

Abstract

Ligand Effects on (De)hydrogenative Catalysis using the $^R\text{PN}^R\text{P}$ Pincer Scaffold

Julia B. Curley

2021

This thesis summarizes synthetic, catalytic, and mechanistic work towards improved understanding of steric and electronic ligand effects in systems supported by the frequently used $^R\text{PN}^R\text{P}$ ($^R\text{PN}^R\text{P} = \text{R}'\text{N}(\text{CH}_2\text{CH}_2\text{PR}_2)_2$) pincer ligand. Chapter 1 provides an overview of previous work on the synthetic and catalytic effects of varying the substituents of the $^R\text{PN}^R\text{P}$ ligand or other ancillary ligands. Chapter 2 describes the synthesis and catalytic activity of a series of novel $^{\text{iPr}}\text{PN}^{\text{Me}}\text{P}$ iron isonitrile complexes to investigate the role of the π -acid ligand. In chapter 3, an active and productive additive-free formic acid dehydrogenation system is developed and optimized using an iron $^{\text{iPr}}\text{PN}^{\text{Me}}\text{P}$ catalyst. Chapter 4 discusses the synthesis of a new N-phenyl ligand $^{\text{iPr}}\text{PN}^{\text{Ph}}\text{P}$ and its coordination to ruthenium, followed by a detailed catalytic and mechanistic comparison between $^{\text{iPr}}\text{PN}^{\text{R}'}\text{P}$ ruthenium complexes which differ only in their N-substitution. In chapter 5, the synthesis and characterization of a series of base metal $^{\text{iPr}}\text{PN}^{\text{Ph}}\text{P}$ complexes is described.

Ligand Effects on (De)hydrogenative Catalysis using the $^R\text{PN}^R\text{P}$ Pincer Scaffold

A Dissertation

Presented to the Faculty of the Graduate School of

Yale University

In Candidacy for the Degree of

Doctor of Philosophy

By

Julia B. Curley

Dissertation Director: Nilay Hazari

December, 2021

© by Julia B. Curley

All rights reserved.

Acknowledgements

I would first like to thank my family for their continued support over my entire life. I know I am moving farther away from home than I've ever been before, but just know I'll always only be a phone call away. To my mom, the original Dr. Curley, thank you for instilling in me a love of science, reading, learning, and chocolate. To my dad, thank you for always reading every single one of my papers and commenting on the figures even though you don't understand a single word. To Matt-Matt, thanks for always remembering to call and for putting up with me as I become even more of a know-it-all, and for finding such an amazing partner to bring into the family. Brittney, thanks for adding to the badass female Curley PhDs.

Thank you to my committee members Bob Crabtree, Pat Holland, and Nilay Hazari for their support and guidance throughout my PhD. In particular, thank you to my advisor Nilay. My five years in the Nilab have been some of the most difficult but fulfilling years in my life, and I thank you for making me a better scientist, writer, and person. To my honorary co-advisor Wes, thank you for all of your incredibly helpful advice over the years, both science-related and not. You've set the gold standard for collaborators and mentors.

Thank you to all Hazari lab members over my time in the lab. Andrew, I will forever observe tie-dye Tuesday in your honor. Megan, thank you for astounding me every day with the quality of both your science and your sass. Jessica, much love from your little croissant. Amira, thank you for always being there to listen if I needed to blow off steam, and for being a great labmate. Nick, thank you for being my mentor, and even more importantly thank you for being my friend. Grad school would have been a much sadder time without your constant influx of memes, cute dogs, and sarcasm. Can't wait for you to

visit. Dav, hey, it's Julia (from the Hazari lab). Thank you for always making sure our interactions are totally normal and not at all awkward. In all seriousness, I'm so glad you were there in my bay to appreciate my niche references and help me calm down and be rational when I was upset, even (especially) when I didn't want to. Matt, thank you for being the absolute worst hood neighbor in history. Our pranks were some of the highlights of my grad school experience (Make Matt's Bench Great Again!), and there's no one I'd rather have gone through all of grad school with. Emily, never let anyone dull your sparkle. You're doing great and you're a badass. Tanya, thanks for continuing to carry the torch for team PNP. Tony, Ligand Boy, the Man with Eight Toes- don't think me leaving means I will ever stop thinking of puns for the pentane Strauss. Also thanks for being the most helpful non-member of the social committee. John, thanks for being such a great addition to the group. I wish you all the best in your grad school experience.

Thank you to everyone that I collaborated with. Thank you to Milad Yirali, Serrae Reed, and Yiren Zhong. You really did your best to teach me materials science, and I appreciate that more than you know. Thank you to Clayton Hert for tirelessly taking care of my complexes and sitting through hours of discussion over how they could have died. Sorry about that time you had to clean out your entire glovebox for me.

Thank you to everyone that holds the Yale chemistry department together. Eric, thank you for keeping the NMRs running and for always being excited to explain something I didn't understand. Brandon, thank you so much for your countless hours of teaching me crystallography, and for your contagious enthusiasm for what you do. It's been amazing working with you; please keep in touch. Fabian, thank you for always going out of your way to help me with mass spec when I need it, and for being a friendly face every

time I saw you in KCL. Daryl and Preston, I will never meet a glassblower that holds a candle to either your skills or your kindness. Thank you for everything you do. Thank you to all members of the front office and stockroom, and especially Brian for being one of the most helpful people in the department. Huge thank you to Ed for being incredibly kind and always willing to take the time to help me out.

Thank you to the best cohort that a girl could ask for- you are all amazing, and I am a better person for knowing each and every one of you. Thank you also to everyone on the second floor of KCL. I've never met a group of such kind, selfless people willing to sacrifice their time to teach me something new or find what I need.

Thank you to some of the best roommates I could have imagined. Noreen, thank you for keeping me young and always putting a smile on my face with your amazingly positive outlook. Kevin- movie night soon? Thank you for being one of my best friends, and for the countless hours of discussions about everything from who the hottest LOTR character is (Aragorn, obviously) to what we want out of life. I couldn't have done grad school without you, Kev.

Thank you to my girls, Lizzy, Danielle, and Maddie. You are all powerful, intelligent, kind, and beautiful souls who inspire me to be a better version of myself. Virtual girls' night ASAP please. Thank you to Sam and Betsy for always supporting me from afar, and for being some of my oldest friends to still put up with me. Alex, thank you for always sending memes.

Thank you to Jack- you got me, always. I love you.

This is for Liam.

Table of Contents

Chapter 1: Understanding Ligand Effects Using the $^R\text{PN}^R\text{P}$ Scaffold.....1

I.	Introduction.....	1
II.	Effects of Altering the $^R\text{PN}^R\text{P}$ Ligand.....	4
	a. Changing the Phosphine Side Arms.....	4
	b. Changing the Nitrogen Substitution.....	12
III.	Effects of Altering the π -Acid Ligand in $^R\text{PN}^H\text{P}$ Complexes.....	19
	a. Isonitrile Ligands.....	19
	b. N-Heterocyclic Carbene Ligands.....	23
IV.	Conclusions and Future Directions.....	25
V.	References.....	25

Chapter 2: Catalytic Formic Acid Dehydrogenation and CO_2 Hydrogenation Using Iron PN^RP Pincer Complexes with Isonitrile Ligands.....37

I.	Introduction.....	37
II.	Results and Discussion.....	40
	a. Synthesis and Characterization of $\text{PN}^{\text{Me}}\text{P}$ Iron Isonitrile Precatalysts.....	40
	b. Catalytic CO_2 Hydrogenation.....	44
	c. Formic Acid Dehydrogenation.....	45
III.	Conclusions.....	48
IV.	References.....	49

Chapter 3: Additive-Free Formic Acid Dehydrogenation Using a Pincer-Supported Iron Catalyst.....57

I.	Introduction.....	57
II.	Results and Discussion.....	59
	a. Optimization of Catalytic Conditions.....	59
	b. Mechanistic Studies.....	63
III.	Conclusions.....	67
IV.	References.....	67

Chapter 4: Control of Catalyst Speciation Using an N-Phenyl Substituted MACHO-Type Ligand in CO₂ Hydrogenation and Formic Acid Dehydrogenation.....73

I.	Introduction.....	73
II.	Results and Discussion.....	76
	a. Synthesis of ⁱ PrPN ^{Ph} P Ligand and Associated Ru Complexes.....	76
	b. Formic Acid Dehydrogenation.....	82
	c. CO ₂ Hydrogenation to Formate.....	88
III.	Conclusions.....	95
IV.	References.....	96

Chapter 5: Iron, Cobalt, and Nickel Complexes Supported by a ⁱPrPN^{Ph}P Pincer Ligand.....109

I.	Introduction.....	109
II.	Results and Discussion.....	112

a.	Synthesis of Iron $iPrPN^{Ph}P$ Complexes.....	112
b.	Synthesis of a Cobalt $iPrPN^{Ph}P$ Complex.....	119
c.	Synthesis of Nickel $iPrPN^{Ph}P$ Complexes.....	121
d.	Formic Acid Dehydrogenation.....	124
III.	Conclusions.....	125
IV.	References.....	126
 Appendix A: Supporting Information for Chapter 2.....		137
Appendix B: Supporting Information for Chapter 3.....		161
Appendix C: Supporting Information for Chapter 4.....		203
Appendix D: Supporting Information for Chapter 5.....		249

List of Figures, Schemes, and Tables

Figure 1.01. Steric and electronic control in common pincer ligands.....	1
Figure 1.02. a.) Modularity of the $^R\text{PN}^{R'}\text{P}$ ligand, and b) examples of reversible (de)hydrogenation reactions catalyzed by $^R\text{PN}^{R'}\text{P}$ complexes.....	2
Figure 1.03. H_2 activation/elimination via MLC using $^R\text{PN}^{\text{HP}}$	3
Table 1.01. Comparison of catalytic ester hydrogenation using 1 , 2 , 3 , and 4	5
Figure 1.04. Transfer of H_2 via MLC from Mn catalysts to methyl benzoate.....	5
Table 1.02. Comparison of catalytic ester hydrogenation using 5 , 6 , and 7	6
Figure 1.05. Iron $^R\text{PN}^{\text{HP}}$ complexes investigated by the Langer group.....	7
Scheme 1.01. a) Previously developed synthetic route used to isolate 5 and 6 , and b) one-pot synthetic procedure used to isolate 7 and generate 8 and 9 <i>in situ</i>	8
Figure 1.06. Proposed product of H_2 elimination from 7 and 8	8
Table 1.03. Selective semihydrogenation of alkynes using 10 and 11	9
Scheme 1.02. Pathway for amine-assisted CO_2 hydrogenation to methanol.....	10
Table 1.04. Comparison of catalytic amine-assisted CO_2 hydrogenation to methanol using 12 , 13 , 14 , and 15	10
Table 1.05. Comparison of catalytic formamide reduction to methanol using 12 , 13 , 14 , and 15	11
Figure 1.07. Catalyst resting state in CO_2 hydrogenation to methanol.....	12
Table 1.06. Comparison of catalytic CO_2 hydrogenation to formate using 16 , 6 , and 17	13
Scheme 1.03. Role of the Lewis acid in formate dissociation from $^{\text{iPr}}\text{PN}^{\text{HP}}$ and $^{\text{iPr}}\text{PN}^{\text{MeP}}$ iron complexes.....	14
Table 1.07. Catalyst screen for CO_2 hydrogenation to formate using 18 and 19	15

Scheme 1.04. Pathway for methanol dehydrogenation.....	15
Scheme 1.05. Rates of methanol dehydrogenation using ruthenium $iPrPN^R P$ complexes.	16
Scheme 1.06. Mechanism of methanol dehydrogenation involving MLC using 12	16
Scheme 1.07. Formic acid dehydrogenation using 12 and 20 under standard conditions compared to using a 1 M phosphoric acid buffer.	17
Table 1.08 $RPN^R P$ ruthenium complexes investigated in the direct amination of alcohols with ammonia.....	18
Scheme 1.08. Synthetic route for the preparation of $iPrPN^H P$ iron isonitrile complexes 26-28	20
Figure 1.08. Bis(isonitrile) byproducts.....	20
Table 1.09. CO ₂ hydrogenation to formate using 28a , 28b and 16	21
Table 1.10. Catalyst screen for neat butanol dehydrogenation using 29a-c and 30	22
Table 1.11. Catalytic comparison for methyl benzoate hydrogenation using 31 with donor ligands and 33	24
Figure 2.01. a) Formic acid dehydrogenation, b) CO ₂ hydrogenation to formate, c) Previous PNP iron catalysts studied by our groups, and d) Complexes studied in this work.....	38
Scheme 2.01. Synthesis of $PN^{Me}P$ iron isonitrile complexes 2a-2c	40
Scheme 2.02. Synthesis of cationic bis(isonitrile) iron species 3a-3c , which were characterized <i>in situ</i>	41
Figure 2.02. Solid-state structures of 2a (top left), 2b (top right), and 2c (bottom) with ellipsoids drawn at 30% probability. Hydrogen atoms besides those attached to iron and boron have been omitted for clarity. All hydrides were located in the difference	

map and freely refined. Only one molecule from the asymmetric unit of 2c shown.....	43
Table 2.01. Selected bond distances (Å) and angles (°) for the (ⁱ PrPN ^{Me} P)Fe isonitrile complexes 2a-2c , as well as the carbonyl complex A	44
Table 2.02. Comparison of iron catalysts for CO ₂ hydrogenation to formate.....	45
Table 2.03. Comparison of iron catalysts for formic acid dehydrogenation.....	46
Figure 3.01. a) Previously reported iron systems for additive-free formic acid dehydrogenation and b) catalysts used in this work.....	58
Table 3.01. Performance of 2 in additive-free FADH in different solvents.....	60
Table 3.02. FADH catalyzed by 2 in using different ratios of toluene: ^t BuOH.....	61
Figure 3.02. Kinetic traces comparing the rates of additive-free FADH using 1 and 2 ; error bars ± 10%.....	62
Table 3.03. Performance of 2 for additive-free FADH at different catalyst loadings.....	63
Scheme 3.01. Proposed mechanism for additive-free FADH using 2	64
Scheme 3.02. Crossover experiments performed to probe the thermodynamic relationship between 3 and 1 ; a) reaction between 3 and 6 and b) reaction between 1 and 2	65
Figure 4.01. a) Previous investigations of ^R PN ^H P and ^R PN ^{Me} P ligated complexes, and b) Ru ⁱ PrPN ^{Ph} P, ⁱ PrPN ^H P, and ⁱ PrPN ^{Me} P complexes compared in this work.....	74
Scheme 4.01. Synthesis of a) ⁱ PrPN ^{Ph} P, and b) (ⁱ PrPN ^{Ph} P)RuHCl(CO) (1) and (ⁱ PrPN ^{Ph} P)Ru(H) ₂ (CO) (2).....	77
Figure 4.02. Solid state structures of a) 1 and b) 2 , with thermal ellipsoids at 30% probability level. There are four molecules in the asymmetric unit of 2 ; only one is	

shown. Hydrogens not bound to Ru omitted for clarity. The hydrides of 2 were located in the difference map and freely refined.....	79
Figure 4.03. a) Reaction of 2 with one atmosphere of CO ₂ and b) solid state structure of (iPrPN ^{Ph} P)RuH(CO){OC(O)H} (3) with thermal ellipsoids at 30% probability. Hydrogens not bound to Ru or the formate ligand omitted for clarity. The hydride of 3 was located in the difference map and freely refined.....	81
Table 4.01. Formic acid dehydrogenation using 2 , 2-Me , and 2-H	83
Scheme 4.02. Proposed mechanism for formic acid dehydrogenation using 2 , 2-H , and 2-Me . For simplicity, only the <i>anti</i> orientation is shown. 2-H operates exclusively in this orientation, 2-Me likely proceeds through both isomers, and 2 operates only in the <i>syn</i> orientation.....	85
Figure 4.04. a) Mechanism of decarboxylation studied computationally for 3 , 3-H , and 3-Me , b) thermodynamics, and c) kinetics of decarboxylation, as determined by DFT. Non rate-determining transition states are faded. CPCM solvation (THF), 298 K, 1 atm CO ₂ , M06 functional, 6-31+G**/LANL2DZ (on Ru) basis sets. <i>Syn/anti</i> refer to the relative orientation between the hydride ligand and N-R moiety; only a schematic of a generic <i>anti</i> isomer is included for simplicity.....	86
Table 4.02. CO ₂ hydrogenation to formate using 2 , 2-H , and 2-Me	89
Scheme 4.03. Investigating an autocatalytic effect in CO ₂ hydrogenation to formate using 2-Me	90
Table 4.03. CO ₂ hydrogenation to formate with a Lewis acid cocatalyst using 2 , 2-H , and 2-Me	91

Scheme 4.04. Proposed mechanism for CO ₂ hydrogenation to formate using 2 , 2-H , and 2-Me . For simplicity, only the <i>anti</i> orientation is shown. 2-H operates exclusively in this orientation, 2-Me likely proceeds through both isomers, and 2 operates only in the <i>syn</i> orientation.....	92
Figure 4.05. Thermodynamics of formate loss as determined by DFT. CPCM solvation (THF), 298 K, M06 functional, 6-31+G**/LANL2DZ (on Ru) basis sets. <i>Syn/anti</i> refer to the relative orientation between the hydride ligand and N-R moiety; only a schematic of a generic <i>anti</i> isomer is included for simplicity.....	93
Figure 4.06. Impact of an intermolecular hydrogen bond between 3-H and a formate molecule on calculated thermodynamics of formate loss. CPCM solvation (THF), 298 K, M06 functional, 6-31+G**/LANL2DZ (on Ru) basis sets. <i>Syn/anti</i> refer to the relative orientation between the hydride ligand and N-R moiety; only a schematic of a generic <i>anti</i> isomer is included for simplicity.....	94
Figure 5.01. a) Previous investigations of ^R PN ^{R'} P complexes; b) Recently published Ru ⁱ PrPN ^{Ph} P complexes; c) Some of the novel ⁱ PrPN ^{Ph} P supported Fe, Co, and Ni complexes synthesized and characterized in this work.....	110
Scheme 5.01. a) Synthesis of (κ ² - ⁱ PrPN ^{Ph} P)FeCl ₂ (1) and b) (ⁱ PrPN ^{Ph} P)FeH(κ ² -BH ₄) (2).112	112
Figure 5.02. Solid-state structures of a) 1 and b) 2 with ellipsoids at 30% probability. Hydrogen atoms not bound to Fe or B omitted for clarity. All hydrides were located in the difference map and freely refined.....	113
Figure 5.03. ⁵⁷ Fe Mössbauer (80 K) of solid powders of a) 1 and b) 2	114

Scheme 5.02. a) Attempted synthesis of $(i\text{PrPN}^{\text{Ph}}\text{P})\text{FeH}(\text{CO})(\text{HBH}_3)$ and isolation of decomposition product $\text{L}\cdot(\text{BH}_3)_2$; b) Attempted synthesis of $(i\text{PrPN}^{\text{Ph}}\text{P})\text{Fe}(\text{H})_2(\text{CO})$ and isolation of $(i\text{PrPN}^{\text{Ph}}\text{P})\text{Fe}(\text{CO})_2$ (3).....	116
Figure 5.04. Solid state structures of decomposition products a) $\text{L}\cdot(\text{BH}_3)_2$ and b) 3 with ellipsoids at 30% probability. Hydrogen atoms not bound to B omitted for clarity. Two molecules of 3 are present in the asymmetric unit; one representative molecule is shown.....	117
Scheme 5.03. Synthesis of $(\kappa^2\text{-}i\text{PrPN}^{\text{Ph}}\text{P})\text{CoCl}_2$ (4).....	119
Figure 5.05. Solid state structure of 4 with ellipsoids at 30% probability. Hydrogen atoms omitted for clarity.....	120
Scheme 5.04. Synthesis of Ni complexes in the a) absence and b) presence of PF_6^-	121
Figure 5.06. Solid state structure of 5 with ellipsoids at 30% probability. Hydrogen atoms and cocrystallized solvent omitted for clarity.....	122
Scheme 5.05. Attempted synthesis of Ni hydride complex $[(i\text{PrPN}^{\text{Ph}}\text{P})\text{NiH}][\text{PF}_6]$ from 5	123
Table 5.01. Formic acid dehydrogenation using 2 and 2-Me	124

Chapter 1: Understanding Ligand Effects Using the $^R\text{PN}^R\text{P}$ Scaffold

I. Introduction

Pincer ligands, traditionally defined as tridentate ligands with a central X-type ligand and two flanking amino- or phosphino- side arms, were first introduced by Moulton and Shaw in 1976 and are now utilized to support a wide variety of transition metal catalysts.¹ This class of ligand occupies three adjacent binding sites around a metal complex, and typically coordinates in a *meridional* geometry. Complexes supported by pincer ligands are particularly advantageous in catalysis due to their high thermal stability and the modular design of the ligand, which enables the steric and electronic properties of pincer-supported catalysts to be readily tuned (Figure 1.01).²

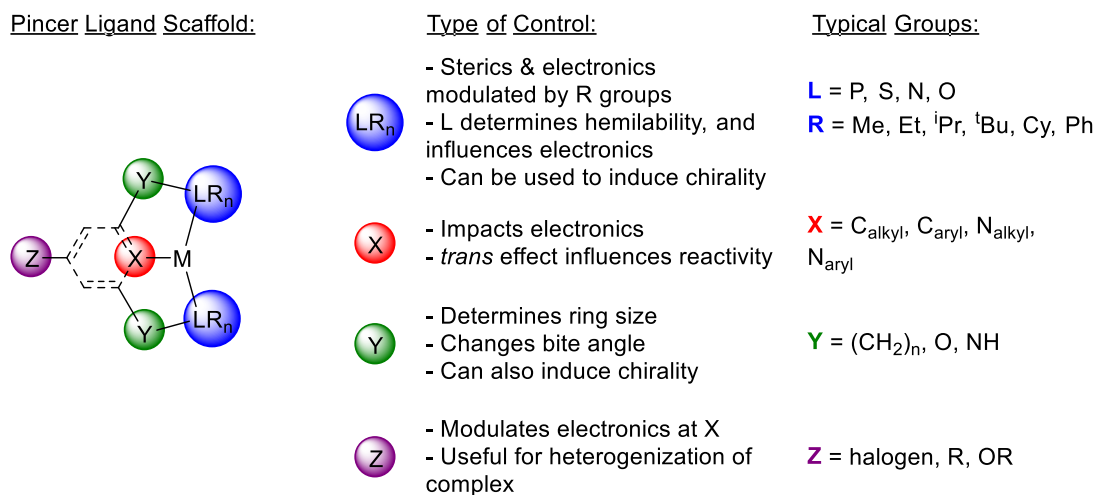


Figure 1.01. Steric and electronic control in common pincer ligands.

Since their introduction, the definition of pincer ligands has expanded to include a wide variety of binding and linking groups that can be systematically altered to control the reactivity of a complex. For example, the central donor (X in Figure 1.01) can be either neutral (L-type) or anionic (X- or X₂-type).³ This has a significant impact on the electronics at the metal center as well as the reactivity at the *trans* coordination site.⁴ If X is aromatic,

a substituent in the *para* position of the ring (Z) can be used to modulate the electronics at X or tether the complex to a surface while having little to no effect on the sterics at the metal center.⁵ The linker arms (Y) can be changed to increase or decrease the pincer bite angle and correspondingly alter the steric properties of the complex. If the central donor X or an adjacent site can be directly involved in bond activation processes with the metal, the pincer ligand may be able to participate in mechanisms that involve metal ligand cooperation (MLC).⁶ Reactions using MLC involve participation by the metal and the ligand in a bond cleavage or bond forming step during which both the ligand and metal are modified, including a change in coordination mode of the participating ligand (*vide infra*). Finally, the choice of side arms (LR_n) has profound effects on pincer complexes: the flanking donors can change the hemilability of the pincer as well as the electronics at the metal, and the substituents on the donors strongly influence the sterics of the primary coordination sphere.

One family of pincer ligands that has been the subject of particular interest is ligands of the type ^RPN^HP (^RPN^HP = HN(CH₂CH₂PR₂)₂, R = Et, ⁱPr, Cy, ^tBu, Ph) (Figure 1.02a). This is because transition metal complexes supported by ^RPN^HP are highly active catalysts for a wide variety of reactions, particularly hydrogenation and dehydrogenation reactions relevant to renewable energy storage^{7,8,9,10,11} and the synthesis of fine and

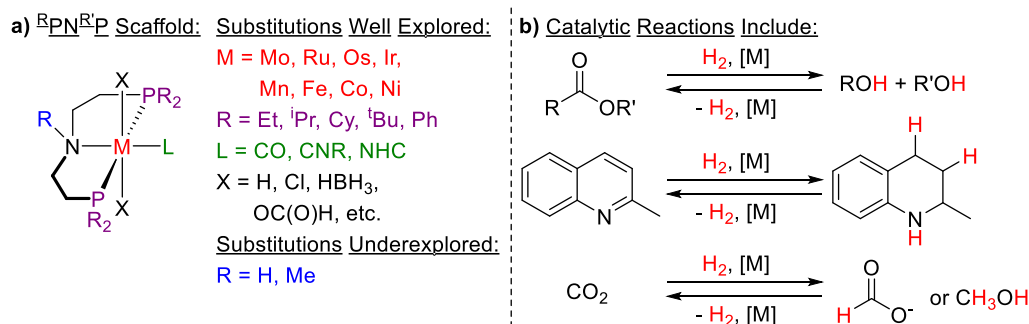


Figure 1.02. a.) Modularity of the ^RPN^RP ligand, and **b.)** examples of reversible (de)hydrogenation reactions catalyzed by ^RPN^RP complexes.

commodity chemicals (Figure 1.02b).^{12,13,14,15,16} These reactions include the hydrogenation of esters, ketones, nitriles, amides, *N*-heterocycles, olefins, and CO₂, the dehydrogenation of formic acid, alcohols, *N*-heterocycles, and ammonia-borane, and the dehydrogenative synthesis of lactones, lactams, amides, ureas, and carbamates. In fact, the complex (^{Ph}PN^HP)RuHCl(CO), known as Ru-MACHO, is used in commercial ester hydrogenation.^{13c}

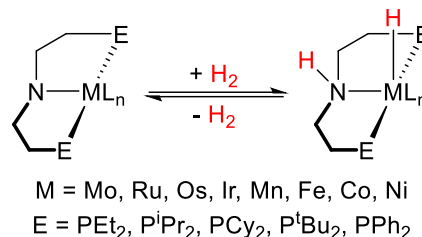


Figure 1.03. H₂ activation/elimination via MLC using ^RPN^HP.

Importantly, it is proposed that many hydrogenation and dehydrogenation reactions catalyzed by ^RPN^HP supported complexes require MLC via the 1,2-addition or elimination of H₂ (Figure 1.03), and this is a key feature of these ligands.

Understanding effects of varying the substituents of the ^RPN^{R'}P scaffold is critical to designing and synthesizing improved catalysts supported by this class of ligand. To date, there are numerous studies on the effects of varying the substituents on the phosphine donors of catalysts ligated by ^RPN^HP.^{7d, 8a, c, e, f, 10b, 11a, 13b, d, 14d, e, 15c-e, 15g, 16a} However, there are comparatively few studies of the synthetic and catalytic effects of changing the substituent on the central nitrogen donor, and most of these focus only on whether or not the catalytic reaction of interest requires a ligand capable of MLC.⁶ For this reason, the N-H substituent in ^RPN^HP has almost always been replaced by a simple methyl group to obtain tertiary amine pincer ligands of the type ^RPN^{Me}P (^RPN^{Me}P = CH₃N(CH₂CH₂PR₂)₂, R = Et, ⁱPr, Cy, ^tBu, Ph).^{8d, g, 9e, g, 10a, c, 13d, g, 14b, c, i, 15e, 16b} Although this minor change to the ligand often results in large impacts on the synthesis and reactivity of ^RPN^{Me}P complexes, few examples of ^RPN^{R'}P ligands exist where R' is not H or Me.¹⁷ Additionally, the most active ^RPN^{R'}P-supported catalysts almost universally contain the π -acidic ligand carbon

monoxide. As a result, there have recently been several reports studying the impact of replacing CO with other π -acidic ligands, such as isonitriles, or even N-heterocyclic carbene (NHC) ligands.¹⁸

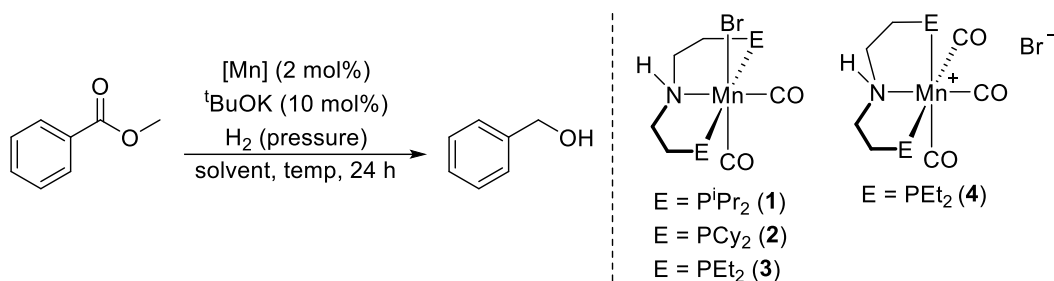
In this chapter, we systematically summarize ligand effects in transition metal catalysts ligated by $^R\text{PN}^R\text{P}$. We begin with changes to the $^R\text{PN}^R\text{P}$ ligand itself, first summarizing studies related to altering the phosphine side arms, followed by discussions of the impact of changing the substituent on the nitrogen donor. Finally, we discuss the consequences of replacing the commonly used CO ligand with an isonitrile or NHC ligand. Variations in the other ancillary ligands (X in Figure 1.02a) do not have a significant impact on catalysis^{8f, 9e, 13a} and will not be discussed in this chapter.

II. Effects of Altering the $^R\text{PN}^R\text{P}$ Ligand

Changing the Phosphine Side Arms

There are many reports that have varied the phosphine side arms of the $^R\text{PN}^R\text{P}$ ligand to study its effects on catalysis (*vide supra*). Given the large number of studies, the discussion here is not comprehensive but uses some leading examples to illustrate the effect of this substitution.

In 2016, the Beller group reported the first well-defined manganese complexes for the hydrogenation of esters into alcohols (Table 1.01).^{16a} They initially synthesized ($^i\text{PrPN}^H\text{P}$)Mn(CO)₂Br (**1**) and ($^{\text{Cy}}\text{PN}^H\text{P}$)Mn(CO)₂Br (**2**), which differ only in their phosphine side arms. Methyl benzoate was chosen as a model substrate for evaluating catalytic activity (Table 1.01). Surprisingly, **1** and **2** both gave low activity for ester hydrogenation, even though it had previously been demonstrated **1** was active for ketone,



Entry	[Mn]	Pressure (bar)	Solvent	Temp. (°C)	Yield
1	1	30	Toluene	100	6%
2	2	30	Toluene	100	2%
3 ^a	1	80	Toluene	120	38%
4	4	30	Toluene	100	82%
5	4	30	1,4-dioxane	100	93%
6	4	10	1,4-dioxane	100	51%
7	3	30	1,4-dioxane	110	97%

Table 1.01. Comparison of catalytic ester hydrogenation using **1**, **2**, **3**, and **4**. Reaction conditions: methyl benzoate (0.5 mmol), [Mn] (2 mol%), ^tBuOK (10 mol%), solvent (1 mL), 24 h. Yield determined using gas chromatography. ^a3 mol% Mn.

aldehyde, and nitrile hydrogenation, and **2** was active nitrile hydrogenation.¹⁹ Specifically, **1** gave only 6% yield at 2 mol% loading and 30 bar H₂ (Table 1.01, Entry 1), while **2** gave 2% yield under the same conditions (Entry 2). Increasing the pressure, temperature, and catalyst loading of **1** still led to only a 38% yield of benzyl alcohol (Entry 3).

The Beller group hypothesized that they could develop an improved catalyst by synthesizing the less sterically hindered diethyl phosphine complex (EtPN^HP)Mn(CO)₂Br (**3**) (Table 1.01). Interestingly, the synthesis of **3** resulted in a mixture of the desired product and [(EtPN^HP)Mn(CO)₃][Br] (**4**), where the EtPN^HP ligand adopts an unusual *facial* geometry. However, **3** and **4** could be isolated independently to evaluate as ester hydrogenation catalysts. Under the same conditions used with **1** and **2**, **4** gives an 82% yield (Table 1.01, Entry 4).

Changing the solvent from toluene to 1,4-dioxane results in a 93% yield (Entry 5), and a 51% yield of benzyl

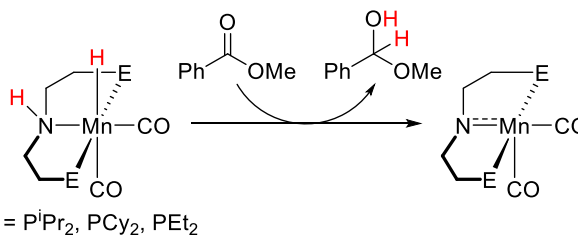
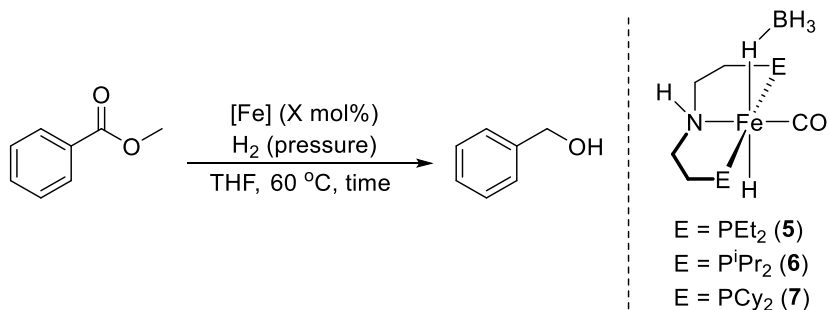


Figure 1.04. Transfer of H₂ via MLC from Mn catalysts to methyl benzoate.

alcohol is observed when the pressure is reduced to only 10 bar H₂ (Entry 6). The related complex **3** gives similar results to **4** under 30 bar H₂, resulting in a yield of 97% (Entry 7). It was proposed that the clear preference for catalysts with small phosphine side arms in this reaction is due to steric effects during the transfer of a hydride from manganese and a proton from the nitrogen ligand to the substrate (Figure 1.04).

Previous results from the Beller group had demonstrated that ⁱPrPN^HP-ligated iron catalysts could effectively hydrogenate a range of esters and lactones without any additives.^{14b} However, the importance of sterics in the manganese-catalyzed system (*vide supra*) inspired the group to investigate iron catalysts with differing sterics at the phosphine side arms, specifically (^RPN^HP)FeH(CO)(HBH₃) (R = Et (**5**), ⁱPr (**6**), or Cy (**7**)) (Table 1.02).^{14d} As expected from the results with manganese, ^{Et}PN^HP ligated **5** was the most active catalyst for the hydrogenation of methyl benzoate, reaching 99% yield at 1 mol% loading after 6 hours at 30 bar H₂ (Table 1.02, entry 1). Under the same conditions, the more sterically bulky complexes **6** and **7** achieved modest yields of 50% and 30%, respectively (Entries 2 & 3). Compound **5** is still capable of achieving an 86% yield of



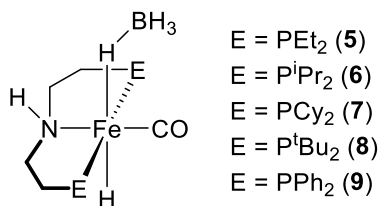
Entry	[Fe]	X mol%	Pressure (bar)	Time (h)	Yield
1	5	1	30	6	99%
2	6	1	30	6	50%
3	7	1	30	6	30%
4	5	0.5	30	16	86%
5	5	1	10	6	82%
6	5	1	2	6	58%

Table 1.02. Comparison of catalytic ester hydrogenation using **5**, **6**, and **7**. Reaction conditions: methyl benzoate (0.5 mmol), [Fe] (1 or 0.5 mol%), THF (1 mL), 60 °C). Yield determined using gas chromatography.

benzyl alcohol at 0.5 mol% loading (Entry 4), and generates the product in 82% and 58% yield at the low pressures of 10 and 2 bar H₂, respectively (Entries 5 & 6).

Time course experiments on the hydrogenation of methyl benzoate using **5**, **6**, and **7** confirmed that **5** is the most active catalyst as well as the most productive. **5** reaches 90% conversion of ester to alcohol within 4 hours, while in the same time **6** and **7** reach only 20% and 18% yield, respectively. This trend is proposed to be a direct result of phosphine group sterics: the smaller phosphine side arms provide less steric hindrance to the substrate molecule as it receives a proton and a hydride from the catalyst (as shown in Figure 1.04 with manganese). The improved ester hydrogenation results achieved in this report are a direct consequence of understanding the effect of phosphine side arm sterics on catalytic activity.

The Langer group performed an extensive study on how phosphine group sterics and electronics affect the synthesis and decomposition of a family of iron ^RPN^HP complexes.^{14e} Initially, they tried to isolate a library of directly comparable complexes of

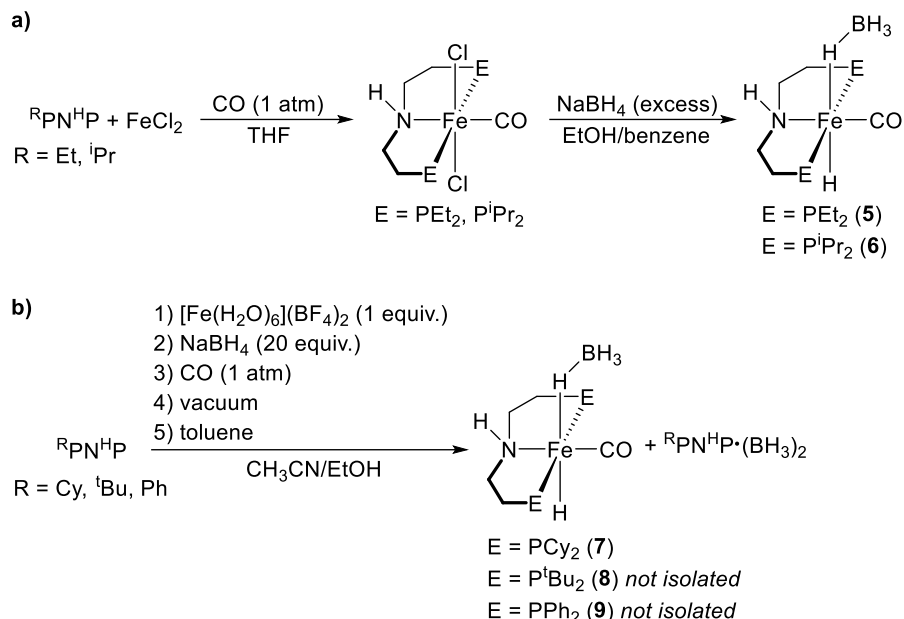


E = PEt₂ (**5**)
 E = PⁱPr₂ (**6**)
 E = PCy₂ (**7**)
 E = P^tBu₂ (**8**)
 E = PPh₂ (**9**)

Figure 1.05. Iron ^RPN^HP complexes investigated by the Langer group.

the type (^RPN^HP)FeH(CO)(HBH₃) (R = Et (**5**), ⁱPr (**6**), Cy (**7**), ^tBu (**8**), or Ph (**9**)) with different phosphine side arms, (Figure 1.05). However,

isolation of **7**, **8**, and **9** was not possible using existing synthetic procedures which proceed via a (^RPN^HP)FeCl₂(CO) (R = Et, ⁱPr) intermediate (Scheme 1.01a),^{9a} and the Langer group therefore utilized a related synthetic pathway to isolate these species (Scheme 1.01b).²⁰ This alternate one-pot synthesis involves the addition of [Fe(H₂O)₆][(BF₄)₂] to ^RPN^HP (R = Cy, ^tBu, Ph) in acetonitrile, followed by reaction with excess NaBH₄, addition of 1 atmosphere CO, and drying *in*



Scheme 1.01. **a)** Previously developed synthetic route used to isolate **5** and **6**, and **b)** one-pot synthetic procedure used to isolate **7** and generate **8** and **9** *in situ*.

vacuo to provide the desired complexes **7-9**. Using this route, **7** was isolated in 31% yield, and **8** and **9** were observed *in situ* by NMR spectroscopy but could not be isolated. ¹H and ¹¹B NMR chemical shifts indicate that BH₃ is bound less tightly in the more sterically bulky (R = Cy, ^tBu) and less electron donating (R = Ph) complexes. In agreement with this observation, **7**, **8**, and **9** all exhibit limited solution stability. **7** and **8** are proposed to lose H₂ via protonation of the coordinated BH₄ by the pincer N-H proton, elimination of H₂, and subsequent B–N bond formation to form an unusual cyclometallated BH₃ complex (Figure 1.06). This species decomposes further to generate unidentified iron-containing products and various RPN^HP-borane adducts. **9** decomposes via loss of BH₃ to transiently form (PhPN^HP)Fe(H)₂(CO), which then loses H₂ to generate PhPN^HP and unidentified products. It is thus proposed that ligands based on less sterically hindered phosphines will generate more active catalysts because the key dihydride

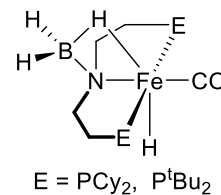


Figure 1.06. Proposed product of H₂ elimination from **7** and **8**.

intermediate is more stable, which is in agreement with catalytic results obtained by the Beller group (*vide supra*).

The groups of Liu and Luo took advantage of the impact of phosphine sterics to generate cobalt RPN^HP ($R = ^iPr, ^tBu$) complexes that selectively catalyze the semihydrogenation of alkynes to provide either the *Z*- or *E*-alkene using ammonia borane as the H_2 source (Table 1.03).^{15e} Base metal catalysts typically selectively generate *Z*-alkenes in semihydrogenation reactions due to *cis*-hydrometallation of the $C\equiv C$ bond. However, *E*-alkenes can be subsequently generated through alkene isomerization via a proposed insertion/ β -H elimination mechanism.²¹ The Liu and Luo groups hypothesized that the alkene insertion step requires a less sterically hindered metal center, and therefore generation of the *E*-alkene could be promoted by a less bulky ligand and prevented by a bulkier ligand.

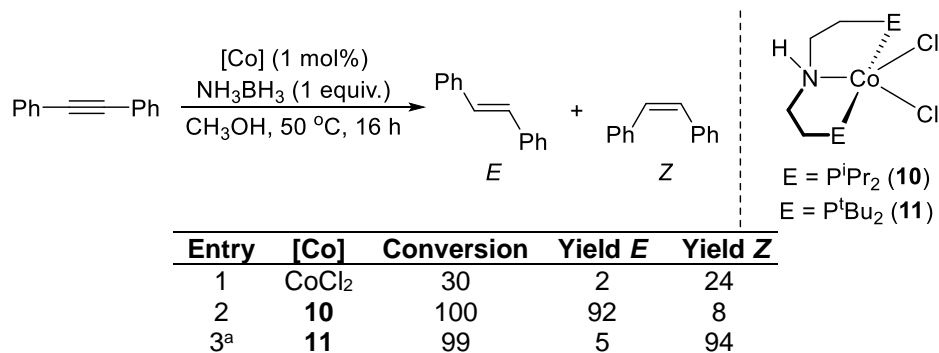
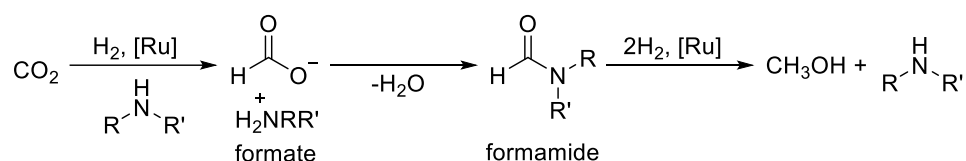


Table 1.03. Selective semihydrogenation of alkynes using **10** and **11**. Reaction conditions: diphenylethyne (0.5 mmol), NH_3BH_3 (0.5 mmol), [Co] (1 mol%), CH_3OH (2 mL), 50 °C, 16 h. Yield determined by gas chromatography. ^a0.6 mmol NH_3BH_3 used.

To investigate this hypothesis, the complexes $(RPN^HP)CoCl_2$ ($R = ^iPr$ (**10**) or tBu (**11**)) were synthesized and tested in transfer hydrogenation of diphenylethyne using ammonia-borane (Table 1.03). Unligated $CoCl_2$ gave only 30% conversion in the reaction, and favored formation of the *Z*-alkene (Entry 1). As anticipated, the less sterically bulky catalyst **10** preferentially formed the *E*-alkene, and provided *trans*-diphenylethylene in

92% yield (Entry 2). Conversely, the more hindered complex **11** generated *cis*-diphenylethylene in 94% yield (Entry 3). This system is another example of how understanding phosphine steric and electronic effects in $^R\text{PN}^H\text{P}$ systems can be used to develop active and selective catalysts.

The effects of varying phosphine side arms have also been studied with ruthenium catalysts. Prakash, Olah, and coworkers initially reported that Ru-MACHO-BH (($^{\text{Ph}}\text{PN}^H\text{P}$)RuH(CO)(HBH₃)) was an active catalyst for amine-assisted hydrogenation of



Scheme 1.02. Pathway for amine-assisted CO₂ hydrogenation to methanol.

CO₂ to methanol, which proceeds via the pathway shown in Scheme 1.02.²² They subsequently published a detailed study on the relationship between phosphine group sterics on the pincer ligand and methanol yield.^{8f} To do so, they synthesized a series of ruthenium complexes which differed only in their phosphine groups: ($^R\text{PN}^H\text{P}$)RuHCl(CO) (R = ⁱPr (**12**), Cy (**13**), ^tBu (**14**), or Ph (**15**)) and assessed the performance of the different catalysts in amine-assisted CO₂ hydrogenation to methanol under the same conditions (Table 1.04). Complexes **12**, **13**, and **14** all gave low yields of methanol, with only 320 and

$\text{CO}_2 + 3\text{H}_2$
75 bar

$\xrightarrow[\text{triglyme, 145 } ^\circ\text{C, 40 h}]{\begin{smallmatrix} [\text{Ru}] (10 \mu\text{mol}) \\ \text{K}_3\text{PO}_4 (1 \text{ mmol}) \\ \text{PEHA} (5.1 \text{ mmol}) \end{smallmatrix}}$

formate + formamide + CH_3OH + H_2O

E = P^iPr_2 (**12**)

E = PCy_2 (**13**)

E = P^tBu_2 (**14**)

E = PPh_2 (**15**)

Entry	[Ru]	TON (formate)	TON (formamide)	TON (CH_3OH)
1	12	110	2,260	320
2	13	100	1,470	50
3	14	160	1,750	0
4	15	160	810	1,040

Table 1.04. Comparison of catalytic amine-assisted CO₂ hydrogenation to methanol using **12**, **13**, **14**, and **15**. PEHA = pentaethylenhexamine. Reaction conditions: 1:3 CO₂:H₂ (75 bar), PEHA (5.1 mmol), [Ru] (10 μmol), K₃PO₄ (1 mmol), triglyme (10 mL), 145 °C, 40 h. Yield determined by ¹H NMR. TON (CH₃OH) = mol CH₃OH formed per mol of [Ru].

50 turnovers achieved by **12** and **13**, respectively (Entries 1 & 2), while ^tBu-substituted **14** did not generate any methanol (Entry 3). ^{Ph}PN^HP ligated **15** was by far the active catalyst for methanol production, giving 1,040 turnovers (Entry 4).

A large amount of formamide was observed in the reactions with **12-14**, indicating that formamide reduction to methanol is the most challenging step for these catalysts (Scheme 1.02, Table 1.04 Entries 1-3). However, when the direct hydrogenation of *N*-formylpiperidine to piperidine and methanol was performed, complexes **12**, **13**, and **15** were all highly proficient catalysts (Table 1.05). **12**, **13**, and **15** reached 1,580, 1,740, and 1,400 turnovers, respectively (Entries 1, 2, & 4). In contrast, **14** is nearly inactive for this reaction and only gives 100 turnovers, presumably due to prohibitive steric clash (Entry 3). Prakash *et al.* therefore proposed that the hydrogenation of CO₂ to methanol using **12** and **13** is inhibited by catalyst decomposition. Mechanistic studies implicated the biscarbonyl complex (^RPN^HP)RuH(CO)₂⁺ (R = ⁱPr, Cy, ^tBu, or Ph) as a catalyst resting state that is inactive for formamide reduction (Figure 1.07). The second CO ligand must dissociate for catalysis to continue past this step, and it was proposed that the lability of the second carbonyl ligand decreases as the electron donating ability of the ^RPN^HP ligand increases due to increased back-bonding into the C-O π* orbital. This hypothesis is supported by the

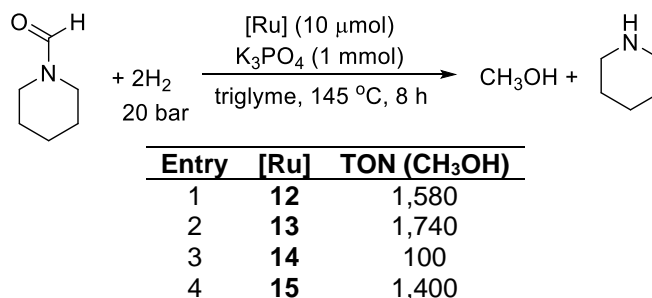
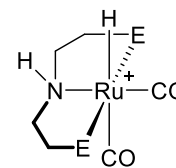


Table 1.05. Comparison of catalytic formamide reduction to methanol using **12**, **13**, **14**, and **15**. Reaction conditions: H₂ (20 bar), *N*-formylpiperidine (20 mmol), [Ru] (10 μmol), K₃PO₄ (1 mmol), triglyme (10 mL), 145 °C, 8 h. Yield determined by ¹H NMR spectroscopy. TON (CH₃OH) = mol CH₃OH formed per mol of [Ru].

IR stretching frequencies of the second CO ligand in each complex, which decrease with increasing electron donation from the phosphine ($\text{Ph} > {}^i\text{Pr} \sim \text{Cy}$), indicating a stronger ruthenium-carbonyl bond. This accounts for the observed differences in catalytic activity; the more electron rich complexes **12** and **13** irreversibly form the decomposition



$\text{E} = \text{P}^i\text{Pr}_2, \text{PCy}_2, \text{P}^t\text{Bu}_2, \text{PPh}_2$

Figure 1.07. Catalyst resting state in CO_2 hydrogenation to methanol.

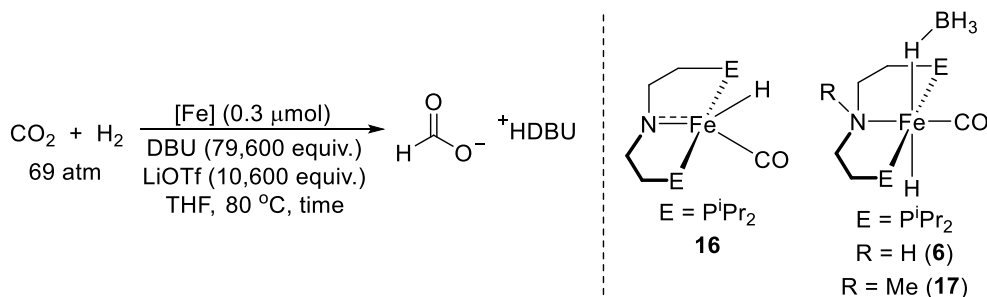
species $({}^R\text{PN}^{\text{H}}\text{P})\text{RuH}(\text{CO})_2^+$ ($\text{R} = {}^i\text{Pr}, \text{Cy}$) and are unable to complete the hydrogenation past formamide because the second CO ligand is not sufficiently labile. Decreased electron donation from the phosphine arms in **15** leads to a weaker Ru–C bond and enables the reversible formation of $({}^{\text{Ph}}\text{PN}^{\text{H}}\text{P})\text{RuH}(\text{CO})_2^+$ via dissociation of CO, and subsequent hydrogenation of formamide to methanol in catalysis. This study, as well as the others described in this section, highlight the subtle interplay of phosphine side arm sterics and electronics on catalytic activity using ${}^R\text{PN}^{\text{H}}\text{P}$ complexes.

Changing the Nitrogen Substitution

Studies investigating the synthetic and catalytic effects of altering the nitrogen substituent on ${}^R\text{PN}^{\text{R}'}\text{P}$ ligands are less common than those exploring changes to the phosphine substituents. Additionally, changes to the nitrogen substituent have been used almost exclusively to determine whether or not a given catalytic reaction requires a ligand capable of MLC (*vide supra*). Thus, they have primarily focused on moving from ${}^R\text{PN}^{\text{H}}\text{P}$ supported complexes, which can participate in MLC, to ${}^R\text{PN}^{\text{Me}}\text{P}$ supported complexes, which are relatively easy to prepare and cannot participate in MLC. Here, we summarize a few key reports that are focused on the catalytic effects of replacing the N–H moiety in

$^R\text{PN}^{\text{H}}\text{P}$ with an N-methyl group. However, we note that there is a void of studies in the literature that explore different substituents on the nitrogen in $^R\text{PN}^{\text{R}'}\text{P}$ -ligated complexes.

In 2015, the Hazari and Bernskoetter groups used $(^{\text{iPr}}\text{PNP})\text{Fe}(\text{H})(\text{CO})$ ($^{\text{iPr}}\text{PNP} = \text{N}(\text{CH}_2\text{CH}_2\text{P}^{\text{iPr}}\text{Pr}_2)_2^-$) (**16**) as a precatalyst for CO_2 hydrogenation to formate (Table 1.06).^{9c} This complex is known to activate H_2 via MLC by 1,2-addition across its Fe–N bond to generate $(^{\text{iPr}}\text{PN}^{\text{H}}\text{P})\text{Fe}(\text{H})_2(\text{CO})$, which is proposed to be on the catalytic cycle.^{9c} Under the optimized conditions, **16** reaches 6,030 turnovers in 24 hours, which corresponds to only an 8% yield of formate (Table 1.06, Entry 1). Subsequently, to investigate the importance of MLC in this reaction, the complexes **6** and $(^{\text{iPr}}\text{PN}^{\text{Me}}\text{P})\text{FeH}(\text{CO})(\text{HBH}_3)$ (**17**) were synthesized, which differ only in their N-substitution. $^{\text{iPr}}\text{PN}^{\text{H}}\text{P}$ complex **6** gives only 1,500 turnovers after 24 hours (Entry 2), displaying even lower activity than **16**. However, tertiary amine-based **17**, which is not capable of MLC, reaches 42,350 turnovers under the same conditions (Entry 3). This corresponds to a 53% yield, and under slightly modified conditions this catalyst gives up to 58,990 turnovers for CO_2 hydrogenation to formate. At the time of the report, this was the highest TON achieved by any base metal catalyst for CO_2 hydrogenation to formate.



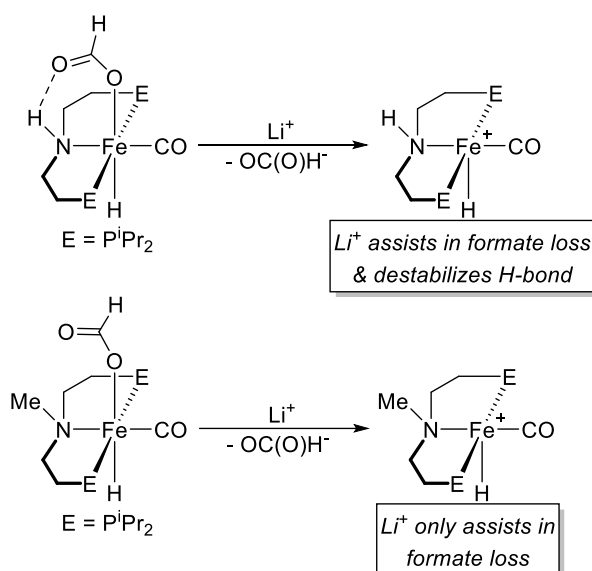
Entry	[Fe]	TON (1 h)	TON (24 h)	Yield ^a
1	16	1,290	6,030	8%
2	6	680	1,500	2%
3	17	18,050	42,350	53%

Table 1.06. Comparison of catalytic CO_2 hydrogenation to formate using **16**, **6**, and **17**. Reaction conditions: 1:1 $\text{CO}_2\text{:H}_2$ (69 atm), $[\text{Fe}]$ (0.3 μmol), DBU (23.9 mmol, 3.60 g), LiOTf (3.18 mmol, 0.497 g), THF (10 mL), 80 °C. Yield determined by ^1H NMR, reported values are the average of two trials. ^aReported yields are based on DBU:formate of 1:1.

These experiments clearly demonstrated that a ligand capable of MLC is not required for CO₂ hydrogenation to formate. Mechanistic studies indicated that the corresponding formate complex (ⁱPrPN^{R'}P)FeH(CO){OC(O)H} (R' = H or Me) was the catalyst resting state for both systems, implicating formate dissociation as the turnover-limiting step. The Lewis acid cocatalyst added to these reactions, LiOTf, was proposed to aid in the dissociation of formate in both systems, as well as disrupting a stabilizing hydrogen bond between the pincer N-H and the formate oxygen in (ⁱPrPN^HP)FeH(CO){OC(O)H} (Scheme 1.03). This hydrogen bond cannot be formed in ⁱPrPN^{Me}P-ligated catalysts, which likely explains why **6** and **16** give inferior activity compared to **17**. This study emphasizes the importance of the N-substitution in ^RPN^{R'}P systems not only for determining whether or not MLC is relevant in catalysis, but also for modulating potential hydrogen bonding

interactions between the pincer ligand and substrates or other ligands.

A few years after this report, the Bernskoetter group investigated cobalt complexes supported by ⁱPrPN^{R'}P ligands for CO₂ hydrogenation to formate.^{10a, c} They synthesized two species, [(ⁱPrPN^{R'}P)Co(CO)₂][Cl] (R' = H (**18**) or Me (**19**)) which differ only in their N-substitution, and investigated catalytic performance under conditions similar to those optimized for iron (Table 1.07). ⁱPrPN^HP-ligated complex **18** gave only 450 turnovers



Scheme 1.03. Role of the Lewis acid in formate dissociation from ⁱPrPN^HP and ⁱPrPN^{Me}P iron complexes.

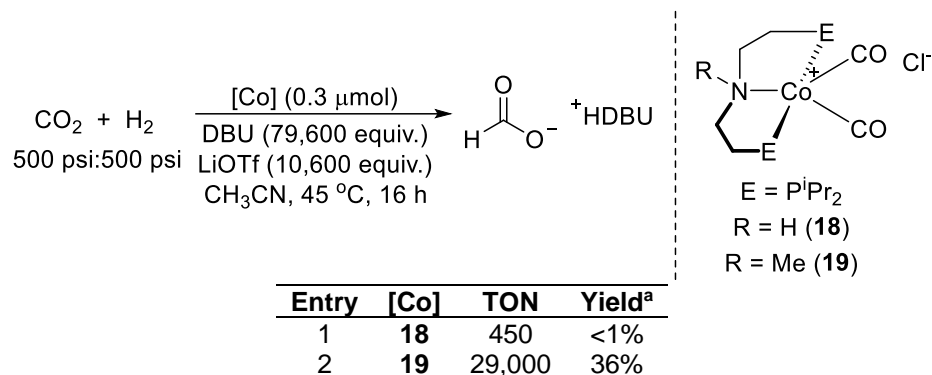
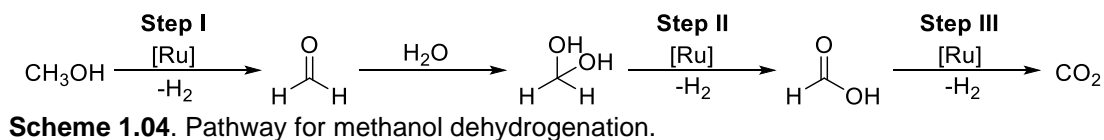
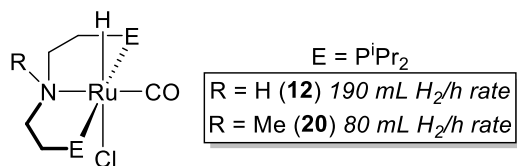
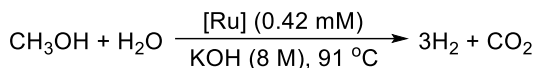


Table 1.07. Catalyst screen for CO₂ hydrogenation to formate using **18** and **19**. Reaction conditions: 1:1 CO₂:H₂ (69 atm), [Co] (0.3 μmol), DBU (23.9 mmol, 3.60 g), LiOTf (3.18 mmol, 0.497 g), CH₃CN (5 mL), 45 °C, 16 h. Yield determined by ¹H NMR, reported values are the average of three trials. ^aReported yields are based on DBU:formate of 1:1.

(Entry 1), while the ⁱPrPN^{Me}P congener **19** achieved 29,000 turnovers (Entry 2), corresponding to an astounding 64-fold increase in productivity simply by changing the pincer N-substitution. This result further emphasizes the fact that a bifunctional ligand is not universally advantageous in catalysis, and that such trends hold across different transition metal catalysts for the same reaction.

In 2016, the Beller group performed a detailed mechanistic study of methanol dehydrogenation to CO₂ (Scheme 1.04) using **12**, one of the state-of-the-art systems for this reaction.^{8a, d} They first investigated whether or not the mechanism requires a bifunctional ligand by synthesizing (ⁱPrPN^{Me}P)RuHCl(CO) (**20**) (Scheme 1.05). Surprisingly, **20** was active for methanol dehydrogenation, although the rate (80 mL H₂ produced per hour) was significantly slower than for the ⁱPrPN^HP-ligated complex **12** (190 mL H₂ produced per hour). However, these two species showed drastically different kinetic isotope effects (KIEs) for reactions with fully deuterated solvents and base: **12**

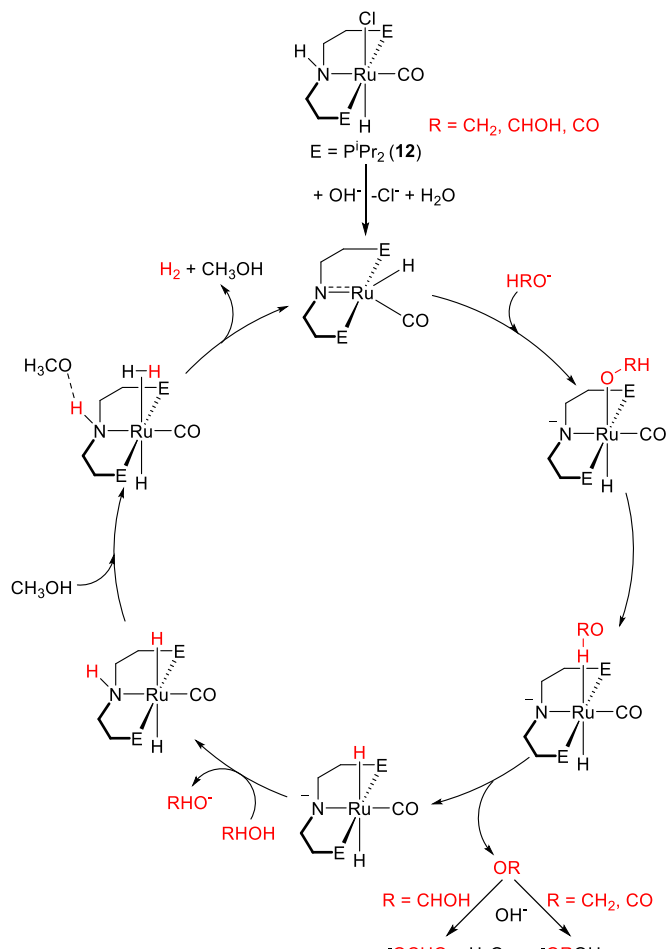




Scheme 1.05. Rates of methanol dehydrogenation using ruthenium $i\text{PrPN}^R\text{P}$ complexes.

showed an isotope effect of 7.07, while **20** only displayed an effect of 1.76. This difference implies the two catalysts operate through different mechanisms, with the turnover limiting step for **20** likely not involving the cleavage of an X–H (X = C, O, Ru) bond. Nevertheless, these data are not straightforward to interpret, as hydrogen is produced over three sequential reductions of methanol (Scheme 1.04).

DFT calculations conclude that **12** operates using a mechanism involving MLC (Scheme 1.06), where formic acid dehydrogenation (Step III in Scheme 1.04, R = CO in Scheme 1.06) is the turnover limiting step. The $i\text{PrPN}^{\text{Me}}\text{P}$ ligand of complex **20** is not capable of operating via a mechanism involving MLC like the one shown in Scheme 1.06, and this system operates using a different mechanism in which methanol dehydrogenation to formaldehyde (Step I in Scheme 1.04) is proposed to be turnover limiting. These results once again

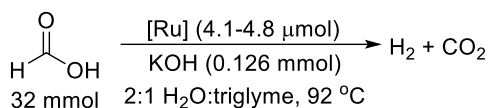


Scheme 1.06. Mechanism of methanol dehydrogenation involving MLC using **12**.

emphasize that the importance of the N-substitution in $^R\text{PN}^{R'}\text{P}$ -supported catalysts extends far beyond simply enabling or shutting down MLC, and can have a significant impact on catalytic activity and mechanism.

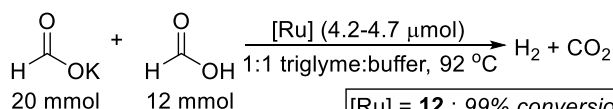
The insights gained in relation to methanol dehydrogenation using **12** and **20** led the Beller group to hypothesize that the $^{\text{iPr}}\text{PN}^{\text{Me}}\text{P}$ -ligated complex **20** should be more active

Not buffered conditions:



[Ru] = **12** : 69% conversion in 3 h
[Ru] = **20** : 82% conversion in 3 h

Buffered conditions:



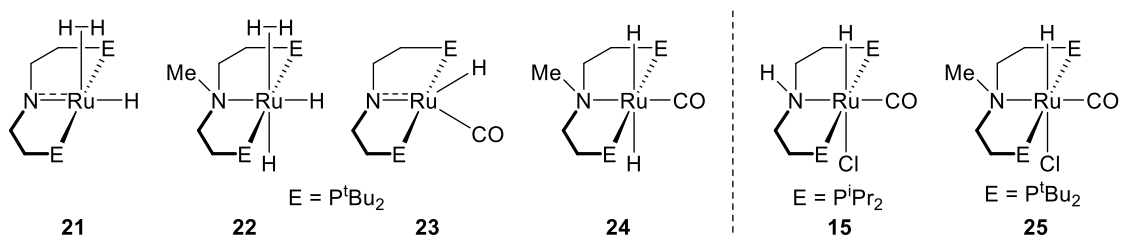
[Ru] = **12** : 99% conversion in 3 h
[Ru] = **20** : 99% conversion in 40 min

Scheme 1.07. Formic acid dehydrogenation using **12** and **20** under standard conditions compared to using a 1 M phosphoric acid buffer.

for formic acid dehydrogenation than **12**, as this step in methanol dehydrogenation was more facile for the $^{\text{iPr}}\text{PN}^{\text{Me}}\text{P}$ species.^{8d} Therefore, they compared the catalytic activity of **12** and **20** in

formic acid dehydrogenation. Complex **20** outperformed **12** under all conditions tested.^{8g} The catalysts were both found to be more active at low pH, and the presence of a 1 M phosphoric acid buffer drastically increased the turnover frequencies (TOFs) of both catalysts (Scheme 1.07) by maintaining a more consistent acidic pH throughout the reaction. However, the difference between the rates of catalysis remained large: **20** had an initial TOF of 9,219 h^{-1} in the buffered solution while **12** only reached a TOF of 2,573 h^{-1} .

In 2018, the Precht and Vogt groups published a report on the direct amination of alcohols with ammonia catalyzed by ruthenium pincer complexes. This study aimed to understand whether or not a system that could participate in MLC was required for the reaction.^{13g} The $^R\text{PN}^{R'}\text{P}$ complexes initially utilized in this report included



Entry	[Ru]	Conversion	Time
1	21	0%	52 h
2	22	75%	52 h
3	23	0%	52 h
4	24	50%	52 h
5	15	0%	52 h
6 ^a	25	95%	32 h

Table 1.08 $\text{RPN}^{\text{R}}\text{P}$ ruthenium complexes investigated in the direct amination of alcohols with ammonia. Reaction conditions: cyclohexanol (5 mmol), [Ru] (0.04 mmol), *t*-amyl alcohol (15 mL), NH_3 (2.5 mL), 150 °C. Conversion determined using NMR spectroscopy. ^a0.5 mmol KO^tBu added.

($^t\text{BuPNP}$)RuH(H_2) (**21**), ($^t\text{BuPN}^{\text{Me}}\text{P}$)Ru(H_2)(H)₂ (**22**), ($^t\text{BuPNP}$)RuH(CO) (**23**), and ($^t\text{BuPN}^{\text{Me}}\text{P}$)Ru(H)₂(CO) (**24**) (Table 1.08). Interestingly, the secondary amine complexes **21** and **23** were both found to be completely inactive in the amination of cyclohexanol using excess ammonia (Table 1.08, Entries 1 & 3). No product was observed even with the addition of a base, when cyclohexanone was added in an attempt to activate the catalysts by accepting H_2 , or when a primary alcohol such as benzyl alcohol was used as a substrate. However, both **22** and **24** were active catalysts for this reaction, giving 75% and 50% conversion to cyclohexylamine after 52 hours, respectively (Entries 2 & 4). These experiments demonstrate that $^t\text{BuPN}^{\text{H}}\text{P}$ complexes are completely inactive for the amination of alcohols, while replacing the pincer N-H with a simple methyl group provides competent (pre)catalysts.

Precht, Vogt, and co-workers next evaluated the activity of commercially available **15** for the same reaction. Once again, this secondary amine complex was inactive, giving

no aminated product under standard conditions, in the presence of base or cyclohexanone, or in different solvents (Table 1.08, Entry 5). Conversely, the $^t\text{BuPN}^{\text{Me}}\text{P}$ complex **25** gives 95% conversion in 32 hours upon addition of cocatalytic base to remove the chloride ligand (Table 1.08, Entry 6). The TOF of **25** in this reaction was measured to be 74 h^{-1} , one of the fastest rates for direct amination of secondary alcohols reported to date.²³ This report, along with the others described in this section, illustrate the importance of the identity of the N-substitution in $^{\text{R}}\text{PN}^{\text{R}'}\text{P}$ catalyst systems. Additionally, if a simple change from N-H to N-Me results in the significant changes in activity described here, it is plausible that even more active, productive, and selective catalysts could be rationally designed by systematically investigating the catalytic impact of novel moieties on this often overlooked substituent.

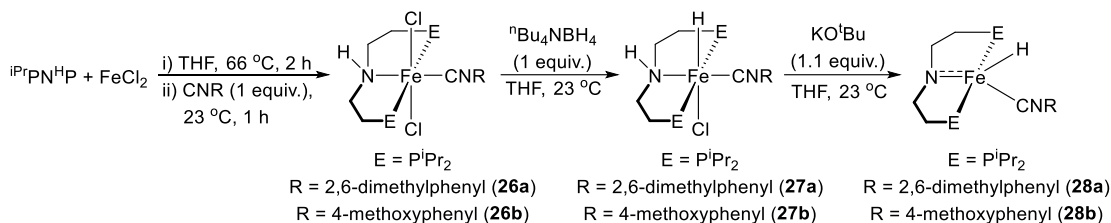
III. Effects of Altering the π -Acid Ligand in $^{\text{R}}\text{PN}^{\text{H}}\text{P}$ Complexes

Isonitrile Ligands

As described in the previous section, modifications to the $^{\text{R}}\text{PN}^{\text{R}'}\text{P}$ ligand backbone have been studied extensively in catalysts of the type $(^{\text{R}}\text{PN}^{\text{R}'}\text{P})\text{MX}_2(\text{CO})$ ($\text{M} = \text{Ir}, \text{Ru}, \text{Fe}, \text{Co}, \text{Mn}$; $\text{X} = \text{H}, \text{Cl}, \text{BH}_4, \text{OC}(\text{O})\text{H}$) (Figure 1.02a). However, research has also been performed on the effects of replacing the commonly used carbonyl ligand in these systems. In particular, isonitrile ligands, which are relatively weak π -acid ligands with tunable steric and electronic properties, have been used as alternatives to carbonyl ligands.²⁴

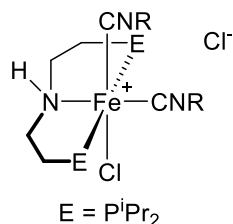
In 2017, the Hazari group described iron $^{\text{R}}\text{PN}^{\text{H}}\text{P}$ complexes with isonitrile ligands.^{18a} They were interested in exploring the electronic effects of changing the π -acid ligand and also the potential steric advantage of isonitrile ligands in hindering bimolecular

decomposition that is commonly proposed to occur in catalysis.^{9c} They first attempted to synthesize isonitrile analogs of previously prepared carbonyl complexes using a related synthetic route (Scheme 1.08).^{9c, 25} Metalation of FeCl₂ with ⁱPrPN^HP and 2,6-dimethylphenyl isonitrile or 4-methoxyphenyl isonitrile resulted primarily in the formation of [(ⁱPrPN^HP)FeCl(CNR)₂][Cl] (R = 2,6-dimethylphenyl or 4-methoxyphenyl) (Figure



Scheme 1.08. Synthetic route for the preparation of ⁱPrPN^HP iron isonitrile complexes **26-28**.

1.08) with the desired complexes (ⁱPrPN^HP)FeCl₂(CNR) (R = 2,6-dimethylphenyl (**26a**) or 4-methoxyphenyl (**26b**)) observed as minor products. The isonitrile was therefore added dropwise as a dilute solution after FeCl₂ was reacted with ⁱPrPN^HP for two hours in order



R = 2,6-dimethylphenyl,
4-methoxyphenyl, ⁱPr,
^tBu, adamantyl

Figure 1.08. Bis(isonitrile) byproducts.

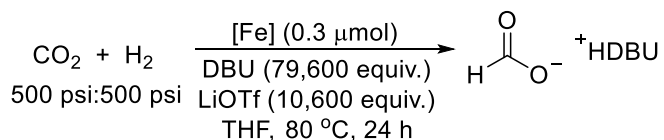
to cleanly isolate **26a** and **26b**. Several attempts were made to synthesize complexes with alkyl isonitriles including ⁱPr, ^tBu, and adamantyl isonitrile, however only bis(isonitrile) species could be isolated (Figure 1.08). This phenomenon is different from analogous carbonyl complexes, where coordination of two CO ligands is not commonly observed

during synthesis.²⁵

The hydrido chloride complexes (ⁱPrPN^HP)FeHCl(CNR) (R = 2,6-dimethylphenyl (**27a**) or 4-methoxyphenyl (**27b**)) were synthesized via the reaction of dichloride complexes **26a** or **26b** with a slight excess of ⁿBu₄NBH₄ in THF (Scheme 1.08). Although these complexes were only prepared in moderate yields (40 and 37%, respectively), these

yields are comparable to those reported for the synthesis of the carbonyl congener $(i\text{PrPN}^{\text{HP}})\text{FeHCl}(\text{CO})$ (38%).²⁵ In an analogous fashion to $(i\text{PrPN}^{\text{HP}})\text{FeHCl}(\text{CO})$, complexes **27a** and **27b** undergo dehydrohalogenation using KO^tBu to generate the amido species $(i\text{PrPNP})\text{FeH}(\text{CNR})$ ($\text{R} = 2,6\text{-dimethylphenyl}$ (**28a**) or 4-methoxyphenyl (**28b**)) (Scheme 1.08).

Complexes **28a** and **28b** display the same kinds of stoichiometric reactivity as their carbonyl congener **16**, such as addition of H_2 across the Fe-N bond to form $(i\text{PrPN}^{\text{HP}})\text{Fe}(\text{H})_2(\text{CNR})$ ($\text{R} = 2,6\text{-dimethylphenyl}$ or 4-methoxyphenyl) and subsequent CO_2 insertion to form $(i\text{PrPN}^{\text{HP}})\text{FeH}(\text{CNR})\{\text{OC}(\text{O})\text{H}\}$ ($\text{R} = 2,6\text{-dimethylphenyl}$ or 4-methoxyphenyl), but the dihydride and formate isonitrile complexes show decreased stability compared to their carbonyl analogues. These differences are also reflected in the catalytic activity of **28a** and **28b** when compared to **16** in CO_2 hydrogenation to formate (Table 1.09). **28a** and **28b** give 613 and 333 turnovers, respectively (Entries 1 & 2), whereas **16** reaches 6,030 turnovers under the same conditions (Entry 3). This study clearly



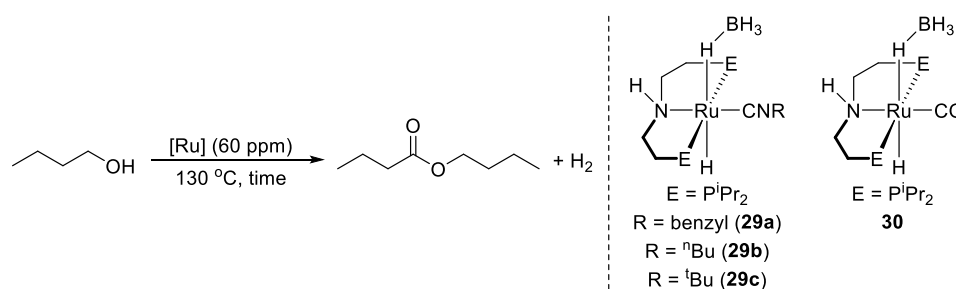
Entry	[Fe]	TON	Yield ^a
1	28a	613	<1%
2	28b	333	<1%
3	16	6,030	8%

Table 1.09. CO_2 hydrogenation to formate using **28a**, **28b** and **16**. Reaction conditions: 1:1 $\text{CO}_2\text{:H}_2$ (69 atm), $[\text{Fe}]$ (0.3 μmol), DBU (23.9 mmol, 3.60 g), LiOTf (3.18 mmol, 0.497 g), THF (10 mL), 80 $^\circ\text{C}$, 24 h. Yield determined by ^1H NMR, reported values are the average of three trials. ^aReported yields are based on DBU:formate of 1:1.

demonstrates the large impact on synthesis and catalysis when the carbonyl ligand in $i\text{PrPN}^{\text{HP}}$ systems is replaced with an isonitrile, and indicates that the more advantageous substitution may be a stronger π -acid.

Recently, the Gauvin group reported the synthesis of a series of $i\text{PrPN}^{\text{H}}\text{P}$ iron and ruthenium complexes with benzyl, ^nBu , or ^tBu isonitrile ligands in order to compare their catalytic performance in acceptorless alcohol dehydrogenation.^{18c} However, similar to the work by the Hazari group (*vide supra*), they were unable to isolate iron $i\text{PrPN}^{\text{H}}\text{P}$ complexes with only one alkyl isonitrile ligand. This precluded a direct catalytic comparison between iron isonitrile complexes and a carbonyl congener, as most iron $i\text{PrPN}^{\text{R}}\text{P}$ bis(carbonyl) complexes have previously been found to be catalytically inactive.^{9c, 14i} In agreement with these results, the isolated complex $[(i\text{PrPN}^{\text{H}}\text{P})\text{FeBr}(\text{CNR})_2][\text{BPh}_4]$ ($\text{R} = \text{benzyl}$) was found to be completely inactive for the dehydrogenation of neat butanol.

Although iron isonitrile complexes with catalytically relevant carbonyl analogues could not be isolated, Gauvin *et al.* were able to generate a series of ruthenium isonitrile complexes to compare in catalysis: $(i\text{PrPN}^{\text{H}}\text{P})\text{RuH}(\text{CNR})(\text{HBH}_3)$ ($\text{R} = \text{benzyl}$ (**29a**), ^nBu (**29b**), or ^tBu (**29c**)) were obtained and compared to $(i\text{PrPN}^{\text{H}}\text{P})\text{RuH}(\text{CO})(\text{HBH}_3)$ (**30**) in neat butanol dehydrogenation (Table 1.10). Surprisingly, isonitrile complexes **29a** and **29b** were found to be initially more active than carbonyl complex **30**, achieving an initial rate



Entry	[Ru]	TOF (h^{-1})	TON (time) ^a	Conversion
1	29a	6,220	10,200 (3 h)	61%
2	29b	5,970	9,000 (3 h)	54%
3	29c	2,930	2,900 (1 h)	17%
4	30	4,300	14,100 (5 h)	85%

Table 1.10. Catalyst screen for neat butanol dehydrogenation using **29a-c** and **30**. Reaction conditions: butanol (10 mL), [Ru] (6.5 μmol), 130 $^\circ\text{C}$. TOFs and TONS determined by ^1H NMR. ^aTime indicates the point at which no further conversion was observed.

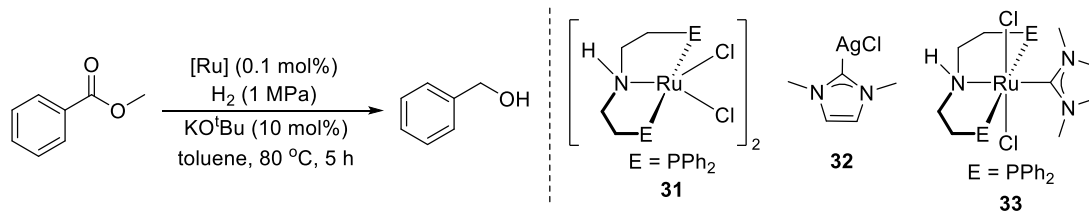
of 6,220, 5,970, and 4,300 turnovers per hour, respectively. However, the isonitrile complexes are less stable under catalytic conditions, and **29a** and **29b** plateau after reaching 10,200 and 9,000 turnovers, respectively, while **30** gives 14,100 turnovers (Table 1.10, Entries 1, 2, & 4). The ^tBu isonitrile complex **29c** is the least active and the least robust, giving only 2,900 turnovers and becoming inactive after 1 hour (Entry 3). These results indicate that increased sterics at the isonitrile ligand do not increase catalyst stability. Additionally, even though **29a-b** are highly active in catalysis, their stability under catalytic conditions is a problem. This conclusion is in agreement with the observations of the Hazari group with iron isonitrile complexes **28a-b** (*vide supra*). Overall, these studies demonstrate that isonitrile ligands can be used to generate active iron and ruthenium ^RPN^HP catalysts, but that further understanding of the impact of isonitrile sterics and electronics on catalyst decomposition is necessary to design improved catalysts.

N-Heterocyclic Carbene Ligands

NHCs are sterically and electronically tunable ligands that have been used to support transition metal complexes in a variety of catalytic transformations.²⁶ In 2016, the Kayaki group hypothesized that a strongly σ -donating NHC ligand could replace the ubiquitous CO ligand in a ruthenium ^{Ph}PN^HP system to increase the nucleophilicity of Ru-H intermediates and generate improved catalysts for ester hydrogenation.^{18d} They first investigated an *in situ* generated system using [(^{Ph}PN^HP)RuCl₂]₂ (**31**) and AgCl(1,3-dimethylimidazol-2-ylidene) (**32**) for the hydrogenation of methyl benzoate (Table 1.11). Dimeric complex **31** was a very poor catalyst for this reaction, giving only 4% yield of benzyl alcohol after 5 hours (Table 1.11, Entry 1). The addition of PPh₃ did not

significantly improve the yield, and only 6% product was observed (Entry 2). However, the addition of 1 equivalent of the NHC precursor **32** sharply increased the productivity of the system and gave a yield of 93% (Entry 3). Many other NHC precursors with varying steric and electronic properties were used as additives with **31** in the model reaction, but none achieved a higher yield than **32**.

The NHC complex (^{Ph}PN^HP)RuCl₂(L) (**33**, L = 1,3-dimethylimidazol-2-ylidene) was isolated and evaluated in catalysis. This species is just as productive as the *in situ* generated system, and gives a 94% yield of benzyl alcohol (Table 1.11, Entry 4). Both the *in situ* and premade NHC catalyst systems were more productive than the corresponding carbonyl complex **15**, which only reached a 49% yield of alcohol under the same conditions (Entry 5). It was further discovered that **33** could catalyze the hydrogenation of methyl benzoate in 74% yield under only one atmosphere of H₂ (Entry 6), which is an important consideration in industrial applications. This report demonstrates the potential power of rationally designing ^RPN^{R'}P catalyst systems by replacing the ubiquitous carbonyl ligand



Entry	[Ru]	Yield
1	31	4%
2	31 + PPh ₃ ^a	6%
3	31 + 32 ^b	93%
4	33	94%
5	15	49%
6 ^c	33	74%

Table 1.11. Catalytic comparison for methyl benzoate hydrogenation using **31** with donor ligands and **33**. Reaction conditions: methyl benzoate (10 mmol), [Ru] (0.05 mol% if using **31** or 0.1 mol% if using **33** or **15**), H₂ (1 MPa), KO^tBu (1.0 mmol), toluene (10 mL), 80 °C, 5 h. Yield determined by GC. ^a0.1 mol% PPh₃ added. ^b0.1 mol% **32** added. ^cConditions: H₂ (balloon), methyl benzoate (1.0 mmol), **33** (1.0 mol%), THF (1 mL), 50 °C.

with a stronger σ -donor such as an NHC, and creates a new path for further catalyst development using this approach.

IV. Conclusions and Future Directions

$^R\text{PN}^{R'}\text{P}$ -ligated transition metal complexes continue to be the subject of broad interest due their ability to facilitate a wide range of catalytic transformations. The effect of phosphine side arm sterics and electronics on catalytic performance has been thoroughly investigated, but the impact of N-substitutions that are not H or Me remains underexplored. This is surprising given that initial results show that the substitution of Me for H has large implications for catalysis. Further, systematic studies on the impact of replacing the commonly used carbonyl ligand with other π -acid or σ -donor ligands are also warranted because understanding the consequences of ligand modification is necessary for rational catalyst design. In this thesis, we strive to understand interconnected ligand effects in $^R\text{PN}^{R'}\text{P}$ systems by filling gaps in the literature related to modifying the π -acid ligand as well as systematically varying the nitrogen substitution to determine its effects on synthesis, catalysis, and mechanism.

V. References

1. Moulton, C. J.; Shaw, B. L., Transition metal–carbon bonds. Part XLII. Complexes of nickel, palladium, platinum, rhodium and iridium with the tridentate ligand 2,6-bis[(di-*t*-butylphosphino)methyl]phenyl. *J. Chem. Soc., Dalton Trans.* **1976**, 1020-1024.
2. (a) Gunanathan, C.; Milstein, D., Bond Activation and Catalysis by Ruthenium Pincer Complexes. *Chem. Rev.* **2014**, *114*, 12024-12087; (b) Lawrence, M. A. W.; Green, K.-A.;

Nelson, P. N.; Lorraine, S. C., Review: Pincer ligands—Tunable, versatile and applicable. *Polyhedron* **2018**, *143*, 11-27; (c) van der Vlugt, J. I.; Reek, J. N. H., Neutral Tridentate PNP Ligands and Their Hybrid Analogues: Versatile Non-Innocent Scaffolds for Homogeneous Catalysis. *Angew. Chem. Int. Ed.* **2009**, *48*, 8832-8846; (d) Alig, L.; Fritz, M.; Schneider, S., First-Row Transition Metal (De)Hydrogenation Catalysis Based On Functional Pincer Ligands. *Chem. Rev.* **2019**, *119*, 2681-2751; (e) Peris, E.; Crabtree, R. H., Key factors in pincer ligand design. *Chem. Soc. Rev.* **2018**, *47*, 1959-1968.

3. Roland, C. D.; Li, H.; Abboud, K. A.; Wagener, K. B.; Veige, A. S., Cyclic polymers from alkynes. *Nature Chemistry* **2016**, *8*, 791-796.

4. (a) Choi, J.; MacArthur, A. H. R.; Brookhart, M.; Goldman, A. S., Dehydrogenation and Related Reactions Catalyzed by Iridium Pincer Complexes. *Chem. Rev.* **2011**, *111*, 1761-1779; (b) van Koten, G.; Milstein, D., *Organometallic Pincer Chemistry*. Springer-Verlag: Berlin-Heidelberg, **2013**.

5. Heimann, J. E.; Bernskoetter, W. H.; Hazari, N.; Mayer, James M., Acceleration of CO₂ insertion into metal hydrides: ligand, Lewis acid, and solvent effects on reaction kinetics. *Chem. Sci.* **2018**, *9*, 6629-6638.

6. Khusnutdinova, J. R.; Milstein, D., Metal–Ligand Cooperation. *Angew. Chem. Int. Ed.* **2015**, *54*, 12236-12273.

7. (a) Schmeier, T. J.; Dobereiner, G. E.; Crabtree, R. H.; Hazari, N., Secondary Coordination Sphere Interactions Facilitate the Insertion Step in an Iridium(III) CO₂ Reduction Catalyst. *J. Am. Chem. Soc.* **2011**, *133*, 9274-9277; (b) Graham, T. W.; Tsang, C.-W.; Chen, X.; Guo, R.; Jia, W.; Lu, S.-M.; Sui-Seng, C.; Ewart, C. B.; Lough, A.; Amoroso, D.; Abdur-Rashid, K., Catalytic Solvolysis of Ammonia Borane. *Angew. Chem.*

Int. Ed. **2010**, *49*, 8708-8711; (c) Ahn, S. T.; Bielinski, E. A.; Lane, E. M.; Chen, Y.; Bernskoetter, W. H.; Hazari, N.; Palmore, G. T. R., Enhanced CO₂ electroreduction efficiency through secondary coordination effects on a pincer iridium catalyst. *Chem. Commun.* **2015**, *51*, 5947-5950; (d) Prichatz, C.; Alberico, E.; Baumann, W.; Junge, H.; Beller, M., Iridium–PNP Pincer Complexes for Methanol Dehydrogenation at Low Base Concentration. *ChemCatChem* **2017**, *9*, 1891-1896; (e) Ramaraj, A.; Nethaji, M.; Jagirdar, B. R., Hydrogenation of CO₂, carbonyl and imine substrates catalyzed by [IrH₃(^{Ph}PN^HP)] complex. *J. Organomet. Chem.* **2019**, *883*, 25-34.

8. (a) Nielsen, M.; Alberico, E.; Baumann, W.; Drexler, H.-J.; Junge, H.; Gladiali, S.; Beller, M., Low-temperature aqueous-phase methanol dehydrogenation to hydrogen and carbon dioxide. *Nature* **2013**, *495*, 85-89; (b) Kothandaraman, J.; Czaun, M.; Goeppert, A.; Haiges, R.; Jones, J.-P.; May, R. B.; Prakash, G. K. S.; Olah, G. A., Amine-Free Reversible Hydrogen Storage in Formate Salts Catalyzed by Ruthenium Pincer Complex without pH Control or Solvent Change. *ChemSusChem* **2015**, *8*, 1442-1451; (c) Rezayee, N. M.; Huff, C. A.; Sanford, M. S., Tandem Amine and Ruthenium-Catalyzed Hydrogenation of CO₂ to Methanol. *J. Am. Chem. Soc.* **2015**, *137*, 1028-1031; (d) Alberico, E.; Lennox, A. J. J.; Vogt, L. K.; Jiao, H.; Baumann, W.; Drexler, H.-J.; Nielsen, M.; Spannenberg, A.; Checinski, M. P.; Junge, H.; Beller, M., Unravelling the Mechanism of Basic Aqueous Methanol Dehydrogenation Catalyzed by Ru–PNP Pincer Complexes. *J. Am. Chem. Soc.* **2016**, *138*, 14890-14904; (e) Kothandaraman, J.; Kar, S.; Sen, R.; Goeppert, A.; Olah, G. A.; Prakash, G. K. S., Efficient Reversible Hydrogen Carrier System Based on Amine Reforming of Methanol. *J. Am. Chem. Soc.* **2017**, *139*, 2549-2552; (f) Kar, S.; Sen, R.; Kothandaraman, J.; Goeppert, A.; Chowdhury, R.; Munoz, S. B.; Haiges, R.; Prakash, G.

K. S., Mechanistic Insights into Ruthenium-Pincer-Catalyzed Amine-Assisted Homogeneous Hydrogenation of CO₂ to Methanol. *J. Am. Chem. Soc.* **2019**, *141*, 3160-3170; (g) Agapova, A.; Alberico, E.; Kammer, A.; Junge, H.; Beller, M., Catalytic Dehydrogenation of Formic Acid with Ruthenium-PNP-Pincer Complexes: Comparing N-Methylated and NH-Ligands. *ChemCatChem* **2019**, *11*, 1910-1914.

9. (a) Alberico, E.; Sponholz, P.; Cordes, C.; Nielsen, M.; Drexler, H.-J.; Baumann, W.; Junge, H.; Beller, M., Selective Hydrogen Production from Methanol with a Defined Iron Pincer Catalyst under Mild Conditions. *Angew. Chem. Int. Ed.* **2013**, *52*, 14162-14166; (b) Bielinski, E. A.; Förster, M.; Zhang, Y.; Bernskoetter, W. H.; Hazari, N.; Holthausen, M. C., Base-Free Methanol Dehydrogenation Using a Pincer-Supported Iron Compound and Lewis Acid Co-catalyst. *ACS Catal.* **2015**, *5*, 2404-2415; (c) Bielinski, E. A.; Lagaditis, P. O.; Zhang, Y.; Mercado, B. Q.; Würtele, C.; Bernskoetter, W. H.; Hazari, N.; Schneider, S., Lewis Acid-Assisted Formic Acid Dehydrogenation Using a Pincer-Supported Iron Catalyst. *J. Am. Chem. Soc.* **2014**, *136*, 10234-10237; (d) Chakraborty, S.; Brennessel, W. W.; Jones, W. D., A Molecular Iron Catalyst for the Acceptorless Dehydrogenation and Hydrogenation of *N*-Heterocycles. *J. Am. Chem. Soc.* **2014**, *136*, 8564-8567; (e) Zhang, Y.; MacIntosh, A. D.; Wong, J. L.; Bielinski, E. A.; Williard, P. G.; Mercado, B. Q.; Hazari, N.; Bernskoetter, W. H., Iron catalyzed CO₂ hydrogenation to formate enhanced by Lewis acid co-catalysts. *Chem. Sci.* **2015**, *6*, 4291-4299; (f) Lane, E. M.; Zhang, Y.; Hazari, N.; Bernskoetter, W. H., Sequential Hydrogenation of CO₂ to Methanol Using a Pincer Iron Catalyst. *Organometallics* **2019**, *38*, 3084-3091; (g) Curley, J. B.; Bernskoetter, W. H.; Hazari, N., Additive-Free Formic Acid Dehydrogenation Using a Pincer-Supported Iron Catalyst. *ChemCatChem* **2020**, *12*, 1934-1938.

10. (a) Spentzos, A. Z.; Barnes, C. L.; Bernskoetter, W. H., Effective Pincer Cobalt Precatalysts for Lewis Acid Assisted CO₂ Hydrogenation. *Inorg. Chem.* **2016**, *55*, 8225-8233; (b) Zhou, W.; Wei, Z.; Spannenberg, A.; Jiao, H.; Junge, K.; Junge, H.; Beller, M., Cobalt-Catalyzed Aqueous Dehydrogenation of Formic Acid. *Chem. Eur. J.* **2019**, *25*, 8459-8464; (c) Mills, M. R.; Barnes, C. L.; Bernskoetter, W. H., Influences of Bifunctional PNP-Pincer Ligands on Low Valent Cobalt Complexes Relevant to CO₂ Hydrogenation. *Inorg. Chem.* **2018**, *57*, 1590-1597.
11. (a) Kar, S.; Goeppert, A.; Kothandaraman, J.; Prakash, G. K. S., Manganese-Catalyzed Sequential Hydrogenation of CO₂ to Methanol via Formamide. *ACS Catal.* **2017**, *7*, 6347-6351; (b) Ryabchuk, P.; Stier, K.; Junge, K.; Checinski, M. P.; Beller, M., Molecularly Defined Manganese Catalyst for Low-Temperature Hydrogenation of Carbon Monoxide to Methanol. *J. Am. Chem. Soc.* **2019**, *141*, 16923-16929; (c) Zubar, V.; Borghs, J. C.; Rueping, M., Hydrogenation or Dehydrogenation of N-Containing Heterocycles Catalyzed by a Single Manganese Complex. *Org. Lett.* **2020**, *22*, 3974-3978; (d) Kaithal, A.; Werlé, C.; Leitner, W., Alcohol-Assisted Hydrogenation of Carbon Monoxide to Methanol Using Molecular Manganese Catalysts. *JACS Au* **2021**, *1*, 130-136.
12. (a) Clarke, Z. E.; Maragh, P. T.; Dasgupta, T. P.; Gusev, D. G.; Lough, A. J.; Abdur-Rashid, K., A Family of Active Iridium Catalysts for Transfer Hydrogenation of Ketones. *Organometallics* **2006**, *25*, 4113-4117; (b) Chen, X.; Jia, W.; Guo, R.; Graham, T. W.; Gullons, M. A.; Abdur-Rashid, K., Highly active iridium catalysts for the hydrogenation of ketones and aldehydes. *Dalton Trans.* **2009**, 1407-1410; (c) Andrushko, N.; Andrushko, V.; Roose, P.; Moonen, K.; Börner, A., Amination of Aliphatic Alcohols and Diols with an Iridium Pincer Catalyst. *ChemCatChem* **2010**, *2*, 640-643; (d) Junge, K.; Wendt, B.;

Jiao, H.; Beller, M., Iridium-Catalyzed Hydrogenation of Carboxylic Acid Esters. *ChemCatChem* **2014**, *6*, 2810-2814.

13. (a) Bertoli, M.; Choualeb, A.; Lough, A. J.; Moore, B.; Spasyuk, D.; Gusev, D. G., Osmium and Ruthenium Catalysts for Dehydrogenation of Alcohols. *Organometallics* **2011**, *30*, 3479-3482; (b) Nielsen, M.; Junge, H.; Kammer, A.; Beller, M., Towards a Green Process for Bulk-Scale Synthesis of Ethyl Acetate: Efficient Acceptorless Dehydrogenation of Ethanol. *Angew. Chem. Int. Ed.* **2012**, *51*, 5711-5713; (c) Kuriyama, W.; Matsumoto, T.; Ogata, O.; Ino, Y.; Aoki, K.; Tanaka, S.; Ishida, K.; Kobayashi, T.; Sayo, N.; Saito, T., Catalytic Hydrogenation of Esters. Development of an Efficient Catalyst and Processes for Synthesising (*R*)-1,2-Propanediol and 2-(1-Menthoxy)ethanol. *Organic Process Research & Development* **2012**, *16*, 166-171; (d) Zhang, L.; Han, Z.; Zhao, X.; Wang, Z.; Ding, K., Highly Efficient Ruthenium-Catalyzed N-Formylation of Amines with H₂ and CO₂. *Angew. Chem. Int. Ed.* **2015**, *54*, 6186-6189; (e) Li, Y.; Nielsen, M.; Li, B.; Dixneuf, P. H.; Junge, H.; Beller, M., Ruthenium-catalyzed hydrogen generation from glycerol and selective synthesis of lactic acid. *Green Chem.* **2015**, *17*, 193-198; (f) Kim, S. H.; Hong, S. H., Ruthenium-Catalyzed Urea Synthesis Using Methanol as the C1 Source. *Org. Lett.* **2016**, *18*, 212-215; (g) Pinggen, D.; Choi, J.-H.; Allen, H.; Murray, G.; Ganji, P.; van Leeuwen, P. W. N. M.; Precht, M. H. G.; Vogt, D., Amide versus amine ligand paradigm in the direct amination of alcohols with Ru-PNP complexes. *Catal. Sci. Technol.* **2018**, *8*, 3969-3976; (h) Thiagarajan, S.; Gunanathan, C., Catalytic Cross-Coupling of Secondary Alcohols. *J. Am. Chem. Soc.* **2019**, *141*, 3822-3827.

14. (a) Chakraborty, S.; Dai, H.; Bhattacharya, P.; Fairweather, N. T.; Gibson, M. S.; Krause, J. A.; Guan, H., Iron-Based Catalysts for the Hydrogenation of Esters to Alcohols.

J. Am. Chem. Soc. **2014**, *136*, 7869-7872; (b) Werkmeister, S.; Junge, K.; Wendt, B.; Alberico, E.; Jiao, H.; Baumann, W.; Junge, H.; Gallou, F.; Beller, M., Hydrogenation of Esters to Alcohols with a Well-Defined Iron Complex. *Angew. Chem. Int. Ed.* **2014**, *53*, 8722-8726; (c) Sharninghausen, L. S.; Mercado, B. Q.; Crabtree, R. H.; Hazari, N., Selective Conversion of Glycerol to Lactic Acid with Iron Pincer Precatalysts. *Chem. Commun.* **2015**, *51*, 16201-16204; (d) Elangovan, S.; Wendt, B.; Topf, C.; Bachmann, S.; Scalone, M.; Spannenberg, A.; Jiao, H.; Baumann, W.; Junge, K.; Beller, M., Improved Second Generation Iron Pincer Complexes for Effective Ester Hydrogenation. *Adv. Synth. Catal.* **2016**, *358*, 820-825; (e) Schneck, F.; Assmann, M.; Balmer, M.; Harms, K.; Langer, R., Selective Hydrogenation of Amides to Amines and Alcohols Catalyzed by Improved Iron Pincer Complexes. *Organometallics* **2016**, *35*, 1931-1943; (f) Rezayee, N. M.; Samblanet, D. C.; Sanford, M. S., Iron-Catalyzed Hydrogenation of Amides to Alcohols and Amines. *ACS Catal.* **2016**, *6*, 6377-6383; (g) Lane, Elizabeth M.; Hazari, N.; Bernskoetter, W. H., Iron-catalyzed urea synthesis: dehydrogenative coupling of methanol and amines. *Chem. Sci.* **2018**, *9*, 4003-4008; (h) Lane, E. M.; Uttley, K. B.; Hazari, N.; Bernskoetter, W., Iron-Catalyzed Amide Formation from the Dehydrogenative Coupling of Alcohols and Secondary Amines. *Organometallics* **2017**, *36*, 2020-2025; (i) Jayarathne, U.; Hazari, N.; Bernskoetter, W. H., Selective Iron-Catalyzed N-Formylation of Amines using Dihydrogen and Carbon Dioxide. *ACS Catal.* **2018**, *8*, 1338-1345; (j) Jayarathne, U.; Zhang, Y.; Hazari, N.; Bernskoetter, W. H., Selective Iron-Catalyzed Deaminative Hydrogenation of Amides. *Organometallics* **2017**, *36*, 409-416.

15. (a) Zhang, G.; Scott, B. L.; Hanson, S. K., Mild and Homogeneous Cobalt-Catalyzed Hydrogenation of C-C, C-O, and C-N Bonds. *Angew. Chem. Int. Ed.* **2012**, *51*, 12102-

12106; (b) Zhang, G.; Hanson, S. K., Cobalt-Catalyzed Transfer Hydrogenation of C-O and C-N Bonds. *Chem. Commun.* **2013**, *49*, 10151-10153; (c) Zhang, G.; Vasudevan, K. V.; Scott, B. L.; Hanson, S. K., Understanding the Mechanisms of Cobalt-Catalyzed Hydrogenation and Dehydrogenation Reactions. *J. Am. Chem. Soc.* **2013**, *135*, 8668-8681; (d) Yin, Z.; Zeng, H.; Wu, J.; Zheng, S.; Zhang, G., Cobalt-Catalyzed Synthesis of Aromatic, Aliphatic, and Cyclic Secondary Amines via a “Hydrogen-Borrowing” Strategy. *ACS Catal.* **2016**, *6*, 6546-6550; (e) Fu, S.; Chen, N.-Y.; Liu, X.; Shao, Z.; Luo, S.-P.; Liu, Q., Ligand-Controlled Cobalt-Catalyzed Transfer Hydrogenation of Alkynes: Stereodivergent Synthesis of *Z*- and *E*-Alkenes. *J. Am. Chem. Soc.* **2016**, *138*, 8588-8594; (f) Yuwen, J.; Chakraborty, S.; Brennessel, W. W.; Jones, W. D., Additive-Free Cobalt-Catalyzed Hydrogenation of Esters to Alcohols. *ACS Catal.* **2017**, *7*, 3735-3740; (g) Junge, K.; Wendt, B.; Cingolani, A.; Spannenberg, A.; Wei, Z.; Jiao, H.; Beller, M., Cobalt Pincer Complexes for Catalytic Reduction of Carboxylic Acid Esters. *Chem. Eur. J.* **2018**, *24*, 1046-1052.

16. (a) Elangovan, S.; Garbe, M.; Jiao, H.; Spannenberg, A.; Junge, K.; Beller, M., Hydrogenation of Esters to Alcohols Catalyzed by Defined Manganese Pincer Complexes. *Angew. Chem. Int. Ed.* **2016**, *55*, 15364-15368; (b) Nguyen, D. H.; Trivelli, X.; Capet, F.; Paul, J.-F.; Dumeignil, F.; Gauvin, R. M., Manganese Pincer Complexes for the Base-Free, Acceptorless Dehydrogenative Coupling of Alcohols to Esters: Development, Scope, and Understanding. *ACS Catal.* **2017**, *7*, 2022-2032; (c) Garbe, M.; Budweg, S.; Papa, V.; Wei, Z.; Hornke, H.; Bachmann, S.; Scalone, M.; Spannenberg, A.; Jiao, H.; Junge, K.; Beller, M., Chemoselective semihydrogenation of alkynes catalyzed by manganese(I)-PNP pincer complexes. *Catal. Sci. Technol.* **2020**, *10*, 3994-4001; (d) Zubar, V.; Dewanji, A.; Rueping,

M., Chemoselective Hydrogenation of Nitroarenes Using an Air-Stable Base-Metal Catalyst. *Org. Lett.* **2021**, *23*, 2742-2747.

17. (a) Bianchini, C.; Glendenning, L.; Peruzzini, M.; Purches, G.; Zanobini, F.; Farnetti, E.; Graziani, M.; Nardin, G., Synthesis of the New Chiral (*R*)- and (*S*)-Aminodiphosphine Ligands *sec*-Butylbis(2-(diphenylphosphino)ethyl)amine, *sec*-Butylbis(2-(dicyclohexylphosphino)ethyl)amine, and (α -Methylbenzyl)bis(2-(dicyclohexylphosphino)ethyl)amine and Their Organometallic Chemistry When Combined with Iridium. *Organometallics* **1997**, *16*, 4403-4414; (b) Dong, Q.; Rose, M. J.; Wong, W.-Y.; Gray, H. B., Dual Coordination Modes of Ethylene-Linked NP₂ Ligands in Cobalt(II) and Nickel(II) Iodides. *Inorg. Chem.* **2011**, *50*, 10213-10224; (c) Ramaraj, A.; Nethaji, M.; Jagirdar, B. R., Contrasting reactivity behaviour of the [RuHCl(CO)(PNP)] complex with electrophilic reagents XOTf (X = H, CH₃, Me₃Si). *Dalton Trans.* **2014**, *43*, 14625-14635; (d) Naicker, D.; Friedrich, H. B.; Omondi, B., Cobalt aminodiphosphine complexes as catalysts in the oxidation of *n*-octane. *RSC Advances* **2015**, *5*, 63123-63129; (e) Ramaraj, A.; Reddy, K. H. K.; Keil, H.; Herbst-Irmer, R.; Stalke, D.; Jemmis, E. D.; Jagirdar, B. R., Approaches to Sigma Complexes via Displacement of Agostic Interactions: An Experimental and Theoretical Investigation. *Organometallics* **2017**, *36*, 2736-2745; (f) Goren Keskin, S.; Stanley, J. M.; Cowley, A. H., Synthesis, characterization and theoretical investigations of molybdenum carbonyl complexes with phosphorus/nitrogen/phosphorus ligand as bidentate and tridentate modes. *Polyhedron* **2017**, *138*, 206-217; (g) Salvarese, N.; Refosco, F.; Seraglia, R.; Roverso, M.; Dolmella, A.; Bolzati, C., Synthesis and characterization of rhenium(III) complexes with (Ph₂PCH₂CH₂)₂NR diphosphinoamine ligands. *Dalton Trans.* **2017**, *46*, 9180-9191; (h) Kostas, I. D.; Antonopoulou, G.;

Potamitis, C.; Raptopoulou, C. P.; Psycharis, V., Platinum complexes with a methoxy-amino phosphine or a nitrogen-containing bis(phosphine) ligand. Synthesis, characterization and application to hydrogenation of trans-cinnamaldehyde. *J. Organomet. Chem.* **2017**, 828, 133-141; (i) Keskin, S. G.; Stanley, J. M.; Mitchell, L. A.; Holliday, B. J., Synthesis, characterization, coordination chemistry, and luminescence studies of copper, silver, palladium, and platinum complexes with a phosphorus/nitrogen/phosphorus ligand. *Inorg. Chim. Acta* **2019**, 486, 200-212.

18. (a) Smith, N. E.; Bernskoetter, W. H.; Hazari, N.; Mercado, B. Q., Synthesis and Catalytic Activity of PNP-Supported Iron Complexes with Ancillary Isonitrile Ligands. *Organometallics* **2017**, 36, 3995-4004; (b) Dai, H.; Li, W.; Krause, J. A.; Guan, H., Experimental Evidence of *syn* H–N–Fe–H Configurational Requirement for Iron-Based Bifunctional Hydrogenation Catalysts. *Inorg. Chem.* **2021**, 60, 6521-6535; (c) Nguyen, D. H.; Merel, D.; Merle, N.; Trivelli, X.; Capet, F.; Gauvin, R. M., Isonitrile ruthenium and iron PNP complexes: synthesis, characterization and catalytic assessment for base-free dehydrogenative coupling of alcohols. *Dalton Trans.* **2021**, 50, 10067-10081; (d) Ogata, O.; Nakayama, Y.; Nara, H.; Fujiwhara, M.; Kayaki, Y., Atmospheric Hydrogenation of Esters Catalyzed by PNP-Ruthenium Complexes with an *N*-Heterocyclic Carbene Ligand. *Org. Lett.* **2016**, 18, 3894-3897.

19. Elangovan, S.; Topf, C.; Fischer, S.; Jiao, H.; Spannenberg, A.; Baumann, W.; Ludwig, R.; Junge, K.; Beller, M., Selective Catalytic Hydrogenations of Nitriles, Ketones, and Aldehydes by Well-Defined Manganese Pincer Complexes. *J. Am. Chem. Soc.* **2016**, 138, 8809-8814.

20. Langer, R.; Diskin-Posner, Y.; Leitun, G.; Shimon, L. J. W.; Ben-David, Y.; Milstein, D., Low-Pressure Hydrogenation of Carbon Dioxide Catalyzed by an Iron Pincer Complex Exhibiting Noble Metal Activity. *Angew. Chem. Int. Ed.* **2011**, *50*, 9948-9952.
21. (a) Karunananda, M. K.; Mankad, N. P., *E*-Selective Semi-Hydrogenation of Alkynes by Heterobimetallic Catalysis. *J. Am. Chem. Soc.* **2015**, *137*, 14598-14601; (b) Srimani, D.; Diskin-Posner, Y.; Ben-David, Y.; Milstein, D., Iron Pincer Complex Catalyzed, Environmentally Benign, *E*-Selective Semi-Hydrogenation of Alkynes. *Angew. Chem. Int. Ed.* **2013**, *52*, 14131-14134.
22. Kothandaraman, J.; Goeppert, A.; Czaun, M.; Olah, G. A.; Prakash, G. K. S., Conversion of CO₂ from Air into Methanol Using a Polyamine and a Homogeneous Ruthenium Catalyst. *J. Am. Chem. Soc.* **2016**, *138*, 778-781.
23. (a) Pinggen, D.; Müller, C.; Vogt, D., Direct Amination of Secondary Alcohols Using Ammonia. *Angew. Chem. Int. Ed.* **2010**, *49*, 8130-8133; (b) Pinggen, D.; Lutz, M.; Vogt, D., Mechanistic Study on the Ruthenium-Catalyzed Direct Amination of Alcohols. *Organometallics* **2014**, *33*, 1623-1629; (c) Pinggen, D.; Lebl, T.; Lutz, M.; Nichol, G. S.; Kamer, P. C. J.; Vogt, D., Catalytic Activity and Fluxional Behavior of Complexes Based on RuHCl(CO)(PPh₃)₃ and Xantphos-Type Ligands. *Organometallics* **2014**, *33*, 2798-2805; (d) Derrah, E. J.; Hanauer, M.; Plessow, P. N.; Schelwies, M.; da Silva, M. K.; Schaub, T., Ru(II)-Triphos Catalyzed Amination of Alcohols with Ammonia via Ionic Species. *Organometallics* **2015**, *34*, 1872-1881.
24. (a) Cotton, F. A.; Zingales, F., The Donor-Acceptor Properties of Isonitriles as Estimated by Infrared Study. *J. Am. Chem. Soc.* **1961**, *83*, 351-355; (b) Bonati, F.; Minghetti, G., Recent advances in the chemistry of isocyanide complexes. *Inorg. Chim.*

Acta **1974**, 9, 95-112; (c) Yamamoto, Y., Zerovalent transition metal complexes of organic isocyanides. *Coord. Chem. Rev.* **1980**, 32, 193-233; (d) Margulieux, G. W.; Weidemann, N.; Lacy, D. C.; Moore, C. E.; Rheingold, A. L.; Figueroa, J. S., Isocyano Analogues of $[\text{Co}(\text{CO})_4]^n$: A Tetraisocyanide of Cobalt Isolated in Three States of Charge. *J. Am. Chem. Soc.* **2010**, 132, 5033-5035; (e) Carpenter, A. E.; Wen, I.; Moore, C. E.; Rheingold, A. L.; Figueroa, J. S., $[1,1\text{-Co}_2(\text{CO})_6(\text{CNAr})_2]$: A Structural Mimic of the Elusive D_{2d} Isomer of $[\text{Co}_2(\text{CO})_8]$. *Chem. Eur. J.* **2013**, 19, 10452-10457; (f) Carpenter, A. E.; Mokhtarzadeh, C. C.; Ripatti, D. S.; Havrylyuk, I.; Kamezawa, R.; Moore, C. E.; Rheingold, A. L.; Figueroa, J. S., Comparative Measure of the Electronic Influence of Highly Substituted Aryl Isocyanides. *Inorg. Chem.* **2015**, 54, 2936-2944; (g) Carpenter, A. E.; Rheingold, A. L.; Figueroa, J. S., A Well-Defined Isocyano Analogue of $\text{HCo}(\text{CO})_4$. 1: Synthesis, Decomposition, and Catalytic 1,1-Hydrogenation of Isocyanides. *Organometallics* **2016**, 35, 2309-2318; (h) Barnett, B. R.; Figueroa, J. S., Zero-valent isocyanides of nickel, palladium and platinum as transition metal σ -type Lewis bases. *Chem. Commun.* **2016**, 52, 13829-13839.

25. Koehne, I.; Schmeier, T. J.; Bielinski, E. A.; Pan, C. J.; Lagaditis, P. O.; Bernskoetter, W. H.; Takase, M. K.; Würtele, C.; Hazari, N.; Schneider, S., Synthesis and Structure of Six-Coordinate Iron Borohydride Complexes Supported by PNP Ligands. *Inorg. Chem.* **2014**, 53, 2133-2143.

26. Peris, E., Smart *N*-Heterocyclic Carbene Ligands in Catalysis. *Chem. Rev.* **2018**, 118, 9988-10031.

Chapter 2: Catalytic Formic Acid Dehydrogenation and CO₂ Hydrogenation Using Iron PN^RP Pincer Complexes with Isonitrile Ligands

This work has previously been published as: Curley, J. B., Smith, N. E., Bernskoetter, W. H., Hazari, N., and Mercado, B. Q. *Organometallics*, **2018**, 37, 3846-3853. Nicholas Smith performed formic acid dehydrogenation catalysis using **B** and provided intellectual contributions and assistance with data analysis.

I. Introduction

Decreased fossil fuel reserves, paired with rising concerns about greenhouse gas emissions, have led to significant interest in the utilization of sustainable energy sources.¹ Unfortunately, many renewable energy sources such as wind and solar are inherently intermittent, and their widespread use will require the development of sustainable methods for energy storage. H₂ is one such clean energy carrier that can be either directly combusted or electrochemically oxidized in a fuel cell.² Gaseous H₂, however, has a low volumetric energy density, hindering its attractiveness as an energy storage medium. Chemical H₂ storage (CHS) based on the reversible (de)hydrogenation of small molecules could promote the use of H₂ as an energy storage vector, and circumvent more costly H₂ compression and liquefaction techniques.³ Formic acid (4.4 wt% H₂), which can be dehydrogenated to form H₂ and CO₂, is a potential liquid CHS material that is currently primarily derived from non-renewable carbon sources.⁴ Renewable formic acid synthesis via the direct hydrogenation of CO₂ using H₂ generated from renewable sources could greatly enhance the value of formic acid as an energy storage medium.^{3b, 4-5} Although the hydrogenation of CO₂ to

formic acid is slightly thermodynamically uphill in organic solvents, typically in academic settings a base is used to generate a formate salt⁶ and drive the reaction forward. On a larger scale, engineering strategies exist to recycle the base and produce formic acid.^{4b} Nevertheless, at this stage, the utilization of formic acid for CHS requires improved catalysts for both formic acid dehydrogenation and CO₂ hydrogenation to formic acid.

Many previously developed homogenous and heterogeneous catalysts for CO₂ hydrogenation to formate or formic acid dehydrogenation have utilized precious metals such as ruthenium and iridium.^{3b, 4-5} Significant efforts are being made to replace these costly, rare, and in some cases toxic metals with more abundant and inexpensive first-row transition metals such as iron.⁷ A number of homogeneous iron catalysts have now been reported for both CO₂ hydrogenation to formate and formic acid dehydrogenation, but in general these systems give inferior activity compared to precious metal systems and are mechanistically less well understood.⁸ We, along with several other groups, have been investigating iron complexes supported by the ligand HN(CH₂CH₂PR₂)₂ (RPN^HP, R = ⁱPr or Cy), which can participate in metal-ligand cooperation (MLC)⁹ to activate substrates

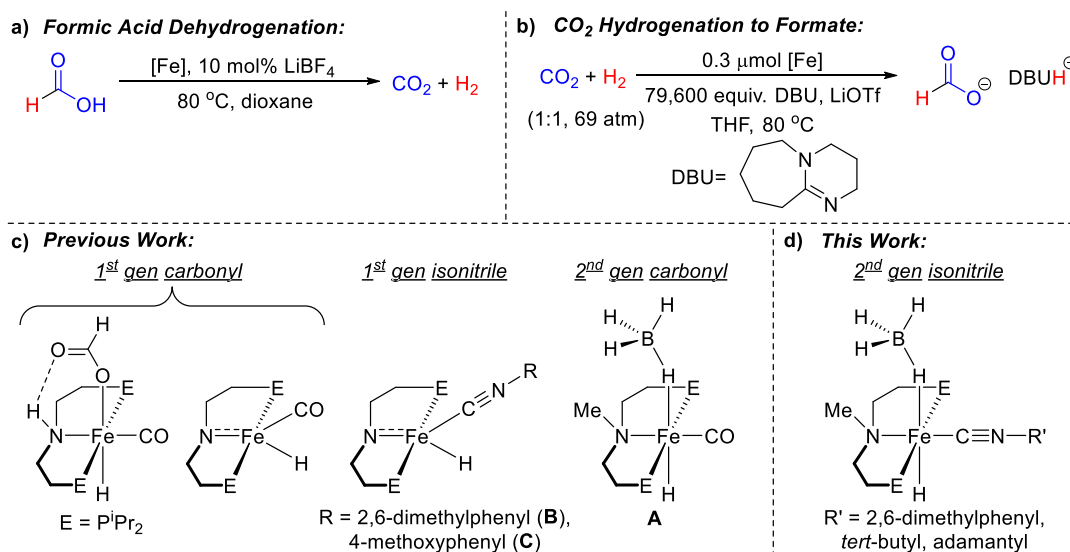


Figure 2.01. **a)** Formic acid dehydrogenation, **b)** CO₂ hydrogenation to formate, **c)** Previous PNP iron catalysts studied by our groups, and **d)** Complexes studied in this work.

when it is in its deprotonated amido form $N(CH_2CH_2P^iPr_2)_2^-$ (RPNP , $R = ^iPr$ or Cy).^{8g, k, 10} We demonstrated that for formic acid dehydrogenation, the iron formate complex $(^iPrPN^H P)Fe(H)\{OC(O)H\}(CO)$ achieves almost 1,000,000 turnovers (TON) with the addition of a Lewis acid (LA) co-catalyst.^{8g} The related precatalyst $(^iPrPNP)Fe(H)(CO)$ gives a TON of almost 9,000 for CO_2 hydrogenation to formate in the presence of a LA co-catalyst and base (Figure 2.01a-c).^{8k} In both cases, these are some of the highest TONs observed for first-row transition metal systems. Subsequently, we developed 2nd generation systems in which the $PN^H P$ ligand was replaced with a PNP ligand containing a tertiary amine that cannot activate substrates via MLC. Complexes of the form $(^RPN^{Me}P)Fe(H)(HBH_3)(CO)$ ($^RPN^{Me}P = CH_3N(CH_2CH_2PR_2)_2$, $R = ^iPr$ or Cy) are an order of magnitude more productive for CO_2 hydrogenation to formate than their 1st generation analogues, affording almost 60,000 TON in the presence of a LA co-catalyst and base (Figure 2.01b-c). However, in both the 1st and 2nd generation systems, catalyst decomposition is a major issue, which needs to be addressed in order to develop improved catalysts.^{8g, k}

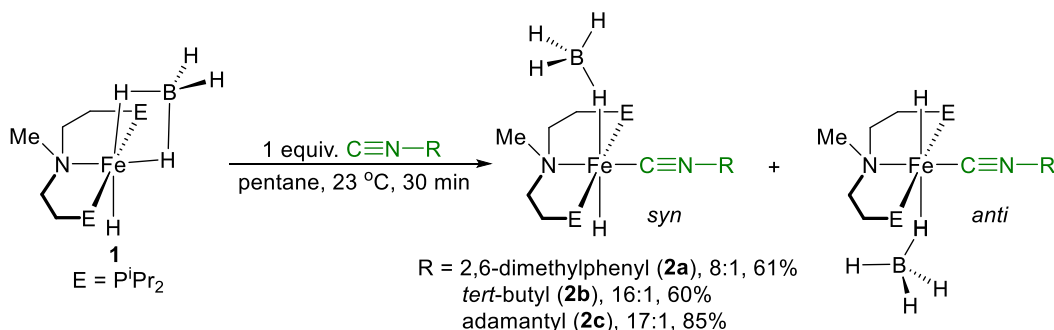
One strategy to prevent catalyst decomposition is to modify the ancillary ligands around the iron. In particular, the replacement of a carbonyl ligand with an isonitrile ligand provides potential benefits because of the tunable steric and electronic properties of isonitriles. In addition, isonitriles could replace the use of carbon monoxide at a late stage of the catalyst synthesis, obviating the need for new method development. Recently, we reported the synthesis of complexes of the form $(^iPrPNP)Fe(H)(C\equiv NR)$ ($R = 2,6$ -dimethylphenyl (**B**), 4-methoxyphenyl (**C**)) (Figure 2.01c), in which the carbonyl ligand of our 1st generation catalysts has been replaced with an isonitrile ligand.¹¹ These complexes

were productive catalysts for CO₂ hydrogenation to formate but showed decreased activity compared to the 1st generation catalysts. Herein, we describe the replacement of the carbonyl ligand with isonitrile ligands in our 2nd generation catalysts featuring ^RPN^{Me}P ligands (Figure 1d). This has resulted in active catalysts for both formic acid dehydrogenation and CO₂ hydrogenation. Our study provides fundamental information about the effect of changing the nature of the π -acid ligand in iron complexes featuring PNP ligands, which may be useful for designing even more active and productive catalysts for a range of hydrogenation and dehydrogenation reactions.

II. Results and Discussion

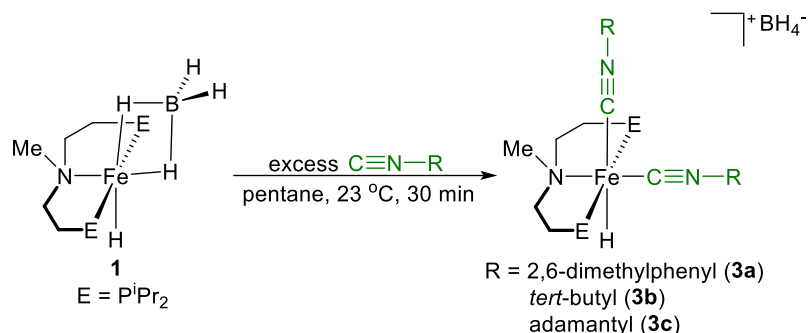
Synthesis and Characterization of PN^{Me}P Iron Isonitrile Precatalysts

The κ^2 -borohydride precursor complex (ⁱPrPN^{Me}P)Fe(H)(κ^2 -H₂BH₂) (**1**) was prepared according to literature procedures.^{8k} Previously, we reported that addition of one atmosphere of carbon monoxide to **1** generates the 2nd generation carbonyl complex (ⁱPrPN^{Me}P)Fe(H)(HBH₃)(CO) (**A**, Figure 2.01c).^{8k} In order to obtain the related isonitrile complexes (ⁱPrPN^{Me}P)Fe(H)(HBH₃)(C \equiv NR) (R = 2,6-dimethylphenyl (**2a**), *tert*-butyl (**2b**), or adamantyl (**2c**)), the procedure was modified and one equivalent of the appropriate isonitrile was added to **1** (Scheme 2.01). Complexes **2a-2c** were obtained in good yields



Scheme 2.01. Synthesis of PN^{Me}P iron isonitrile complexes **2a-2c**.

after purification by recrystallization, provided exactly one equivalent of isonitrile was added. Addition of any excess isonitrile resulted in the formation of cationic bis(isonitrile) iron species of the form $[(^i\text{PrPN}^{\text{Me}}\text{P})\text{Fe}(\text{H})(\text{C}\equiv\text{NR})_2][\text{BH}_4^-]$ ($\text{R} = 2,6\text{-dimethylphenyl}$ (**3a**),



Scheme 2.02. Synthesis of cationic bis(isonitrile) iron species **3a-3c**, which were characterized *in situ*.

tert-butyl (**3b**), or adamantyl (**3c**)) (Scheme 2.02), which were difficult to separate from the desired mono(isonitrile) iron products. Complexes **3a-3c** were not isolated but characterized on the basis of their ^1H NMR spectra, which clearly indicated that two isonitrile ligands were present (see Appendix A). A similar problem involving coordination of two isonitrile ligands was observed in the synthesis of 1st generation isonitrile complexes.¹¹ In fact, the successful isolation of alkyl isonitrile complexes **2b** and **2c** is noteworthy, since in the case of 1st generation isonitrile complexes it was not possible to isolate any complexes with alkyl isonitrile ligands due to the concomitant formation of bis(isonitrile) species.

NMR spectroscopy showed that complexes **2a-2c** are diamagnetic, with two isomers present in solution. We propose, based on observations with related complexes,^{8k} that the two isomers differ in having either *syn*- or *anti*-coplanar arrangements of the N-Me and Fe-HBH₃ moieties, with the *syn*-isomer being the predominant species (Scheme 2.01). At room temperature in C₆D₆, ^{31}P NMR resonances were observed at 91.4 and 95.2 ppm in a 8:1 ratio for **2a**, at 91.3 and 95.6 ppm in a 16:1 ratio for **2b**, and at 91.2 and 95.6

ppm in a 17:1 ratio for **2c**. The ratio of the isomers remains constant when solutions of **2a-2c** are left at room temperature for extended periods of time (~2-3 days) in C₆D₆. However, when a sample of **2b** was heated to 50 °C in C₆D₆ the ratio changed to 5:1, before returning to its original value when the sample was cooled back down to room temperature. This suggests that we are observing the thermodynamic ratio of the isomers and that the isomers interconvert slowly on the NMR timescale. The hydride regions of the room temperature ¹H NMR spectra of **2a-2c** in C₆D₆ were also consistent with the presence of two isomers. Apparent triplet resonances were observed at -21.5 and -21.8 ppm for **2a**, at -22.1 and -22.3 ppm for **2b**, and at -22.1 and -22.3 ppm for **2c**, in the same ratio as the peaks in the ³¹P NMR spectra. At room temperature all three complexes exhibit a broad borohydride signal around -3 ppm that is consistent with κ^1 -BH₄ coordination and suggests rapid interchange of the bound and free B-H protons on the NMR timescale.^{10h, 12} The solid-state IR spectra of **2a-2c** showed broad C-N absorptions at 1970 cm⁻¹ for **2a**, 1990 cm⁻¹ for **2b**, and 2015 cm⁻¹ for **2c**. The C-N absorptions of the free isonitrile ligands occur at 2126 cm⁻¹ (2,6-dimethylphenyl isonitrile), 2137 cm⁻¹ (*tert*-butyl isonitrile), and 2150 cm⁻¹ (adamantyl isonitrile).¹³ Given that the differences between the free isonitrile stretch and coordinated isonitrile stretch are approximately the same for all three complexes, the relative extent of back donation from the iron into the isonitrile π^* -orbital is presumably similar for **2a-2c**.

The solid-state structures of **2a-c** were determined using single-crystal X-ray diffraction (Figure 2.02, Table 2.01). The high quality of the data allowed for the location and free refinement of the Fe-H and B-H hydrogen atoms. The coordination geometry about the iron centers of **2a-c** is distorted octahedral, similar to the carbonyl analog **A**.^{8k}

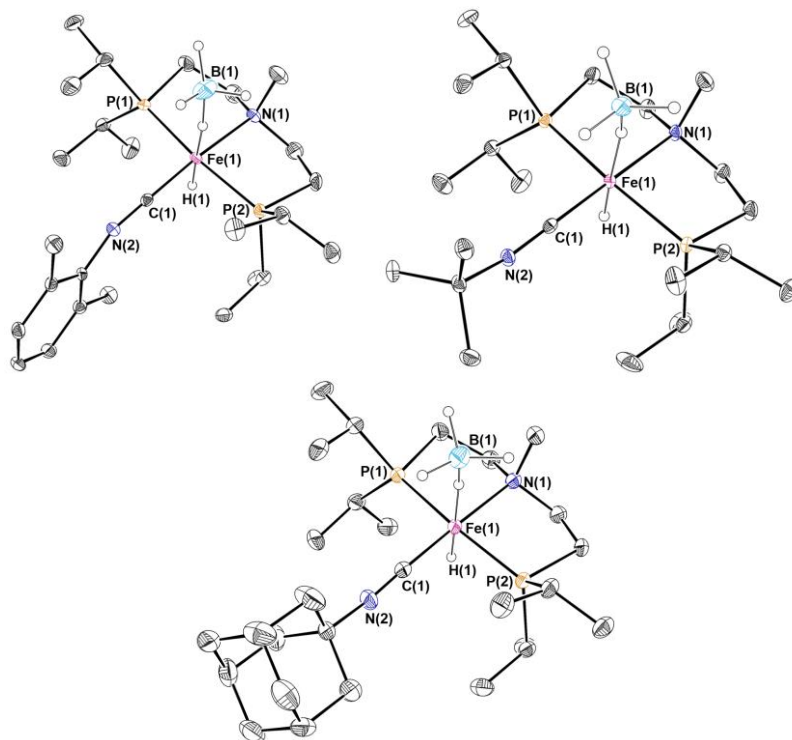


Figure 2.02. Solid-state structures of **2a** (top left), **2b** (top right), and **2c** (bottom) with ellipsoids drawn at 30% probability. Hydrogen atoms besides those attached to iron and boron have been omitted for clarity. All hydrides were located in the difference map and freely refined. Only one molecule from the asymmetric unit of **2c** shown.

As expected the pincer ligand occupies three meridional coordination sites, with the isonitrile ligand *trans* to the nitrogen donor of the pincer ligand. The hydride and κ^1 -BH₄ ligands are *trans* to each other and all three complexes crystallize as the *syn* isomers. Nevertheless, when crystals of **2a**, **2b**, or **2c** were dissolved in C₆D₆ at room temperature a thermodynamic mixture of the *syn* and *anti*-isomers was immediately observed in all cases, suggesting that the establishment of a dynamic equilibrium is rapid. The only major difference in the solid-state structures of the isonitrile complexes and **A** is the Fe–C bond length, which is significantly longer in **2a–2c**. This indicates that the isonitrile ligands are weaker π -acceptors than carbon monoxide. Additionally, the Fe–C bond lengths for **2a–c** are the same within error, which suggests that changing the electronics of the substituent on the isonitrile ligand from aryl (**2a**) to alkyl (**2b** and **2c**) does not have a significant effect

Table 2.01. Selected bond distances (Å) and angles (°) for the (*i*PrPN^{Me}P)Fe isonitrile complexes **2a-2c**, as well as the carbonyl complex **A**.

Complex	Fe–B	Fe–H	Fe–C	Fe–N	Fe–P	C≡Y	P–Fe–P	C≡N–C
2a	2.971(6)	1.39(5)	1.766(3)	2.126(3)	2.2118(9) 2.2159(9)	1.180(4) (Y=N)	169.42(4)	163.0(3)
2b	2.895(4)	1.40(3)	1.776(3)	2.132(2)	2.1985(8) 2.2070(8)	1.182(4) (Y=N)	167.76(3)	157.3(3)
2c^a	2.888(6) 2.927(6)	1.57(4) 1.54(5)	1.776(4) 1.803(5)	2.119(3) 2.128(3)	2.1867(12) 2.1936(12) 2.1885(12) 2.1995(12)	1.175(5) 1.159(5) (Y=N)	165.87(5) 166.83(5)	160.8(4) 165.8(5)
A^{8k}	2.864(3)	1.47(2)	1.728(2)	2.136(1)	2.2031(7) 2.2034(6)	1.162(2) (Y=O)	165.45(3)	-

^aTwo independent molecules are present in the asymmetric unit.

on their back-bonding ability. This is further supported by the similar C≡N–C bond angles observed in the isonitrile ligands of all three complexes, which is also consistent with comparable back-bonding.

Catalytic CO₂ Hydrogenation

The isonitrile iron complexes were tested for their ability to catalyze CO₂ hydrogenation to formate using the optimized conditions previously utilized for **A**.^{8k} Complexes **2a-2c** were found to be effective precatalysts (Table 2.02), with the 2,6-dimethylphenyl isonitrile complex **2a** achieving 5,300 TON, the highest out of these complexes (Table 2.02, entry 2). The alkyl isonitrile complexes **2b** and **2c** achieved 1,300 and 710 TON, respectively (Table 2.02, entries 3 and 4). All three of the 2nd generation isonitrile precatalysts gave considerably higher TON than the 1st generation isonitrile species **B**. We note that under the reaction conditions **B** undergoes a 1,2-addition of H₂ across Fe–N bond to form (*i*PrPN^HP)Fe(H)₂(C≡NR).¹¹ As a consequence, our results with **B** are comparable to those obtained with **2a-2c**, which we propose lose BH₃ in the presence of DBU to form (*i*PrPN^{Me}P)Fe(H)₂(C≡NR). Specifically, the 2,6-dimethylphenyl complex **2a** achieves about an order of magnitude higher TON for this reaction than its 1st generation

isonitrile analog **B** (Table 2.02, entries 2 and 5). This agrees with the previously observed trend that 2nd generation complexes are approximately an order of magnitude more productive for CO₂ hydrogenation than their 1st generation congeners, and suggests that this is a general phenomenon.^{8k} It also indicates that the preparation and evaluation of tertiary PN^RP ligands with other substituents on the nitrogen may lead to more productive catalysts and that ligands capable of MLC are not required for this reaction. Although complexes **2a-2c** are about an order of magnitude less productive than the 2nd generation carbonyl species **A** (Table 2.02, entry 1), they achieve comparable or higher TONs than the majority of the iron catalysts currently described in the literature.^{4b} This demonstrates the privileged nature of ^RPN^{R'}P ligands in generating productive iron catalysts for CO₂ hydrogenation.

Table 2.02. Comparison of iron catalysts for CO₂ hydrogenation to formate.^a

$$\text{CO}_2 + \text{H}_2 \xrightarrow[\text{THF, 80 } ^\circ\text{C, 24 hr}]{\begin{array}{c} 0.3 \text{ } \mu\text{mol [Fe]} \\ 79,600 \text{ equiv. DBU, LiOTf} \end{array}} \text{H}-\text{C}(=\text{O})-\text{O}^- \quad \text{DBUH}^+$$

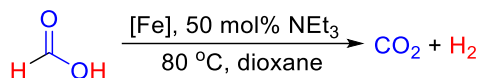
DBU =

Entry	Catalyst	DBU/LiOTf	TON ^{b,c}
1 ^{8k}	A	7.5/1	42,000
2	2a	7.5/1	5,300
3	2b	7.5/1	1,300
4	2c	7.5/1	710
5 ¹¹	B	7.5/1	610

^aReaction conditions: 69 atm of CO₂:H₂ (1:1), 0.3 μmol of catalyst in 10 mL THF (ca 0.01 M), 3.60 g DBU at 80 °C. ^bFormate production quantified by ¹H NMR spectroscopy. ^cReported values are the average of two trials.

Formic Acid Dehydrogenation

The isonitrile complexes **2a-2c** were also investigated for their ability to dehydrogenate formic acid to CO₂ and H₂. In order to provide an accurate comparison to the 2nd generation carbonyl complexes, **A** was also tested in formic acid dehydrogenation

Table 2.03. Comparison of iron catalysts for formic acid dehydrogenation.^a

Entry	Catalyst	mol% [Fe]	TOF (h ⁻¹) ^b	TON (time) ^c
1	A	0.1	750	1,000 (3 h)
2	A	0.01	2,100	2,600 (4 h)
3	2a	0.1	120	140 (4 h)
4	2b	0.1	100	120 (4 h)
5	2c	0.1	110	120 (4 h)
6	B	0.1	30	57 (18 h)

^aReaction conditions: Formic acid (110 μL , 2.91 mmol), [Fe] (0.1 or 0.01 mol%), 50 mol% NEt₃, 5 mL dioxane, 80 $^{\circ}\text{C}$. ^bTurnover frequencies (TOF) were measured after the first hour.

^cTurnover numbers (TON) were measured using a gas burette. The time indicates the point at which no further increase in TON was observed. Reported results are the average of two trials.

(Table 2.03). Triethylamine (NEt₃) was used as an additive at 50 mol% loading, instead of a Lewis acid, in order to remove BH₃ from the precatalysts and generate the proposed catalytically active dihydride species *in situ*. The NEt₃ was added before the precatalysts were treated with formic acid to ensure activation before the NEt₃ was protonated by formic acid. At 0.1 mol% iron loading, complete conversion of formic acid to CO₂ and H₂ was observed in 3 hours using **A** as the precatalyst (Table 2.03, entry 1). When the catalyst loading was decreased to 0.01 mol% iron, the total TON increased to 2,600 over 4 hours (Table 2.03, entry 2). The gas mixture produced from catalysis was analyzed by gas chromatography and no CO was observed. The three isonitrile complexes **2a-2c** were all found to be viable precatalysts, although their TONs were approximately an order of magnitude lower than their carbonyl congener **A**. This follows the trend observed in CO₂ hydrogenation; the isonitrile π -acceptor ligands are less effective at stabilizing catalytic systems than carbonyl ligands. Precatalyst **2a** achieves 140 TON over 4 hours (Table 2.03, entry 3), and **2b** and **2c** both reach 120 TON over 4 hours (Table 2.03, entries 4 and 5) at 0.1 mol% catalyst loading. In addition, the rate of formation of gaseous products from catalysis using **2a** was monitored (see Appendix A) to better understand the activity and

decomposition of the isonitrile complexes **2a-2c**. In the first 30 minutes of catalysis, **2a** reaches an average of 96 out of 140 total TON, or 69% of its total productivity. In contrast, the carbonyl precatalyst **A** reaches 500 TON after 30 minutes, which is only 50% of its total TON. In general, the isonitrile complexes **2a-2c** exhibit high initial activities, but deactivate much more quickly than their carbonyl congener **A**. A comparison was also performed between the 1st and 2nd generation iron isonitrile complexes for formic acid dehydrogenation. Complex **B** reaches only 57 TON over 18 hours (Table 2.03, entry 6). A more direct comparison between **2a-2c** and the analogous 1st generation isonitrile precatalyst (ⁱPrPN^HP)Fe(H)(HBH₃)(2,6-dimethylphenylisonitrile)¹¹ indicated that the 1st generation system was completely inactive for catalysis, although this may be related to the instability of this species at elevated temperatures. Nevertheless, these results demonstrate that the 2nd generation isonitrile complexes **2a-2c** are more productive than their 1st generation congener **B**.

In order to further probe the reason for the relatively poor catalytic performance and rapid deactivation of **2a-2c**, we attempted to synthesize and isolate either the dihydride species (ⁱPrPN^{Me}P)Fe(H)₂(C≡NR) or the formate species (ⁱPrPN^HP)Fe(H){OC(O)H}(C≡NR) (R = 2,6-dimethylphenyl, *tert*-butyl, adamantyl), which are proposed to be catalytic intermediates in both formic acid dehydrogenation and CO₂ hydrogenation.^{8g, k} However, none of these complexes were stable to isolation, and none could be generated cleanly *in situ* (see Appendix A). The instability of these important catalytic intermediates is a likely cause for the decreased catalytic activity of the 2nd generation isonitrile complexes compared to their carbonyl analog **A**. Overall, the catalytic activity of **A** and **2a-2c** for formic acid dehydrogenation highlights the general principle

that a ligand which can cooperate with the metal is not a prerequisite to promote this type of dehydrogenation reaction.¹⁴ This is notable for the design of improved catalytic systems, as the potential to incorporate a substituent other than hydrogen on the nitrogen donor of the pincer ligands expands our ability to tune the properties of these ligands for catalysis.

III. Conclusions

In this work we have prepared three novel $\text{PN}^{\text{Me}}\text{P}$ supported iron precatalysts with isonitrile ligands that are analogs of the related 1st and 2nd generation PN^{HP} and $\text{PN}^{\text{Me}}\text{P}$ iron carbonyl complexes studied extensively in the literature. In contrast to our findings with PN^{HP} supported iron complexes with isonitrile ancillary ligands, it was possible to synthesize $\text{PN}^{\text{Me}}\text{P}$ supported iron precatalysts with both alkyl and aryl isonitrile ligands. The 2nd generation isonitrile complexes are active for both CO_2 hydrogenation to formate as well as formic acid dehydrogenation, however they achieve about an order of magnitude fewer TON for these reactions than the 2nd generation carbonyl complex. While the iron isonitrile complexes reach TON comparable to other published iron catalysts for CO_2 hydrogenation, their decrease in activity relative to the 2nd generation carbonyl system is most likely related to the instability of their catalytic intermediates, which we were unable to cleanly generate. Nevertheless, the catalytic data presented here provides valuable insight into the design of improved iron catalysts for CO_2 hydrogenation and formic acid dehydrogenation. It indicates that for CO_2 hydrogenation $\text{PN}^{\text{Me}}\text{P}$ supported iron catalysts are more productive than the corresponding systems containing a PN^{HP} ligand, and that further modification of the identity of the substituent on the nitrogen donor could lead to systems that give higher TON. It also demonstrates that a ligand that can participate in MLC is not required for formic acid dehydrogenation, which will impact ligand design.

Finally, our results suggest that if the carbonyl ancillary ligand is to be replaced in 1st and 2nd generation PN^HP and PN^{Me}P supported iron catalysts, stronger π -acceptor ligands, such as a nitrosyl ligand, should be pursued rather than weaker π -acceptor ligands. Future work in our laboratories will focus on using these guidelines to modify the primary ligand environment around iron to design more active and productive catalysts.

Supporting Information

For supporting information, including experimental details and procedures, additional experimental information, and information on X-ray diffraction, see Appendix A.

Acknowledgements

Upul Jayarathne and Matthew Mills evaluated the activity of isonitrile containing species for CO₂ hydrogenation.

IV. References

1. (a) Lewis, N. S.; Nocera, D. G., Powering the Planet: Chemical Challenges in Solar Energy Utilization. *Proc. Natl. Acad. Sci. USA* **2006**, *103*, 15729-15735; (b) Ellabban, O.; Abu-Rub, H.; Blaabjerg, F., Renewable Energy Resources: Current Status, Future Prospects and their Enabling Technology. *Renew. Sust. Energ. Rev.* **2014**, *39*, 748-764.
2. Eberle, U.; Felderhoff, M.; Schuth, F., Chemical and Physical Solutions for Hydrogen Storage. *Angew. Chem. Int. Ed.* **2009**, *48*, 6608-6630.
3. (a) Dalebrook, A. F.; Gan, W.; Grasemann, M.; Moret, S.; Laurenczy, G., Hydrogen Storage: Beyond Conventional Methods. *Chem. Commun.* **2013**, *49*, 8735-51; (b) Sordakis, K.; Tang, C.; Vogt, L. K.; Junge, H.; Dyson, P. J.; Beller, M.; Laurenczy, G., Homogeneous

Catalysis for Sustainable Hydrogen Storage in Formic Acid and Alcohols. *Chem. Rev.* **2018**, *118*, 372-433.

4. (a) Mellmann, D.; Sponholz, P.; Junge, H.; Beller, M., Formic acid as a hydrogen storage material - development of homogeneous catalysts for selective hydrogen release. *Chem. Soc. Rev.* **2016**, *45*, 3954-3988; (b) Bernskoetter, W. H.; Hazari, N., Reversible Hydrogenation of Carbon Dioxide to Formic Acid and Methanol: Lewis Acid Enhancement of Base Metal Catalysts. *Acc. Chem. Res.* **2017**, *50*, 1049-1058.

5. Wang, W.-H.; Himeda, Y.; Muckerman, J. T.; Manbeck, G. F.; Fujita, E., CO₂ Hydrogenation to Formate and Methanol as an Alternative to Photo- and Electrochemical CO₂ Reduction. *Chem. Rev.* **2015**, *115*, 12936-12973.

6. When formate is generated instead of formic acid, the wt% H₂ is significantly reduced from 4.4 wt%. For the atom efficient production of formic acid from CO₂ and H₂ for use in H₂ storage it is crucial to generate formic acid and not formate.

7. (a) Chirik, P. J.; Gunnoe, T. B., A Meeting of Metals—A Joint Virtual Issue between Organometallics and ACS Catalysis on First-Row Transition Metal Complexes. *ACS Catal.* **2015**, *5*, 5584-5585; (b) Fuerstner, A., Iron Catalysis in Organic Synthesis: A Critical Assessment of What It Takes To Make This Base Metal a Multitasking Champion. *ACS Cent. Sci.* **2016**, *2*, 778-789.

8. (a) Boddien, A.; Loges, B.; Gärtner, F.; Torborg, C.; Fumino, K.; Junge, H.; Ludwig, R.; Beller, M., Iron-Catalyzed Hydrogen Production from Formic Acid. *J. Am. Chem. Soc.* **2010**, *132*, 8924-8934; (b) Christopher, F.; Albert, B.; Ralf, J.; Reiko, J.; Dyson, P. J.; Rosario, S.; Gabor, L.; Matthias, B., A Well-Defined Iron Catalyst for the Reduction of Bicarbonates and Carbon Dioxide to Formates, Alkyl Formates, and Formamides. *Angew.*

Chem. Int. Ed. **2010**, *49*, 9777-9780; (c) Boddien, A.; Mellmann, D.; Gärtner, F.; Jackstell, R.; Junge, H.; Dyson, P. J.; Laurenczy, G.; Ludwig, R.; Beller, M., Efficient Dehydrogenation of Formic Acid Using an Iron Catalyst. *Science* **2011**, *333*, 1733-1736; (d) Robert, L.; Yael, D. P.; Gregory, L.; Shimon, L. J. W.; Ben-David, Y.; David, M., Low-Pressure Hydrogenation of Carbon Dioxide Catalyzed by an Iron Pincer Complex Exhibiting Noble Metal Activity. *Angew. Chem. Int. Ed.* **2011**, *50*, 9948-9952; (e) Ziebart, C.; Federsel, C.; Anbarasan, P.; Jackstell, R.; Baumann, W.; Spannenberg, A.; Beller, M., Well-Defined Iron Catalyst for Improved Hydrogenation of Carbon Dioxide and Bicarbonate. *J. Am. Chem. Soc.* **2012**, *134*, 20701-20704; (f) Zell, T.; Butschke, B.; Ben-David, Y.; Milstein, D., Efficient Hydrogen Liberation from Formic Acid Catalyzed by a Well-Defined Iron Pincer Complex under Mild Conditions. *Chem. Eur. J.* **2013**, *19*, 8068-8072; (g) Bielinski, E. A.; Lagaditis, P. O.; Zhang, Y.; Mercado, B. Q.; Würtele, C.; Bernskoetter, W. H.; Hazari, N.; Schneider, S., Lewis Acid-Assisted Formic Acid Dehydrogenation Using a Pincer-Supported Iron Catalyst. *J. Am. Chem. Soc.* **2014**, *136*, 10234-10237; (h) Bertini, F.; Mellone, I.; Ienco, A.; Peruzzini, M.; Gonsalvi, L., Iron(II) Complexes of the Linear rac-Tetraphos-1 Ligand as Efficient Homogeneous Catalysts for Sodium Bicarbonate Hydrogenation and Formic Acid Dehydrogenation. *ACS Catal.* **2015**, *5*, 1254-1265; (i) Fong, H.; Peters, J. C., Hydricity of an Fe–H Species and Catalytic CO₂ Hydrogenation. *Inorg. Chem.* **2015**, *54*, 5124-5135; (j) Rivada-Wheelaghan, O.; Dauth, A.; Leitus, G.; Diskin-Posner, Y.; Milstein, D., Synthesis and Reactivity of Iron Complexes with a New Pyrazine-Based Pincer Ligand, and Application in Catalytic Low-Pressure Hydrogenation of Carbon Dioxide. *Inorg. Chem.* **2015**, *54*, 4526-4538; (k) Zhang, Y.; MacIntosh, A. D.; Wong, J. L.; Bielinski, E. A.; Williard, P. G.; Mercado, B. Q.; Hazari,

N.; Bernskoetter, W. H., Iron Catalyzed CO₂ Hydrogenation to Formate Enhanced by Lewis Acid Co-Catalysts. *Chem. Sci.* **2015**, *6*, 4291-4299; (l) Mellone, I.; Gorgas, N.; Bertini, F.; Peruzzini, M.; Kirchner, K.; Gonsalvi, L., Selective Formic Acid Dehydrogenation Catalyzed by Fe-PNP Pincer Complexes Based on the 2,6-Diaminopyridine Scaffold. *Organometallics* **2016**, *35*, 3344-3349; (m) Bertini, F.; Gorgas, N.; Stöger, B.; Peruzzini, M.; Veiros, L. F.; Kirchner, K.; Gonsalvi, L., Efficient and Mild Carbon Dioxide Hydrogenation to Formate Catalyzed by Fe(II) Hydrido Carbonyl Complexes Bearing 2,6-(Diaminopyridyl)diphosphine Pincer Ligands. *ACS Catal.* **2016**, *6*, 2889-2893.

9. The standard definition of metal-ligand cooperation (MLC) is that both the metal and the ligand are directly involved in the bond activation process. For more information see: Khusnutdinova, J. R.; Milstein, D. Metal–Ligand Cooperation. *Angew. Chem. Int. Ed.* **2015**, *54*, 12236-12273.

10. (a) Alberico, E.; Sponholz, P.; Cordes, C.; Nielsen, M.; Drexler, H. J.; Baumann, W.; Junge, H.; Beller, M., Selective Hydrogen Production from Methanol with a Defined Iron Pincer Catalyst under Mild Conditions. *Angew. Chem. Int. Ed.* **2013**, *52*, 14162-14166; (b) Chakraborty, S.; Dai, H.; Bhattacharya, P.; Fairweather, N. T.; Gibson, M. S.; Krause, J. A.; Guan, H., Iron-Based Catalysts for the Hydrogenation of Esters to Alcohols. *J. Am. Chem. Soc.* **2014**, *136*, 7869-7872; (c) Chakraborty, S.; Lagaditis, P. O.; Forster, M.; Bielinski, E. A.; Hazari, N.; Holthausen, M. C.; Jones, W. D.; Schneider, S., Well-Defined Iron Catalysts for the Acceptorless Reversible Dehydrogenation-Hydrogenation of Alcohols and Ketones. *ACS Catal.* **2014**, *4*, 3994-4003; (d) Chakraborty, S.; Brennessel, W. W.; Jones, W. D., A Molecular Iron Catalyst for the Acceptorless Dehydrogenation and

Hydrogenation of N-Heterocycles. *J. Am. Chem. Soc.* **2014**, *136*, 8564-8567; (e) Bornschein, C.; Werkmeister, S.; Wendt, B.; Jiao, H.; Alberico, E.; Baumann, W.; Junge, H.; Junge, K.; Beller, M., Mild and Selective Hydrogenation of Aromatic and Aliphatic (di)nitriles with a Well-Defined Iron Pincer Complex. *Nat. Commun.* **2014**, *5*, 4111; (f) Qu, S.; Dai, H.; Dang, Y.; Song, C.; Wang, Z.-X.; Guan, H., Computational Mechanistic Study of Fe-Catalyzed Hydrogenation of Esters to Alcohols: Improving Catalysis by Accelerating Precatalyst Activation with a Lewis Base. *ACS Catal.* **2014**, *4*, 4377-4388; (g) Fillman, K. L.; Bielinski, E. A.; Schmeier, T. J.; Nesvet, J. C.; Woodruff, T. M.; Pan, C. J.; Takase, M. K.; Hazari, N.; Neidig, M. L., Flexible Binding of PNP Pincer Ligands to Monomeric Iron Complexes. *Inorg. Chem.* **2014**, *53*, 6066-6072; (h) Koehne, I.; Schmeier, T. J.; Bielinski, E. A.; Pan, C. J.; Lagaditis, P. O.; Bernskoetter, W. H.; Takase, M. K.; Würtele, C.; Hazari, N.; Schneider, S., Synthesis and Structure of Six-Coordinate Iron Borohydride Complexes Supported by PNP Ligands. *Inorg. Chem.* **2014**, *53*, 2133-2143; (i) Bielinski, E. A.; Förster, M.; Zhang, Y.; Bernskoetter, W. H.; Hazari, N.; Holthausen, M. C., Base-Free Methanol Dehydrogenation Using a Pincer-Supported Iron Compound and Lewis Acid Co-catalyst. *ACS Catal.* **2015**, *5*, 2404-2415; (j) Fairweather, N. T.; Gibson, M. S.; Guan, H., Homogeneous Hydrogenation of Fatty Acid Methyl Esters and Natural Oils under Neat Conditions. *Organometallics* **2015**, *34*, 335-339; (k) Bonitatibus, P. J., Jr.; Doherty, M. D.; Siclovan, O.; Soloveichik, G. L.; Chakraborty, S.; Jones, W. D., Reversible Catalytic Dehydrogenation of Alcohols for Energy Storage. *Proc. Natl. Acad. Sci. USA* **2015**, *112*, 1687-92; (l) Sharninghausen, L. S.; Mercado, B. Q.; Crabtree, R. H.; Hazari, N., Selective Conversion of Glycerol to Lactic Acid with Iron Pincer Precatalysts. *Chem. Commun.* **2015**, *51*, 16201-16204; (m) Glüer, A.; Foerster, M.;

Celinski, V. R.; Schmedt auf der Guenne, J.; Holthausen, M. C.; Schneider, S., Highly Active Iron Catalyst for Ammonia Borane Dehydrocoupling at Room Temperature. *ACS Catal.* **2015**, *5*, 7214-7217; (n) Yang, X., Bio-inspired computational design of iron catalysts for the hydrogenation of carbon dioxide. *Chem. Commun.* **2015**, *51*, 13098-13101; (o) Peña-López, M.; Neumann, H.; Beller, M., Iron(II) Pincer-Catalyzed Synthesis of Lactones and Lactams through a Versatile Dehydrogenative Domino Sequence. *ChemCatChem* **2015**, *7*, 865-871; (p) Lange, S.; Elangovan, S.; Cordes, C.; Spannenberg, A.; Jiao, H.; Junge, H.; Bachmann, S.; Scalone, M.; Topf, C.; Junge, K.; Beller, M., Selective Catalytic Hydrogenation of Nitriles to Primary Amines Using Iron Pincer Complexes. *Catal. Sci. Technol.* **2016**, *6*, 4768-4772; (q) Rezayee, N. M.; Samblanet, D. C.; Sanford, M. S., Iron-Catalyzed Hydrogenation of Amides to Alcohols and Amines. *ACS Catal.* **2016**, *6*, 6377-6383; (r) Xu, R.; Chakraborty, S.; Bellows, S. M.; Yuan, H.; Cundari, T. R.; Jones, W. D., Iron-Catalyzed Homogeneous Hydrogenation of Alkenes under Mild Conditions by a Stepwise, Bifunctional Mechanism. *ACS Catal.* **2016**, *6*, 2127-2135; (s) Schneck, F.; Assmann, M.; Balmer, M.; Harms, K.; Langer, R., Selective Hydrogenation of Amides to Amines and Alcohols Catalyzed by Improved Iron Pincer Complexes. *Organometallics* **2016**, *35*, 1931-1943; (t) Sawatlon, B.; Surawatanawong, P., Mechanisms for dehydrogenation and hydrogenation of N-heterocycles using PNP-pincer-supported iron catalysts: a density functional study. *Dalton Trans.* **2016**, *45*, 14965-14978; (u) Bornschein, C.; Gustafson Karl, P. J.; Verho, O.; Beller, M.; E., B. J.-. Evaluation of Fe and Ru Pincer-Type Complexes as Catalysts for the Racemization of Secondary Benzylic Alcohols. *Chem. Eur. J.* **2016**, *22*, 11583-11586; (v) Dong, K.; Elangovan, S.; Sang, R.; Spannenberg, A.; Jackstell, R.; Junge, K.; Li, Y.; Beller, M., Selective Catalytic

Two-Step Process for Ethylene Glycol from Carbon Monoxide. *Nature Commun.* **2016**, *7*, 12075; (w) Kothandaraman, J.; Goeppert, A.; Czaun, M.; Olah, G. A.; Surya Prakash, G. K., CO₂ capture by amines in aqueous media and its subsequent conversion to formate with reusable ruthenium and iron catalysts. *Green Chem.* **2016**, *18*, 5831-5838; (x) Xia, T.; Wei, Z.; Spiegelberg, B.; Jiao, H.; Hinze, S.; de Vries Johannes, G., Isomerization of Allylic Alcohols to Ketones Catalyzed by Well-Defined Iron PNP Pincer Catalysts. *Chem. Eur. J.* **2017**, *24*, 4043-4049; (y) Jayarathne, U.; Zhang, Y.; Hazari, N.; Bernskoetter, W. H., Selective Iron-Catalyzed Deaminative Hydrogenation of Amides. *Organometallics* **2017**, *36*, 409-416; (z) Bellows, S. M.; Chakraborty, S.; Gary, J. B.; Jones, W. D.; Cundari, T. R., An Uncanny Dehydrogenation Mechanism: Polar Bond Control over Stepwise or Concerted Transition States. *Inorg. Chem.* **2017**, *56*, 5519-5524; (aa) Anke, F.; Han, D.; Klahn, M.; Spannenberg, A.; Beweries, T., Formation of high-molecular weight polyaminoborane by Fe hydride catalysed dehydrocoupling of methylamine borane. *Dalton Trans.* **2017**, *46*, 6843-6847; (ab) Nguyen Duc, H.; Morin, Y.; Zhang, L.; Trivelli, X.; Capet, F.; Paul, S.; Desset, S.; Dumeignil, F.; Gauvin Régis, M., Oxidative Transformations of Biosourced Alcohols Catalyzed by Earth-Abundant Transition Metals. *ChemCatChem* **2017**, *9*, 2652-2660; (ac) Lane, E. M.; Uttley, K. B.; Hazari, N.; Bernskoetter, W. H., Iron-Catalyzed Amide Formation from the Dehydrogenative Coupling of Alcohols and Secondary Amines. *Organometallics* **2017**, *36*, 2020-2025; (ad) Yi, Y.; Liu, H.; Xiao, L. P.; Wang, B.; Song, G., Highly Efficient Hydrogenation of Levulinic Acid into γ -Valerolactone using an Iron Pincer Complex. *ChemSusChem* **2018**, *11*, 1474-1478; (ae) Lane, E. M.; Hazari, N.; Bernskoetter, W. H., Iron-Catalyzed Urea

Synthesis: Dehydrogenative Coupling of Methanol and Amines. *Chem. Sci.* **2018**, 9, 4003-4008.

11. Smith, N. E.; Bernskoetter, W. H.; Hazari, N.; Mercado, B. Q., Synthesis and Catalytic Activity of PNP-Supported Iron Complexes with Ancillary Isonitrile Ligands. *Organometallics* **2017**, 36, 3995-4004.

12. (a) Marks, T. J.; Kolb, J. R., Covalent Transition Metal, Lanthanide, and Actinide Tetrahydroborate Complexes. *Chem. Rev.* **1977**, 77, 263-293; (b) Langer, R.; Iron Mark, A.; Konstantinovski, L.; Diskin-Posner, Y.; Leitun, G.; Ben-David, Y.; Milstein, D., Iron Borohydride Pincer Complexes for the Efficient Hydrogenation of Ketones under Mild, Base-Free Conditions: Synthesis and Mechanistic Insight. *Chem. Eur. J.* **2012**, 18, 7196-7209.

13. (a) Sasaki, T.; Eguchi, S.; Katada, T., Synthesis of Adamantane Derivatives. XXV. Synthesis and Reactions of 1- and 2-Adamantyl Isocyanides. *J. Org. Chem.* **1974**, 39, 1239-1242; (b) Kool, L. B.; Rausch, M. D.; Alt, H. G.; Engelhardt, H. E.; Herberhold, M., Synthesis and characterization of bis-isonitrile complexes $\text{Cp}_2\text{M}(\text{CNR})_2$ ($\text{M} = \text{Ti}, \text{Zr}$; $\text{R} = 2,6\text{-dimethylphenyl}$). *J. Organomet. Chem.* **1986**, 317, C38-C40; (c) Edwards, D. A.; Tetrick, S. M.; Walton, R. A., The Vibrational Spectra of t-butyl Isocyanide and the Homoleptic Cations $[\text{M}(\text{CNCMe}_3)_6]^{n+}$ ($\text{M} = \text{Re}$, $n = 1$; $\text{M} = \text{Ru}$ and Os , $n = 2$) as their Hexafluorophosphate Salts. *J. Organomet. Chem.* **1988**, 349, 383-391.

14. Dub, P. A.; Gordon, J. C., Metal–Ligand Bifunctional Catalysis: The “Accepted” Mechanism, the Issue of Concertedness, and the Function of the Ligand in Catalytic Cycles Involving Hydrogen Atoms. *ACS Catal.* **2017**, 7, 6635-6655.

Chapter 3: Additive-Free Formic Acid Dehydrogenation Using a Pincer-Supported Iron Catalyst

This work has been previously published as: Curley, J. B., Bernskoetter, W. H., and Hazari, N. *ChemCatChem*, **2020**, 12, 1934-1938.

I. Introduction

The potentially devastating environmental and economic consequences associated with the continued use of fossil fuels make the replacement of these finite feedstocks with clean and renewable energy sources one of the most significant challenges facing society.¹ However, many sustainable energy sources such as wind and solar are inherently intermittent, and their widespread adoption will require the development of efficient methods for energy storage. H₂ is a clean energy carrier that can be directly combusted or electrochemically oxidized in a fuel cell, while only producing water as a byproduct.² Although H₂ has a high energy density by weight, its low volumetric density limits its practicality for large scale applications. Therefore, liquid organic hydrogen carriers (LOHCs) that can release H₂ on demand are currently being widely studied as alternatives to energy intensive and expensive H₂ compression and liquification.³ Formic acid (4.4 wt% H₂), which can in principle be renewably obtained from biomass oxidation or CO₂ hydrogenation, could be an attractive LOHC if efficient catalysts for the dehydrogenation of formic acid to generate H₂ and CO₂ are developed.

The vast majority of homogeneous catalysts for formic acid dehydrogenation (FADH) utilize precious metals such as ruthenium and iridium.^{3b,4} Recently, there has been growing interest in replacing these expensive and rare metals with more cost effective

catalysts based on earth abundant first row transition metals such as iron, cobalt, nickel, and manganese.⁵ Although a number of base metal catalysts have been developed for FADH, in most cases significant activity is only observed in the presence of additives such as excess ligand, exogenous base, or a Lewis acid.^{3b} For example, we reported that $(i\text{PrPN}^{\text{H}}\text{P})\text{Fe}(\text{H})(\text{CO})\{\text{OC}(\text{O})\text{H}\}$ (**1**, $i\text{PrPN}^{\text{H}}\text{P} = \text{HN}(\text{CH}_2\text{CH}_2\text{P}^i\text{Pr}_2)_2$) gives 980,000 turnovers for FADH in dioxane, but only when the Lewis acid LiBF_4 is used as a co-catalyst to assist in turnover-limiting decarboxylation. In contrast, **1** gives a maximum of only 180 turnovers under related conditions without a Lewis acid.⁶ The use of additives is not thermodynamically required in FADH, and complicates the incorporation of a catalyst into a device.

To date, there are a limited number of precious metal catalysts for additive-free FADH, and it is rare that they achieve turnover numbers (TONs) greater than 100,000.^{3b, 7} Similarly, the few additive-free base metal catalysts give a maximum TON of only approximately 1,000 (Figure 3.01a).⁸ In these base metal systems the active catalyst is

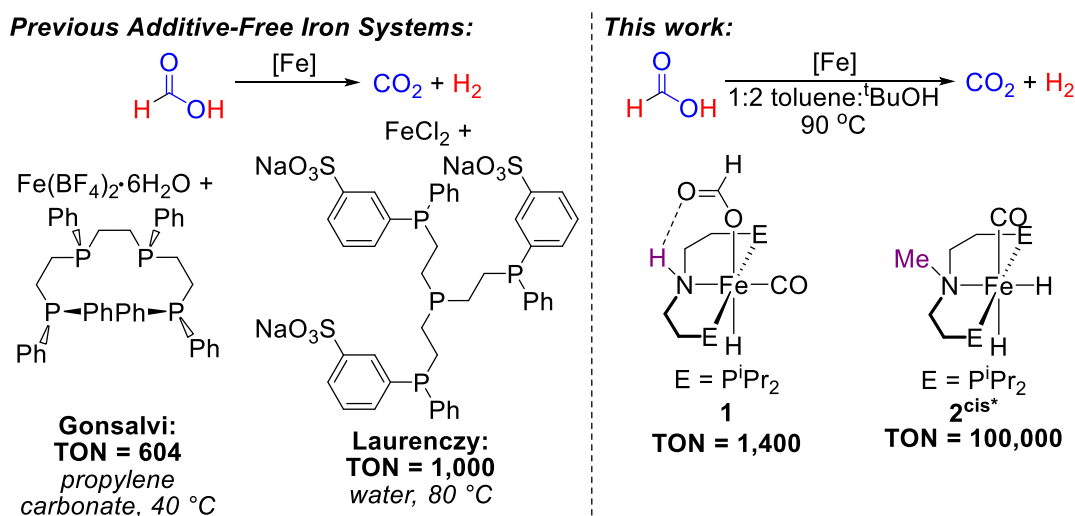


Figure 3.01. a) Previously reported iron systems for additive-free formic acid dehydrogenation⁸ and **b)** catalysts used in this work. *When **2** is used as a catalyst, **2^{trans}**, where the two hydride ligands are *trans* to each other, is present in addition to **2^{cis}**. At room temperature the equilibrium ratio between **2^{cis}** and **2^{trans}** is approximately 3:1.

generated *in situ*, which means that free ligand, potentially present from incomplete formation of the active catalyst, could be playing a role in the catalytic reaction. Herein, we report a well-defined pincer-supported iron catalyst for additive-free FADH which gives TONs of up to 100,000 (Figure 3.01b). This is two orders of magnitude larger than any previous base metal system for additive-free FADH. Mechanistic studies provide both an explanation for the high productivity of our system as well as guidance for future catalyst design.

II. Results and Discussion

Optimization of Catalytic Conditions

Recent work exploring the kinetics of CO₂ insertion into transition metal hydrides, the microscopic reverse of the proposed turnover-limiting decarboxylation step in FADH, indicate that these reactions are faster in polar solvents.⁹ Similarly, computational work on the elementary steps involved in FADH indicate that the barrier to decarboxylation is lower in polar solvents.¹⁰ This suggests that the development of systems for additive-free FADH would be aided by the use of polar solvents. However finding transition metal hydrides, especially first-row complexes, that are stable in polar solvents is challenging. For example, iron hydrides related to **1** are unstable in both non-polar and polar solvents.⁶ Our groups recently reported the syntheses of iron complexes featuring the tertiary amine ligand ⁱPrPN^{Me}P (ⁱPrPN^{Me}P = CH₃N(CH₂CH₂PⁱPr₂)₂) and demonstrated that the resulting hydride complexes were significantly more stable than those supported by the ⁱPrPN^HP ligand.¹¹ Therefore, we postulated that species containing the ⁱPrPN^{Me}P ligand should be superior catalysts for additive-free FADH compared to **1**.

To evaluate our hypothesis, (ⁱPrPN^{Me}P)Fe(H)₂(CO) (**2**, present at room temperature as a 3:1 ratio of the *cis*-dihydride species **2^{cis}** and the *trans*-dihydride species **2^{trans}**)¹² was used for additive-free FADH in a variety of high boiling solvents (Table 3.01). In dioxane, **2** gives 1000 turnovers after 4 hours, which is approximately five times larger than that previously reported for **1** (180, 48 hours).⁶ In fact, our unoptimized results show that **2** gives comparable productivity to other state-of-the-art base metal catalysts for additive-free FADH⁸ and is active in solvents ranging from water to toluene. However, contrary to our expectations, the highest TONs were observed in relatively non-polar solvents such as dioxane, diphenyl ether, and toluene (Entries 8-10) rather than more polar solvents such as 1,3-dimethyl-2-imidazolidinone (DMI), N-methyl-2-pyrrolidone (NMP) or *tert*-amyl alcohol (Entries 3-5), which we proposed would aid decarboxylation. Kinetic analysis of these reactions showed that initial turnover frequencies (TOFs) in polar solvents were quite high, but that catalyst death was also rapid. In many cases, no turnovers were observed after 2 hours in polar solvents, whereas in non-polar solvents the catalyst was active for up

Table 3.01. Performance of **2** in additive-free FADH in different solvents.^a

$\text{H}-\overset{\text{O}}{\parallel}\text{C}-\text{OH} \xrightarrow[80\text{ }^{\circ}\text{C}]{\text{2 (0.01 mol\%)}} \text{CO}_2 + \text{H}_2$					
Entry	Solvent	Dielectric Constant	TOF (h ⁻¹) ^b	TON (time) ^c	Yield
1	Propylene carbonate	64.0	360	400 (2 h)	4.0%
2	Water	78.5	480	650 (5 h)	6.5%
3	NMP	32.0	590	670 (2 h)	6.7%
4	DMI	37.6	830	850 (2 h)	8.5%
5	<i>tert</i> -amyl alcohol	5.82	770	890 (2 h)	8.9%
6	Chlorobenzene	2.71	880	940 (4 h)	9.4%
7	Diglyme	7.23	750	970 (4 h)	9.7%
8	1,4-Dioxane	2.21	890	1,000 (4 h)	10%
9	Diphenyl ether	3.65	1,000	1,100 (4 h)	11%
10	Toluene	2.42	950	1,100 (6 h)	11%
11	Propyl acetate	8.10	1,000	1,200 (6 h)	12%

^aReaction conditions: Formic acid (110 μ L, 2.91 mmol), **2** (0.01 mol%, 291 μ L of a 1 mM stock solution in toluene), 4.70 mL solvent, 80 $^{\circ}$ C. ^bTOFs (turnover frequencies) were measured after the first hour. ^cTONs were measured using a gas buret. The time indicates the point at which no further increase in TON was observed. Reported results are the average of two trials, errors \pm 10%. NMP=N-methyl-2-pyrrolidone, DMI=1,3-dimethyl-2-imidazolidinone.

to 6 hours. We hypothesized that by using a mixed solvent system consisting of a non-polar solvent to slow down catalyst decomposition and a polar solvent to aid decarboxylation, we would see improved activity and productivity. A series of experiments were performed in varying mixtures of toluene and ^tBuOH (Table 3.02). At a toluene:^tBuOH ratio of 1:2, a maximum TON of 1,700 was reached after 6 hours (Entry 4), significantly higher than the 1,100 turnovers obtained in pure toluene. In general, the best results were obtained with toluene:^tBuOH mixtures of between 2:1 and 1:2 (Entries 2-4), with little variation in catalytic activity within this range. When mixtures with higher amounts of toluene or ^tBuOH were used (Entries 1 & 5), we observed decreased performance. The temperature and initial formic acid concentration used in catalysis were subsequently optimized using a 1:2 toluene:^tBuOH mixture (see Appendix B for optimization). Under our optimized conditions, a TON of 2,600 in 5 hours at 90 °C was obtained using 0.01 mol% **2**. Gas chromatography performed on the gaseous reaction products confirmed production of a 1:1 mixture of H₂ and CO₂ with no CO detected, indicating that **2** is highly selective for FADH (see Appendix B).

Table 3.02. FADH catalyzed by **2** in using different ratios of toluene:^tBuOH.^a

$\text{H}-\overset{\text{O}}{\parallel}\text{C}-\text{OH} \xrightarrow[\text{toluene:}^t\text{BuOH, 80 }^\circ\text{C}]{\textbf{2 (0.01 mol\%)}} \text{CO}_2 + \text{H}_2$				
Entry	Toluene: ^t BuOH	TOF (h ⁻¹) ^b	TON (time) ^c	Yield
1	3:1	980	1,200 (4 h)	12%
2	2:1	1,200	1,600 (8 h)	16%
3	1:1	1,200	1,400 (8 h)	14%
4	1:2	1,300	1,700 (6 h)	17%
5	1:3	1,100	1,300 (6 h)	13%

^aReaction conditions: Formic acid (110 μL, 2.91 mmol), **2** (0.01 mol%), 291 μL of a 1 mM stock solution in toluene), 5.00 mL total reaction volume, 80 °C. ^bTurnover frequencies (TOF) were measured after the first hour. ^cTurnover numbers (TON) were measured using a gas buret. The time indicates the point at which no further increase in TON was observed. Reported results are the average of two trials, errors ± 10%.

We tested a series of iron complexes supported by a pincer ligand containing either a secondary amine, ⁱPrPN^HP, or tertiary amine, ⁱPrPN^{Me}P, using the optimized catalytic

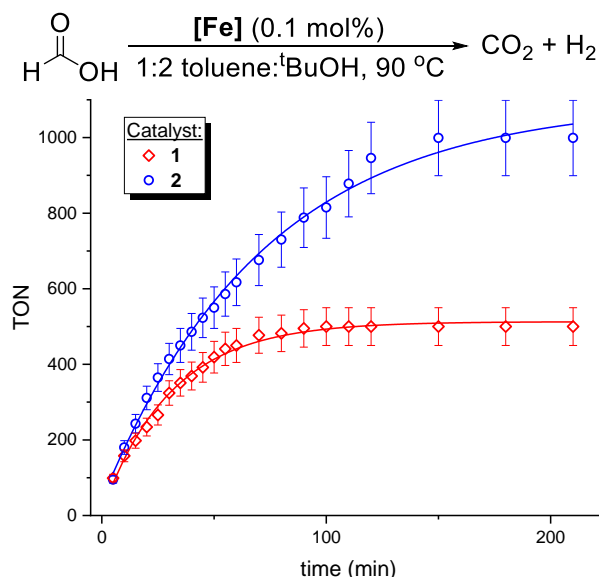


Figure 3.02. Kinetic traces comparing the rates of additive-free FADH using **1** and **2**; error bars $\pm 10\%$.

conditions for **2** (see Table B.03) to identify the most efficient catalyst. All $i\text{PrPN}^{\text{MeP}}$ species evaluated achieved higher TONs than the $i\text{PrPN}^{\text{HP}}$ complexes, and **2** was found to be the most productive catalyst (see Appendix B). Complex **1** only gave 1,400 turnovers after 7 hours compared to 2,600 for **2** at 0.01 mol% catalyst loading. This supports our hypothesis that catalytic intermediates ligated by $i\text{PrPN}^{\text{MeP}}$ are more stable than those ligated by $i\text{PrPN}^{\text{HP}}$, and this is likely why **2** shows superior productivity for additive-free FADH. We attribute the improved performance of **1** in additive-free FADH in a toluene: $t\text{BuOH}$ mixture compared to our previous results in dioxane⁶ to the presence of the polar solvent mixture which promotes decarboxylation to a greater degree than it enhances the rate of catalyst decomposition.⁹ The difference between **1** and **2** is even larger at 0.1 mol% catalyst loading (Figure 3.02), with **2** reaching full conversion in 3 hours, while **1** only gives 500 turnovers and is inactive after less than 2 hours. Additionally, **2** is a more active catalyst than **1** under these conditions, as its initial TOF is significantly higher (see Appendix B). The catalyst loading of our best catalyst, **2**, was lowered to assess if even higher TONs could be reached

Table 3.03. Performance of **2** for additive-free FADH at different catalyst loadings.^a

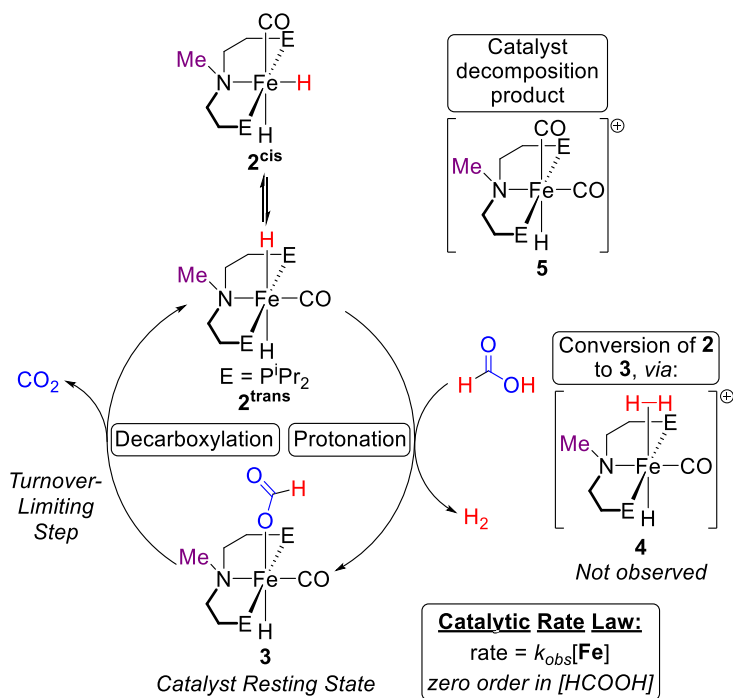
$\text{H}-\overset{\text{O}}{\parallel}{\text{C}}-\text{OH} \xrightarrow[\text{1:2 toluene:}^t\text{BuOH, 90 }^\circ\text{C}]{\text{2 (X mol\%)}} \text{CO}_2 + \text{H}_2$				
Entry	X (mol%)	TOF (h ⁻¹) ^b	TON (time) ^c	Yield
1	0.1	640	1,000 (3 h)	100%
2	0.01	2,100	2,600 (5 h)	26%
3	0.001	13,000	16,000 (5 h)	16%
4	0.0001	62,000	100,000 (6 h)	10%

^a**Reaction conditions:** Formic acid (110 μL , 2.91 mmol), **2** (1 mM stock solution in toluene), 1.67 mL toluene (total), 3.33 mL ^tBuOH, 90 $^\circ\text{C}$. ^bTOFs were measured after the first hour. ^cTONs were measured using a gas buret. The time indicates the point at which no further increase in TON was observed. Reported results are the average of two trials, errors \pm 10%.

(Table 3.03). At 0.001 mol%, **2** achieves 16,000 turnovers (Entry 3), and when the loading is further decreased to 0.0001 mol%, **2** gives a TON of 100,000 (Entry 4). The observed increase in TONs as iron concentration decreases suggests a catalyst decomposition mechanism that is greater than first order in iron. This is the highest TON reported for any homogeneous base metal catalyst for additive-free FADH and is comparable to some of the best precious metal systems.^{3b, 7d-g}

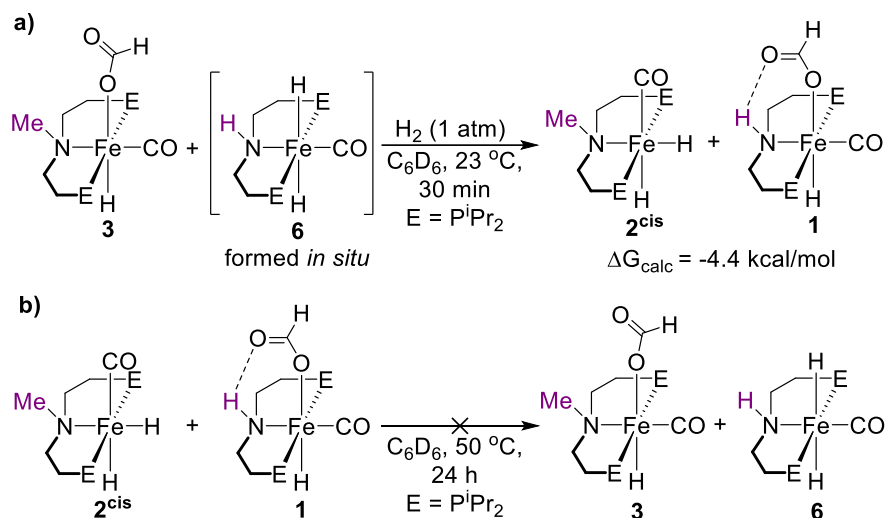
Mechanistic Studies

Given the high activity of **2**, we performed mechanistic studies to elucidate the elementary steps in the catalytic cycle. A stoichiometric experiment indicated that addition of one equivalent of formic acid to **2** resulted in clean formation of (ⁱPrPN^{Me}P)Fe(H)(CO){OC(O)H} (**3**)¹³ and H₂, likely via the unobserved dihydrogen complex **4**. Only the isomers of **3** with the formate *trans* to the hydride are observed, and we propose that regardless of which isomer of **2** is protonated, the formate rapidly equilibrates to form only the *trans* isomers (see Appendix B). Heating **3** under static vacuum regenerates **2** and releases CO₂. Presumably, under our catalytic conditions, where gaseous products are removed from the reaction mixture, there is also sufficient driving force to liberate CO₂ from **3**. On the basis of these experiments, we propose the simple two



Scheme 3.01. Proposed mechanism for additive-free FADH using **2**.

step mechanism shown in Scheme 3.01, which is analogous to that proposed for FADH using **1** and a Lewis acid.⁶ *In situ* ^{31}P NMR spectroscopy performed on a model reaction showed that the formate complex **3** is the catalytic resting state, indicating that decarboxylation is turnover-limiting (see Appendix B). In agreement with this proposal, kinetics experiments show that the reaction is zero order in [formic acid] and first order in [iron] (see Appendix B).¹⁴ Additionally, ^{31}P , ^1H , and ^{13}C NMR and IR spectroscopies indicate that **2** decomposes to the inactive species $[(^i\text{PrPN}^{\text{Me}}\text{P})\text{Fe}(\text{H})(\text{CO})_2]^+$ (**5**) during catalysis (see Appendix B). An experiment performed with ^{13}C -labelled formic acid determined that the second carbonyl ligand in **5** is not generated via dehydration of formic acid to form CO and H_2O . These results again suggest a catalyst decomposition mechanism that is greater than first order in iron. Notably, our proposed mechanism does not involve any elementary steps requiring metal-ligand cooperation (MLC), in which both the metal and ligand are directly involved in bond activation. This is one of only a few examples of



Scheme 3.02. Crossover experiments performed to probe the thermodynamic relationship between **3** and **1**; **a**) reaction between **3** and **6** and **b**) reaction between **1** and **2**.

high activity in a dehydrogenation reaction catalyzed by a base metal that does not involve a MLC pathway.^{11b, 15}

Several experiments were performed to understand the differences in catalysis between **1** and **2**. First, variable temperature NMR experiments show that **2** and **3** are in equilibrium under static vacuum, which indicates that decarboxylation of **3** is kinetically accessible and approximately thermoneutral under those conditions (see Appendix B). In contrast, no (ⁱPrPN^HP)Fe(H)₂(CO) is formed when **1** is exposed to vacuum for prolonged times at elevated temperatures, consistent with a significantly higher kinetic barrier for decarboxylation and/or with decarboxylation from **1** being thermodynamically disfavored. To further establish that decarboxylation of **1** is less favorable than decarboxylation of **3**, crossover experiments were performed. Initially, the ⁱPrPN^{Me}P formate complex **3** and amido complex (ⁱPrPNP)Fe(H)(CO) (ⁱPrPNP = N(CH₂CH₂PⁱPr₂)₂⁻) were combined in a 1:1 ratio. An atmosphere of H₂ was added to generate (ⁱPrPN^HP)Fe(H)₂(CO) (**6**) *in situ*,⁶ and complete conversion to the dihydride **2** and formate **1** were observed after 30 minutes at room temperature (Scheme 3.02a). Conversely, a 1:1 mixture of **2** and **1** monitored for 24

hours at 50 °C did not undergo any exchange (Scheme 3.02b). Taken together these experiments illustrate that decarboxylation from **3** is kinetically accessible under mild conditions in the absence of additives and that the formation of **1** from **6** and CO₂ is more thermodynamically preferred than the formation of **3** from **2** and CO₂. DFT calculations were performed to quantify these results. They indicate that thermodynamically (ΔG), decarboxylation of **1** is 8.5 kcal/mol uphill, whereas decarboxylation of **3** is unfavorable by only 4.0 kcal/mol (see Appendix B), which agrees with our experimental results. The corresponding kinetic barriers (ΔG^\ddagger) for decarboxylation of **1** and **3** are 20.2 and 26.7 kcal/mol, respectively. This shows that even though decarboxylation of **1** is thermodynamically disfavored relative to **3**, it is kinetically more facile. Therefore, we attribute the higher catalytic activity we observe using **2** compared with **1** to the increased stability of the ⁱPrPN^{Me}P system under the reaction conditions.^{15e}

Given that decarboxylation is turnover-limiting, it was postulated that catalysis using **2** could be improved by adding Lewis acids. However, when FADH was performed under our optimized conditions in the presence of different Lewis acids (LiOTf, NaOTf, and LiNTf), no improvement in activity was observed, and instead these additives had a deleterious effect on catalyst performance (see Appendix B). This is in agreement with previous mechanistic studies that show that Lewis acid effects on CO₂ insertion (or the microscopic reverse, decarboxylation) are highly solvent dependent.⁹ In this case, they also suggest that the presence of Lewis acids leads to more rapid catalyst decomposition, which has previously been observed in hydrogenation reactions using an ⁱPrPN^{Me}P iron precatalyst.¹⁶

III. Conclusions

In conclusion, we have developed an iron catalyst for additive-free FADH that can achieve 100,000 turnovers, which is the highest of any base metal system to date and is comparable to many precious metal systems. The excellent performance of catalysts ligated by the $i\text{PrPN}^{\text{Me}}\text{P}$ ligand can be attributed to their improved stability relative to catalysts ligated by $i\text{PrPN}^{\text{H}}\text{P}$. Our work is significant on a fundamental level as it is one of only a few to establish that a pathway involving MLC is not required to generate highly active and productive dehydrogenation catalysts.¹⁷ It also suggests that further improvement in catalysis can be achieved by lowering the barrier for decarboxylation and improving catalyst stability. Future work in our groups will focus on modifying the pincer ligand to solve these challenges.

Supporting Information

For supporting information, including experimental details and procedures as well as additional experimental information, see Appendix B.

Acknowledgements

All computational work was supported by the facilities and staff of the Yale University Faculty of Arts and Sciences High Performance Computing Center.

IV. References

1. (a) Lewis, N. S.; Nocera, D. G., Powering the Planet: Chemical Challenges in Solar Energy Utilization. *Proc. Natl. Acad. Sci. U.S.A* **2006**, *103*, 15729-15735; (b) Ellabban, O.; Abu-Rub, H.; Blaabjerg, F., Renewable Energy Resources: Current Status, Future Prospects and their Enabling Technology. *Renew. Sustain. Energy Rev.* **2014**, *39*, 748-764;

- (c) Burkart, M. D.; Hazari, N.; Tway, C. L.; Zeitler, E. L., Opportunities and Challenges for Catalysis in Carbon Dioxide Utilization. *ACS Catal.* **2019**, *9*, 7937-7956.
2. Eberle, U.; Felderhoff, M.; Schuth, F., Chemical and Physical Solutions for Hydrogen Storage. *Angew. Chem. Int. Ed.* **2009**, *48*, 6608-6630.
3. (a) Dalebrook, A. F.; Gan, W.; Grasemann, M.; Moret, S.; Laurenczy, G., Hydrogen Storage: Beyond Conventional Methods. *Chem. Commun.* **2013**, *49*, 8735-51; (b) Sordakis, K.; Tang, C.; Vogt, L. K.; Junge, H.; Dyson, P. J.; Beller, M.; Laurenczy, G., Homogeneous Catalysis for Sustainable Hydrogen Storage in Formic Acid and Alcohols. *Chem. Rev.* **2018**, *118*, 372-433.
4. (a) Wang, W.-H.; Himeda, Y.; Muckerman, J. T.; Manbeck, G. F.; Fujita, E., CO₂ Hydrogenation to Formate and Methanol as an Alternative to Photo- and Electrochemical CO₂ Reduction. *Chem. Rev.* **2015**, *115*, 12936-12973; (b) Mellmann, D.; Sponholz, P.; Junge, H.; Beller, M., Formic acid as a hydrogen storage material - development of homogeneous catalysts for selective hydrogen release. *Chem. Soc. Rev.* **2016**, *45*, 3954-3988; (c) Bernskoetter, W. H.; Hazari, N., Reversible Hydrogenation of Carbon Dioxide to Formic Acid and Methanol: Lewis Acid Enhancement of Base Metal Catalysts. *Acc. Chem. Res.* **2017**, *50*, 1049-1058.
5. (a) Chirik, P. J.; Gunnoe, T. B., A Meeting of Metals—A Joint Virtual Issue between Organometallics and ACS Catalysis on First-Row Transition Metal Complexes. *ACS Catal.* **2015**, *5*, 5584-5585; (b) Fuerstner, A., Iron Catalysis in Organic Synthesis: A Critical Assessment of What It Takes To Make This Base Metal a Multitasking Champion. *ACS Cent. Sci.* **2016**, *2*, 778-789.

6. Bielinski, E. A.; Lagaditis, P. O.; Zhang, Y.; Mercado, B. Q.; Würtele, C.; Bernskoetter, W. H.; Hazari, N.; Schneider, S., Lewis Acid-Assisted Formic Acid Dehydrogenation Using a Pincer-Supported Iron Catalyst. *J. Am. Chem. Soc.* **2014**, *136*, 10234-10237.
7. (a) Wang, Z.; Lu, S.-M.; Li, J.; Wang, J.; Li, C., Unprecedentedly High Formic Acid Dehydrogenation Activity on an Iridium Complex with an N,N'-Diimine Ligand in Water. *Chem. Eur. J.* **2015**, *21*, 12592-12595; (b) Jantke, D.; Pardatscher, L.; Drees, M.; Cokoja, M.; Herrmann, W. A.; Kühn, F. E., Hydrogen Production and Storage on a Formic Acid/Bicarbonate Platform using Water-Soluble N-Heterocyclic Carbene Complexes of Late Transition Metals. *ChemSusChem* **2016**, *9*, 2849-2854; (c) Iguchi, M.; Himeda, Y.; Manaka, Y.; Kawanami, H., Development of an Iridium-Based Catalyst for High-Pressure Evolution of Hydrogen from Formic Acid. *ChemSusChem* **2016**, *9*, 2749-2753; (d) Prichatz, C.; Trincado, M.; Tan, L.; Casas, F.; Kammer, A.; Junge, H.; Beller, M.; Grützmacher, H., Highly Efficient Base-Free Dehydrogenation of Formic Acid at Low Temperature. *ChemSusChem* **2018**, *11*, 3092-3095; (e) Wang, S.; Huang, H.; Roisnel, T.; Bruneau, C.; Fischmeister, C., Base-Free Dehydrogenation of Aqueous and Neat Formic Acid with Iridium(III) Cp*(dipyridylamine) Catalysts. *ChemSusChem* **2019**, *12*, 179-184; (f) Fink, C.; Laurency, G., A Precious Catalyst: Rhodium-Catalyzed Formic Acid Dehydrogenation in Water. *Euro. J. Inorg. Chem.* **2019**, 2381-2387; (g) Onishi, N.; Kanega, R.; Fujita, E.; Himeda, Y., Carbon Dioxide Hydrogenation and Formic Acid Dehydrogenation Catalyzed by Iridium Complexes Bearing Pyridyl-Pyrazole Ligands: Effect of an Electron-Donating Substituent on the Pyrazole Ring on the Catalytic Activity and Durability. *Adv. Synth. Catal.* **2019**, *361*, 289-296.

8. (a) Bertini, F.; Mellone, I.; Ienco, A.; Peruzzini, M.; Gonsalvi, L., Iron(II) Complexes of the Linear *rac*-Tetraphos-1 Ligand as Efficient Homogeneous Catalysts for Sodium Bicarbonate Hydrogenation and Formic Acid Dehydrogenation. *ACS Catal.* **2015**, *5*, 1254-1265; (b) Montandon-Clerc, M.; Dalebrook, A. F.; Laurenczy, G., Quantitative Aqueous Phase Formic Acid Dehydrogenation Using Iron(II) Based Catalysts. *J. Catal.* **2016**, *343*, 62-67; (c) Neary, M. C.; Parkin, G., Nickel-Catalyzed Release of H₂ from Formic Acid and a New Method for the Synthesis of Zerovalent Ni(PMe₃)₄. *Dalton Trans.* **2016**, *45*, 14645-14650.
9. (a) Heimann, J. E.; Bernskoetter, W. H.; Hazari, N.; Mayer, J. M., Acceleration of CO₂ Insertion into Metal Hydrides: Ligand, Lewis Acid, and Solvent Effects on Reaction Kinetics. *Chem. Sci.* **2018**, *8*, 6629-6638; (b) Heimann, J. E.; Bernskoetter, W. H.; Hazari, N., Understanding the Individual and Combined Effects of Solvent and Lewis Acid on CO₂ Insertion into a Metal Hydride. *J. Am. Chem. Soc.* **2019**, *141*, 10520-10529.
10. Govindarajan, N.; Meijer, E. J., Elucidating cation effects in homogeneously catalyzed formic acid dehydrogenation. *Faraday Discuss.* **2019**.
11. (a) Zhang, Y.; MacIntosh, A. D.; Wong, J. L.; Bielinski, E. A.; Williard, P. G.; Mercado, B. Q.; Hazari, N.; Bernskoetter, W. H., Iron Catalyzed CO₂ Hydrogenation to Formate Enhanced by Lewis Acid Co-Catalysts. *Chem. Sci.* **2015**, *6*, 4291-4299; (b) Curley, J. B.; Smith, N. E.; Bernskoetter, W. H.; Hazari, N.; Mercado, B. Q., Catalytic Formic Acid Dehydrogenation and CO₂ Hydrogenation Using Iron PN^RP Pincer Complexes with Isonitrile Ligands. *Organometallics* **2018**, *37*, 3846-3853.
12. For another example of cis/trans dihydride species implicated in (de)hydrogenative catalysis, see: Gorgas, N.; Stöger, B.; Veiros, L. F.; Kirchner, K. Highly Efficient and

Selective Hydrogenation of Aldehydes: A Well-Defined Fe(II) Catalyst Exhibits Noble-Metal Activity. *ACS Catal.* **2016**, *6*, 2664-2672.

13. Complex 3 is observed as a 5:1 mixture of 2 isomers at room temperature. Only the major isomer is shown in the figures. Further details about the isomers can be found in the SI, section SII.

14. A same-excess experiment showed that a negligible amount of catalyst decomposition occurs in the initial regime where we performed our kinetic analysis (see SI). Therefore, we do not think that catalyst decomposition influences our results.

15. (a) Khusnutdinova, J. R.; Milstein, D., Metal–Ligand Cooperation. *Angew. Chem. Int. Ed.* **2015**, *54*, 12236-12273; (b) Alig, L.; Fritz, M.; Schneider, S., First-Row Transition Metal (De)Hydrogenation Catalysis Based On Functional Pincer Ligands. *Chem. Rev.* **2019**, *119*, 2681-2751; (c) Bauer, G.; Kirchner, K. A., Well-Defined Bifunctional Iron Catalysts for the Hydrogenation of Ketones: Iron, the New Ruthenium. *Angew. Chem. Int. Ed.* **2011**, *50*, 5798-5800; (d) Eisenstein, O.; Crabtree, R. H., Outer sphere hydrogenation catalysis. *New J. Chem.* **2013**, *37*, 21-27; (e) Gusev, D. G., Dehydrogenative Coupling of Ethanol and Ester Hydrogenation Catalyzed by Pincer-Type YNP Complexes. *ACS Catal.* **2016**, *6*, 6967-6981; (f) Mellone, I.; Gorgas, N.; Bertini, F.; Peruzzini, M.; Kirchner, K.; Gonsalvi, L., Selective Formic Acid Dehydrogenation Catalyzed by Fe-PNP Pincer Complexes Based on the 2,6-Diaminopyridine Scaffold. *Organometallics* **2016**, *35*, 3344-3349; (g) Zhao, B.; Han, Z.; Ding, K., The N–H Functional Group in Organometallic Catalysis. *Angew. Chem. Int. Ed.* **2013**, *52*, 4744-4788.

16. Jayarathne, U.; Hazari, N.; Bernskoetter, W. H., Selective Iron-Catalyzed N-Formylation of Amines using Dihydrogen and Carbon Dioxide. *ACS Catalysis* **2018**, *8*, 1338-1345.
17. (a) Pinggen, D.; Choi, J.-H.; Allen, H.; Murray, G.; Ganji, P.; van Leeuwen, P. W. N. M.; Prechtel, M. H. G.; Vogt, D., Amide versus amine ligand paradigm in the direct amination of alcohols with Ru-PNP complexes. *Catalysis Science & Technology* **2018**, *8*, 3969-3976; (b) Ye, X.; Plessow, P. N.; Brinks, M. K.; Schelwies, M.; Schaub, T.; Rominger, F.; Paciello, R.; Limbach, M.; Hofmann, P., Alcohol Amination with Ammonia Catalyzed by an Acridine-Based Ruthenium Pincer Complex: A Mechanistic Study. *Journal of the American Chemical Society* **2014**, *136*, 5923-5929; (c) Agapova, A.; Alberico, E.; Kammer, A.; Junge, H.; Beller, M., Catalytic Dehydrogenation of Formic Acid with Ruthenium-PNP-Pincer Complexes: Comparing N-Methylated and NH-Ligands. *ChemCatChem* **2019**, *11*, 1910-1914; (d) Marziale, A. N.; Friedrich, A.; Klopsch, I.; Drees, M.; Celinski, V. R.; Schmedt auf der Gönne, J.; Schneider, S., The Mechanism of Borane–Amine Dehydrocoupling with Bifunctional Ruthenium Catalysts. *Journal of the American Chemical Society* **2013**, *135*, 13342-13355; (e) Choi, J.-H.; Heim, L. E.; Ahrens, M.; Prechtel, M. H. G., Selective conversion of alcohols in water to carboxylic acids by in situ generated ruthenium trans dihydrido carbonyl PNP complexes. *Dalton Transactions* **2014**, *43*, 17248-17254.

Chapter 4: Control of Catalyst Speciation Using an N-Phenyl Substituted MACHO-Type Ligand in CO₂ Hydrogenation and Formic Acid Dehydrogenation

Clayton Hert performed all CO₂ hydrogenation experiments and assisted in interpreting the catalytic data.

I. Introduction

Transition metal complexes supported by pincer ligands are ubiquitous in catalysis due to their high thermal stability, modular design, and facile tunability.¹ In particular, pincer ligands of the type ^RPN^HP (^RPN^HP = HN(CH₂CH₂PR₂)₂, R = Et, ⁱPr, Cy, ^tBu, Ph) have attracted significant interest due to their ability to support highly active catalysts for a wide variety of transformations.² For example, ^RPN^HP supported complexes have been extensively utilized to perform dehydrogenation and hydrogenation reactions relevant to both renewable energy storage^{3,4,5,6,7} and the synthesis of fine and commodity chemicals.^{8,9,10,11,12} Notably, the complex Ru-MACHO ((^{Ph}PN^HP)RuHCl(CO)) is used commercially in the hydrogenation of esters.^{9c} As a result of the high activity and versatility of catalysts supported by ^RPN^HP ligands, a large amount of research has been performed to understand the effects of varying the substituents on the phosphine donors of ^RPN^HP type ligands, and there is considerable understanding about how to optimize these substituents to maximize catalytic activity.^{3d, 4a, c, e, f, 6b, 7a, 9b, d, 10d, e, 11c-e, 11g, 12a} Conversely, there are few reports exploring the consequences of changing the substituent on the nitrogen donor, and there is little knowledge about how this impacts catalytic performance (Figure 4.01a).

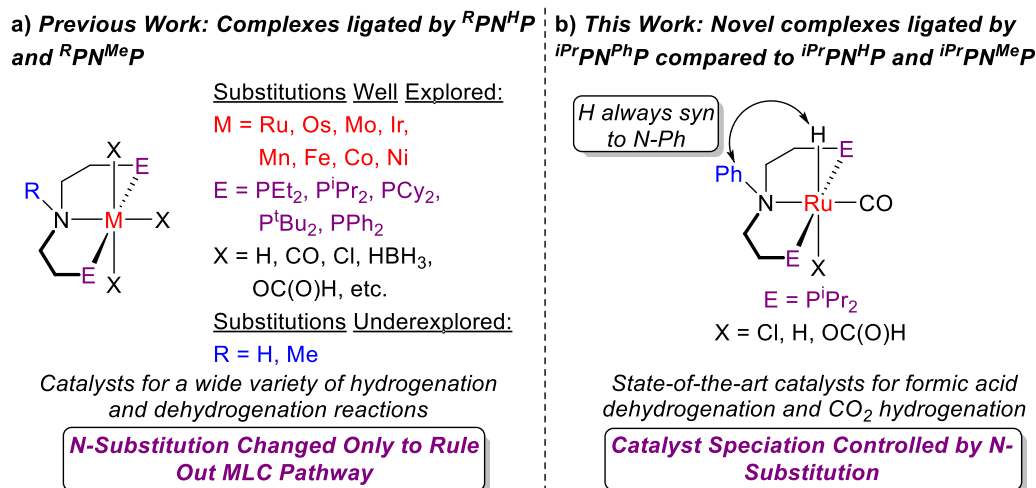


Figure 4.01. a) Previous investigations of $^R\text{PN}^H\text{P}$ and $^R\text{PN}^{\text{Me}}\text{P}$ ligated complexes, and b) Ru $^i\text{PrPN}^{\text{Ph}}\text{P}$, $^i\text{PrPN}^H\text{P}$, and $^i\text{PrPN}^{\text{Me}}\text{P}$ complexes compared in this work.

The limited studies investigating the influence of changing the N-substituent on $^R\text{PN}^H\text{P}$ type ligands have typically solely explored whether the mechanism of catalysis involves metal-ligand cooperativity (MLC).¹³ For this reason, the simple tertiary amine-based $^R\text{PN}^{\text{Me}}\text{P}$ ($^R\text{PN}^{\text{Me}}\text{P} = \text{CH}_3\text{N}(\text{CH}_2\text{CH}_2\text{PR}_2)_2$, $R = \text{Et, } ^i\text{Pr, Cy, } ^t\text{Bu, Ph}$) ligand has been almost exclusively utilized.^{4d, g, 5e, g, 6a, c, 9d, g, 10b, c, i, 11e, 12b} However, even this small change to the ligand results in large differences in chemistry. For example, $^R\text{PN}^{\text{Me}}\text{P}$ supported complexes often require different synthetic routes compared to their $^R\text{PN}^H\text{P}$ congeners.^{5e, 11c, 12b} Additionally, metal hydride complexes ligated by $^R\text{PN}^{\text{Me}}\text{P}$ are frequently observed as a mixture of isomers in solution, with both *syn* and *anti* conformations present (*syn* and *anti* refer in this report to the orientation of the hydride ligand with respect to the substituent on the N donor), which complicates understanding of their reactivity.^{4d, 5g} In contrast, largely due to hydrogen bonding, metal hydrides supported by $^R\text{PN}^H\text{P}$ ligands almost always have an *anti* conformation^{4d, 5c, 14} and at this stage, it is difficult to selectively form *syn* hydride complexes supported by $^R\text{PN}^R\text{P}$ type ligands.

The change in ligand from $^R\text{PN}^{\text{H}}\text{P}$ to $^R\text{PN}^{\text{Me}}\text{P}$ can also have a profound impact on catalytic performance. Two notable examples relate to carbon dioxide hydrogenation and formic acid hydrogenation, which are important transformations in the development of sustainable strategies for renewable energy storage.¹⁵ Although Fe catalysts ligated by $^{\text{iPr}}\text{PN}^{\text{Me}}\text{P}$ give more than 60,000 turnovers for CO_2 hydrogenation to formate, their $^{\text{iPr}}\text{PN}^{\text{H}}\text{P}$ analogues give only approximately 9,000 turnovers under the same conditions.^{5e} Similarly, in the microscopic reverse formic acid dehydrogenation reaction, an Fe catalyst supported by $^{\text{iPr}}\text{PN}^{\text{Me}}\text{P}$ gives approximately 100,000 turnovers, while the related catalyst supported by $^{\text{iPr}}\text{PN}^{\text{H}}\text{P}$ gives only 1,400 turnovers under the same conditions.^{5g} These examples illustrate the general principle that in many hydrogenation and dehydrogenation reactions, a ligand that can participate in MLC is not required. Further, the stark differences in activity and speciation between $^{\text{iPr}}\text{PN}^{\text{H}}\text{P}$ and $^{\text{iPr}}\text{PN}^{\text{Me}}\text{P}$ complexes demonstrate the need for detailed studies exploring $^R\text{PN}^{\text{R'}}\text{P}$ ligands with N-substituents that are not a proton or a methyl group to design improved catalysts.¹⁶

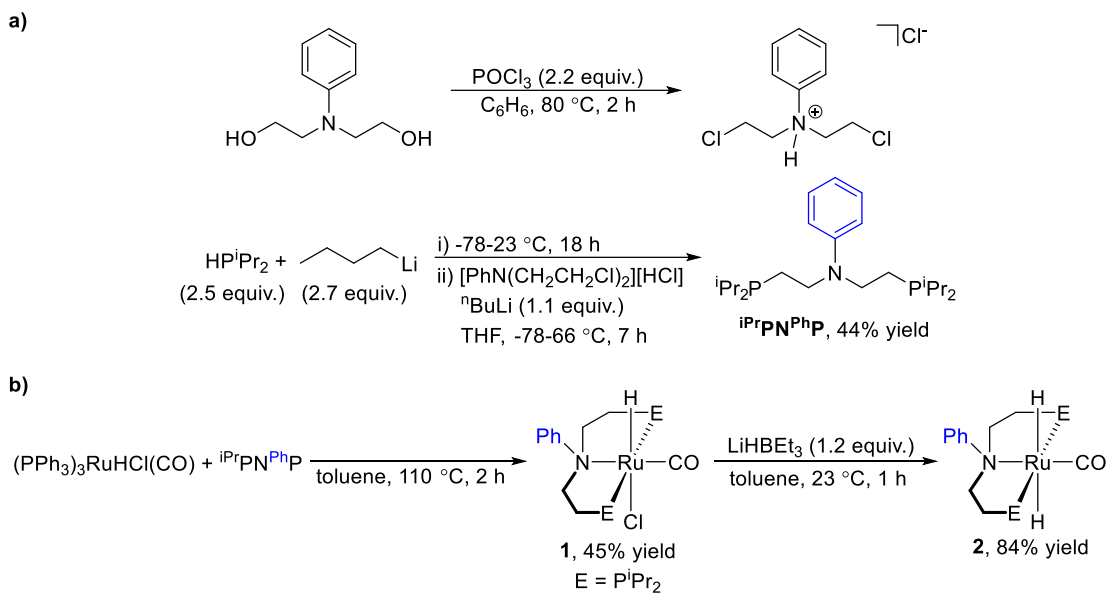
Here, we report the synthesis and characterization of the novel pincer ligand $^{\text{iPr}}\text{PN}^{\text{Ph}}\text{P}$ ($^{\text{iPr}}\text{PN}^{\text{Ph}}\text{P} = \text{PhN}(\text{CH}_2\text{CH}_2\text{P}^{\text{iPr}}_2)_2$), which contains a phenyl substituent on the nitrogen donor. By preparing Ru hydride complexes supported by the new ligand, we demonstrate that the $^{\text{iPr}}\text{PN}^{\text{Ph}}\text{P}$ ligand results in the first set of $^R\text{PN}^{\text{R'}}\text{P}$ ligated complexes that adopt only the *syn* conformation both in solution and in the solid state (Figure 4.01b). This provides a new strategy for controlling the speciation of complexes supported by $^R\text{PN}^{\text{R'}}\text{P}$ ligands, which has rarely been studied.¹⁷ We extend our synthetic results to catalysis by comparing the catalytic performance of three Ru complexes ($^{\text{iPr}}\text{PN}^{\text{R'}}\text{P}$)Ru(H)₂(CO) ($\text{R}' = \text{H}, \text{Me}, \text{or Ph}$) in formic acid dehydrogenation and CO_2 hydrogenation to formate. We

observe that the catalyst ligated by $i\text{PrPN}^{\text{Ph}}\text{P}$ is the most active in both reactions under the optimal conditions, with performance that is comparable to the leading molecular catalysts. In the case of CO_2 hydrogenation, the stability of the $(i\text{PrPN}^{\text{R}'}\text{P})\text{Ru}(\text{H})_2(\text{CO})$ complexes allow us to elucidate a previously unidentified autocatalytic effect in which the product formate salt increases activity. For both reactions, we perform mechanistic studies including DFT calculations to understand the activity of the $i\text{PrPN}^{\text{Ph}}\text{P}$ ligated complexes. These studies show that in formic acid dehydrogenation there is a kinetic advantage for catalysts that operate through the *syn* isomer. Overall, this work provides fundamental information about developing improved catalysts for dehydrogenation and hydrogenation reactions by highlighting the importance of varying the substituent on the nitrogen donor in $\text{RPN}^{\text{R}'}\text{P}$ type ligands. It also suggests that even greater improvements in catalytic activity can be obtained by further tuning of this often overlooked substituent.

II. Results and Discussion

Synthesis of $i\text{PrPN}^{\text{Ph}}\text{P}$ Ligand and Associated Ru Complexes

The N-phenyl substituted pincer ligand $i\text{PrPN}^{\text{Ph}}\text{P}$ was synthesized using a modified procedure to that utilized to prepare $i\text{PrPN}^{\text{Me}}\text{P}$ (Scheme 4.01a).^{10b} Specifically, in the first step commercially available $\text{PhN}(\text{CH}_2\text{CH}_2\text{OH})_2$ was chlorinated with an excess of phosphorus oxychloride to generate $[\text{PhN}(\text{CH}_2\text{CH}_2\text{Cl})_2][\text{HCl}]$, which can also be purchased commercially. The $[\text{PhN}(\text{CH}_2\text{CH}_2\text{Cl})_2][\text{HCl}]$ salt was then treated with lithium diisopropylphosphide, which was generated *in situ* through the reaction of HP^iPr with a slight excess of $^n\text{BuLi}$. This produced crude $i\text{PrPN}^{\text{Ph}}\text{P}$, which could easily be purified by extraction in pentane to give the pure ligand as a lightly colored oil in 44% yield. We



Scheme 4.01. Synthesis of **a)** $iPrPN^{Ph}P$, and **b)** $(iPrPN^{Ph}P)RuHCl(CO)$ (**1**) and $(iPrPN^{Ph}P)Ru(H)_2(CO)$ (**2**).

typically used this synthesis, which technically only requires one synthetic step from commercially available precursors, to generate one gram of ligand at a time. The free $iPrPN^{Ph}P$ ligand was characterized using NMR spectroscopy and mass spectrometry, and is air sensitive due to the tendency of the phosphorus atoms to oxidize upon exposure to oxygen.

Given the high catalytic activity of Ru monohydride and dihydride complexes supported by $iPrPN^{H}P$ and $iPrPN^{Me}P$ ligands in a range of hydrogenation and dehydrogenation reactions,^{4, 9} we coordinated our new $iPrPN^{Ph}P$ ligand to Ru. Using a procedure modified from that for the synthesis of $(iPrPN^{Me}P)RuHCl(CO)$ (**1-Me**),^{4d} we prepared $(iPrPN^{Ph}P)RuHCl(CO)$ (**1**) via the reaction of $iPrPN^{Ph}P$ with the commonly utilized Ru precursor $(PPh_3)_3RuHCl(CO)$ in refluxing toluene (Scheme 4.01b). The moderate yield, 45%, is related to the need to perform a number of successive recrystallizations of **1** from cold Et_2O in order to remove residual triphenylphosphine. Compound **1** has a single

resonance in the $^{31}\text{P}\{^1\text{H}\}$ NMR spectrum at 67.4 ppm corresponding to ligated $^{\text{iPr}}\text{PN}^{\text{Ph}}\text{P}$, and a triplet resonance in the ^1H spectrum at -14.40 ppm corresponding to a Ru hydride.

Interestingly, the peak at 8.01 ppm which corresponds to the two aromatic protons *ortho* to the N atom on the $^{\text{iPr}}\text{PN}^{\text{Ph}}\text{P}$ ligand is broad at room temperature. At -50 °C, this peak separates into two distinct resonances, each corresponding to a single proton, at 9.05 and 7.07 ppm (see Appendix C). In fact, at -50 °C all five of the aromatic protons on the $^{\text{iPr}}\text{PN}^{\text{Ph}}\text{P}$ ligand have distinct chemical shifts, indicating free rotation of the phenyl ring in solution at room temperature and restricted rotation at lower temperatures (see Appendix C). In contrast to $(^{\text{iPr}}\text{PN}^{\text{H}}\text{P})\text{RuHCl}(\text{CO})$ (**1-H**) and **1-Me**, which exist as mixtures of *syn* and *anti* isomers in solution, only one isomer of **1** is observed by NMR spectroscopy. Two dimensional ^1H NOESY NMR spectroscopy indicates that in this isomer the hydride ligand is *syn* to the N-phenyl group (see Appendix C). We propose that the increased steric bulk of the N-phenyl substituent in $^{\text{iPr}}\text{PN}^{\text{Ph}}\text{P}$ disfavors the formation of the *anti* isomer, which would place the sterically more demanding Cl ligand on the same face as the phenyl group.

Single crystals of **1** suitable for X-ray diffraction were grown by slow diffusion of hexamethyldisiloxane (HMDSO) into a concentrated THF solution at -35 °C. The solid state structure, shown in Figure 4.02a, is distorted octahedral about Ru, with the $^{\text{iPr}}\text{PN}^{\text{Ph}}\text{P}$ ligand binding in the expected *meridional* fashion. The hydride was not located in the difference map, but the position of the ‘vacant’ coordination site indicates that it is oriented *syn* to the phenyl group on the nitrogen donor, consistent with the proposed solution state structure (*vide supra*). The Ru–N distance in **1** is 2.327(5) Å, which is significantly longer than the corresponding Ru–N distances in **1-H** and **1-Me**, which are 2.1949(18) Å and 2.247(2) Å, respectively.^{4d} This suggests that the nitrogen atom in $^{\text{iPr}}\text{PN}^{\text{Ph}}\text{P}$ is a weaker

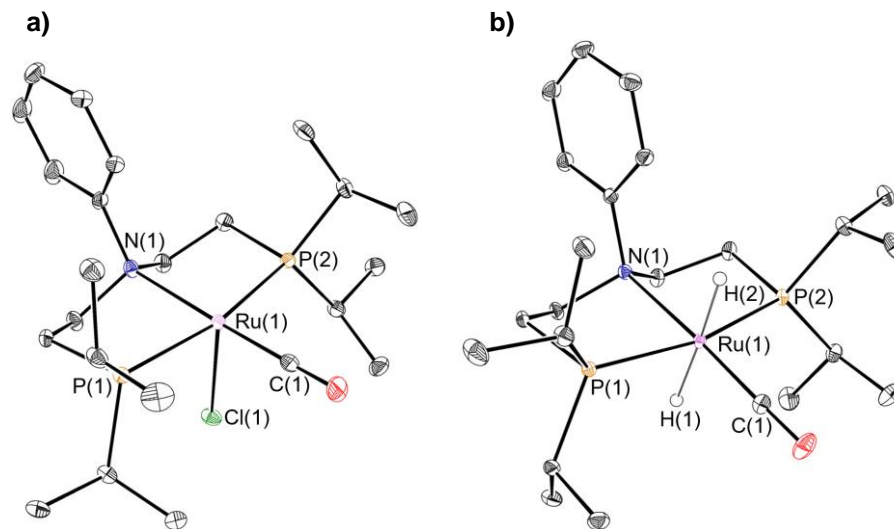


Figure 4.02. Solid state structures of **a) 1** and **b) 2**, with thermal ellipsoids at 30% probability level. There are four molecules in the asymmetric unit of **2**; only one is shown. Hydrogens not bound to Ru omitted for clarity. The hydrides of **2** were located in the difference map and freely refined. Selected bond lengths (Å) and angles (°) for **1**: Ru(1)-P(1) 2.3257(15), Ru(1)-P(2) 2.3365(15), Ru(1)-N(1) 2.327(5), Ru(1)-Cl(1) 2.5491(15), Ru(1)-C(1) 1.803(6), P(1)-Ru(1)-P(2) 166.48(5), P(1)-Ru(1)-N(1) 83.54(12), P(1)-Ru(1)-Cl(1) 89.46(5), P(1)-Ru(1)-C(1) 95.88(19), P(2)-Ru(1)-N(1) 82.94(12), P(2)-Ru(1)-Cl(1) 89.75(5), P(2)-Ru(1)-C(1) 97.63(19), N(1)-Ru(1)-Cl(1) 86.92(12), N(1)-Ru(1)-C(1) 176.9(2), Cl(1)-Ru(1)-C(1) 96.2(2). For a representative molecule of **2**: Ru(1)-P(1) 2.3157(5), Ru(1)-P(2) 2.2985(5), Ru(1)-N(1) 2.3326(16), Ru(1)-C(1) 1.810(2), P(1)-Ru(1)-P(2) 164.941(18), P(1)-Ru(1)-N(1) 82.78(4), P(1)-Ru(1)-C(1) 98.19(7), P(2)-Ru(1)-N(1) 82.16(4), P(2)-Ru(1)-C(1) 96.82(7), N(1)-Ru(1)-C(1) 175.07(7). Data for the other three molecules in the asymmetric unit is included in Appendix C.

donor than the nitrogen atoms in $i\text{PrPN}^{\text{H}}\text{P}$ or $i\text{PrPN}^{\text{Me}}\text{P}$, which is also supported by IR spectroscopy. Specifically, the $\text{C}\equiv\text{O}$ stretching frequency in **1** is observed at 1913 cm^{-1} , whereas the corresponding $\text{C}\equiv\text{O}$ stretch is observed at 1897 cm^{-1} in **1-Me** and at 1906 cm^{-1} in **1-H**,^{4d} indicating that there is less back-bonding from Ru to CO in **1** and presumably a less electron rich Ru center. Overall, the solution state, IR, and X-ray data show that the simple substitution of a proton or methyl substituent for a phenyl substituent on the nitrogen donor in ligands of the type $i\text{PrPN}^{\text{R}}\text{P}$ results in significant differences in the coordination chemistry of the resulting complexes.

The dihydride complex ($i\text{PrPN}^{\text{Ph}}\text{P}$)Ru(H)₂(CO) (**2**) was synthesized from **1** using 1.2 equivalents of lithium triethylborohydride in toluene (Scheme 4.01b). The colorless solid,

isolated in 84% yield, has a single $^{31}\text{P}\{^1\text{H}\}$ NMR resonance at 85.23 ppm and two nearly overlapping hydride resonances at -4.99 and -5.15 ppm in its ^1H NMR spectrum. The similar downfield chemical shifts of the hydride resonances are consistent with a *trans* relationship between these ligands.¹⁸ Analogous to **1**, the two aromatic protons *ortho* to the nitrogen moiety of the $^{i\text{Pr}}\text{PN}^{\text{Ph}}\text{P}$ ligand are observed as a broad peak at 8.43 ppm at room temperature, again indicating free rotation of the phenyl ring in the solution state. The solid state structure of **2** determined by X-ray diffraction (Figure 4.02b) supports this assignment, and the two hydrides were located in the difference map. Similar to **1**, complex **2** has a distorted octahedral geometry, and the Ru–N distance is 2.3326(16) Å. This is again significantly longer than the Ru–N distance in $(^{i\text{Pr}}\text{PN}^{\text{H}}\text{P})\text{Ru}(\text{H})_2(\text{CO})$ (**2-H**), which is 2.2060(11) Å.^{4d} Further, the C≡O stretching frequency in **2** is observed at 1874 cm^{-1} , while the corresponding C≡O stretches for **2-Me** and **2-H** are observed at 1868 and 1853 cm^{-1} , respectively. This shows that the Ru center in **2** is less electron rich than those in either **2-H** or **2-Me** and once again emphasizes the poorer σ -donating ability of the nitrogen donor in $^{i\text{Pr}}\text{PN}^{\text{Ph}}\text{P}$ compared to $^{i\text{Pr}}\text{PN}^{\text{H}}\text{P}$ and $^{i\text{Pr}}\text{PN}^{\text{Me}}\text{P}$.

The insertion of CO_2 into Ru dihydride complexes supported by $^{i\text{Pr}}\text{PN}^{\text{H}}\text{P}$ and $^{i\text{Pr}}\text{PN}^{\text{Me}}\text{P}$ is a crucial step in catalytic CO_2 hydrogenation.^{4b, f} Exposure of **2** to one atmosphere of CO_2 in C_6D_6 led to the disappearance of all peaks corresponding to **2** in the NMR spectrum in less than five minutes at room temperature (Figure 4.03a). The formation of one new species with a single resonance at 66.18 ppm was observed in the $^{31}\text{P}\{^1\text{H}\}$ NMR spectrum, as well as a triplet hydride peak at -16.12 ppm and a singlet resonance at 9.34 ppm in the ^1H NMR spectrum. We assign the peak at 9.34 ppm to a coordinated formate ligand and propose the product is the formate complex $(^{i\text{Pr}}\text{PN}^{\text{Ph}}\text{P})\text{RuH}(\text{CO})\{\text{OC}(\text{O})\text{H}\}$ (**3**).

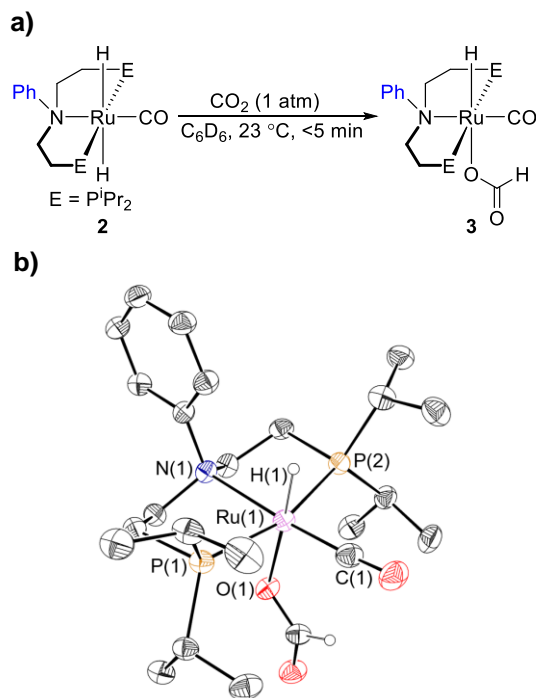


Figure 4.03. a) Reaction of **2** with one atmosphere of CO₂ and **b)** solid state structure of (iPrPNPhP)RuH(CO){OC(O)H} (**3**) with thermal ellipsoids at 30% probability. Hydrogens not bound to Ru or the formate ligand omitted for clarity. The hydride of **3** was located in the difference map and freely refined. Selected bond lengths (Å) and angles (°) for **3**: Ru(1)-P(1) 2.3453(16), Ru(1)-P(2) 2.3366(16), Ru(1)-N(1) 2.297(5), Ru(1)-O(1) 2.220(4), Ru(1)-C(1) 1.810(7), P(1)-Ru(1)-P(2) 163.73(6), P(1)-Ru(1)-N(1) 82.18(13), P(1)-Ru(1)-O(1) 90.78(12), P(1)-Ru(1)-C(1) 97.9(2), P(2)-Ru(1)-N(1) 82.14(13), P(2)-Ru(1)-O(1) 91.87(12), P(2)-Ru(1)-C(1) 97.3(2), N(1)-Ru(1)-O(1) 83.96(16), N(1)-Ru(1)-C(1) 175.1(2), O(1)-Ru(1)-C(1) 101.0(2).

Based on the upfield hydride chemical shift, it is likely that the hydride ligand is oriented *trans* to the relatively weakly donating formate ligand.^{4d, 18} Two dimensional ¹H NOESY NMR spectroscopy again indicates a *syn* orientation between the hydride and the N-phenyl group (see Appendix C). This stands in contrast to the related complex (iPrPN^{Me}P)RuH(CO){OC(O)H} (**3-Me**), which is a mixture of the *syn* and *anti* isomers in solution, while (iPrPN^HP)RuH(CO){OC(O)H} (**3-H**) is only present as the *anti* isomer, presumably due to the stabilizing hydrogen bond that is formed between the formate carbonyl oxygen and the pincer ligand N-H moiety.^{4d} Our assignment of the geometry of **3** in the solution state is supported by the solid state structure, which indicates that the formate ligand is on the opposite face of the metal center from the phenyl ring (Figure

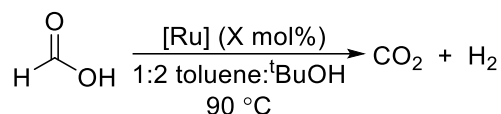
4.03b). To the best of our knowledge, this is the first example of an $^R\text{PN}^{R'}\text{P}$ -ligated transition metal formate complex where the solid state structure has the hydride ligand *syn* and the formate ligand *anti* to the N-substituent. As in **1** and **2**, the geometry of **3** is distorted octahedral about Ru, and the Ru–N distance of 2.297(5) Å is again substantially longer than the corresponding distance of 2.185(3) in **3-H**.^{4d} In agreement with our observations, DFT calculations in benzene predict that the *syn* isomer of **3** is 3.0 kcal/mol lower in energy than the *anti* isomer.

Interestingly, although it was possible to obtain single crystals of **3** by crystallization under an atmosphere of CO₂, we were not able to isolate **3** on scale due to its instability under vacuum. Exposure of **3** to vacuum for even a minute at room temperature results in partial conversion back to **2** via decarboxylation. **3-Me** also begins forming **2-Me** immediately under vacuum, precluding its isolation (see Appendix C). The instability of these two complexes stands in contrast to **3-H**, which is isolable on scale and is not observed to decarboxylate under ambient conditions.^{4d} These significant differences in the stability and geometry of the formate complexes again highlights the substantial effects of changing the N-substituent of the $^{\text{iPr}}\text{PN}^{R'}\text{P}$ ligand. In the following sections we assess the differences in catalytic performance of Ru complexes which differ only in the nitrogen substitution of their $^{\text{iPr}}\text{PN}^{R'}\text{P}$ ligands.

Formic Acid Dehydrogenation

Formic acid is an attractive liquid for hydrogen storage if efficient catalysts for the dehydrogenation of formic acid to generate H₂ and CO₂ are developed.^{15a, 15c-e} Although a large number of homogeneous catalysts for formic acid dehydrogenation have been developed, most of these require basic additives such as NEt₃, a Lewis acid, or excess

ligand in order to achieve high activity.^{15a, e} Thus, despite intensive research efforts there is still a need for selective and active catalysts that do not require additives. Previously, both our group and others have provided evidence that the mechanism of formic acid



Entry	[Ru]	X (mol%)	TOF (h ⁻¹) ^a	TON ^b (time)	Yield
1	2-H		2,900	9,500 (7 h)	95%
2	2-Me	0.01	5,500	10,000 (130 min)	100%
3	2		7,400	10,000 (80 min)	100%
4	2-H		14,000	20,000 (24 h)	20%
5	2-Me	0.001	15,000	68,000 (78 h)	68%
6	2		20,000	69,000 (48 h)	69%

Table 4.01. Formic acid dehydrogenation using **2**, **2-Me**, and **2-H**. Reaction conditions: Formic acid (110 μL , 2.91 mmol), [Ru] (0.01 or 0.001 mol%, 291 μL of a stock solution in toluene), 5.00 mL total reaction volume, 90 $^{\circ}\text{C}$. Turnover numbers (TON) were measured using a gas buret. ^aThis value is the TON after the first hour. ^bThis value is the maximum TON that was recorded. The time indicates how long it took for catalysis to stop and for the maximum TON to be obtained.

dehydrogenation with ^RPN^{R'}P-supported Fe and Ru complexes does not involve MLC.^{4g, 5c}

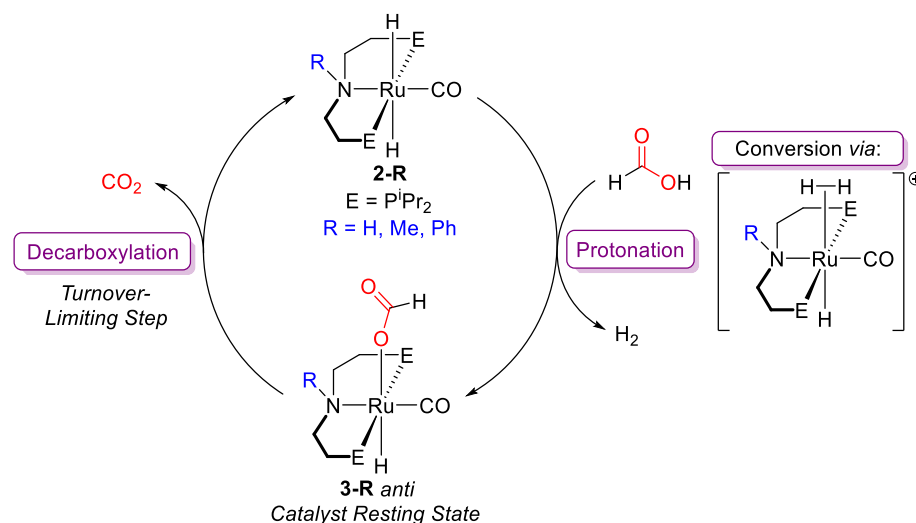
In fact, complexes supported by ^RPN^{Me}P ligands give superior performance to those supported by ^RPN^HP ligands. We tested **2**, **2-H**, and **2-Me** as catalysts for additive free formic acid dehydrogenation in the first direct catalytic comparison between more than two ^RPN^{R'}P-ligated catalysts which differ *only* in their N-substitution. We used conditions previously optimized for a related ^{iPr}PN^{Me}P-ligated Fe system (Table 4.01).^{5g} At 0.01 mol% catalyst loading, **2-H** reaches only 9,500 TON after 7 hours, while **2** and **2-Me** both quantitatively convert formic acid to CO₂ and H₂ in 80 and 130 minutes, respectively (Table 4.01, entries 1-3). The N-phenyl substituted complex **2** not only reaches full conversion in the shortest time, but also gives the highest initial TOF. Importantly, analysis of the headspace of a catalytic reaction by GC indicates that no CO, which could in principle

poison the catalyst, is detected when **2** is used as a catalyst (see Appendix C). The superior activity and productivity of **2-Me** and **2-Ph** compared to **2-H** is consistent with previously published results which propose that a MLC mechanism is not operative in this reaction.^{4g}

5g, 19

To further compare the relative performance of the three catalysts, the catalyst loading was reduced by an order of magnitude to 0.001 mol%. **2-H** gives a maximum of 20,000 turnovers after 24 hours, which corresponds to a yield of 20% (Table 4.01, entry 4). Both **2-Me** and **2** give comparable yields, 68% and 69%, respectively, but the TOF with **2** is approximately 33% higher than the TOF with **2-Me**, and **2** attains its maximum yield approximately one day faster than **2-Me** (Table 4.01, entries 5 & 6). This implies faster turnover but also faster decomposition for **2** compared to **2-Me**. Unfortunately, comparing the catalytic activity of **2** to other homogeneous catalysts for formic acid dehydrogenation is challenging because many systems report TOFs that are extrapolated to one hour from initial rates obtained in the first 3-10 minutes of catalysis, and also operate under different conditions.²⁰ However, of the catalysts that are active for 1 hour, **2** gives one of the highest TOFs reported, although its TON is not as high as others.²¹ This suggests that understanding the reasons for the high activity of **2** is important for the design of the next generation of catalysts.

To gain insight into the catalytic activity of **2**, we investigated the mechanism of formic acid dehydrogenation. Initially, the resting states in catalysis for **2**, **2-H**, and **2-Me** were determined using *in situ* NMR spectroscopy. In all three cases, the corresponding formate complexes **3**, **3-H**, or **3-Me** were identified as the resting state (see Appendix C). Additionally, **2** was reacted stoichiometrically with formic acid in toluene-*d*₈. Immediate



Scheme 4.02. Proposed mechanism for formic acid dehydrogenation using **2**, **2-H**, and **2-Me**. For simplicity, only the *anti* orientation is shown. **2-H** operates exclusively in this orientation, **2-Me** likely proceeds through both isomers, and **2** operates only in the *syn* orientation.

gas formation was observed upon addition of the acid, and NMR spectroscopy confirmed the formation of **3** along with H_2 (see Appendix C). On the basis of these results and the similarity between systems based on **2** and those previously studied on Fe^{5c} and Ru^{4g} we propose the simple mechanism for formic acid dehydrogenation shown in Scheme 4.02 for all three catalysts.^{4g, 5g} First, protonation of the dihydride complex **2** generates an unobserved molecular hydrogen complex, which rapidly loses H_2 and binds the formate ion to generate **3**, the catalytic resting state. Turnover-limiting decarboxylation, the microscopic reverse of the stoichiometric CO_2 insertion reactions described earlier, produces CO_2 and regenerates **2**.

The mechanism of decarboxylation from **3**, **3-H**, and **3-Me** was probed using DFT calculations using THF^{22} as the solvent (Figure 4.04). We propose that decarboxylation is a two-step process (Figure 4.04a), as has been reported for related complexes.^{5c, 23} In the first step, which proceeds via a transition state labelled TS1, the Ru-O bond is broken and a Ru-H bond is formed as the formate ligand rotates from being bound through O to bound

through H. This leads to the formation of an intermediate H-bound formate complex ($i^i\text{Pr}^R\text{PN}^R\text{P})\text{RuH}(\text{CO})(\text{H}-\text{CO}_2)$). The second transition state (TS2) involves cleavage of the Ru–H bond to form free CO_2 and **2**. Only the *anti* isomer of **3-H** and the *syn* isomer of **3** were considered, as these are the only isomers observed in solution by NMR spectroscopy.²⁴ Both the *syn* and *anti* isomers were calculated for **3-Me** as both are observed experimentally and therefore could in principle facilitate formic acid

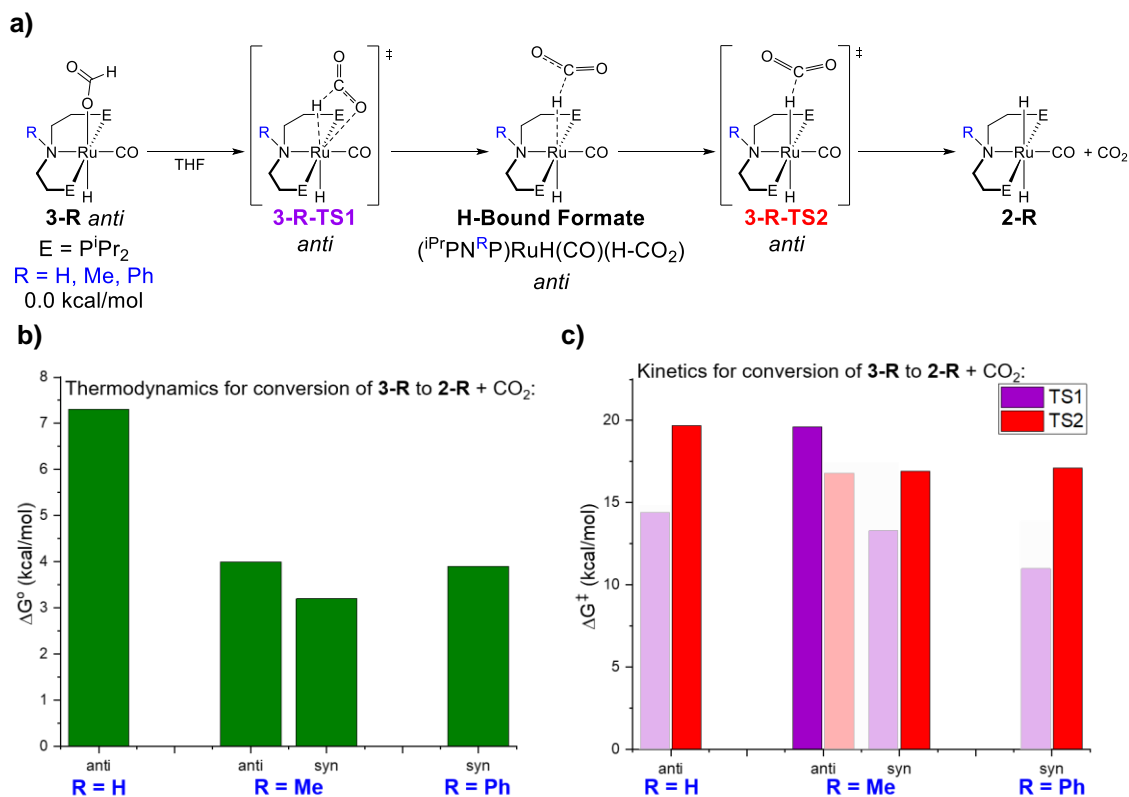


Figure 4.04. a) Mechanism of decarboxylation studied computationally for **3**, **3-H**, and **3-Me**, **b)** thermodynamics, and **c)** kinetics of decarboxylation, as determined by DFT. Non rate-determining transition states are faded. CPCM solvation (THF), 298 K, 1 atm CO_2 , M06 functional, 6-31+G**/LANL2DZ (on Ru) basis sets. *Syn/anti* refer to the relative orientation between the hydride ligand and N-R moiety; only a schematic of a generic *anti* isomer is included for simplicity.

dehydrogenation.

Thermodynamically, decarboxylation is the most uphill for **3-H** at 7.3 kcal/mol, while it is significantly less uphill for **3** at 3.9 kcal/mol (Figure 4.04b). Kinetically, the

trend is similar: the barrier for decarboxylation from **3-H** *anti* is calculated to be 19.7 kcal/mol, while the barrier for **3** *syn* is 16.9 kcal/mol (Figure 4.04c). This corresponds to a predicted rate increase of almost two orders of magnitude for decarboxylation from **3** compared to **3-H**. The higher barrier for decarboxylation from **3-H** compared to **3** is attributed to the presence of the stabilizing hydrogen bond between the formate carbonyl oxygen and the pincer N-H moiety,^{4d} which must be broken to release CO₂ and generate **2-H**. The calculated energies also agree with the observation that **3** undergoes decarboxylation at room temperature under vacuum, while **3-H** can be isolated (*vide supra*). In the case of both **3** and **3-H**, the second step, involving TS2, is rate-determining.

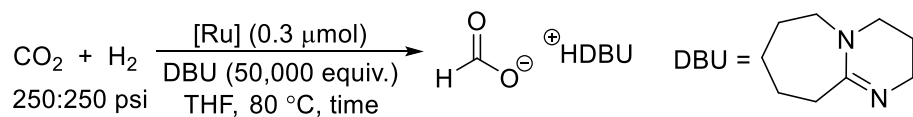
The situation for **3-Me** is more complicated. The computed free energies for decarboxylation from the *syn* and *anti* isomers of **3-Me** are 3.2 and 4.0 kcal/mol, respectively (Figure 4.04b). The trend in thermodynamics matches the trend in kinetics, and the calculated barrier for decarboxylation from the *syn* isomer of **3-Me** is 17.1 kcal/mol, while the corresponding value for the *anti* isomer is 19.6 kcal/mol (Figure 4.04c). There is, however, a change in the rate-determining step for decarboxylation between the isomers of **3-Me**. For the *syn* isomer TS2 is rate-determining, whereas for the *anti* isomer TS1 is rate-determining. We propose that this change in rate-determining step is related to steric factors, as in TS1 *anti* there are close contacts between the formate ligand and two of the N-methyl protons (2.25 and 2.35 Å). In contrast, there is only one analogous close contact between the formate ligand and a ⁱPrPN^{Me}P backbone proton in TS1 *syn* (2.17 Å).

Given that decarboxylation from the *syn* isomer of **3-Me** is both thermodynamically and kinetically preferred, the *syn* isomer is likely to result in more rapid generation of products in catalysis than the *anti* isomer. The barrier for decarboxylation from the *anti*

isomer of **3-Me** is slightly higher than the barrier for **3**, which is consistent with our experimental results that **3** is the most active catalyst. Given that the *syn* isomer of **3** is preferred, our results imply that in complexes supported by $i\text{PrPN}^{\text{R}}\text{P}$ ligands, it is preferable for the catalyst to adopt a *syn* geometry for reactions that do not proceed via a mechanism involving MLC in order to avoid steric clash or a stabilizing hydrogen bond with the substituent on the nitrogen donor.¹⁷ This trend has not been previously proposed or investigated, presumably due to a dearth of systems that only adopt the *syn* configuration. The $i\text{PrPN}^{\text{Ph}}\text{P}$ ligand provides a framework for rationally designing a range of systems that meet these criteria in the future.

CO₂ Hydrogenation to Formate

The hydrogenation of CO₂ to formate or formic acid represents an atom economical method to synthesize an important commodity chemical, and is also directly relevant to the utilization of formate or formic acid as a sustainable medium for hydrogen storage.¹⁵ Both our groups and others have demonstrated using $\text{RPN}^{\text{Me}}\text{P}$ (R = *i*Pr, Ph) supported Fe and Ru catalysts that a ligand capable of MLC is not required for CO₂ hydrogenation to formate.^{4b, 5e} Therefore, we directly compared the activity of **2**, **2-H**, and **2-Me** as catalysts for CO₂ hydrogenation to formate using similar but far less forcing conditions to those previously described with related Fe catalysts that utilize DBU (DBU = 1,5-diazabicyclo(4.3.0)non-5-ene) as an organic base (Table 4.02).^{5e} We first compared the initial activities of the three catalysts by determining the TON after one hour of catalysis (Table 4.02, column 3). **2** and **2-H** achieve the same TON within error in the first hour, 900 and 1050, respectively (Entries 1 & 3). In contrast, **2-Me** gives a TON of only 550 in the first hour, approximately half the activity of the other two catalysts (Entry 2). We used these initial TONs to predict

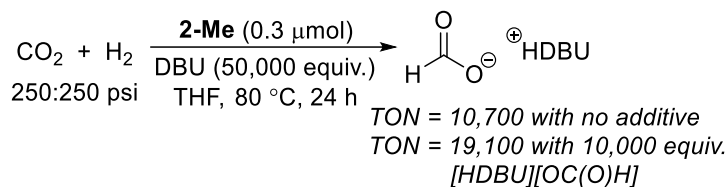


Entry	[Ru]	TON (1 h)	Predicted TON (24 h) ^a	TON (24 h)	TON (48 h)	TON (72 h)
1	2-H	1,050 (130)	25,200	39,000	58,800 ^b	--
2	2-Me	550 (50)	13,200	10,700	31,000	48,000
3	2	900	21,600	48,300	--	--

Table 4.02. CO₂ hydrogenation to formate using **2**, **2-H**, and **2-Me**. Reaction conditions: 250 psi CO₂:250 psi H₂, [Ru] (0.3 μmol), DBU (2.34 g, 15.0 mmol), THF (10 mL), 80 °C. TONs quantified using ¹H NMR spectroscopy; reported values are the average of three trials with the standard deviation in parentheses. Values without a standard deviation are from only one experiment. ^aThis number is the observed TON after 1 hour multiplied by 24. ^bTONs slightly greater than 50,000 are possible due to one protonated DBU molecule stabilizing more than one formate molecule.

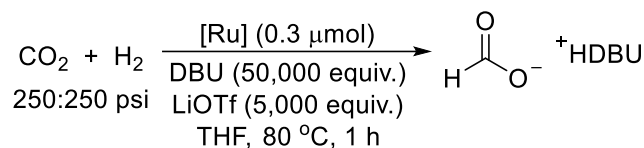
the productivity of each catalyst after 24 hours, assuming a constant rate of formate production (Column 4). To our surprise, in actuality both **2-H** and **2** achieve far higher TONs after 24 hours than predicted (Column 5). **2-H** gives a TON of 39,000 (Entry 1), which is 55% more than the predicted value, while **2** achieves a TON of 48,300 (Entry 3), which is 110% more than the predicted turnovers. Although **2-Me** only gives a TON of 10,700 TON after 24 hours (Entry 2, column 5, 19% fewer than predicted²⁵), the rate of formate production also actually increases over time for this system, with 31,000 turnovers reached after 48 hours and 48,000 turnovers reached after 72 hours (Entry 2, columns 6 & 7). This corresponds to 10,700 turnovers in the first 24 hours, 20,300 in the second 24 hours, and 17,000 in the final 24 hours. Experiments to determine the standard deviations in all of the values in Table 4.02 are ongoing.

We hypothesized that this unusual increase in the rate of product formation over time could be due to an autocatalytic effect in which the product, [HDBU][formate], acts as a weak Lewis acid. This proposal is based on previous observations that Lewis acid co-catalysts such as Li⁺ increase the catalytic activity of related ⁱPrPN^RP-ligated Fe complexes



Scheme 4.03. Investigating an autocatalytic effect in CO₂ hydrogenation to formate using **2-Me**. Reaction conditions: 250 psi CO₂:250 psi H₂, **2-Me** (0.3 μmol), DBU (2.34 g, 15.0 mmol), [HDBU][OC(O)H] (0 g or 0.510 g, 3.00 mmol), THF (10 mL), 80 °C, 24 h. TONs quantified using ¹H NMR spectroscopy; reported values are the average of three trials. In the reaction in which [HDBU][OC(O)H] was used as an additive, the amount of formate initially present was subtracted from the overall yield of formate.

(R' = H, Me) for CO₂ hydrogenation by assisting in the dissociation of formate from the catalyst.^{5e} In order to elucidate the role of the formate product on the rate of catalysis, we performed an experiment using **2-Me** as a catalyst under the same conditions as those in Table 4.02, but with 10,000 equivalents of [HDBU][formate] added (Scheme 4.03). After 24 hours, **2-Me** gives a TON of 19,100, which is 79% more than the TON achieved in the first 24 hours without the product salt added and very close to the TON reached in the second 24 hours (Table 4.02, entry 2). This result confirms that the presence of [HDBU][formate] increases the rate of formate production. It is likely that this product enhancement also occurs in many other systems for CO₂ hydrogenation that use DBU,^{5e, 6a, 26} but has remained unobserved both because of catalyst instability, as well as the challenges associated with monitoring product formation as a function of time in high pressure reactions. In fact, a notable feature of the ⁱPrPN^{R'}P catalysts studied in this work is their stability, as all give essentially complete conversion to formate despite the low catalyst loadings and are still operative after 24 hours. This is unusual compared to other homogeneous catalysts for CO₂ hydrogenation, which often decompose relatively quickly^{15b} and as a result are not suitable for incorporation in practical devices.^{15c} Overall,



Entry	[Ru]	TON (1 h)
1	2-H	7,800 (200)
2	2-Me	15,300 (400)
3	2	17,500

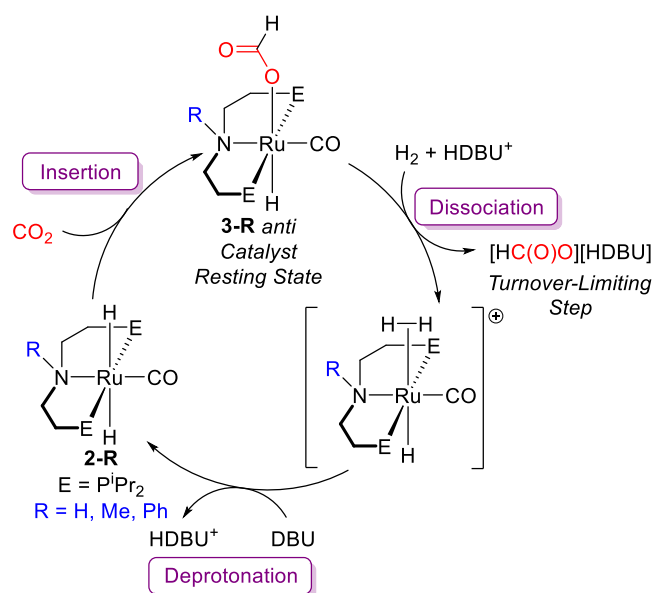
Table 4.03. CO₂ hydrogenation to formate with a Lewis acid cocatalyst using **2**, **2-H**, and **2-Me**. Reaction conditions: 250 psi CO₂:250 psi H₂, [Ru] (0.3 μmol), DBU (2.34 g, 15.0 mmol, 50,000 equiv. to [Ru]), LiOTf (0.230 g, 1.5 mmol, 5,000 equiv. to [Ru]), THF (10 mL), 80 °C. TONs quantified using ¹H NMR spectroscopy; reported values are the average of three trials with the standard deviation in parentheses. Values without a standard deviation are from only one experiment.

2, containing the new ⁱPrPN^{Ph}P ligand, gives the best performance followed by **2-H** and **2-Me**.

The product [HDBU][formate] is a weak Lewis acid in comparison to alkali metal halides such as Li⁺. Therefore, we performed CO₂ hydrogenation reactions with our series of Ru catalysts under the same conditions as those in Table 4.02, but in the presence of 5,000 equivalents of LiOTf to determine if a larger co-catalytic effect could be observed with a stronger Lewis acid (Table 4.03). Initially we monitored the TON after 1 hour. Under these conditions **2-H** gives a TON of 7,800 (Entry 1), which is a substantial increase compared to its initial TON of 1,050 without a Lewis acid (Table 4.02, entry 1). The activity of **2-Me** increases even more dramatically from 550 turnovers in the absence of a Lewis acid to 15,300 turnovers in the presence of a Lewis acid (Table 4.03, entry 2). This corresponds to a greater than 27-fold increase in productivity. The ⁱPrPN^{Ph}P supported catalyst **2** gives the highest TON of 17,500 under these conditions (Entry 3), and displays approximately a 20-fold increase in TON in the presence of the Lewis acid. We hypothesize based on results in the Fe system that in catalysis with **2-H**, the Lewis acid assists with

both formate extrusion and in disrupting a stabilizing hydrogen bond between the pincer N-H moiety and bound formate.^{5e} This dual role for the Lewis acid in **2-H** relative to **2** or **2-Me** (where the Lewis acid only assists in formate extrusion) explains why the Lewis acid effect is less pronounced for **2-H**. These results illustrate the profound effect of Lewis acid co-catalysts in this reaction, and confirm that **2** remains the most active catalyst of those studied. In fact, the initial TONs for **2**, **2-H**, and **2-Me** with LiOTf are among the highest of any known homogeneous Ru system,^{15b} suggesting that unprecedented activity could be possible through further tuning of the substituent on the N-donor. Experiments to find the standard deviation in Table 4.03 for **2** are ongoing, as well as catalysis using a higher DBU loading to investigate the maximum possible TON that can be reached by each catalyst.

To gain insight into the excellent activity of **2** in CO₂ hydrogenation, we investigated the mechanism of the reaction. First, the resting states in catalysis for **2**, **2-H**, and **2-Me** were determined using *in situ* NMR spectroscopy. In all three cases, the formate complex **3**, **3-H**, or **3-Me** was identified as the resting state (see Appendix C). This formate



Scheme 4.04. Proposed mechanism for CO₂ hydrogenation to formate using **2**, **2-H**, and **2-Me**. For simplicity, only the *anti* orientation is shown. **2-H** operates exclusively in this orientation, **2-Me** likely proceeds through both isomers, and **2** operates only in the *syn* orientation.

complex presumably forms via facile CO₂ insertion into **2**, **2-H**, or **2-Me** (*vide supra*). A control reaction between **3** and excess DBU and H₂ results in the formation of the salt [HDBU][formate] and dihydride **2** (see Appendix C). We propose that this reaction involves dissociation of formate and binding of H₂ to form an unobserved dihydrogen complex.²⁷ The dihydrogen intermediate is then deprotonated by DBU to regenerate **2**. On the basis of these results and the similarity to those previously studied,^{4b,5e} we propose the mechanism for CO₂ hydrogenation to formate shown in Scheme 4.04, which is likely operative for all three systems. The mechanism involves three steps: (i) facile CO₂ insertion into **2**, (ii) turnover-limiting substitution of the formate ligand in **3** with an H₂ ligand to form a molecular H₂ complex, and (iii) rapid deprotonation of the H₂ complex to regenerate **2**.

To understand the differences in performance between **2**, **2-H**, and **2-Me**, we used DFT to calculate the thermodynamics of turnover-limiting formate dissociation in THF (Figure 4.05). Given that the formate complexes **3**, **3-H**, and **3-Me** are coordinatively saturated, we assumed a dissociative mechanism for ligand exchange, with no involvement

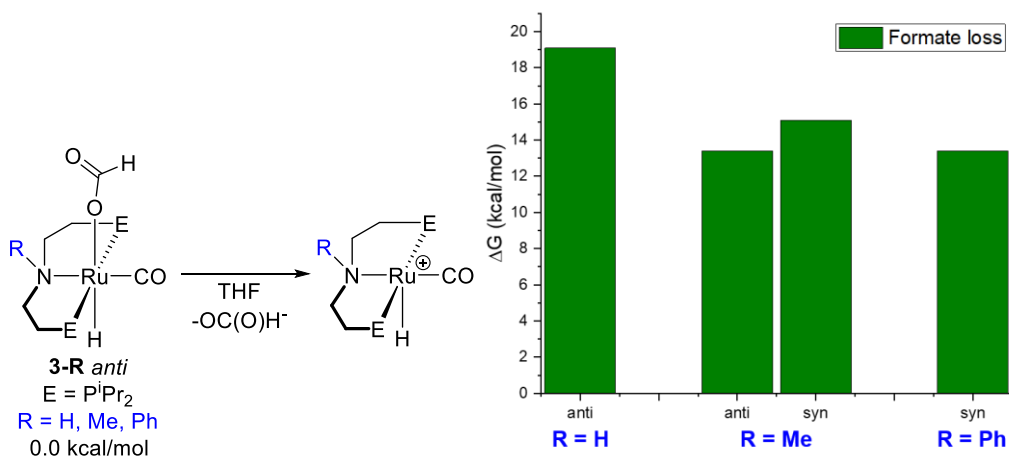


Figure 4.05. Thermodynamics of formate loss as determined by DFT. CPCM solvation (THF), 298 K, M06 functional, 6-31+G**/LANL2DZ (on Ru) basis sets. *Syn/anti* refer to the relative orientation between the hydride ligand and N-R moiety; only a schematic of a generic *anti* isomer is included for simplicity.

of the incoming H₂ ligand. Formate loss from **3-H** to generate a coordinatively unsaturated cation is the most uphill at 19.1 kcal/mol. This is likely because in **3-H** an intramolecular hydrogen bond between the formate ligand and the pincer N-H group must be broken in order to dissociate formate.^{4d} Formate dissociation from the isomers of **3-Me** is 13.4 kcal/mol and 15.1 kcal/mol uphill for the *anti* and *syn* isomers, respectively, while for **3** dissociation is disfavored by 13.4 kcal/mol. The unfavorability of formate dissociation is consistent with a high pressure of H₂ being required in catalysis to efficiently trap the coordinatively unsaturated cation when it is formed. However, this calculated thermodynamic trend does not match our experimental results, as **2-H** shows roughly twice the productivity of **2-Me** in the first hour (Table 4.02, entries 1 & 2), but our calculations indicate that it should be the slowest catalyst.

We postulated that the computed free energy of formate loss from **3-H** may not be accurate because the speciation of **3-H** in solution was not correctly modelled in our initial calculations. It has previously been demonstrated that the N-H group in the ⁱPrPN^HP ligand can participate in intermolecular hydrogen bonding.¹⁴ On this basis, we hypothesized that the N-H moiety of the ⁱPrPN^HP ligand could engage in intermolecular hydrogen bonding with one or more product formate molecule(s). Calculations in which a formate molecule

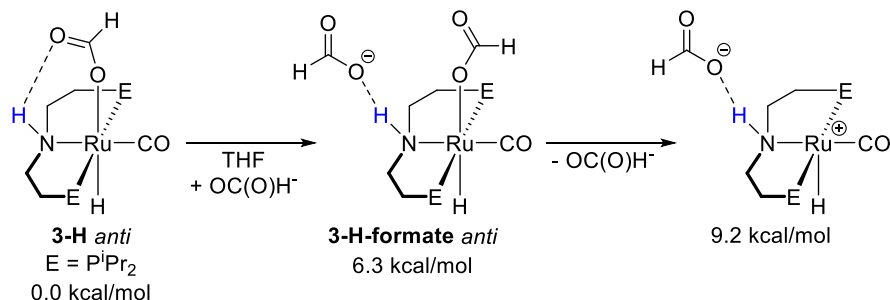


Figure 4.06. Impact of an intermolecular hydrogen bond between **3-H** and a formate molecule on calculated thermodynamics of formate loss. CPCM solvation (THF), 298 K, M06 functional, 6-31+G**/LANL2DZ (on Ru) basis sets. *Syn/anti* refer to the relative orientation between the hydride ligand and N-R moiety; only a schematic of a generic *anti* isomer is included for simplicity.

hydrogen bonds to the N-H group of the $i\text{PrPN}^{\text{H}}\text{P}$ ligand change the thermodynamics for formate loss from **3-H** (Figure 4.06). Although the initial binding of formate to **3-H** to form **3-H-formate** is uphill by 6.3 kcal/mol (consistent with free formate not impacting the NMR spectrum of **3-H**), the loss of the coordinated formate molecule from **3-H-formate** is much more facile. The overall penalty for formate loss is reduced to 9.2 kcal/mol, which suggests that, consistent with our experimental results, **2-H** should be the fastest catalyst followed by **2** and **2-Me**.²⁸ These results also demonstrate the complications encountered when attempting to computationally predict reactivity in systems where hydrogen bonding is possible between the catalyst and the solvent and/or substrate.

III. Conclusions

In this work, we have synthesized a novel N-phenyl ligand $i\text{PrPN}^{\text{Ph}}\text{P}$ and characterized a series of its coordination complexes with Ru. We then performed the first systematic study of the impact of N-substitution on catalysis by utilizing three $i\text{PrPN}^{\text{R}}\text{P}$ Ru complexes (R = H, Me, Ph) in formic acid dehydrogenation and CO₂ hydrogenation to formate. The experimental and computational results for formic acid dehydrogenation discussed here contain new insights into the large effects that changing the N-substitution of the $i\text{PrPN}^{\text{R}}\text{P}$ ligand scaffold has on catalysis. There is evidence that the weaker N σ -donor in $i\text{PrPN}^{\text{Ph}}\text{P}$, combined with the propensity for this system to undergo reactivity solely on the catalyst face *anti* to the N-phenyl group, leads to a significant decrease in the barrier for decarboxylation and a corresponding increase in formic acid dehydrogenation TOF. However, catalyst instability in the novel system remains an issue, likely also due to the change in electronics in the N-phenyl ligand compared to its N-H and N-Me analogues.

We found that the $i\text{PrPN}^{\text{Ph}}\text{P}$ complex was also the most active for CO_2 hydrogenation to formate, and the stability of the catalysts used here enabled us to identify an autocatalytic effect that has not previously been noticed. A co-catalytic Lewis acid effect was utilized to achieve some of the highest reported turnover frequencies for homogenous Ru catalysts in CO_2 hydrogenation. Work is ongoing in our lab to complete the CO_2 hydrogenation data presented in this chapter, and to use the insights gained here to design improved catalysts supported by $i\text{PrPN}^{\text{R}}\text{P}$ ligands.

Supporting Information

For supporting information, including experimental details and procedures, additional experimental information, and information on X-ray diffraction and computations, see Appendix C.

Acknowledgements

All computational work was supported by the facilities and staff of the Yale University Faculty of Arts and Sciences High Performance Computing Center. Dr. Fabian Menges performed mass spectrometry experiments.

IV. References

1. (a) van der Vlugt, J. I.; Reek, J. N. H., Neutral Tridentate PNP Ligands and Their Hybrid Analogues: Versatile Non-Innocent Scaffolds for Homogeneous Catalysis. *Angew. Chem. Int. Ed.* **2009**, *48*, 8832-8846; (b) Gunanathan, C.; Milstein, D., Bond Activation and Catalysis by Ruthenium Pincer Complexes. *Chem. Rev.* **2014**, *114*, 12024-12087; (c) Lawrence, M. A. W.; Green, K.-A.; Nelson, P. N.; Lorraine, S. C., Review: Pincer ligands—Tunable, versatile and applicable. *Polyhedron* **2018**, *143*, 11-27; (d) Peris, E.;

- Crabtree, R. H., Key factors in pincer ligand design. *Chem. Soc. Rev.* **2018**, *47*, 1959-1968;
- (e) Alig, L.; Fritz, M.; Schneider, S., First-Row Transition Metal (De)Hydrogenation Catalysis Based On Functional Pincer Ligands. *Chem. Rev.* **2019**, *119*, 2681-2751.
2. Schneider, S.; Meiners, J.; Askevold, B., Cooperative Aliphatic PNP Amido Pincer Ligands—Versatile Building Blocks for Coordination Chemistry and Catalysis. *Euro. J. Inorg. Chem.* **2012**, *2012*, 412-429.
3. For leading references that use Ir catalysts supported by ^RPN^HP ligands see: (a) Schmeier, T. J.; Dobereiner, G. E.; Crabtree, R. H.; Hazari, N., Secondary Coordination Sphere Interactions Facilitate the Insertion Step in an Iridium(III) CO₂ Reduction Catalyst. *J. Am. Chem. Soc.* **2011**, *133*, 9274-9277; (b) Graham, T. W.; Tsang, C.-W.; Chen, X.; Guo, R.; Jia, W.; Lu, S.-M.; Sui-Seng, C.; Ewart, C. B.; Lough, A.; Amoroso, D.; Abdur-Rashid, K., Catalytic Solvolysis of Ammonia Borane. *Angew. Chem. Int. Ed.* **2010**, *49*, 8708-8711; (c) Ahn, S. T.; Bielinski, E. A.; Lane, E. M.; Chen, Y.; Bernskoetter, W. H.; Hazari, N.; Palmore, G. T. R., Enhanced CO₂ electroreduction efficiency through secondary coordination effects on a pincer iridium catalyst. *Chem. Commun.* **2015**, *51*, 5947-5950; (d) Prichatz, C.; Alberico, E.; Baumann, W.; Junge, H.; Beller, M., Iridium—PNP Pincer Complexes for Methanol Dehydrogenation at Low Base Concentration. *ChemCatChem* **2017**, *9*, 1891-1896; (e) Ramaraj, A.; Nethaji, M.; Jagirdar, B. R., Hydrogenation of CO₂, Carbonyl and Imine Substrates Catalyzed by [IrH₃(^{Ph}PN^HP)] Complex. *J. Organomet. Chem.* **2019**, *883*, 25-34.
4. For leading references that use Ru catalysts supported by ^RPN^HP ligands see: (a) Nielsen, M.; Alberico, E.; Baumann, W.; Drexler, H.-J.; Junge, H.; Gladiali, S.; Beller, M., Low-temperature aqueous-phase methanol dehydrogenation to hydrogen and carbon dioxide.

Nature **2013**, *495*, 85-89; (b) Kothandaraman, J.; Czaun, M.; Goeppert, A.; Haiges, R.; Jones, J.-P.; May, R. B.; Prakash, G. K. S.; Olah, G. A., Amine-Free Reversible Hydrogen Storage in Formate Salts Catalyzed by Ruthenium Pincer Complex without pH Control or Solvent Change. *ChemSusChem* **2015**, *8*, 1442-1451; (c) Rezayee, N. M.; Huff, C. A.; Sanford, M. S., Tandem Amine and Ruthenium-Catalyzed Hydrogenation of CO₂ to Methanol. *J. Am. Chem. Soc.* **2015**, *137*, 1028-1031; (d) Alberico, E.; Lennox, A. J. J.; Vogt, L. K.; Jiao, H.; Baumann, W.; Drexler, H.-J.; Nielsen, M.; Spannenberg, A.; Checinski, M. P.; Junge, H.; Beller, M., Unravelling the Mechanism of Basic Aqueous Methanol Dehydrogenation Catalyzed by Ru–PNP Pincer Complexes. *J. Am. Chem. Soc.* **2016**, *138*, 14890-14904; (e) Kothandaraman, J.; Kar, S.; Sen, R.; Goeppert, A.; Olah, G. A.; Prakash, G. K. S., Efficient Reversible Hydrogen Carrier System Based on Amine Reforming of Methanol. *J. Am. Chem. Soc.* **2017**, *139*, 2549-2552; (f) Kar, S.; Sen, R.; Kothandaraman, J.; Goeppert, A.; Chowdhury, R.; Munoz, S. B.; Haiges, R.; Prakash, G. K. S., Mechanistic Insights into Ruthenium-Pincer-Catalyzed Amine-Assisted Homogeneous Hydrogenation of CO₂ to Methanol. *J. Am. Chem. Soc.* **2019**, *141*, 3160-3170; (g) Agapova, A.; Alberico, E.; Kammer, A.; Junge, H.; Beller, M., Catalytic Dehydrogenation of Formic Acid with Ruthenium-PNP-Pincer Complexes: Comparing N-Methylated and NH-Ligands. *ChemCatChem* **2019**, *11*, 1910-1914.

5. For leading references that use Fe catalysts supported by ^RPN^HP ligands see: (a) Alberico, E.; Sponholz, P.; Cordes, C.; Nielsen, M.; Drexler, H.-J.; Baumann, W.; Junge, H.; Beller, M., Selective Hydrogen Production from Methanol with a Defined Iron Pincer Catalyst under Mild Conditions. *Angew. Chem. Int. Ed.* **2013**, *52*, 14162-14166; (b) Bielinski, E. A.; Förster, M.; Zhang, Y.; Bernskoetter, W. H.; Hazari, N.; Holthausen, M.

C., Base-Free Methanol Dehydrogenation Using a Pincer-Supported Iron Compound and Lewis Acid Co-catalyst. *ACS Catal.* **2015**, *5*, 2404-2415; (c) Bielinski, E. A.; Lagaditis, P. O.; Zhang, Y.; Mercado, B. Q.; Würtele, C.; Bernskoetter, W. H.; Hazari, N.; Schneider, S., Lewis Acid-Assisted Formic Acid Dehydrogenation Using a Pincer-Supported Iron Catalyst. *J. Am. Chem. Soc.* **2014**, *136*, 10234-10237; (d) Chakraborty, S.; Brennessel, W. W.; Jones, W. D., A Molecular Iron Catalyst for the Acceptorless Dehydrogenation and Hydrogenation of N-Heterocycles. *J. Am. Chem. Soc.* **2014**, *136*, 8564-8567; (e) Zhang, Y.; MacIntosh, A. D.; Wong, J. L.; Bielinski, E. A.; Williard, P. G.; Mercado, B. Q.; Hazari, N.; Bernskoetter, W. H., Iron catalyzed CO₂ hydrogenation to formate enhanced by Lewis acid co-catalysts. *Chem. Sci.* **2015**, *6*, 4291-4299; (f) Lane, E. M.; Zhang, Y.; Hazari, N.; Bernskoetter, W. H., Sequential Hydrogenation of CO₂ to Methanol Using a Pincer Iron Catalyst. *Organometallics* **2019**, *38*, 3084-3091; (g) Curley, J. B.; Bernskoetter, W. H.; Hazari, N., Additive-Free Formic Acid Dehydrogenation Using a Pincer-Supported Iron Catalyst. *ChemCatChem* **2020**, *12*, 1934-1938.

6. For leading references that use Co catalysts supported by ^RPN^HP ligands see: (a) Spentzos, A. Z.; Barnes, C. L.; Bernskoetter, W. H., Effective Pincer Cobalt Precatalysts for Lewis Acid Assisted CO₂ Hydrogenation. *Inorg. Chem.* **2016**, *55*, 8225-8233; (b) Zhou, W.; Wei, Z.; Spannenberg, A.; Jiao, H.; Junge, K.; Junge, H.; Beller, M., Cobalt-Catalyzed Aqueous Dehydrogenation of Formic Acid. *Chem. Eur. J.* **2019**, *25*, 8459-8464; (c) Mills, M. R.; Barnes, C. L.; Bernskoetter, W. H., Influences of Bifunctional PNP-Pincer Ligands on Low Valent Cobalt Complexes Relevant to CO₂ Hydrogenation. *Inorg. Chem.* **2018**, *57*, 1590-1597.

7. For leading references that use Mn catalysts supported by $^R\text{PN}^H\text{P}$ ligands see: (a) Kar, S.; Goeppert, A.; Kothandaraman, J.; Prakash, G. K. S., Manganese-Catalyzed Sequential Hydrogenation of CO₂ to Methanol via Formamide. *ACS Catal.* **2017**, 7, 6347-6351; (b) Ryabchuk, P.; Stier, K.; Junge, K.; Checinski, M. P.; Beller, M., Molecularly Defined Manganese Catalyst for Low-Temperature Hydrogenation of Carbon Monoxide to Methanol. *J. Am. Chem. Soc.* **2019**, 141, 16923-16929; (c) Zubar, V.; Borghs, J. C.; Rueping, M., Hydrogenation or Dehydrogenation of N-Containing Heterocycles Catalyzed by a Single Manganese Complex. *Org. Lett.* **2020**, 22, 3974-3978; (d) Kaithal, A.; Werlé, C.; Leitner, W., Alcohol-Assisted Hydrogenation of Carbon Monoxide to Methanol Using Molecular Manganese Catalysts. *JACS Au* **2021**, 1, 130-136.

8. For leading references that use Ir catalysts supported by $^R\text{PN}^H\text{P}$ ligands see: (a) Clarke, Z. E.; Maragh, P. T.; Dasgupta, T. P.; Gusev, D. G.; Lough, A. J.; Abdur-Rashid, K., A Family of Active Iridium Catalysts for Transfer Hydrogenation of Ketones. *Organometallics* **2006**, 25, 4113-4117; (b) Chen, X.; Jia, W.; Guo, R.; Graham, T. W.; Gullons, M. A.; Abdur-Rashid, K., Highly active iridium catalysts for the hydrogenation of ketones and aldehydes. *Dalton Trans.* **2009**, 1407-1410; (c) Andrushko, N.; Andrushko, V.; Roose, P.; Moonen, K.; Börner, A., Amination of Aliphatic Alcohols and Diols with an Iridium Pincer Catalyst. *ChemCatChem* **2010**, 2, 640-643; (d) Junge, K.; Wendt, B.; Jiao, H.; Beller, M., Iridium-Catalyzed Hydrogenation of Carboxylic Acid Esters. *ChemCatChem* **2014**, 6, 2810-2814.

9. For leading references that use Ru catalysts supported by $^R\text{PN}^H\text{P}$ ligands see: (a) Bertoli, M.; Choualeb, A.; Lough, A. J.; Moore, B.; Spasyuk, D.; Gusev, D. G., Osmium and Ruthenium Catalysts for Dehydrogenation of Alcohols. *Organometallics* **2011**, 30, 3479-

3482; (b) Nielsen, M.; Junge, H.; Kammer, A.; Beller, M., Towards a Green Process for Bulk-Scale Synthesis of Ethyl Acetate: Efficient Acceptorless Dehydrogenation of Ethanol. *Angew. Chem. Int. Ed.* **2012**, *51*, 5711-5713; (c) Kuriyama, W.; Matsumoto, T.; Ogata, O.; Ino, Y.; Aoki, K.; Tanaka, S.; Ishida, K.; Kobayashi, T.; Sayo, N.; Saito, T., Catalytic Hydrogenation of Esters. Development of an Efficient Catalyst and Processes for Synthesising (R)-1,2-Propanediol and 2-(l-Menthoxy)ethanol. *Org. Proc. Res. Dev.* **2012**, *16*, 166-171; (d) Zhang, L.; Han, Z.; Zhao, X.; Wang, Z.; Ding, K., Highly Efficient Ruthenium-Catalyzed N-Formylation of Amines with H₂ and CO₂. *Angew. Chem. Int. Ed.* **2015**, *54*, 6186-6189; (e) Li, Y.; Nielsen, M.; Li, B.; Dixneuf, P. H.; Junge, H.; Beller, M., Ruthenium-Catalyzed Hydrogen Generation from Glycerol and Selective Synthesis of Lactic Acid. *Green Chem.* **2015**, *17*, 193-198; (f) Kim, S. H.; Hong, S. H., Ruthenium-Catalyzed Urea Synthesis Using Methanol as the C1 Source. *Org. Lett.* **2016**, *18*, 212-215; (g) Pinggen, D.; Choi, J.-H.; Allen, H.; Murray, G.; Ganji, P.; van Leeuwen, P. W. N. M.; Prechtl, M. H. G.; Vogt, D., Amide Versus Amine Ligand Paradigm in the Direct Amination of Alcohols with Ru-PNP Complexes. *Catal. Sci. Tech.* **2018**, *8*, 3969-3976; (h) Thiagarajan, S.; Gunanathan, C., Catalytic Cross-Coupling of Secondary Alcohols. *J. Am. Chem. Soc.* **2019**, *141*, 3822-3827.

10. For leading references that use Fe catalysts supported by ^RPN^HP ligands see: (a) Chakraborty, S.; Dai, H.; Bhattacharya, P.; Fairweather, N. T.; Gibson, M. S.; Krause, J. A.; Guan, H., Iron-Based Catalysts for the Hydrogenation of Esters to Alcohols. *J. Am. Chem. Soc.* **2014**, *136*, 7869-7872; (b) Werkmeister, S.; Junge, K.; Wendt, B.; Alberico, E.; Jiao, H.; Baumann, W.; Junge, H.; Gallou, F.; Beller, M., Hydrogenation of Esters to Alcohols with a Well-Defined Iron Complex. *Angew. Chem. Int. Ed.* **2014**, *53*, 8722-8726;

(c) Sharninghausen, L. S.; Mercado, B. Q.; Crabtree, R. H.; Hazari, N., Selective Conversion of Glycerol to Lactic Acid with Iron Pincer Precatalysts. *Chem. Commun.* **2015**, *51*, 16201-16204; (d) Elangovan, S.; Wendt, B.; Topf, C.; Bachmann, S.; Scalone, M.; Spannenberg, A.; Jiao, H.; Baumann, W.; Junge, K.; Beller, M., Improved Second Generation Iron Pincer Complexes for Effective Ester Hydrogenation. *Adv. Synth. Catal.* **2016**, *358*, 820-825; (e) Schneck, F.; Assmann, M.; Balmer, M.; Harms, K.; Langer, R., Selective Hydrogenation of Amides to Amines and Alcohols Catalyzed by Improved Iron Pincer Complexes. *Organometallics* **2016**, *35*, 1931-1943; (f) Rezayee, N. M.; Samblanet, D. C.; Sanford, M. S., Iron-Catalyzed Hydrogenation of Amides to Alcohols and Amines. *ACS Catal.* **2016**, *6*, 6377-6383; (g) Lane, Elizabeth M.; Hazari, N.; Bernskoetter, W. H., Iron-catalyzed urea synthesis: dehydrogenative coupling of methanol and amines. *Chem. Sci.* **2018**, *9*, 4003-4008; (h) Lane, E. M.; Uttley, K. B.; Hazari, N.; Bernskoetter, W., Iron-Catalyzed Amide Formation from the Dehydrogenative Coupling of Alcohols and Secondary Amines. *Organometallics* **2017**, *36*, 2020-2025; (i) Jayarathne, U.; Hazari, N.; Bernskoetter, W. H., Selective Iron-Catalyzed N-Formylation of Amines using Dihydrogen and Carbon Dioxide. *ACS Catal.* **2018**, *8*, 1338-1345; (j) Jayarathne, U.; Zhang, Y.; Hazari, N.; Bernskoetter, W. H., Selective Iron-Catalyzed Deaminative Hydrogenation of Amides. *Organometallics* **2017**, *36*, 409-416.

11. For leading references that use Co catalysts supported by $R^N P^N H^P$ ligands see: (a) Zhang, G.; Scott, B. L.; Hanson, S. K., Mild and Homogeneous Cobalt-Catalyzed Hydrogenation of C-C, C-O, and C-N Bonds. *Angew. Chem. Int. Ed.* **2012**, *51*, 12102-12106; (b) Zhang, G.; Hanson, S. K., Cobalt-Catalyzed Transfer Hydrogenation of C-O and C-N Bonds. *Chem. Commun.* **2013**, *49*, 10151-10153; (c) Zhang, G.; Vasudevan, K. V.; Scott, B. L.;

Hanson, S. K., Understanding the Mechanisms of Cobalt-Catalyzed Hydrogenation and Dehydrogenation Reactions. *J. Am. Chem. Soc.* **2013**, *135*, 8668-8681; (d) Yin, Z.; Zeng, H.; Wu, J.; Zheng, S.; Zhang, G., Cobalt-Catalyzed Synthesis of Aromatic, Aliphatic, and Cyclic Secondary Amines via a “Hydrogen-Borrowing” Strategy. *ACS Catal.* **2016**, *6*, 6546-6550; (e) Fu, S.; Chen, N.-Y.; Liu, X.; Shao, Z.; Luo, S.-P.; Liu, Q., Ligand-Controlled Cobalt-Catalyzed Transfer Hydrogenation of Alkynes: Stereodivergent Synthesis of Z- and E-Alkenes. *J. Am. Chem. Soc.* **2016**, *138*, 8588-8594; (f) Yuwen, J.; Chakraborty, S.; Brennessel, W. W.; Jones, W. D., Additive-Free Cobalt-Catalyzed Hydrogenation of Esters to Alcohols. *ACS Catal.* **2017**, *7*, 3735-3740; (g) Junge, K.; Wendt, B.; Cingolani, A.; Spannenberg, A.; Wei, Z.; Jiao, H.; Beller, M., Cobalt Pincer Complexes for Catalytic Reduction of Carboxylic Acid Esters. *Chem. Eur. J.* **2018**, *24*, 1046-1052.

12. For leading references that use Mn catalysts supported by ^RPN^HP ligands see: (a) Elangovan, S.; Garbe, M.; Jiao, H.; Spannenberg, A.; Junge, K.; Beller, M., Hydrogenation of Esters to Alcohols Catalyzed by Defined Manganese Pincer Complexes. *Angew. Chem. Int. Ed.* **2016**, *55*, 15364-15368; (b) Nguyen, D. H.; Trivelli, X.; Capet, F.; Paul, J.-F.; Dumeignil, F.; Gauvin, R. M., Manganese Pincer Complexes for the Base-Free, Acceptorless Dehydrogenative Coupling of Alcohols to Esters: Development, Scope, and Understanding. *ACS Catal.* **2017**, *7*, 2022-2032; (c) Garbe, M.; Budweg, S.; Papa, V.; Wei, Z.; Hornke, H.; Bachmann, S.; Scalone, M.; Spannenberg, A.; Jiao, H.; Junge, K.; Beller, M., Chemoselective Semihydrogenation of Alkynes Catalyzed by Manganese(I)-PNP Pincer Complexes. *Catal. Sci. Tech.* **2020**, *10*, 3994-4001; (d) Zubar, V.; Dewanji, A.;

Rueping, M., Chemoselective Hydrogenation of Nitroarenes Using an Air-Stable Base-Metal Catalyst. *Org. Lett.* **2021**, *23*, 2742-2747.

13. Khusnutdinova, J. R.; Milstein, D., Metal–Ligand Cooperation. *Angew. Chem. Int. Ed.* **2015**, *54*, 12236-12273.

14. Smith, N. E.; Bernskoetter, W. H.; Hazari, N., The Role of Proton Shuttles in the Reversible Activation of Hydrogen via Metal–Ligand Cooperation. *J. Am. Chem. Soc.* **2019**, *141*, 17350-17360.

15. (a) Joó, F., Breakthroughs in Hydrogen Storage-Formic Acid as a Sustainable Storage Material for Hydrogen. *ChemSusChem* **2008**, *1*, 805-808; (b) Wang, W.-H.; Himeda, Y.; Muckerman, J. T.; Manbeck, G. F.; Fujita, E., CO₂ Hydrogenation to Formate and Methanol as an Alternative to Photo-and Electrochemical CO₂ Reduction. *Chem. Rev.* **2015**, *115*, 12936-12973; (c) Eppinger, J. r.; Huang, K.-W., Formic Acid as a Hydrogen Energy Carrier. *ACS Energy Lett.* **2017**, *2*, 188-195; (d) Bernskoetter, W. H.; Hazari, N., Reversible Hydrogenation of Carbon Dioxide to Formic Acid and Methanol: Lewis Acid Enhancement of Base Metal Catalysts. *Acc. Chem. Res.* **2017**, *50*, 1049-1058; (e) Sordakis, K.; Tang, C.; Vogt, L. K.; Junge, H.; Dyson, P. J.; Beller, M.; Laurenczy, G., Homogeneous Catalysis for Sustainable Hydrogen Storage in Formic Acid and Alcohols. *Chem. Rev.* **2018**, *118*, 372-433.

16. (a) Bianchini, C.; Glendenning, L.; Peruzzini, M.; Purches, G.; Zanolini, F.; Farnetti, E.; Graziani, M.; Nardin, G., Synthesis of the New Chiral (R)- and (S)-Aminodiphosphine Ligands *sec*-Butylbis(2-(diphenylphosphino)ethyl)amine, *sec*-Butylbis(2-(dicyclohexylphosphino)ethyl)amine, and (α -Methylbenzyl)bis(2-(dicyclohexylphosphino)ethyl)amine and Their Organometallic Chemistry When

Combined with Iridium. *Organometallics* **1997**, *16*, 4403-4414; (b) Dong, Q.; Rose, M. J.; Wong, W.-Y.; Gray, H. B., Dual Coordination Modes of Ethylene-Linked NP2 Ligands in Cobalt(II) and Nickel(II) Iodides. *Inorg. Chem.* **2011**, *50*, 10213-10224; (c) Ramaraj, A.; Nethaji, M.; Jagirdar, B. R., Contrasting reactivity behaviour of the [RuHCl(CO)(PNP)] complex with electrophilic reagents XOTf (X = H, CH₃, Me₃Si). *Dalton Trans.* **2014**, *43*, 14625-14635; (d) Naicker, D.; Friedrich, H. B.; Omondi, B., Cobalt Aminodiphosphine Complexes as Catalysts in the Oxidation of n-Octane. *RSC Adv.* **2015**, *5*, 63123-63129; (e) Ramaraj, A.; Reddy, K. H. K.; Keil, H.; Herbst-Irmer, R.; Stalke, D.; Jemmis, E. D.; Jagirdar, B. R., Approaches to Sigma Complexes via Displacement of Agostic Interactions: An Experimental and Theoretical Investigation. *Organometallics* **2017**, *36*, 2736-2745; (f) Goren Keskin, S.; Stanley, J. M.; Cowley, A. H., Synthesis, characterization and theoretical investigations of molybdenum carbonyl complexes with phosphorus/nitrogen/phosphorus ligand as bidentate and tridentate modes. *Polyhedron* **2017**, *138*, 206-217; (g) Salvarese, N.; Refosco, F.; Seraglia, R.; Roverso, M.; Dolmella, A.; Bolzati, C., Synthesis and characterization of rhenium(iii) complexes with (Ph₂PCH₂CH₂)₂NR diposphinoamine ligands. *Dalton Trans.* **2017**, *46*, 9180-9191; (h) Kostas, I. D.; Antonopoulou, G.; Potamitis, C.; Raptopoulou, C. P.; Psycharis, V., Platinum complexes with a methoxy-amino phosphine or a nitrogen-containing bis(phosphine) ligand. Synthesis, characterization and application to hydrogenation of trans-cinnamaldehyde. *J. Organomet. Chem.* **2017**, *828*, 133-141; (i) Keskin, S. G.; Stanley, J. M.; Mitchell, L. A.; Holliday, B. J., Synthesis, characterization, coordination chemistry, and luminescence studies of copper, silver, palladium, and platinum complexes with a phosphorus/nitrogen/phosphorus ligand. *Inorg. Chim. Acta* **2019**, *486*, 200-212.

17. Dai, H.; Li, W.; Krause, J. A.; Guan, H., Experimental Evidence of syn H–N–Fe–H Configurational Requirement for Iron-Based Bifunctional Hydrogenation Catalysts. *Inorg. Chem.* **2021**, *60*, 6521-6535.
18. Chatt, J.; Coffey, R. S.; Shaw, B. L., 1355. Hydrido-Complexes of Iridium(III) Stabilised by Tertiary Phosphines and Arsines. *J. Chem. Soc.* **1965**, 7391-7405.
19. Curley, J. B.; Smith, N. E.; Bernskoetter, W. H.; Hazari, N.; Mercado, B. Q., Catalytic Formic Acid Dehydrogenation and CO₂ Hydrogenation Using Iron PN^RP Pincer Complexes with Isonitrile Ligands. *Organometallics* **2018**, *37*, 3846-3853.
20. (a) Barnard, J. H.; Wang, C.; Berry, N. G.; Xiao, J., Long-Range Metal–Ligand Bifunctional Catalysis: Cyclometallated Iridium Catalysts for the Mild and Rapid Dehydrogenation of Formic Acid. *Chem. Sci.* **2013**, *4*, 1234-1244; (b) Manaka, Y.; Wang, W.-H.; Suna, Y.; Kambayashi, H.; Muckerman, J. T.; Fujita, E.; Himeda, Y., Efficient H₂ Generation From Formic Acid Using Azole Complexes in Water. *Catal. Sci. Tech.* **2014**, *4*, 34-37; (c) Hull, J. F.; Himeda, Y.; Wang, W.-H.; Hashiguchi, B.; Periana, R.; Szalda, D. J.; Muckerman, J. T.; Fujita, E., Reversible Hydrogen Storage Using CO₂ and a Proton-Switchable Iridium Catalyst in Aqueous Media Under Mild Temperatures and Pressures. *Nature Chem.* **2012**, *4*, 383-388.
21. (a) Kar, S.; Rauch, M.; Leitus, G.; Ben-David, Y.; Milstein, D., Highly Efficient Additive-Free Dehydrogenation of Neat Formic Acid. *Nature Catal.* **2021**, *4*, 193-201; (b) Celaje, J. J. A.; Lu, Z.; Kedzie, E. A.; Terrile, N. J.; Lo, J. N.; Williams, T. J., A Prolific Catalyst for Dehydrogenation of Neat Formic Acid. *Nature Commun.* **2016**, *7*, 11308; (c) Boddien, A.; Loges, B.; Junge, H.; Beller, M., Hydrogen Generation at Ambient Conditions: Application in Fuel Cells. *ChemSusChem* **2008**, *1*, 751-758.

22. In catalysis, a 2:1 mixture of ^tBuOH to toluene was used. However, THF was selected as the solvent for calculations because its dielectric constant of 7.58 is conveniently close to a 2:1 weighted average of ^tBuOH (10.06) and toluene (2.38).
23. Hazari, N.; Heimann, J. E., Carbon Dioxide Insertion into Group 9 and 10 Metal–Element σ Bonds. *Inorg. Chem.* **2017**, *56*, 13655-13678.
24. NMR experiments indicate that protonation of **2** with formic acid results exclusively in the formation of **3 syn** before any decarboxylation. Therefore, it is unlikely that **3 anti** plays a role in catalysis, although a mechanism in which **3 syn** undergoes turnover limiting isomerization to **3 anti** followed by fast decarboxylation cannot be rigorously excluded. In the case of **2-H**, previous work (see: *J. Am. Chem. Soc.* **2016**, *138*, 14890-14904) has shown that protonation with formic acid results exclusively in the formation of **3-H anti** before any decarboxylation. Therefore, in this case it is unlikely that **3-H syn** plays a role in catalysis.
25. These two values are likely within error of each other.
26. (a) Bertini, F.; Gorgas, N.; Stöger, B.; Peruzzini, M.; Veiros, L. F.; Kirchner, K.; Gonsalvi, L., Efficient and Mild Carbon Dioxide Hydrogenation to Formate Catalyzed by Fe(II) Hydrido Carbonyl Complexes Bearing 2,6-(Diaminopyridyl)diphosphine Pincer Ligands. *ACS Catal.* **2016**, *6*, 2889-2893; (b) Filonenko, G. A.; Hensen, E. J. M.; Pidko, E. A., Mechanism of CO₂ Hydrogenation to Formates by Homogeneous Ru-PNP Pincer Catalyst: From a Theoretical Description to Performance Optimization. *Catal. Sci. Tech.* **2014**, *4*, 3474-3485; (c) Filonenko, G. A.; van Putten, R.; Schulpen, E. N.; Hensen, E. J. M.; Pidko, E. A., Highly Efficient Reversible Hydrogenation of Carbon Dioxide to Formates Using a Ruthenium PNP-Pincer Catalyst. *ChemCatChem* **2014**, *6*, 1526-1530.

27. A ⁱPrPN^HP ligated Fe complex with a dihydrogen ligand was recently crystallographically characterized. See Curley, J. B.; Smith, N. E.; Bernskoetter, W. H.; Ertem, M. Z.; Hazari, N.; Mercado, B. Q.; Townsend, T. M.; Wang, X. Understanding the Properties and Decomposition of Highly Active Iron Pincer Complexes for Hydrogenation and Dehydrogenation Reactions. **2021**, *11*, In Press.
28. No stabilizing interactions between free formate and **3** or **3-Me** were identified by DFT.

Chapter 5: Iron, Cobalt, and Nickel Complexes Supported by a $i\text{PrPN}^{\text{Ph}}\text{P}$

Pincer Ligand

Tanya Townsend performed the experiments in the “Synthesis of a Cobalt $i\text{PrPN}^{\text{Ph}}\text{P}$ Complex” section and crystallized complex **4**.

I. Introduction

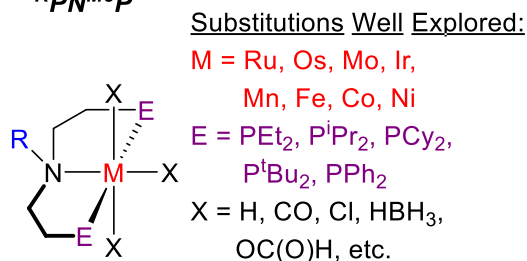
Pincer ligands are commonly used to support transition metal complexes due to their ability to generate species with high thermal stability as well as their modular design, which allows for facile tuning of both steric and electronic properties.¹ One notable application of pincer ligated complexes is in catalysis. For example, metal complexes supported by $\text{RPN}^{\text{H}}\text{P}$ ($\text{RPN}^{\text{H}}\text{P} = \text{HN}(\text{CH}_2\text{CH}_2\text{PR}_2)_2$, $\text{R} = \text{Et}$, $i\text{Pr}$, Cy , $t\text{Bu}$, Ph) ligands can catalyze a wide range of transformations, including (de)hydrogenation reactions relevant to renewable energy storage^{2,3,4,5,6} and the synthesis of fine and commodity chemicals.^{7,8,9,10,11} In fact, the complex $(\text{PhPN}^{\text{H}}\text{P})\text{RuHCl}(\text{CO})$, known as Ru-MACHO, is commercially used for the hydrogenation of esters.^{8c} To date, many studies have explored the effect of varying the phosphine substituents of $\text{RPN}^{\text{H}}\text{P}$ ligands in order to understand their reactivity and generate improved catalysts.^{2d, 3a, c, e, f, 5b, 6a, 8b, d, 9d, e, 10c-e, 10g, 11a} In contrast, there is a relative paucity of information on the synthetic and catalytic consequences of varying the substituent on the central nitrogen donor (Figure 5.01a).

The vast majority of studies that have explored the influence of the substituent on the nitrogen donor have compared complexes supported by $\text{RPN}^{\text{H}}\text{P}$ ligands to species with simple tertiary amine-containing $\text{RPN}^{\text{Me}}\text{P}$ ($\text{RPN}^{\text{Me}}\text{P} = \text{CH}_3\text{N}(\text{CH}_2\text{CH}_2\text{PR}_2)_2$, $\text{R} = \text{Et}$, $i\text{Pr}$, Cy , $t\text{Bu}$, Ph) ligands.^{3d, g, 4d, g, 5a, c, 8d, g, 9b, c, j, 10c, 11b} The primary purpose of most of these

investigations was to determine whether or not the pincer ligand was engaging in metal-ligand cooperation (MLC).¹² Nevertheless, this relatively small change in the ligand backbone has large synthetic and catalytic consequences. For example, complexes containing the $^R\text{PN}^{\text{Me}}\text{P}$ ligand often require different synthetic routes compared to analogous complexes with $^R\text{PN}^{\text{H}}\text{P}$ ligands.^{4d, 10c, 11b} Additionally, changing from a $^R\text{PN}^{\text{H}}\text{P}$ ligand to a $^R\text{PN}^{\text{Me}}\text{P}$ ligand can in some cases completely inhibit catalysis or in other cases result in systems that are orders of magnitude more productive.^{3g, 4d} For instance, whereas Fe catalysts supported by a $^i\text{PrPN}^{\text{H}}\text{P}$ ligand give approximately 9,000 turnovers for CO_2 hydrogenation to formate, Fe catalysts supported by a $^i\text{PrPN}^{\text{Me}}\text{P}$ ligand give more than 60,000 turnovers under the same conditions.^{4d} Despite these studies demonstrating the profound difference in reactivity when the substituent on the nitrogen donor is changed, there are few examples of ligands of the type $^R\text{PN}^{R'}\text{P}$ where R' is not a hydrogen or methyl

Previous Work:

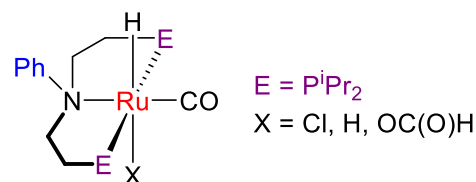
a) Complexes ligated by $^R\text{PN}^{\text{H}}\text{P}$ and $^R\text{PN}^{\text{Me}}\text{P}$



Substitutions Underexplored:
 $R = \text{H, Me}$

Catalysts for numerous reactions

b) Ru complexes ligated by $^i\text{PrPN}^{\text{Ph}}\text{P}$



Catalysts for formic acid dehydrogenation and CO_2 hydrogenation

c) This Work: First-row complexes ligated by $^i\text{PrPN}^{\text{Ph}}\text{P}$

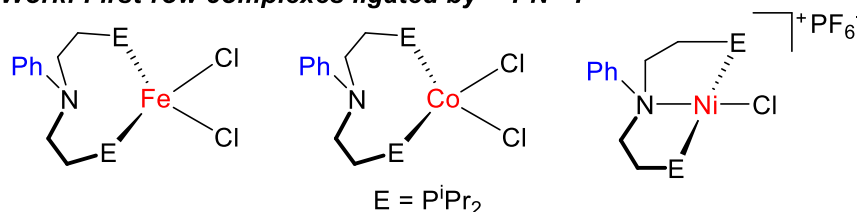


Figure 5.01. a) Previous investigations of $^R\text{PN}^{R'}\text{P}$ complexes; b) Recently published Ru $^i\text{PrPN}^{\text{Ph}}\text{P}$ complexes; c) Some of the novel $^i\text{PrPN}^{\text{Ph}}\text{P}$ supported Fe, Co, and Ni complexes synthesized and characterized in this work.

substituent.¹³ This severely limits our understanding of how to tune the substituent on the nitrogen donor of $^R\text{PN}^{R'}\text{P}$ type ligands to improve catalytic performance.

We recently reported the synthesis of the novel $^i\text{PrPN}^{\text{Ph}}\text{P}$ ($^i\text{PrPN}^{\text{Ph}}\text{P} = \text{PhN}(\text{CH}_2\text{CH}_2\text{P}^i\text{Pr}_2)_2$) ligand, which contains a phenyl substituent on the nitrogen donor (Figure 5.01b). A series of Ru hydride complexes containing the $^i\text{PrPN}^{\text{Ph}}\text{P}$ ligand were prepared. These complexes exhibit significantly longer Ru–N bond lengths than their $^i\text{PrPN}^{\text{Me}}\text{P}$ and $^i\text{PrPN}^{\text{H}}\text{P}$ congeners, indicating that the nitrogen ligand is a worse σ -donor. The relatively large steric bulk of the phenyl group also resulted in the characterization of a formate complex where the formate ligand is oriented *anti* to the N-phenyl moiety.¹⁴ In contrast, the more stable isomer in the analogous Ru complexes containing $^i\text{PrPN}^{\text{H}}\text{P}$ and $^i\text{PrPN}^{\text{Me}}\text{P}$ ligands has the formate ligand oriented *syn* to the nitrogen substituent.^{3d} Potentially as a result of their different coordination chemistry, the $^i\text{PrPN}^{\text{Ph}}\text{P}$ supported Ru complexes demonstrated improved activity for additive free formic acid dehydrogenation and CO_2 hydrogenation compared to related Ru complexes with $^i\text{PrPN}^{\text{H}}\text{P}$ and $^i\text{PrPN}^{\text{Me}}\text{P}$ ligands. This study illustrated the promise of exploring novel substituents on the nitrogen donor of the privileged $^R\text{PN}^{R'}\text{P}$ scaffold.

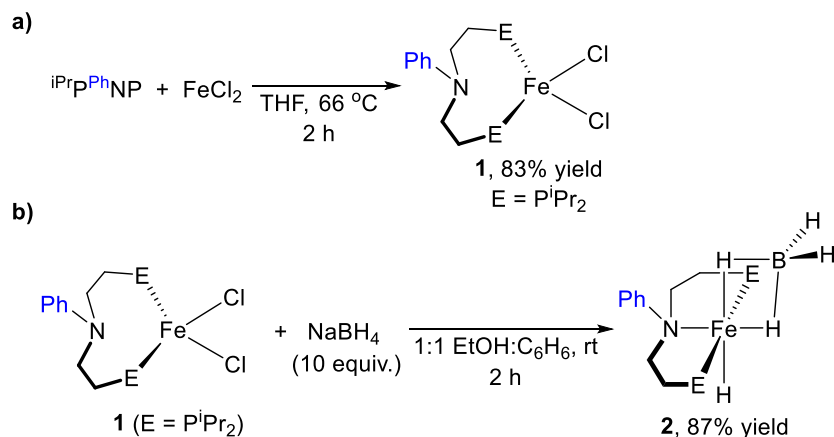
Over the last decade, there has been interest in using catalysts containing cheaper, more abundant, and frequently less toxic first-row transition metals, such as Fe, Co, and Ni instead of more traditional systems based on costly and rare second and third-row transition metals such as Ru and Ir.¹⁵ Accordingly, there are now many examples of base metal catalysts for (de)hydrogenative reactions that achieve high turnover frequencies (TOFs) and numbers (TONs), including systems supported by $^R\text{PN}^{\text{H}}\text{P}$ or $^R\text{PN}^{\text{Me}}\text{P}$ ligands.^{4-6, 9-11} Here, we describe the synthesis of a series of Fe, Co, and Ni complexes supported by the

$i\text{PrPN}^{\text{Ph}}\text{P}$ ligand (Figure 5.01c). We characterize these complexes using IR, UV-Vis, NMR, and Mössbauer spectroscopies, as well as X-ray crystallography. This allows us to show that there are significant differences in the properties and reactivity of base metal complexes containing the $i\text{PrPN}^{\text{Ph}}\text{P}$ ligand compared to those containing $i\text{PrPN}^{\text{HP}}$ or $i\text{PrPN}^{\text{MeP}}$ ligands. Additionally, we compare the catalytic performance of a $i\text{PrPN}^{\text{Ph}}\text{P}$ -ligated Fe hydride complex with a $i\text{PrPN}^{\text{MeP}}$ -ligated Fe hydride complex in additive free formic acid dehydrogenation. All of these data highlight the importance of the substituent on the nitrogen atom in complexes containing $^{\text{R}}\text{PN}^{\text{R'}}\text{P}$ ligands, which will be valuable for the design of improved catalysts.

II. Results and Discussion

Synthesis of Iron $i\text{PrPN}^{\text{Ph}}\text{P}$ Complexes

The $i\text{PrPN}^{\text{Ph}}\text{P}$ ligand was metallated to Fe by refluxing the ligand in THF for two hours with anhydrous FeCl_2 , an analogous procedure to that used to prepare the related $i\text{PrPN}^{\text{HP}}$ and $i\text{PrPN}^{\text{MeP}}$ ligated derivatives (Scheme 5.01a).^{4d, 16} After purification, $(\kappa^2\text{-}i\text{PrPN}^{\text{Ph}}\text{P})\text{FeCl}_2$ (**1**) was isolated as a white solid in 83% yield. Complex **1** is paramagnetic and a solution magnetic measurement using the Evans NMR method was consistent with



Scheme 5.01. a) Synthesis of $(\kappa^2\text{-}i\text{PrPN}^{\text{Ph}}\text{P})\text{FeCl}_2$ (**1**) and b) $(i\text{PrPN}^{\text{Ph}}\text{P})\text{FeH}(\kappa^2\text{-BH}_4)$ (**2**).

an $S = 2$ ground state ($4.5 \pm 0.3 \mu_B$). Surprisingly, X-ray crystallography showed that the nitrogen donor of the $iPrPN^{Ph}P$ ligand is not bound to the Fe center in **1** (Figure 5.02a). As a result, the geometry around the Fe is distorted tetrahedral. This is indicated by the four-coordinate geometry index, τ_4 , which is 0.91 for this complex.¹⁷ This type of bidentate coordination mode is uncommon for $RPN^R P$ ligands, but is also observed in the analogous Co complex (*vide infra*). The Fe–P (2.465(2) Å & 2.460(2) Å) and Fe–Cl (2.245(2) Å & 2.246(2) Å) bond lengths of **1** are shorter than the corresponding bond distances in $(iPrPN^H P)FeCl_2$ (**1-H**) and $(iPrPN^{Me} P)FeCl_2$ (**1-Me**), as expected for a complex with a lower coordination number.^{4d, 16} The P–Fe–P bond angle is $109.61(8)^\circ$, as opposed to the approximately linear angle observed when $RPN^R P$ ligands bind in a tridentate fashion. The structure of **1** suggests that the nitrogen atom of the pincer ligand is a poorer σ -donor in

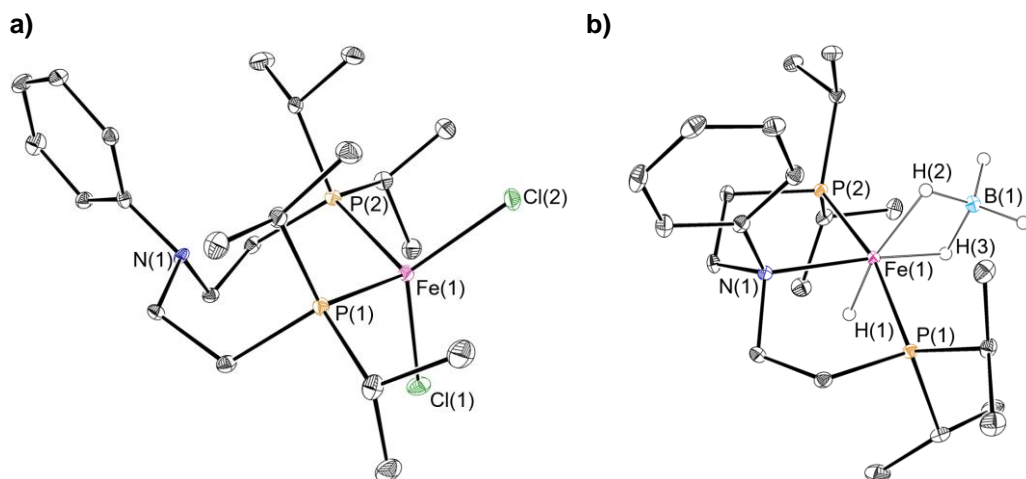


Figure 5.02. Solid-state structures of **a) 1** and **b) 2** with ellipsoids at 30% probability. Hydrogen atoms not bound to Fe or B omitted for clarity. All hydrides were located in the difference map and freely refined. Selected bond lengths (Å) and angles ($^\circ$) for **1**: Fe(1)–P(1) 2.465(2), Fe(1)–P(2) 2.460(2), Fe(1)–Cl(1) 2.245(2), Fe(1)–Cl(2) 2.246(2), P(1)–Fe(1)–P(2) $109.61(8)$, P(1)–Fe(1)–Cl(1) $103.45(9)$, P(1)–Fe(1)–Cl(2) $109.06(9)$, P(2)–Fe(1)–Cl(1) $104.50(9)$, P(2)–Fe(1)–Cl(2) $107.10(9)$, Cl(1)–Fe(1)–Cl(2) $122.65(10)$. For **2**: Fe(1)–N(1) 2.1711(14), Fe(1)–P(1) 2.1918(6), Fe(1)–P(2) 2.1874(6), Fe(1)–H(1) 1.43(3), Fe(1)–H(2) 1.68(2), Fe(1)–H(3) 1.54(2), P(1)–Fe(1)–P(2) $166.23(2)$, P(1)–Fe(1)–N(1) $85.90(5)$, P(1)–Fe(1)–H(1) $83.0(12)$, P(1)–Fe(1)–H(2) $98.4(9)$, P(1)–Fe(1)–H(3) $92.8(10)$, P(2)–Fe(1)–N(1) $85.93(5)$, P(2)–Fe(1)–H(1) $84.9(12)$, P(2)–Fe(1)–H(2) $95.1(9)$, P(2)–Fe(1)–H(3) $94.4(10)$, N(1)–Fe(1)–H(1) $82.2(10)$, N(1)–Fe(1)–H(2) $115.5(7)$, N(1)–Fe(1)–H(3) $175.2(8)$, H(1)–Fe(1)–H(2) $162.4(12)$, H(1)–Fe(1)–H(3) $93.1(12)$, H(2)–Fe(1)–H(3) $69.3(10)$.

$i\text{PrPN}^{\text{Ph}}\text{P}$ than in its N–H and N–Me analogues, although steric factors could also cause the decoordination of the nitrogen donor.

^{57}Fe Mössbauer spectroscopy was performed on a powder sample of **1** to gain further insight into its electronic structure (Figure 5.03a). The 80 K Mössbauer spectrum of **1** is well fit to a single Fe species, with $\delta = 0.75$ mm/s and $\Delta E_Q = 2.88$ mm/s. This isomer shift is consistent with a high-spin, $S = 2$, Fe(II) species, as expected.¹⁸ However, the isomer shift of **1** is less positive than that of **1-H** ($\delta = 0.86$ mm/s).¹⁶ This indicates greater s-electron density at the Fe center in **1** compared to its congener with a $i\text{PrPN}^{\text{H}}\text{P}$ ligand, as expected when comparing four and five coordinate species within a series of high spin

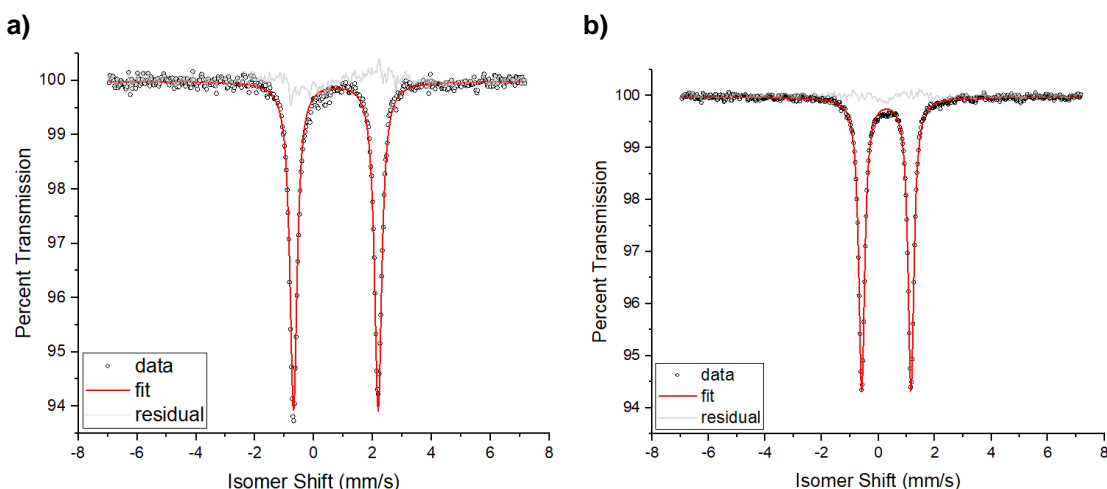


Figure 5.03. ^{57}Fe Mössbauer (80 K) of solid powders of **a) 1** and **b) 2**.

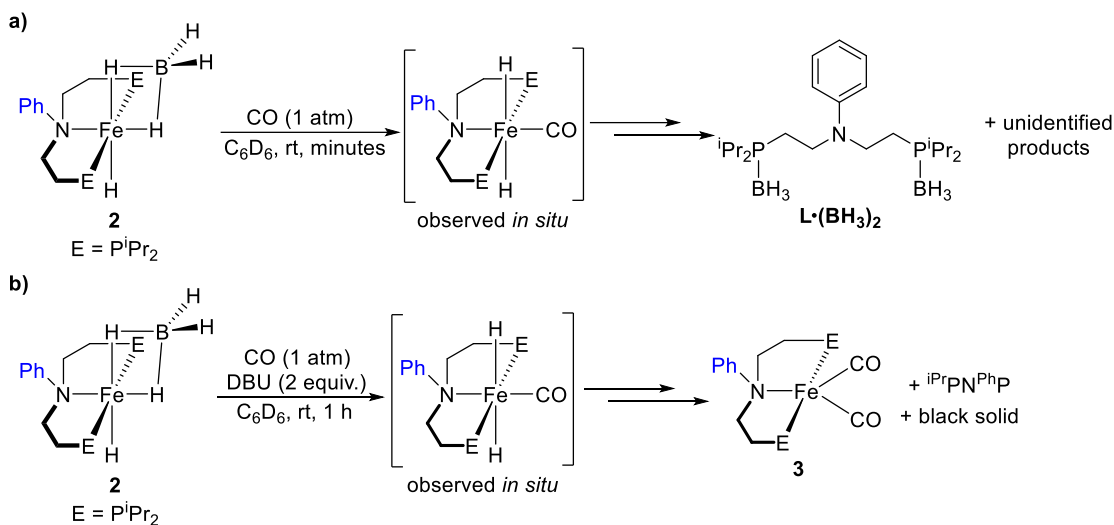
iron(II) complexes.¹⁸⁻¹⁹

Studies on Fe complexes supported by $\text{RPN}^{\text{H}}\text{P}$ and $\text{RPN}^{\text{Me}}\text{P}$ ligands demonstrate that six-coordinate hydride complexes with ancillary CO ligands typically give the highest TONs and TOFs in catalytic hydrogenation and dehydrogenation reactions.^{1d} We therefore added CO to **1**. Unfortunately, addition of one atmosphere of CO to **1** does not lead to the formation of a carbonyl containing species. In fact, no change to the NMR spectra of **1** are observed upon stirring for 24 hours under CO. Therefore, in order to generate a carbonyl

hydride complex, we treated **1** with a hydride source. The reaction of **1** with excess NaBH₄ in a 1:1 solvent mixture of benzene and ethanol gives the diamagnetic complex (iPrPN^{Ph}P)FeH(κ^2 -BH₄) (**2**) in 87% yield, analogous to the iPrPN^{Me}P congener (Scheme 5.01b).^{4d} In the solid state, the Fe center in **2** has a distorted octahedral geometry, as shown in Figure 5.02b. The Fe–N bond length in **2** is 2.1711(14) Å, which is significantly longer than the Fe–N bond in (iPrPN^{Me}P)FeH(κ^2 -BH₄) (**2-Me**, 2.079(2) Å). This is consistent with the weaker σ -donating ability of the nitrogen donor in the iPrPN^{Ph}P ligand compared to the iPrPN^{Me}P ligand. In **2**, the P–Fe–P bond angle is 166.23(2)°, analogous to other species where the ^RPN^RP ligand binds in a standard tridentate fashion.^{4d, 20} A surprising feature of **2** is that it is unstable when placed under vacuum for more than approximately ten minutes. This stands in contrast to **2-Me**, which is stable indefinitely under vacuum.^{4d}

⁵⁷Fe Mössbauer spectra were obtained at 80 K of powder samples of **2** (Figure 5.03b) and **2-Me** (see Appendix D). The Mössbauer spectrum of **2** is well fit to a single Fe species, with δ = 0.29 mm/s and ΔE_Q = 1.74 mm/s. For **2-Me**, these values are δ = -0.25 mm/s and ΔE_Q = 1.53 mm/s. Both are consistent with low-spin, S = 0, Fe(II) complexes, but the 0.54 mm/s difference in isomer shifts is striking. This disparity suggests significantly greater s-electron density at the Fe center in **2-Me**, which leads to a more negative isomer shift due to the more negative effective Fe nuclear charge. This is consistent with increased σ -donation from the nitrogen moiety in iPrPN^{Me}P compared to iPrPN^{Ph}P.¹⁸

With **2** in hand, we again endeavored to prepare a Fe carbonyl hydride complex supported by the iPrPN^{Ph}P ligand. Addition of one atmosphere of CO to **2** leads to the immediate formation of the desired dihydride product (iPrPN^{Ph}P)Fe(H)₂(CO) *in situ*. This



Scheme 5.02. a) Attempted synthesis of $(iPrPN^{Ph}P)FeH(CO)(HBH_3)$ and isolation of decomposition product $L \cdot (BH_3)_2$; b) Attempted synthesis of $(iPrPN^{Ph}P)Fe(H)_2(CO)$ and isolation of $(iPrPN^{Ph}P)Fe(CO)_2$ (**3**).

is followed, however, by rapid decomposition to a complex mixture of products and an intractable black precipitate within minutes (Scheme 5.02a). Identification of $(iPrPN^{Ph}P)Fe(H)_2(CO)$ by NMR spectroscopy was based on spectroscopic similarities to the $iPrPN^{Me}P$ congener $(iPrPN^{Me}P)Fe(H)_2(CO)$ (see Appendix D).^{4b} An analogous mixture of products is obtained when **2** is treated with one equivalent of other π -acid ligands, such as 2,6-dimethylphenyl isonitrile or *tert*-butyl isonitrile. In almost all of these reactions, a broad peak was observed at 31 ppm in the ^{31}P NMR spectra (see Appendix D). This species was also observed in small amounts when solid samples of **2** were exposed to vacuum for more than approximately fifteen minutes. Single crystals grown in pentane from the reaction of **2** and CO revealed that this peak corresponds to a Lewis acid-base adduct between the demetallated $iPrPN^{Ph}P$ ligand and an equivalent of BH_3 bound to each phosphorus atom ($PhN\{CH_2CH_2P^{iPr}_2(BH_3)\}_2$, $L \cdot (BH_3)_2$) (Figure 5.04a). $L \cdot (BH_3)_2$ was also independently synthesized through the reaction of $iPrPN^{Ph}P$ with a solution of $BH_3 \cdot THF$ in THF. The fate of the remainder of the $iPrPN^{Ph}P$ ligand originally bound to Fe

is unknown. Analogous borane adducts have been isolated with $^R\text{PN}^H\text{P}$ ($R = \text{Cy}, \text{Ph}, ^t\text{Bu}$) upon decomposition of unstable Fe borohydride complexes.^{9e} Nevertheless, presumably adducts of this type are more likely to form with the $^i\text{PrPN}^{\text{Ph}}\text{P}$ ligand because of the weaker binding of the nitrogen donor to the Fe center. The geometry about the nitrogen in $\text{L}\cdot(\text{BH}_3)_2$ is trigonal planar (sum of the angles about N = 360.02°). This orientation presumably hinders the nitrogen lone pair from donating to the metal center, further complicating its ligation to Fe. Attempts to isolate the desired carbonyl dihydride product by decreasing

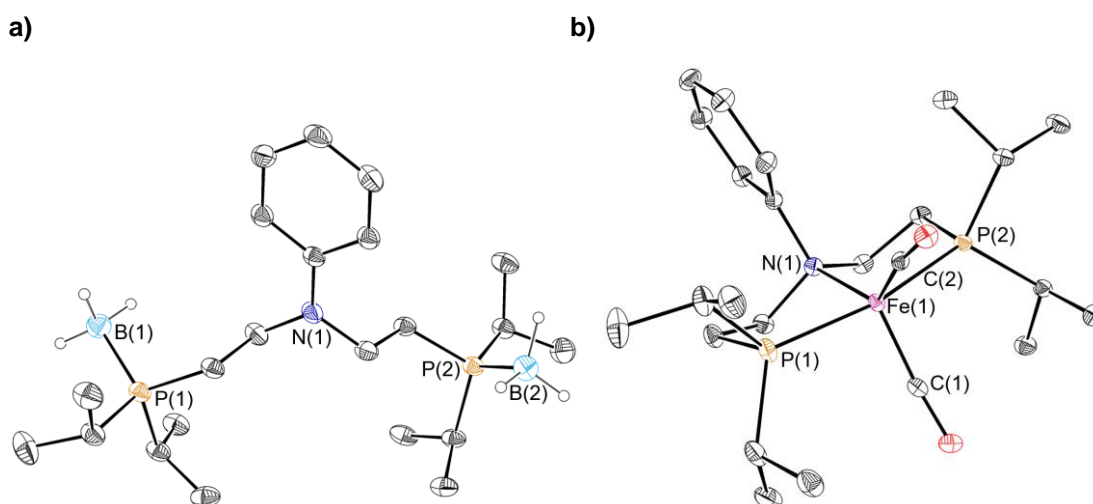


Figure 5.04. Solid state structures of decomposition products **a)** $\text{L}\cdot(\text{BH}_3)_2$ and **b)** **3** with ellipsoids at 30% probability. Hydrogen atoms not bound to B omitted for clarity. Two molecules of **3** are present in the asymmetric unit; one representative molecule is shown. Selected bond lengths (Å) and angles ($^\circ$) for depicted molecule of **3** (data for other molecule in SI): Fe(1)-P(1) 2.2348(5), Fe(1)-P(2) 2.2235(5), Fe(1)-N(1) 2.2529(14), Fe(1)-C(1) 1.7388(18), Fe(1)-C(2) 1.7236(17), P(1)-Fe(1)-P(2) 166.28(2), P(1)-Fe(1)-N(1) 83.48(4), P(1)-Fe(1)-C(1) 94.42(6), P(1)-Fe(1)-C(2) 95.72(6), P(2)-Fe(1)-N(1) 83.34(4), P(2)-Fe(1)-C(1) 94.43(6), P(2)-Fe(1)-C(2) 90.57(6), N(1)-Fe(1)-C(1) 114.17(7), N(1)-Fe(1)-C(2) 133.36(7), C(1)-Fe(1)-C(2) 112.39(8).

reaction time, temperature, or changing the solvent were unsuccessful.

In order to sequester the free BH_3 formed upon reaction of **2** with CO and potentially prevent demetallation of the ligand, base was added to the reaction. Inclusion of two equivalents of 1,8-diazabicyclo-(5.4.0)-undec-7-ene (DBU) led to the observation of the desired dihydride complex $(^i\text{PrPN}^{\text{Ph}}\text{P})\text{Fe}(\text{H})_2(\text{CO})$ *in situ*, but the species again could not be isolated. Over the course of approximately one hour, a 1:1 mixture of products was

observed by ^{31}P NMR spectroscopy (Scheme 5.02b). One product is the free $^{\text{iPr}}\text{PN}^{\text{Ph}}\text{P}$ ligand, and the second product, which has a ^{31}P NMR shift of 96 ppm and no hydride peaks in the ^1H NMR spectrum, was revealed by X-ray spectroscopy to be the Fe(0) species $(^{\text{iPr}}\text{PN}^{\text{Ph}}\text{P})\text{Fe}(\text{CO})_2$ (**3**) (Figure 5.04b). Once again, attempts to isolate the desired dihydride product using different reaction conditions or bases were unsuccessful.

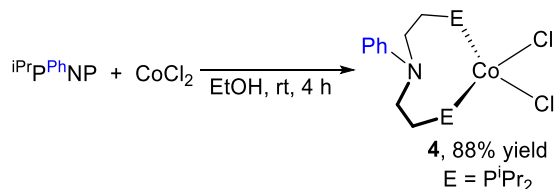
Complex **3** is an analogue of the commonly observed decomposition products $(^{\text{iPr}}\text{PN}^{\text{H}}\text{P})\text{Fe}(\text{CO})_2$ (**3-H**) and $(^{\text{iPr}}\text{PN}^{\text{Me}}\text{P})\text{Fe}(\text{CO})_2$ (**3-Me**), which have been isolated from catalytic mixtures using $^{\text{iPr}}\text{PN}^{\text{H}}\text{P}$ and $^{\text{iPr}}\text{PN}^{\text{Me}}\text{P}$ ligated catalysts.^{4b, 9j, 20} The geometry index τ_5 for **3** is 0.55,²¹ indicating that the geometry around the Fe center in **3** is in between trigonal bipyramidal and square pyramidal.²² In contrast, for **3-H** the τ_5 value is 0.33 which corresponds to a more square pyramidal geometry,²⁰ while for **3-Me** the τ_5 value is 0.62 indicating the geometry is more trigonal bipyramidal.^{9j} The Fe–N bond in **3** (2.2529(14) Å) is again significantly lengthened in comparison to the $^{\text{iPr}}\text{PN}^{\text{H}}\text{P}$ (2.1281(12) Å) and $^{\text{iPr}}\text{PN}^{\text{Me}}\text{P}$ (2.18(1) Å) supported analogues, indicating a weaker bond. The IR spectrum of **3** has two strong C≡O stretching bands at 1835 and 1772 cm^{-1} . These are very close to those attributed to the analogous bands in **3-H**, which are found at 1838 and 1767 cm^{-1} .²⁰ Although this implies a similar amount of back-donation from the Fe centers in the two complexes, this may arise because of the significant differences in geometry of the complexes. The $^{13}\text{C}\{^1\text{H}\}$ NMR spectrum of **3** contains two peaks corresponding to the carbonyl carbons, at 223.2 and 219.1 ppm. These also match well with **3-H**, which has peaks assigned to the carbonyl carbons at 222.4 and 226.2 ppm, and **3-Me**, which has peaks at 223.1 and 220.5 ppm.^{9j, 20} Unfortunately, reproducible isolation of **3** on scale was not possible, precluding its full characterization. This was partially due to its high solubility in all common organic

solvents, including pentane and hexamethyldisiloxane. Attempts to synthesize **3** via irradiation of $\text{Fe}(\text{CO})_5$ and $i\text{PrPN}^{\text{Ph}}\text{P}$ led to an inseparable mixture of products including **3** and several unidentified species (see Appendix D).

Addition of other simple L-type ligands to **2** such as pyridine and monodentate phosphines including PMe_3 and PPh_3 resulted in complex mixtures of products that could not be isolated (see Appendix D). As of yet, a synthetic strategy for the isolation of a six coordinate $i\text{PrPN}^{\text{Ph}}\text{P}$ Fe carbonyl hydride complex that can be compared catalytically to related congeners containing $i\text{PrPN}^{\text{H}}\text{P}$ and $i\text{PrPN}^{\text{Me}}\text{P}$ ligands has not been discovered. However, it is clear from our work that the Fe coordination chemistry of the $i\text{PrPN}^{\text{Ph}}\text{P}$ ligand deviates substantially from related $i\text{PrPN}^{\text{H}}\text{P}$ and $i\text{PrPN}^{\text{Me}}\text{P}$ analogues due to poorer σ -donation from the nitrogen, which influences ground state properties and frequently causes decreased stability in coordination complexes. This again demonstrates the significant role of the substituent on the nitrogen.

Synthesis of a Cobalt $i\text{PrPN}^{\text{Ph}}\text{P}$ Complex

Reaction of $i\text{PrPN}^{\text{Ph}}\text{P}$ with CoCl_2 in ethanol formed $(\kappa^2\text{-}i\text{PrPN}^{\text{Ph}}\text{P})\text{CoCl}_2$ (**4**) in 88% yield after 4 hours (Scheme 5.03). Single crystal X-ray crystallography indicates a distorted tetrahedral complex ($\tau_4 = 0.92$)¹⁷ in which the N of the $i\text{PrPN}^{\text{Ph}}\text{P}$ ligand is not coordinated to the metal center, analogous to Fe complex **1** (Figure 5.05). This is in contrast to $(i\text{PrPN}^{\text{H}}\text{P})\text{CoCl}_2$ (**4-H**), where the Co–N distance of 2.336(2) Å indicates the presence of a Co–N bond.²³ The P–Co–P bond angle is 114.0083(10)°, which is consistent with both



Scheme 5.03. Synthesis of $(\kappa^2\text{-}i\text{PrPN}^{\text{Ph}}\text{P})\text{CoCl}_2$ (**4**).

bidentate binding of the $i\text{PrPN}^{\text{Ph}}\text{P}$ ligand and the approximately tetrahedral geometry around Co. This is also reflected by the four-coordinate geometry index, τ_4 , which is 0.92 for **4**.¹⁷ This complex closely resembles the previously prepared distorted tetrahedral species $(\kappa^2\text{-}^{\text{Ph}}\text{PN}^{\text{Ph}}\text{P})\text{CoI}_2$, which has a Co–N distance of 3.684 Å and a P–Co–P angle of 113.829(9)°. ^{13b} The spin-only effective magnetic moment of **4** was determined using the Evans NMR method to be $4.1 \pm 0.3 \mu_{\text{B}}$, which is consistent with a $S = 3/2$ ground state. Similar to **1**, complex **4** was found to be unreactive toward CO even upon prolonged heating, precluding synthesis of a Co(II) carbonyl complex.

The synthesis of a Co(I) species with a bound $i\text{PrPN}^{\text{Ph}}\text{P}$ ligand was attempted via several routes. Following an analogous procedure for the synthesis of $(i\text{PrPN}^{\text{H}}\text{P})\text{Co}(\text{CO})_2\text{Cl}^{5\text{c}}$ and $(i\text{PrPN}^{\text{Me}}\text{P})\text{Co}(\text{CO})_2\text{Cl}^{5\text{a}}$ which have been utilized in formic acid dehydrogenation catalysis, metallation of $i\text{PrPN}^{\text{Ph}}\text{P}$ with $(\text{PPh}_3)_3\text{CoCl}$ under 1 atm CO yielded an inseparable mixture of products. Attempts to synthesize $(i\text{PrPN}^{\text{Ph}}\text{P})\text{CoCl}$ via metallation under a N_2 atmosphere also resulted in a mixture of products, including

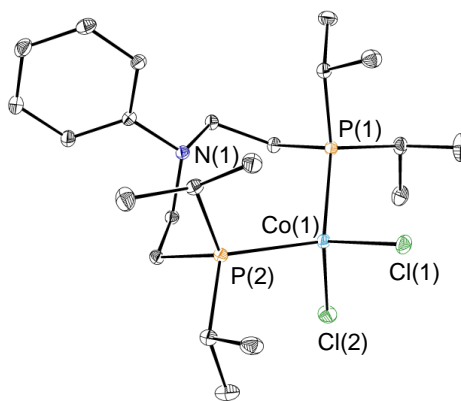


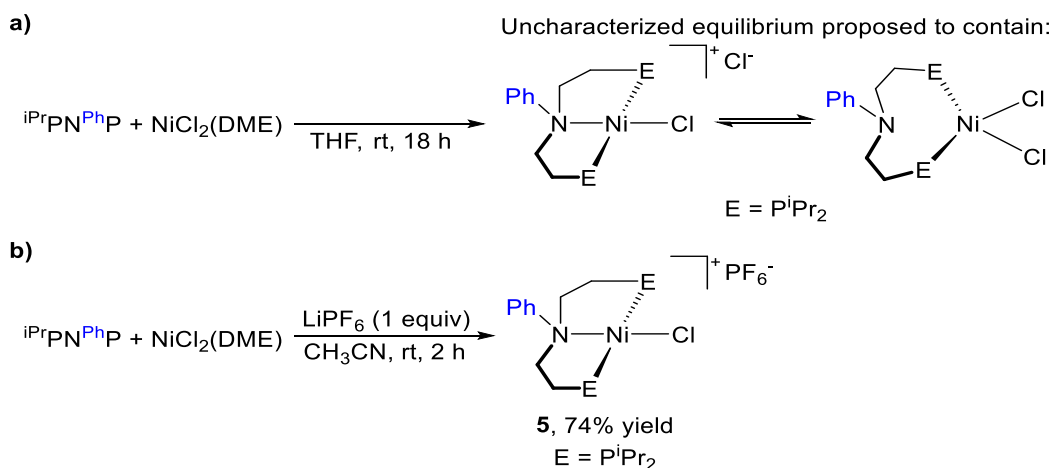
Figure 5.05. Solid state structure of **4** with ellipsoids at 30% probability. Hydrogen atoms omitted for clarity. Selected bond lengths (Å) and angles (°) for **4**: Co(1)–P(1) 2.38612(4), Co(1)–P(2) 2.38864(5), Co(1)–Cl(1) 2.23344(4), Co(1)–Cl(2) 2.23821(5), P(1)–Co(1)–P(2) 114.0083(10), P(1)–Co(1)–Cl(1) 107.2662(16), P(1)–Co(1)–Cl(2) 105.7718(8), P(2)–Co(1)–Cl(1) 109.8251(10), P(2)–Co(1)–Cl(2) 103.8767(11), Cl(1)–Co(1)–Cl(2) 116.25385(15).

paramagnetic species such as **4** (see Appendix D). This indicates that complexes of type

(ⁱPrPN^{Ph}P)Co^I may be susceptible to decomposition via disproportionation. The reaction of **4** with hydride sources such as ⁿBu₄NBH₄ resulted in the formation of an intractable black precipitate and identification of free ⁱPrPN^{Ph}P, which is similar to the problems encountered when preparing Fe carbonyl hydrides supported by the ⁱPrPN^{Ph}P ligand.

Synthesis of Nickel ⁱPrPN^{Ph}P Complexes

The ⁱPrPN^{Ph}P ligand was initially coordinated to Ni by stirring ⁱPrPN^{Ph}P with one equivalent of NiCl₂(DME) (DME = 1,2-dimethoxyethane) in THF at room temperature for 18 hours (Scheme 5.04a). A dark red-orange solid was isolated from the reaction. However, we were unable to unequivocally determine the speciation and structure of the product. This was because, although the ³¹P NMR spectrum in C₆D₆ of the isolated product contained only one broad peak at 57.7 ppm, the ¹H NMR spectrum contained resonances consistent with the presence of both paramagnetic and diamagnetic species. Further, variable temperature NMR data collected in different solvents indicated a possible solvent- and/or temperature-dependent equilibrium between the paramagnetic and diamagnetic species (see Appendix D). We propose that the diamagnetic complex is square planar [(ⁱPrPN^{Ph}P)NiCl]⁺[Cl]⁻, in which the ⁱPrPN^{Ph}P is bound to Ni in the standard tridentate



Scheme 5.04. Synthesis of Ni complexes in the **a)** absence and **b)** presence of PF₆⁻.

meridional fashion. The paramagnetic resonances may arise because the nitrogen donor of $i\text{PrPN}^{\text{Ph}}\text{P}$ decoordinates from the metal center and the outer-sphere chloride binds to give a neutral tetrahedral complex with the formula $(\kappa^2-i\text{PrPN}^{\text{Ph}}\text{P})\text{NiCl}_2$, analogous to Fe complex **1**. An equilibrium of this type would be expected to vary depending on the nature of the solvent and the temperature. In support of the presence of a square planar complex, we were able to crystallize $[(i\text{PrPN}^{\text{Ph}}\text{P})\text{NiCl}][1/2\text{NiCl}_4]$, which contains the $i\text{PrPN}^{\text{Ph}}\text{P}$ ligand bound in a tridentate meridional fashion from the reaction mixture (see Appendix D), although the source of the NiCl_4^{2-} anion is unclear. We note that the complexes $[(i\text{PrPN}^{\text{Me}}\text{P})\text{NiCl}][\text{Cl}]$ and $[(i\text{PrPN}^{\text{H}}\text{P})\text{NiBr}][\text{Br}]$ have previously been isolated and there is no evidence that they are in equilibrium with other species,²³⁻²⁴ which again highlights the different coordination chemistry between the $i\text{PrPN}^{\text{Ph}}\text{P}$ and $i\text{PrPN}^{\text{H}}\text{P}$ and $i\text{PrPN}^{\text{Me}}\text{P}$ ligands.

In order to avoid potential complications associated with having an outer-sphere Cl⁻ ligand, a reaction was performed between $i\text{PrPN}^{\text{Ph}}\text{P}$ and $\text{NiCl}_2(\text{DME})$ in the presence of one equivalent of LiPF_6 (Scheme 5.04b). After stirring for two hours at room temperature in CH_3CN , a bright orange solid was isolated. After workup, this species had no observable

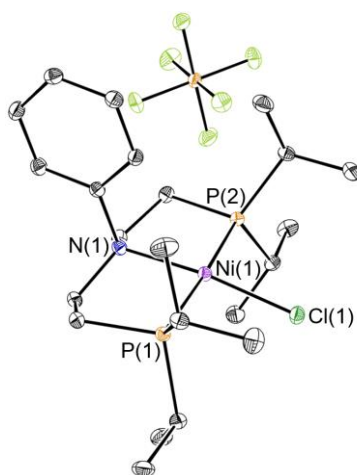
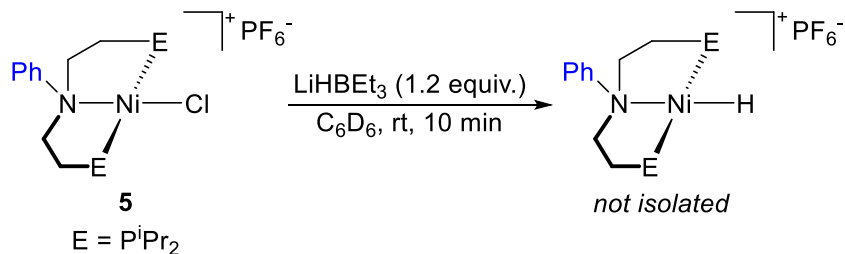


Figure 5.06. Solid state structure of **5** with ellipsoids at 30% probability. Hydrogen atoms and cocrystallized solvent omitted for clarity. Selected bond lengths (Å) and angles (°): Ni(1)-P(1) 2.2203(4), Ni(1)-P(2) 2.2203(4), Ni(1)-N(1) 1.9956(17), Ni(1)-Cl(1) 2.1656(6), P(1)-Ni(1)-P(2) 175.94(2) P(1)-Ni(1)-N(1) 88.129(12), P(1)-Ni(1)-Cl(1) 91.727(12), P(2)-Ni(1)-N(1) 88.129(12), P(2)-Ni(1)-Cl(1) 91.727(12), N(1)-Ni(1)-Cl(1) 171.09(5).

paramagnetic peaks in its ^1H NMR spectrum, and resonances consistent with a diamagnetic complex containing a bound $^i\text{PrPN}^{\text{Ph}}\text{P}$ ligand were present. The ^{31}P NMR spectrum contained a diagnostic resonance corresponding to an outer-sphere PF_6^- anion at -143.2 ppm, which integrated to half the intensity of the metallated $^i\text{PrPN}^{\text{Ph}}\text{P}$ peak at 40.8 ppm. This is similar to the broad ^{31}P NMR resonance observed that was proposed to correspond to $[(^i\text{PrPN}^{\text{Ph}}\text{P})\text{NiCl}][\text{Cl}]$ in the equilibrium mixture (*vide supra*). Single crystals grown by slow diffusion of benzene into a concentrated THF solution at room temperature were shown by X-ray diffraction to have the structure $[(^i\text{PrPN}^{\text{Ph}}\text{P})\text{NiCl}][\text{PF}_6]$ (**5**) (Figure 5.06). The $^i\text{PrPN}^{\text{Ph}}\text{P}$ binds in a tridentate meridional fashion, and the geometry around Ni is distorted square planar ($\tau_4 = 0.092$).¹⁷ The Ni–N bond distance in **5** is 1.9956(17) Å, which is significantly longer than the 1.953 Å distance in the congener $[(^i\text{PrPN}^{\text{Me}}\text{P})\text{NiCl}][\text{BPh}_4]$,²⁴ again consistent with weaker donation from the $^i\text{PrPN}^{\text{Ph}}\text{P}$ ligand. The P–Ni–P angle in **5** is 175.94(2)°, which is indicative of tridentate binding.

The complexes $[(^{\text{Cy}}\text{PN}^{\text{H}}\text{P})\text{NiH}][\text{BPh}_4]$ and $[(^{\text{Cy}}\text{PN}^{\text{Me}}\text{P})\text{NiH}][\text{BPh}_4]$ were previously found to be active catalysts for alkene hydrogenation²⁵ and therefore we endeavored to convert **5** into a Ni hydride complex. Reactions with multiple hydride sources including NaBH_4 and $(^n\text{Bu})_4\text{BH}_4$ led to a complex mixture of products and rapid demetallation of the $^i\text{PrPN}^{\text{Ph}}\text{P}$ ligand. In contrast, a reaction between **5** and a slight excess of LiHBEt_3 resulted in the clean formation of a complex containing a triplet resonance in the ^1H NMR spectrum



Scheme 5.05. Attempted synthesis of Ni hydride complex $[(^i\text{PrPN}^{\text{Ph}}\text{P})\text{NiH}][\text{PF}_6]$ from **5**.

in C₆D₆ at -20.98 ppm, which is consistent with a hydride. Additionally, the ³¹P NMR spectrum contained peaks at 56.4 ppm, corresponding to the coordinated ⁱPrPN^{Ph}P ligand, and -141.7 ppm, corresponding to the PF₆ anion (see Appendix D). Based on spectral similarities to previously isolated complexes,²⁵ we propose this species is the desired product [(ⁱPrPN^{Ph}P)NiH][PF₆] (Scheme 5.05). Unfortunately, all attempts at isolation of the hydride were unsuccessful due to the apparent instability of the complex. For example, exposure of the reaction solution to vacuum resulted in partial regeneration of **5** along with substantial decomposition to an insoluble precipitate and free ⁱPrPN^{Ph}P. This undesirable reaction also occurred when the solution was filtered before exposure to vacuum, suggesting that even trace amounts of chloride containing by-products are problematic. Overall, our results with Ni are analogous to those with Fe and Co, and indicate that it is difficult to form stable first-row metal hydride containing species with the ⁱPrPN^{Ph}P ligand.

Formic Acid Dehydrogenation

Formic acid is an attractive liquid for hydrogen storage if efficient catalysts for the dehydrogenation of formic acid to generate H₂ and CO₂ are developed.²⁶ It has previously been demonstrated that Fe carbonyl hydride complexes supported by either ⁱPrPN^HP or ⁱPrPN^{Me}P ligands are highly active catalysts for formic acid dehydrogenation.^{4b, g} Although

$$\text{H}-\text{C}(=\text{O})-\text{OH} \xrightarrow[90\text{ }^{\circ}\text{C}]{\text{[Fe] (0.1 mol\%), 1:2 toluene:t-BuOH}} \text{CO}_2 + \text{H}_2$$

Entry	[Fe]	TOF (h ⁻¹) ^a	TON ^b (time)	Yield
1	2	110	160 (5 h)	16%
2	2-Me	130	170 (4 h)	17%

Table 5.01. Formic acid dehydrogenation using **2** and **2-Me**. Reaction conditions: Formic acid (110 μL, 2.91 mmol), [Fe] (0.1 mol%, 291 μL of a 1 mM stock solution in toluene), 5.00 mL total reaction volume, 90 °C. Turnover numbers (TON) were measured using a gas buret. ^aThis value is the TON after the first hour. ^bThis value is the maximum TON that was recorded. The time indicates how long it took for catalysis to stop and for the maximum TON to be obtained.

we were unable to isolate a Fe carbonyl hydride complex supported by the $i\text{PrPN}^{\text{Ph}}\text{P}$ ligand which we could directly compare to catalysts in the literature, we studied the catalytic performance of **2** and **2-Me** in additive free formic acid dehydrogenation to observe any changes in activity that may arise from changing *only* the N-substituent on $i\text{PrPN}^{\text{R}}\text{P}$ -ligated Fe complexes. We utilized conditions previously optimized with the related catalyst $(i\text{PrPN}^{\text{Me}}\text{P})\text{Fe}(\text{H})_2(\text{CO})$ for this reaction (Table 5.01).^{4g} At 0.1 mol% catalyst loading, $i\text{PrPN}^{\text{Ph}}\text{P}$ -ligated complex **2** achieves a TON of 160 after 5 hours, and the $i\text{PrPN}^{\text{Me}}\text{P}$ congener **2-Me** reaches 170 TON in 4 hours (Table 5.01, entries 1 & 2). These results are within the error of our measurements ($\pm 10\%$). The yields of product for each catalyst are not high ($(i\text{PrPN}^{\text{Me}}\text{P})\text{Fe}(\text{H})_2(\text{CO})$ reaches full conversion under these conditions),^{4g} but they are comparable to the productivity of $i\text{PrPN}^{\text{Me}}\text{P}$ Fe isonitrile complexes that were previously studied under similar catalytic conditions with exogenous base added.²⁷ These results highlight that a Fe carbonyl hydride will be required to fully assess the catalytic performance of $i\text{PrPN}^{\text{Ph}}\text{P}$ ligated Fe complexes.

III. Conclusions

In this work, we have coordinated the recently developed $i\text{PrPN}^{\text{Ph}}\text{P}$ pincer ligand to Fe, Co, and Ni. Specifically, five new complexes were isolated and characterized using IR, UV-Vis, NMR, and Mössbauer spectroscopies, as well as X-ray crystallography. A frequently observed decomposition product of the demetallated ligand was also isolated and characterized. The properties and reactivity of the new $i\text{PrPN}^{\text{Ph}}\text{P}$ ligated complexes are markedly different compared to their $i\text{PrPN}^{\text{H}}\text{P}$ and $i\text{PrPN}^{\text{Me}}\text{P}$ analogues. For example, our results indicate that the nitrogen donor of $i\text{PrPN}^{\text{Ph}}\text{P}$ is a poorer σ -donor than the nitrogen

donors in $i\text{PrPN}^{\text{H}}\text{P}$ or $i\text{PrPN}^{\text{Me}}\text{P}$. This leads to an uncommon κ^2 -coordination of the pincer ligand in both Fe and Co dichloride complexes and difficulty synthesizing carbonyl hydride complexes supported by the $i\text{PrPN}^{\text{Ph}}\text{P}$ ligand. Nevertheless, we were able to directly compare a $i\text{PrPN}^{\text{Ph}}\text{P}$ Fe hydride complex with its $i\text{PrPN}^{\text{Me}}\text{P}$ analogue in catalytic formic acid dehydrogenation. The two catalysts showed similar low activity, highlighting the importance of isolating carbonyl hydride complexes. Future work in our labs will focus on using these insights to rationally design novel $i\text{PrPN}^{\text{R}}\text{P}$ ligands to better support a variety of transition metal complexes and generate improved catalysts.

Supporting Information

For supporting information, including experimental details and procedures, additional experimental information, and information on X-ray diffraction and Mössbauer spectroscopy, see Appendix D.

Acknowledgements

Dr. Dongyoung Kim, Dr. Majed Fataftah, and Prof. Patrick Holland assisted in obtaining and interpreting Mössbauer data, and Dr. Fabian Menges obtained high resolution mass spectrometry data.

IV. References

1. (a) van der Vlugt, J. I.; Reek, J. N. H., Neutral Tridentate PNP Ligands and Their Hybrid Analogues: Versatile Non-Innocent Scaffolds for Homogeneous Catalysis. *Angew. Chem. Int. Ed.* **2009**, *48*, 8832-8846; (b) Gunanathan, C.; Milstein, D., Bond Activation and Catalysis by Ruthenium Pincer Complexes. *Chem. Rev.* **2014**, *114*, 12024-12087; (c) Lawrence, M. A. W.; Green, K.-A.; Nelson, P. N.; Lorraine, S. C., Review: Pincer

- ligands—Tunable, versatile and applicable. *Polyhedron* **2018**, *143*, 11-27; (d) Alig, L.; Fritz, M.; Schneider, S., First-Row Transition Metal (De)Hydrogenation Catalysis Based On Functional Pincer Ligands. *Chem. Rev.* **2019**, *119*, 2681-2751.
2. (a) Schmeier, T. J.; Dobereiner, G. E.; Crabtree, R. H.; Hazari, N., Secondary Coordination Sphere Interactions Facilitate the Insertion Step in an Iridium(III) CO₂ Reduction Catalyst. *J. Am. Chem. Soc.* **2011**, *133*, 9274-9277; (b) Graham, T. W.; Tsang, C.-W.; Chen, X.; Guo, R.; Jia, W.; Lu, S.-M.; Sui-Seng, C.; Ewart, C. B.; Lough, A.; Amoroso, D.; Abdur-Rashid, K., Catalytic Solvolysis of Ammonia Borane. *Angew. Chem. Int. Ed.* **2010**, *49*, 8708-8711; (c) Ahn, S. T.; Bielinski, E. A.; Lane, E. M.; Chen, Y.; Bernskoetter, W. H.; Hazari, N.; Palmore, G. T. R., Enhanced CO₂ Electroreduction Efficiency Through Secondary Coordination Effects on a Pincer Iridium Catalyst. *Chem. Commun.* **2015**, *51*, 5947-5950; (d) Prichatz, C.; Alberico, E.; Baumann, W.; Junge, H.; Beller, M., Iridium–PNP Pincer Complexes for Methanol Dehydrogenation at Low Base Concentration. *ChemCatChem* **2017**, *9*, 1891-1896; (e) Ramaraj, A.; Nethaji, M.; Jagirdar, B. R., Hydrogenation of CO₂, Carbonyl and Imine Substrates Catalyzed by [IrH₃(^{Ph}PN^HP)] Complex. *J. Organomet. Chem.* **2019**, *883*, 25-34.
3. (a) Nielsen, M.; Alberico, E.; Baumann, W.; Drexler, H.-J.; Junge, H.; Gladiali, S.; Beller, M., Low-Temperature Aqueous-Phase Methanol Dehydrogenation to Hydrogen and Carbon Dioxide. *Nature* **2013**, *495*, 85-89; (b) Kothandaraman, J.; Czaun, M.; Goeppert, A.; Haiges, R.; Jones, J.-P.; May, R. B.; Prakash, G. K. S.; Olah, G. A., Amine-Free Reversible Hydrogen Storage in Formate Salts Catalyzed by Ruthenium Pincer Complex without pH Control or Solvent Change. *ChemSusChem* **2015**, *8*, 1442-1451; (c) Rezayee, N. M.; Huff, C. A.; Sanford, M. S., Tandem Amine and Ruthenium-Catalyzed

Hydrogenation of CO₂ to Methanol. *J. Am. Chem. Soc.* **2015**, *137*, 1028-1031; (d) Alberico, E.; Lennox, A. J. J.; Vogt, L. K.; Jiao, H.; Baumann, W.; Drexler, H.-J.; Nielsen, M.; Spannenberg, A.; Checinski, M. P.; Junge, H.; Beller, M., Unravelling the Mechanism of Basic Aqueous Methanol Dehydrogenation Catalyzed by Ru–PNP Pincer Complexes. *J. Am. Chem. Soc.* **2016**, *138*, 14890-14904; (e) Kothandaraman, J.; Kar, S.; Sen, R.; Goeppert, A.; Olah, G. A.; Prakash, G. K. S., Efficient Reversible Hydrogen Carrier System Based on Amine Reforming of Methanol. *J. Am. Chem. Soc.* **2017**, *139*, 2549-2552; (f) Kar, S.; Sen, R.; Kothandaraman, J.; Goeppert, A.; Chowdhury, R.; Munoz, S. B.; Haiges, R.; Prakash, G. K. S., Mechanistic Insights into Ruthenium-Pincer-Catalyzed Amine-Assisted Homogeneous Hydrogenation of CO₂ to Methanol. *J. Am. Chem. Soc.* **2019**, *141*, 3160-3170; (g) Agapova, A.; Alberico, E.; Kammer, A.; Junge, H.; Beller, M., Catalytic Dehydrogenation of Formic Acid with Ruthenium-PNP-Pincer Complexes: Comparing N-Methylated and NH-Ligands. *ChemCatChem* **2019**, *11*, 1910-1914.

4. (a) Alberico, E.; Sponholz, P.; Cordes, C.; Nielsen, M.; Drexler, H.-J.; Baumann, W.; Junge, H.; Beller, M., Selective Hydrogen Production from Methanol with a Defined Iron Pincer Catalyst under Mild Conditions. *Angew. Chem. Int. Ed.* **2013**, *52*, 14162-14166; (b) Bielinski, E. A.; Lagaditis, P. O.; Zhang, Y.; Mercado, B. Q.; Würtele, C.; Bernskoetter, W. H.; Hazari, N.; Schneider, S., Lewis Acid-Assisted Formic Acid Dehydrogenation Using a Pincer-Supported Iron Catalyst. *J. Am. Chem. Soc.* **2014**, *136*, 10234-10237; (c) Chakraborty, S.; Brennessel, W. W.; Jones, W. D., A Molecular Iron Catalyst for the Acceptorless Dehydrogenation and Hydrogenation of N-Heterocycles. *J. Am. Chem. Soc.* **2014**, *136*, 8564-8567; (d) Zhang, Y.; MacIntosh, A. D.; Wong, J. L.; Bielinski, E. A.; Williard, P. G.; Mercado, B. Q.; Hazari, N.; Bernskoetter, W. H., Iron Catalyzed CO₂

Hydrogenation to Formate Enhanced by Lewis Acid Co-Catalysts. *Chem. Sci.* **2015**, *6*, 4291-4299; (e) Bielinski, E. A.; Förster, M.; Zhang, Y.; Bernskoetter, W. H.; Hazari, N.; Holthausen, M. C., Base-Free Methanol Dehydrogenation Using a Pincer-Supported Iron Compound and Lewis Acid Co-catalyst. *ACS Catal.* **2015**, *5*, 2404-2415; (f) Lane, E. M.; Zhang, Y.; Hazari, N.; Bernskoetter, W. H., Sequential Hydrogenation of CO₂ to Methanol Using a Pincer Iron Catalyst. *Organometallics* **2019**, *38*, 3084-3091; (g) Curley, J. B.; Bernskoetter, W. H.; Hazari, N., Additive-Free Formic Acid Dehydrogenation Using a Pincer-Supported Iron Catalyst. *ChemCatChem* **2020**, *12*, 1934-1938.

5. (a) Spentzos, A. Z.; Barnes, C. L.; Bernskoetter, W. H., Effective Pincer Cobalt Precatalysts for Lewis Acid Assisted CO₂ Hydrogenation. *Inorg. Chem.* **2016**, *55*, 8225-8233; (b) Zhou, W.; Wei, Z.; Spannenberg, A.; Jiao, H.; Junge, K.; Junge, H.; Beller, M., Cobalt-Catalyzed Aqueous Dehydrogenation of Formic Acid. *Chem. Eur. J.* **2019**, *25*, 8459-8464; (c) Mills, M. R.; Barnes, C. L.; Bernskoetter, W. H., Influences of Bifunctional PNP-Pincer Ligands on Low Valent Cobalt Complexes Relevant to CO₂ Hydrogenation. *Inorg. Chem.* **2018**, *57*, 1590-1597.

6. (a) Kar, S.; Goeppert, A.; Kothandaraman, J.; Prakash, G. K. S., Manganese-Catalyzed Sequential Hydrogenation of CO₂ to Methanol via Formamide. *ACS Catal.* **2017**, *7*, 6347-6351; (b) Ryabchuk, P.; Stier, K.; Junge, K.; Checinski, M. P.; Beller, M., Molecularly Defined Manganese Catalyst for Low-Temperature Hydrogenation of Carbon Monoxide to Methanol. *J. Am. Chem. Soc.* **2019**, *141*, 16923-16929; (c) Zubar, V.; Borghs, J. C.; Rueping, M., Hydrogenation or Dehydrogenation of N-Containing Heterocycles Catalyzed by a Single Manganese Complex. *Org. Lett.* **2020**, *22*, 3974-3978; (d) Kaithal, A.; Werlé,

C.; Leitner, W., Alcohol-Assisted Hydrogenation of Carbon Monoxide to Methanol Using Molecular Manganese Catalysts. *JACS Au* **2021**, *1*, 130-136.

7. (a) Clarke, Z. E.; Maragh, P. T.; Dasgupta, T. P.; Gusev, D. G.; Lough, A. J.; Abdur-Rashid, K., A Family of Active Iridium Catalysts for Transfer Hydrogenation of Ketones. *Organometallics* **2006**, *25*, 4113-4117; (b) Chen, X.; Jia, W.; Guo, R.; Graham, T. W.; Gullons, M. A.; Abdur-Rashid, K., Highly Active Iridium Catalysts for the Hydrogenation of Ketones and Aldehydes. *Dalton Trans.* **2009**, 1407-1410; (c) Andrushko, N.; Andrushko, V.; Roose, P.; Moonen, K.; Börner, A., Amination of Aliphatic Alcohols and Diols with an Iridium Pincer Catalyst. *ChemCatChem* **2010**, *2*, 640-643; (d) Junge, K.; Wendt, B.; Jiao, H.; Beller, M., Iridium-Catalyzed Hydrogenation of Carboxylic Acid Esters. *ChemCatChem* **2014**, *6*, 2810-2814.

8. (a) Bertoli, M.; Choualeb, A.; Lough, A. J.; Moore, B.; Spasyuk, D.; Gusev, D. G., Osmium and Ruthenium Catalysts for Dehydrogenation of Alcohols. *Organometallics* **2011**, *30*, 3479-3482; (b) Nielsen, M.; Junge, H.; Kammer, A.; Beller, M., Towards a Green Process for Bulk-Scale Synthesis of Ethyl Acetate: Efficient Acceptorless Dehydrogenation of Ethanol. *Angew. Chem. Int. Ed.* **2012**, *51*, 5711-5713; (c) Kuriyama, W.; Matsumoto, T.; Ogata, O.; Ino, Y.; Aoki, K.; Tanaka, S.; Ishida, K.; Kobayashi, T.; Sayo, N.; Saito, T., Catalytic Hydrogenation of Esters. Development of an Efficient Catalyst and Processes for Synthesising (R)-1,2-Propanediol and 2-(1-Menthoxy)ethanol. *Org. Proc. Res. Dev.* **2012**, *16*, 166-171; (d) Zhang, L.; Han, Z.; Zhao, X.; Wang, Z.; Ding, K., Highly Efficient Ruthenium-Catalyzed N-Formylation of Amines with H₂ and CO₂. *Angew. Chem. Int. Ed.* **2015**, *54*, 6186-6189; (e) Li, Y.; Nielsen, M.; Li, B.; Dixneuf, P. H.; Junge, H.; Beller, M., Ruthenium-Catalyzed Hydrogen Generation from Glycerol and

Selective Synthesis of Lactic Acid. *Green Chem.* **2015**, *17*, 193-198; (f) Kim, S. H.; Hong, S. H., Ruthenium-Catalyzed Urea Synthesis Using Methanol as the C1 Source. *Org. Lett.* **2016**, *18*, 212-215; (g) Pinggen, D.; Choi, J.-H.; Allen, H.; Murray, G.; Ganji, P.; van Leeuwen, P. W. N. M.; Prechtl, M. H. G.; Vogt, D., Amide Versus Amine Ligand Paradigm in the Direct Amination of Alcohols with Ru-PNP Complexes. *Catal. Sci. Tech.* **2018**, *8*, 3969-3976; (h) Thiagarajan, S.; Gunanathan, C., Catalytic Cross-Coupling of Secondary Alcohols. *J. Am. Chem. Soc.* **2019**, *141*, 3822-3827.

9. (a) Chakraborty, S.; Dai, H.; Bhattacharya, P.; Fairweather, N. T.; Gibson, M. S.; Krause, J. A.; Guan, H., Iron-Based Catalysts for the Hydrogenation of Esters to Alcohols. *J. Am. Chem. Soc.* **2014**, *136*, 7869-7872; (b) Werkmeister, S.; Junge, K.; Wendt, B.; Alberico, E.; Jiao, H.; Baumann, W.; Junge, H.; Gallou, F.; Beller, M., Hydrogenation of Esters to Alcohols with a Well-Defined Iron Complex. *Angew. Chem. Int. Ed.* **2014**, *53*, 8722-8726; (c) Sharninghausen, L. S.; Mercado, B. Q.; Crabtree, R. H.; Hazari, N., Selective Conversion of Glycerol to Lactic Acid with Iron Pincer Precatalysts. *Chem. Commun.* **2015**, *51*, 16201-16204; (d) Elangovan, S.; Wendt, B.; Topf, C.; Bachmann, S.; Scalone, M.; Spannenberg, A.; Jiao, H.; Baumann, W.; Junge, K.; Beller, M., Improved Second Generation Iron Pincer Complexes for Effective Ester Hydrogenation. *Adv. Synth. Catal.* **2016**, *358*, 820-825; (e) Schneck, F.; Assmann, M.; Balmer, M.; Harms, K.; Langer, R., Selective Hydrogenation of Amides to Amines and Alcohols Catalyzed by Improved Iron Pincer Complexes. *Organometallics* **2016**, *35*, 1931-1943; (f) Rezayee, N. M.; Samblanet, D. C.; Sanford, M. S., Iron-Catalyzed Hydrogenation of Amides to Alcohols and Amines. *ACS Catal.* **2016**, *6*, 6377-6383; (g) Lane, E. M.; Uttley, K. B.; Hazari, N.; Bernskoetter, W., Iron-Catalyzed Amide Formation from the Dehydrogenative Coupling of Alcohols and

Secondary Amines. *Organometallics* **2017**, *36*, 2020-2025; (h) Jayarathne, U.; Zhang, Y.; Hazari, N.; Bernskoetter, W. H., Selective Iron-Catalyzed Deaminative Hydrogenation of Amides. *Organometallics* **2017**, *36*, 409-416; (i) Lane, Elizabeth M.; Hazari, N.; Bernskoetter, W. H., Iron-Catalyzed Urea Synthesis: Dehydrogenative Coupling of Methanol and Amines. *Chem. Sci.* **2018**, *9*, 4003-4008; (j) Jayarathne, U.; Hazari, N.; Bernskoetter, W. H., Selective Iron-Catalyzed N-Formylation of Amines using Dihydrogen and Carbon Dioxide. *ACS Catal.* **2018**, *8*, 1338-1345.

10. (a) Zhang, G.; Scott, B. L.; Hanson, S. K., Mild and Homogeneous Cobalt-Catalyzed Hydrogenation of C-C, C-O, and C-N Bonds. *Angew. Chem. Int. Ed.* **2012**, *51*, 12102-12106; (b) Zhang, G.; Hanson, S. K., Cobalt-Catalyzed Transfer Hydrogenation of C-O and C-N Bonds. *Chem. Commun.* **2013**, *49*, 10151-10153; (c) Zhang, G.; Vasudevan, K. V.; Scott, B. L.; Hanson, S. K., Understanding the Mechanisms of Cobalt-Catalyzed Hydrogenation and Dehydrogenation Reactions. *J. Am. Chem. Soc.* **2013**, *135*, 8668-8681; (d) Yin, Z.; Zeng, H.; Wu, J.; Zheng, S.; Zhang, G., Cobalt-Catalyzed Synthesis of Aromatic, Aliphatic, and Cyclic Secondary Amines via a “Hydrogen-Borrowing” Strategy. *ACS Catal.* **2016**, *6*, 6546-6550; (e) Fu, S.; Chen, N.-Y.; Liu, X.; Shao, Z.; Luo, S.-P.; Liu, Q., Ligand-Controlled Cobalt-Catalyzed Transfer Hydrogenation of Alkynes: Stereodivergent Synthesis of Z- and E-Alkenes. *J. Am. Chem. Soc.* **2016**, *138*, 8588-8594; (f) Yuwen, J.; Chakraborty, S.; Brennessel, W. W.; Jones, W. D., Additive-Free Cobalt-Catalyzed Hydrogenation of Esters to Alcohols. *ACS Catal.* **2017**, *7*, 3735-3740; (g) Junge, K.; Wendt, B.; Cingolani, A.; Spannenberg, A.; Wei, Z.; Jiao, H.; Beller, M., Cobalt Pincer Complexes for Catalytic Reduction of Carboxylic Acid Esters. *Chem. Eur. J.* **2018**, *24*, 1046-1052.

11. (a) Elangovan, S.; Garbe, M.; Jiao, H.; Spannenberg, A.; Junge, K.; Beller, M., Hydrogenation of Esters to Alcohols Catalyzed by Defined Manganese Pincer Complexes. *Angew. Chem. Int. Ed.* **2016**, *55*, 15364-15368; (b) Nguyen, D. H.; Trivelli, X.; Capet, F.; Paul, J.-F.; Dumeignil, F.; Gauvin, R. M., Manganese Pincer Complexes for the Base-Free, Acceptorless Dehydrogenative Coupling of Alcohols to Esters: Development, Scope, and Understanding. *ACS Catal.* **2017**, *7*, 2022-2032; (c) Garbe, M.; Budweg, S.; Papa, V.; Wei, Z.; Hornke, H.; Bachmann, S.; Scalone, M.; Spannenberg, A.; Jiao, H.; Junge, K.; Beller, M., Chemoselective Semihydrogenation of Alkynes Catalyzed by Manganese(I)-PNP Pincer Complexes. *Catal. Sci. Tech.* **2020**, *10*, 3994-4001; (d) Zubar, V.; Dewanji, A.; Rueping, M., Chemoselective Hydrogenation of Nitroarenes Using an Air-Stable Base-Metal Catalyst. *Org. Lett.* **2021**, *23*, 2742-2747.
12. Khusnutdinova, J. R.; Milstein, D., Metal–Ligand Cooperation. *Angew. Chem. Int. Ed.* **2015**, *54*, 12236-12273.
13. (a) Bianchini, C.; Glendenning, L.; Peruzzini, M.; Purches, G.; Zanobini, F.; Farnetti, E.; Graziani, M.; Nardin, G., Synthesis of the New Chiral (R)- and (S)-Aminodiphosphine Ligands *sec*-Butylbis(2-(diphenylphosphino)ethyl)amine, *sec*-Butylbis(2-(dicyclohexylphosphino)ethyl)amine, and (α -Methylbenzyl)bis(2-(dicyclohexylphosphino)ethyl)amine and Their Organometallic Chemistry When Combined with Iridium. *Organometallics* **1997**, *16*, 4403-4414; (b) Dong, Q.; Rose, M. J.; Wong, W.-Y.; Gray, H. B., Dual Coordination Modes of Ethylene-Linked NP2 Ligands in Cobalt(II) and Nickel(II) Iodides. *Inorg. Chem.* **2011**, *50*, 10213-10224; (c) Ramaraj, A.; Nethaji, M.; Jagirdar, B. R., Contrasting Reactivity Behaviour of the [RuHCl(CO)(PNP)] Complex with Electrophilic Reagents XOTf (X = H, CH₃, Me₃Si). *Dalton Trans.* **2014**,

43, 14625-14635; (d) Naicker, D.; Friedrich, H. B.; Omondi, B., Cobalt Aminodiphosphine Complexes as Catalysts in the Oxidation of n-Octane. *RSC Adv.* **2015**, *5*, 63123-63129; (e) Ramaraj, A.; Reddy, K. H. K.; Keil, H.; Herbst-Irmer, R.; Stalke, D.; Jemmis, E. D.; Jagirdar, B. R., Approaches to Sigma Complexes via Displacement of Agostic Interactions: An Experimental and Theoretical Investigation. *Organometallics* **2017**, *36*, 2736-2745; (f) Goren Keskin, S.; Stanley, J. M.; Cowley, A. H., Synthesis, Characterization and Theoretical Investigations of Molybdenum Carbonyl Complexes with Phosphorus/Nitrogen/Phosphorus Ligand as Bidentate and Tridentate Modes. *Polyhedron* **2017**, *138*, 206-217; (g) Salvarese, N.; Refosco, F.; Seraglia, R.; Roverso, M.; Dolmella, A.; Bolzati, C., Synthesis and Characterization of Rhenium(iii) Complexes with (Ph₂PCH₂CH₂)₂NR Diphosphinoamine Ligands. *Dalton Trans.* **2017**, *46*, 9180-9191; (h) Kostas, I. D.; Antonopoulou, G.; Potamitis, C.; Raptopoulou, C. P.; Psycharis, V., Platinum Complexes with a Methoxy-Amino Phosphine or a Nitrogen-Containing Bis(phosphine) Ligand. Synthesis, Characterization and Application to Hydrogenation of Trans-Cinnamaldehyde. *J. Organomet. Chem.* **2017**, *828*, 133-141; (i) Keskin, S. G.; Stanley, J. M.; Mitchell, L. A.; Holliday, B. J., Synthesis, Characterization, Coordination Chemistry, and Luminescence Studies of Copper, Silver, Palladium, and Platinum Complexes with a Phosphorus/Nitrogen/Phosphorus Ligand. *Inorg. Chim. Acta* **2019**, *486*, 200-212.

14. In this article, *anti* means that the formate ligand is positioned on the opposite face of the complex to the substituent on the nitrogen donor. *Syn* means that the formate ligand is positioned on the same face of the complex to the substituent on the nitrogen donor.

15. (a) Chirik, P. J. G., T. Brent, A Meeting of Metals—A Joint Virtual Issue between *Organometallics* and *ACS Catalysis* on First-Row Transition Metal Complexes. *ACS*

- Catal.* **2015**, *5*, 5584-5585; (b) Fürstner, A., Iron Catalysis in Organic Synthesis: A Critical Assessment of What It Takes To Make This Base Metal a Multitasking Champion. *ACS Cent. Sci.* **2016**, *2*, 778-789; (c) Egorova, K. S.; Ananikov, V. P., Toxicity of Metal Compounds: Knowledge and Myths. *Organometallics* **2017**, *36*, 4071-4090.
16. Fillman, K. L.; Bielinski, E. A.; Schmeier, T. J.; Nesvet, J. C.; Woodruff, T. M.; Pan, C. J.; Takase, M. K.; Hazari, N.; Neidig, M. L., Flexible Binding of PNP Pincer Ligands to Monomeric Iron Complexes. *Inorg. Chem.* **2014**, *53*, 6066-6072.
17. Yang, L.; Powell, D. R.; Houser, R. P., Structural Variation in Copper(I) Complexes with Pyridylmethanamide Ligands: Structural Analysis with a New Four-Coordinate Geometry index, τ_4 . *Dalton Trans.* **2007**, 955-964.
18. Gütllich, P.; Bill, E.; Trautwein, A. X., *Mössbauer Spectroscopy and Transition Metal Chemistry: Fundamentals and Applications*. Springer-Verlag: Berlin, **2011**.
19. McWilliams, S. F.; Brennan-Wydra, E.; MacLeod, K. C.; Holland, P. L., Density Functional Calculations for Prediction of ^{57}Fe Mössbauer Isomer Shifts and Quadrupole Splittings in β -Diketiminato Complexes. *ACS Omega* **2017**, *2*, 2594-2606.
20. Koehne, I.; Schmeier, T. J.; Bielinski, E. A.; Pan, C. J.; Lagaditis, P. O.; Bernskoetter, W. H.; Takase, M. K.; Würtele, C.; Hazari, N.; Schneider, S., Synthesis and Structure of Six-Coordinate Iron Borohydride Complexes Supported by PNP Ligands. *Inorg. Chem.* **2014**, *53*, 2133-2143.
21. Addison, A. W.; Rao, T. N.; Reedijk, J.; van Rijn, J.; Verschoor, G. C., Synthesis, Structure, and Spectroscopic Properties of Copper(II) Compounds Containing Nitrogen–Sulphur Donor Ligands; The Crystal and Molecular Structure of Aqua[1,7-bis(N-

- methylbenzimidazol-2'-yl)-2,6-dithiaheptane]copper(II) Perchlorate. *J. Chem. Soc., Dalton Trans.* **1984**, 1349-1356.
22. Hartwig, J. F., *Organotransition Metal Chemistry: From Bonding to Catalysis*. University Science Books: United States, **2010**.
23. Rozenel, S. S.; Kerr, J. B.; Arnold, J., Metal Complexes of Co, Ni and Cu with the Pincer Ligand $\text{HN}(\text{CH}_2\text{CH}_2\text{P}^i\text{Pr}_2)_2$: Preparation, Characterization and Electrochemistry. *Dalton Trans.* **2011**, *40*, 10397-10405.
24. Tamizmani, M.; Sivasankar, C., Synthesis, Characterization and Catalytic Application of Some Novel PNP-Ni(II) Complexes: Regio-Selective [2+2+2] Cycloaddition Reaction of Alkyne. *J. Organomet. Chem.* **2017**, *845*, 82-89.
25. Vasudevan, K. V.; Scott, B. L.; Hanson, S. K., Alkene Hydrogenation Catalyzed by Nickel Hydride Complexes of an Aliphatic PNP Pincer Ligand. *Euro. J. Inorg. Chem.* **2012**, *2012*, 4898-4906.
26. (a) Joó, F., Breakthroughs in Hydrogen Storage-Formic Acid as a Sustainable Storage Material for Hydrogen. *ChemSusChem* **2008**, *1*, 805-808; (b) Sordakis, K.; Tang, C.; Vogt, L. K.; Junge, H.; Dyson, P. J.; Beller, M.; Laurenczy, G., Homogeneous Catalysis for Sustainable Hydrogen Storage in Formic Acid and Alcohols. *Chem. Rev.* **2018**, *118*, 372-433.
27. Curley, J. B.; Smith, N. E.; Bernskoetter, W. H.; Hazari, N.; Mercado, B. Q., Catalytic Formic Acid Dehydrogenation and CO_2 Hydrogenation Using Iron $\text{PN}^{\text{R}}\text{P}$ Pincer Complexes with Isonitrile Ligands. *Organometallics* **2018**, *37*, 3846-3853.

Appendix A: Supporting Information for Chapter 2

Adapted from the Supporting Information for: Curley, J. B., Smith, N. E., Bernskoetter, W. H., Hazari, N., and Mercado, B. Q. *Organometallics*, **2018**, 37, 3846-3853.

I. Experimental Procedures

General Methods

Experiments were performed under a dinitrogen atmosphere in an M-Braun glovebox or using standard Schlenk techniques unless otherwise noted. Under typical operating conditions, the glovebox was not purged between use of benzene, diethyl ether, pentane, THF, dioxane, or toluene. As a consequence, each solvent should be assumed to contain trace amounts of the others. All moisture and air-sensitive liquids were either transferred inside the glovebox or using a stainless steel cannula on a Schlenk line. Solvents were dried by passage through a column of activated alumina and stored under dinitrogen unless otherwise noted.

Ethanol (200 proof) was purchased from Decon Laboratories, Inc., and degassed and stored under dinitrogen prior to use. All commercial chemicals were used as received except where noted. Anhydrous FeCl_2 was purchased from Alfa Aesar. Sodium borohydride was purchased from Acros Organics. 2,6-dimethylphenyl isonitrile, *tert*-butyl isonitrile, and adamantyl isonitrile were used as received from Santa Cruz Biotech or Sigma-Aldrich. Formic acid was purchased from EMD Millipore Inc. and degassed prior to use. Triethylamine was purchased from Fisher Scientific, degassed, and dried over

calcium hydride prior to use. Deuterated solvents were obtained from Cambridge Isotope Laboratories. C₆D₆ was dried by passage through a plug of activated alumina.

NMR spectra were recorded on Bruker AMX-400, AMX-500, or AMX-600 spectrometers at ambient probe temperatures, unless otherwise noted. Chemical shifts are reported in ppm with respect to residual internal protio solvent for ¹H and ¹³C{¹H} NMR spectra. ³¹P{¹H} NMR spectra are referenced via the ¹H resonances based on the relative gyromagnetic ratios.¹ All *J* coupling constant values are given in Hertz. Elemental analyses were performed by Robertson Microlit Laboratories, Inc. Infrared data were obtained on a Bruker ALPHA FTIR spectrometer with a platinum ATR attachment inside a N₂-filled glovebox. All samples were taken of the neat solid. UV-Vis data were collected on a Hewlett-Packard 8453 diode array spectrophotometer. Literature procedures were used to synthesize **1**,² **A**,² and **B**.³

X-ray Crystallography

Crystal samples were mounted on polyimide loops with immersion oil. Low-temperature diffraction data (ω -scans) were collected on a Rigaku MicroMax-007HF diffractometer coupled to a Saturn994+ CCD detector with Cu K α (λ = 1.54178 Å) for the structure of **2c**. The diffraction images for **2c** were processed and scaled using Rigaku Oxford Diffraction software. A Rigaku SCX Mini diffractometer coupled to a Rigaku Mercury275R CCD with Mo K α radiation (λ = 0.71073 Å) was used for **2a** and **2b**. The diffraction images for **2a** and **2b** were processed and scaled using the Rigaku CrystalClear software.⁴ The structures were solved with SHELXT and refined against F^2 on all data by full-matrix least squares with SHELXL.⁵ Details of the crystal and refinement data for **2a**, **2b**, and **2c** are described in Section IX of this Appendix.

Gas Chromatography

Gas Chromatography was performed on a ThermoFisher Trace 1300 GC apparatus equipped with a thermal conductivity detector and a Supelco fused silica capillary column (5 Å molecular sieves, 30 m x 0.53 mm). The system uses N₂ as a carrier gas and allows for determination of H₂ at concentrations greater than 1 ppm and CO at concentrations greater than 100 ppm.

II. Synthetic Procedures and Characterizing Data for New Compounds

(ⁱPrPN^{Me}P)Fe(H)(HBH₃)(2,6-dimethylphenyl isonitrile) (**2a**)

A Schlenk flask was charged with (ⁱPrPN^{Me}P)Fe(H)(κ²-H₂BH₂) (**1**) (25 mg, 0.064 mmol), 2,6-dimethylphenyl isonitrile (8.4 mg, 0.064 mmol), and pentane (5 mL). The mixture was stirred for 30 minutes at room temperature to afford a heterogeneous yellow mixture with a yellow precipitate. The volatiles were removed *in vacuo*. The crude product was extracted in 3x2 mL THF and concentrated. Yellow crystals were grown from the slow diffusion of 5 mL pentane into the THF solution at -35 °C and afforded clean **2a** (20 mg, 0.039 mmol, 61%). Crystals suitable for X-ray diffraction were also grown from slow diffusion of pentane into a concentrated THF solution at -35 °C.

Anal. Found (calc'd) for C₂₆H₅₃P₂N₂BFe: C, 60.07 (59.79); H, 10.40 (10.23); N, 5.08 (5.36). ¹H NMR (500 MHz, C₆D₆): The following peaks were overlapping in both the major and minor isomers: 6.80 (d, 2H, CH_{Ar} *J*=7.5 Hz), 6.70 (m, 1H, CH_{Ar}), 3.13 (m, 2H, CH₂), 2.18 (m, 2H, CH₂), 2.06 (s, 3H, N-CH₃), 1.87 (m, 4H, CH₂), 1.75 (m, 4H, CH), 1.64 (m, 6H, CHCH₃), 1.22 (m, 12H, CHCH₃), 1.06 (m, 6H, CHCH₃), -2.64 ppm (br, 4H, HBH₃). The following peaks were distinct in the major and minor isomers: Major isomer: 2.56 (s,

6H, C_{Ar}CH₃), -21.48 ppm (t, 1H, Fe-*H*, *J*=53.5 Hz). Minor isomer: 2.49 (s, 6H, C_{Ar}CH₃), -21.83 ppm (t, 1H, Fe-*H*, *J*=52.2 Hz). ¹³C{¹H} (151 MHz, C₆D₆): 133.7, 124.1, 65.6, 50.5, 29.8 (t, *J*=7.6 Hz), 27.4 (t, *J*=6.1 Hz), 26.0 (t, 12.9), 21.1 (m), 20.3 (m), 19.8, 19.6, 18.3 ppm (m). ³¹P{¹H} NMR (202 MHz, C₆D₆): Major isomer: 91.4 ppm. Minor isomer: 95.2 ppm. IR (cm⁻¹): 1970 (ν_{CN}, br). UV-Vis (THF, (λ_{max}, ε)): (440 nm, 913 M⁻¹ cm⁻¹)

(ⁱPrPN^{Me}P)Fe(H)(HBH₃)(*tert*-butyl isonitrile) (**2b**)

A Schlenk flask was charged with (ⁱPrPN^{Me}P)Fe(H)(κ²-H₂BH₂) (**1**) (25 mg, 0.064 mmol), *tert*-butyl isonitrile (7.2 μL, 0.064 mmol), and pentane (5 mL). The mixture was stirred for 30 minutes at room temperature to afford a yellow solution. The volatiles were removed *in vacuo*. The crude product was extracted in 3x2 mL THF and concentrated. Yellow crystals were grown from the slow diffusion of 5 mL pentane into the THF solution at -35 °C and afforded clean **2b** (18 mg, 0.038 mmol, 60%). Crystals suitable for X-ray diffraction were also grown from slow diffusion of pentane into a concentrated THF solution at -35 °C.

Anal. Found (calc'd) for C₂₂H₅₃P₂N₂BFe: C, 55.65 (55.71); H, 11.11 (11.26); N, 5.94 (5.91). ¹H NMR (500 MHz, C₆D₆): The following peaks were overlapping in both the major and minor isomers: 3.07 (m, 2H, CH₂), 2.27 (m, 2H, CH₂), 2.00 (s, 3H, N-CH₃), 1.84 (m, 4H, CH₂), 1.77 (m, 6H, CHCH₃), 1.68 (m, 4H, CH), 1.31 (m, 6H, CHCH₃), 1.25 (m, 6H, CHCH₃), 1.14 (s, 9H, CH₃), 1.08 ppm (m, 6H, CHCH₃). The following peaks were distinct in the major and minor isomers: Major isomer: -22.1 ppm (t, 1H, Fe-*H*, *J*=54.3 Hz). Minor isomer: -22.3 ppm (t, 1H, Fe-*H*, *J*=52.7 Hz). ¹³C{¹H} (151 MHz, C₆D₆): 65.4, 50.6, 31.3, 31.1 (t, *J*=6.9 Hz), 28.4 (t, *J*=6.1 Hz), 26.1 (t, *J*=11.5 Hz), 21.3, 19.4, 18.5 ppm. ³¹P{¹H}

NMR (202 MHz, C₆D₆): Major isomer: 91.3 ppm. Minor isomer: 95.7 ppm. IR (cm⁻¹): 1990 (ν_{CN}, br). UV-Vis (THF, (λ_{max}, ε)): (438 nm, 989 M⁻¹cm⁻¹).

(ⁱPrPN^{Me}P)Fe(H)(HBH₃)(adamantyl isonitrile) (**2c**)

A Schlenk flask was charged with (ⁱPrPN^{Me}P)Fe(H)(κ²-H₂BH₂) **1** (25 mg, 0.064 mmol), adamantyl isonitrile (10 mg, 0.064 mmol), and pentane (5 mL). The mixture was stirred for 30 minutes at room temperature to afford a heterogeneous yellow mixture with a yellow precipitate. The volatiles were removed *in vacuo*. The crude product was extracted in 3x2 mL THF and concentrated. Yellow crystals were grown from the slow diffusion of 5 mL pentane into the THF solution at -35 °C and afforded clean **2c** (30 mg, 0.054 mmol, 85%). Crystals suitable for X-ray diffraction were also grown from slow diffusion of pentane into a concentrated THF solution at -35 °C.

Anal. Found (calc'd) for C₂₈H₅₉P₂N₂BFe: C, 61.11 (60.88); H, 10.69 (10.77); N, 5.33 (5.07). ¹H NMR (500 MHz, C₆D₆): The following peaks were overlapping in both the major and minor isomers: 3.11 (m, 2H, CH₂), 2.31 (m, 2H, CH₂), 2.02 (s, 3H, N-CH₃), 1.73-1.95 (m, 15H, adamantyl), 1.70 (br, 4H, CH), 1.34 (m, 18H, CHCH₃), 1.11 ppm (m, 6H, CHCH₃). The following peaks were distinct in the major and minor isomers: Major isomer: -22.1 ppm (t, 1H, Fe-H, J=54.4 Hz). Minor isomer: -22.3 ppm (t, 1H, Fe-H, J=51.6 Hz). ¹³C{¹H} (151 MHz, C₆D₆): 65.5 (t, J=5.6 Hz), 56.0, 50.6, 44.7, 36.0, 31.2 (t, J=6.9 Hz), 29.5, 28.5 (t, J=6.2 Hz), 26.2 (t, J=12.4 Hz), 21.5 (m), 19.5, 18.6 (m), 14.3 ppm. ³¹P{¹H} NMR (202 MHz, C₆D₆): Major isomer: 91.2 ppm. Minor isomer: 95.6 ppm. IR (cm⁻¹): 2015 (ν_{CN}, br). UV-Vis (THF, (λ_{max}, ε)): (437 nm, 901 M⁻¹cm⁻¹).

III. Procedures for Catalysis

General Methods for CO₂ Hydrogenation

In a glovebox, a 50 mL glass reactor liner was charged with catalyst as a stock solution in THF (*ca.* 0.02 M, 0.3 μ mol catalyst), LiOTf (492 mg, 3.15 mmol), DBU (3.6 g, 24 mmol), and 10 mL of THF. The cylinder liner was placed into a 50 mL Parr reactor and the vessel sealed. The reactor was removed from the glovebox and pressurized sequentially with 34 atm of CO₂ and then 34 atm of H₂ via a Y-value inlet at ambient temperature. The reactor was then heated to 80 °C, a process which occurred in approximately 10 minutes, and mechanically stirred for 24 hours. The reaction was stopped by removal of the heat source, cooling in an ice water bath, and venting of the vessel's atmosphere. The reaction solution, which contained some suspended solid, was then transferred to a 100 mL round-bottomed flask, using D₂O to dissolve the solid products. All volatiles were removed *in vacuo*. The residue was then dissolved in D₂O and DMF was added as an internal standard for quantification of the formate product by ¹H NMR spectroscopy. Delay times of 60 seconds were used between scans to ensure accurate integrations.

General Methods for Formic Acid Dehydrogenation

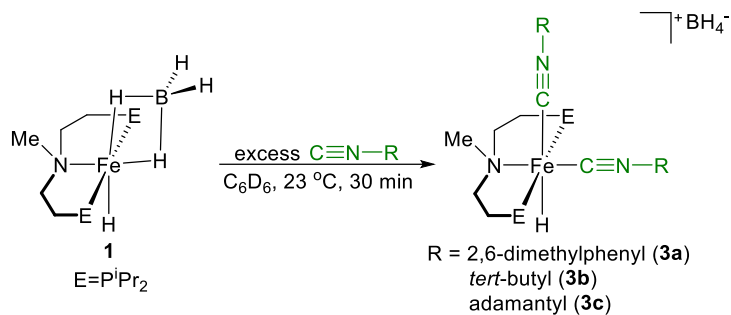
In a glovebox, a 25 mL Schlenk flask was charged with catalyst as a stock solution in dioxane (10.0 mM, 2.91 μ mol catalyst), and dioxane (4.7 mL). The Schlenk flask was sealed with a septum, removed from the glovebox and attached to a gas burette setup (see SI). The gas burette and tubing were subjected to three vacuum/N₂ purge cycles. Triethylamine (202 μ L, 1.46 mmol) was added to the reaction flask via syringe. The Schlenk flask was lowered into an oil bath preheated to 80 °C and allowed to equilibrate

for 5 min. Formic acid (110 μ L, 2.91 mmol) was then injected via syringe and the change in water level in the gas burette was used to determine the TOF and TON.

IV. Observation of Bis-isonitrile Complexes

The following is a general procedure which was used to observed bis-isonitrile complexes *in situ* (Scheme A.01):

To a J. Young NMR tube were added **1** (5 mg, 0.01 mmol), an excess of the appropriate isonitrile (~6 equivalents), and C₆D₆ (0.5 mL). The tube was mixed for 30 minutes, the volatiles were removed *in vacuo*, and the residue was filtered and redissolved in C₆D₆. Shown below are ¹H and ³¹P NMR spectra of this reaction using 2,6-dimethylphenyl isonitrile (to generate **3a**, Figures A.01 and A.02), *tert*-butyl isonitrile (to generate **3b**, Figures A.03 and A.04), and adamantyl isonitrile (to generate **3c**, Figures A.05 and A.06). The ¹H and ³¹P NMR spectra of a mixture of **2c** and **3c** which was generated when a slight excess of adamantyl isonitrile was added to **1** are shown in Figures A.07 and A.08. In this reaction, **1** (25 mg, 0.06 mmol) and adamantyl isonitrile (11 mg, 0.07 mmol) were stirred in pentane (5 mL) at room temperature for 30 minutes. The volatiles were removed *in vacuo*, the solid was extracted in 3x2 mL THF and concentrated. Crystals of a mixture of **2c** and **3c** were grown from the slow diffusion of pentane at -35 °C. In general, the bis-isonitrile iron complexes **3a-3c** were observed whenever an excess of any isonitrile ligand was added to **1**.



Scheme A.01. Formation of bis-isonitrile complexes through the reaction of excess isonitrile with **1**.

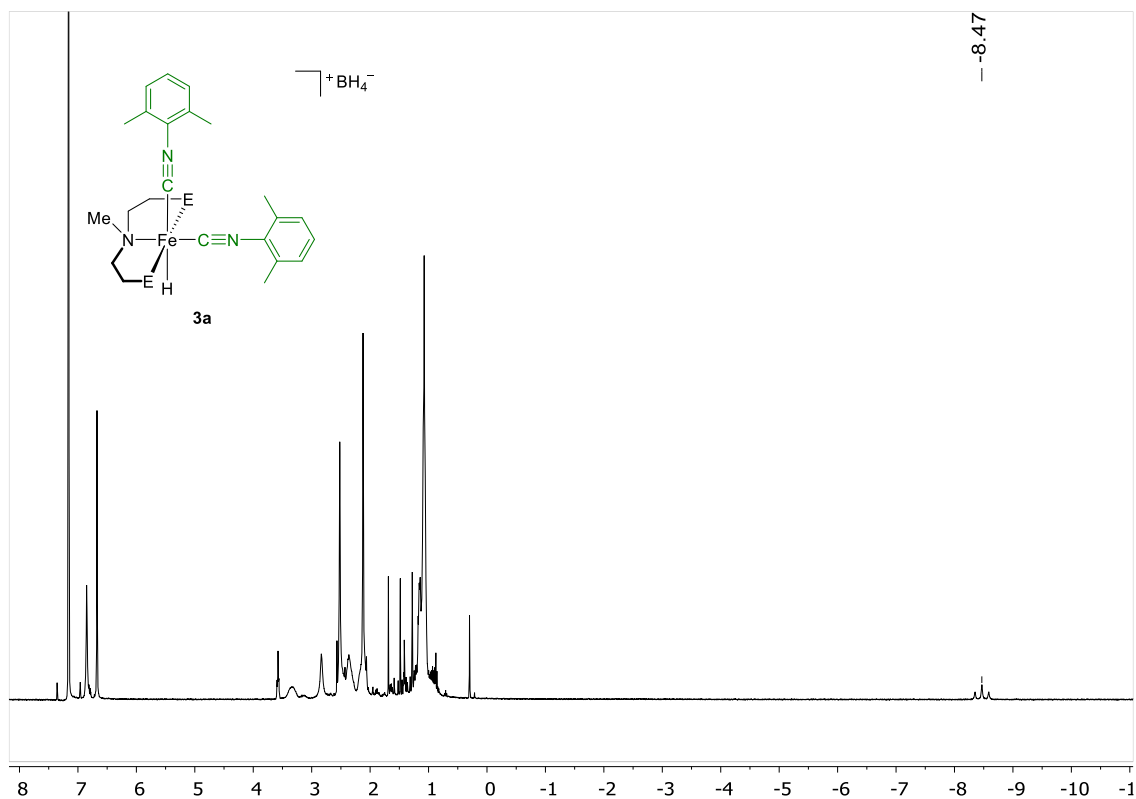


Figure A.01. ^1H NMR spectrum of **3a** generated *in situ* from the addition of excess 2,6-dimethylphenyl isonitrile to **1**; peak at 7.16 ppm is the residual solvent peak.

$[(^i\text{PrPN}^{\text{Me}}\text{PFe}(\text{H})(2,6\text{-dimethylphenyl isonitrile})_2)][\text{BH}_4]$. ^1H NMR (400 MHz, C_6D_6): 6.85 (br, 2H, ArCH), 6.67 (br, 4H, ArCH), 3.32 (br, 2H, CH_2), 2.83 (s, 3H, N- CH_3), 2.52 (br, 8H, Ar CH_3 + CH_2), 2.37 (br, 6H, CH_2), 2.16 (br, 4H, CH), 2.12 (s, 6H, Ar CH_3), 1.28 (q,

4H, BH_4 , $J=81.6$ Hz), 1.07 (m, 24H, $CHCH_3$) -8.47 (t, 1H, Fe- H , $J=46.3$ Hz). $^{31}P\{^1H\}$
 NMR (162 MHz, C_6D_6): 94.1.

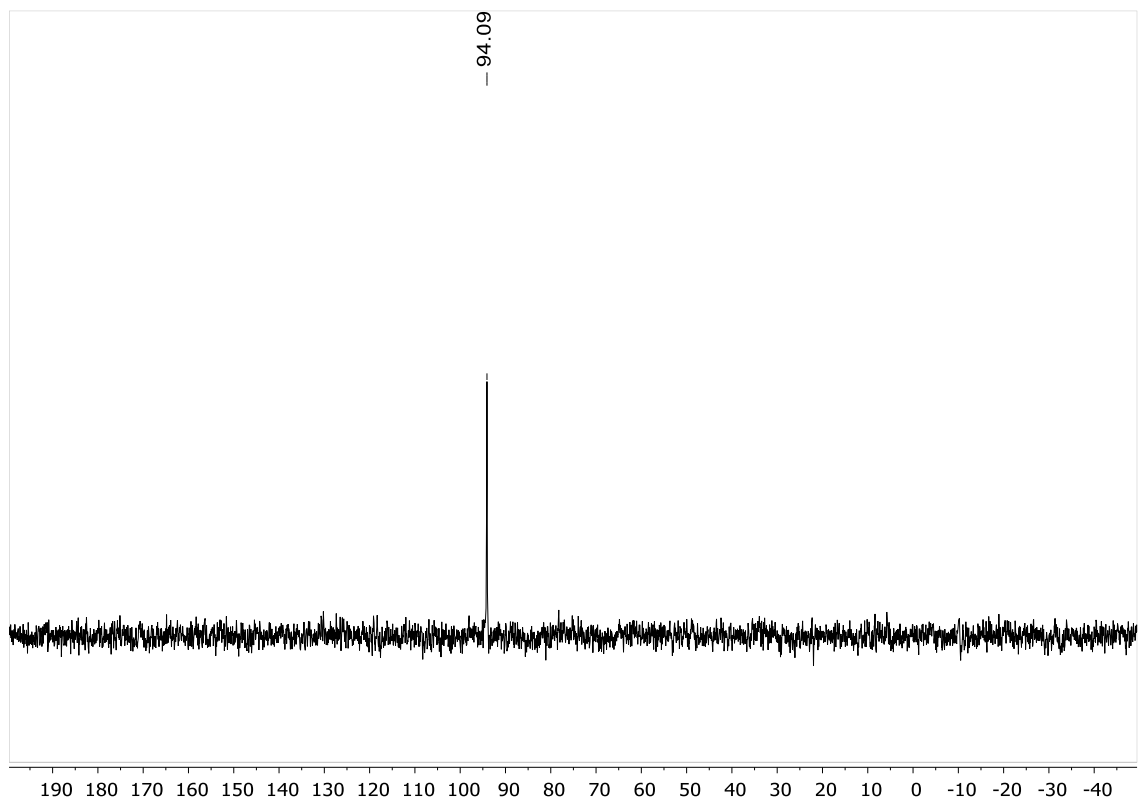


Figure A.02. $^{31}P\{^1H\}$ NMR spectrum of **3a** generated *in situ* from the addition of excess 2,6-dimethylphenyl isonitrile to **1**.

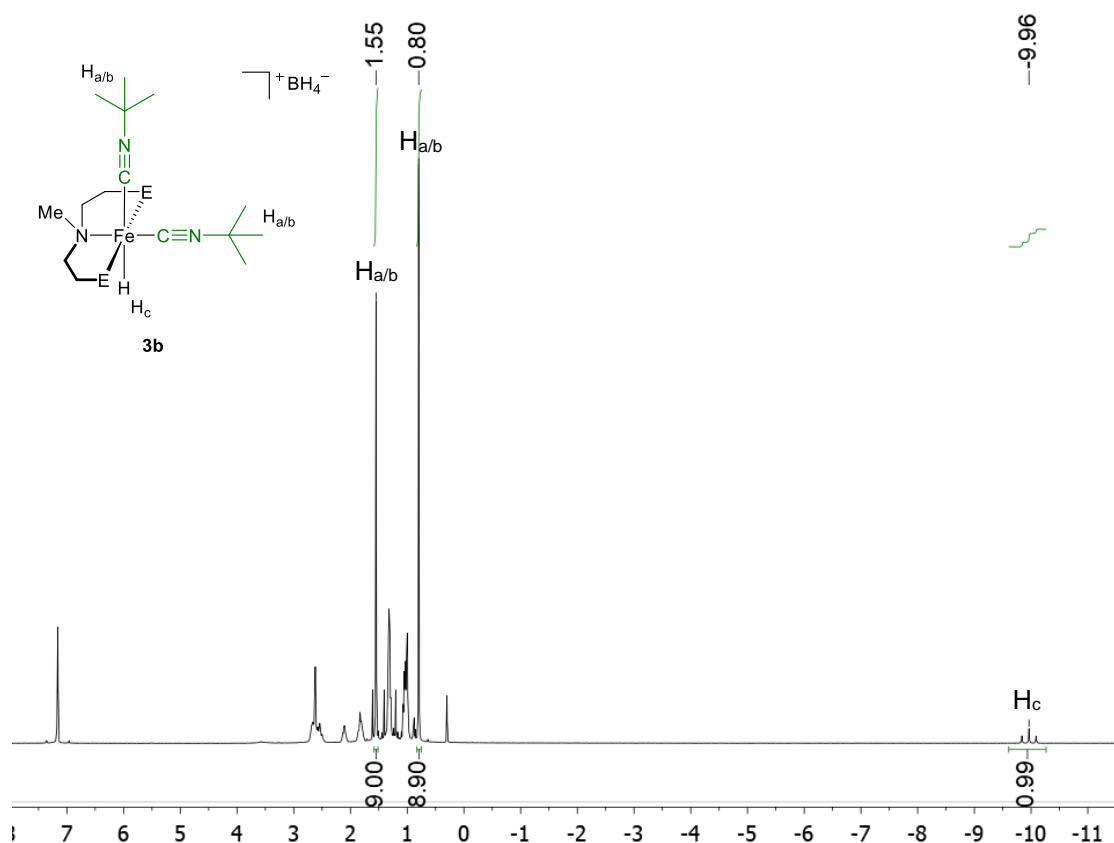


Figure A.03. ^1H NMR spectrum of the reaction of **1** with excess *tert*-butyl isonitrile in C_6D_6 to generate **3b**; peak at 7.16 ppm is the residual solvent peak.

$[(^i\text{PrPN}^{\text{Me}}\text{PFe}(\text{H})(\text{tert-butyl isonitrile})_2)][\text{BH}_4]$. ^1H NMR (400 MHz, C_6D_6): 2.67 (m, 2H, CH_2), 2.62 (s, 3H, N- CH_3), 2.54 (m, 4H, CH_2), 2.11 (m, 2H, CH_2), 1.83 (m, 4H, CH), 1.55 (s, 9H, CH_3), 1.32 (m, 12H, CHCH_3), 1.30 (q, 4H, BH_4 , $J=81.5$ Hz), 1.02 (m, 12H, CHCH_3), 0.80 (s, 9H, CH_3), -9.96 (t, 1H, Fe-H, $J=50.1$ Hz). $^{31}\text{P}\{^1\text{H}\}$ NMR (162 MHz, C_6D_6): 95.0.

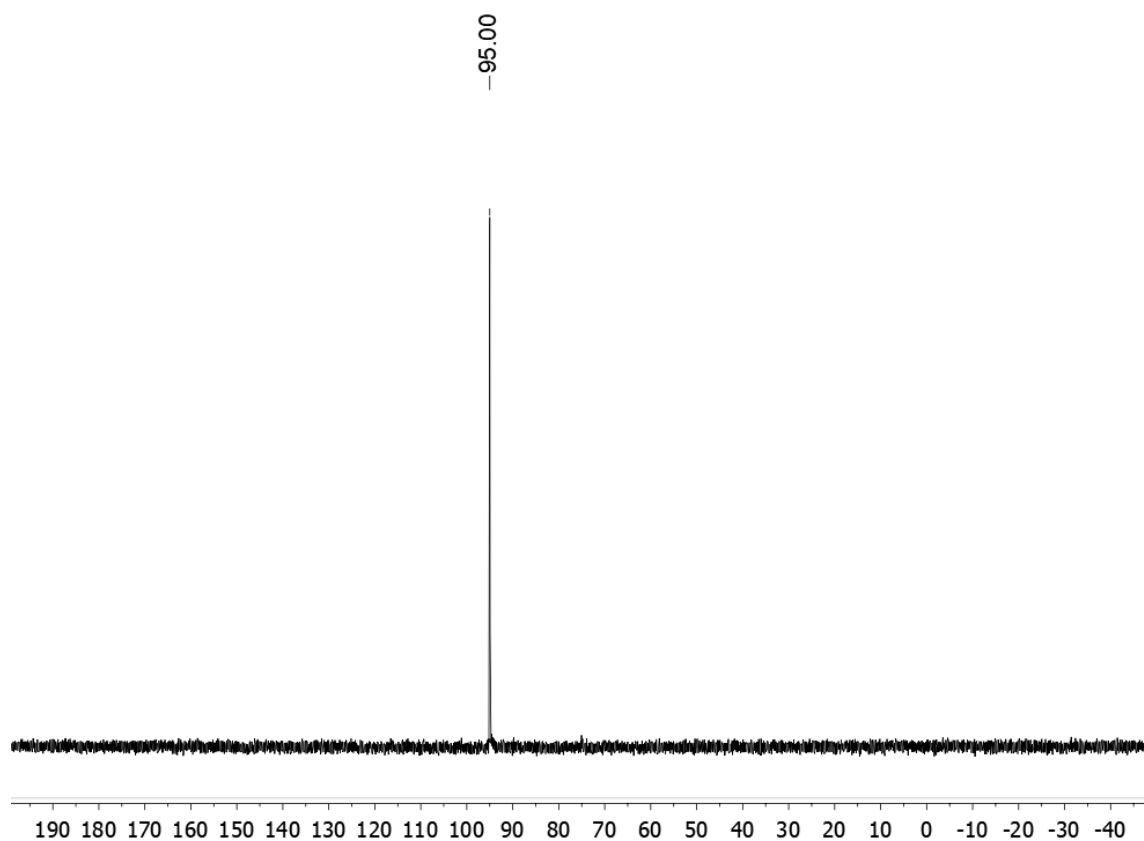


Figure A.04. $^{31}\text{P}\{^1\text{H}\}$ NMR spectrum of the reaction of **1** with excess *tert*-butyl isonitrile to generate **3b**.

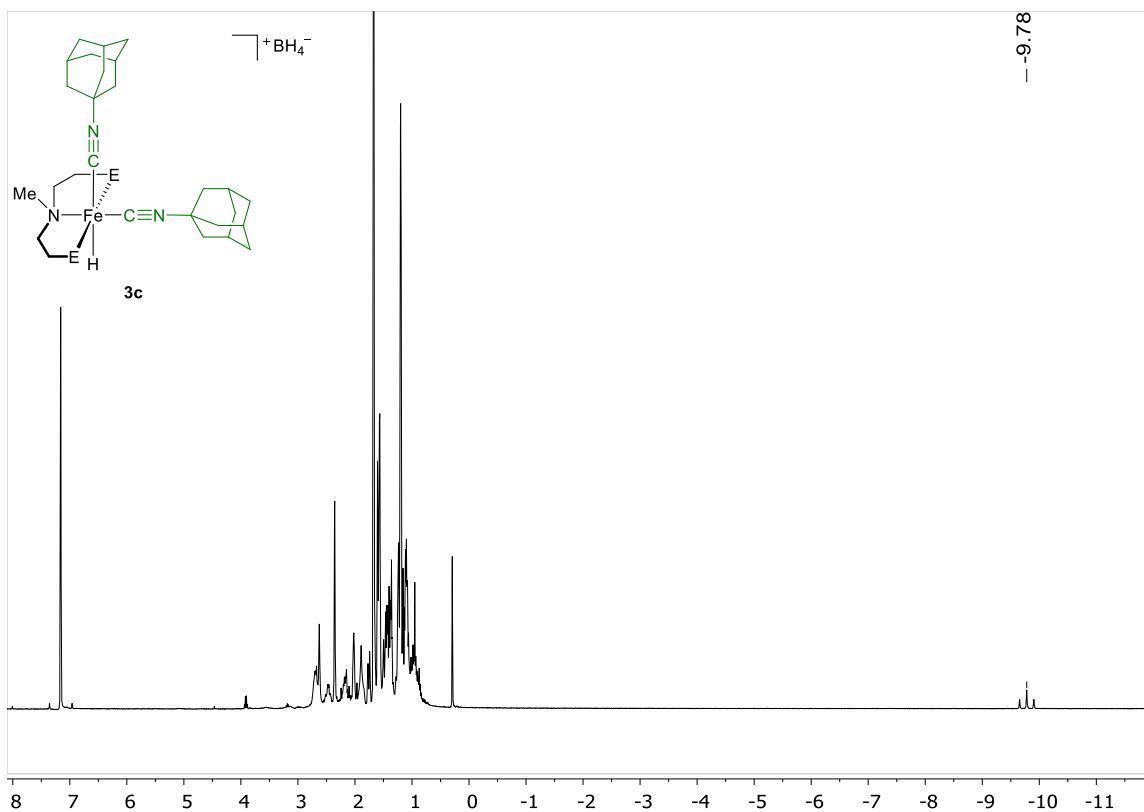


Figure A.05. ^1H NMR spectrum of **3c** generated *in situ* from the addition of excess adamantyl isonitrile to **1**; peak at 7.16 ppm is the residual solvent peak.

$[(^i\text{PrPN}^{\text{Me}}\text{PFe}(\text{H})(\text{adamantyl isonitrile})_2)][\text{BH}_4]$. Peaks in the aliphatic region of the ^1H

NMR were overlapping and could not be assigned. ^1H NMR (400 MHz, C_6D_6): 2.69 (m, 3H), 2.62 (s, 2H), 2.47 (br, 2H), 2.35 (s, 4H), 2.15 (m, 2H), 2.02 (br, 3H), 1.89 (br, 3H), 1.75 (br, 2H), 1.58 (m, 12H), 1.30-1.53 (m, 13H), 1.24 (br, 4H), 1.16 (br, 3H), 1.10 (m, 10H), 0.95 (m, 6H), -9.78 (t, 1H, Fe-H, $J=50.1$ Hz). $^{31}\text{P}\{^1\text{H}\}$ NMR (162 MHz, C_6D_6):

94.9.

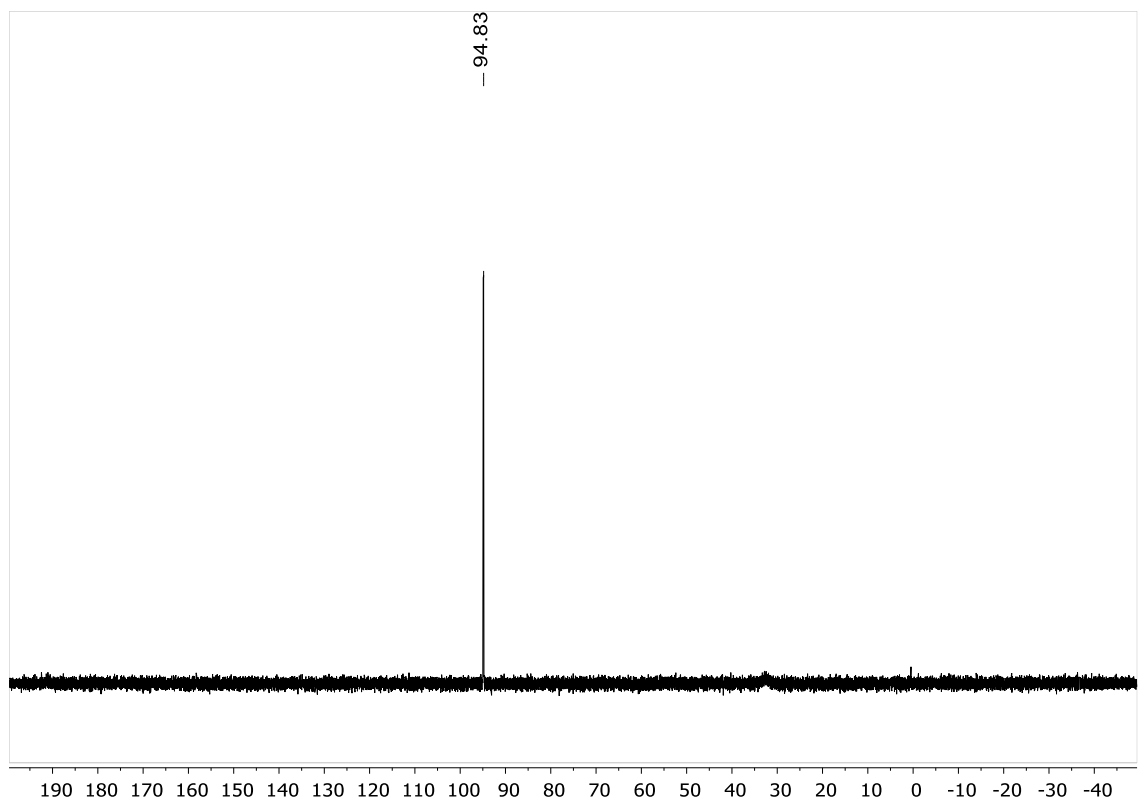


Figure A.06. $^{31}\text{P}\{^1\text{H}\}$ NMR spectrum of **3c** generated *in situ* from the addition of excess adamantyl isonitrile to **1**; small broad peak at 32 ppm is due to the presence of an $^{\text{iPr}}\text{PN}^{\text{Me}}\text{P-BH}_3$ adduct.

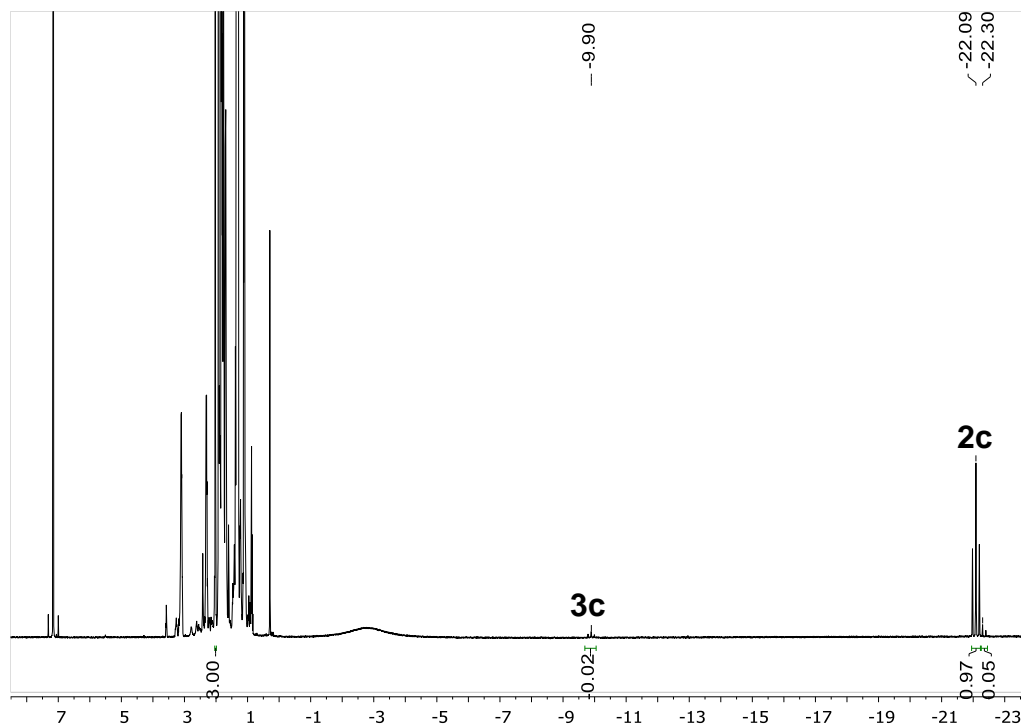


Figure A.07. ^1H NMR spectrum of a mixture of **2c** (2 isomers) and **3c** formed when a slight excess of adamantyl isonitrile was added to **1** in pentane, then the mixture was recrystallized from THF/pentane.

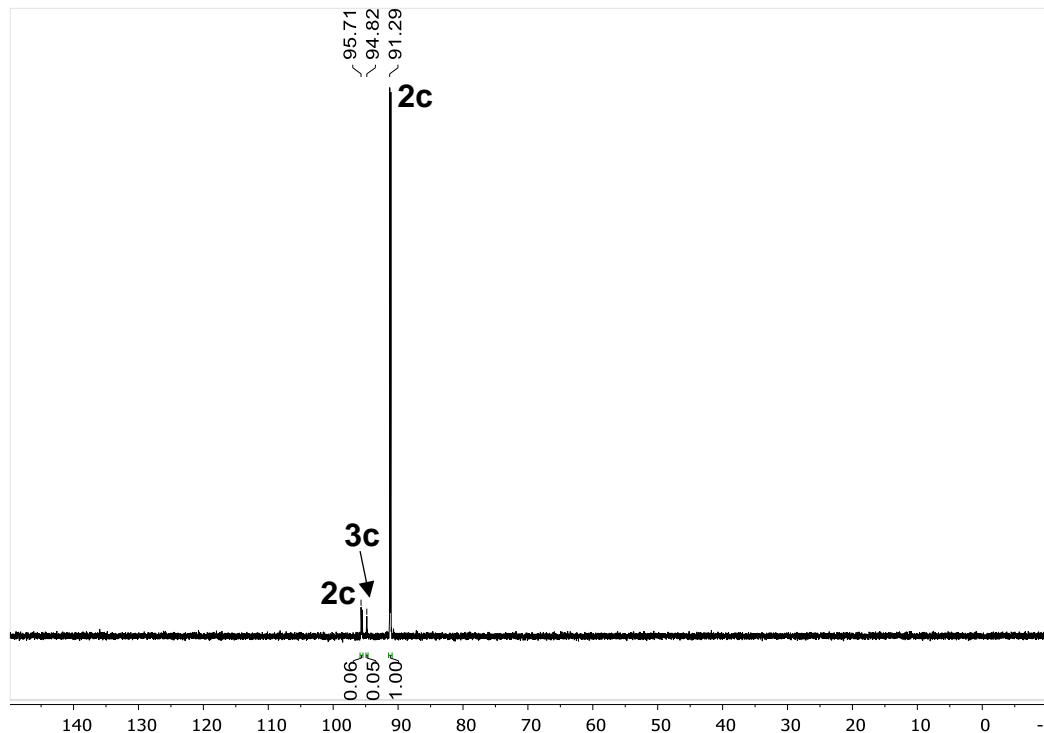


Figure A.08. $^{31}\text{P}\{^1\text{H}\}$ NMR spectrum of a mixture of **2c** (2 isomers) and **3c** formed when a slight excess of adamantyl isonitrile was added to **1** in pentane, then the mixture was recrystallized from THF/pentane.

V. *In Situ* Observation of Catalytic Intermediates

*Attempted Synthesis of $(i\text{PrPN}^{\text{Me}}\text{P})\text{Fe}(\text{H})_2(2,6\text{-dimethylphenyl isonitrile})$ from **2a***

In the glovebox, to a J. Young NMR tube were added **2a** (5 mg, 0.01 mmol), C_6D_6 (0.5 mL), and triethylamine (0.1 mL, 0.8 mmol). The J. Young tube was mixed on a shake tray for 4 hours, then heated to 45 °C in an oil bath overnight.

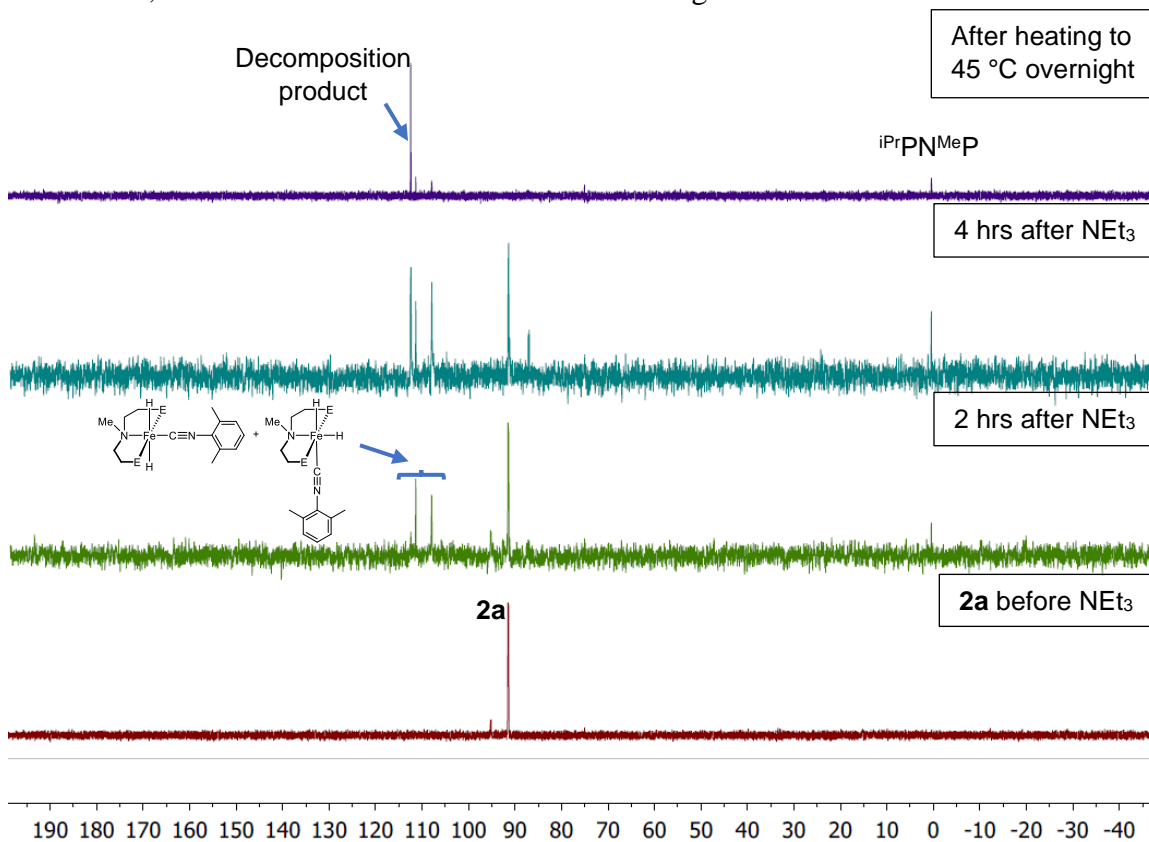


Figure A.09. Stacked $^{31}\text{P}\{^1\text{H}\}$ NMR spectra of the *in situ* reaction to form $(i\text{PrPN}^{\text{Me}}\text{P})\text{Fe}(\text{H})_2(2,6\text{-dimethylphenyl isonitrile})$ from **2a**. The decomposition product at 113 ppm was the only observed species after all attempts at isolation. Similar results were obtained in reactions with **2b** and **2c**.

Attempted Synthesis of (ⁱPrPN^{Me}P)Fe(H){OC(O)H}(2,6-dimethylphenyl isonitrile)

In a glovebox, to a J. Young NMR tube were added **2a** (5 mg, 0.01 mmol), C₆D₆ (0.5 mL), and triethylamine (0.1 mL, 0.8 mmol). The reaction was removed from the box, subjected to one freeze-pump-thaw cycle, and 1 atm of CO₂ was added. After 2 hours of mixing at room temperature, the volatiles were removed *in vacuo* and the residue was filtered and redissolved in C₆D₆.

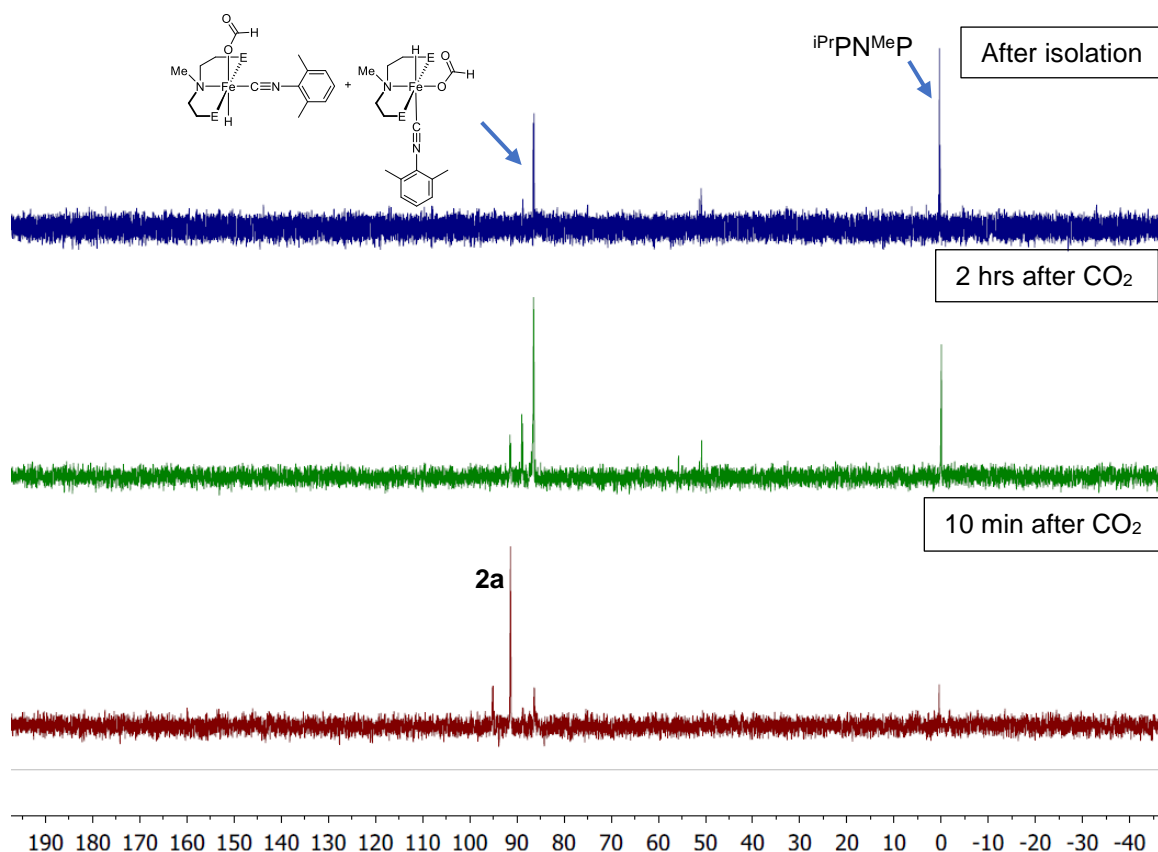


Figure A.10. Stacked ³¹P{¹H} NMR spectra of the *in situ* reaction to form (ⁱPrPN^{Me}P)Fe(H)(OC(O)H)(2,6-dimethylphenyl isonitrile) from **2a**. Removal of the CO₂ atmosphere *in vacuo* led to further decomposition to demetallated ligand and an intractable precipitate. Similar results were obtained in reactions with **2b** and **2c**.

VI. Formic Acid Dehydrogenation TON Quantification

A gas burette was used to order to measure TON in formic acid dehydrogenation.

First, a blank reaction was performed in which no catalyst was added to the reaction

solution. The volume of gas obtained from this reaction (trace solvent and FA) was recorded as V_{blank} . The corrected volume of gas produced from a catalytic reaction was then calculated using the following expression:

$$V_{\text{corr}} = V_{\text{obs}} - V_{\text{blank}}$$

Where V_{obs} is the observed change in water level in the gas burette during catalysis. It was assumed that a 1:1 mixture of H and CO₂ was produced in the catalytic reaction. The number of moles of gas produced (n_{prod}) in the reaction was determined using the following expression that utilizes the ideal gas law:

$$n_{\text{prod}} = \frac{V_{\text{corr}}}{2(22.4 \frac{\text{L}}{\text{mol}})}$$

The TON was then determined using the following expression:

$$\text{TON} = \frac{n_{\text{prod}}}{n_{\text{cat}}}$$

Where n_{cat} is the molar quantity of the catalyst.

The TOF was determined to be the TON that occurred in the first hour.

VII. Kinetic Trace of Formic Acid Dehydrogenation

In order to study the kinetics of formic acid dehydrogenation, a blank reaction was first performed with no iron precatalyst added, and the volume of gas produced from trace solvent and formic acid was recorded at a series of timepoints. The blank reaction was performed twice to ensure consistent values. Next, catalytic trials were run under standard conditions as reported in Table 2.03 of the main text using complex **2a** as the precatalyst. The reaction was monitored until completion, and the values of the blank kinetics trial were used to correct the TON recorded at each timepoint, as described in Appendix A, section

VI. This experiment was also repeated to ensure consistent results. The kinetic traces of both trials are shown below in Figure A.11.

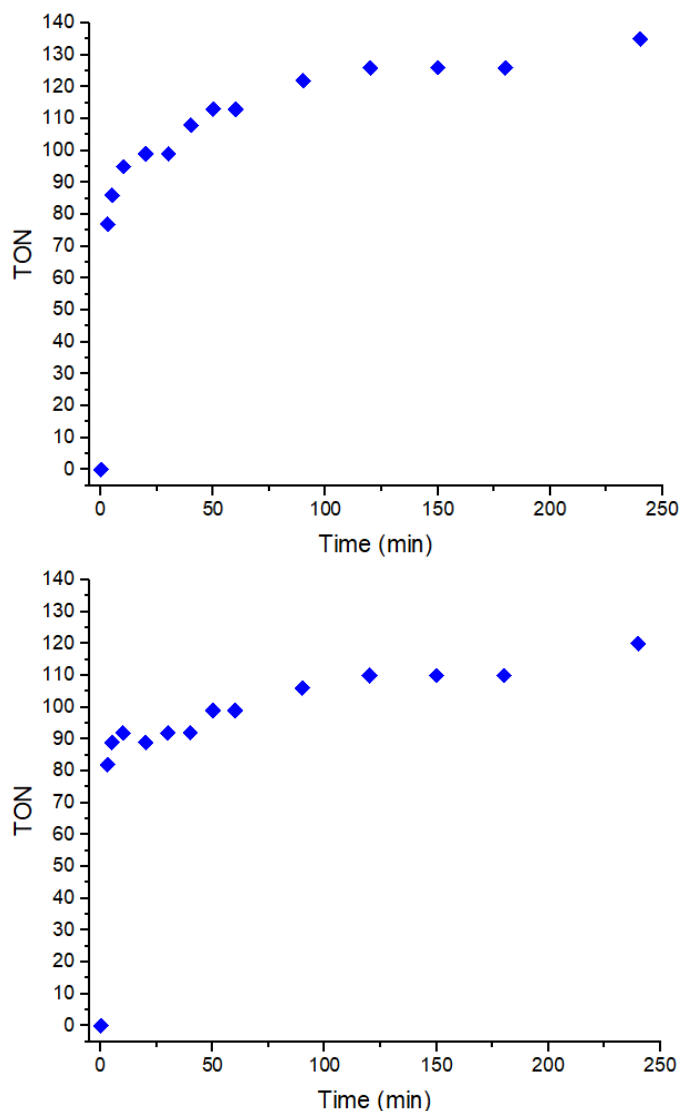


Figure A.11. Kinetic traces of two trials of formic acid dehydrogenation catalyzed by **2a**. Catalytic conditions are described in Table 3 of the main text. TON values were measured using a gas burette after correction using a blank trial.

VIII. Gas Chromatography of Catalytic Products

GC was performed to identify H_2 as a product in formic acid dehydrogenation and ensure that no CO was observed. The GC trace below is an example for formic acid

dehydrogenation using **A** as a catalyst under conditions described in Table 2.03. It is representative of GC results from FADH performed using **B**, **2a**, **2b**, and **2c**.

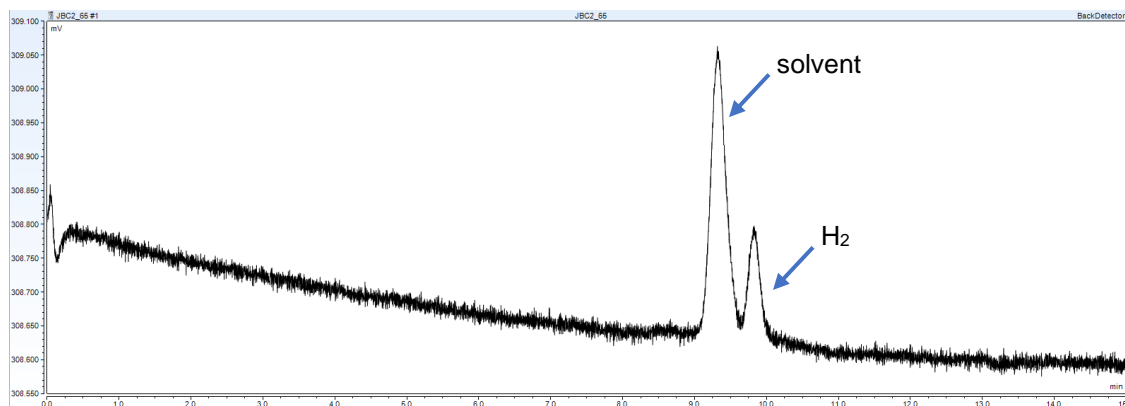


Figure A.12. GC trace of gas produced from FA dehydrogenation using **A**.

IX. X-ray Crystallographic Information

Details about the structure of 2a (CCDC 1858636)

Refinement details for **2a**:

Refinement of F^2 against all reflections. 8 low angle reflections were omitted due to interference with the beam stop. The weighted R-factor wR and goodness of fit S are based on F^2 , conventional R-factors R are based on F, with F set to zero for negative F^2 . The threshold expression of $F^2 > 2\sigma(F^2)$ is used only for calculating R-factors(gt) etc. and is not relevant to the choice of reflections for refinement. R-factors based on F^2 are statistically about twice as large as those based on F, and R-factors based on all data will be even larger.

The hydrogen atoms were first found in the difference map, then generated geometrically and refined as riding atoms with C-H distances = 0.95-0.99 Å and $U_{iso}(H) = 1.2$ times $U_{eq}(C)$ for CH and CH₂ groups and $U_{iso}(H) = 1.5$ times $U_{eq}(C)$ for CH₃

groups. The only exceptions were H1C, H1D, H1E, H1F (bound to B1), and H (bound to Fe1), which were found on the difference map and then freely refined.

Table A.01. Crystal data and structure refinement for **2a**.

Empirical formula	C ₂₆ H ₅₃ B Fe N ₂ P ₂	
Formula weight	522.30	
Temperature	93.15 K	
Wavelength	0.71073 Å	
Crystal system	Orthorhombic	
Space group	Pca2 ₁	
Unit cell dimensions	a = 15.7841(4) Å	a = 90°.
	b = 12.7521(3) Å	b = 90°.
	c = 14.6571(3) Å	g = 90°.
Volume	2950.19(12) ³	
Z	4	
Density (calculated)	1.176 Mg/m ³	
Absorption coefficient	0.636 mm ⁻¹	
F(000)	1136	
Crystal size	0.4 x 0.2 x 0.1 mm ³	
Crystal color and habit	Yellow block	
Theta range for data collection	2.931 to 28.720°.	
Index ranges	-21 ≤ h ≤ 21, -17 ≤ k ≤ 17, -19 ≤ l ≤ 19	
Reflections collected	54439	
Independent reflections	7615 [R(int) = 0.0503]	
Observed reflections (I > 2σ(I))	6826	
Completeness to theta = 25.242°	99.8 %	
Absorption correction	Semi-empirical from equivalents	
Max. and min. transmission	1.00000 and 0.94334	
Solution method	SHELXT 2014/5 (Sheldrick, 2014)	
Refinement method	ShelXL (Sheldrick, 2015)	
Data / restraints / parameters	7615 / 1 / 320	
Goodness-of-fit on F ²	1.046	
Final R indices [I > 2σ(I)]	R1 = 0.0373, wR2 = 0.0901	
R indices (all data)	R1 = 0.0453, wR2 = 0.0945	
Absolute structure parameter	-0.004(7)	
Extinction coefficient	n/a	
Largest diff. peak and hole	0.855 and -0.266 e.Å ⁻³	

Details about the structure of 2b (CCDC 1858637)

Refinement details for **2b**:

Refinement of F^2 against all reflections. 8 low angle reflections were omitted due to interference with the beam stop. The weighted R-factor wR and goodness of fit S are based on F^2 , conventional R-factors R are based on F, with F set to zero for negative F^2 . The threshold expression of $F^2 > 2\sigma(F^2)$ is used only for calculating R-factors(gt) etc. and is not relevant to the choice of reflections for refinement. R-factors based on F^2 are statistically about twice as large as those based on F, and R- factors based on all data will be even larger.

The hydrogen atoms were first found in the difference map, then generated geometrically and refined as riding atoms with C-H distances = 0.95-0.99 Å and Uiso(H) = 1.2 times Ueq(C) for CH and CH₂ groups and Uiso(H) = 1.5 times Ueq(C) for CH₃ groups. The only exceptions were H1A, H1B, H1C, H1D (bound to B1), and H (bound to Fe1), which were found on the difference map and then freely refined.

Table A.02. Crystal data and structure refinement for **3b**.

Empirical formula	C ₂₂ H ₅₃ B Fe N ₂ P ₂	
Formula weight	474.26	
Temperature	93(2) K	
Wavelength	0.71073 Å	
Crystal system	Orthorhombic	
Space group	Pbca	
Unit cell dimensions	a = 17.8973(8) Å	a = 90°.
	b = 15.8658(8) Å	b = 90°.
	c = 19.2679(10) Å	g = 90°.
Volume	5471.2(5) Å ³	
Z	8	
Density (calculated)	1.152 Mg/m ³	
Absorption coefficient	0.679 mm ⁻¹	
F(000)	2080	
Crystal size	0.300 x 0.200 x 0.100 mm ³	
Crystal color and habit	Yellow block	
Theta range for data collection	2.819 to 26.417°.	

Index ranges	-22<=h<=22, -19<=k<=19, -24<=l<=24
Reflections collected	83009
Independent reflections	5598 [R(int) = 0.1406]
Observed reflections ($I > 2\sigma(I)$)	4019
Completeness to $\theta = 25.242^\circ$	99.8 %
Solution method	SHELXT 2014/5 (Sheldrick, 2014)
Refinement method	SHELXL-2016/6 (Sheldrick, 2016)
Data / restraints / parameters	5598 / 0 / 285
Goodness-of-fit on F^2	1.023
Final R indices [$I > 2\sigma(I)$]	R1 = 0.0440, wR2 = 0.0929
R indices (all data)	R1 = 0.0739, wR2 = 0.1055
Extinction coefficient	n/a
Largest diff. peak and hole	0.697 and -0.291 e. \AA^{-3}

Details about the structure of 2c (CCDC 1858638)

Refinement details for **2c**:

Refinement of F^2 against all reflections. The weighted R-factor wR and goodness of fit S are based on F^2 , conventional R-factors R are based on F, with F set to zero for negative F^2 . The threshold expression of $F^2 > 2\sigma(F^2)$ is used only for calculating R-factors(gt) etc. and is not relevant to the choice of reflections for refinement. R-factors based on F^2 are statistically about twice as large as those based on F, and R-factors based on all data will be even larger.

The hydrogen atoms were first found in the difference map, then generated geometrically and refined as riding atoms with C-H distances = 0.95-0.99 Å and Uiso(H) = 1.2 times Ueq(C) for CH and CH₂ groups and Uiso(H) = 1.5 times Ueq(C) for CH₃ groups. The only exceptions were H1, H2, H1C, H1D, H1E, H1F, H2C, H2D, H2E and H2F, which were found on the difference map and then freely refined.

Table A.03. Crystal data and structure refinement for **2c**.

Empirical formula	C ₂₈ H ₅₉ B Fe N ₂ P ₂
Formula weight	552.37
Temperature	93(2) K
Wavelength	1.54184 Å

Crystal system	Orthorhombic
Space group	Pbca
Unit cell dimensions	a = 26.8871(6) Å a = 90°. b = 12.8928(5) Å b = 90°. c = 35.5088(9) Å g = 90°.
Volume	12309.1(6) Å ³
Z	16
Density (calculated)	1.192 Mg/m ³
Absorption coefficient	5.031 mm ⁻¹
F(000)	4832
Crystal size	0.050 x 0.020 x 0.010 mm ³
Crystal color and habit	Yellow Plate
Theta range for data collection	2.489 to 66.620°.
Index ranges	-32<=h<=32, -15<=k<=15, -42<=l<=42
Reflections collected	441402
Independent reflections	10888 [R(int) = 0.3254]
Observed reflections (I > 2sigma(I))	7315
Completeness to theta = 66.620°	100.0 %
Absorption correction	Semi-empirical from equivalents
Max. and min. transmission	1.00000 and 0.77007
Solution method	SHELXT-2014/5 (Sheldrick, 2014)
Refinement method	SHELXL-2014/7 (Sheldrick, 2014)
Data / restraints / parameters	10888 / 0 / 671
Goodness-of-fit on F ²	1.044
Final R indices [I>2sigma(I)]	R1 = 0.0661, wR2 = 0.1341
R indices (all data)	R1 = 0.1071, wR2 = 0.1526
Extinction coefficient	n/a
Largest diff. peak and hole	0.618 and -0.556 e.Å ⁻³

X. References

1. Harris, R. K.; Becker, E. D.; Cabral De Menezes, S. M.; Granger, P.; Hoffman, R. E.; Zilm, K. W., Further Conventions for NMR Shielding and Chemical Shifts: (IUPAC Recommendations 2008). *Pure Appl. Chem.* **2008**, *80*, 59-84.
2. Zhang, Y.; MacIntosh, A. D.; Wong, J. L.; Bielinski, E. A.; Williard, P. G.; Mercado, B. Q.; Hazari, N.; Bernskoetter, W. H., Iron Catalyzed CO₂ Hydrogenation to Formate Enhanced by Lewis Acid Co-Catalysts. *Chem. Sci.* **2015**, *6*, 4291-4299.

3. Smith, N. E.; Bernskoetter, W. H.; Hazari, N.; Mercado, B. Q., Synthesis and Catalytic Activity of PNP-Supported Iron Complexes with Ancillary Isonitrile Ligands. *Organometallics* **2017**, *36*, 3995-4004.
4. *CrysAlis Pro*, Rigaku OD. The Woodlands, TX, 2015.
5. Sheldrick, G., A Short History of SHELX. *Acta Cryst. A* **2008**, *64*, 112-122.

Appendix B: Supporting Information for Chapter 3

Adapted from the Supporting Information for: Curley, J. B., Bernskoetter, W. H., and Hazari, N. *ChemCatChem*, **2020**, *12*, 1934-1938.

I. Experimental Procedures

General Methods

Experiments were performed under a dinitrogen atmosphere in an M-Braun glovebox or using standard Schlenk techniques unless otherwise noted. Under typical operating conditions, the glovebox was not purged between uses of benzene, diethyl ether, pentane, THF, dioxane, or toluene. As a consequence, each solvent should be assumed to contain trace amounts of the others. All moisture and air-sensitive liquids were either transferred inside the glovebox or using a stainless steel cannula on a Schlenk line. Solvents were dried by passage through a column of activated alumina and stored under dinitrogen unless otherwise noted.

Ethanol (200 proof) was purchased from Decon Laboratories, Inc., and degassed and stored under dinitrogen prior to use. 1,3-dimethyl-2-imidazolidinone was purchased at 98% purity from Alfa Aesar, distilled, and dried by passage through a plug of activated alumina. Propylene carbonate was purchased from Acros at 99.5% purity and dried by passage through a plug of activated alumina. Deionized water was degassed prior to use. N-methyl-2-pyrrolidinone was purchased from Santa Cruz and dried by passage through a plug of activated alumina. *tert*-Amyl alcohol was purchased from Alfa Aesar, dried over CaH_2 , and distilled. 99.8% anhydrous chlorobenzene was purchased from Sigma-Aldrich

and dried by passage through a plug of activated alumina. Diglyme was purchased at 99% purity from Acros and dried by passage through a plug of activated alumina. Diphenyl ether was purchased at 99% purity from Alfa Aesar. Propyl acetate was purchased from Alfa Aesar and dried by passage through a plug of activated alumina.

All commercial chemicals were used as received except where noted. Anhydrous FeCl_2 was purchased from Alfa Aesar. Sodium borohydride was purchased from Acros Organics. Formic acid was purchased at 98+% purity from Millipore, degassed, and purified by partial freezing at 5 °C prior to use. Anhydrous *tert*-butanol was purchased from Sigma. Formic acid and *tert*-butanol were degassed *via* three freeze/pump/thaw cycles every week during regular usage. LiOTf , NaOTf and LiNTf_2 were purchased as the highest available purity from Sigma. ^{13}C -formic acid was purchased from Cambridge Isotope Laboratories. Deuterated solvents were obtained from Cambridge Isotope Laboratories. C_6D_6 and toluene- d_8 were dried by passage through a plug of activated alumina.

NMR spectra were recorded on Bruker AMX-400, AMX-500 or AMX-600, spectrometers at ambient probe temperatures, unless otherwise noted. Chemical shifts are reported in ppm with respect to residual internal protio solvent for ^1H and $^{13}\text{C}\{^1\text{H}\}$ NMR spectra. $^{31}\text{P}\{^1\text{H}\}$ NMR spectra are referenced via the ^1H resonances based on the relative gyromagnetic ratios.¹ Infrared data were obtained on a Bruker ALPHA FTIR spectrometer with a platinum ATR attachment inside a N_2 -filled glovebox. All samples were taken of the neat solid. Literature procedures were used to synthesize **1**, **2**, **3**, **6**, **7**, and **8**.²

Gas Chromatography

Gas Chromatography was performed on a ThermoFisher Trace 1300 GC apparatus equipped with a thermal conductivity detector and a Supelco fused silica capillary column (5 Å molecular sieves, 30 m x 0.53 mm). The system uses N₂ as a carrier gas and allows for determination of H₂ at concentrations greater than 1 ppm. He carrier gas was used for determination of CO₂ and CO at concentrations greater than 1 ppm. CH₄ was used as a gas detection standard.

II. Discussion of the Isomers of **2** and **3**

Complex **2** was previously reported as a mixture of isomers.^{2a} Due to its importance in our catalytic mechanism and calculations, as part of this work we conclusively determined which isomers were present and their relative ratio. ³¹P{¹H} and ¹H NMR spectra of **2** at room temperature are shown in Figure B.01-B.02.

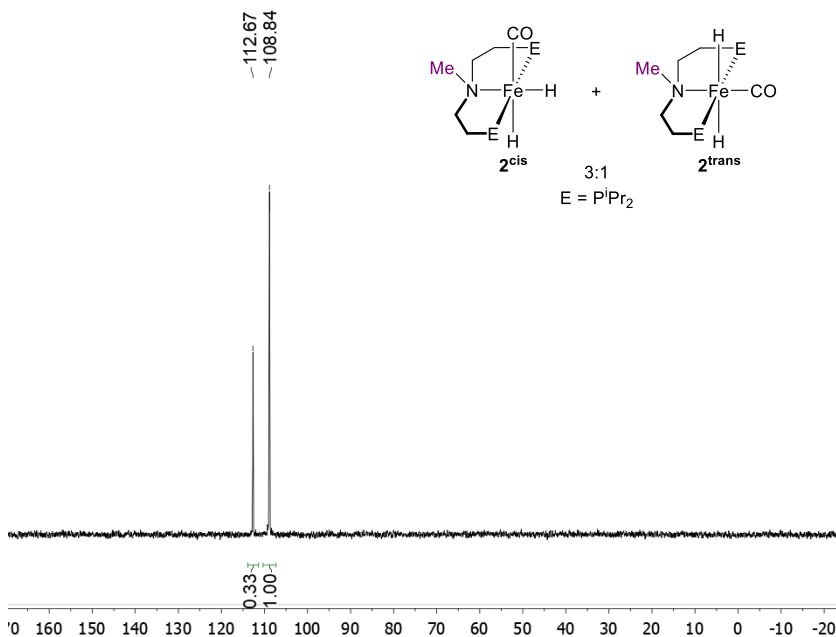


Figure B.01. ³¹P{¹H} NMR spectrum of the isomers of **2** at room temperature in C₆D₆.

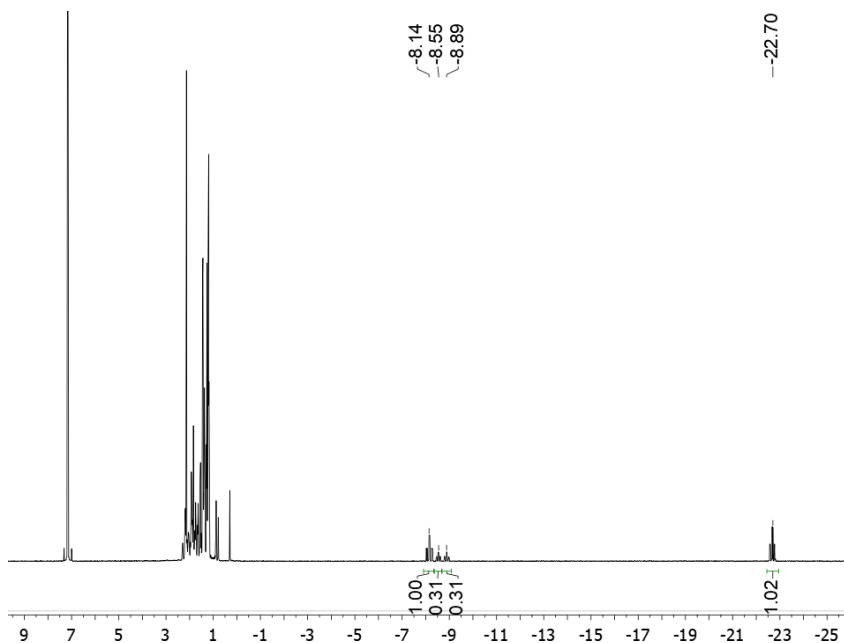


Figure B.02. ^1H NMR spectrum of the isomers of **2** at room temperature in C_6D_6 .

The two isomers are present in a 3:1 ratio. The upfield shift of one of the hydride peaks (-22.7 ppm) indicates that the cis isomer is the major component,³ but Nuclear Overhauser Spectroscopy (NOESY) was used to confirm this by looking at any interactions between the N-methyl moiety of the $^{\text{iPr}}\text{PN}^{\text{Me}}\text{P}$ ligand and the apical ligand, shown in Figure B.03.

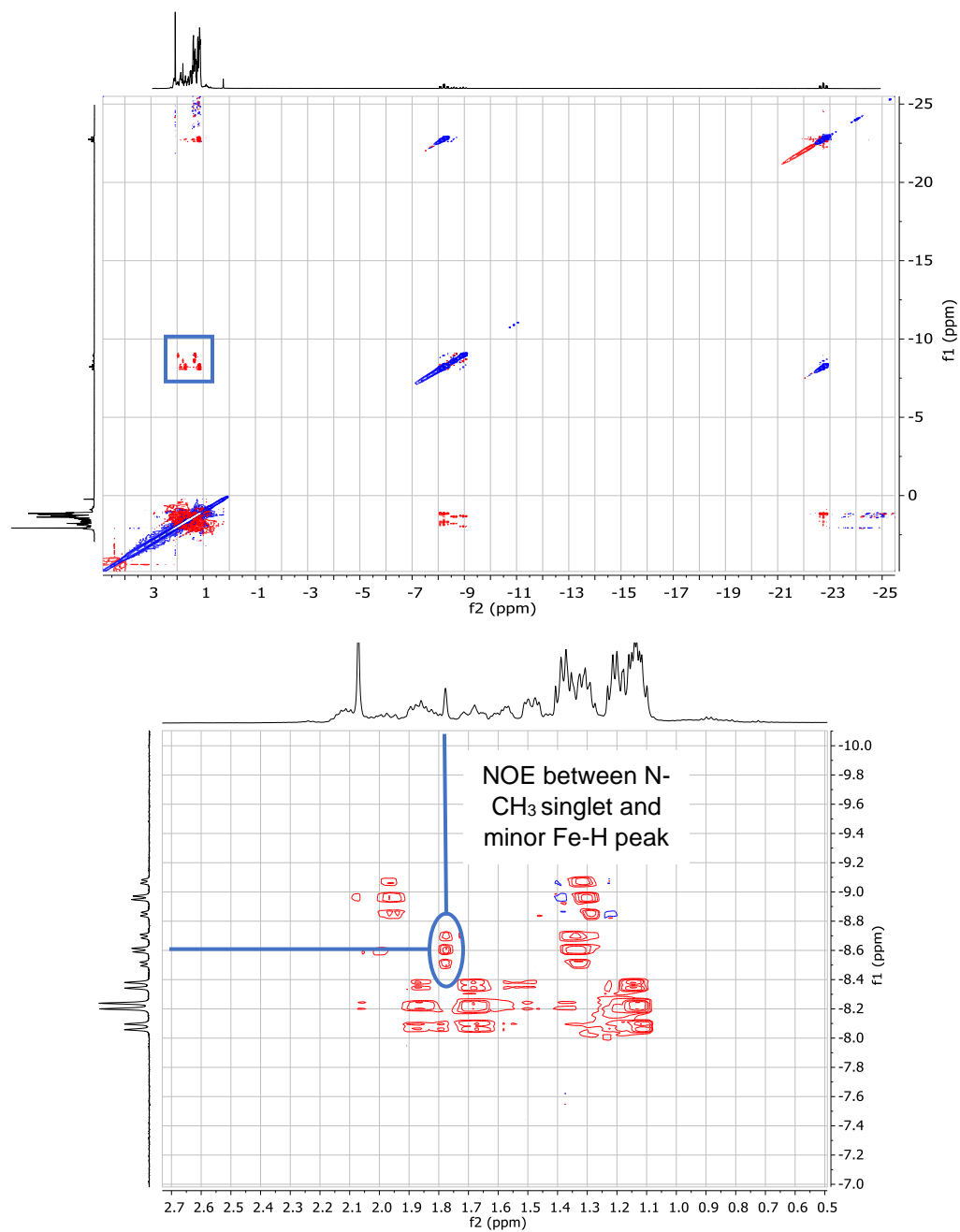


Figure B.03. NOESY spectrum in C_6D_6 of **2** (top) with an inset of the relevant portion of the spectrum (bottom).

This spectrum shows a Nuclear Overhauser Effect (NOE) between the N-methyl moiety of the $\text{iPrPN}^{\text{Me}}\text{P}$ ligand and a hydride from the minor isomer of **2**. This, combined

with the hydride shift data and the fact that **2^{cis}** is the isomer that is obtained upon crystallization,^{2a} led us to conclude that **2^{cis}** is the major isomer, and **2^{trans}** is the minor isomer.

Similarly, formate complex **3** is a mixture of 2 isomers at room temperature. Representative NMR spectra are shown in Figure B.04-B.05. Note that in a dinitrogen atmosphere some dihydride **2** is always observed with **3** due to the equilibrium between these species (see B.VIII). The 2% impurity at 103 ppm is (ⁱPrPN^{Me}P)Fe(CO)₂.⁴

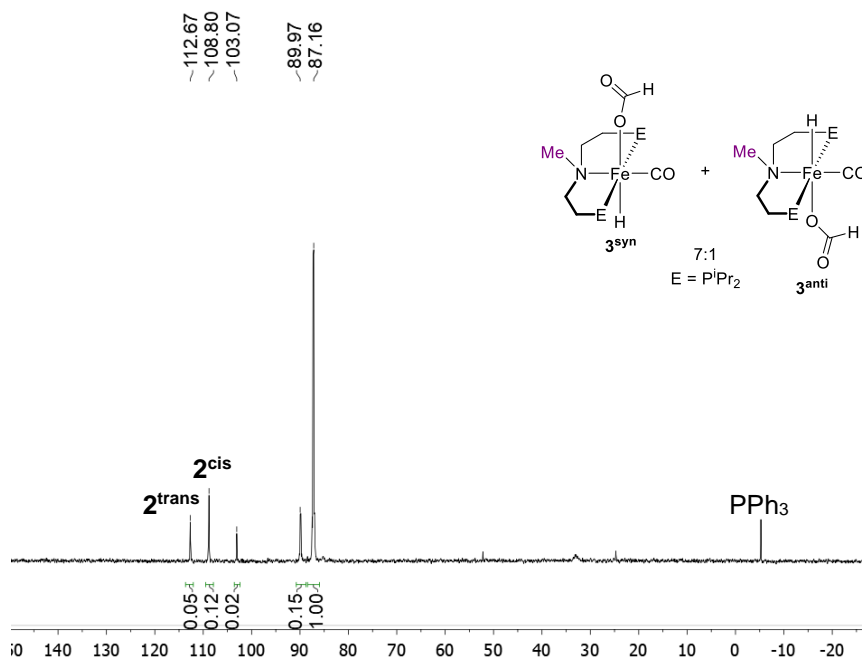


Figure B.04. ³¹P{¹H} spectrum of the isomers of **3** at room temperature in C₆D₆.

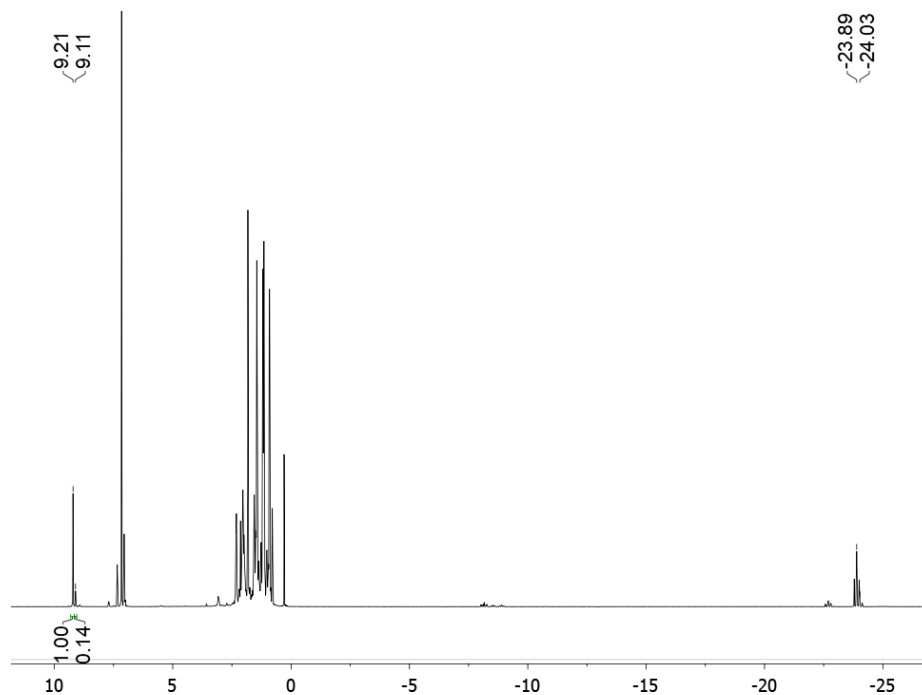


Figure B.05. ^1H NMR spectrum of the isomers of **3** at room temperature in C_6D_6 .

The hydride shifts here indicate that both isomers have the formate moiety *trans* to the hydride, but it is not possible to tell whether the formate or hydride ligand is located on the same face of the molecule as the N-methyl substituent. To determine this, another NOESY experiment was performed, with the area of interest highlighted in Figure B.06.

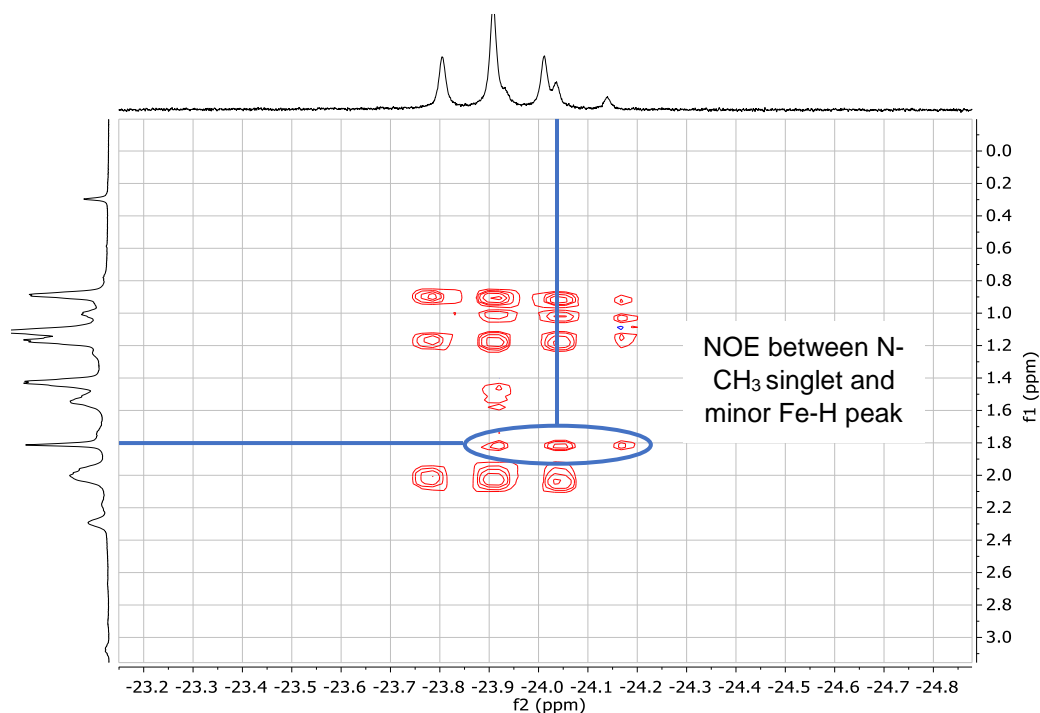
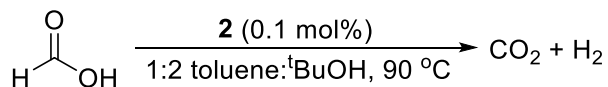


Figure B.06. Inset of the NOESY spectrum of **3** in C₆D₆.

In this case, an NOE is again observed between the minor isomer's hydride peak and the ligand N-Methyl group (this peak overlaps for the major and minor isomers). This indicates that the major isomer of **3** has the formate group adjacent to the N-methyl substituent, named **3^{syn}** for its position relative to the N-Methyl group. **3^{anti}** is the minor isomer, and has the hydride *syn* to the N-methyl.

III. General Procedure for Formic Acid Dehydrogenation

Representative Procedure for Additive-Free Formic Acid Dehydrogenation



In the glovebox, to a 25 mL Schlenk flask equipped with a magnetic stir bar were added toluene (1.37 mL) and **2** (291 μL of a 10 mM stock solution in toluene). The flask

was sealed, removed from the glovebox, and put under N₂ on a Schlenk line. A reflux condenser with a Kontes sidearm for addition of reagents was attached to a Kontes pin 3-way valve *via* Tygon tubing, thoroughly purged with N₂, then attached to the reaction flask. Anhydrous ^tBuOH (3.33 mL) was added to the reaction flask through a rubber septum placed on the condenser sidearm. The Tygon tubing leading from the 3-way valve to the oil bubbler was purged with N₂, then the bubbler was attached to a gas buret filled with mineral oil to prevent gas dissolution. The reaction flask was lowered into an oil bath preheated to 90 °C and allowed to equilibrate. Formic acid (110 μL, 2.91 mmol) was added through a rubber septum placed on the condenser sidearm, then the sidearm was rapidly resealed with a Kontes pin, the system was cut off from active N₂ flow, and the reaction flask was opened to the gas buret *via* the 3-way valve. As gas evolution lowered the level of the oil in the buret, the separatory funnel was lowered to keep the oil levels approximately even and maintain roughly atmospheric pressure in the reaction. A second catalytic reaction was always run in parallel and the numbers reported are the average of at least two experiments.

TON Quantification:

Before running a catalytic reaction, a blank reaction was performed in which no catalyst was added to the reaction solution. The volume of gas obtained from this reaction (trace solvent and formic acid) was recorded as V_{blank}. The corrected volume of gas produced from a catalytic reaction was then calculated using the following expression:

$$V_{corr} = V_{obs} - V_{blank}$$

Where V_{obs} is the observed change in oil level in the gas buret during catalysis. For kinetics experiments, blank reactions were performed where V_{blank} was measured at each desired

timepoint. It was assumed that a 1:1 mixture of H₂ and CO₂ was produced in the catalytic reaction. The number of moles of gas produced (n_{prod}) in the reaction was determined using the following expression that utilizes the ideal gas law:

$$n_{prod} = \frac{V_{corr}}{2(22.4 \frac{L}{mol})}$$

The TON was then determined using the following expression:

$$TON = \frac{n_{prod}}{n_{cat}}$$

Where n_{cat} is the molar quantity of the catalyst.

The TOF was determined to be the TON that occurred in the first hour.

Gas Volume Determination

The volume/height ratio of each gas buret was determined before using them in catalysis. To do this, water was placed in the buret, and the meniscus was marked. Some water was drained from the column into a tared flask, and the new water level was marked again. The weight of the water drained from the flask was used to determine its volume, and this was divided by the change in height in the buret to determine the mL/cm calibration of the buret.

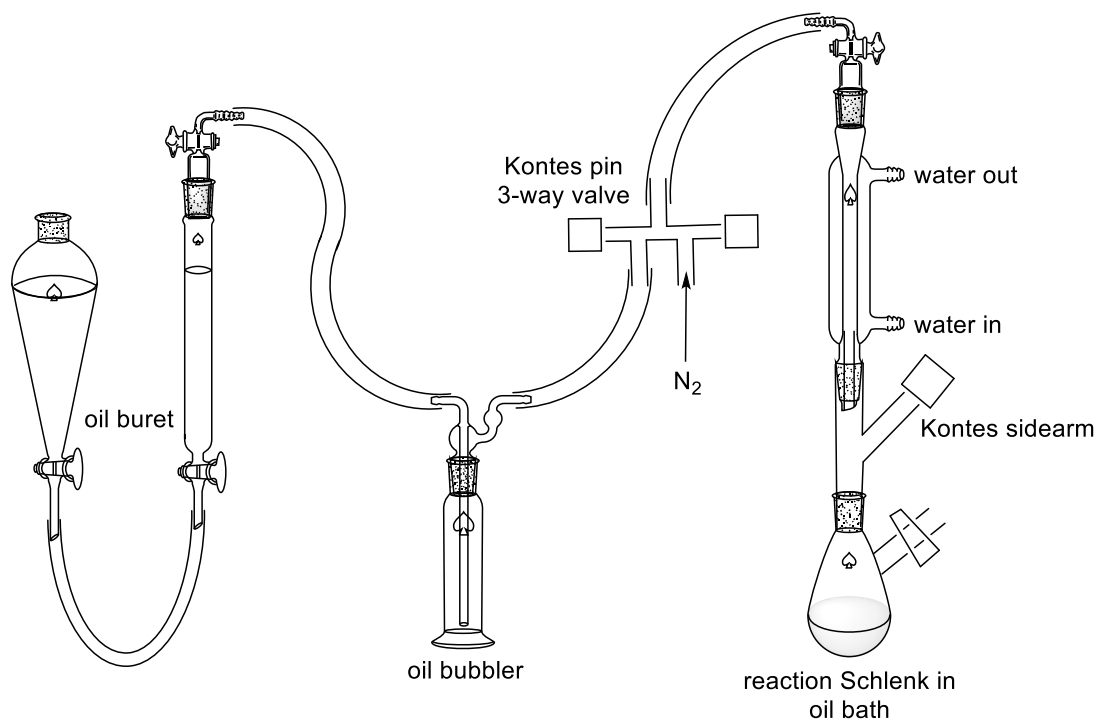


Figure B.07. Diagram of experimental setup for formic acid dehydrogenation.

IV. Optimization of Formic Acid Dehydrogenation Conditions

Table B.01. Temperature screen for formic acid dehydrogenation.^a

$$\text{H}-\overset{\text{O}}{\parallel}{\text{C}}-\text{OH} \xrightarrow[1:2 \text{ toluene:}^t\text{BuOH}]{\text{2 (0.01 mol\%)}} \text{CO}_2 + \text{H}_2$$

Entry	Temperature	TOF (h ⁻¹) ^b	TON (time) ^c	Yield
1	50 °C	760	980 (6 h)	9.8%
2	60 °C	1,000	1,400 (8 h)	14%
3	70 °C	1,000	1,300 (6 h)	13%
4	80 °C	1,300	1,700 (6 h)	17%
5	90 °C	2,100	2,600 (5 h)	26%
6	100 °C	760	930 (2 h)	9.3%

^aReaction conditions: Formic acid (110 μL , 2.91 mmol), **2** (0.01 mol%, 291 μL of a 1 mM stock solution in toluene), 1.67 mL toluene (total), 3.33 mL *tert*-butanol. ^bTurnover frequencies (TOF) were measured after the first hour. ^cTurnover numbers (TON) were measured using a gas buret. The time indicates the point at which no further increase in TON was observed. Reported results are the average of two trials, errors $\pm 10\%$.

Table B.02. Formic acid concentration screen for formic acid dehydrogenation.^a

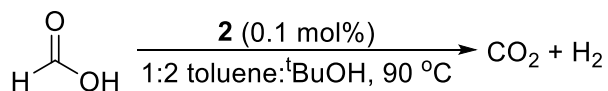
$$\text{H}-\overset{\text{O}}{\parallel}{\text{C}}-\text{OH} \xrightarrow[1:2 \text{ toluene:}^t\text{BuOH, } 90\text{ }^\circ\text{C}]{\text{2 (0.01 mol\%)}} \text{CO}_2 + \text{H}_2$$

Entry	Solvent Volume	[FA] _i	TOF (h ⁻¹) ^b	TON (time) ^c	Yield
1	2 mL	1.5 M	1,000	1,300 (4 h)	13%
2	4 mL	0.73 M	1,000	1,500 (4 h)	14%
3	5 mL	0.58 M	2,100	2,600 (5 h)	26%
4	6 mL	0.49 M	1,200	1,400 (6 h)	14%
5	8 mL	0.36 M	1,200	1,400 (6 h)	14%

^aReaction conditions: Formic acid (110 μL , 2.91 mmol), **2** (0.01 mol%, 291 μL of a 1 mM stock solution in toluene), 90 $^\circ\text{C}$. ^bTurnover frequencies (TOF) were measured after the first hour. ^cTurnover numbers (TON) were measured using a gas buret. The time indicates the point at which no further increase in TON was observed. Reported results are the average of two trials, errors $\pm 10\%$.

V. GC Measurements of Gaseous Reaction Products

GC was performed to confirm the products of formic acid dehydrogenation using **2** as a 1:1 ratio of CO_2 and H_2 with little to no CO generation. A standard catalytic reaction was run under the optimized conditions in order to ensure the desired gaseous products were being formed. GC samples were taken from the headspace of the gas buret and measured against a CH_4 standard. The traces are shown in Figures B.08 and B.09. The CO_2 and H_2 peaks integrate to 1:1 using calibration curves obtained for each gas, and no CO formation was observed.



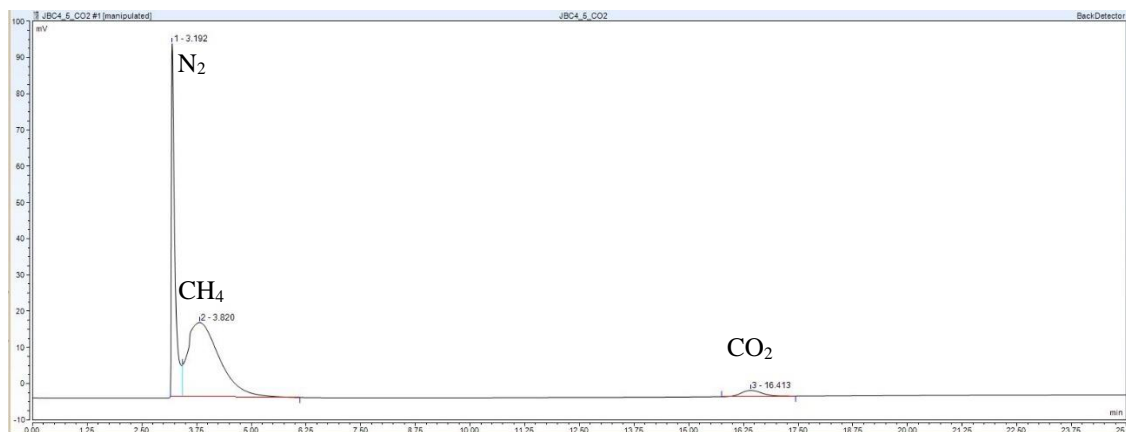


Figure B.08. GC trace of CO_2 detection using He carrier gas and a CH_4 standard; no CO peak observed (retention time 7 minutes).

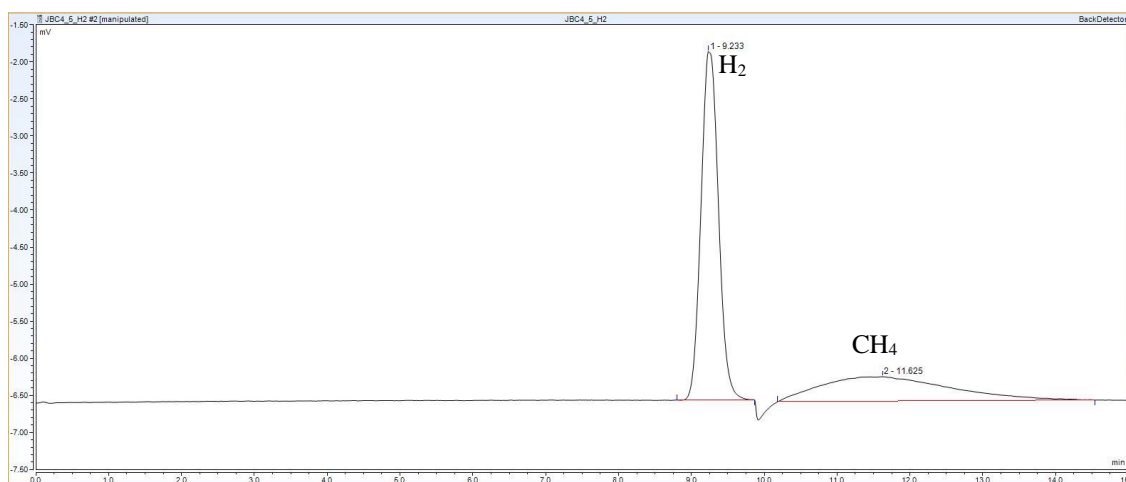
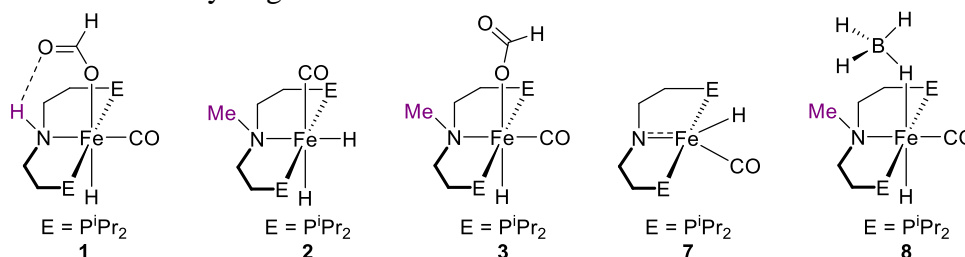


Figure B.09. GC trace of H_2 detection using N_2 carrier gas and a CH_4 standard.

VI. Precatalyst Screen

Table B.03. Performance of different pincer supported iron complexes for additive-free formic acid dehydrogenation.^a



$\text{H}-\text{C}(=\text{O})-\text{OH} \xrightarrow[\text{1:2 toluene:}^t\text{BuOH, 90 }^\circ\text{C}]{[\text{Fe}] (0.01 \text{ mol}\%)} \text{CO}_2 + \text{H}_2$				
Entry	[Fe]	TOF (h^{-1}) ^b	TON (time) ^c	Yield
1	2	2,100	2,600 (5 h)	26%
2	8	1,300	1,700 (4 h)	17%
3	3	1,600	1,900 (6 h)	19%
4	7	1,000	1,300 (4 h)	13%
5	1	1,100	1,400 (7 h)	14%

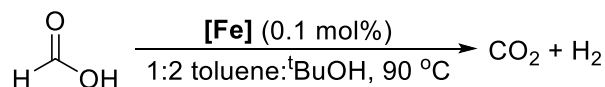
^aReaction conditions: Formic acid (110 μL , 2.91 mmol), **[Fe]** (0.01 mol%, 291 μL of a 1 mM stock solution in toluene), 1.67 mL toluene (total), 3.33 mL $^t\text{BuOH}$, 90 $^\circ\text{C}$. ^bTOFs were measured after the first hour. ^cTONs were measured using a gas buret. The time indicates the point at which no further increase in TON was observed. Reported results are the average of two trials, errors $\pm 10\%$.

Using the optimized catalytic conditions for **2**, we tested a series of iron complexes containing either a secondary amine, $^i\text{PrPN}^{\text{H}}\text{P}$, or tertiary amine, $^i\text{PrPN}^{\text{Me}}\text{P}$, pincer ligand, as shown in Table B.03. Also included in the screen was the five coordinate species $(^i\text{PrPNP})\text{Fe}(\text{H})(\text{CO})$ (**7**, $^i\text{PrPNP} = \text{N}(\text{CH}_2\text{CH}_2\text{P}^i\text{Pr}_2)_2^-$), which is known to undergo 1,2-addition across the Fe-N bond with formic acid to form complex **1**.^{2b} Unsurprisingly, complexes **1** and **7** had similar catalytic activities of around ~1200 turnovers, but this was inferior to any system with the tertiary amine-containing pincer ligand. We attribute the improved performance of **1** in additive-free dehydrogenation in a toluene: $^t\text{BuOH}$ mixture compared to our previous results in dioxane to the presence of the polar solvent mixture

which promotes decarboxylation.⁵ The complex $(i\text{PrPN}^{\text{Me}}\text{P})\text{Fe}(\text{H})(\kappa^1\text{-HBH}_3)(\text{CO})$ (**8**), which needs to lose BH_3 to generate **2**, gave inferior performance to **2**, presumably because there are side processes such that the conversion of **8** to **2** is not clean under the catalytic conditions. Unexpectedly, the formate complex **3** gives lower catalytic activity than **2**. In order to investigate this difference in productivity, an NMR stability test was performed, where solutions of **2** and **3** were prepared in a 1:2 toluene: $t\text{BuOH}$ mixture in J Young NMR tubes. The tubes were heated to 90 °C in order to mimic the reaction conditions. After 1 hour, **3** showed 13% decomposition, while **2** was only 7% decomposed. After 3 hours, **3** was 33% decomposed and **2** was only 16% decomposition products. Decomposition products observed included the free $i\text{PrPN}^{\text{Me}}\text{P}$ ligand and the iron(0) species $(i\text{PrPN}^{\text{Me}}\text{P})\text{Fe}(\text{CO})_2$. Protonation of this species by formic acid leads to formation of the catalytic decomposition product **5**.⁴ From this experiment, we hypothesize that **3** is a less productive catalyst than **2** because it is less stable under catalytic conditions, and more of the catalytic stock solution decomposes before catalysis begins.

VII. Comparison of the Initial Kinetics of **1** and **2**

The kinetics of formic acid dehydrogenation using catalysts **1** and **2** were compared under optimized conditions at 0.1 mol% loading. Full kinetics traces are shown in Figure 3.02. The initial kinetics of the reactions are shown in Figure B.10.



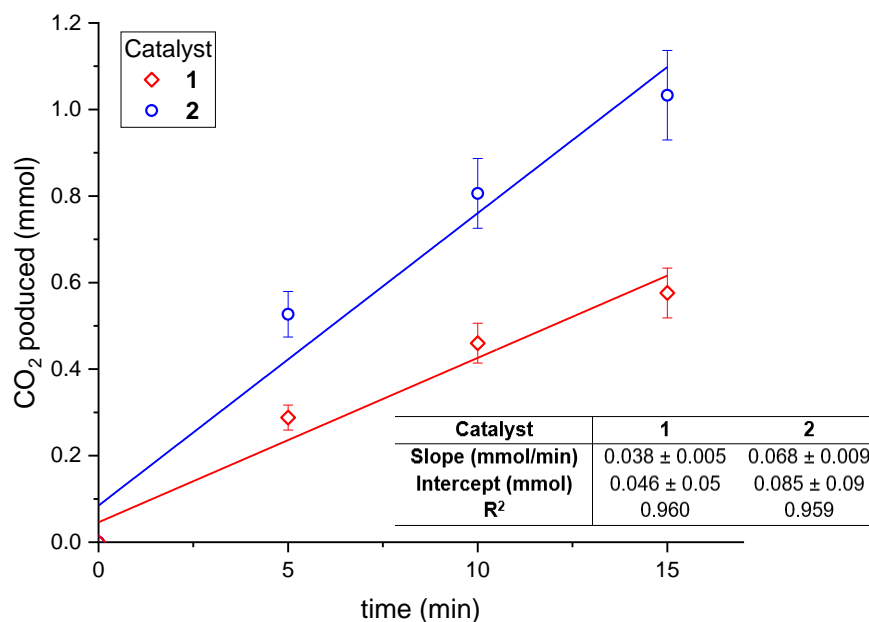
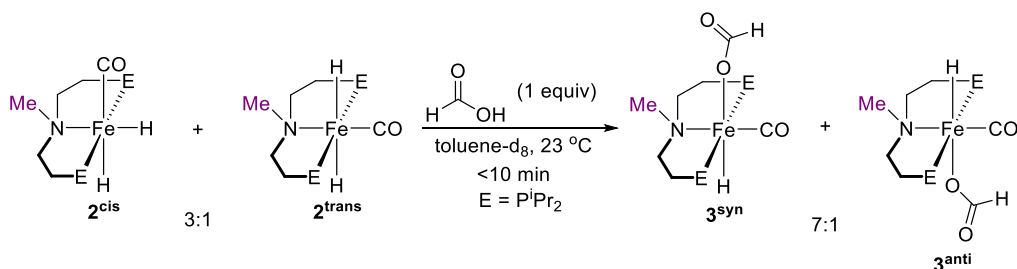
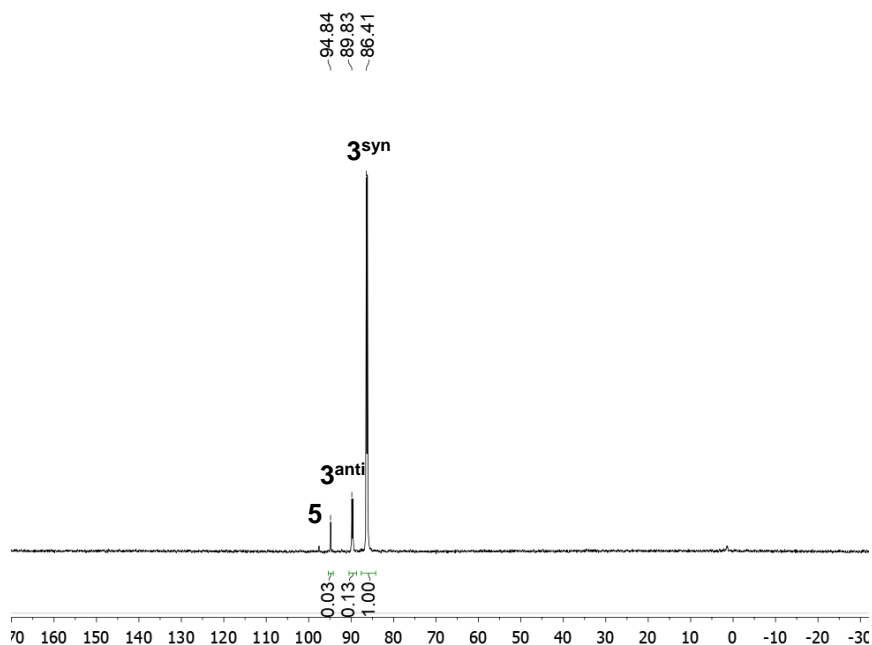


Figure B.10. Initial kinetics of additive-free FADH using **1** and **2** at 0.1 mol% loading, error bars $\pm 10\%$.

VIII. Stoichiometric Reactions Relevant to Catalysis

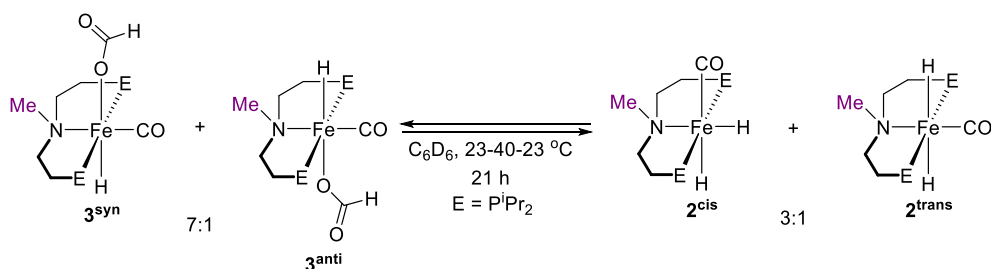
In the glovebox, to a J Young NMR tube were added **2** (5.0 mg, 0.012 mmol), formic acid (0.5 μ L, 0.012 mmol, added as a stock solution in toluene- d_8), and toluene- d_8 (600 μ L). The solution immediately deepened in color from pale yellow to bright yellow. The reaction scheme and $^3\text{P}\{^1\text{H}\}$ NMR spectrum is shown in Scheme B.01. The 3% impurity is decomposition product **5**.

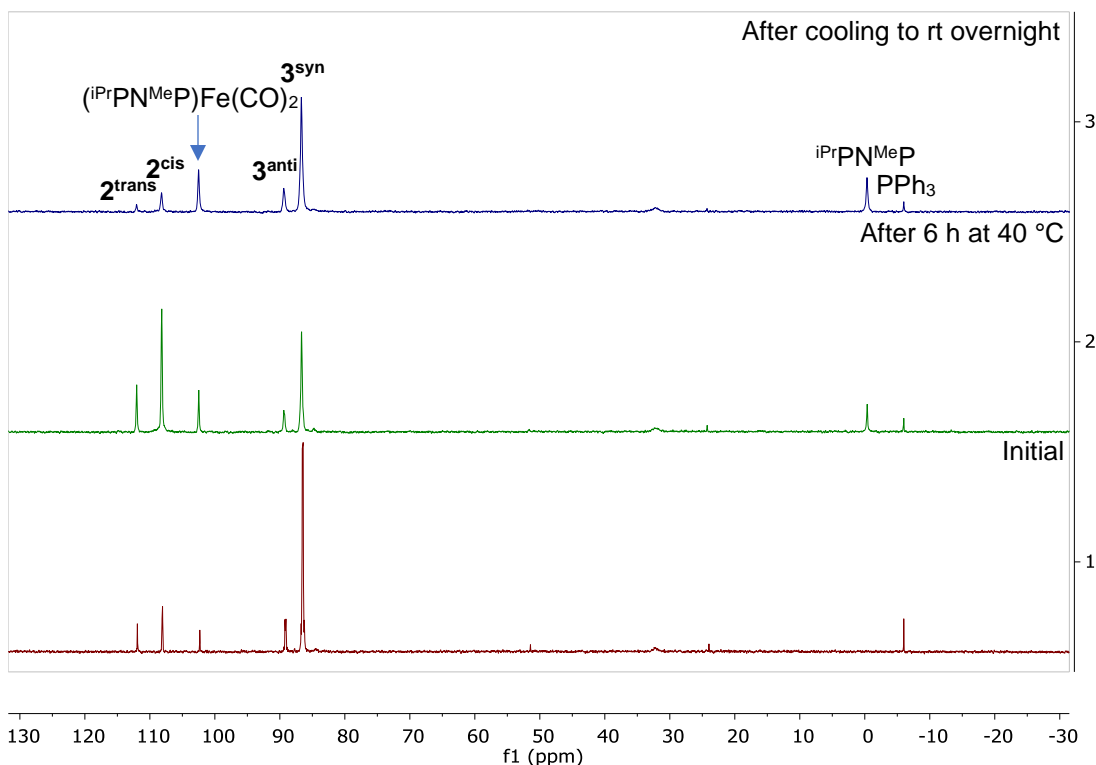




Scheme B.01. Stoichiometric reaction of **2** and formic acid to generate **3**, and the reaction $^{31}\text{P}\{^1\text{H}\}$ NMR spectrum in toluene- d_8 .

Next, to a J Young NMR tube were added **3** (5.6 mg, 0.012 mmol), a capillary containing PPh_3 in toluene- d_8 as a standard, and C_6D_6 (500 μL). The tube was degassed and sealed under vacuum. Initial NMR data showed 84% **3** and 13% **2** with 3% decomposition. The tube was heated to 40 $^\circ\text{C}$ for 6 hours to give 44% **3**, 48% **2** and 8% decomposition, then cooled to room temperature overnight (an additional 15 hours). The final spectrum showed 72% **3**, 11% **2**, and 17% decomposition. Reaction scheme and $^{31}\text{P}\{^1\text{H}\}$ NMR spectra are shown in Scheme B.02.

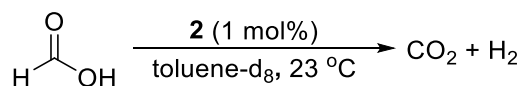


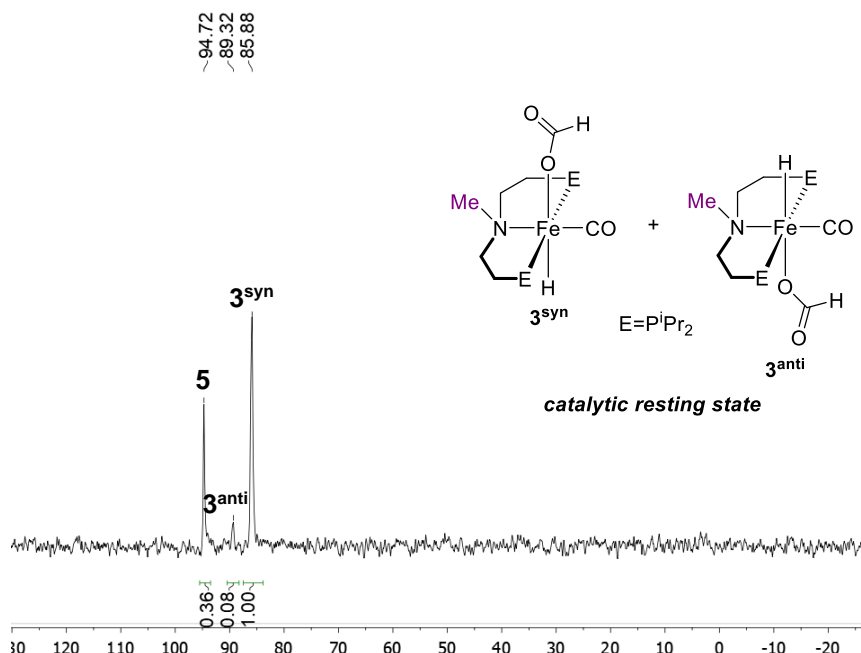


Scheme B.02. Reaction scheme and $^{31}\text{P}\{^1\text{H}\}$ spectra of **3** in C_6D_6 under static vacuum initially (bottom), after heating for 6 hours at 40°C (middle), and after cooling to room temperature overnight (top).

IX. Determination of the Catalytic Resting State

In the glovebox, to a J Young NMR tube were added **2** (1.5 mg, 0.0036 mmol), toluene- d_8 (600 μL) formic acid (14 μL). Vigorous bubbling was immediately observed, and the color deepened to bright yellow as soon as the formic acid was added. NMR spectra were taken as soon as possible (<10 min). The reaction scheme and $^{31}\text{P}\{^1\text{H}\}$ NMR spectrum is shown in Scheme B.03.





Scheme B.03. *In situ* $^{31}\text{P}\{^1\text{H}\}$ NMR experiment performed in toluene- d_8 to determine the resting state of **2** in formic acid dehydrogenation.

X. Determination of the Order in [Formic Acid]

To determine the catalytic order in [formic acid], experiments were performed with 5 different initial concentrations of formic acid. Origin was used to linearly fit the first 15 minutes of kinetics data and determine the observed initial rates. These observed rates were then plotted against the initial concentration of formic acid in order to determine the order in formic acid. Data for these experiments are shown in Table B.04 and Figures B.11 and B.12.

Table B.04. Initial rates data for order in formic acid experiments.

	$\text{H}-\text{C}(=\text{O})-\text{OH} \xrightarrow[1:2 \text{ toluene:}^t\text{BuOH}, 90^\circ\text{C}]{\text{2 (2.91 } \mu\text{mol)}} \text{CO}_2 + \text{H}_2$				
	X M				
[FA] _i	0.58 M	0.41 M	0.29 M	0.22 M	0.14 M
Slope	0.054 ± 0.007	0.063 ± 0.005	0.058 ± 0.004	0.046 ± 0.005	0.052 ± 0.011
Intercept	0.056 ± 0.06	0.023 ± 0.05	-0.033 ± 0.04	-0.039 ± 0.04	0.024 ± 0.1
R ²	0.971	0.987	0.991	0.980	0.913

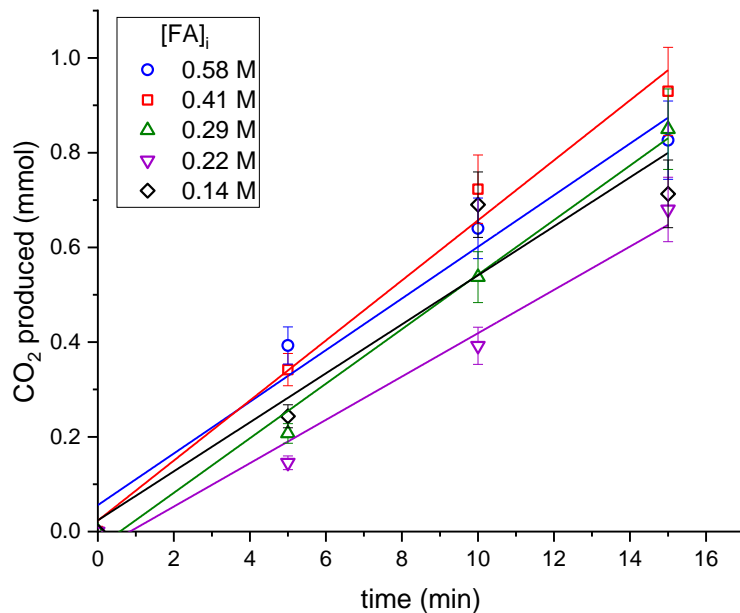


Figure B.11. Plot of the initial kinetics of formic acid dehydrogenation at varying initial concentrations of formic acid, error bars $\pm 10\%$.

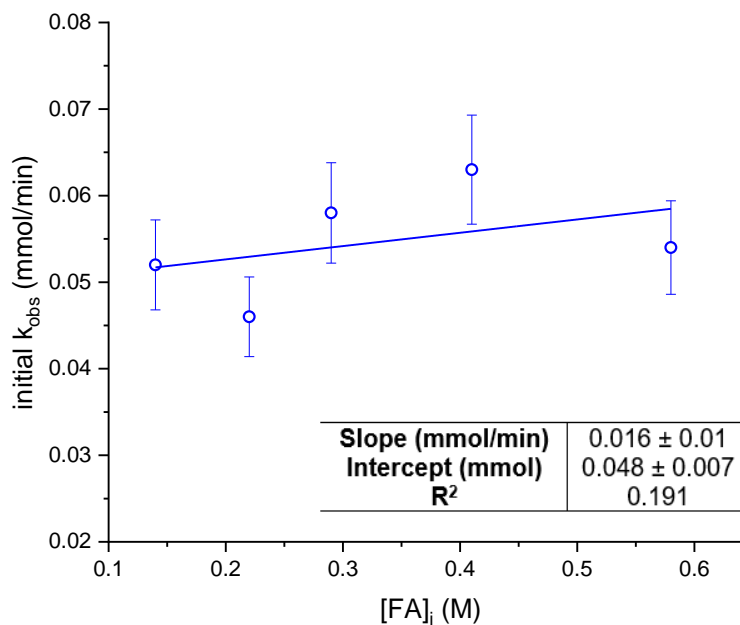


Figure B.12. Plot of initial observed rate vs initial concentration of formic acid, error bars $\pm 10\%$.

Figure B.12 shows that the rate of FADH has no dependence on the concentration of formic acid, as all of the k_{obs} are essentially within error of each other. This indicates that this FADH system has a zero order dependence on [formic acid].

XI. Determination of the Order in [Iron]

In order to find the catalytic order in [iron], experiments were performed with 4 different initial concentrations of **2**. Origin was used to linearly fit the first 15-20 minutes of kinetics data and determine the observed initial rates. These observed rates then were plotted against the initial concentration of **2** in order to determine the order in formic acid. Data for these experiments are shown in Table B.05 and Figures B.13 and B.14.

Table B.05. Initial rates data for order in formic acid experiments.

	$\text{H}-\overset{\text{O}}{\parallel}{\text{C}}-\text{OH} \xrightarrow[1:2 \text{ toluene:}^t\text{BuOH, } 90\text{ }^\circ\text{C}]{\text{2 (X mM)}} \text{CO}_2 + \text{H}_2$			
[2]_i	0.73 mM	0.58 mM	0.44 mM	0.29 mM
Slope	0.079 ± 0.005	0.067 ± 0.009	0.057 ± 0.006	0.044 ± 0.003
Intercept	0.044 ± 0.05	0.085 ± 0.09	0.10 ± 0.08	0.052 ± 0.04
R²	0.992	0.958	0.966	0.985

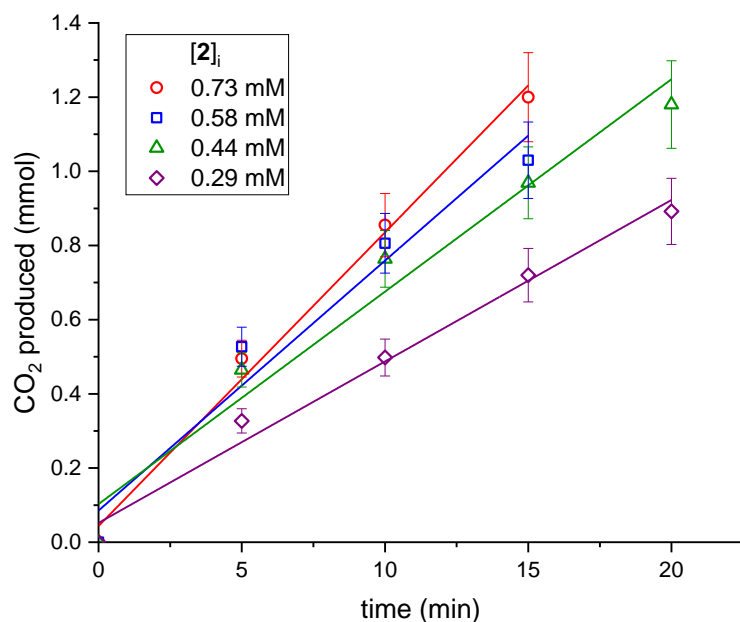


Figure B.13. Plot of the initial kinetics of formic acid dehydrogenation at varying initial concentrations of **2**, error bars $\pm 10\%$.

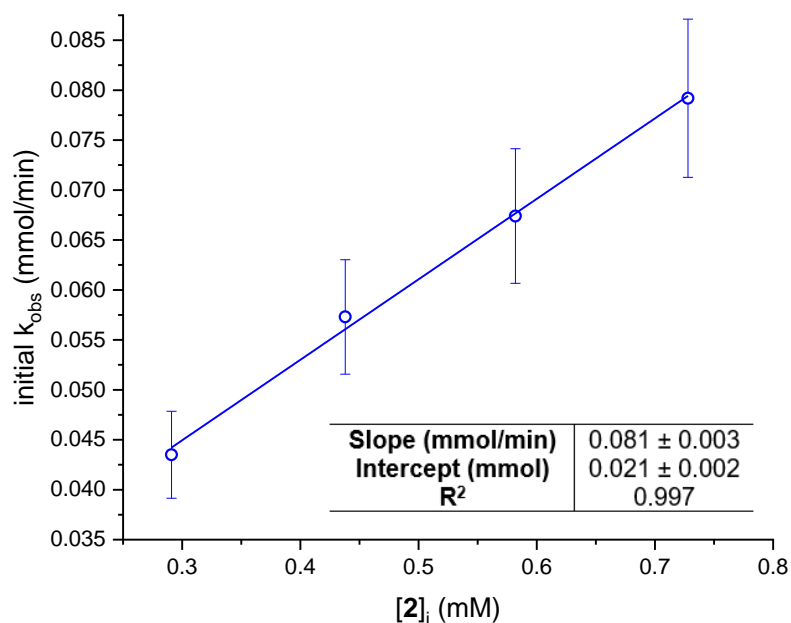


Figure B.14. Plot of initial observed rate vs initial concentration of **2**, error bars $\pm 10\%$.

Figure B.14 shows that the rate of formic acid dehydrogenation has a first order dependence on the initial concentration of **2**, and therefore a first order dependence on [iron].

XII. Same-Excess Experiments Using 1 and 2

A same-excess experiment was performed using **2** in order to investigate catalyst decomposition in formic acid dehydrogenation.⁶ Optimized conditions were used at 0.1 mol% **2**, and the same-excess experiment was started with 70% of the usual amount of formic acid, thus imitating starting the reaction at 30% conversion. The kinetics traces of these experiments and comparison of the initial rates are shown below in Figures B.15 and B.16.

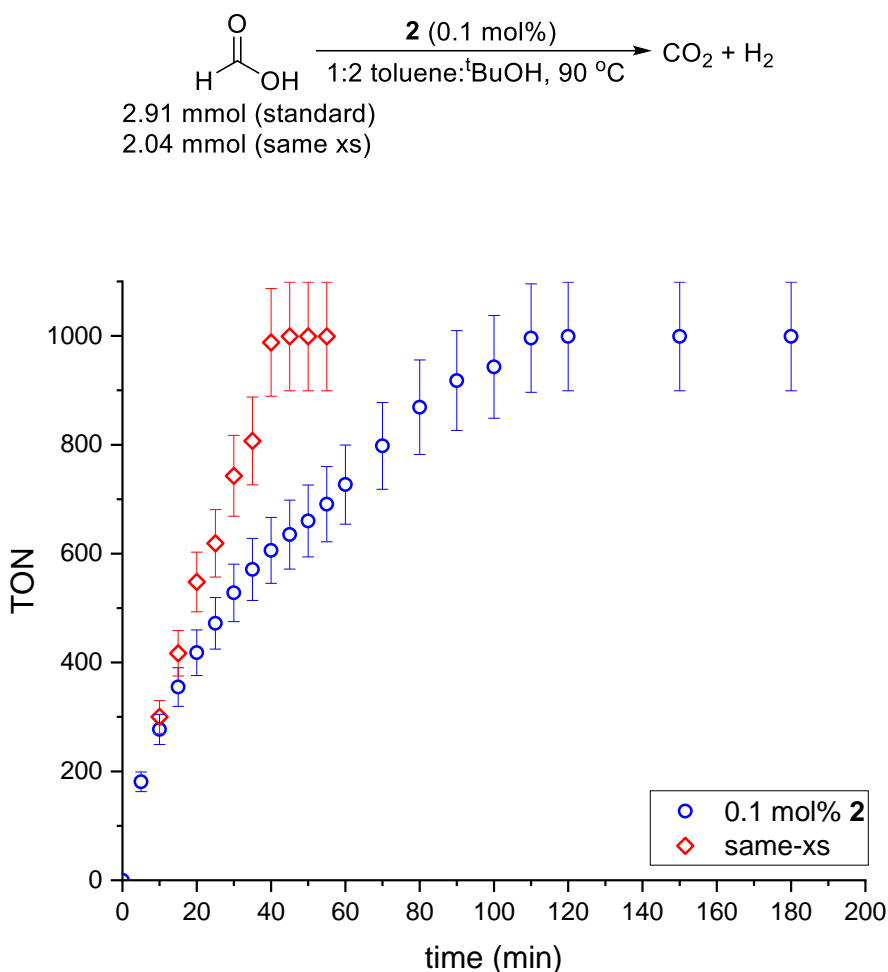


Figure B.15. Same-excess experiment using **2**; same-xs reaction kinetics have been time-adjusted for easier comparison to the standard reaction kinetics, error bars $\pm 10\%$.

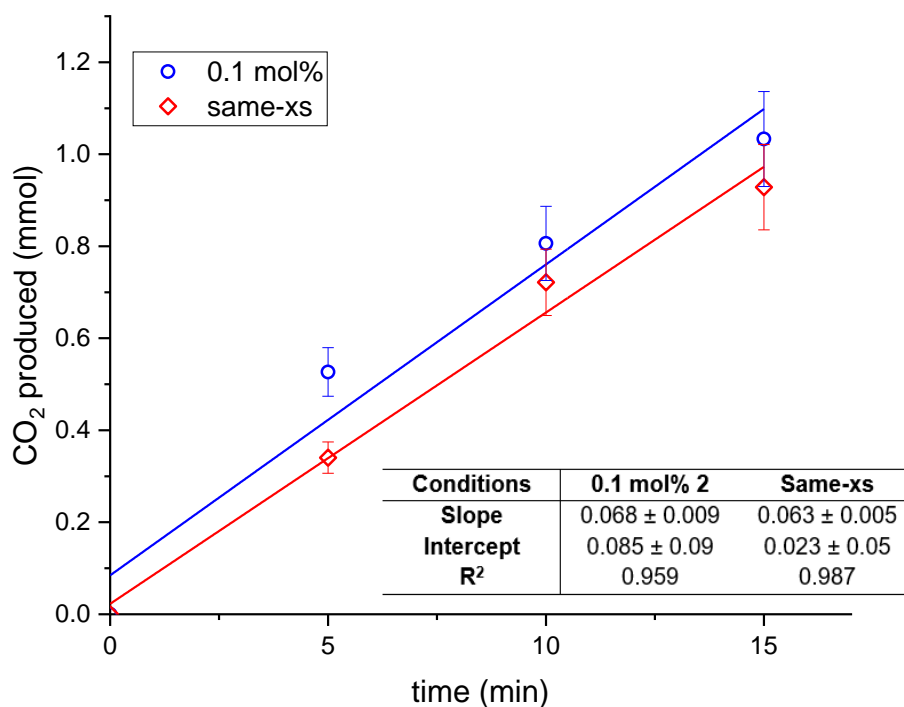
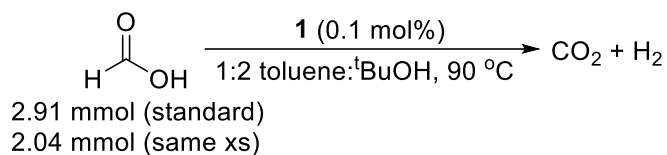


Figure B.16. Comparison of the initial rates of formic acid dehydrogenation under standard conditions with 0.1 mol% **2** and the same-xs experiment, error bars $\pm 10\%$.

These experiments show little or no catalyst decomposition within the first 15 minutes of catalysis using **2** (slopes in Figure B.16 are within error), but catalyst decomposition does occur over the course of the reaction because the two kinetics traces do not overlay (Figure B.15).

A same-excess experiment was similarly performed using **1**. The kinetics traces of these experiments and comparison of the initial rates are shown in Figures B.17 and B.18.



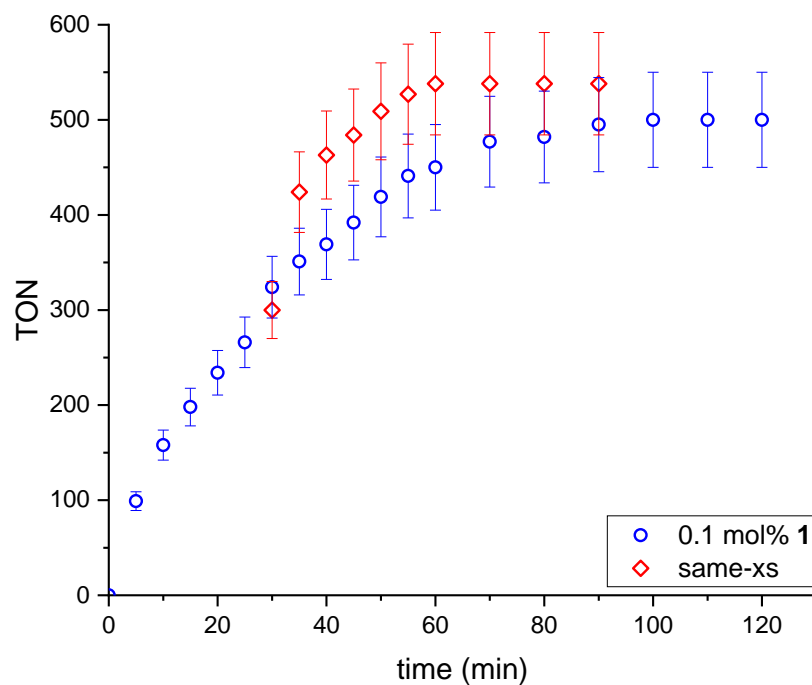


Figure B.17. Same-excess experiment using **1**; same-xs reaction kinetics have been time-adjusted for easier comparison to the standard reaction kinetics, error bars $\pm 10\%$.

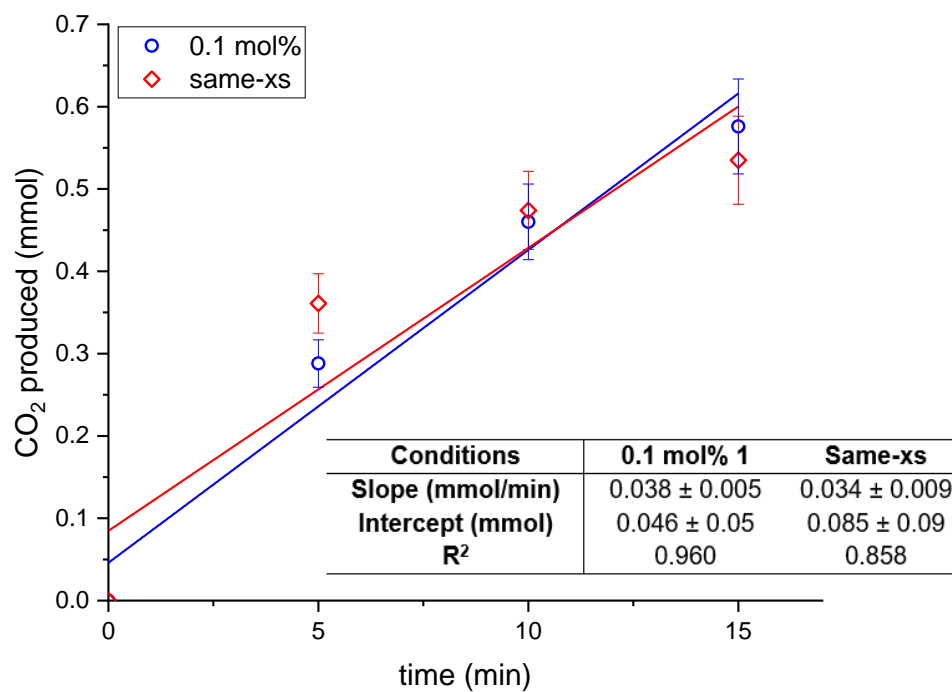
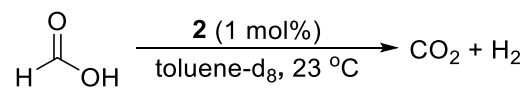


Figure B.18. Comparison of the initial rates of formic acid dehydrogenation under standard conditions with 0.1 mol% **1** and the same-xs experiment, error bars $\pm 10\%$.

The nonlinearity of these data makes it difficult to conclude if there is significant catalyst decomposition of **1** during the first 15 minutes. However, the poor behavior of **1** compared with **2** suggests that it is likely that **1** or related catalytic intermediates is/are more unstable under catalytic conditions.

XIII. Identification of the Catalytic Decomposition Product

In a glovebox, to a J Young NMR tube were added **2** (1.5 mg, 3.6 μmol), toluene- d_8 (0.600 μL), and formic acid (14 μL , 0.36 mmol). The reaction color deepened from pale yellow to bright yellow upon addition of formic acid, and vigorous gas formation was observed. The reaction mixture was frozen in liquid N_2 , degassed, and sealed under vacuum. The solution color slowly bleached to colorless and an off-white precipitate formed. Spectroscopic data are given in Figures B.19-B.22.



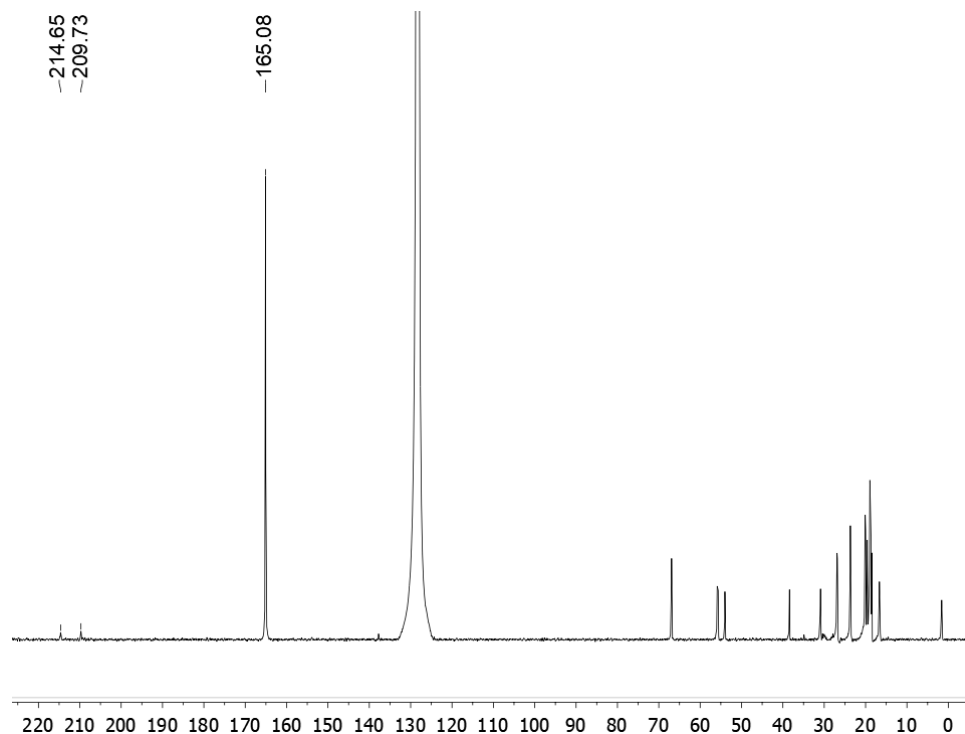


Figure B.21. $^{13}\text{C}\{^1\text{H}\}$ NMR spectrum of formic acid dehydrogenation decomposition product **5** in C_6D_6 ; ^1H and $^{13}\text{C}\{^1\text{H}\}$ spectra are shown after a pentane wash was performed to remove the equivalent of free $^{\text{iPr}}\text{PN}^{\text{Me}}\text{P}$ formed concomitantly with **5**.

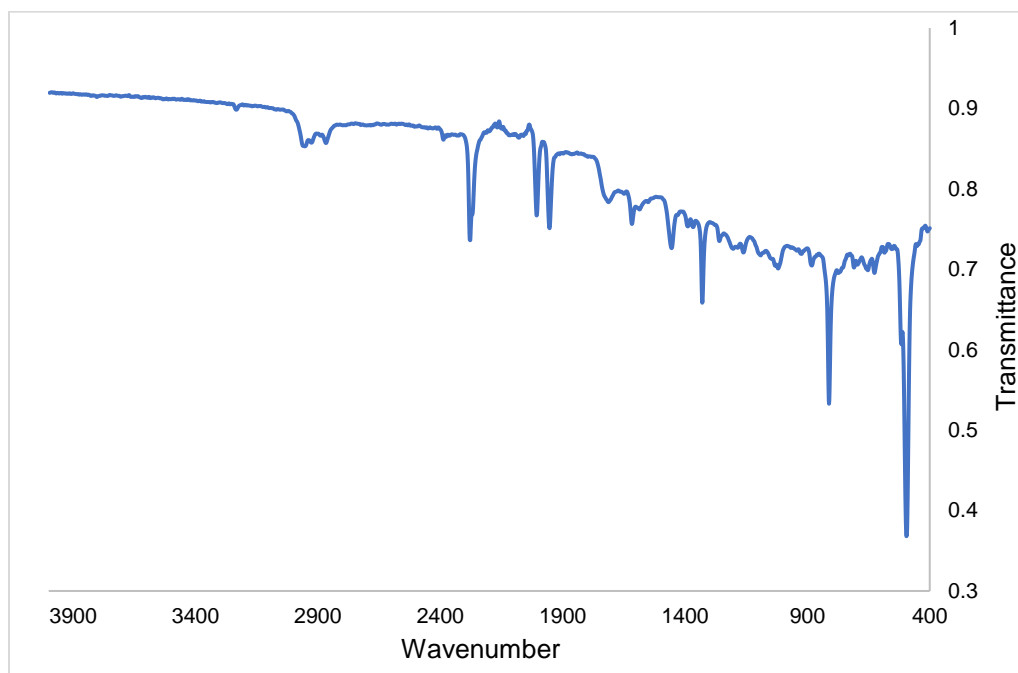


Figure B.22. IR spectrum of formic acid dehydrogenation decomposition product **5**.

All of these spectra are very similar to the related complex $[(^i\text{PrPN}^{\text{Me}}\text{P})\text{FeH}(\text{CO})_2][\text{OTf}]$,⁴ as well as the secondary amine-based $^i\text{PrPN}^{\text{HP}}$ congener $[(^i\text{PrPN}^{\text{HP}})\text{FeH}(\text{CO})_2][\text{Cl}]$.⁷ It was thus concluded that $[(^i\text{PrPN}^{\text{Me}}\text{P})\text{FeH}(\text{CO})_2][\text{OC}(\text{O})\text{H}]$ (**5**) was the decomposition product of formic acid dehydrogenation using **2**.

XIV. ¹³C-Formic Acid Decomposition Experiment

In the glovebox, to a J Young NMR tube were added **2** (1.6 mg, 4.0 μmol), C₆D₆ (600 μL), and ¹³C-formic acid (15 μL, 0.40 mmol). The solution immediately deepened in color to bright yellow, and the tube was sealed. The ¹³C{¹H} NMR spectrum is shown in Figure B.23.

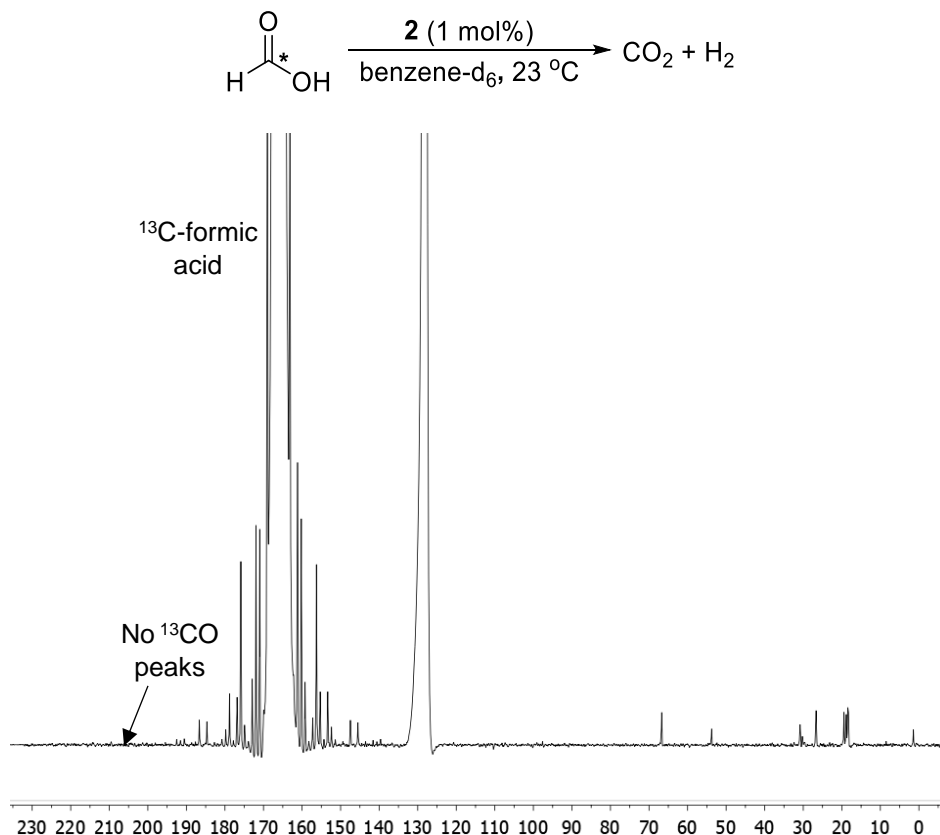
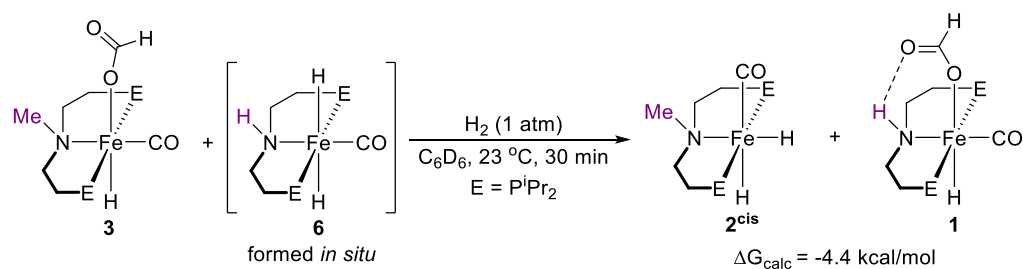


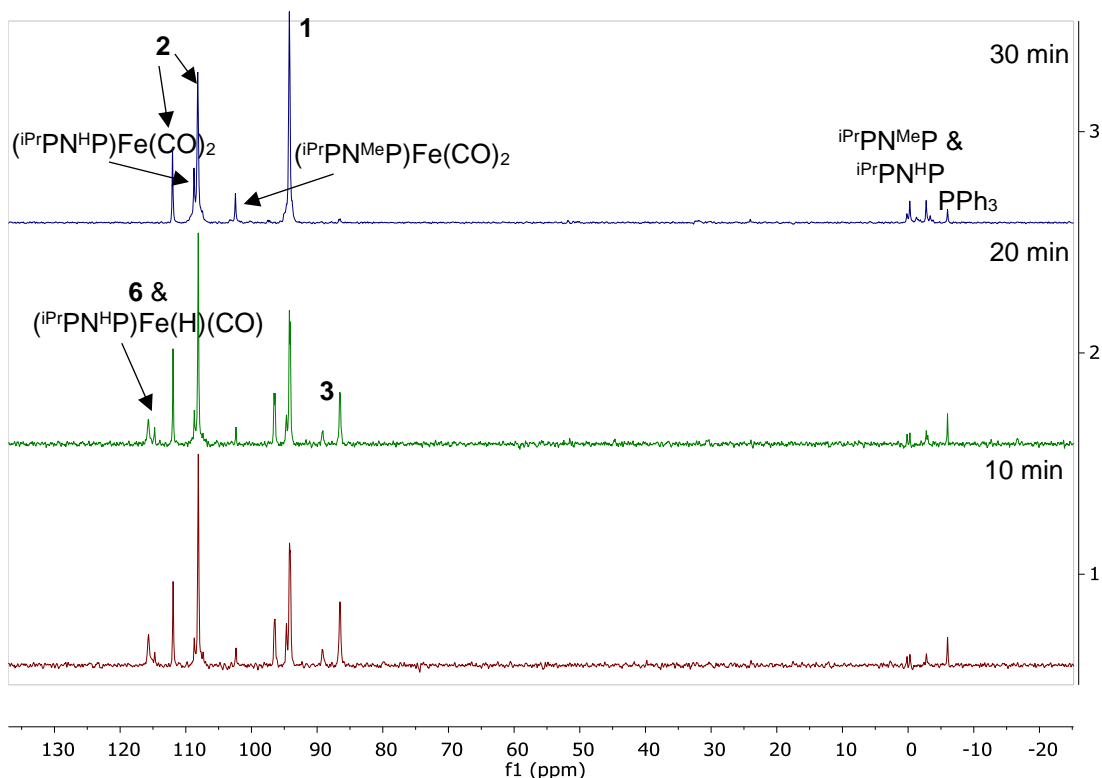
Figure B.23. ¹³C{¹H} NMR of formic acid dehydrogenation decomposition product using ¹³C-formic acid in C₆D₆.

XV. Crossover Experiments Between $i\text{PrPN}^{\text{Me}}\text{P}$ and $i\text{PrPN}^{\text{H}}\text{P}$ Complexes

Crossover Between **3** and **6**

In the glovebox, to a J Young NMR tube were added **3** (6.0 mg, 0.012 mmol), $(i\text{PrPNP})\text{Fe}(\text{H})(\text{CO})$ (**7**) (4.5 mg, 0.012 mmol), a PPh_3 in toluene- d_8 capillary, and C_6D_6 (600 μL). The tube was removed from the box, degassed via 3 freeze-pump-thaw cycles, and H_2 (1 atm) was added to generate dihydride **6** *in situ*. The solution changed color from pink-orange to golden yellow over the course of about 20-30 minutes. The reaction shows complete conversion to **1** and **2** by NMR spectroscopy after 30 minutes. $^{31}\text{P}\{^1\text{H}\}$ NMR spectra of the reaction are shown in Scheme B.04.

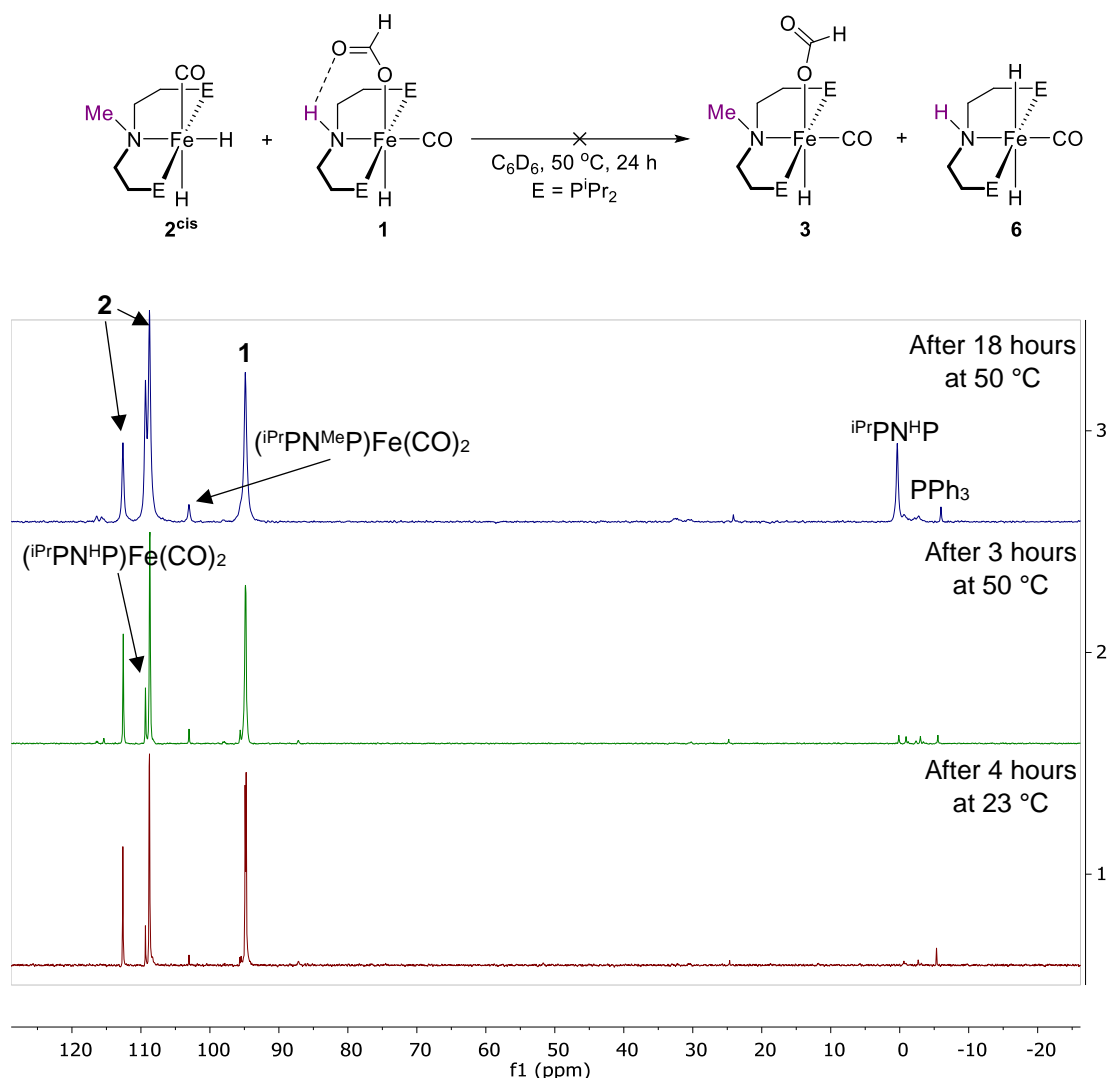




Scheme B.04. $^{31}\text{P}\{^1\text{H}\}$ NMR spectra in C_6D_6 of the exchange experiment between **3** and **6** (generated *in situ*) after 10 minutes (bottom), 20 minutes (middle) and 30 minutes (top); <10% decomposition to $(^{\text{iPr}}\text{PN}^{\text{R}}\text{P})\text{Fe}(\text{CO})_2$ ($\text{R}=\text{H}, \text{Me}$) was observed over the course of the reaction.

Crossover Between 2 and 1

In the glovebox, to a J Young NMR tube were added **2** (4.7 mg, 0.011 mmol), **1** (5.0 mg, 0.011 mmol), a PPh_3 in toluene- d_8 capillary, and C_6D_6 (600 μL). The reaction was monitored using $^{31}\text{P}\{^1\text{H}\}$ NMR spectroscopy, and the spectra are shown in Scheme B.05. After 4 hours at room temperature, no change was observed (bottom spectrum), so the tube was heated to 50 $^\circ\text{C}$ for 3 hours (middle spectrum). Since no conversion was observed, the tube was heated at 50 $^\circ\text{C}$ overnight, but only minor decomposition to $(^{\text{iPr}}\text{PN}^{\text{R}}\text{P})\text{Fe}(\text{CO})_2$ ($\text{R} = \text{H}, \text{Me}$) was observed (top spectrum).



Scheme B.05. $^{31}\text{P}\{^1\text{H}\}$ NMR spectra in C_6D_6 of the exchange experiment between **2** and **1** after 4 hours at 23°C (bottom), 3 hours at 50°C (middle) and 18 hours at 50°C (top); only slow decomposition to $(\text{iPrPN}^{\text{R}}\text{P})\text{Fe}(\text{CO})_2$ ($\text{R} = \text{H}, \text{Me}$) was observed over the course of the reaction.

XVI. Effects of Lewis Acids on Formic Acid Dehydrogenation with **2**

In order to investigate the effect of adding co-catalytic amounts of Lewis acids (LAs) to formic acid dehydrogenation catalyzed by **2**, the representative procedure for additive-free formic acid dehydrogenation experimental setup (Section B.III) was modified to add either LiOTf (45.4 mg, 0.291 mmol), LiNTf₂ (83.5 mg, 0.291 mmol), or NaOTf

(50.1 mg, 0.291 mmol) while the reaction flask was still in the glovebox. Kinetics data for these reactions are shown in Figure B.24.

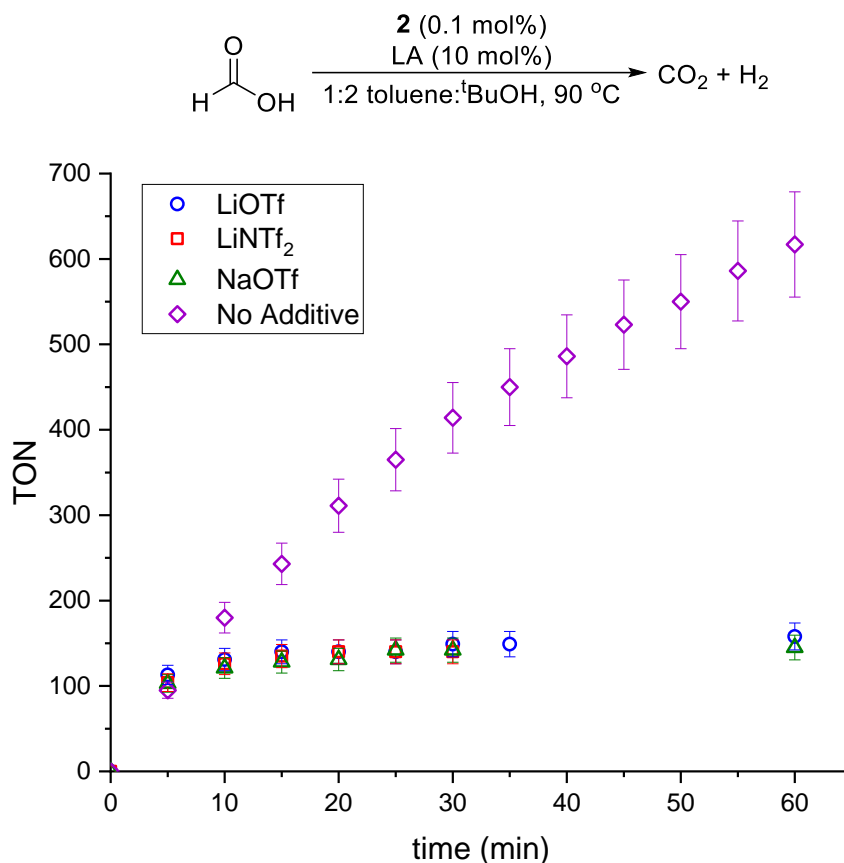


Figure B.24. Kinetics of formic acid dehydrogenation using 0.1 mol% **2** and 10 mol% LiOTf, LiINTf₂ or NaOTf LA co-catalyst.

As illustrated in Figure B.24, all LAs added to formic acid dehydrogenation with **2** resulted in a rapid loss of activity, and no turnovers were observed after 1 hour. In order to further investigate how LAs decrease productivity in catalysis, formic acid dehydrogenation was run with 3 different concentrations of LiOTf: 100 equivalents (shown in Figure B.24), 10 equivalents, and 1 equivalent relative to **2**. Kinetics data from these experiments are shown in Figure B.25. Surprisingly, all three experiments reached only 100-150 TONs, and again in all cases no activity was observed after 1 hour. These results

are strikingly different from those with no LA, where **2** reaches 1000 turnovers in just under 3 hours. All of these results indicate that not only do LAs not enhance the catalytic activity of **2** for formic acid dehydrogenation under these conditions, but they in fact significantly increase the rate of catalyst decomposition.

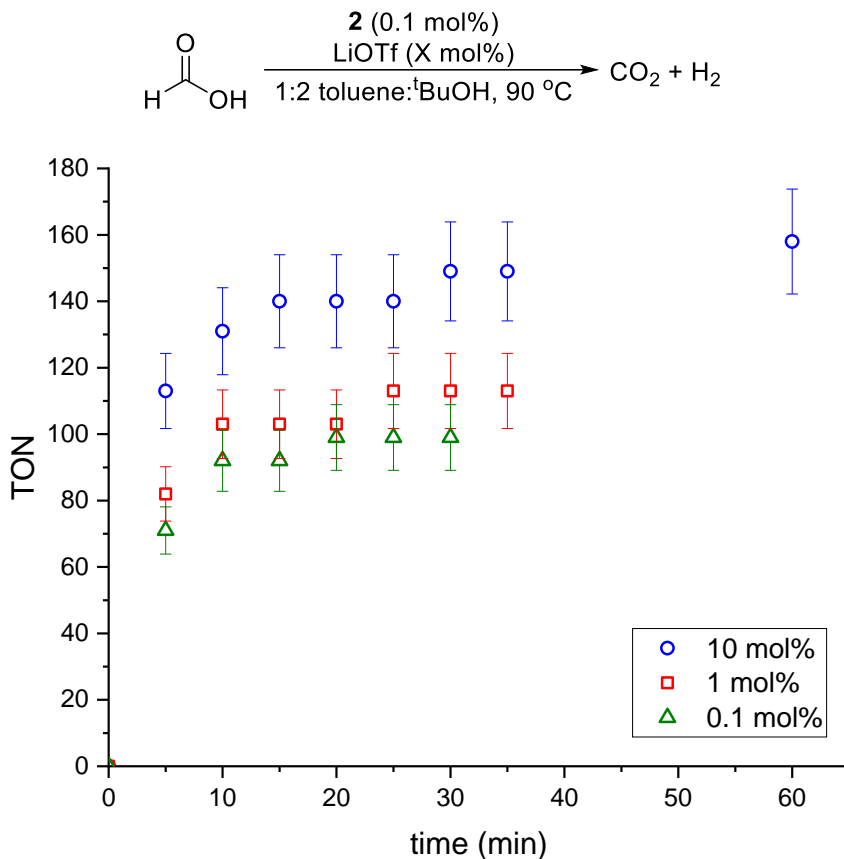


Figure B.25. Kinetics of formic acid dehydrogenation using **2** and varying amounts of LiOTf.

XVII. Computational Details

DFT studies were performed to probe the thermodynamics and kinetics of CO₂ insertion/decarboxylation with ⁱPrPN^{Me}P and ⁱPrPN^HP complexes. The calculations were carried out with the Gaussian16 software package.⁸ The hybrid meta-GGA M06 functional⁹

was selected on the basis of previous geometry and energy benchmarking.¹⁰ Structures were fully optimized without any geometry or symmetry constraints, combining the double-z LANL2DZ (on Fe, including pseudopotentials¹¹) and 6-31+G** (on all other elements¹²) basis sets. Vibrational frequencies were computed at the same level of theory to classify all stationary points as either saddle points (transition states, with a single imaginary frequency) or energy minima (reactants, intermediates and products, with only real frequencies). These calculations were also used to obtain the thermochemistry corrections (zero-point, thermal and entropy energies) The energies reported in the text were obtained by adding the thermochemistry corrections to the refined potential energies. The solvation effects of toluene were included using the continuum CPCM model.

First, the relative energies of relevant isomers of dihydride and formate complexes **1**, **2**, **3**, and **6** were calculated. The results and isomer nomenclature are shown in Figures B.26 and B.27.

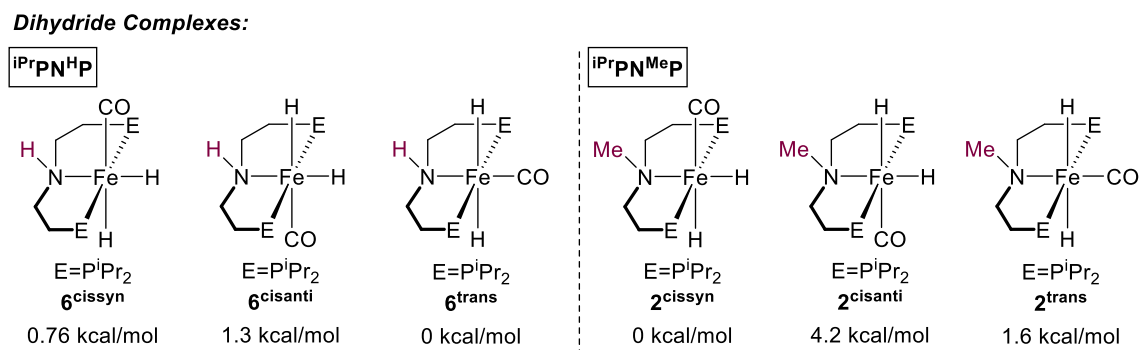


Figure B.26. Computed relative energies of the relevant isomers of **2** and **6**. Energies given are relative to the lowest energy isomer of that complex.

Formate Complexes:

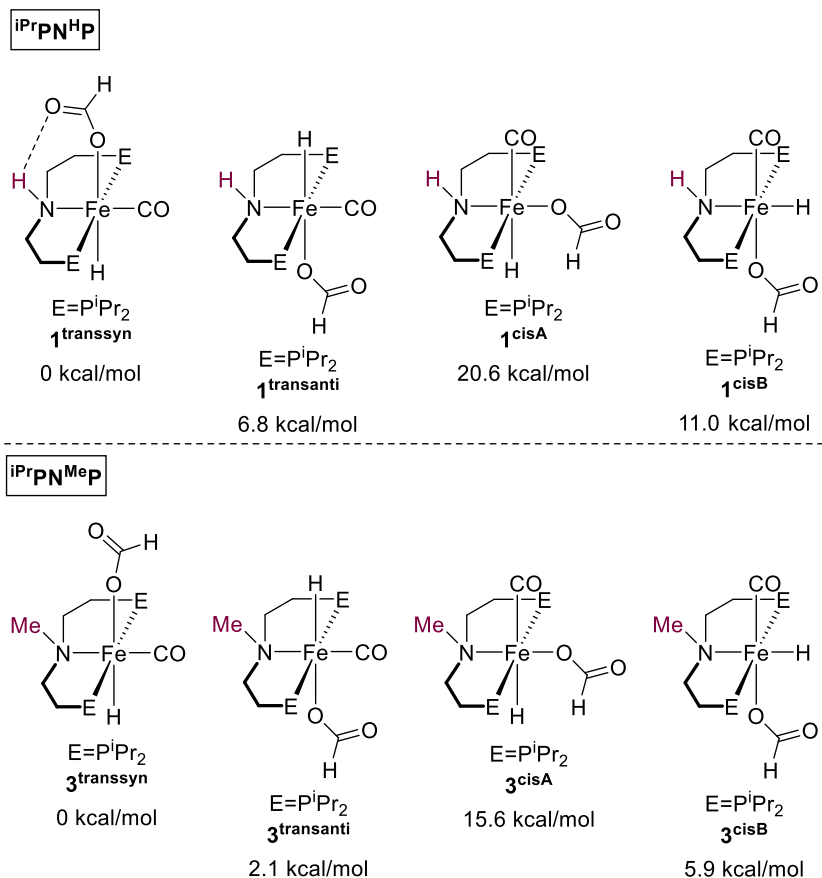


Figure B.27. Computed relative energies of the relevant isomers of **1** and **3**. Formate complex isomers calculated were chosen based on the two lowest energy isomers of the dihydride complexes. Energies given are relative to the lowest energy isomer of that complex.

These theoretical energies match well with experimental observations. For example, the major isomer of **6** in solution is **6^{trans}**, with one of the *cis* isomers observed at roughly 15% at room temperature. **2^{cissyn}** is the major isomer seen for **2**, existing at room temperature as a 3:1 ratio with **2^{trans}**.

The iPrPN^HP formate complex is only ever observed to be the **1^{transsyn}** isomer, where a stabilizing H-bond with the ligand N-H moiety is possible. This is also supported by the calculations, which show an almost 7 kcal/mol preference for this isomer over any other.

Experimentally, $i\text{PrPN}^{\text{Me}}\text{P}$ formate **3** is obtained as a 5:1 ratio of **3^{transsyn}**:**3^{transanti}** in solution at room temperature. This agrees with the DFT calculations which predict **3^{transsyn}** to be the most stable formate isomer, and **3^{transanti}** to be less stable by only 2.1 kcal/mol.

From this information, we assumed dihydride complex isomers **6^{cisanti}** and **2^{cisanti}** and formate complex isomers **1^{transanti}**, **1^{cisA}**, **1^{cisB}**, **3^{cisA}** and **3^{cisB}** were too high in energy to be relevant to catalysis, so we did not investigate them further. Next, we considered the thermodynamics of turnover-limiting decarboxylation of **1^{transsyn}**, **3^{transsyn}** and **3^{transanti}**. The calculated ΔG for each reaction is shown in Figure B.28.

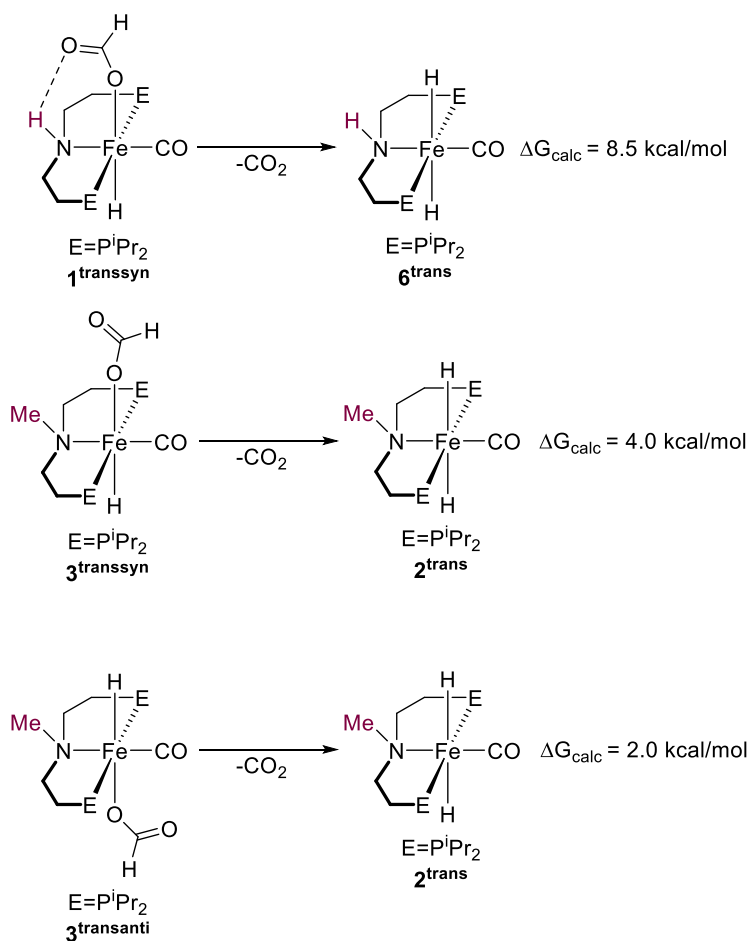


Figure B.28. Calculated thermodynamics for decarboxylation from formate complexes **1^{transsyn}**, **3^{transsyn}** and **3^{transanti}**.

These results further emphasize the importance of the hydrogen bond in thermodynamically stabilizing and favoring **1^{transsyn}**. Decarboxylation from the equivalent formate isomer with the ⁱPrPN^{Me}P ligand (**3^{transsyn}**) is 4.5 kcal/mol less unfavorable than decarboxylation from **1^{transsyn}**. These theoretical results match well with our crossover experiments (Section B.XV) that demonstrated a strong thermodynamic preference for the formation of **1** and **2** over **6** and **3**, and also begin to explain the superior additive-free formic acid dehydrogenation activity of **2** compared to **1**.

Next, the kinetics of decarboxylation were considered. Based on previous results we propose the two-step mechanism, shown in Figure B.29, wherein the first step is rearrangement of the O-bound formate to a less stable H-bound species, followed by the formation of the Fe–H bond and breaking of the C–H bond.^{2b, 13} It is predicted that the first step of this process will be rate-limiting.

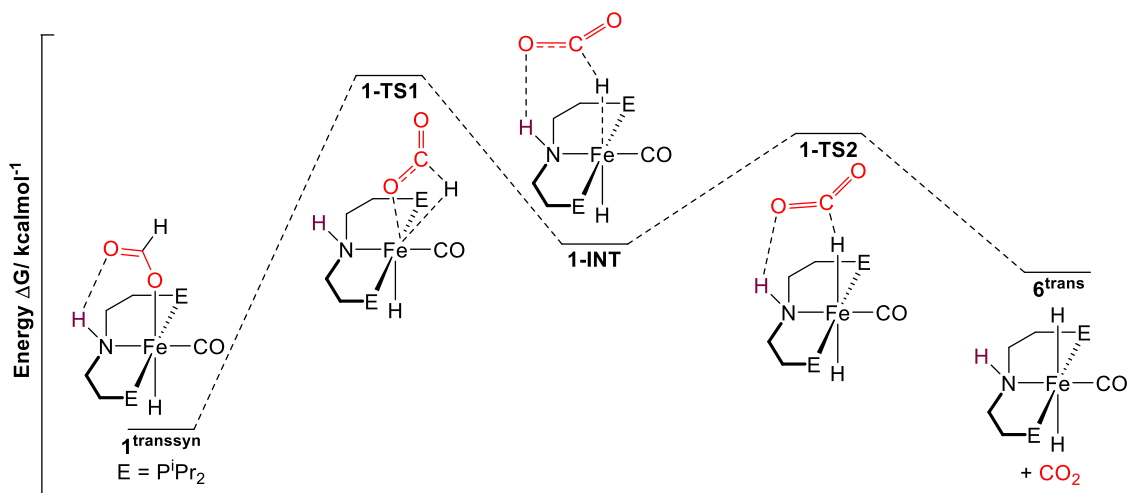


Figure B.29. Representative potential energy surface for decarboxylation, shown here from **1^{transsyn}** to **6^{trans}** and CO₂.

First, the kinetics of decarboxylation from **1**^{transsyn} to **6**^{trans} and CO₂ were calculated, and the results are shown in Figure B.30. The barrier for this reaction was found to be 20.2 kcal/mol, which is in agreement with previous calculations.^{2b}

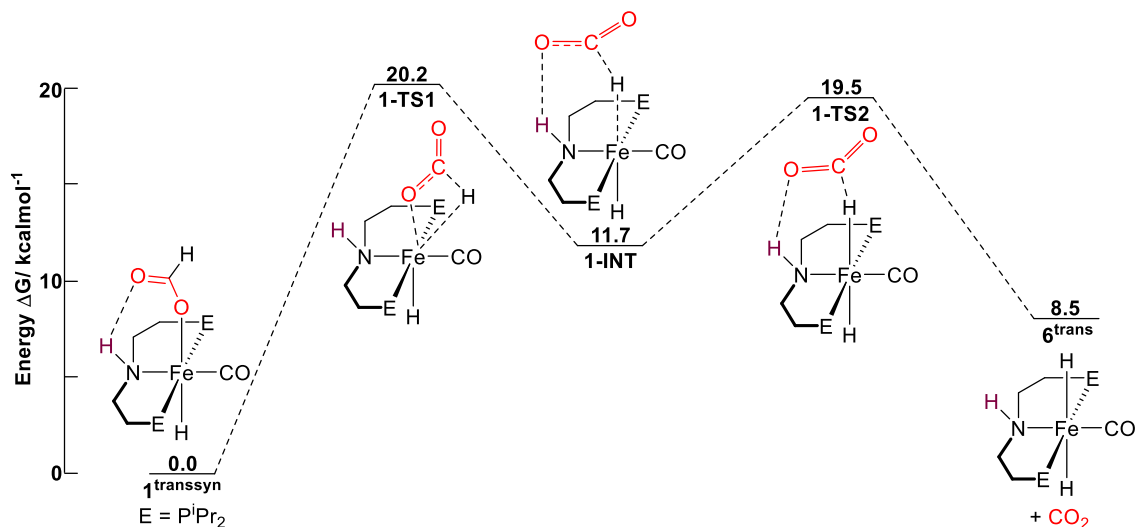


Figure B.30. Calculated potential energy surface for decarboxylation from **1**^{transsyn} to **6**^{trans} and CO₂.

The kinetics of decarboxylation from **3**^{transsyn} to **2**^{trans} and CO₂ were also calculated, and the barrier was found to be 26.7 kcal/mol. The results are detailed in Figure B.31.

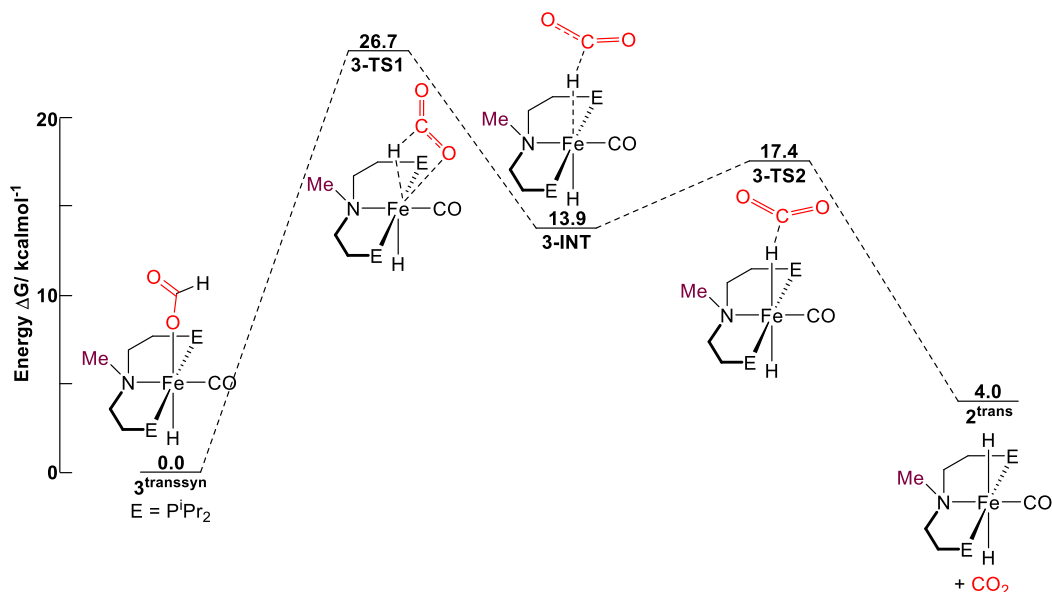


Figure B.31. Calculated potential energy surface for decarboxylation from **3**^{transsyn} to **2**^{trans} and CO₂.

XVIII. References

1. Harris, R. K.; Becker, E. D.; Cabral De Menezes, S. M.; Granger, P.; Hoffman, R. E.; Zilm, K. W., Further Conventions for NMR Shielding and Chemical Shifts: (IUPAC Recommendations 2008). *Pure Appl. Chem.* **2008**, *80*, 59-84.
2. (a) Zhang, Y.; MacIntosh, A. D.; Wong, J. L.; Bielinski, E. A.; Williard, P. G.; Mercado, B. Q.; Hazari, N.; Bernskoetter, W. H., Iron Catalyzed CO₂ Hydrogenation to Formate Enhanced by Lewis Acid Co-Catalysts. *Chem. Sci.* **2015**, *6*, 4291-4299; (b) Bielinski, E. A.; Lagaditis, P. O.; Zhang, Y.; Mercado, B. Q.; Würtele, C.; Bernskoetter, W. H.; Hazari, N.; Schneider, S., Lewis Acid-Assisted Formic Acid Dehydrogenation Using a Pincer-Supported Iron Catalyst. *J. Am. Chem. Soc.* **2014**, *136*, 10234-10237.
3. Crabtree, R. H., *The Organometallic Chemistry of the Transition Metals*. Fifth ed.; John Wiley & Sons, Inc: Hoboken, New Jersey, **2009**.
4. Jayarathne, U.; Hazari, N.; Bernskoetter, W. H., Selective Iron-Catalyzed N-Formylation of Amines using Dihydrogen and Carbon Dioxide. *ACS Catal.* **2018**, *8*, 1338-1345.
5. (a) Heimann, J. E.; Bernskoetter, W. H.; Hazari, N.; Mayer, J. M., Acceleration of CO₂ Insertion into Metal Hydrides: Ligand, Lewis Acid, and Solvent Effects on Reaction Kinetics. *Chem. Sci.* **2018**, *8*, 6629-6638; (b) Heimann, J. E.; Bernskoetter, W. H.; Hazari, N., Understanding the Individual and Combined Effects of Solvent and Lewis Acid on CO₂ Insertion into a Metal Hydride. *J. Am. Chem. Soc.* **2019**, *141*, 10520-10529.
6. Blackmond, D. G., Kinetic Profiling of Catalytic Organic Reactions as a Mechanistic Tool. *J. Am. Chem. Soc.* **2015**, *137*, 10852-10866.

7. Koehne, I.; Schmeier, T. J.; Bielinski, E. A.; Pan, C. J.; Lagaditis, P. O.; Bernskoetter, W. H.; Takase, M. K.; Würtele, C.; Hazari, N.; Schneider, S., Synthesis and Structure of Six-Coordinate Iron Borohydride Complexes Supported by PNP Ligands. *Inorg. Chem.* **2014**, *53*, 2133-2143.
8. Frisch, M. J.; Trucks, G. W.; Schlegel, H. B.; Scuseria, G. E.; Robb, M. A.; Cheeseman, J. R.; Scalmani, G.; Barone, V.; Petersson, G. A.; Nakatsuji, H.; Li, X.; Caricato, M.; Marenich, A. V.; Bloino, J.; Janesko, B. G.; Gomperts, R.; Mennucci, B.; Hratchian, H. P.; Ortiz, J. V.; Izmaylov, A. F.; Sonnenberg, J. L.; Williams; Ding, F.; Lipparini, F.; Egidi, F.; Goings, J.; Peng, B.; Petrone, A.; Henderson, T.; Ranasinghe, D.; Zakrzewski, V. G.; Gao, J.; Rega, N.; Zheng, G.; Liang, W.; Hada, M.; Ehara, M.; Toyota, K.; Fukuda, R.; Hasegawa, J.; Ishida, M.; Nakajima, T.; Honda, Y.; Kitao, O.; Nakai, H.; Vreven, T.; Throssell, K.; Montgomery Jr., J. A.; Peralta, J. E.; Ogliaro, F.; Bearpark, M. J.; Heyd, J. J.; Brothers, E. N.; Kudin, K. N.; Staroverov, V. N.; Keith, T. A.; Kobayashi, R.; Normand, J.; Raghavachari, K.; Rendell, A. P.; Burant, J. C.; Iyengar, S. S.; Tomasi, J.; Cossi, M.; Millam, J. M.; Klene, M.; Adamo, C.; Cammi, R.; Ochterski, J. W.; Martin, R. L.; Morokuma, K.; Farkas, O.; Foresman, J. B.; Fox, D. J. *Gaussian 16 Rev. C.01*, Wallingford, CT, 2016.
9. Zhao, Y.; Truhlar, D. G., The M06 suite of density functionals for main group thermochemistry, thermochemical kinetics, noncovalent interactions, excited states, and transition elements: two new functionals and systematic testing of four M06-class functionals and 12 other functionals. *Theoretical Chemistry Accounts* **2008**, *120*, 215-241.
10. Artús Suárez, L.; Culakova, Z.; Balcells, D.; Bernskoetter, W. H.; Eisenstein, O.; Goldberg, K. I.; Hazari, N.; Tilset, M.; Nova, A., The Key Role of the Hemiaminal

Intermediate in the Iron-Catalyzed Deaminative Hydrogenation of Amides. *ACS Catal.* **2018**, *8*, 8751-8762.

11. Hay, P. J.; Wadt, W. R., Ab initio effective core potentials for molecular calculations. Potentials for the transition metal atoms Sc to Hg. *J. Chem. Phys.* **1985**, *82*, 270-283.

12. (a) Hehre, W. J.; Ditchfield, R.; Pople, J. A., Self—Consistent Molecular Orbital Methods. XII. Further Extensions of Gaussian—Type Basis Sets for Use in Molecular Orbital Studies of Organic Molecules. *J. Chem. Phys.* **1972**, *56*, 2257-2261; (b) Francl, M. M.; Pietro, W. J.; Hehre, W. J.; Binkley, J. S.; Gordon, M. S.; DeFrees, D. J.; Pople, J. A., Self-consistent molecular orbital methods. XXIII. A polarization-type basis set for second-row elements. *J. Chem. Phys.* **1982**, *77*, 3654-3665.

13. Bielinski, E. A.; Förster, M.; Zhang, Y.; Bernskoetter, W. H.; Hazari, N.; Holthausen, M. C., Base-Free Methanol Dehydrogenation Using a Pincer-Supported Iron Compound and Lewis Acid Co-catalyst. *ACS Catal.* **2015**, *5*, 2404-2415.

Appendix C: Supporting Information for Chapter 4

I. Experimental Procedures

General Methods

Experiments were performed under a dinitrogen atmosphere in an M-Braun glovebox or using standard Schlenk techniques unless otherwise noted. Under typical operating conditions, the glovebox was not purged between uses of benzene, diethyl ether, pentane, THF, 1,4-dioxane, or toluene. As a consequence, each solvent should be assumed to contain trace amounts of the others. All moisture and air-sensitive liquids were either transferred inside the glovebox or using a stainless steel cannula on a Schlenk line. Solvents were dried by passage through a column of activated alumina and stored under dinitrogen unless otherwise noted. All commercial chemicals were used as received except where noted.

Diisopropylphosphine was purchased as a 10 wt% solution in hexanes from Strem Chemicals. LiHBEt_3 was purchased as a 1.7 M solution in THF from Acros Organics. Formic acid was purchased from EMD Millipore Inc., purified by recrystallization at 5 °C, and degassed prior to use. Toluene was distilled prior to use in catalysis. 1,8-Diazabicyclo[5.4.0]undec-7-ene (DBU) was purchased from Oakwood Chemicals, dried over calcium hydride, and vacuum distilled prior to use. Deuterated solvents were obtained from Cambridge Isotope Laboratories. C_6D_6 was dried by passage through a plug of activated alumina.

NMR spectra were recorded on Bruker AMX-400, AMX-500 or AMX-600, spectrometers at ambient probe temperatures, unless otherwise noted. Chemical shifts are

reported in ppm with respect to residual internal protio solvent for ^1H and $^{13}\text{C}\{^1\text{H}\}$ NMR spectra. $^{31}\text{P}\{^1\text{H}\}$ NMR spectra are referenced via the ^1H resonances based on the relative gyromagnetic ratios.¹ All J coupling constant values are given in Hertz. Elemental analyses were performed by Robertson Microlit Laboratories, Inc. Infrared data were obtained on a Bruker ALPHA FTIR spectrometer with a platinum ATR attachment inside a dinitrogen-filled glovebox. All samples were taken of the neat solid.

Mass spectrometric measurements were performed with a Thermo Fisher QExactive Orbitrap LC-MS system using continuous injection with a syringe. Samples were prepared in a glove box and loaded into a gas tight syringe. The syringe and the PEEK capillaries to the ion source of the MS were cleaned with dry and oxygen-free solvents before sample injection. Samples were held at room temperature and continuously injected using a syringe pump at 30 $\mu\text{L}/\text{min}$. Electrospray was used for desolvatization and ionization, with the electrospray needle held at +3.5kV. Compressed air was used as the desolvatization gas, the capillary temperature was set at 320 $^{\circ}\text{C}$, the probe heater temperature at 40 $^{\circ}\text{C}$, and the sheath gas flow at 5 L/min. The resolution was set to 14,000 $\text{M}/\Delta\text{M}$. Mass spectra were recorded in the range of 150 to 2000 m/z in positive ion mode. Measurements and data post-processing were performed with Thermo Xcalibur 4.1.31.9.

Gas Chromatography was performed on a ThermoFisher Trace 1300 GC apparatus equipped with a thermal conductivity detector and a Supelco fused silica capillary column (5 \AA molecular sieves, 30 m x 0.53 mm). He carrier gas was used for determination of CO_2 and CO at concentrations greater than 1 ppm.

Literature procedures were used to synthesize $(\text{PPh}_3)_3\text{RuHCl}(\text{CO})$,² $(^i\text{PrPN}^{\text{H}}\text{P})\text{Ru}(\text{H})_2(\text{CO})$ (**2-H**),³ and $(^i\text{PrPN}^{\text{Me}}\text{P})\text{Ru}(\text{H})_2(\text{CO})$ (**2-Me**).⁴ IR data was not previously published for **1-H**, **2-H**, or **2-Me**. Solid-state spectra were obtained for these compounds and are provided in Section XIV.

II. Synthetic Procedures and Characterizing Data

$[\text{PhN}(\text{CH}_2\text{CH}_2\text{Cl})_2][\text{HCl}]$

A 250 mL 3-neck round bottom flask equipped with a magnetic stirring bar was charged with $\text{PhN}(\text{CH}_2\text{CH}_2\text{OH})_2$ (2.50 g, 13.8 mmol) and benzene (100 mL). The flask was equipped with a reflux condenser, and POCl_3 (2.80 mL, 30.4 mmol) was added through a septum on one of the necks. The reaction was heated to 80 °C and stirred for two hours, during which time a white precipitate formed in the flask. After cooling to room temperature, the benzene was filtered off and the solid was washed with 3x15 mL petroleum ether. Drying *in vacuo* afforded the product as a white solid, yield 2.70 g (77%). The ^1H NMR spectrum matches that previously described in the literature.⁵

$^i\text{PrPN}^{\text{Ph}}\text{P}$

A 250 mL Schlenk flask equipped with a magnetic stirring bar was charged with diisopropylphosphine (10 wt% in hexanes, 15.0 g, 12.7 mmol) and pentane (20 mL). The flask was cooled to -78 °C in a dry ice/isopropanol bath and *n*-butyllithium (2.1 M in hexanes, 6.52 mL, 13.7 mmol) was added slowly via syringe. The solution was stirred for five minutes in the cold bath, then warmed gradually to room temperature and stirred overnight as a white precipitate formed. The solid was isolated via filter cannula, and $[\text{PhN}(\text{CH}_2\text{CH}_2\text{Cl})_2][\text{HCl}]$ (1.29 g, 5.07 mmol) was added to the flask under positive N_2

flow. THF (30 mL) cooled to -78 °C was added to the flask via cannula. Additional *n*-butyllithium (2.1 M in hexanes, 2.66 mL, 5.58 mmol) was added slowly via syringe to deprotonate the amine and regenerate any hydrolyzed lithium diisopropylphosphide salt. After stirring at room temperature for five minutes, the flask was equipped with a reflux condenser and refluxed at 66 °C for 7 hours. The reaction was then cooled to room temperature, and the solvent was removed *in vacuo*. The product was extracted in 5x5 mL pentane and isolated *in vacuo* to obtain a lightly colored oil (849 mg, 2.22 mmol, 44%).

¹H NMR (600 MHz, C₆D₆): 7.28 (t, 2H, CH_{Ar}, *J*=8.7 Hz), 6.84 (d, 2H, CH_{Ar}, *J*=8.3 Hz), 6.76 (t, 1H, CH_{Ar}, *J*=7.2 Hz), 3.57 (m, 4H, CH₂), 1.66 (m, 4H, CH₂), 1.56 (m, 4H, CHCH₃), 0.99 ppm (m, 24H, CHCH₃). ¹³C{¹H} (151 MHz, C₆D₆): 129.51, 116.22, 112.50, 50.65 (d, *J*=32.1 Hz), 23.30 (d, *J*=13.5 Hz), 19.89 (d, *J*=16.5 Hz), 18.54 ppm (d, *J*=9.8 Hz). ³¹P{¹H} (202 MHz, C₆D₆): -0.42 ppm (s). HRMS (E⁺): 381.27 [M⁺]. Calc for [C₂₂H₄₇P₂N]: 381.27.

(ⁱPrPN^{Ph}P)RuHCl(CO) (1)

A 100 mL Schlenk flask equipped with a magnetic stirring bar was charged with ⁱPrPN^{Ph}P (150 mg, 0.393 mmol), (PPh₃)₃RuHCl(CO) (374 mg, 0.393 mmol), and toluene (20 mL). The flask was equipped with a reflux condenser and heated at 110 °C for 4 hours. After cooling to room temperature, the solvent was removed *in vacuo*. The product was extracted in 4x3 mL THF, then concentrated *in vacuo*. Clean product was obtained as a white solid from sequential crystallizations in concentrated Et₂O at -35 °C to remove residual PPh₃ (96 mg, 0.175 mmol, 45%). Crystals suitable for X-ray diffraction were grown by slow diffusion of pentane into a concentrated THF solution at room temperature.

Anal. Found (calc'd) for C₂₃H₄₂P₂NOClRu: C, 50.57 (50.50); H, 7.62 (7.74); N, 2.53 (2.56). ¹H NMR (500 MHz, C₆D₆): 8.01 (br, 2H, CH_{Ar}), 7.00 (t, 2H, CH_{Ar}, *J*=8.6 Hz), 6.92

(t, 1H, CH_{Ar} , $J=7.3$ Hz), 4.60 (m, 2H, CH_2), 2.99 (m, 2H, CH_2), 2.78 (m, 2H, CH_2), 1.78 (m, 6H, $CHCH_3$), 1.72 (m, 2H, CH_2), 1.43 (m, 2H, $CHCH_3$), 1.12 (m, 6H, $CHCH_3$), 1.06 (m, 8H, $2CHCH_3 + 6CHCH_3$), 0.94 (m, 6H, $CHCH_3$), -14.40 ppm (t, 1H, RuH , $J=17.9$ Hz). $^{13}C\{^1H\}$ (151 MHz, C_6D_6): 207.68, 149.46, 128.35, 127.61, 58.11, 26.30 (t, $J=8.8$ Hz), 25.34 (t, $J=12.4$ Hz), 24.50 (t, $J=10.7$ Hz), 21.17 (t, $J=2.5$ Hz), 20.52 (t, $J=2.6$ Hz), 19.99, 17.32 ppm. $^{31}P\{^1H\}$ (202 MHz, C_6D_6): 67.36 ppm. IR, solid state (cm^{-1}): 1913 ($C\equiv O$).

$(iPrPN^{Ph}P)Ru(H)_2(CO)$ (2)

A 50 mL Schlenk flask equipped with a magnetic stirring bar was charged with **1** (72 mg, 0.132 mmol), $LiHBEt_3$ (1.7 M in THF, 94 μ L, 0.158 mmol), and toluene (7 mL). The reaction was stirred at room temperature for 2 hours, then the volatiles were removed *in vacuo*. The product was extracted in 5x2 mL pentane, and isolated *in vacuo* to yield a white solid (57 mg, 0.111 mmol, 84%). Crystals suitable for X-ray diffraction were grown from a concentrated pentane solution at -35 °C.

This compound is not stable under prolonged vacuum and therefore elemental analysis was not attempted. 1H NMR (600 MHz, C_6D_6): 8.43 (br, 2H, CH_{Ar}), 7.04 (t, 2H, CH_{Ar} , $J=7.6$ Hz), 6.91 (t, 1H, CH_{Ar} , $J=7.3$ Hz), 3.22 (m, 2H, CH_2), 2.97 (m, 2H, CH_2), 1.93 (m, 2H, CH_2), 1.81 (m, 2H, CH_2), 1.47 (m, 2H, $CHCH_3$), 1.39 (m, 6H, $CHCH_3$), 1.34 (m, 2H, $CHCH_3$), 1.28 (m, 6H, $CHCH_3$), 1.23 (m, 6H, $CHCH_3$), 1.19 (m, 6H, $CHCH_3$), -4.99 (t, 1H, RuH , $J=17.5$ Hz), -5.15 ppm (t, 1H, RuH , $J=18.6$ Hz). $^{13}C\{^1H\}$ (151 MHz, C_6D_6): 209.20, 148.37, 127.97, 126.94, 64.74 (t, $J=5.0$ Hz), 28.56 (t, $J=12.0$ Hz), 27.56 (t, $J=12.4$ Hz), 26.57 (t, $J=8.4$ Hz), 19.32 (t, $J=2.3$ Hz), 18.95 (m), 18.91 (m), 18.80 ppm. $^{31}P\{^1H\}$ (162 MHz, C_6D_6): 85.23 ppm. IR, solid state (cm^{-1}): 1874 ($C\equiv O$).

$(iPrPN^{Ph}P)RuH(CO)\{OC(O)H\}$ (3)

A J Young tube was charged with **2** (8 mg, 0.014 mmol) and C₆D₆ (0.50 mL). The solution was frozen in N₂(l), degassed, thawed, and 1 atm CO₂ was added. Crystals suitable for X-ray diffraction precipitated from solution overnight in the J Young tube from the NMR scale reaction in C₆D₆ at room temperature under an atmosphere of CO₂. Some back conversion to the dihydride starting material was observed upon removal of the CO₂ atmosphere and replacement with N₂, precluding isolation of this species on scale.

¹H NMR (600 MHz, C₆D₆): 9.34 (s, 1H, OC(O)H), 7.39 (m, 1H, CH_{Ar}), 7.03 (m, 3H, CH_{Ar}), 6.96 (t, 1H, CH_{Ar}, *J*=7.3 Hz), 4.06 (m, 2H, CH₂), 2.84 (m, 2H, CH₂), 2.26 (m, 2H, CH₂), 1.68 (m, 2H, CH₂), 1.52 (m, 6H, CHCH₃), 1.38 (m, 2H, CHCH₃), 1.00-1.10 (m, 14H, 2CHCH₃ + 12CHCH₃), 0.93 (m, 6H, CHCH₃), -16.12 ppm (t, 1H, RuH, *J*=18.3 Hz).
¹³C{¹H} (101 MHz, C₆D₆): 168.02, 148.98, 128.19, 127.80, 57.38 (t, *J*=4.3 Hz), 25.57 (t, *J*=8.5 Hz), 25.33 (t, *J*=14.1 Hz), 23.77 (t, *J*=9.7 Hz), 20.16 (m), 19.86 (t, *J*=2.6 Hz), 19.60, 17.27 ppm. ³¹P{¹H} (202 MHz, C₆D₆): 66.18 ppm.

III. Variable Temperature ¹H NMR Spectra of **1**

The variable temperature ¹H NMR spectra of **1** in Figures C.01-C.03 demonstrate that the broad aromatic peak present at 8.01 ppm at room temperature sharpens into two peaks at 9.05 and 7.07 ppm at -50 °C. In fact, at -50 °C all 5 aromatic protons have distinct chemical shifts (Figure C.03). This indicates free rotation of the phenyl ring in solution at room temperature, and restricted rotation at low temperatures.

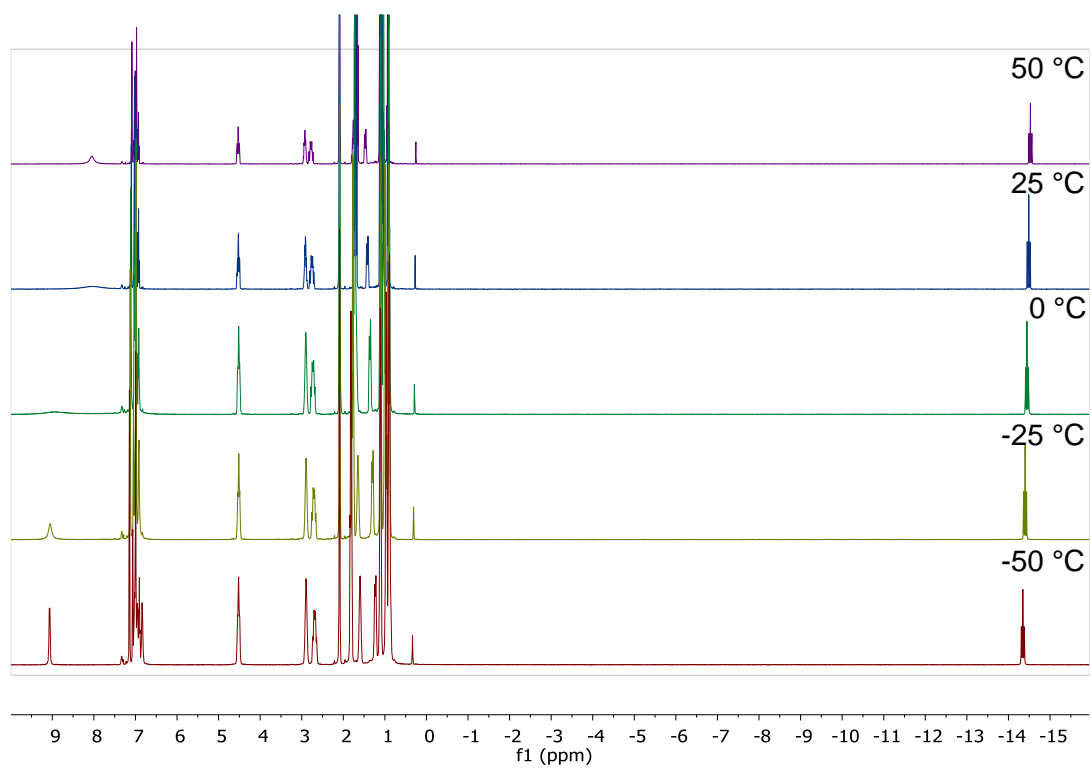
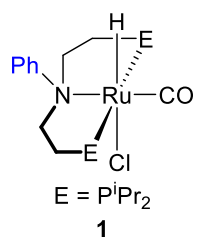


Figure C.01. ^1H NMR spectra of **1** in $\text{toluene-}d_8$ at -50 , -25 , 0 , 25 , and $50\text{ }^\circ\text{C}$.

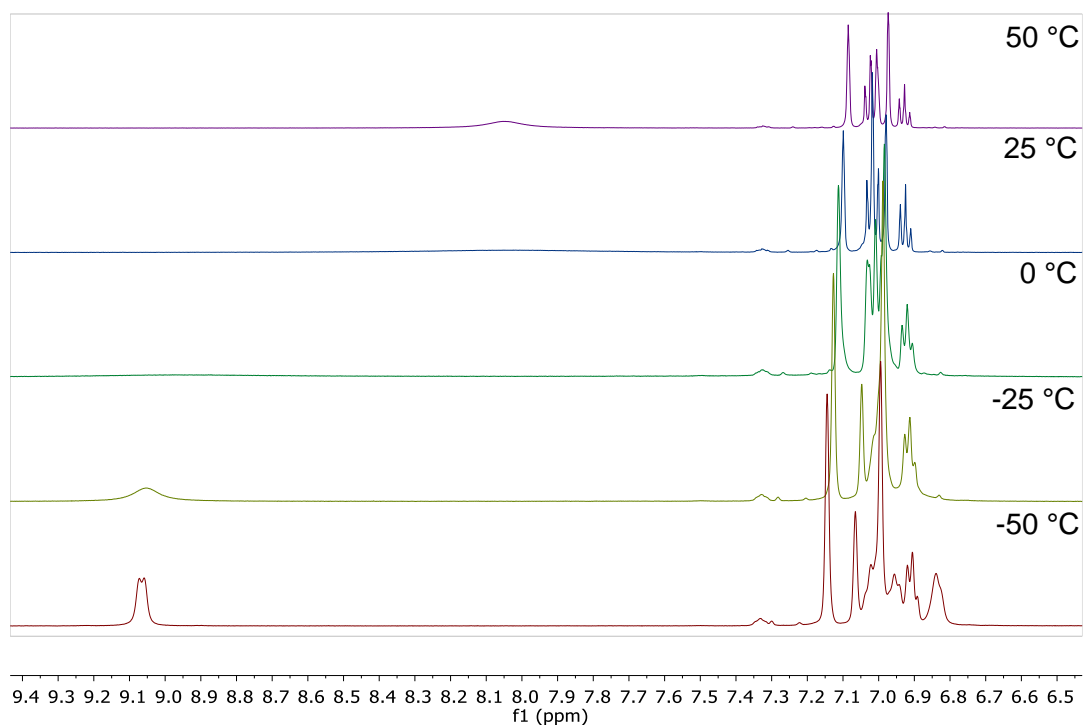


Figure C.02. The aromatic region of the ^1H NMR spectra of **1** in toluene- d_8 taken -50, -25, 0, 25, and 50 $^\circ\text{C}$.

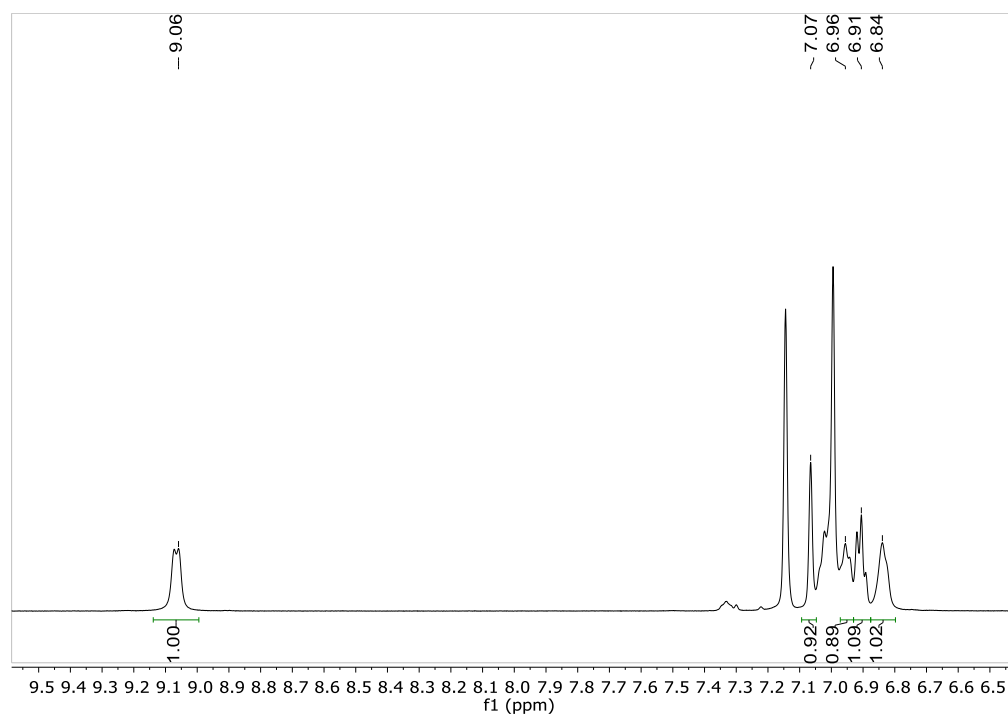


Figure C.03. The aromatic region of the ^1H NMR spectrum of **1** in toluene- d_8 at -50 $^\circ\text{C}$. All 5 aromatic protons of $i\text{PrPN}^{\text{Ph}}\text{P}$ have distinct chemical shifts.

IV. Determination of the Solution State Isomer of **1**

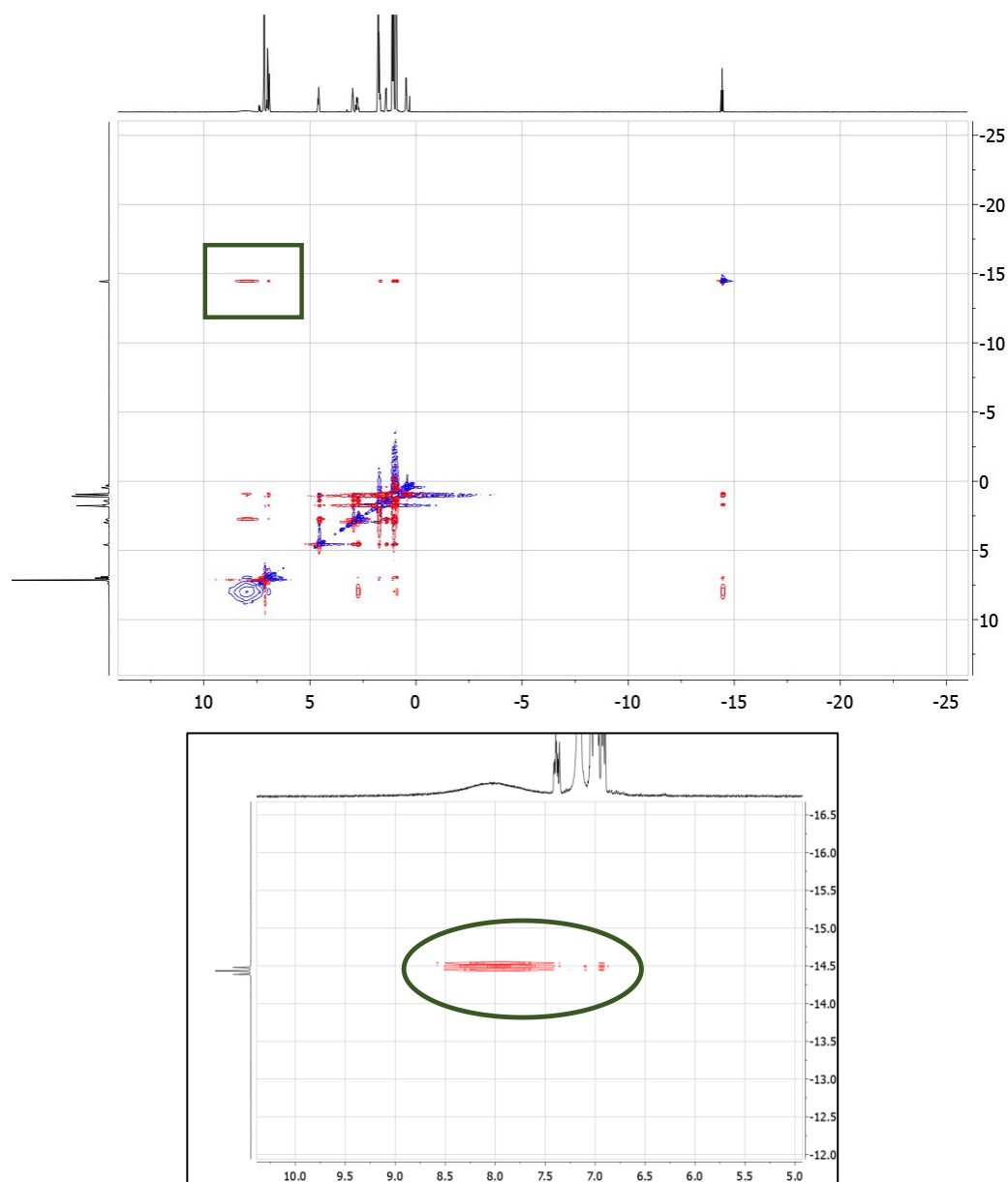
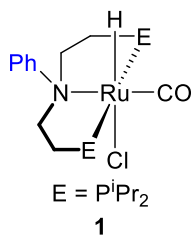


Figure C.04. ^1H NOESY NMR of **1** in C_6D_6 (top) and an inset (bottom) showing an NOE between the hydride ligand and the aromatic protons, indicating the hydride is *syn* with respect to the N-phenyl group.

V. Determination of the Solution State Isomer of **3**

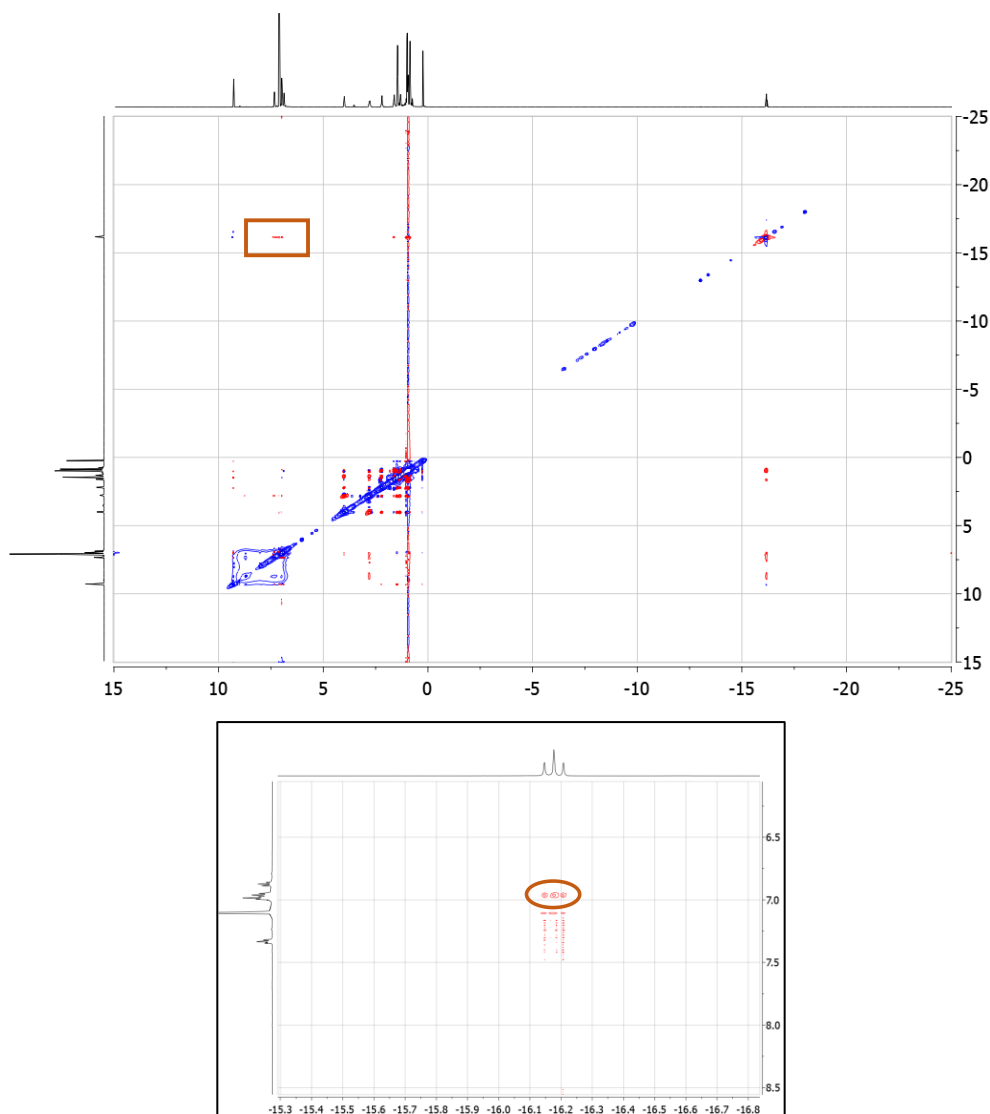
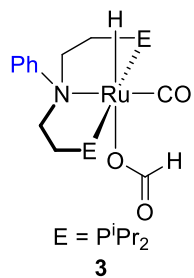


Figure C.05. ^1H NOESY NMR of **3** in C_6D_6 (top) and an inset (bottom) showing an NOE between the hydride ligand and the aromatic protons, indicating the hydride is *syn* with respect to the N-phenyl group.

VI. Vacuum Stability of **3** and **3-Me**

General Procedure: In the glovebox, to a J. Young NMR tube were added either **2** or **2-Me** (~5 mg) and C₆D₆ (0.5 mL). The samples were then degassed and one atmosphere of CO₂ was added. NMR spectra of the formate complex were obtained (bottom spectra in Figures C.06-C.09). The solvent was then removed *in vacuo*, and the solid was left under vacuum for one minute after the solvent was evaporated. The sample was redissolved in C₆D₆ and NMR spectra were again obtained (top spectra in Figures C.06-C.09).

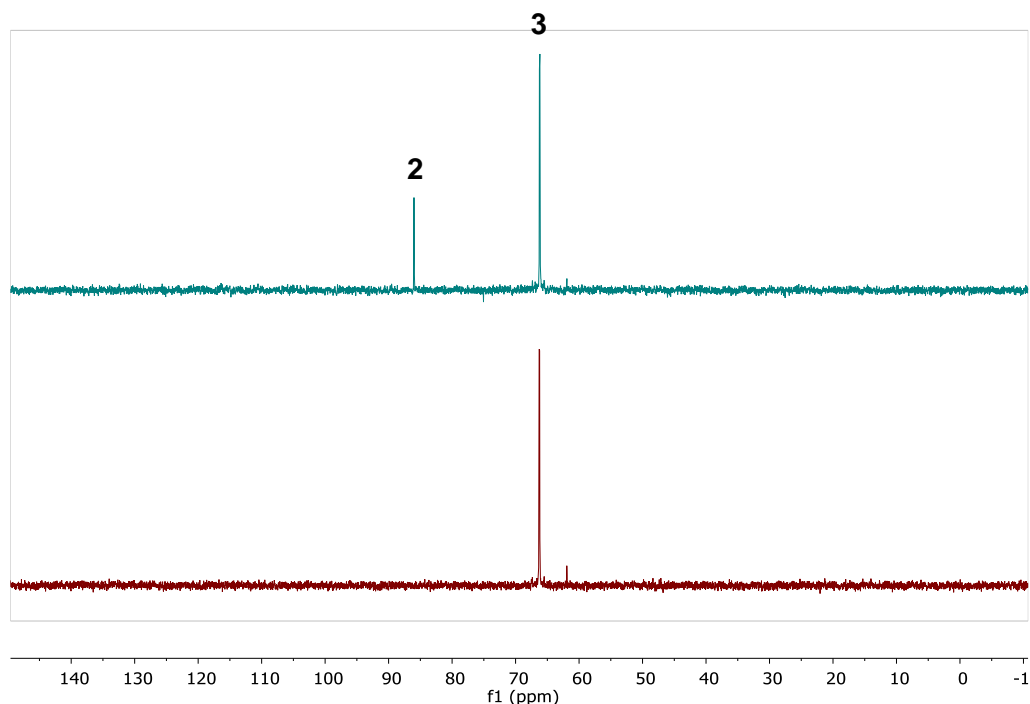


Figure C.06. ³¹P{¹H} NMR spectra of **3** in C₆D₆ taken under an atmosphere of CO₂ (bottom) and then after drying the sample *in vacuo* and replacing the headspace with N₂ (top). Roughly 20% conversion to **2** observed.

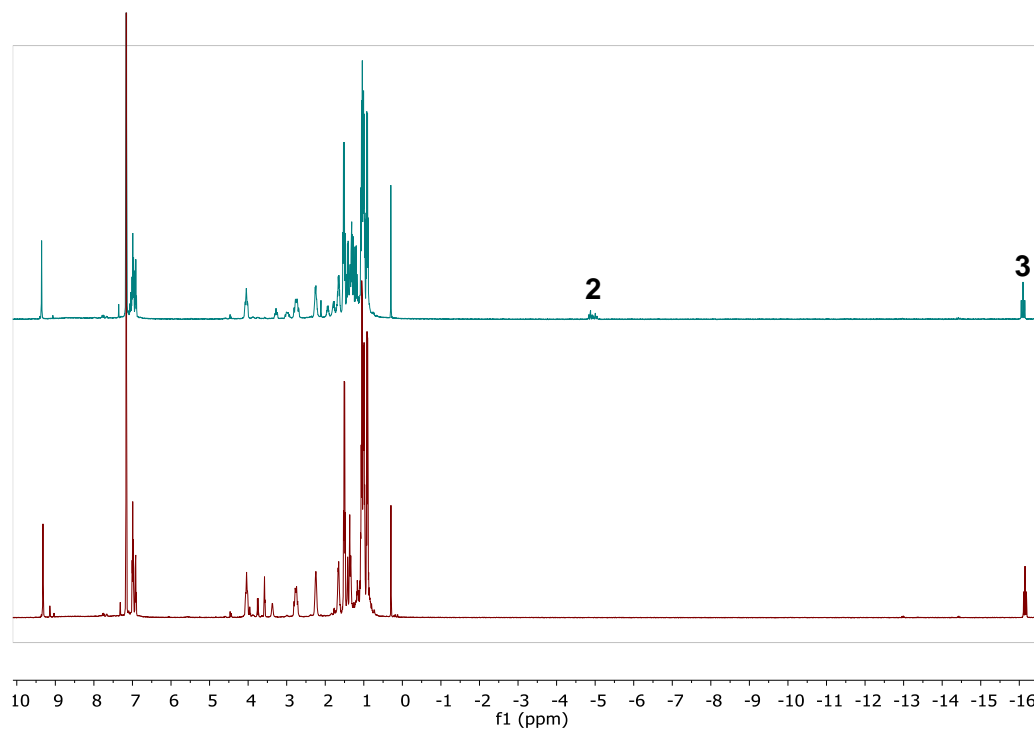


Figure C.07. ^1H NMR spectra of **3** in C_6D_6 taken under an atmosphere of CO_2 (bottom) and then after drying the sample *in vacuo* and replacing the headspace with N_2 (top). Roughly 20% conversion to **2** observed.

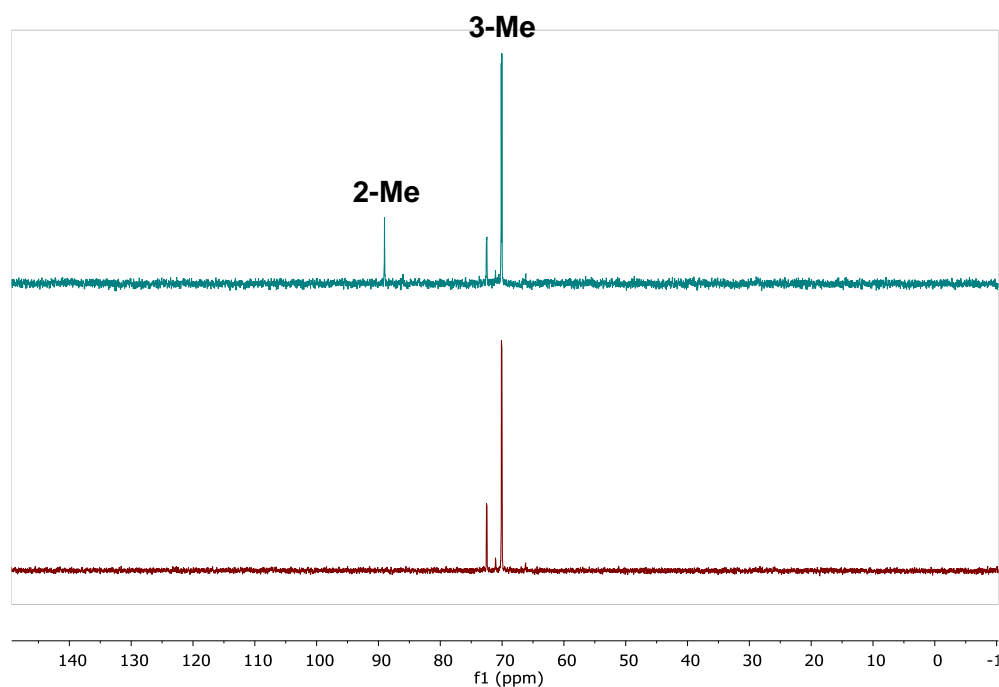


Figure C.08. $^{31}\text{P}\{^1\text{H}\}$ NMR spectra of **3-Me** (two isomers) in C_6D_6 taken under an atmosphere of CO_2 (bottom) and then after drying the sample *in vacuo* and replacing the headspace with N_2 (top). Roughly 15% conversion to **2-Me** observed.

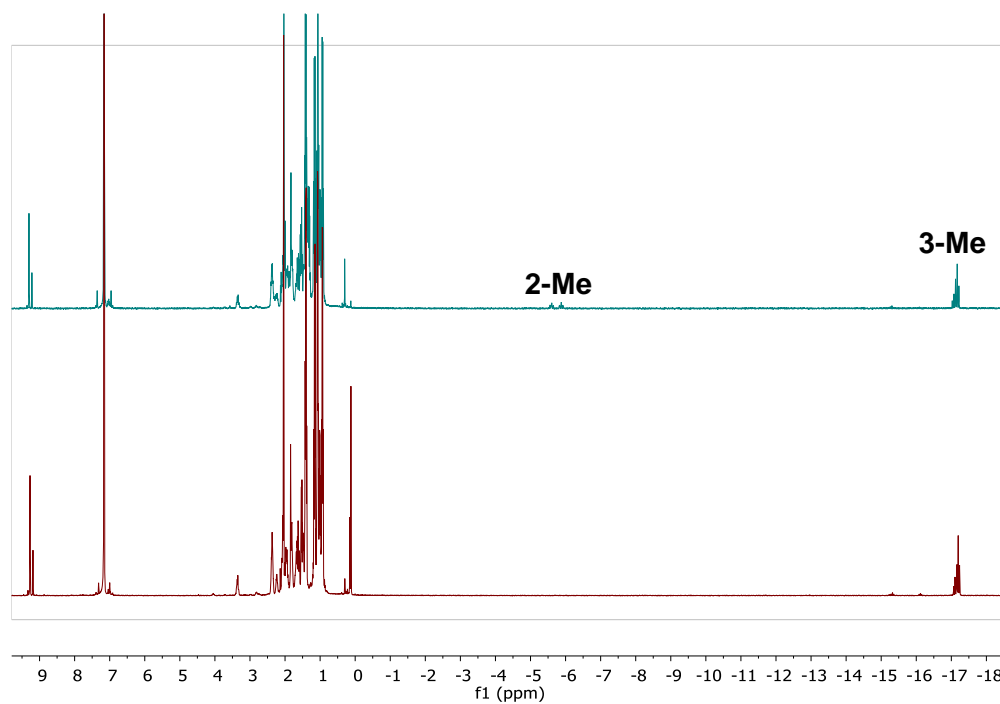
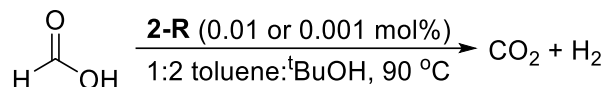


Figure C.09. ^1H NMR spectra of **3-Me** (two isomers) in C_6D_6 taken under an atmosphere of CO_2 (bottom) and then after drying the sample *in vacuo* and replacing the headspace with N_2 (top). Roughly 15% conversion to **2-Me** observed.

VII. Details of Catalytic Formic Acid Dehydrogenation



In the glovebox, to a 25 mL Schlenk flask equipped with a magnetic stir bar were added either **2**, **2-H**, or **2-Me** (291 μL of a 1.0 or 0.1 mM stock solution in toluene) and toluene (1.67 mL total). The flask was sealed, removed from the glovebox, and placed under an N_2 atmosphere on a Schlenk line. A reflux condenser with a Kontes sidearm for addition of reagents was attached to a Kontes pin 3-way valve *via* Tygon tubing, thoroughly purged with N_2 , then attached to the reaction flask. Anhydrous $^t\text{BuOH}$ (3.33 mL) was added to the reaction flask through a rubber septum placed on the condenser sidearm. The Tygon tubing leading from the 3-way valve to the oil bubbler was purged with N_2 , then the bubbler was attached to a gas buret filled with mineral oil to prevent gas dissolution (Figure C.10). The reaction flask was lowered into an oil bath preheated to $90\text{ }^\circ\text{C}$ and allowed to equilibrate. Formic acid (110 μL , 2.91 mmol) was added through a rubber septum placed on the condenser sidearm, then the sidearm was rapidly resealed with a Kontes pin, the system was cut off from active N_2 flow, and the reaction flask was opened to the gas buret *via* the 3-way valve. As gas evolution lowered the level of the oil in the buret, the separatory funnel was lowered to keep the oil levels approximately even and maintain roughly atmospheric pressure in the reaction. A second catalytic reaction was always performed in parallel and the turnover numbers reported are the average of the two experiments.

TON Quantification:

Before running a catalytic reaction, a blank reaction was performed in which no catalyst was added to the reaction solution. The volume of gas obtained from this reaction

(trace solvent and FA) was recorded as V_{blank} . The corrected volume of gas produced from a catalytic reaction was then calculated using the following expression:

$$V_{corr} = V_{obs} - V_{blank}$$

Where V_{obs} is the observed change in oil level in the gas buret during catalysis. It was assumed that a 1:1 mixture of H_2 and CO_2 was produced in the catalytic reaction. The number of moles of gas produced (n_{prod}) in the reaction was determined using the following expression that utilizes the ideal gas law:

$$n_{prod} = \frac{V_{corr}}{2(22.4 \frac{L}{mol})}$$

The TON was then determined using the following expression:

$$TON = \frac{n_{prod}}{n_{cat}}$$

Where n_{cat} is the molar quantity of the catalyst.

The TOF was determined to be the TON that occurred in the first hour.

Gas Volume Determination

The volume/height ratio of each gas buret was determined before using them in catalysis. To do this, water was placed in the buret, and the meniscus was marked. Some water was drained from the column into a tared flask, and the new water level was marked again. The weight of the water drained from the flask was used to determine its volume, and this was divided by the change in height in the buret to determine the mL/cm calibration of the buret.

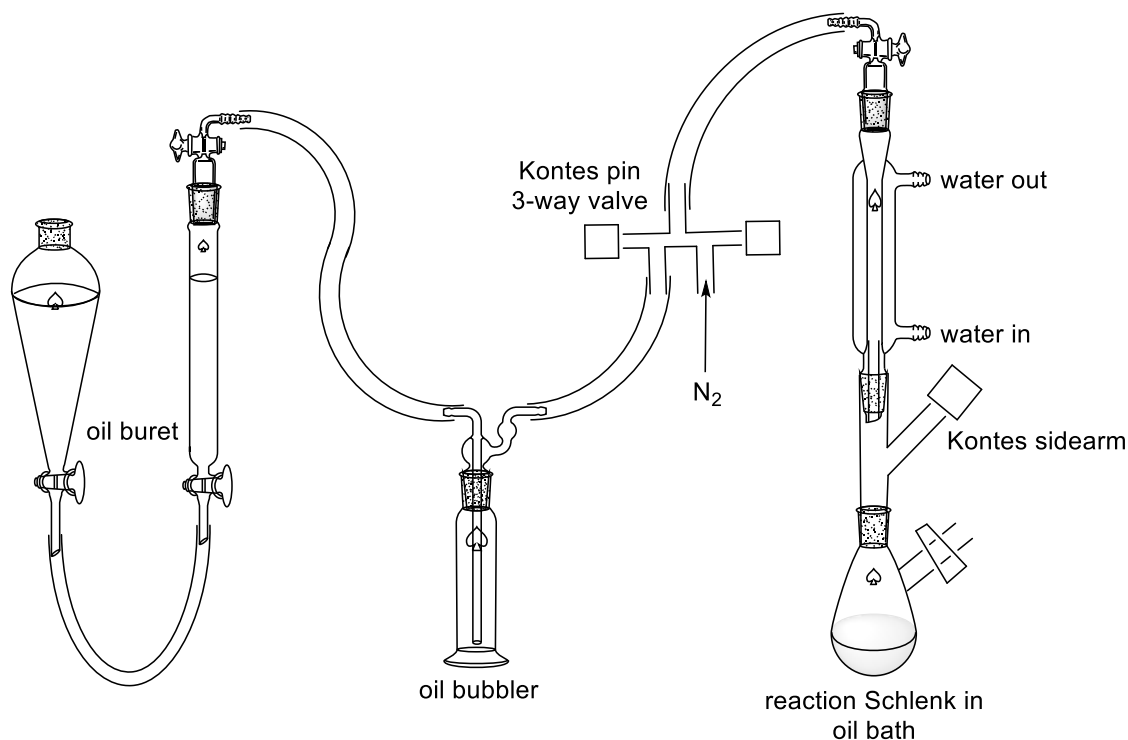
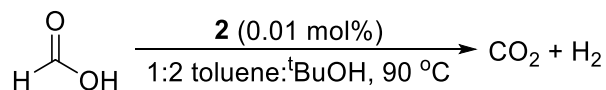


Figure C.10. Diagram of experimental setup for formic acid dehydrogenation.

VIII. GC Detection of Gaseous Reaction Products in Formic Acid Dehydrogenation

GC was performed to confirm the products of formic acid dehydrogenation using **2** as a 1:1 ratio of CO₂ and H₂ with no observable CO generation. A standard catalytic reaction was run in order to ensure the desired gaseous products were being formed. GC samples were taken from the headspace of the gas buret. The GC trace is shown in Figure C.11. No CO formation was observed (retention time 7 minutes).



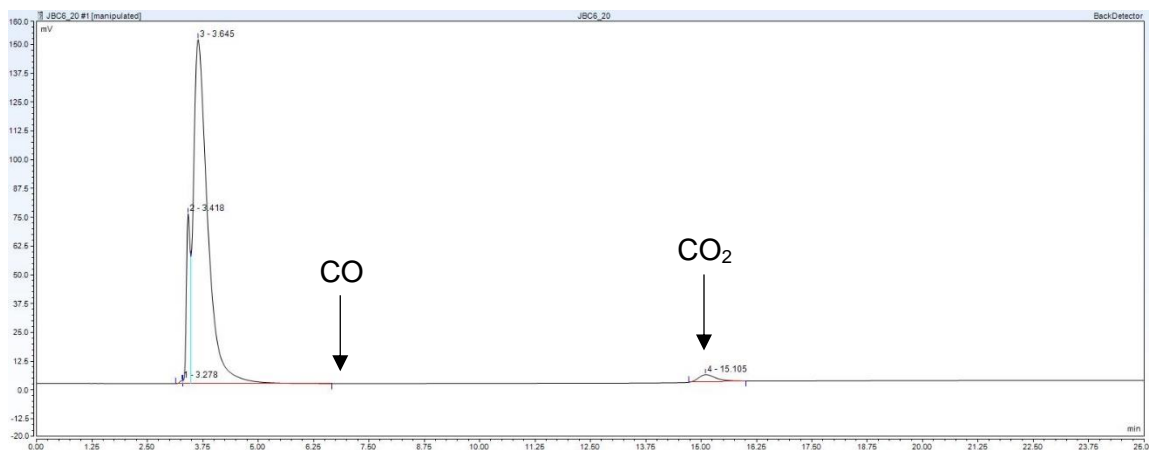
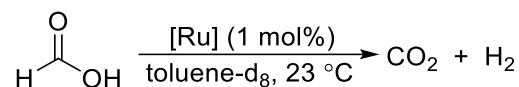


Figure C.11. GC trace of CO₂ detection using He carrier gas; no CO peak observed. Large peak is N₂/solvent vapor.

IX. Determination of Resting State in Formic Acid Dehydrogenation Using **2**, **2-Me**, and **2-H**



General Procedure: In the glovebox, to a J. Young NMR tube were added either **2**, **2-Me**, or **2-H** (3.7 μmol), toluene-*d*₈ (600 μL), and formic acid (14 μL, 3.7 mmol). In all cases effervescence was observed upon addition of the acid. The tube was then capped, frozen in N₂(*l*), degassed, sealed, and warmed to room temperature. NMR spectra were recorded after 15 minutes to determine the catalytic resting state. ³¹P{¹H} NMR data for each catalyst is shown in Figures C.12-C.14.

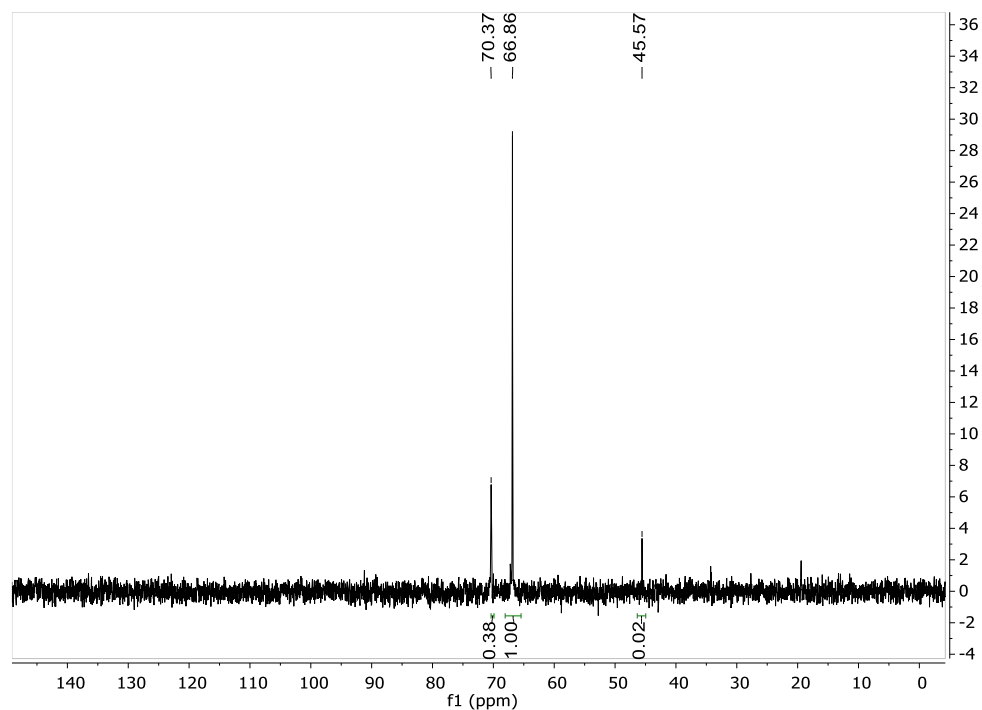
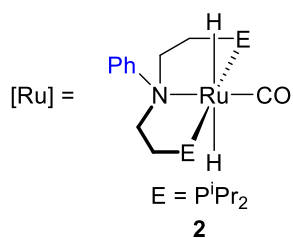


Figure C.12. *In situ* $^{31}P\{^1H\}$ NMR spectrum of formic acid dehydrogenation in toluene- d_8 catalyzed by **2**. Resting state **3** is observed at 66.86 ppm, minor unknown products observed at 70.37 and 45.57 ppm.

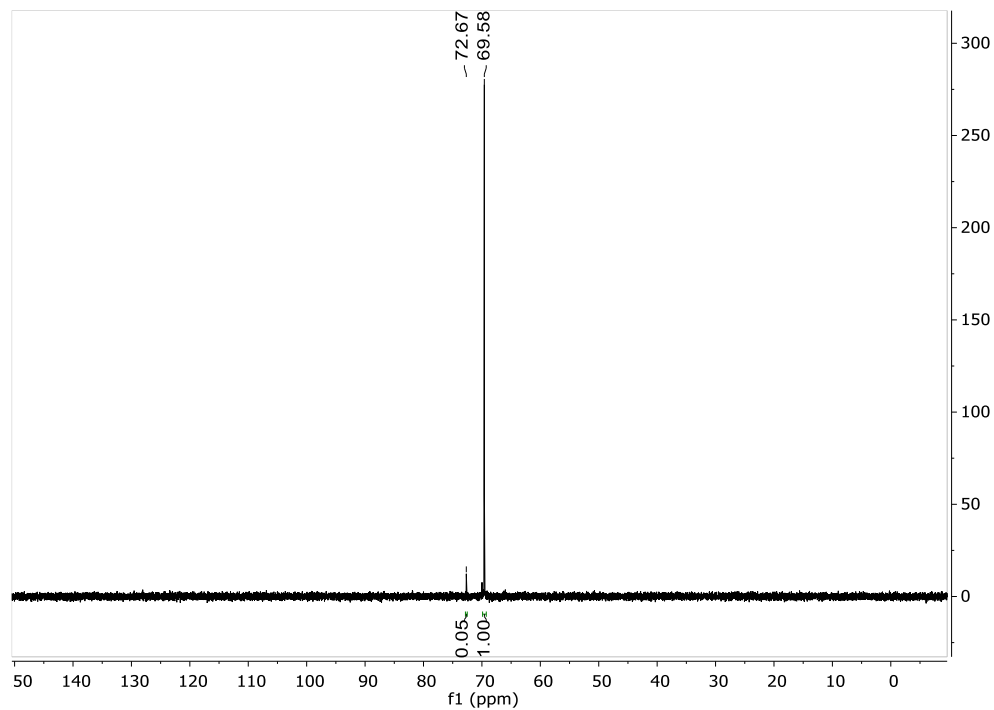
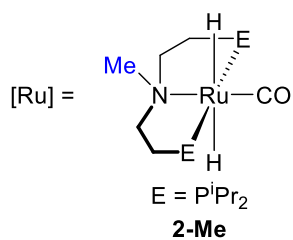


Figure C.13. *In situ* $^{31}\text{P}\{^1\text{H}\}$ NMR spectrum of formic acid dehydrogenation in toluene- d_8 catalyzed by **2-Me**. Resting state **3-Me** is observed as two isomers at 69.58 and 72.67 ppm.

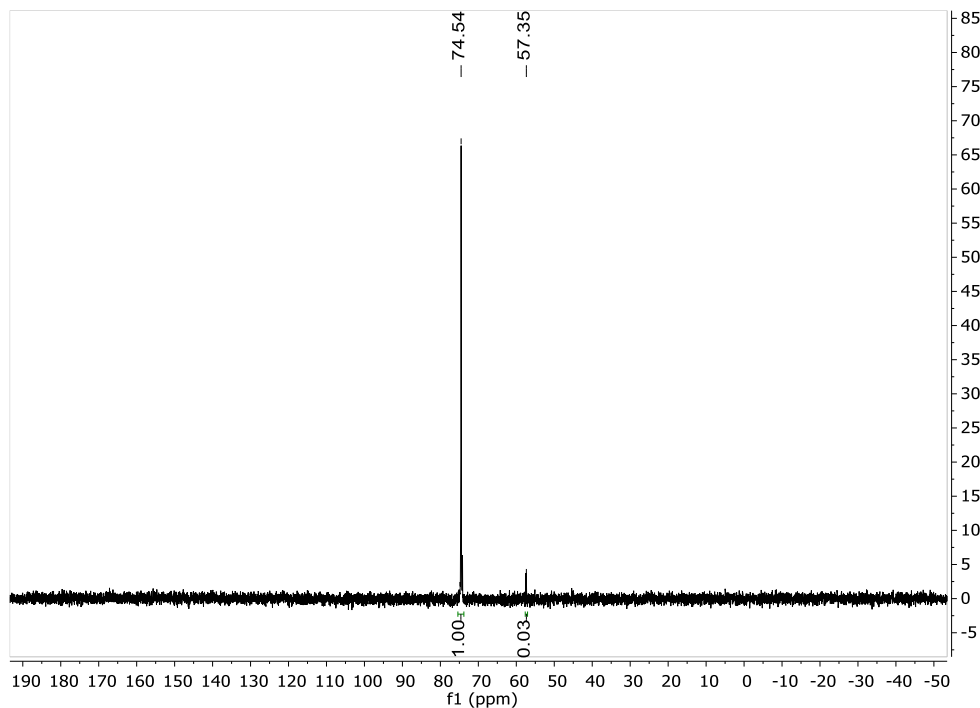
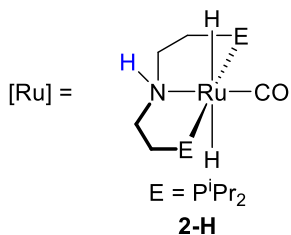
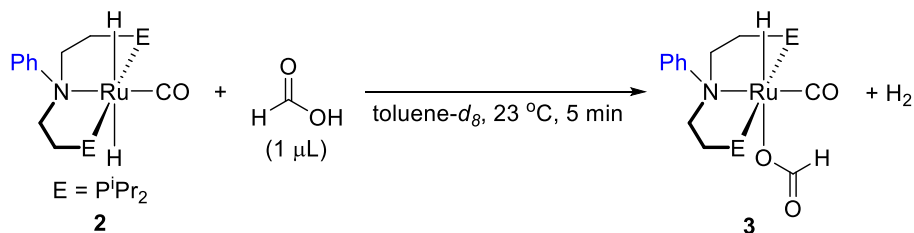


Figure C.14. *In situ* $^{31}\text{P}\{^1\text{H}\}$ NMR spectrum of formic acid dehydrogenation in toluene- d_8 catalyzed by **2-H**. Resting state **3-H** is observed at 74.54 ppm, minor unknown product observed at 57.35 ppm.

X. Reaction of **2** with Formic Acid



In a glovebox, to a J. Young NMR tube were added **2** (4.0 mg, 0.0078 mmol), toluene- d_8 (0.50 mL), and formic acid (1 μL). Immediate effervescence was observed upon

addition of the acid. The NMR tube was capped and the spectra shown in Figures C.15-C.16 were taken, showing formation of **3**, H₂, and a minor unknown decomposition product.

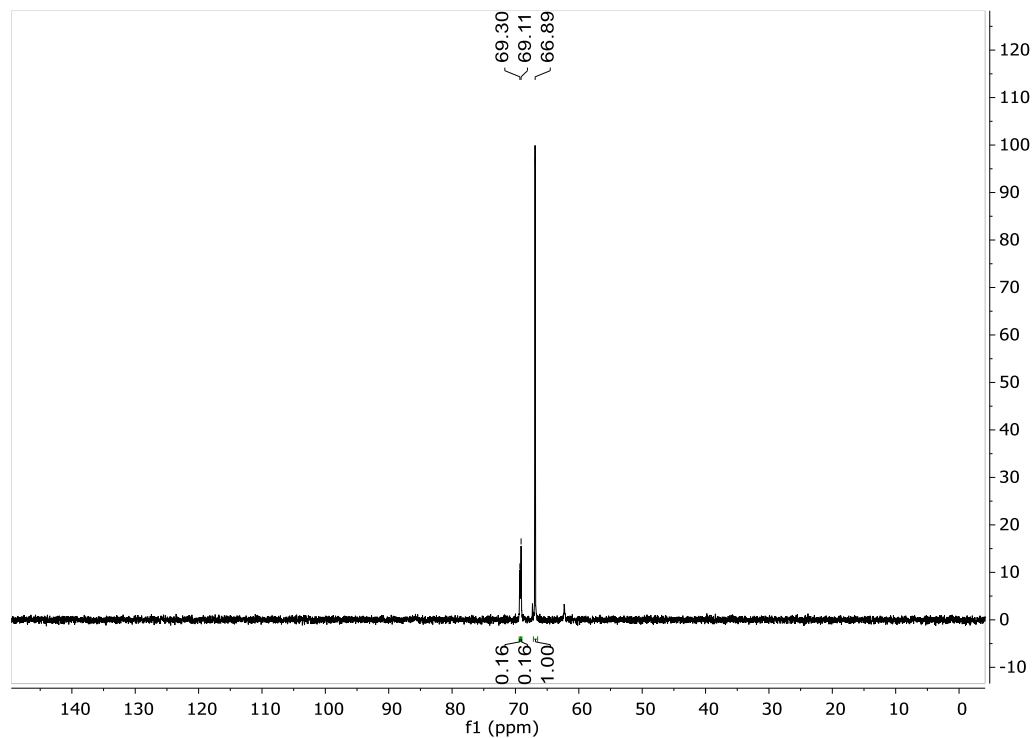


Figure C.15. ³¹P{¹H} NMR spectrum of the reaction of **2** with formic acid in toluene-*d*₈. **3** is observed at 66.89 ppm, and two minor unknown decomposition products are observed at 69.11 and 69.30 ppm.

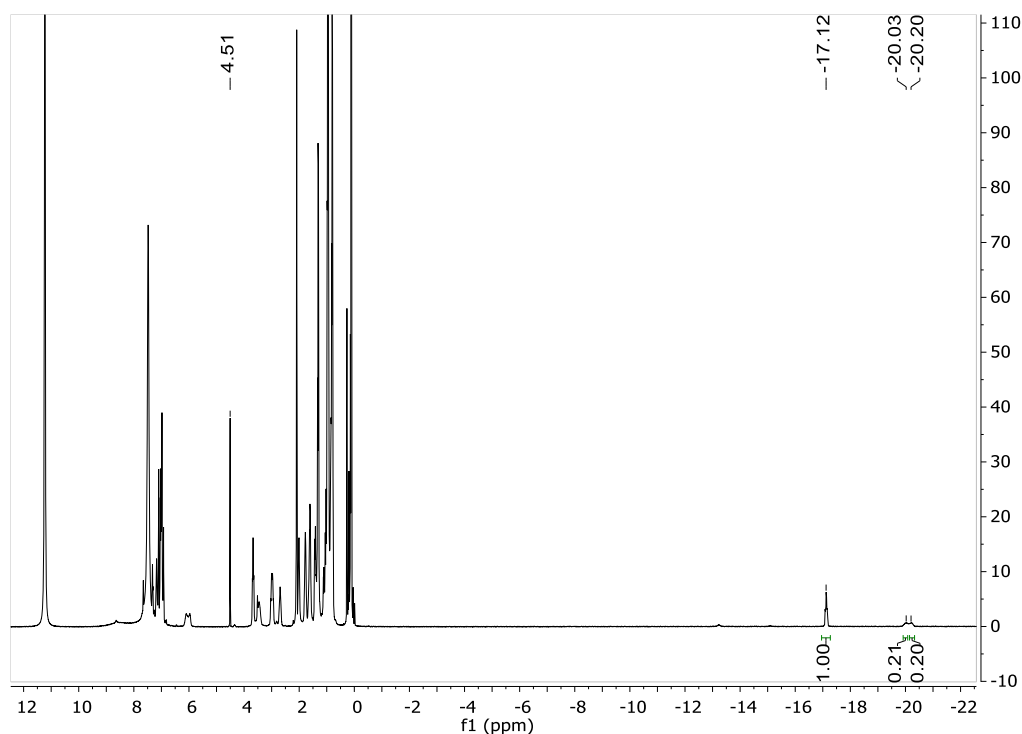


Figure C.16. ^1H NMR spectrum of the reaction of **2** with formic acid in toluene- d_8 . The hydride of **3** is observed at -17.12 ppm, and hydrides for two minor unknown decomposition products are observed at -20.03 and -20.20 ppm. H_2 is present at 4.51 ppm.

XI. Details of Catalytic CO_2 Hydrogenation

Representative Procedure for Catalytic CO_2 Hydrogenation

In a glovebox, a 50 mL glass reactor liner was charged with catalyst as a stock solution in THF (*ca.* 20 mM, 0.3 μmol catalyst), LiOTf (if an additive was used, 234 mg, 1.5 mmol), DBU (2.31 g, 15 mmol), and 10 mL of THF. The cylinder liner was placed into a 50 mL Parr reactor and the vessel sealed. The reactor was removed from the glovebox and pressurized sequentially with 17 atm of CO_2 and then 17 atm of H_2 via a Y-value inlet at ambient temperature. The reactor was then heated to 80 $^\circ\text{C}$, a process which occurred in approximately 10 minutes, and mechanically stirred for the desired length of time. The reaction was stopped by removal of the heat source, cooling in an ice water bath, and

venting of the vessel's atmosphere. The reaction solution, which contained some suspended solid, was then transferred to a 100 mL round-bottomed flask, using D₂O to dissolve the solid products. All volatiles were removed *in vacuo*. The residue was then dissolved in D₂O and DMF was added as an internal standard for quantification of the formate product by ¹H NMR spectroscopy. Delay times of 1 second were used between scans. Catalytic trials were run in triplicate, and errors in TON are given as the standard deviation.

XII. Determination of Resting State in CO₂ Hydrogenation Using **2, **2-Me**, and **2-H****

General Procedure: In the glovebox, to a J. Young NMR tube were added either **2**, **2-Me**, or **2-H** (14 μmol), THF (500 μL), DBU (21 μL, 0.14 mmol), and a CDCl₃/PPh₃ capillary. The tube was frozen, degassed, and 1 atm of 1:1 CO₂:H₂ was added. NMR spectra were recorded after 15 minutes to determine the catalyst resting state. A peak corresponding to [HDBU][formate] was observed in all ¹H NMR spectra. ³¹P{¹H} NMR data for each catalyst is shown in Figures C.17-C.19.

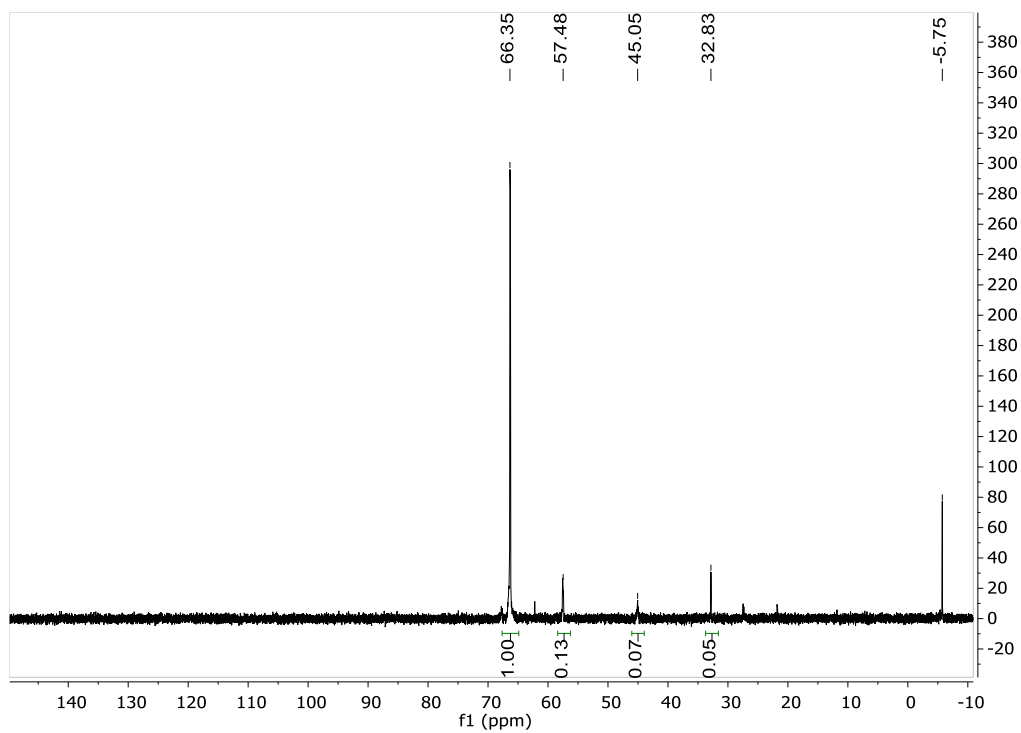
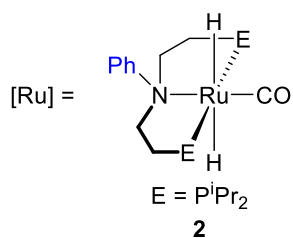


Figure C.17. *In situ* $^{31}\text{P}\{^1\text{H}\}$ NMR spectrum of CO_2 hydrogenation in THF catalyzed by **2**. Resting state **3** is observed at 66.35 ppm, minor unknown products observed at 57.48, 45.05, and 32.83 ppm. PPh_3 standard at -5.75 ppm.

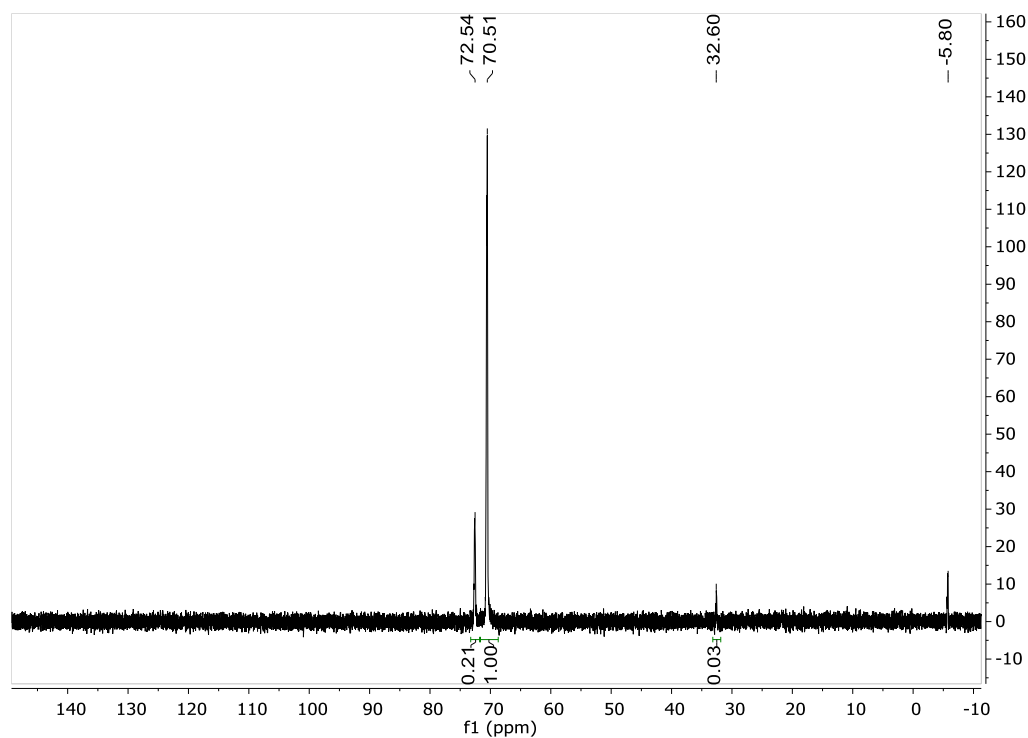
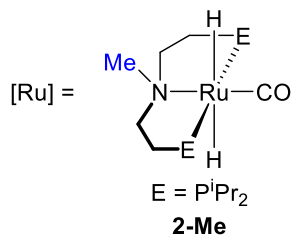


Figure C.18. *In situ* $^{31}\text{P}\{^1\text{H}\}$ NMR spectrum of CO_2 hydrogenation in THF catalyzed by **2-Me**. Resting state **3-Me** is observed as two isomers at 70.51 and 72.54 ppm, minor unknown product observed at 32.60 ppm. PPh_3 standard at -5.80 ppm.

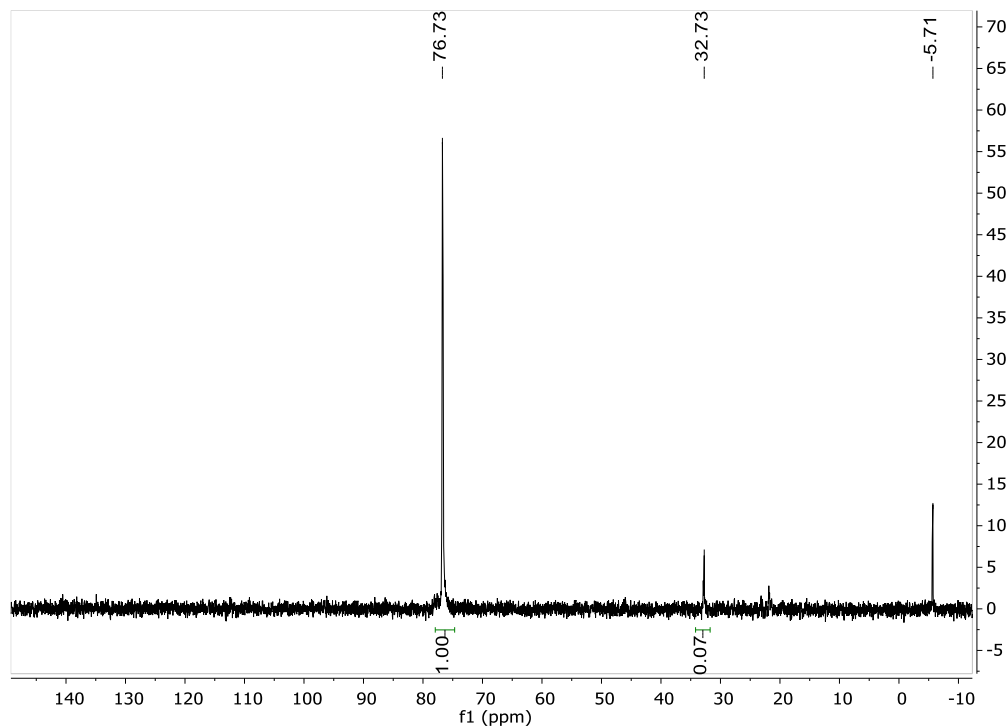
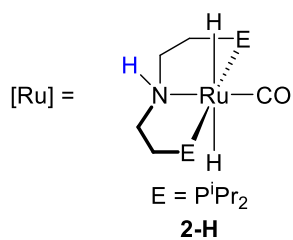
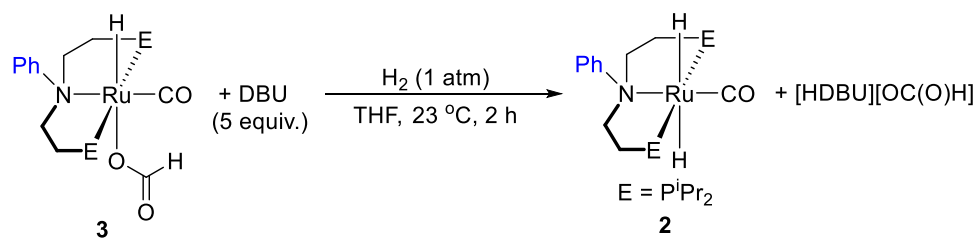


Figure C.19. *In situ* $^{31}\text{P}\{^1\text{H}\}$ NMR spectrum of CO_2 hydrogenation in THF catalyzed by **2-H**. Resting state **3-H** is observed at 72.54 ppm, minor unknown product observed at 32.73 ppm. PPh_3 standard at -5.71 ppm.

XIII. Reaction of **3** with H_2 and DBU



In a glovebox, to a J. Young NMR tube were added **3** (6.0 mg, 0.011 mmol), THF (0.50 mL), DBU (8 μ L, 0.05 mmol), and a $\text{CDCl}_3/\text{PPh}_3$ capillary. The tube was frozen in $\text{N}_2(l)$, degassed, and 1 atm H_2 was added. The NMR tube was capped and warmed to room temperature, and the spectra shown in Figures C.20-C.21 were taken after two hours, showing formation of **2**, $[\text{HDBU}][\text{formate}]$, and some minor decomposition.

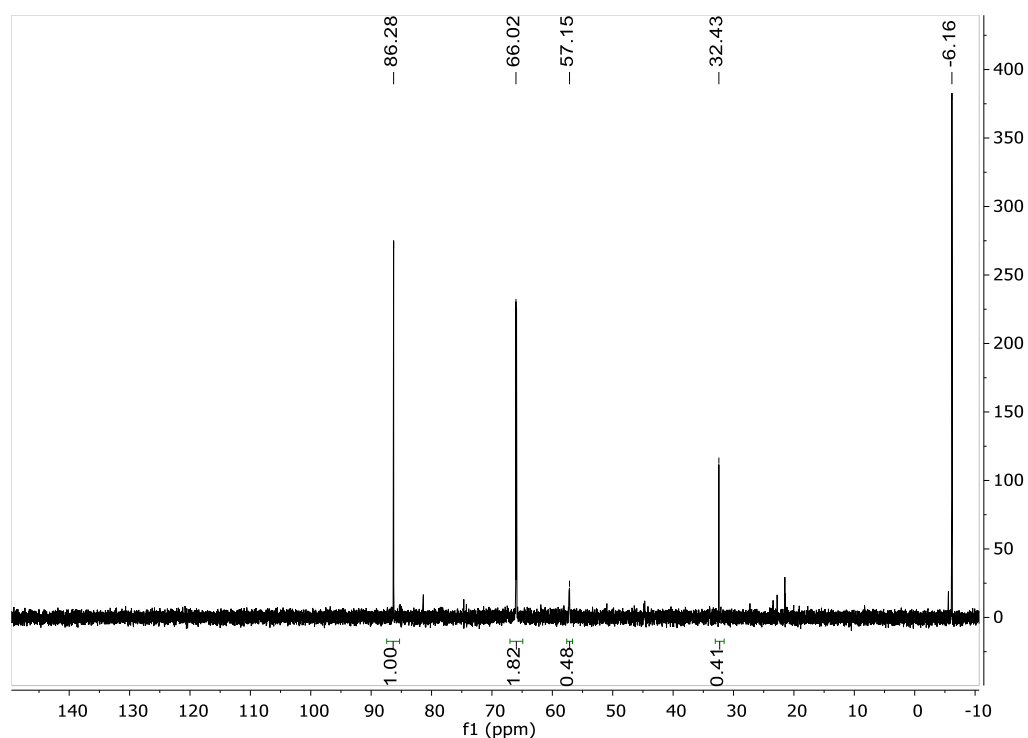


Figure C.20. $^{31}\text{P}\{^1\text{H}\}$ NMR spectrum of the reaction of **3** with H_2 and DBU in THF. **3** is observed at 66.02 ppm, **2** is observed at 86.28 ppm, and two minor unknown decomposition products are observed at 57.15 and 32.43 ppm. PPh_3 standard at -6.16 ppm.

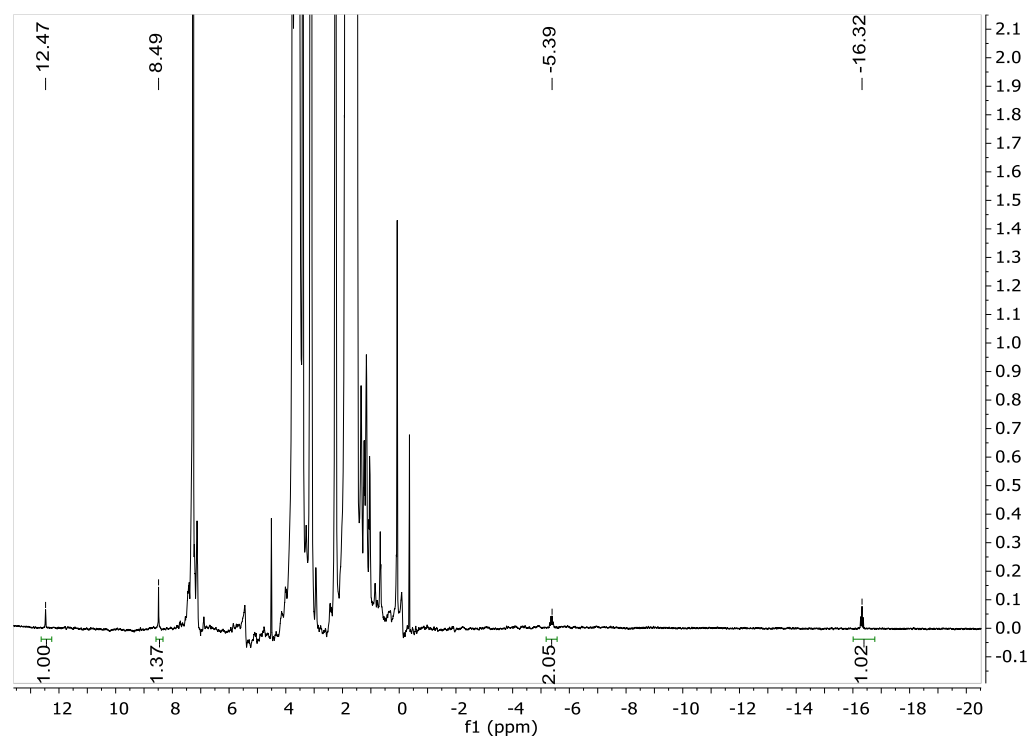


Figure C.21. ^1H NMR spectrum of the reaction of **3** with H_2 and DBU in THF. The hydride of **3** is observed at -16.32 ppm and its formate peak is shifted downfield at 12.47 ppm. Hydrides of **2** are observed at -5.39 ppm and [HDBU][formate] is present at 8.49 ppm. Inconsistency in baseline is due to solvent suppression.

XIV. Full Spectra of Novel Compounds

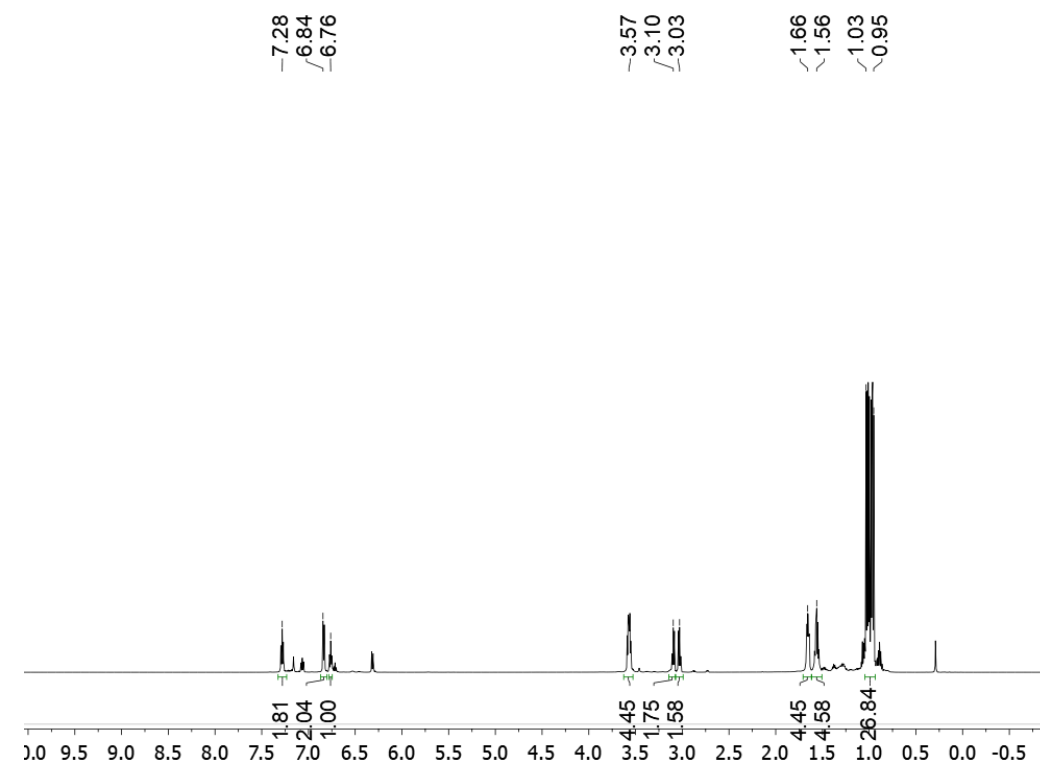
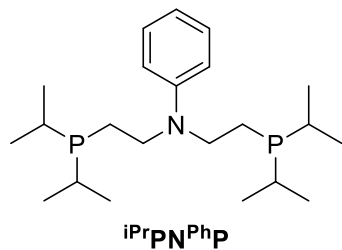
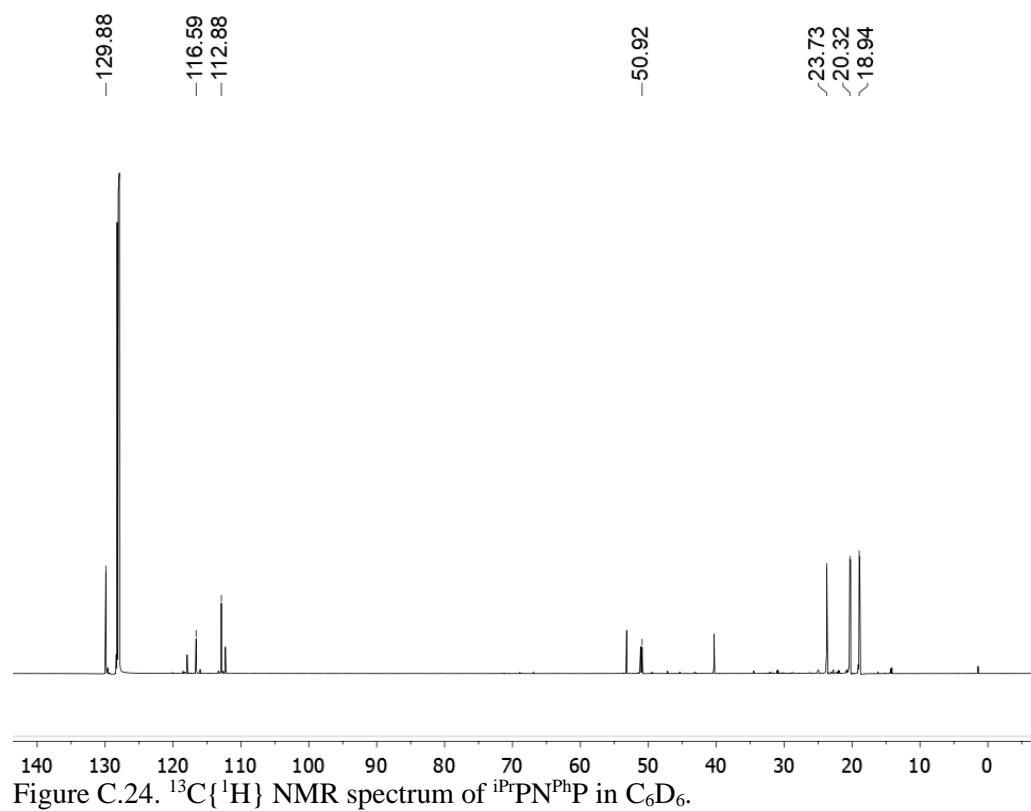
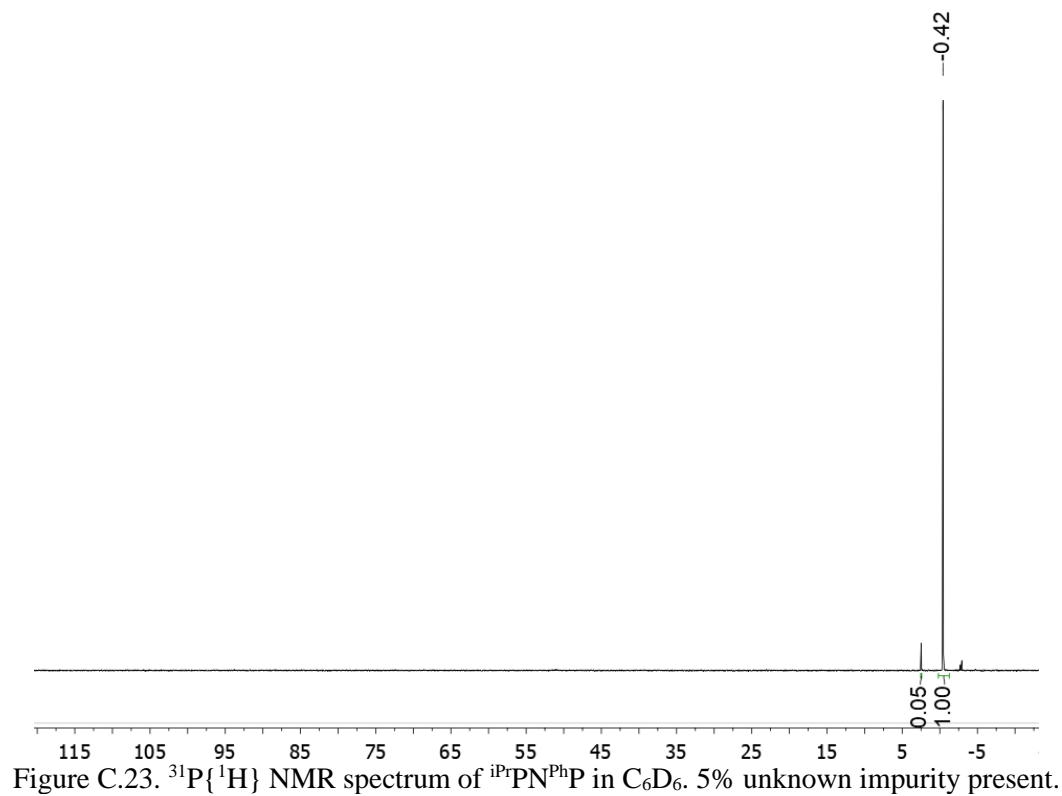


Figure C.22. ^1H NMR spectrum of $\text{iPrPN}^{\text{Ph}}\text{P}$ in C_6D_6 .



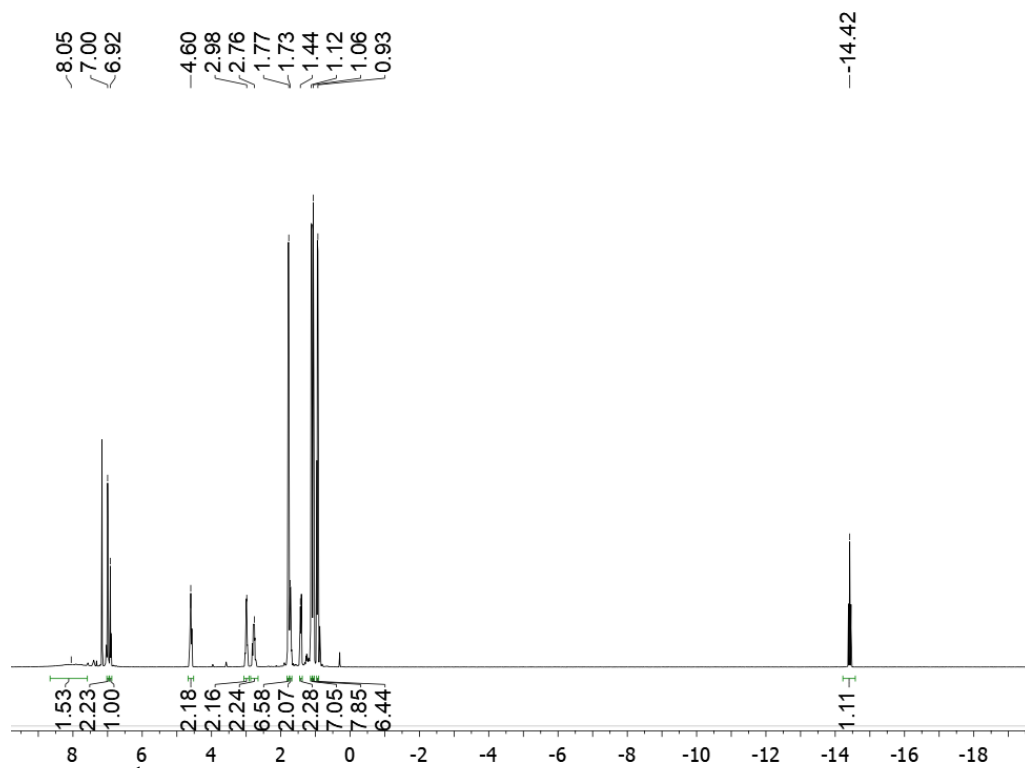
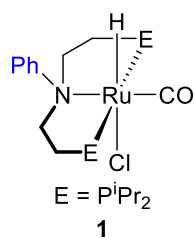


Figure C.25. ^1H NMR spectrum of **1** in C_6D_6 .

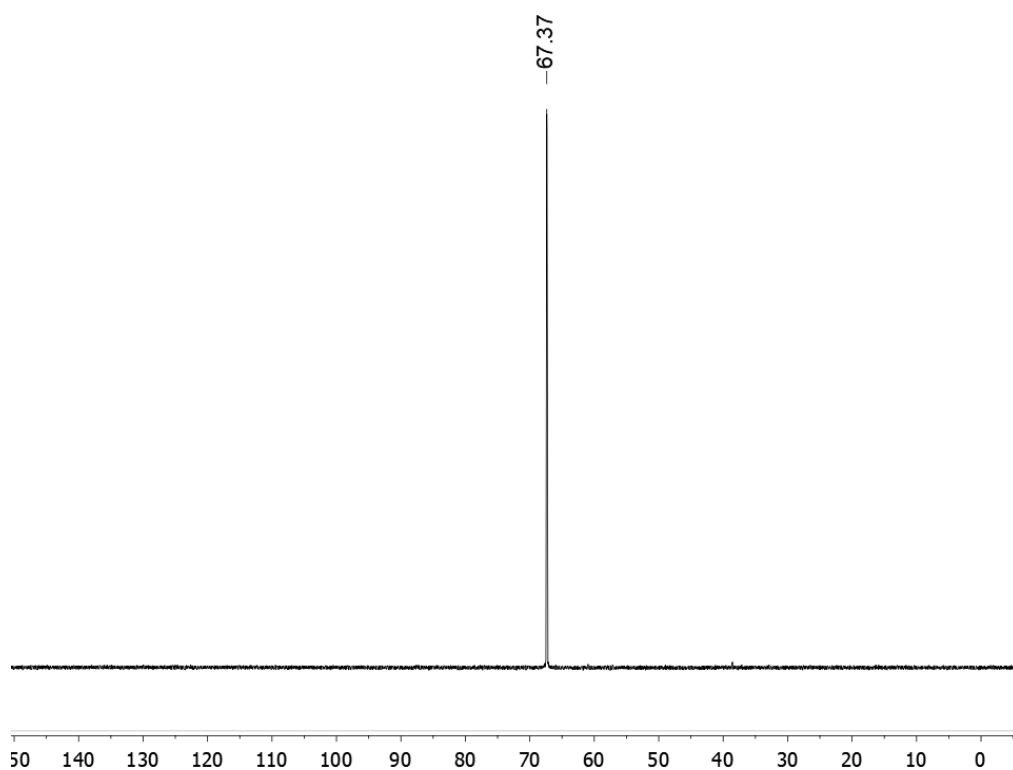


Figure C.26. $^{31}\text{P}\{^1\text{H}\}$ NMR spectrum of **1** in C_6D_6 .

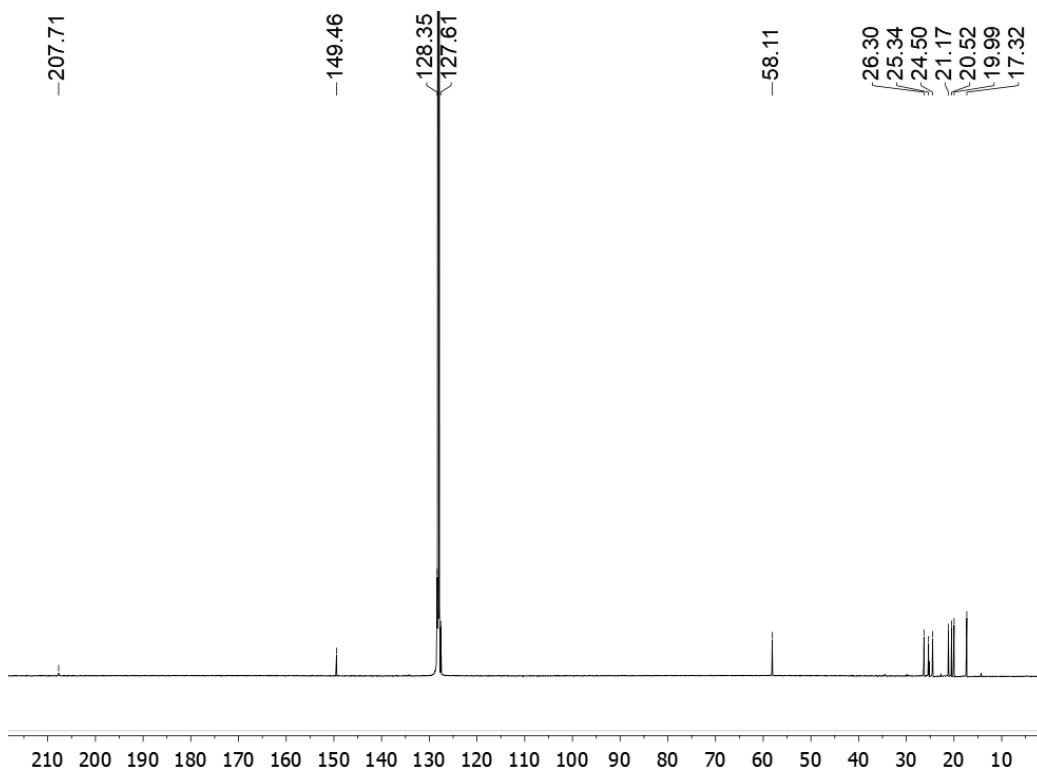


Figure C.27. $^{13}\text{C}\{^1\text{H}\}$ NMR spectrum of **1** in C_6D_6 .

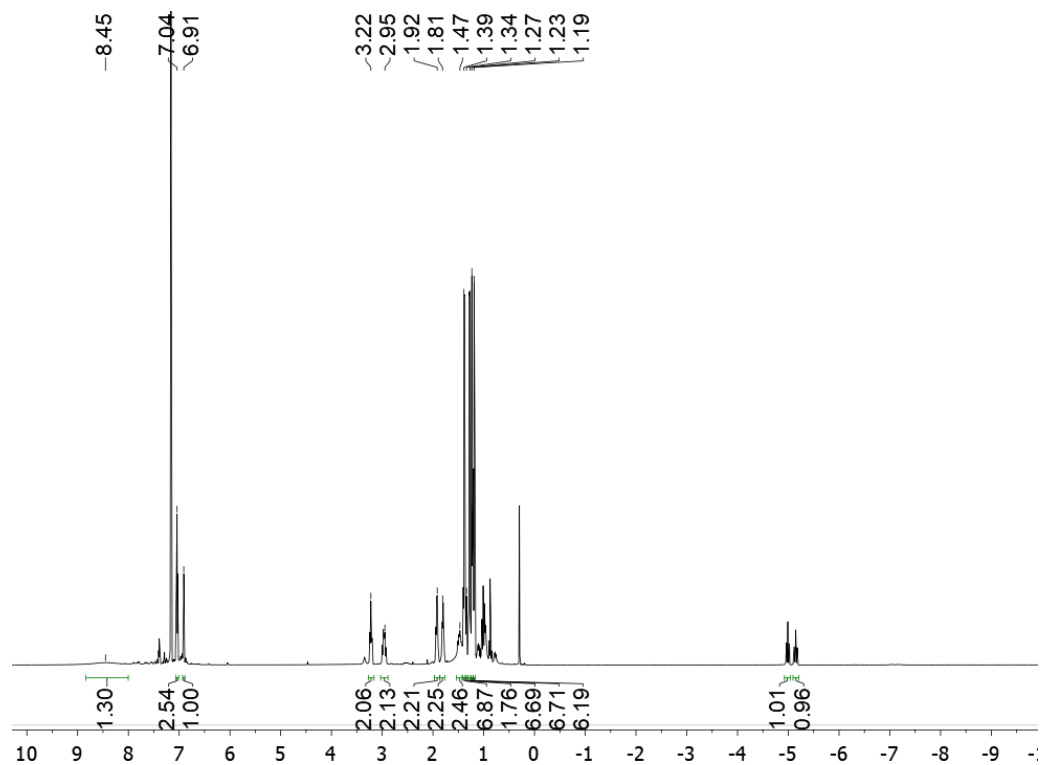
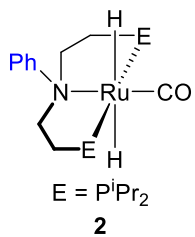


Figure C.28. ^1H NMR spectrum of **2** in C_6D_6 .

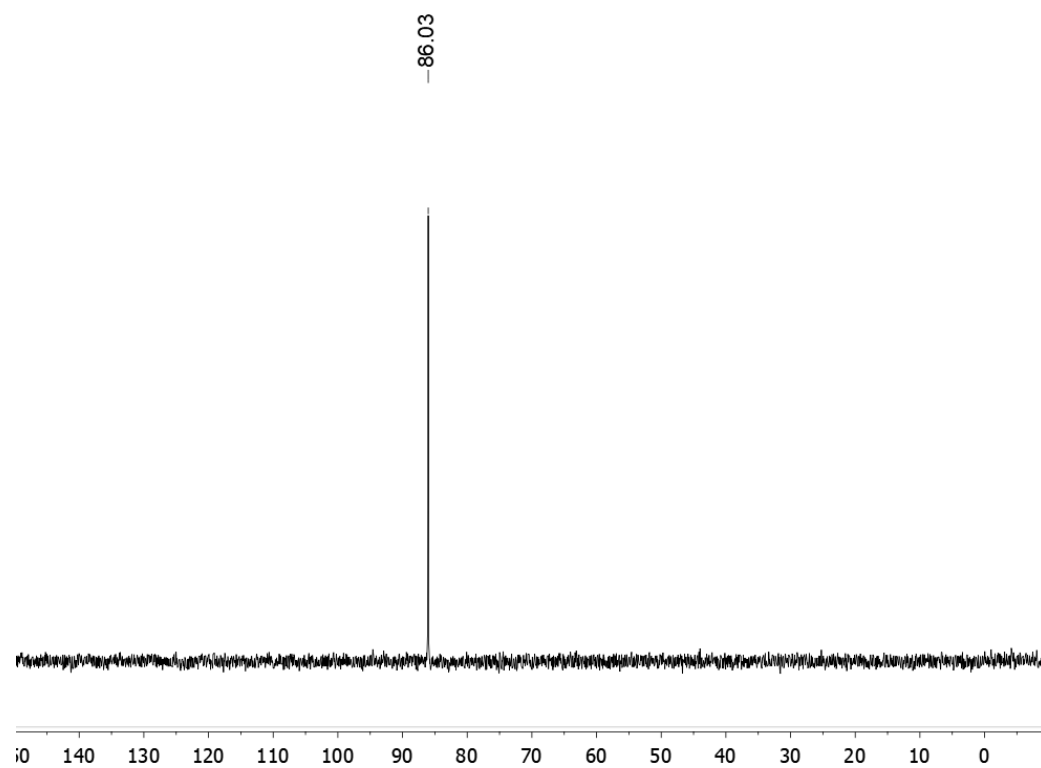


Figure C.29. $^{31}\text{P}\{^1\text{H}\}$ NMR spectrum of **2** in C₆D₆.

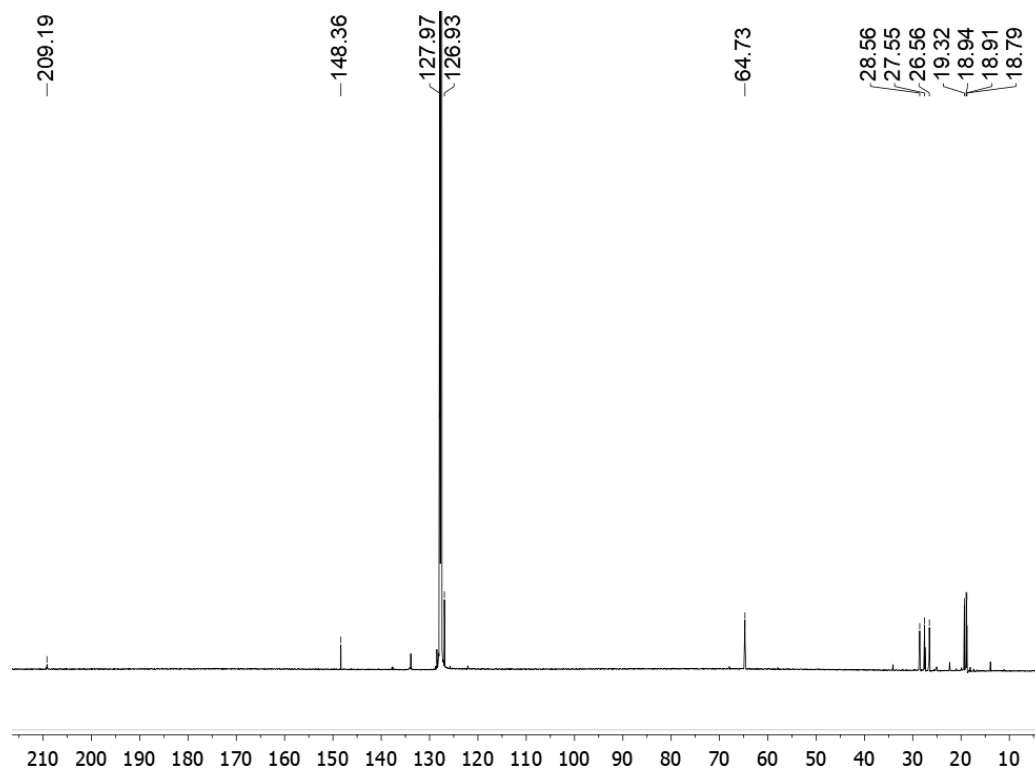


Figure C.30. $^{13}\text{C}\{^1\text{H}\}$ NMR spectrum of **2** in C₆D₆.

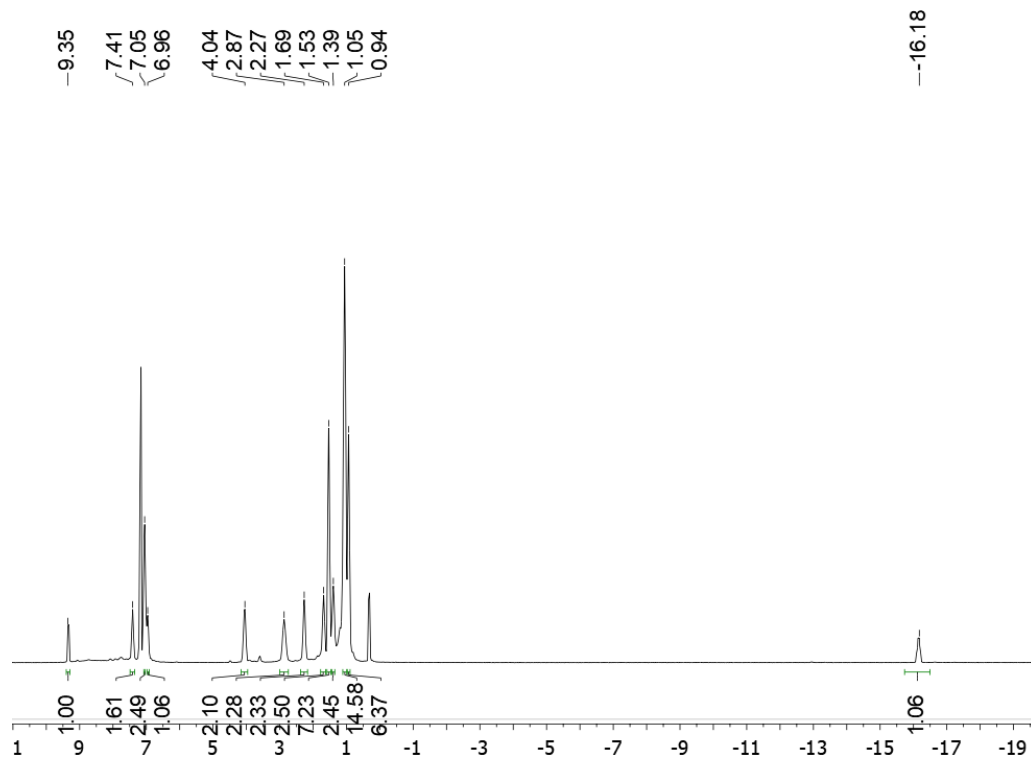
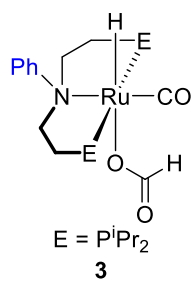


Figure C.31. ^1H NMR spectrum of **3** in C_6D_6 .

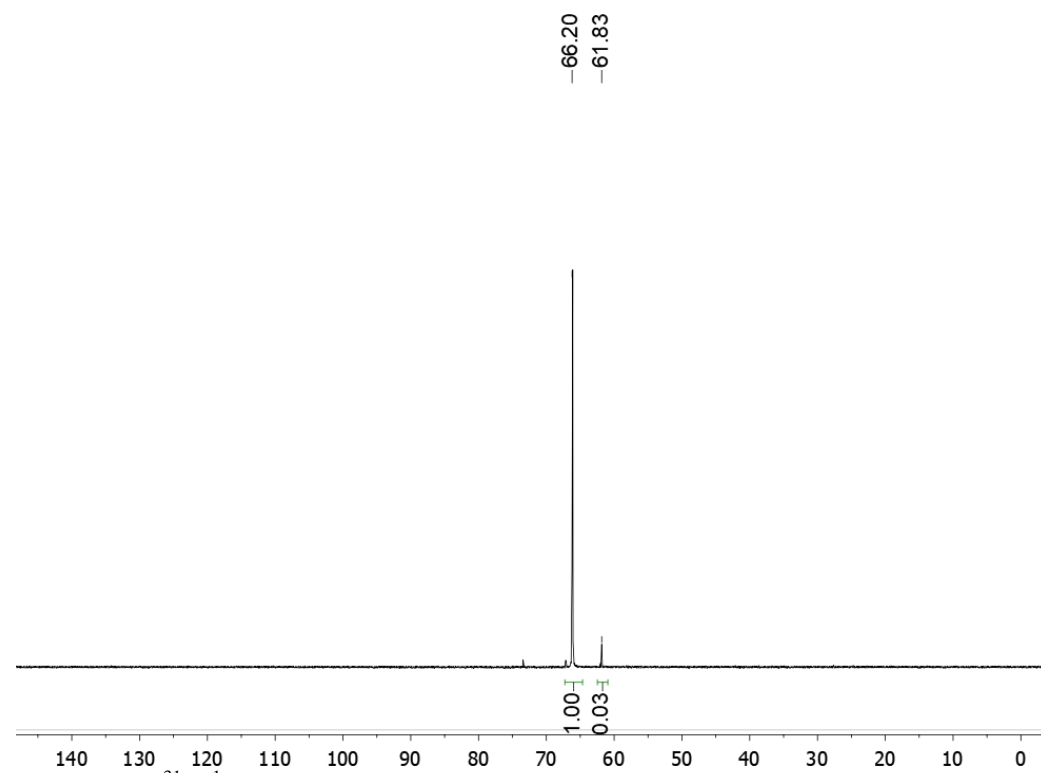


Figure C.32. $^{31}\text{P}\{^1\text{H}\}$ NMR spectrum of **3** in C_6D_6 . Minor impurity at 61.83 ppm.

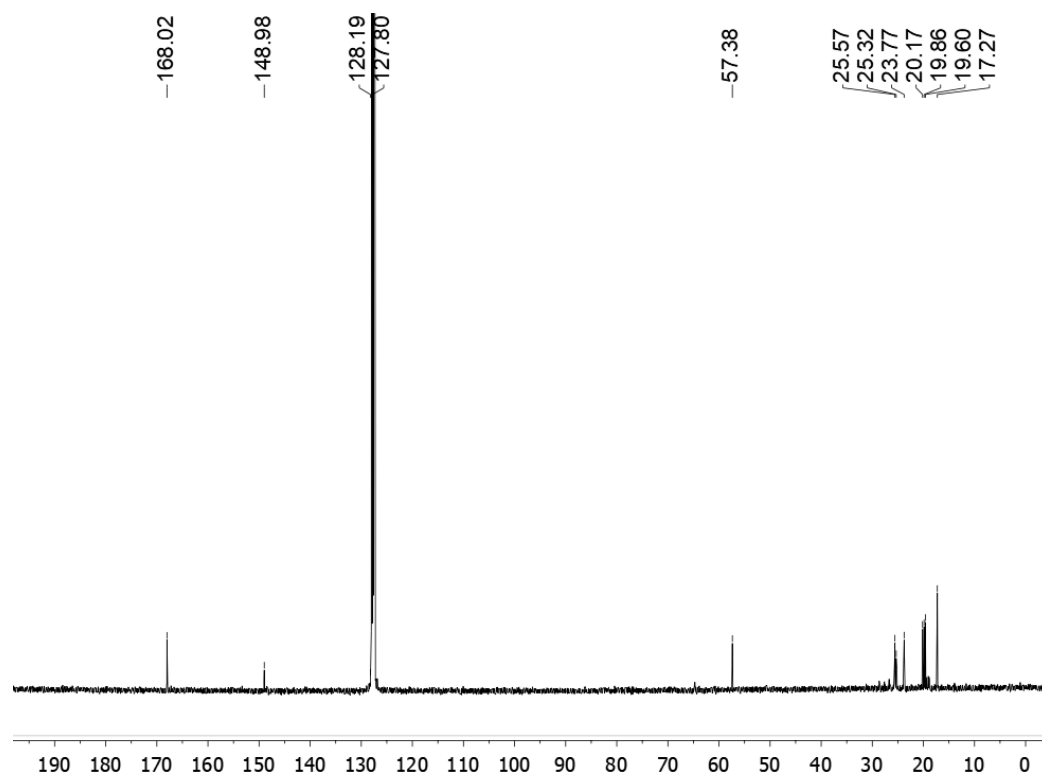


Figure C.33. $^{13}\text{C}\{^1\text{H}\}$ NMR spectrum of **3** in C_6D_6 .

Previously isolated compounds **1-H**, **2-H**, and **2-Me** did not have published IR spectra, so we obtained them for this report. They are shown in Figures C.34-C.36, below.

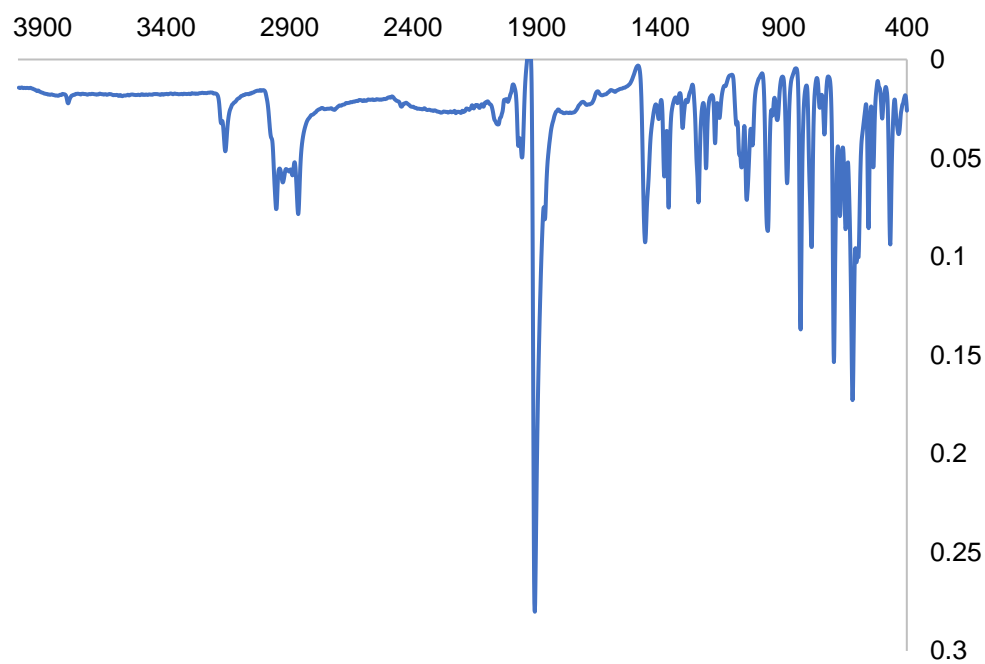
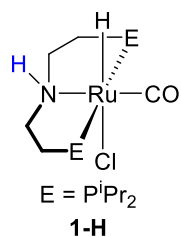


Figure C.34. Solid-state IR spectrum of **1-H**. C=O stretch present at 1906 cm⁻¹.

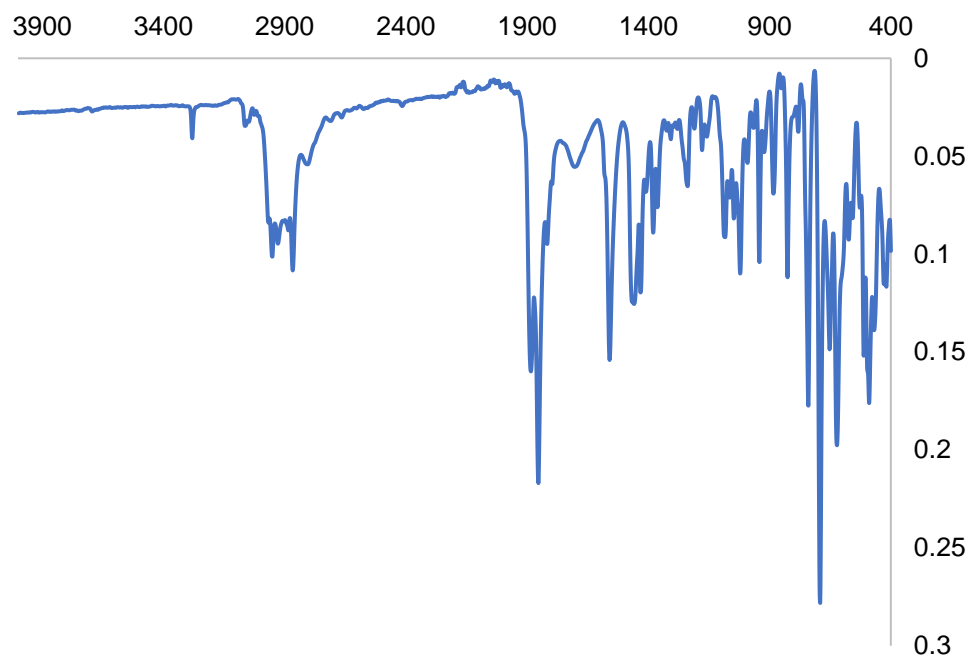
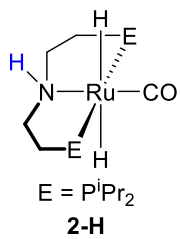


Figure C.35. Solid-state IR spectrum of **2-H**. $\text{C}\equiv\text{O}$ stretch present at 1853 cm^{-1} .

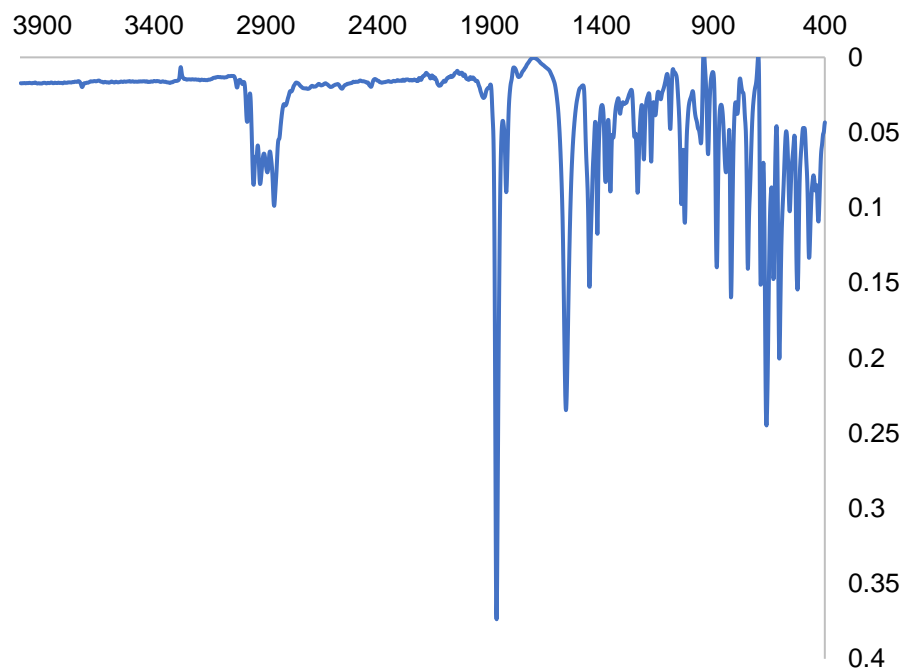
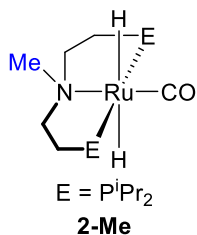


Figure C.36. Solid-state IR spectrum of **2-Me**. C≡O stretch present at 1868 cm⁻¹.

XV. X-ray Crystallographic Information

(ⁱPrPN^{Ph}P)RuHCl(CO) (**1**) (CCDC:XX)

Low-temperature diffraction data (ω -scans) were collected on a Rigaku SCX Mini diffractometer coupled to a Rigaku Mercury275R CCD with Mo K α radiation ($\lambda = 0.71073$ Å) for the structure of **1**.⁶ The diffraction images were processed and scaled using Rigaku Oxford Diffraction software. The structure was solved with SHELXT and was refined against F^2 on all data by full-matrix least squares with SHELXL.⁷ All non-hydrogen atoms

were refined anisotropically. Hydrogen atoms were included in the model at geometrically calculated positions and refined using a riding model. The isotropic displacement parameters of all hydrogen atoms were fixed to 1.2 times the U value of the atoms to which they are linked (1.5 times for methyl groups). The full numbering scheme of **1** can be found in the full details of the X-ray structure determination (CIF), which is included as Supporting Information. CCDC number XXXXXX (**1**) contains the supplementary crystallographic data for this paper. These data can be obtained free of charge from The Cambridge Crystallographic Data Center via www.ccdc.cam.ac.uk/data_request/cif.

Table C.01. Crystal data and structure refinement for **1**.

Empirical formula	C ₂₃ H ₄₂ Cl N O P ₂ Ru	
Formula weight	547.03	
Temperature	93(2) K	
Wavelength	0.71073 Å	
Crystal system	Triclinic	
Space group	P-1	
Unit cell dimensions	a = 10.4036(7) Å	α = 102.420(5)°.
	b = 10.4816(6) Å	β = 100.463(5)°.
	c = 13.7676(8) Å	γ = 113.778(6)°.
Volume	1279.82(15) Å ³	
Z	2	
Density (calculated)	1.420 Mg/m ³	
Absorption coefficient	0.856 mm ⁻¹	
F(000)	572	
Crystal size	0.200 x 0.200 x 0.200 mm ³	
Crystal color and habit	Colorless Block	
Theta range for data collection	2.329 to 25.021°.	
Index ranges	-12 ≤ h ≤ 12, -12 ≤ k ≤ 12, -16 ≤ l ≤ 16	
Reflections collected	18480	
Independent reflections	4522 [R(int) = 0.0881]	
Observed reflections (I > 2σ(I))	3487	
Completeness to theta = 25.021°	99.9 %	
Absorption correction	Semi-empirical from equivalents	
Max. and min. transmission	1.00000 and 0.93376	
Solution method	SHELXT-2018/2 (Sheldrick, 2014)	
Refinement method	SHELXL-2014/7 (Sheldrick, 2014)	
Data / restraints / parameters	4522 / 0 / 274	
Goodness-of-fit on F ²	1.044	
Final R indices [I > 2σ(I)]	R1 = 0.0448, wR2 = 0.0744	
R indices (all data)	R1 = 0.0711, wR2 = 0.0821	
Largest diff. peak and hole	0.744 and -0.592 e.Å ³	

(ⁱPrPN^{Ph}P)Ru(H)₂(CO) (**2**) (CCDC: XX)

Low-temperature diffraction data (ω -scans) were collected on a Rigaku MicroMax-007HF diffractometer coupled to a Dectris Pilatus3R detector with Mo K α ($\lambda = 0.71073$ Å) for the structure of **2**. The diffraction images were processed and scaled using Rigaku Oxford Diffraction software.⁶ The structure was solved with SHELXT and was refined against F² on all data by full-matrix least squares with SHELXL.⁷ All non-hydrogen atoms were refined anisotropically. Hydrogen atoms were included in the model at geometrically calculated positions and refined using a riding model. The isotropic displacement parameters of all hydrogen atoms were fixed to 1.2 times the U value of the atoms to which they are linked (1.5 times for methyl groups). Three reflections were not properly recorded due to instrument artifacts. These reflections were subsequently omitted. The full numbering scheme of compound **2** can be found in the full details of the X-ray structure determination (CIF), which is included as Supporting Information. CCDC number XXXXXX (**2**) contains the supplementary crystallographic data for this paper. These data can be obtained free of charge from The Cambridge Crystallographic Data Center via www.ccdc.cam.ac.uk/data_request/cif.

Table C.02. Crystal data and structure refinement for **2**.

Empirical formula	C ₂₃ H ₄₃ N O P ₂ Ru	
Formula weight	512.59	
Temperature	93(2) K	
Wavelength	0.71073 Å	
Crystal system	Triclinic	
Space group	P-1	
Unit cell dimensions	$a = 14.3901(2)$ Å	$\alpha = 116.3750(10)^\circ$
	$b = 19.0902(2)$ Å	$\beta = 101.2770(10)^\circ$
	$c = 21.4046(3)$ Å	$\gamma = 95.9650(10)^\circ$
Volume	$5042.98(12)$ Å ³	
Z	8	
Density (calculated)	1.350 Mg/m ³	
Absorption coefficient	0.762 mm ⁻¹	

F(000)	2160
Crystal size	0.180 x 0.080 x 0.070 mm ³
Crystal color and habit	Colorless Plate
Theta range for data collection	2.844 to 27.484°.
Index ranges	-18<=h<=18, -24<=k<=24, -27<=l<=27
Reflections collected	192954
Independent reflections	23128 [R(int) = 0.0543]
Observed reflections (I > 2sigma(I))	20505
Completeness to theta = 25.242°	99.8 %
Absorption correction	Semi-empirical from equivalents
Max. and min. transmission	1.00000 and 0.48130
Solution method	SHELXT-2014/5 (Sheldrick, 2014)
Refinement method	SHELXL-2014/7 (Sheldrick, 2014)
Data / restraints / parameters	23128 / 0 / 1073
Goodness-of-fit on F ²	1.067
Final R indices [I>2sigma(I)]	R1 = 0.0277, wR2 = 0.0642
R indices (all data)	R1 = 0.0336, wR2 = 0.0664
Largest diff. peak and hole	1.071 and -0.767 e.Å ⁻³

(ⁱPrPN^{Ph}P)RuH(CO){OC(O)H} (**3**) (CCDC: XX)

Low-temperature diffraction data (ω -scans) were collected on a Rigaku MicroMax-007HF diffractometer coupled to a Saturn994+ CCD detector with Cu K α (λ = 1.54178 Å) for the structure of **3**. The diffraction images were processed and scaled using Rigaku Oxford Diffraction software.⁶ The structure was solved with SHELXT and was refined against F² on all data by full-matrix least squares with SHELXL.⁷ All non-hydrogen atoms were refined anisotropically. Hydrogen atoms were included in the model at geometrically calculated positions and refined using a riding model. The isotropic displacement parameters of all hydrogen atoms were fixed to 1.2 times the U value of the atoms to which they are linked (1.5 times for methyl groups). The only exception was H1RU, which was found in the difference map and freely refined. The full numbering scheme of compound **3** can be found in the full details of the X-ray structure determination (CIF), which is included as Supporting Information. CCDC number XXXXXX (**3**) contains the

supplementary crystallographic data for this paper. These data can be obtained free of charge from The Cambridge Crystallographic Data Center via www.ccdc.cam.ac.uk/data_request/cif.

Table C.03. Crystal data and structure refinement for **3**.

Empirical formula	C ₂₄ H ₄₃ N O ₃ P ₂ Ru	
Formula weight	556.60	
Temperature	93(2) K	
Wavelength	1.54184 Å	
Crystal system	Monoclinic	
Space group	P ₂ ₁ /n	
Unit cell dimensions	a = 14.1273(5) Å	$\alpha = 90^\circ$
	b = 10.2513(3) Å	$\beta = 109.126(4)^\circ$
	c = 19.6615(6) Å	$\gamma = 90^\circ$
Volume	2690.26(16) Å ³	
Z	4	
Density (calculated)	1.374 Mg/m ³	
Absorption coefficient	6.026 mm ⁻¹	
F(000)	1168	
Crystal size	0.200 x 0.140 x 0.050 mm ³	
Crystal color and habit	Yellow Plate	
Theta range for data collection	3.386 to 66.581°.	
Index ranges	-16 ≤ h ≤ 16, -12 ≤ k ≤ 12, -23 ≤ l ≤ 23	
Reflections collected	90205	
Independent reflections	4714 [R(int) = 0.1367]	
Observed reflections (I > 2σ(I))	3832	
Completeness to theta = 66.581°	99.2 %	
Absorption correction	Semi-empirical from equivalents	
Max. and min. transmission	1.00000 and 0.79239	
Solution method	SHELXT-2014/5 (Sheldrick, 2014)	
Refinement method	SHELXL-2014/7 (Sheldrick, 2014)	
Data / restraints / parameters	4714 / 0 / 292	
Goodness-of-fit on F ²	1.100	
Final R indices [I > 2σ(I)]	R1 = 0.0578, wR2 = 0.1415	
R indices (all data)	R1 = 0.0729, wR2 = 0.1535	
Largest diff. peak and hole	0.619 and -1.250 e.Å ⁻³	

XVI. Computational Details

DFT studies were performed to probe the isomers of **3** in solution, the thermodynamics and kinetics of decarboxylation, and the thermodynamics of formate loss.

The calculations were carried out with the Gaussian16 software package.⁸ The hybrid meta-GGA M06 functional⁹ was selected on the basis of previous geometry and energy benchmarking.¹⁰ Structures were fully optimized without any geometry or symmetry constraints, using the double-z LANL2DZ for Ru, including pseudopotentials,¹¹ and 6-31+G** for all other elements¹² basis sets. Vibrational frequencies were computed at the same level of theory to classify all stationary points as either saddle points (transition states with a single imaginary frequency) or energy minima (reactants, products, and intermediates with only real frequencies). These calculations were also used to obtain the thermochemistry corrections (zero-point, thermal, and entropy energies). The energies reported in the text were obtained by adding the thermochemistry corrections at 298.15 K to the refined potential energies. Solvation effects of benzene for the isomers of **3** and THF for all other calculations were included using the continuum CPCM model.

XVII. References

1. Harris, R. K.; Becker, E. D.; Cabral De Menezes, S. M.; Granger, P.; Hoffman, R. E.; Zilm, K. W., Further Conventions for NMR Shielding and Chemical Shifts: (IUPAC Recommendations 2008). *Pure Appl. Chem.* **2008**, *80*, 59-84.
2. Ahmad, N.; Levison, J. J.; Robinson, S. D.; Uttley, M. F.; Wonchoba, E. R.; Parshall, G. W., Complexes of Ruthenium, Osmium, Rhodium, and Iridium Containing Hydride Carbonyl, or Nitrosyl Ligands. *Inorg. Synth.* **1974**, 45-64.
3. Bertoli, M.; Choualeb, A.; Lough, A. J.; Moore, B.; Spasyuk, D.; Gusev, D. G., Osmium and Ruthenium Catalysts for Dehydrogenation of Alcohols. *Organometallics* **2011**, *30*, 3479-3482.

4. Alberico, E.; Lennox, A. J. J.; Vogt, L. K.; Jiao, H.; Baumann, W.; Drexler, H.-J.; Nielsen, M.; Spannenberg, A.; Checinski, M. P.; Junge, H.; Beller, M., Unravelling the Mechanism of Basic Aqueous Methanol Dehydrogenation Catalyzed by Ru–PNP Pincer Complexes. *J. Am. Chem. Soc.* **2016**, *138*, 14890-14904.
5. Lee, J. Y.; Lee, Y. H.; Byun, Y. G., Characterization and study of piperazinium salts, degradation products of nitrogen mustards by nuclear magnetic resonance spectroscopy and liquid chromatography–mass spectrometry. *Journal of Chromatography A* **2012**, *1227*, 163-173.
6. *CrysAlis Pro, Rigaku OD*. The Woodlands, TX, **2015**.
7. Sheldrick, G., A Short History of SHELX. *Acta Cryst. A* **2008**, *64*, 112-122.
8. Frisch, M. J.; Trucks, G. W.; Schlegel, H. B.; Scuseria, G. E.; Robb, M. A.; Cheeseman, J. R.; Scalmani, G.; Barone, V.; Petersson, G. A.; Nakatsuji, H.; Li, X.; Caricato, M.; Marenich, A. V.; Bloino, J.; Janesko, B. G.; Gomperts, R.; Mennucci, B.; Hratchian, H. P.; Ortiz, J. V.; Izmaylov, A. F.; Sonnenberg, J. L.; Williams; Ding, F.; Lipparini, F.; Egidi, F.; Goings, J.; Peng, B.; Petrone, A.; Henderson, T.; Ranasinghe, D.; Zakrzewski, V. G.; Gao, J.; Rega, N.; Zheng, G.; Liang, W.; Hada, M.; Ehara, M.; Toyota, K.; Fukuda, R.; Hasegawa, J.; Ishida, M.; Nakajima, T.; Honda, Y.; Kitao, O.; Nakai, H.; Vreven, T.; Throssell, K.; Montgomery Jr., J. A.; Peralta, J. E.; Ogliaro, F.; Bearpark, M. J.; Heyd, J. J.; Brothers, E. N.; Kudin, K. N.; Staroverov, V. N.; Keith, T. A.; Kobayashi, R.; Normand, J.; Raghavachari, K.; Rendell, A. P.; Burant, J. C.; Iyengar, S. S.; Tomasi, J.; Cossi, M.; Millam, J. M.; Klene, M.; Adamo, C.; Cammi, R.; Ochterski, J. W.; Martin, R. L.; Morokuma, K.; Farkas, O.; Foresman, J. B.; Fox, D. J. *Gaussian 16 Rev. C.01*, Wallingford, CT, 2016.

9. Zhao, Y.; Truhlar, D. G., The M06 Suite of Density Functionals for Main Group Thermochemistry, Thermochemical Kinetics, Noncovalent Interactions, Excited States, and Transition Elements: Two New Functionals and Systematic Testing of Four M06-Class Functionals and 12 Other Functionals. *Theoretical Chemistry Accounts* **2008**, *120*, 215-241.
10. Artús Suárez, L.; Culakova, Z.; Balcells, D.; Bernskoetter, W. H.; Eisenstein, O.; Goldberg, K. I.; Hazari, N.; Tilset, M.; Nova, A., The Key Role of the Hemiaminal Intermediate in the Iron-Catalyzed Deaminative Hydrogenation of Amides. *ACS Catal.* **2018**, *8*, 8751-8762.
11. Hay, P. J.; Wadt, W. R., Ab Initio Effective Core Potentials for Molecular Calculations. Potentials for the Transition Metal Atoms Sc to Hg. *J. Chem. Phys.* **1985**, *82*, 270-283.
12. Franchl, M. M.; Pietro, W. J.; Hehre, W. J.; Binkley, J. S.; Gordon, M. S.; DeFrees, D. J.; Pople, J. A., Self-Consistent Molecular Orbital Methods. XXIII. A Polarization-Type Basis Set for Second-Row Elements. *J. Chem. Phys.* **1982**, *77*, 3654-3665.

Appendix D: Supporting Information for Chapter 5

I. Experimental Procedures

General Methods

Experiments were performed under a dinitrogen atmosphere in an M-Braun glovebox or using standard Schlenk techniques unless otherwise noted. Under typical operating conditions, the glovebox was not purged between use of benzene, diethyl ether, pentane, THF, 1,4-dioxane, or toluene. As a consequence, each solvent should be assumed to contain trace amounts of the others. All moisture and air-sensitive liquids were either transferred inside the glovebox or using a stainless steel cannula on a Schlenk line. Solvents were dried by passage through a column of activated alumina and stored under dinitrogen unless otherwise noted.

Ethanol (200 proof) was purchased from Decon Laboratories, Inc., and degassed and stored under dinitrogen prior to use. All commercial chemicals were used as received except where noted. Anhydrous FeCl_2 was purchased from Alfa Aesar. NaBH_4 and $n\text{Bu}_4\text{NBH}_4$ were purchased from Acros. LiHBEt_3 was purchased as a 1.7 M solution in THF from Acros. DBU was purchased from Fisher Scientific, dried over calcium hydride, and distilled prior to use. $\text{Fe}(\text{CO})_5$, $\text{NiCl}_2(\text{DME})$, CoCl_2 , PMe_3 , and PPh_3 were purchased from MilliporeSigma. Anhydrous pyridine was purchased from MilliporeSigma and distilled prior to use. 99.9% LiPF_6 was purchased from Strem. HPLC standard grade formic acid was purchased from Fisher, crystallized at 5 °C, and degassed prior to use. C_6D_6 was obtained from Cambridge Isotope Laboratories and dried by passage through a plug of activated alumina.

NMR spectra were recorded on Bruker AMX-400, AMX-500 or AMX-600 spectrometers at ambient probe temperatures, unless otherwise noted. Chemical shifts are reported in ppm with respect to residual internal protio solvent for ^1H and $^{13}\text{C}\{^1\text{H}\}$ NMR spectra. $^{31}\text{P}\{^1\text{H}\}$ NMR spectra are referenced via the ^1H resonances based on the relative gyromagnetic ratios.¹ All J coupling constant values are given in Hertz. Elemental analyses were performed by Robertson Microlit Laboratories, Inc. Infrared data were obtained on a Bruker ALPHA FTIR spectrometer with a platinum ATR attachment inside a N_2 -filled glovebox. All samples were taken of the neat solid. UV-Vis data were collected on a Shimadzu UV-3600 Plus spectrophotometer.

Mass spectrometric measurements were performed with a Thermo Fisher QExactive Orbitrap LC-MS system using continuous injection with a syringe. A sample of $\text{L}\cdot(\text{BH}_3)_2$ was prepared in a glove box and loaded into a gas tight syringe. The syringe and the PEEK capillaries to the ion source of the MS were cleaned with dry and oxygen-free solvents before sample injection. The sample was held at room temperature and continuously injected using a syringe pump at 30 $\mu\text{L}/\text{min}$. Electrospray was used for desolvatization and ionization, with the electrospray needle held at +3.5kV. Compressed air was used as the desolvatization gas, the capillary temperature was 320 $^\circ\text{C}$, the probe heater temperature 40 $^\circ\text{C}$, and the sheath gas flow was 5 L/min. The resolution was set to 14,000 $\text{M}/\Delta\text{M}$. Mass spectra were recorded in the range of 150 to 2000 m/z in positive ion mode. Measurements and data post-processing were performed with Thermo Xcalibur 4.1.31.9. Literature procedures were used to synthesize $^{\text{iPr}}\text{PN}^{\text{Ph}}\text{P}$ and **2-Me**.²

Mössbauer Spectroscopy

Mössbauer data were recorded on a See Co. MS4 Mössbauer spectrometer with alternating constant acceleration integrated with a Janis SVT-400T He/N₂ cryostat with a 50 mT applied magnetic field. All measurements were performed at 80 K. Isomer shifts were determined relative to α -Fe at 298 K. Mössbauer spectra were fit to Lorentzian doublets using the program WMoss (SEECO). Mössbauer spectra were recorded on 30-40 mg of compound with natural abundance Fe.

II. Synthetic Procedures and Characterizing Data for New Compounds

(κ^2 -ⁱPrPN^{Ph}P)FeCl₂ (1)

To a 100 mL Schlenk flask equipped with a magnetic stir bar were added ⁱPrPN^{Ph}P (344 mg, 0.901 mmol), FeCl₂ (114 mg, 0.901 mmol), and THF (20 mL). The flask was equipped with a reflux condenser and heated at reflux for 2 hours, then cooled to room temperature. The volatiles were then removed *in vacuo*. The crude product was extracted in 3x5 mL THF and concentrated to ~5 mL. Pentane (8 mL) was layered on top and the solution cooled to -35 °C. The product precipitated from solution overnight as a white powder, yield 380 mg (83%). Single crystals suitable for X-ray diffraction were grown by slow diffusion of Et₂O into a concentrated THF solution at -35 °C.

Anal. Found (calc'd) for FeNP₂Cl₂C₂₂H₄₁: C, 51.83 (51.99); H, 7.89 (8.13); N, 2.75 (2.76). ¹H NMR (500 MHz, C₆D₆): 72.97, 70.98, 15.91, 6.98, 6.76, 4.33 ppm. Effective magnetic moment (C₆D₆): 4.52 μ_B . IR, solid state (cm⁻¹) 2959, 2928, 2865, 2791, 1595, 1493, 1456, 1166, 1132, 771, 705, 655.

(ⁱPrPN^{Ph}P)FeH(κ^2 -BH₄) (2)

To a 50 mL Schlenk flask equipped with a magnetic stir bar were added **1** (63.0 mg, 0.124 mmol), NaBH₄ (46.8 mg, 1.24 mmol), benzene (5 mL), and ethanol (5 mL). Upon addition of ethanol, the reaction solution darkened from colorless to deep brown, and gas evolution was observed. The reaction was stirred at room temperature for 2 hours, then the volatiles were removed *in vacuo*. The crude product was extracted in 4x2 mL pentane and the solution concentrated to 4 mL. The product precipitated from solution as a brown crystalline solid at -35 °C, yield 49.0 mg (87%). Single crystals suitable for X-ray diffraction were grown from a concentrated pentane solution at -35 °C.

The solid was not stable to vacuum for more than 10 minutes, so elemental analysis could not be performed, although it was possible to dry a sample for Mössbauer spectroscopy. ¹H NMR (400 MHz, C₆D₆): 7.70 (d, 2H, CH_{Ar}, *J*=7.89 Hz), 6.89 (t, 2H, CH_{Ar}, *J*=7.14 Hz), 6.81 (t, 1H, CH_{Ar}, *J*=7.14 Hz), 2.91 (m, 2H, CH₂), 2.52 (m, 2H, CH₂), 2.40 (m, 2H, CH₂), 1.92 (m, 2H, CH₂), 1.56 (m, 8H, CHCH₃ + CHCH₃), 1.47 (m, 8H, CHCH₃ + CHCH₃), 1.23 (m, 6H, CHCH₃), 1.14 (m, 8H, CHCH₃ + BH₂), -10.96 (br, 1H, FeH), -24.25 (t, 1H, FeH, *J*=53.1 Hz), -40.32 ppm (br, 1H, FeH). ³¹P{¹H} NMR (162 MHz, C₆D₆): 90.2 ppm. ¹³C{¹H} NMR (151 MHz, C₆D₆): 148.50, 128.35, 127.98, 127.74, 126.92, 65.36, 26.37 (t, *J*=11.57 Hz), 23.31 (t, *J*=5.5 Hz), 21.36 (t, *J*=5.93 Hz), 20.02 (t, *J*=2.62 Hz), 19.49, 19.45 (m), 17.41 ppm (m). IR, solid state (cm⁻¹): 2926, 2863, 2380, 2345, 2306, 1878, 1717, 1597. UV-Vis (THF, (λ_{max}, ε)): 362 nm, 930 M⁻¹cm⁻¹.

(PhN{CH₂CH₂PⁱPr₂(BH₃)}₂(L•(BH₃)₂))

In a dinitrogen glovebox, to a 15 mL scintillation vial were added ⁱPrPN^{Ph}P (60.0 mg, 0.157 mmol), THF (3 mL), and BH₃•THF (1 M in THF, 472 μL, 0.472 mmol). The vial was capped and shaken briefly, then the volatiles were removed *in vacuo*. The resulting white

solid was washed with 2x2 mL pentane and dried to obtain pure product as a white crystalline solid, yield 59.9 mg (93%). Single crystals suitable for X-ray diffraction were grown from a reaction of **2** and CO in a concentrated pentane solution at -35 °C.

^1H NMR (400 MHz, C_6D_6): 7.29 (t, 2H, CH_{Ar} , $J=7.61$ Hz) 6.93 (d, 2H, CH_{Ar} , $J=8.21$ Hz), 6.78 (t, 1H, CH_{Ar} , $J=7.25$ Hz), 3.95 (t, 2H, CH_2 , $J=6.45$ Hz), 3.68 (m, 4H, CH_2), 3.53 (m, 2H, CH_2), 1.63 (m, 4H, CHCH_3), 1.52 (m, 6H, BH_3), 0.98-0.92 (m, 12H, CHCH_3) 0.88-0.83 ppm (m, 12H, CHCH_3). $^{31}\text{P}\{^1\text{H}\}$ NMR (162 MHz, C_6D_6): 31.69 ppm (br d, $J=66.8$ Hz). $^{13}\text{C}\{^1\text{H}\}$ NMR (151 MHz, C_6D_6): 147.11, 130.17, 128.35, 117.83, 113.25, 63.29, 46.05 (d, $J=5.58$ Hz), 34.17, 22.26 (d, $J=32.55$ Hz), 19.46, 17.07, 16.89, 16.85, 16.72 ppm (m). IR, solid state (cm^{-1}): 2955, 2873, 2361, 1595, 1505, 1354, 1040, 742. HRMS (E^+): 410.3437 $[\text{M}+\text{H}]^+$. Calc for $[\text{C}_{22}\text{H}_{48}\text{P}_2\text{B}_2\text{N}]$: 410.3443.

$(^{\text{iPr}}\text{PN}^{\text{Ph}}\text{P})\text{Fe}(\text{CO})_2$ (**3**)

To a 50 mL Kontes valve flask equipped with a magnetic stir bar were added **2** (25.0 mg, 0.0551 mmol), DBU (16 μL , 0.11 mmol), and benzene (5 mL). The solution was frozen at -196 °C, degassed, and 1 atm CO was added. The reaction flask was sealed, allowed to warm to room temperature, and stirred for one hour, during which time the color lightened from brown to bright orange. The volatiles were then removed *in vacuo* and the crude product was extracted in 3x3 mL pentane. This solution was concentrated to ~3 mL, and single crystals suitable for X-ray diffraction were grown at -35 °C. There was difficulty reproducing this synthesis to isolate clean material without the presence of free $^{\text{iPr}}\text{PN}^{\text{Ph}}\text{P}$. Select characterizing data that was obtained are provided below.

^1H NMR (500 MHz, C_6D_6): 7.95 (br, 2H, CH_{Ar}), 6.98 (t, 2H, CH_{Ar} , $J=7.56$ Hz), 6.89 (t, 1H, CH_{Ar} , $J=7.24$ Hz), 2.97 (m, 4H, CH_2), 2.21 (m, 2H, CH_2), 2.05 (m, 2H, CH_2), 1.30-

1.41 (m, 15H, $\text{CHCH}_3 + \text{CHCH}_3$), 1.23-1.15 ppm (m, 13H, $\text{CHCH}_3 + \text{CHCH}_3$). $^{31}\text{P}\{^1\text{H}\}$ NMR (202 MHz, C_6D_6): 96.26 ppm. $^{13}\text{C}\{^1\text{H}\}$ NMR (151 MHz, C_6D_6): 223.00 (FeCO), 218.93 (FeCO), 148.73, 128.35, 127.50, 63.12 (t, $J=4.38$ Hz), 28.24 (t, $J=10.8$ Hz), 26.99 (t, $J=11.0$ Hz), 25.34 (t, $J=5.17$ Hz), 19.11, 18.78, 18.34 ppm. IR, solid state (cm^{-1}): 2926, 2871, 1835 ($\text{C}=\text{O}$), 1772 ($\text{C}\equiv\text{O}$).

$(\kappa^2\text{-iPrPN}^{\text{Ph}}\text{P})\text{CoCl}_2$ (**4**)

To a 100 mL Schlenk flask equipped with a magnetic stir bar were added CoCl_2 (25.0 mg, 0.193 mmol) and ethanol (20 mL). In a vial, $\text{iPrPN}^{\text{Ph}}\text{P}$ (90.0 g, 0.236 mmol) was dissolved in ethanol (10 mL). This solution was then added dropwise to the CoCl_2 solution while swirling the Schlenk flask, which generated a bright blue suspension. The flask was sealed and stirred at room temperature for 4 hours, during which time the reaction became homogenous. The volatiles were removed *in vacuo*, producing a bright blue powder. The crude product was extracted with toluene (3x5 mL) and then concentrated to 5 mL and layered with 2 mL pentane. After allowing the solution to stand at $-35\text{ }^\circ\text{C}$ overnight, the product was obtained as blue block crystals, yield 79.0 mg (79%). Single crystals suitable for X-ray diffraction were also grown by slow diffusion of pentane into a concentrated toluene solution at $-35\text{ }^\circ\text{C}$.

^1H NMR (400 MHz, C_6D_6) 105.65, 89.26, 16.55, 6.52-5.71, 5.38, 4.73 ppm. Effective magnetic moment (C_6D_6): 4.1 μ_{B} . IR, solid state (cm^{-1}): 2967, 2875, 2803, 1602, 1505. UV-Vis (THF, (λ_{max} , ϵ)): 349 nm, 4663 $\text{M}^{-1}\text{cm}^{-1}$; 445 nm, 1723 $\text{M}^{-1}\text{cm}^{-1}$. Despite multiple attempts, we were unable to obtain a satisfactory elemental analysis of this compound.

$[(\text{iPrPN}^{\text{Ph}}\text{P})\text{NiCl}][\text{PF}_6]$ (**5**)

To a 50 mL Schlenk flask equipped with a magnetic stir bar were added $i\text{PrPN}^{\text{Ph}}\text{P}$ (100 mg, 0.262 mmol), $\text{NiCl}_2(\text{DME})$ (57.6 mg, 0.262 mmol), LiPF_6 (39.8 mg, 0.262 mmol), and CH_3CN (10 mL). The solution immediately turned bright red, then darkened over two hours while stirring at room temperature. The volatiles were removed *in vacuo*, and the residue was washed with 4x3 mL pentane. The crude product was extracted in 4x3 mL THF, concentrated to 6 mL, and 3 mL pentane was layered on top. The product precipitated from solution at $-35\text{ }^\circ\text{C}$ as an orange powder, yield 120 mg (74%). Single crystals suitable for X-ray diffraction were obtained by slow diffusion of benzene into a concentrated THF solution at room temperature.

^1H NMR (400 MHz, CH_3CN): 10.78 (br, 2H, CH_{Ar}), 7.65 (br, 2H, CH_{Ar}), 7.54 (t, 1H, CH_{Ar} , $J=7.12\text{ Hz}$), 3.43 (m, 2H, CH_2), 3.24 (m, 2H, CH_2), 2.51 (m, 2H, CH_2), 2.17 (m, 2H, CH_2), 1.80 (m, 2H, CHCH_3), 1.67 (m, 6H, CHCH_3), 1.54 (m, 6H, CHCH_3), 1.31 (m, 8H, CHCH_3 + CHCH_3), 1.14 ppm (m, 6H, CHCH_3). $^{31}\text{P}\{^1\text{H}\}$ NMR (162 MHz, CH_3CN): 41.31 (s, 2P, $i\text{PrPN}^{\text{Ph}}\text{P}$), -144.67 ppm (sept, 1P, PF_6 , $J=706\text{ Hz}$). ^{19}F NMR (376 MHz, CH_3CN): 72.98 ppm (d, 6F, PF_6 , $J=706\text{ Hz}$). $^{13}\text{C}\{^1\text{H}\}$ NMR (126 MHz, CH_3CN): 146.35, 131.34, 68.25, 65.93, 26.21, 25.52 (t, $J=10.6\text{ Hz}$), 24.60 (t, $J=12.1\text{ Hz}$), 20.74 (t, $J=8.7\text{ Hz}$), 19.99, 19.13, 18.66, 18.16 ppm. IR, solid state (cm^{-1}): 2963, 2955, 2887, 1458, 1248, 1028. UV-Vis (CH_3CN , (λ_{max} , ϵ)): 491 nm, $1109\text{ M}^{-1}\text{cm}^{-1}$. Despite multiple attempts, we were unable to obtain a satisfactory elemental analysis of this compound.

III. Procedures for Catalysis

General Methods for Catalytic Formic Acid Dehydrogenation

In the glovebox, to a 25 mL Schlenk flask equipped with a magnetic stir bar were added catalyst (291 μ L of a 1 mM stock solution in toluene) and toluene (1.67 mL total). The flask was sealed, removed from the glovebox, and placed under an N₂ atmosphere on a Schlenk line. A reflux condenser with a Kontes sidearm for addition of reagents was attached to a Kontes pin 3-way valve *via* Tygon tubing, thoroughly purged with N₂, then attached to the reaction flask (see SI for diagram). Anhydrous ^tBuOH (3.33 mL) was added to the reaction flask through a rubber septum placed on the condenser sidearm. The Tygon tubing leading from the 3-way valve to the oil bubbler was purged with N₂, then the bubbler was attached to a gas buret filled with mineral oil to prevent gas dissolution. The reaction flask was lowered into an oil bath preheated to 90 °C and allowed to equilibrate. Formic acid (110 μ L, 2.91 mmol) was added through a rubber septum placed on the condenser sidearm, then the sidearm was rapidly resealed with a Kontes pin, the system was cut off from active N₂ flow, and the reaction flask was opened to the gas buret *via* the 3-way valve. As gas evolution lowered the level of the oil in the buret, the separatory funnel was lowered to keep the oil levels approximately even and maintain roughly atmospheric pressure in the reaction. A second catalytic reaction was always performed in parallel and the turnover numbers reported are the average of the two experiments. A diagram showing the reaction setup used for formic acid dehydrogenation is provided in this Appendix, section XX.

IV. Full Spectra of Isolated Compounds 1-5, $L \cdot (BH_3)_2$

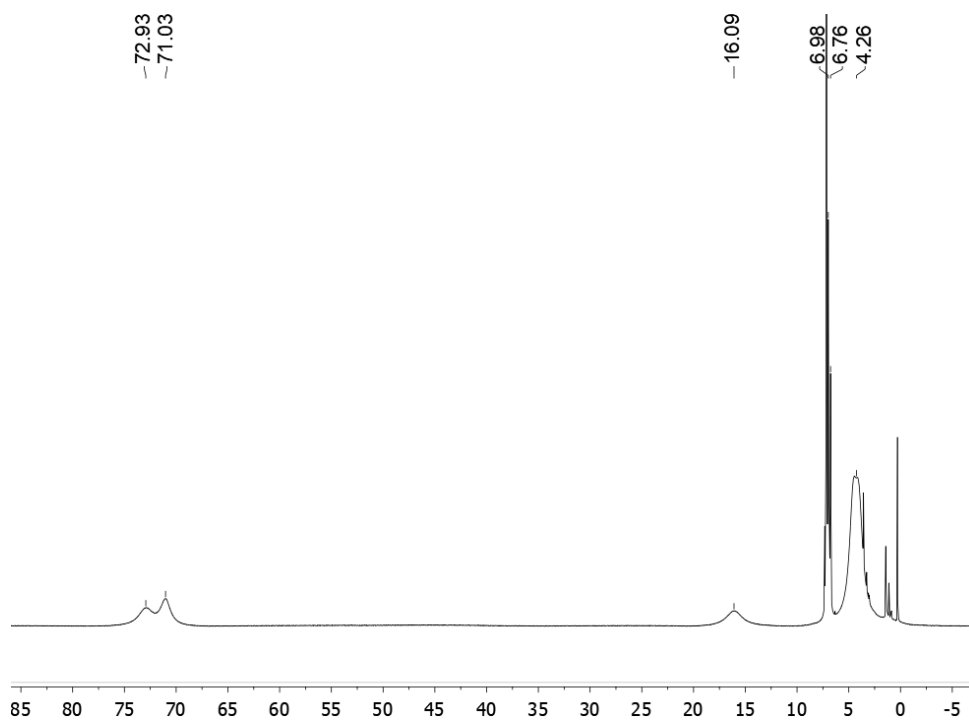
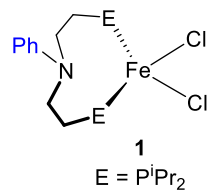


Figure D.01. ¹H NMR spectrum of **1** in C₆D₆.

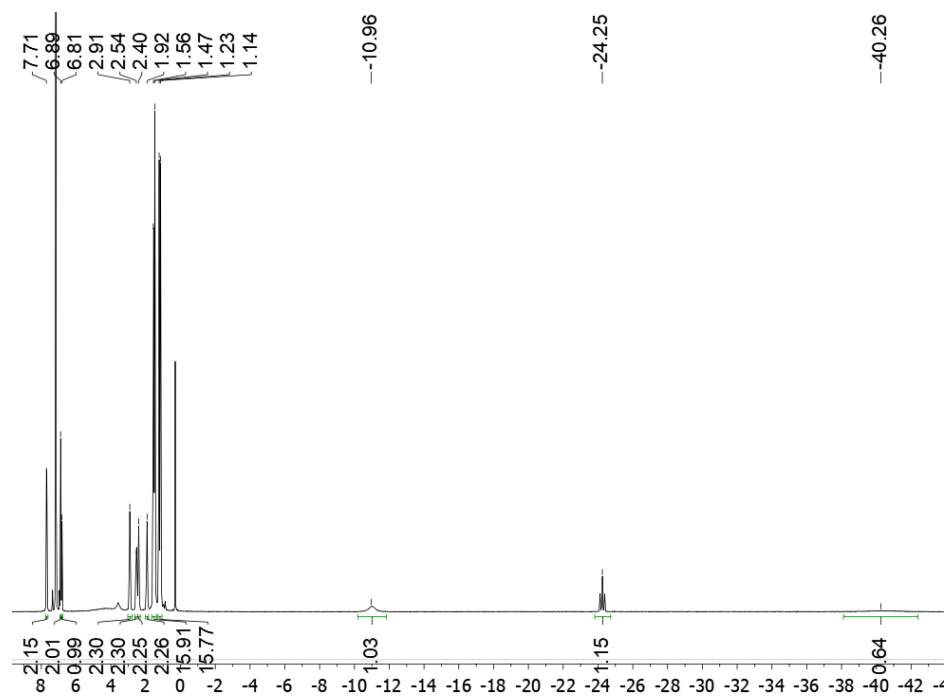
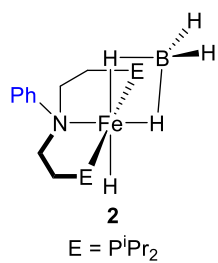
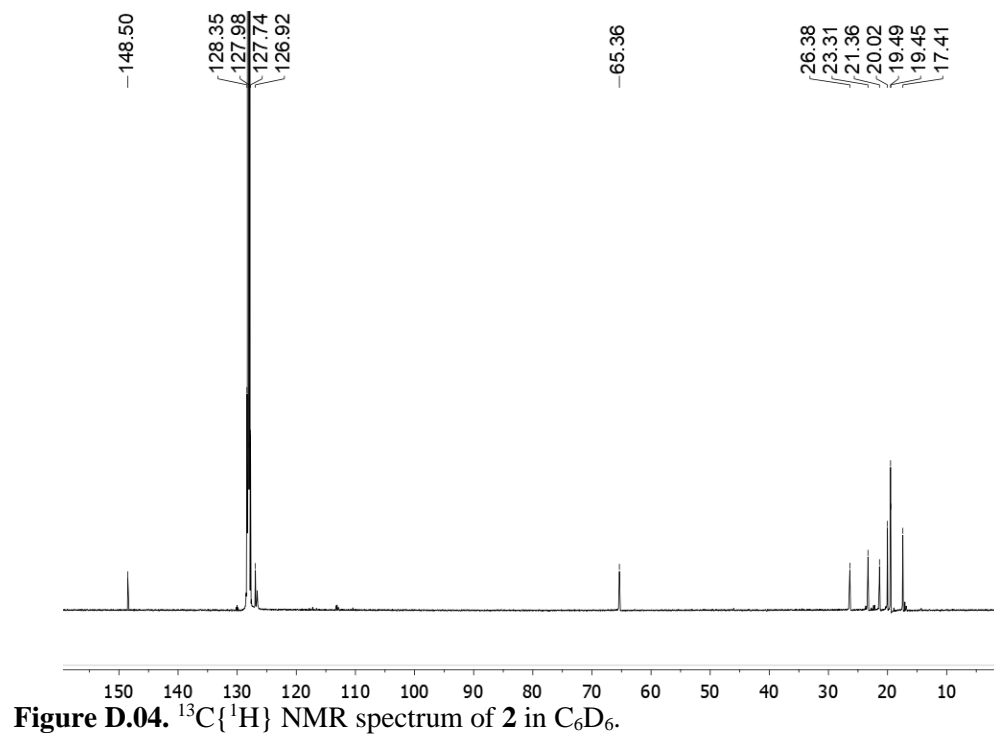
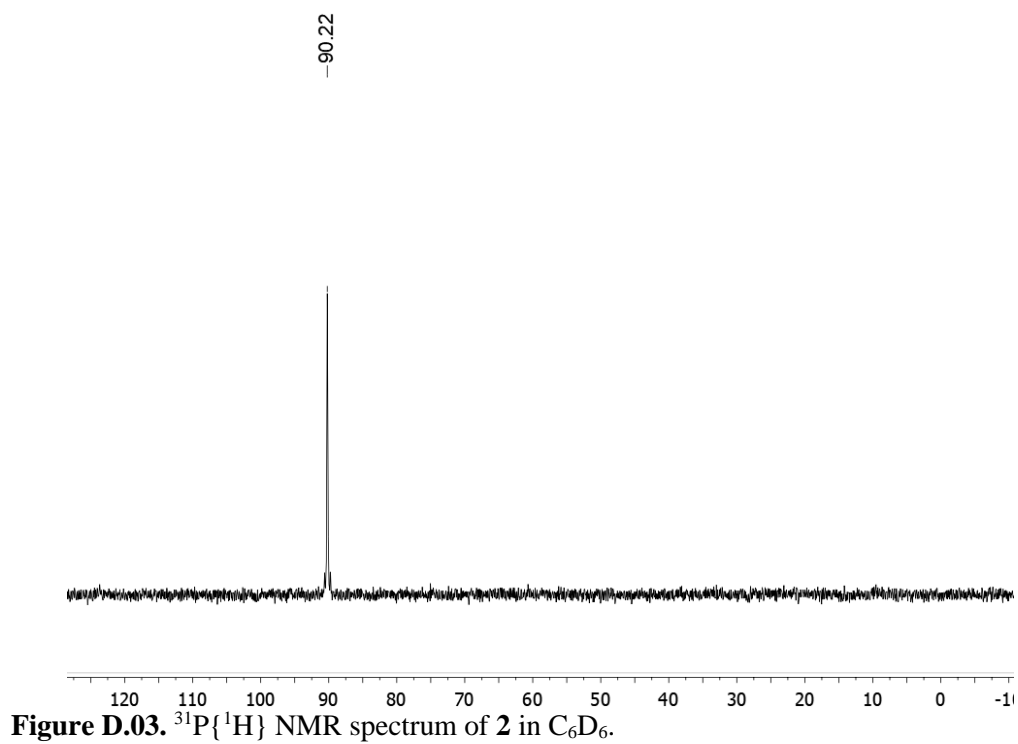


Figure D.02. 1H NMR spectrum of **2** in C_6D_6 .



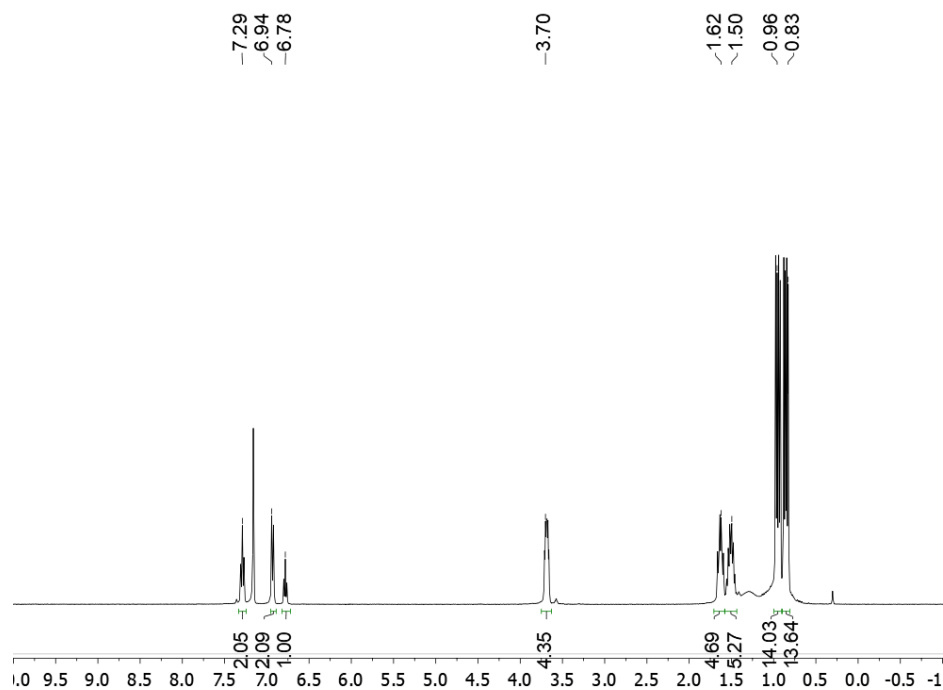
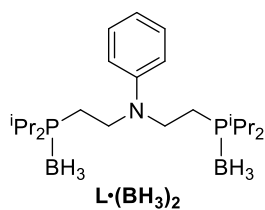
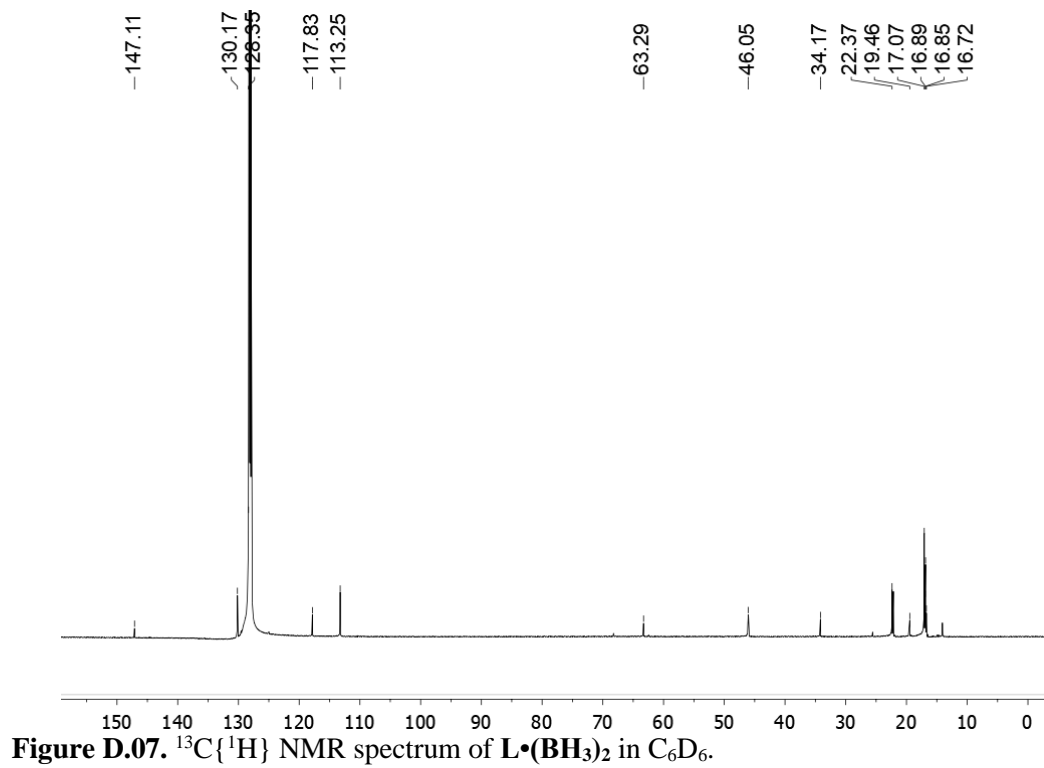
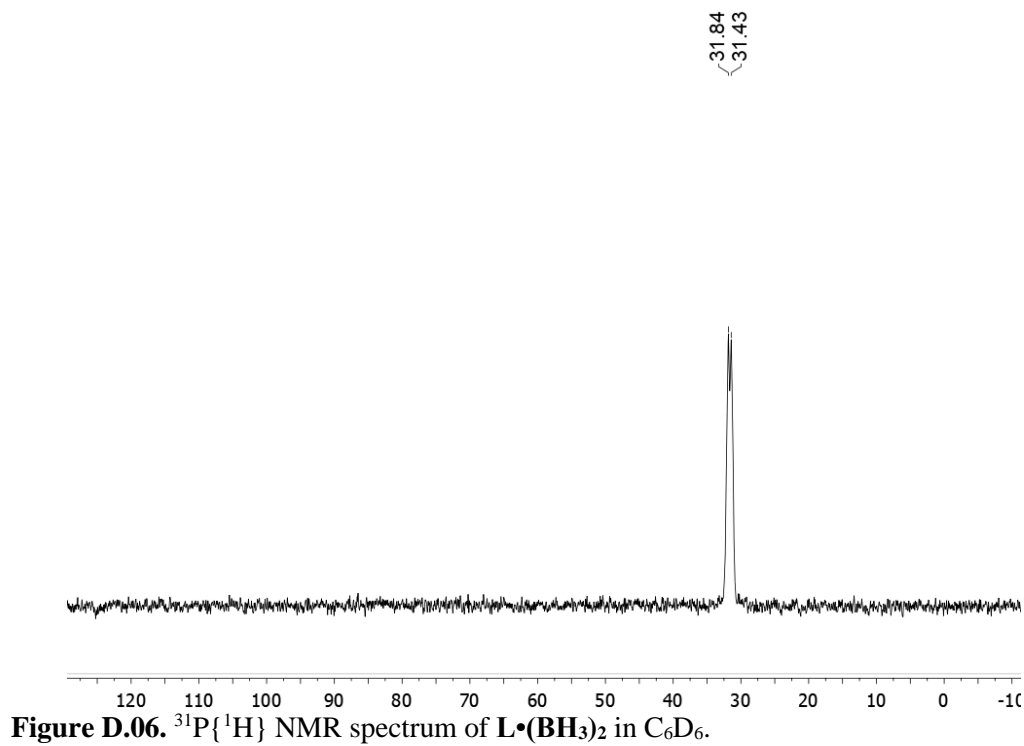


Figure D.05. ¹H NMR spectrum of **L•(BH₃)₂** in C₆D₆.



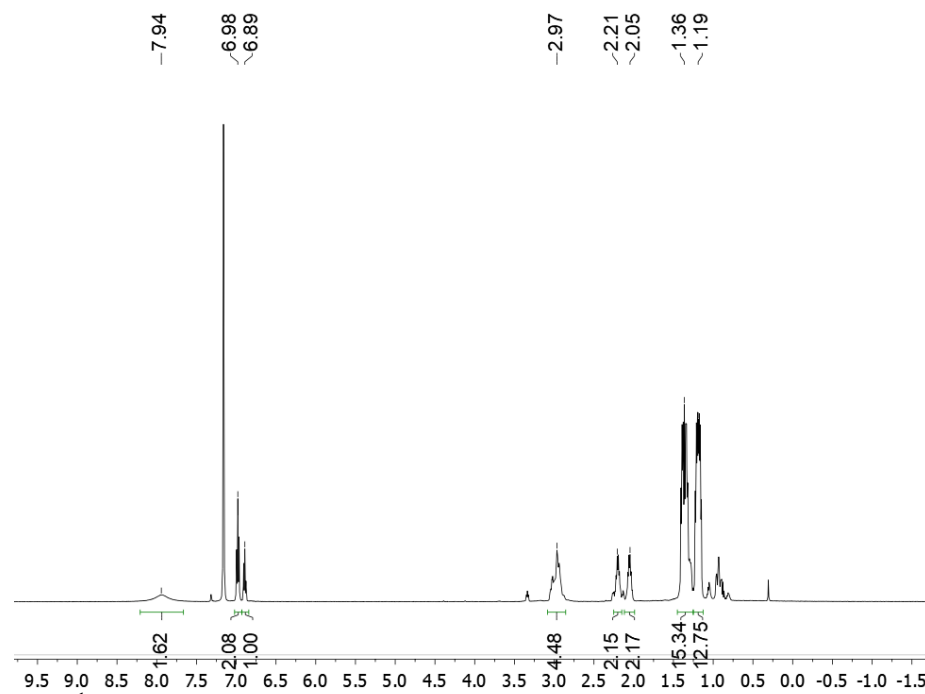
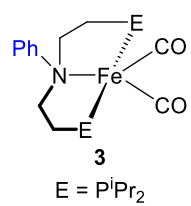
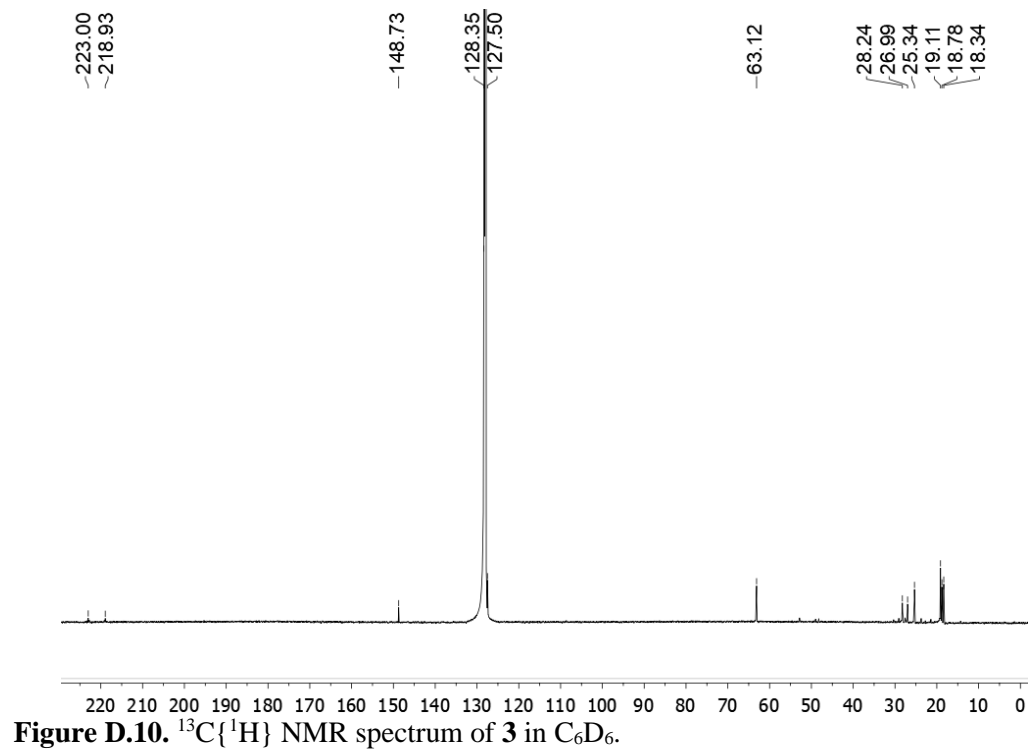
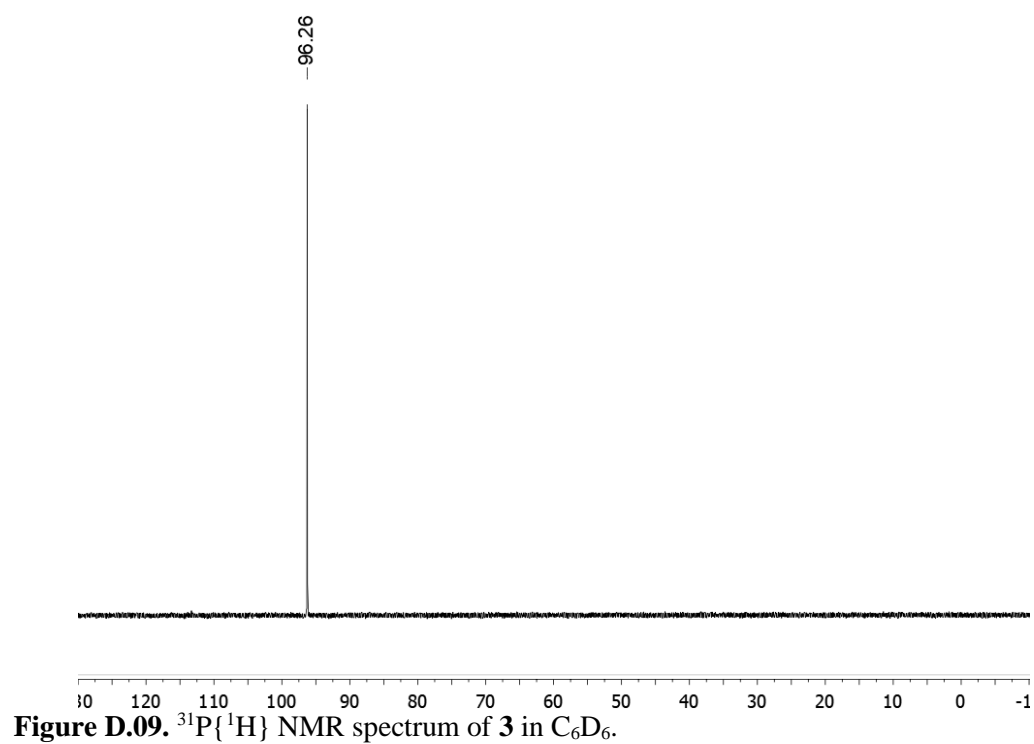


Figure D.08. 1H NMR spectrum of **3** in C_6D_6 .



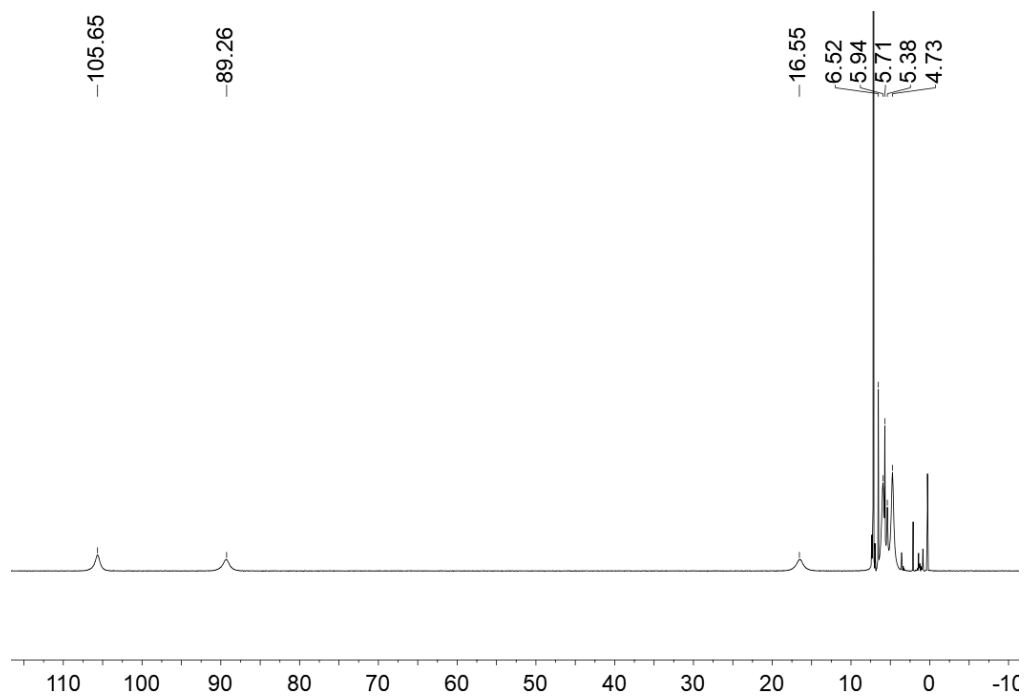
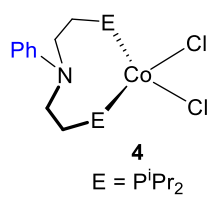


Figure D.11. 1H NMR spectrum of **4** in C_6D_6 .

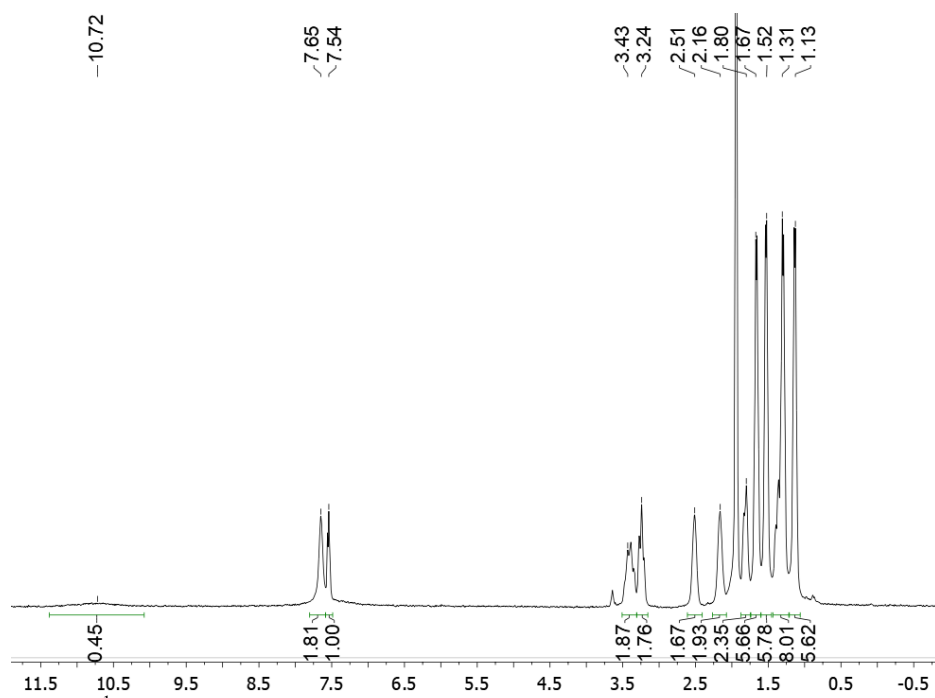
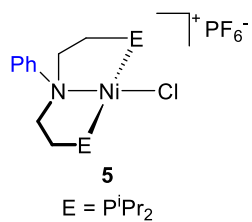
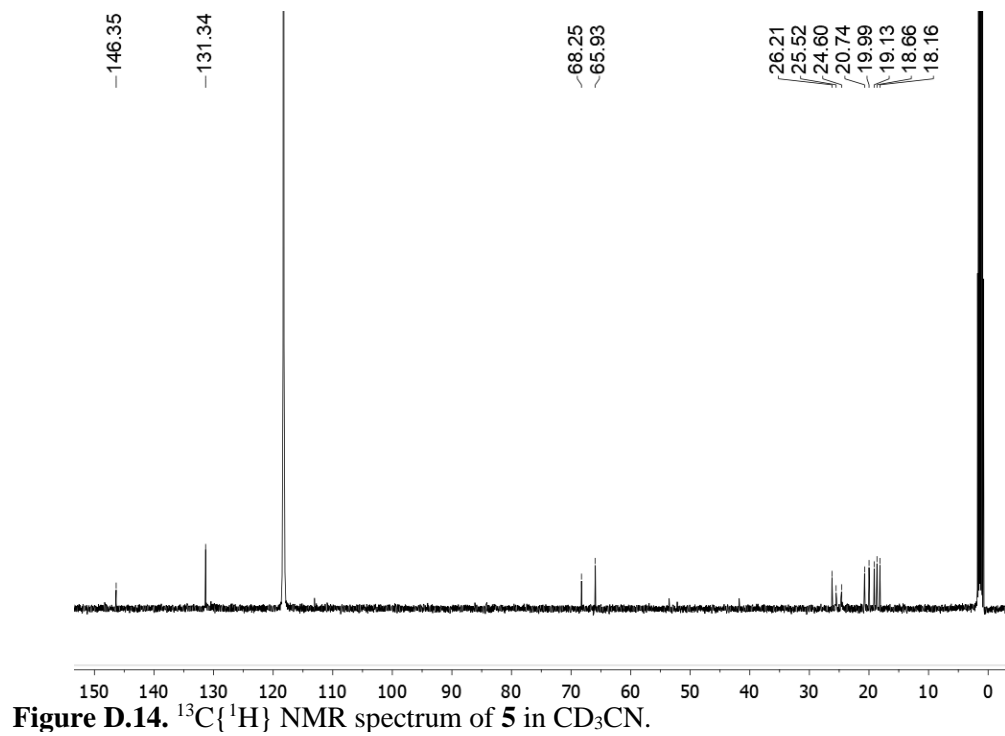
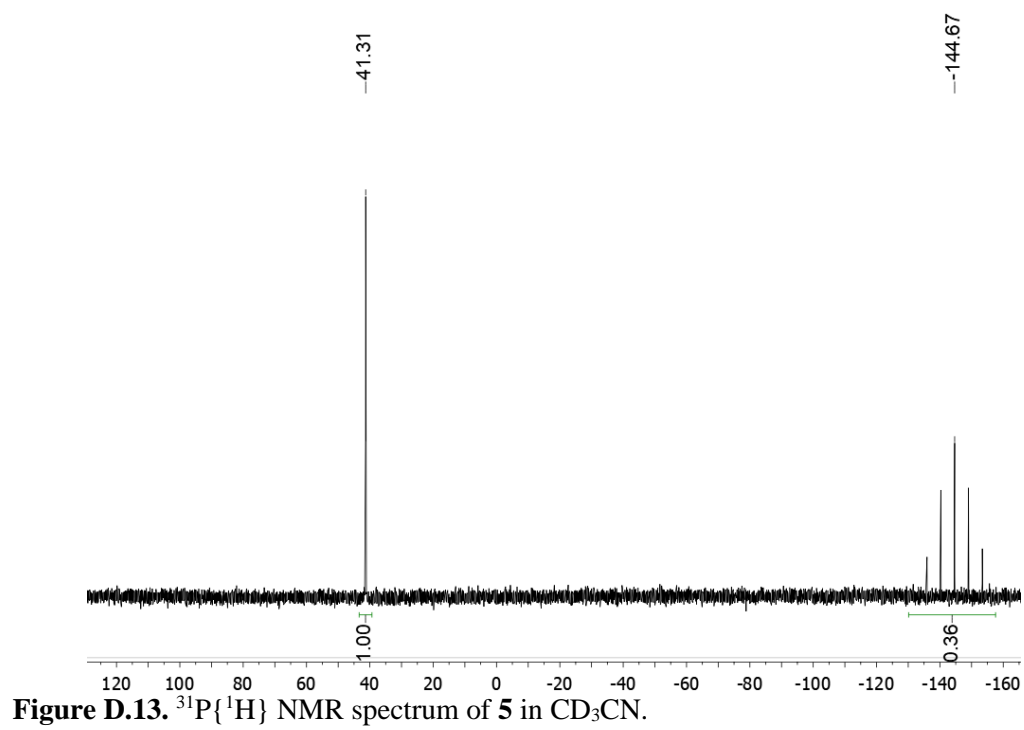
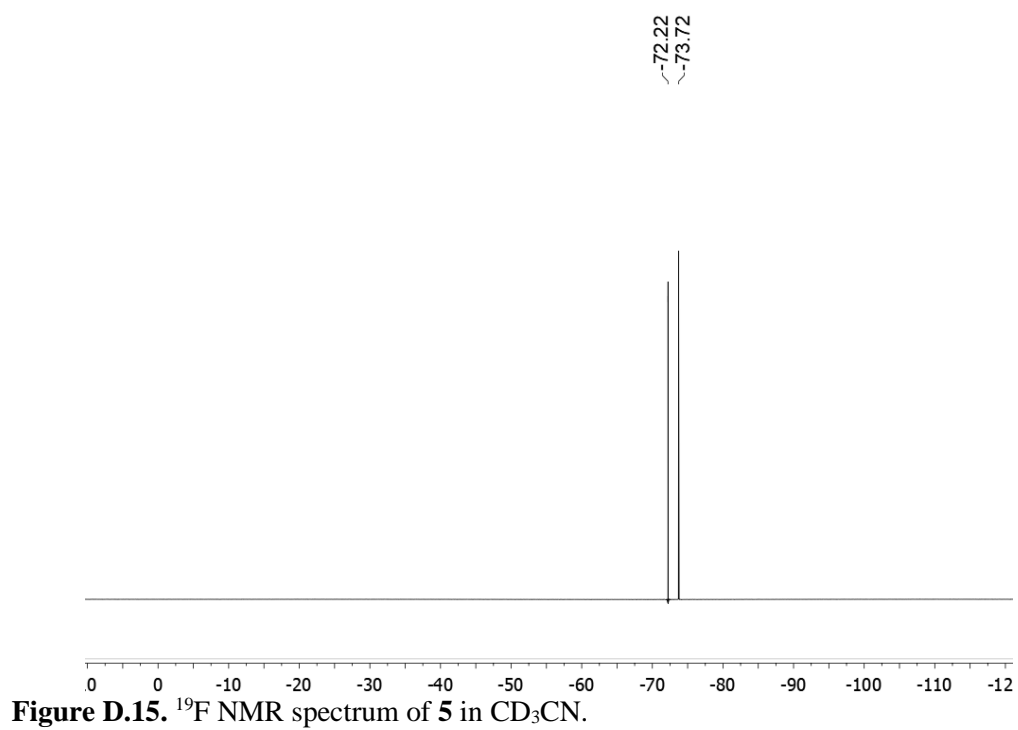


Figure D.12. 1H NMR spectrum of **5** in CD_3CN .





V. Mössbauer Spectrum of 2-Me

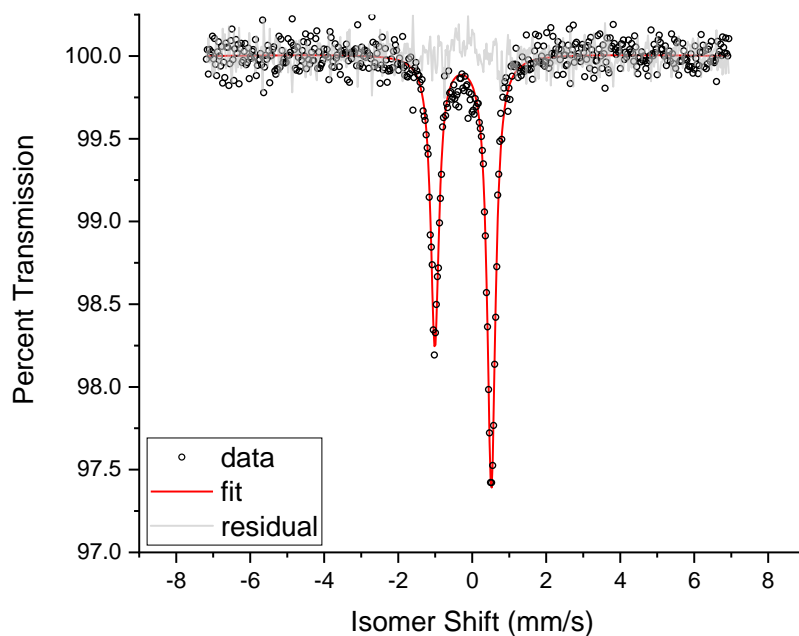
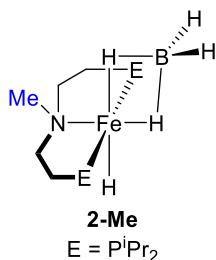
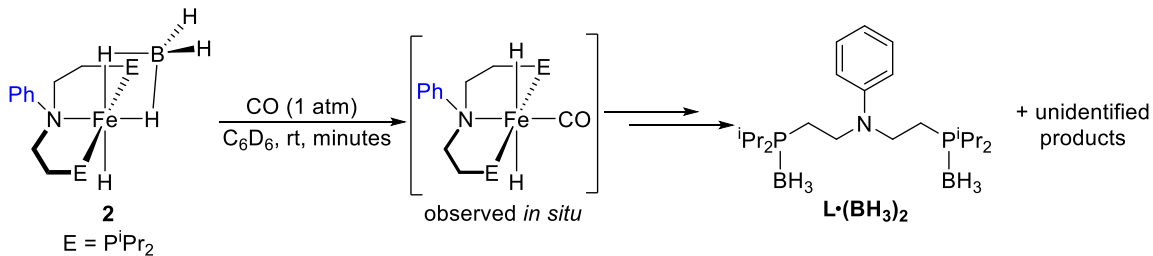


Figure D.16. ⁵⁷Fe Mössbauer spectrum obtained on a powder sample of **2-Me**; $\delta = -0.246$ mm/s, $\Delta E_Q = 1.53$ mm/s. Asymmetry in the doublet is due to crystallinity in the sample.

VI. Addition of CO to 2



NMR data for the reaction of **2** with CO in C₆D₆ is shown in Figures D.17-D.19, below. We propose based on the close similarity between the hydride chemical shifts in Figures D.18-D.19 and the previously isolated complex (iPrPN^{Me}P)Fe(H)₂(CO) (-8.90 and

-22.69 ppm) that the desired product ($i\text{PrPN}^{\text{Ph}}\text{P})\text{Fe}(\text{H})_2(\text{CO})$ is formed *in situ*,² however this is not the only product that is formed and it could not be isolated. After isolation, only $\text{L}\cdot(\text{BH}_2)_2$ was observed by ^{31}P NMR spectroscopy.

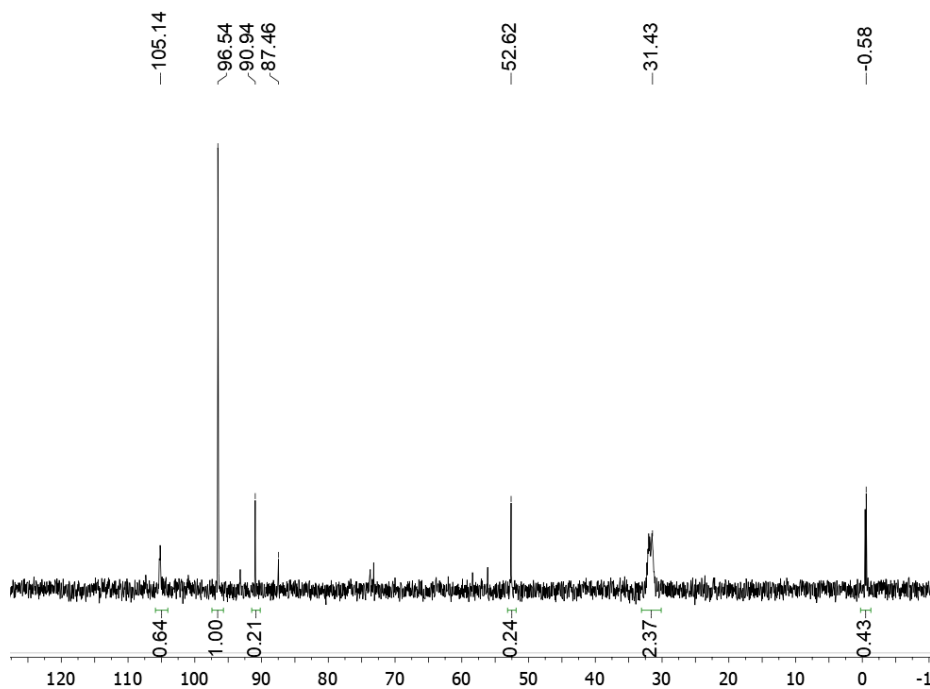


Figure D.17. $^{31}\text{P}\{^1\text{H}\}$ NMR spectrum from the reaction of **2** with CO in C_6D_6 after 15 minutes. ($i\text{PrPN}^{\text{Ph}}\text{P})\text{Fe}(\text{CO})_2$ (**3**) observed at 96.54 ppm, $\text{L}\cdot(\text{BH}_3)_2$ observed at 31.43 ppm, and $i\text{PrPN}^{\text{Ph}}\text{P}$ observed at -0.58 ppm. Identities of the other peaks are unknown.

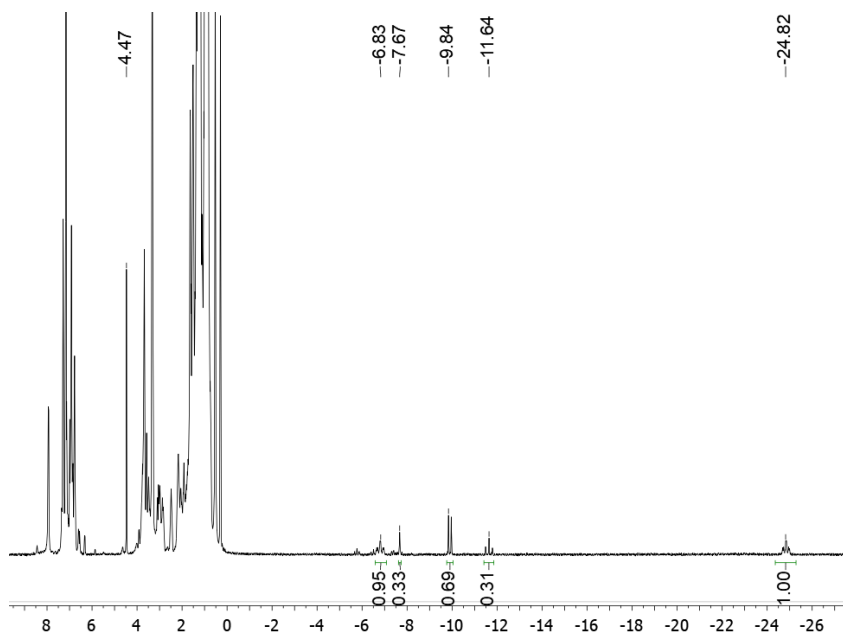


Figure D.18. ^1H NMR spectrum from the reaction of **2** with CO in C_6D_6 after 15 minutes. H_2 peak at 4.47 ppm.

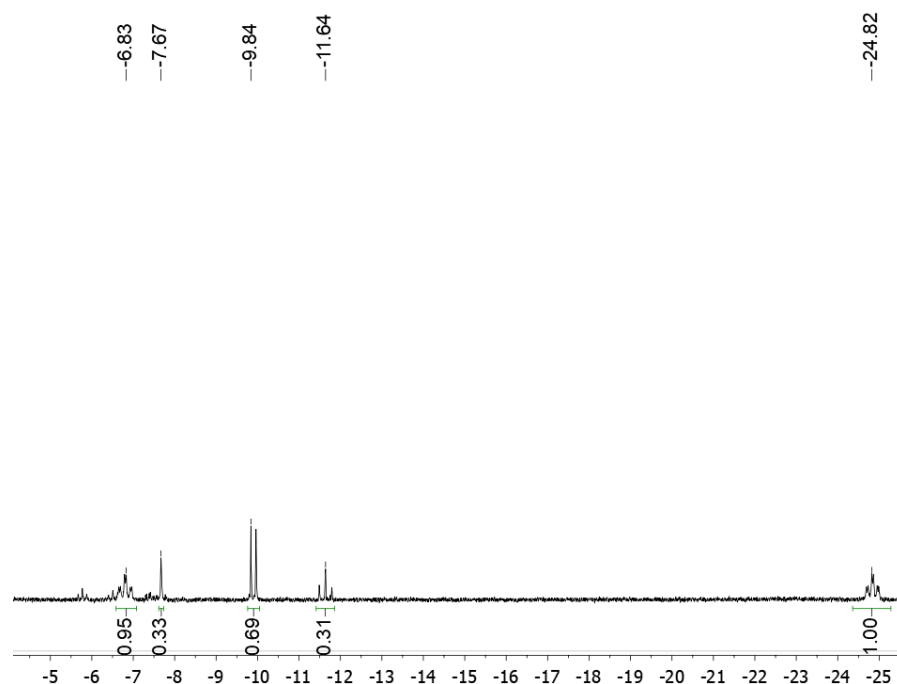
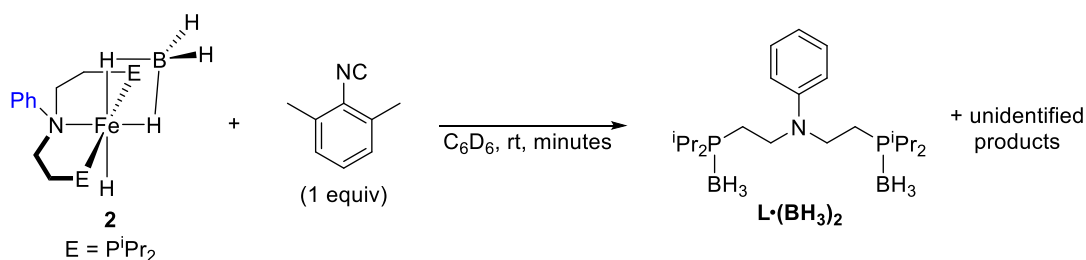


Figure D.19. Hydride region of the ^1H NMR spectrum from the reaction of **2** with CO in C_6D_6 after 15 minutes. 1:1 hydride peaks at -6.83 and -24.82 ppm are close to those of the major isomer of $\text{iPrPN}^{\text{Me}}\text{PFe}(\text{H})_2(\text{CO})$ (-8.90 and -22.69 ppm) and the td splitting is as expected for a dihydride complex.

VII. Reaction of **2** with 2,6-Dimethylphenyl Isonitrile



NMR data for the reaction of **2** with 2,6-dimethylphenyl isonitrile in C_6D_6 are shown in Figures D.20-D.21, below. Multiple unknown products were observed along with $\text{L} \cdot (\text{BH}_2)_2$, which was the only product observed after isolation.

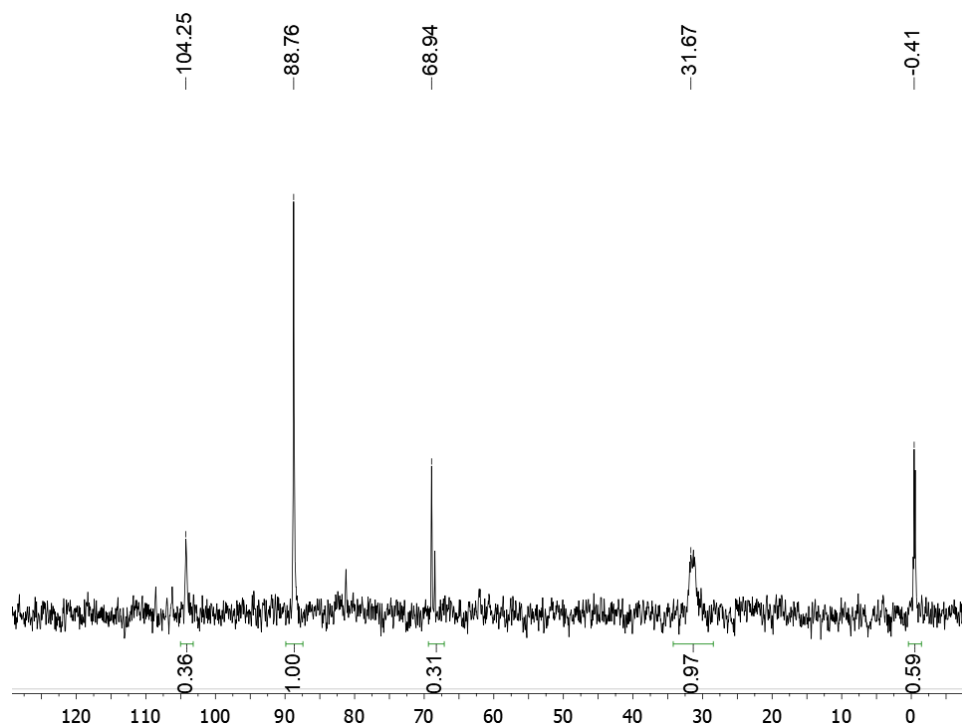


Figure D.20. $^{31}\text{P}\{^1\text{H}\}$ NMR spectrum from the reaction of **2** with 2,6-dimethylphenyl isonitrile in C_6D_6 after 15 minutes. $\text{L}\cdot(\text{BH}_3)_2$ observed at 31.67 ppm and $^{\text{iPr}}\text{PN}^{\text{Ph}}\text{P}$ observed at -0.41 ppm. Identities of the other peaks are unknown.

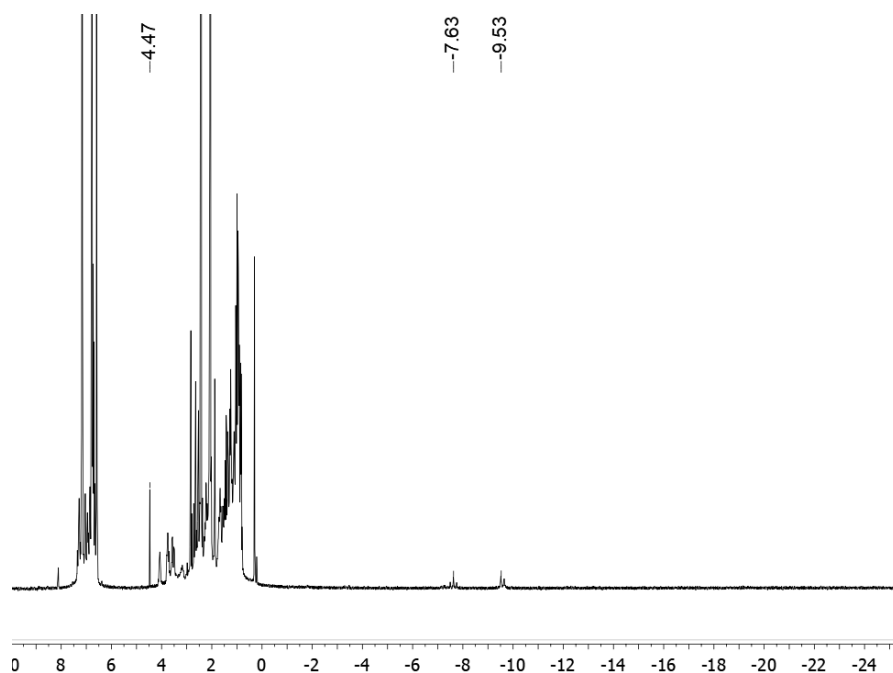
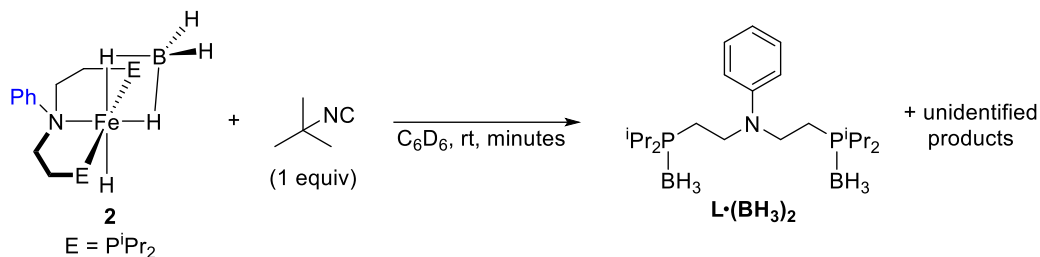


Figure D.21. ^1H NMR spectrum from the reaction of **2** with 2,6-dimethylphenyl isonitrile in C_6D_6 after 15 minutes. H_2 peak at 4.47 ppm.

VIII. Reaction of **2** with *tert*-butyl Isonitrile



NMR data for the reaction of **2** with *tert*-butyl isocyanide in C_6D_6 are shown in Figures D.22-D.23, below. Multiple unknown products were observed along with $L \cdot (BH_2)_2$, which was the only product observed after isolation.

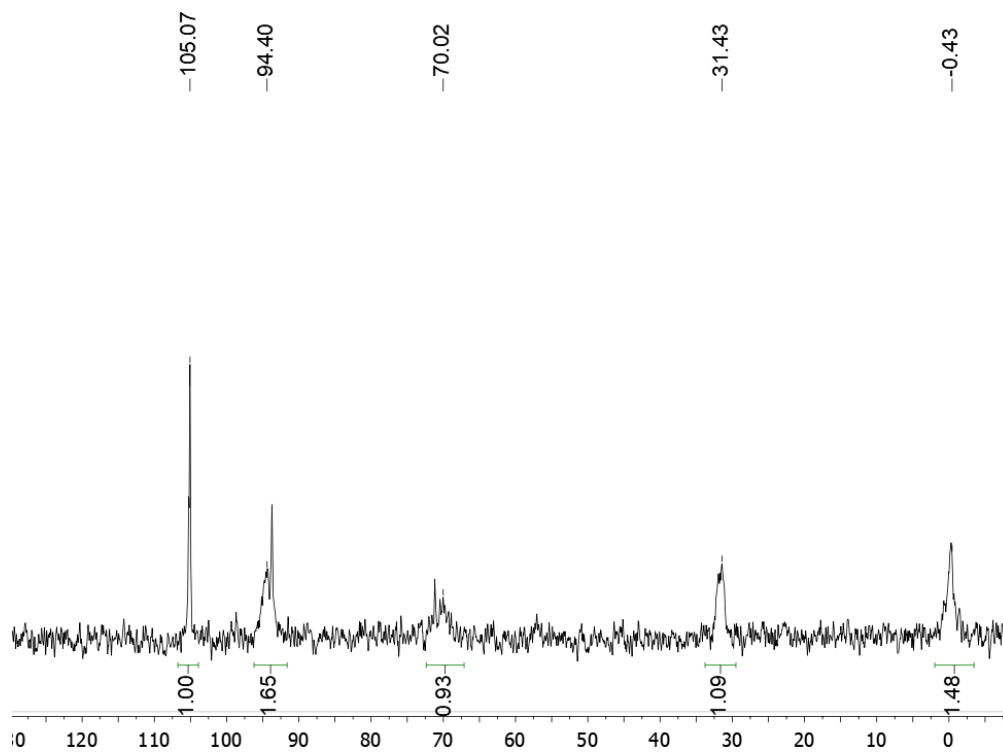


Figure D.22. $^{31}P\{^1H\}$ NMR spectrum from the reaction of **2** with *tert*-butyl isocyanide in C_6D_6 after 15 minutes. $L \cdot (BH_3)_2$ observed at 31.43 ppm and $iPrPN^{Ph}P$ observed at -0.43 ppm. Identities of the other peaks are unknown.

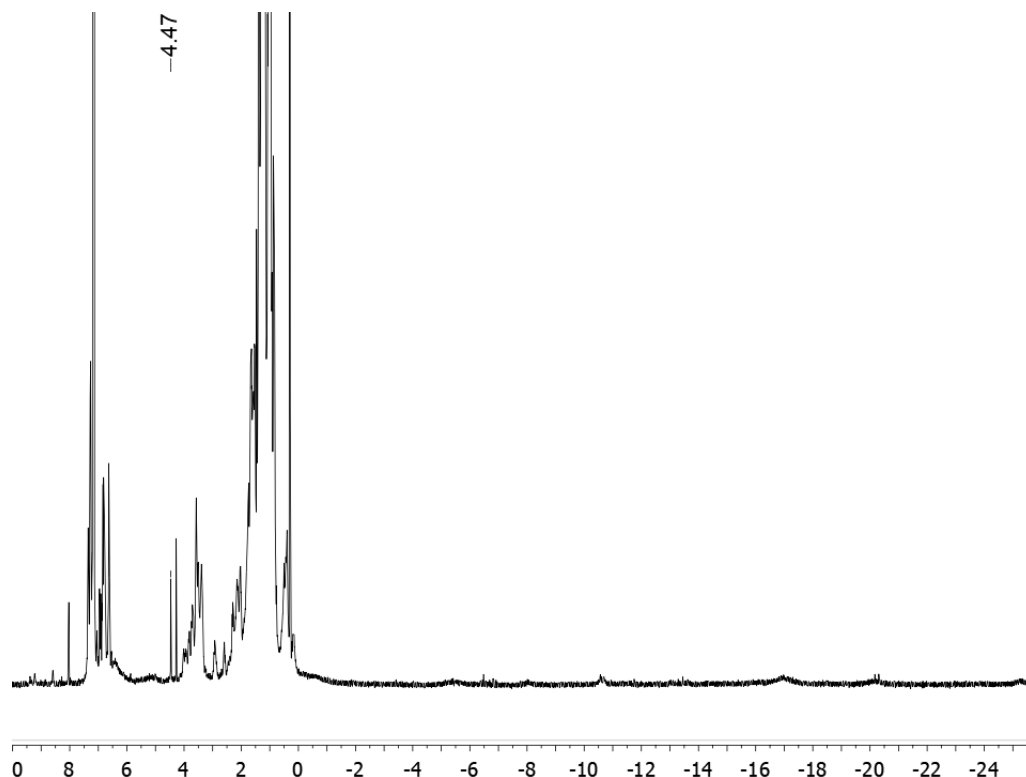
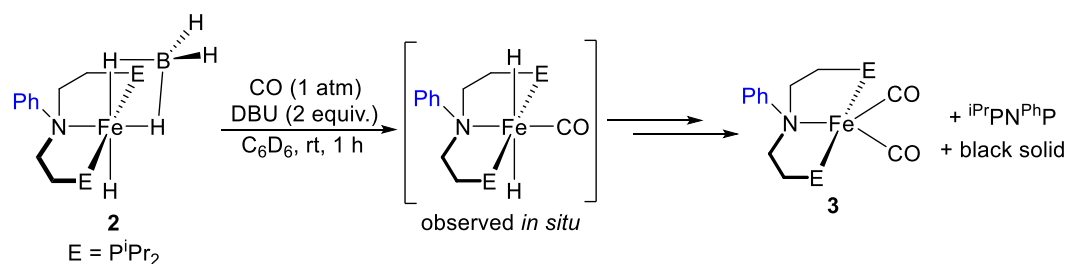


Figure D.23. ¹H NMR spectrum from the reaction of **2** with *tert*-butyl isonitrile in C₆D₆ after 15 minutes. H₂ peak at 4.47 ppm.

IX. Reaction of **2** with CO and DBU



NMR spectra for the reaction between **2**, CO, and DBU in C₆D₆ are shown in Figures D.24-D.25. Although the formation of a precipitate in the J. Young NMR tube caused poor shimming and broad spectra, we propose based on the identical hydride chemical shifts here and in Figures D.18-D.19 that the desired product (*i*PrPN^{Ph}P)Fe(H)₂(CO) was formed *in situ*,² but only **3** was observed after isolation.

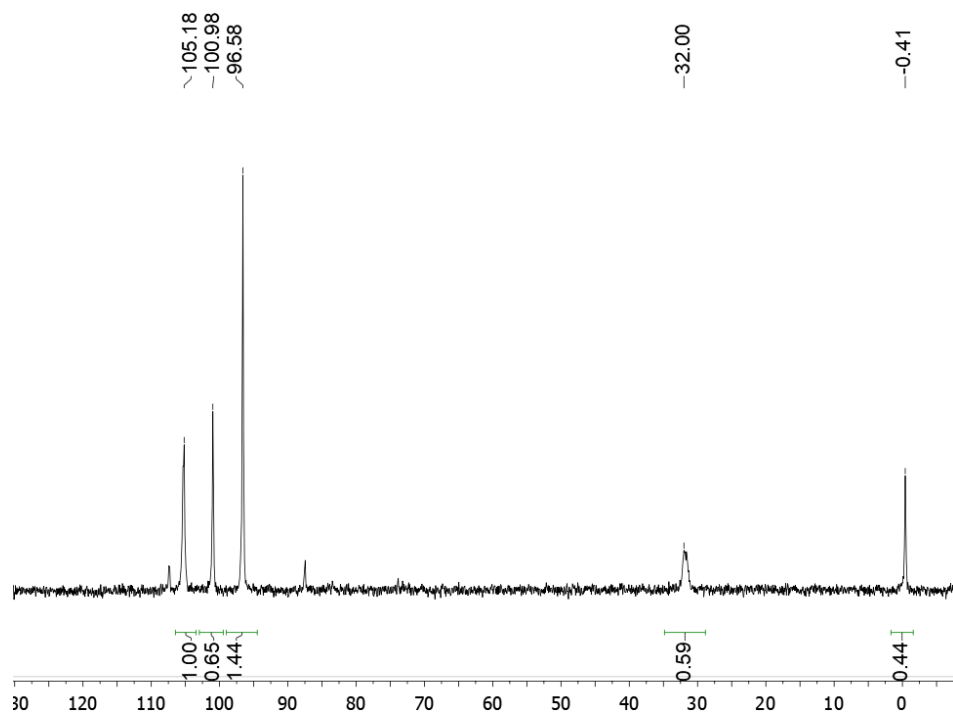


Figure D.24. $^{31}\text{P}\{^1\text{H}\}$ NMR spectrum from the reaction of **2** with CO and DBU in C_6D_6 after 15 minutes. $(^{\text{iPr}}\text{PN}^{\text{Ph}}\text{P})\text{Fe}(\text{CO})_2$ (**3**) observed at 96.58 ppm, $\text{L}\cdot(\text{BH}_3)_2$ observed at 32.00 ppm, and $^{\text{iPr}}\text{PN}^{\text{Ph}}\text{P}$ observed at -0.41 ppm. Identities of the other peaks are unknown.

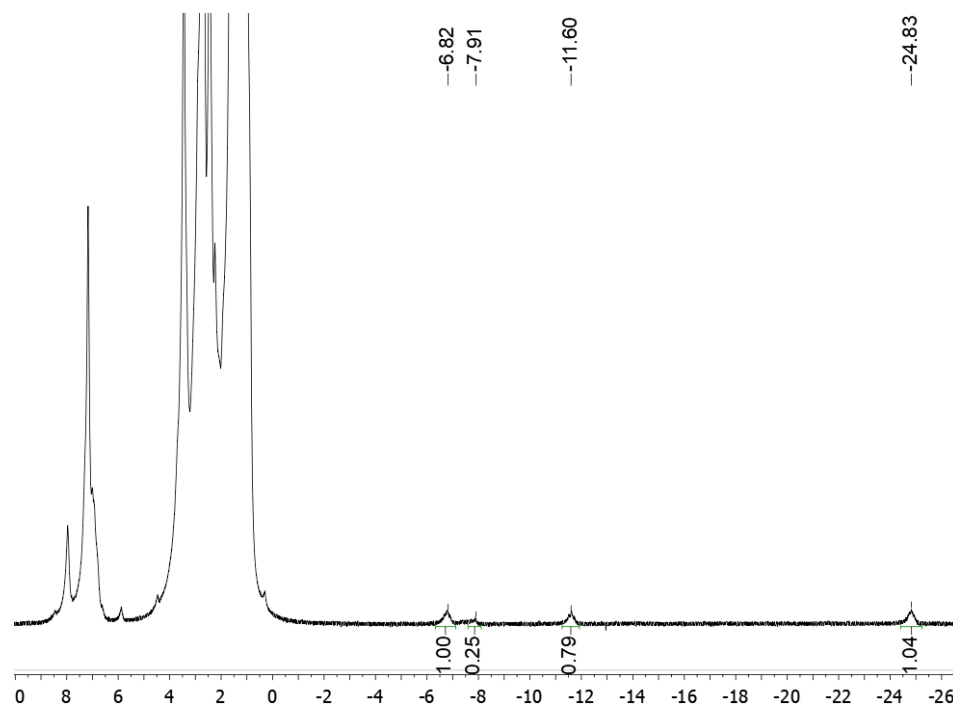
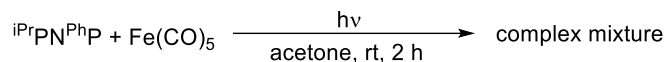


Figure D.25. ^1H NMR spectrum from the reaction of **2** with CO and DBU in C_6D_6 after 15 minutes. Peaks at -6.82 and -24.83 ppm are proposed to correspond to the hydrides of $(^{\text{iPr}}\text{PN}^{\text{Ph}}\text{P})\text{Fe}(\text{H})_2(\text{CO})$.

X. Irradiation of $\text{Fe}(\text{CO})_5$ and ${}^i\text{PrPN}^{\text{Ph}}\text{P}$



A solution of ${}^i\text{PrPN}^{\text{Ph}}\text{P}$ and $\text{Fe}(\text{CO})_5$ in acetone was irradiated using a 100 W Xenon lamp for two hours at room temperature. The quartz cuvette used for the reaction was topped with a rubber septum, and a needle leading to an oil bubbler was used to allow irradiated CO to vent from the reaction headspace without air contaminating the reaction. The solution turned dark red-orange after irradiation. No clean products could be isolated. The procedure used is the same as that in the literature for $({}^i\text{PrPN}^{\text{H}}\text{P})\text{Fe}(\text{CO})_2$.³ NMR data shown in Figure D.26-D.27.

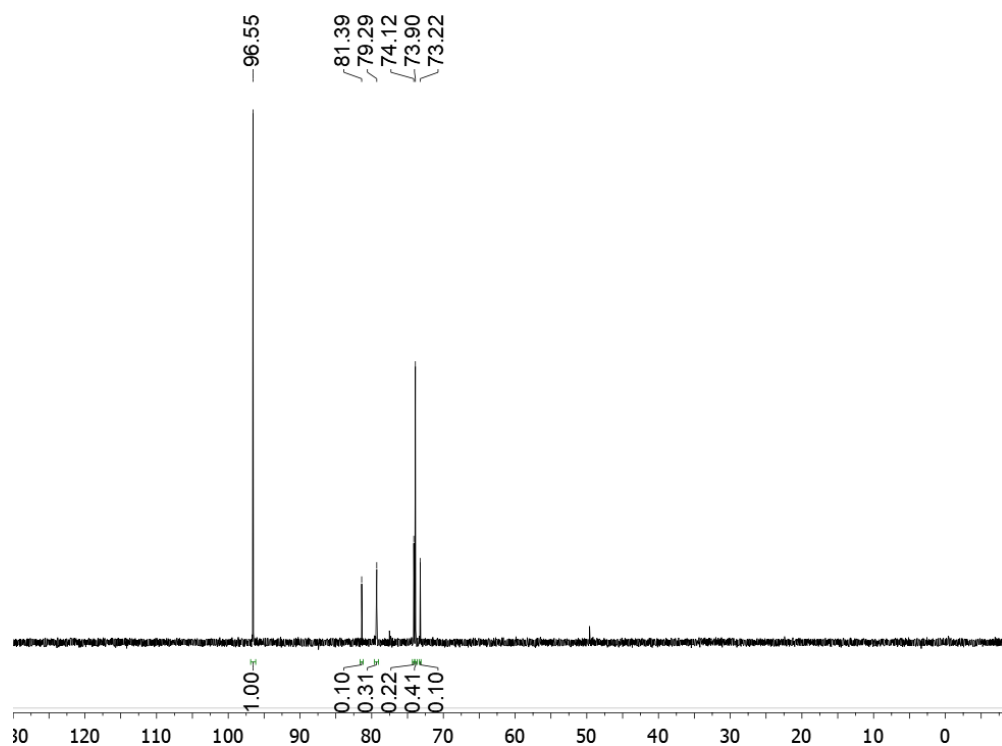


Figure D.26. ${}^{31}\text{P}\{^1\text{H}\}$ NMR spectrum from the irradiation of ${}^i\text{PrPN}^{\text{Ph}}\text{P}$ with $\text{Fe}(\text{CO})_5$ after pumping down, extracting in pentane, and redissolving in C_6D_6 . $({}^i\text{PrPN}^{\text{Ph}}\text{P})\text{Fe}(\text{CO})_2$ (**3**) is observed at 96.58 ppm but could not be isolated cleanly.

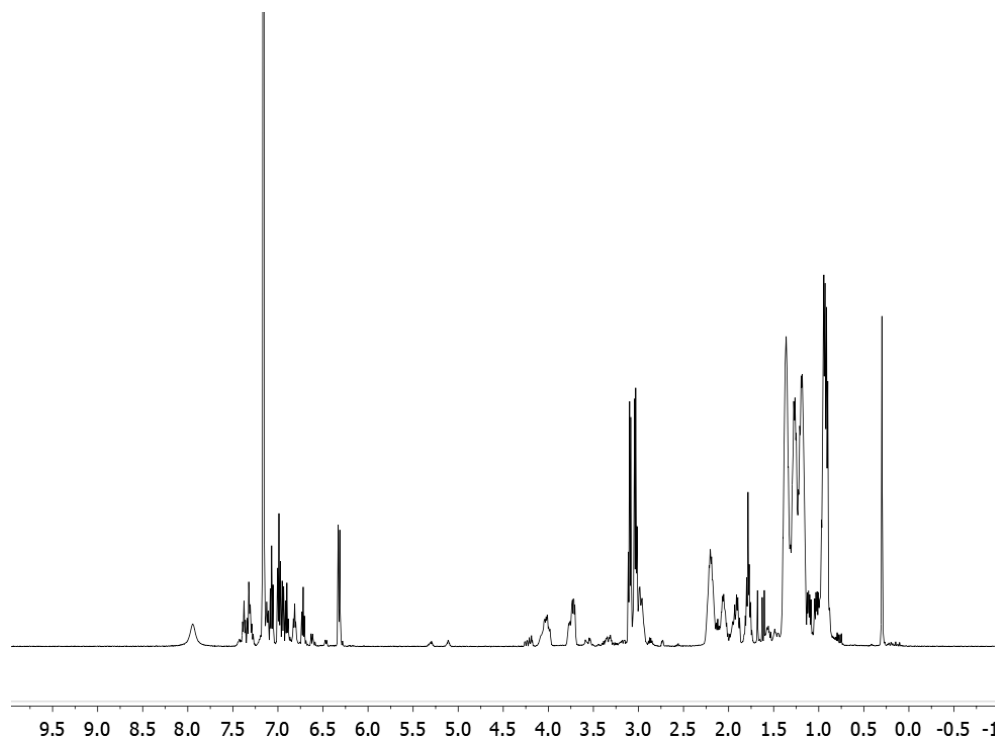
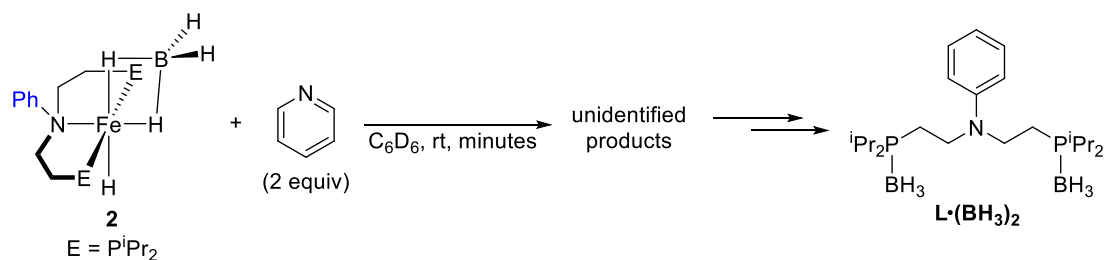


Figure D.27. ^1H NMR spectrum from the irradiation of $i\text{PrPN}^{\text{Ph}}\text{P}$ with $\text{Fe}(\text{CO})_5$ after pumping down, extracting in pentane, and redissolving in C_6D_6 . $(i\text{PrPN}^{\text{Ph}}\text{P})\text{Fe}(\text{CO})_2$ (**3**) could not be isolated cleanly.

XI. Reaction of **2** with Pyridine



In situ NMR data for the reaction of **2** and pyridine in C_6D_6 is shown in Figures D.28-D.29. While one major product is observed in the $^{31}\text{P}\{^1\text{H}\}$ NMR spectrum, clean isolation of this species was unsuccessful. Workup procedures led only to isolation of $i\text{PrPN}^{\text{Ph}}\text{P}$ and/or $\text{L} \cdot (\text{BH}_3)_2$. Additionally, NMR spectra for this reaction were always broad

even after filtering, indicating potential fluctional binding of pyridine and a possible explanation for the difficulty isolating the unidentified product(s).

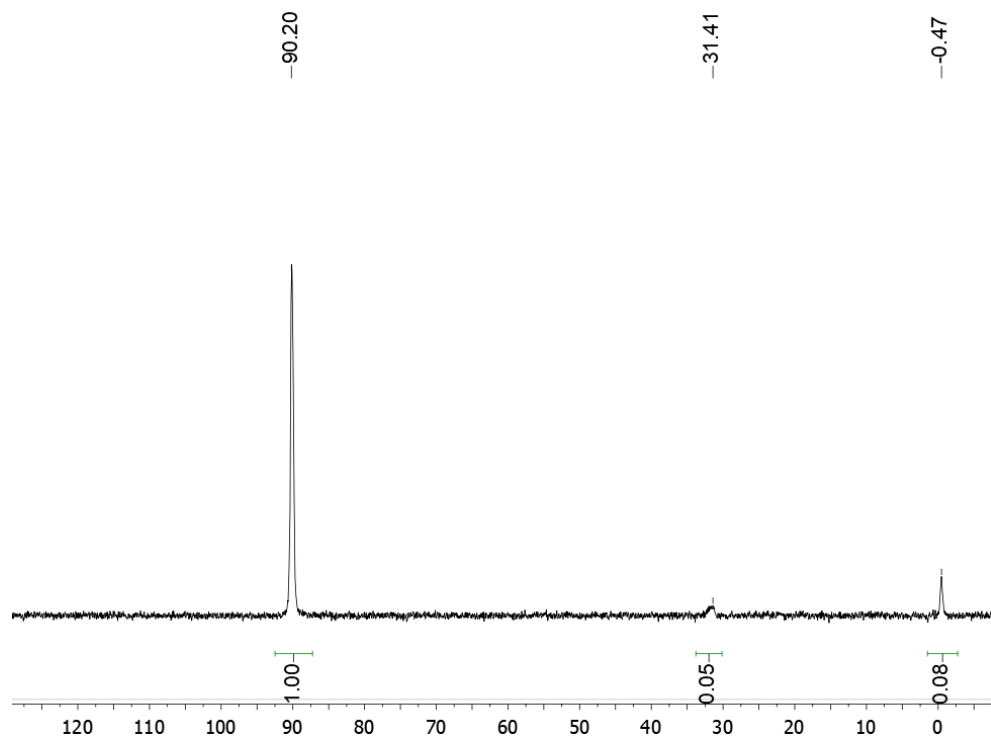


Figure D.28. $^{31}\text{P}\{^1\text{H}\}$ NMR spectrum from the reaction of **2** with pyridine in C_6D_6 after 15 minutes. $\text{L}\cdot(\text{BH}_3)_2$ observed at 31.41 ppm, and $^{\text{iPr}}\text{PN}^{\text{Ph}}\text{P}$ observed at -0.47 ppm.

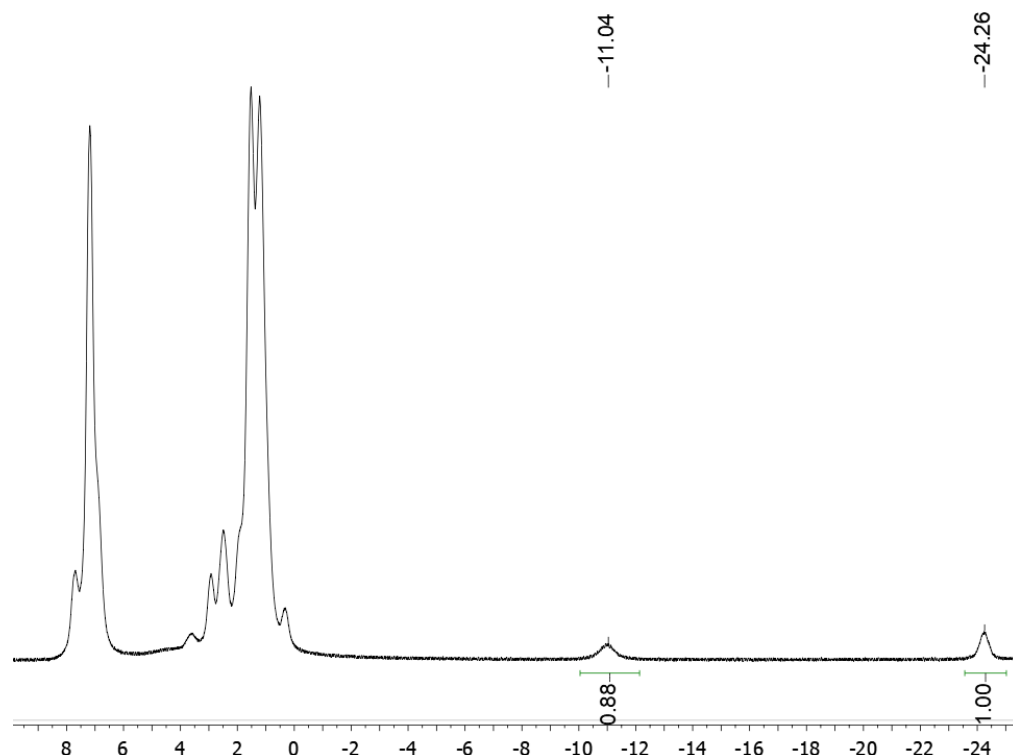
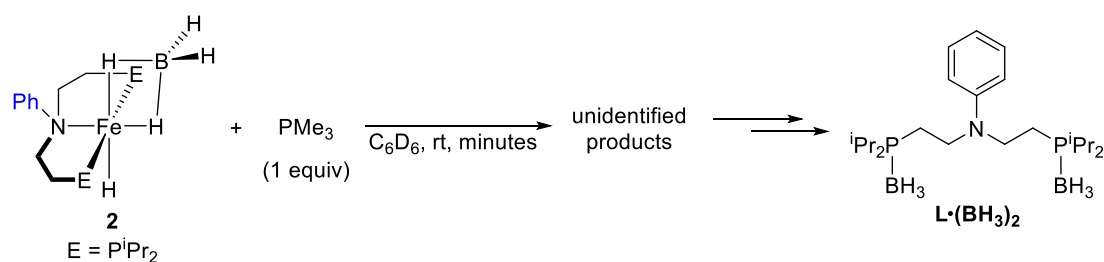


Figure D.29. ^1H NMR spectrum from the reaction of **2** with pyridine in C_6D_6 after 15 minutes. All ^1H spectra of this reaction were similarly broad, even after filtering the solution.

XII. Reaction of **2** with PMe_3



In situ NMR spectra for the reaction of **2** with PMe_3 in C_6D_6 are shown in Figures D.30-D.31. Similar to the reaction with pyridine, these spectra were always broad, and no clean $i\text{PrPN}^{\text{Ph}}\text{P}$ -ligated products could be isolated.

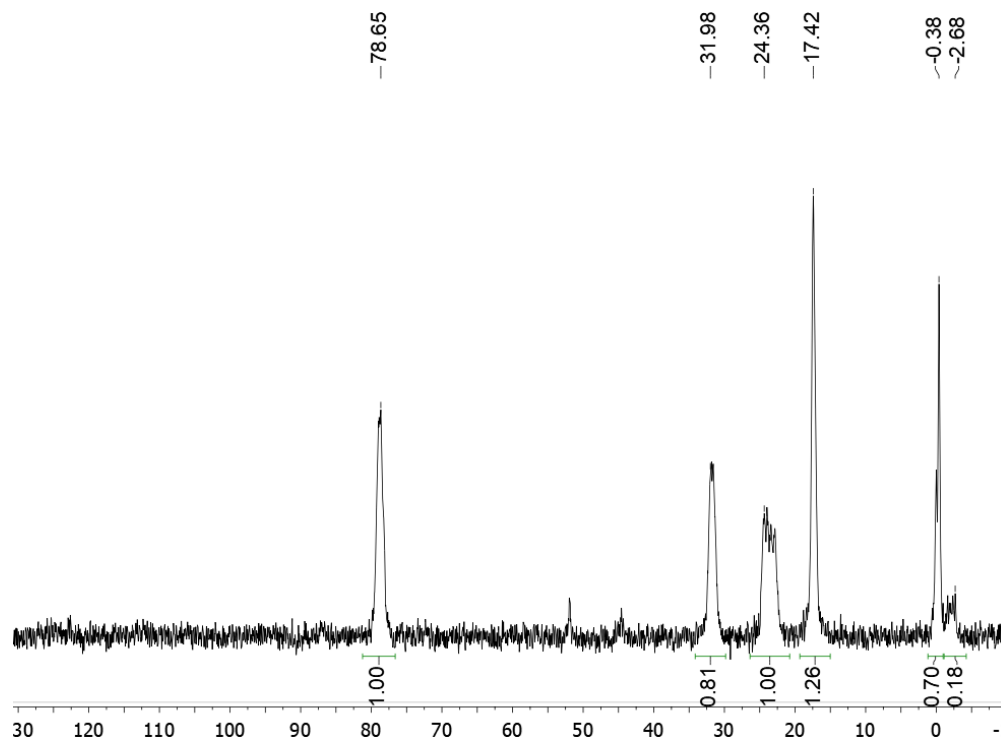


Figure D.30. $^{31}\text{P}\{^1\text{H}\}$ NMR spectrum from the reaction of **2** with PMe_3 in C_6D_6 after 15 minutes. $\text{L} \cdot (\text{BH}_3)_2$ observed at 31.98 ppm, $\text{iPrPN}^{\text{Ph}}\text{P}$ observed at -0.38 ppm, and free PMe_3 observed at -2.68 ppm.

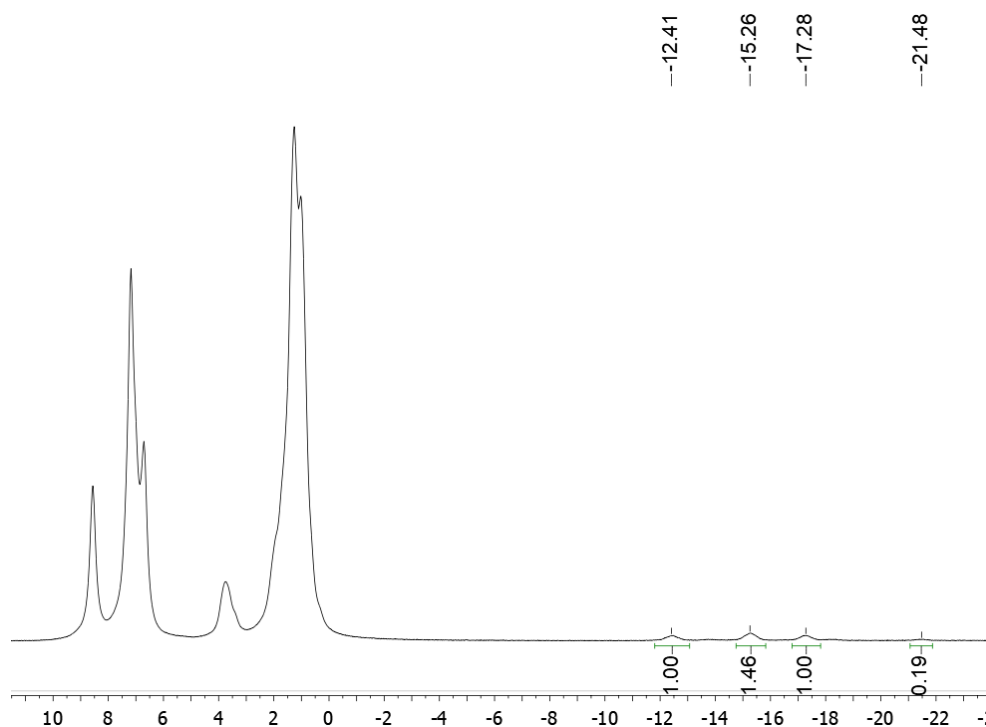
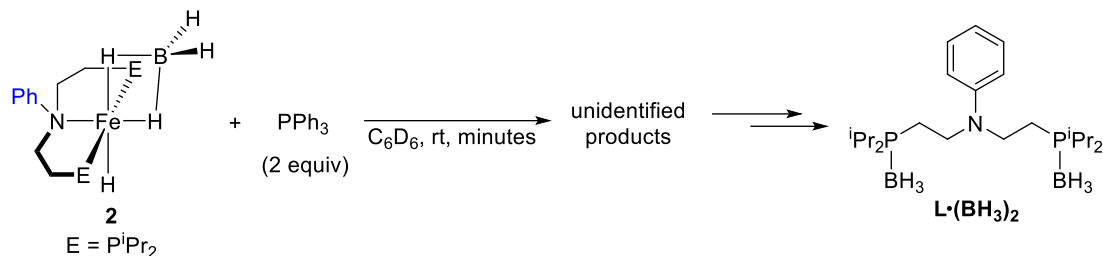


Figure D.31. ^1H NMR spectrum from the reaction of **2** with PMe_3 in C_6D_6 after 15 minutes. All ^1H spectra of this reaction were similarly broad, even after filtering the solution.

XIII. Reaction of **2** with PPh₃



In situ NMR spectra for the reaction of **2** with PPh₃ in C₆D₆ are shown in Figures D.32-D.33. Similar to the reaction with pyridine, these spectra were always broad, and no clean ⁱPrPN^{Ph}P-ligated products could be isolated.

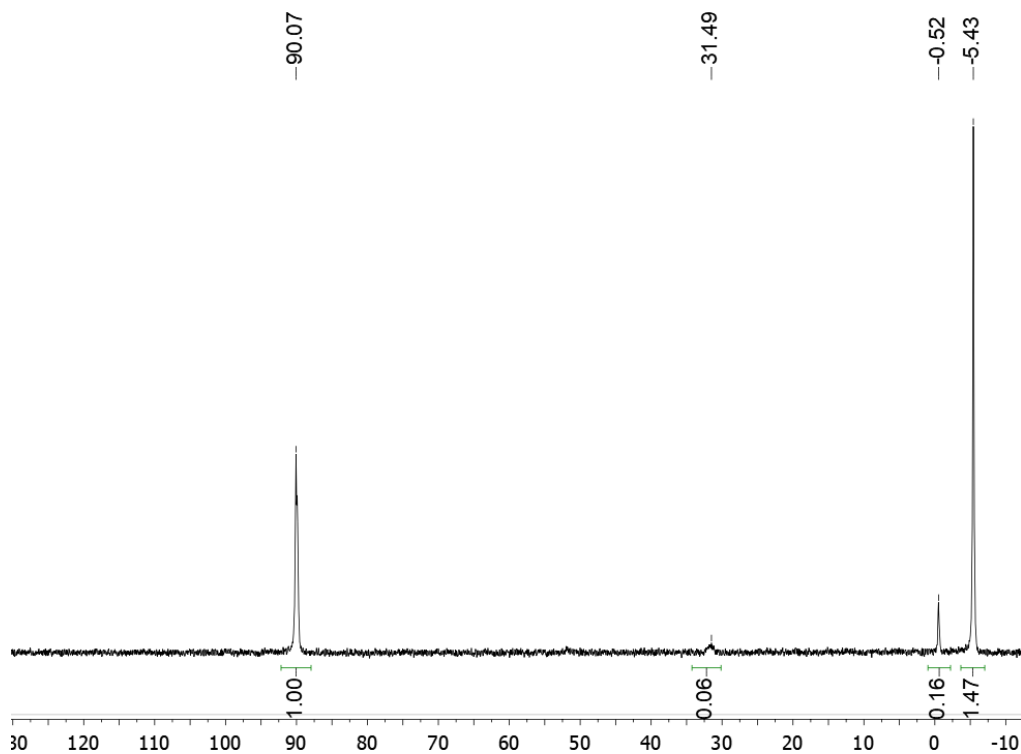


Figure D.32. ³¹P{¹H} NMR spectrum from the reaction of **2** with PPh₃ in C₆D₆ after 15 minutes. L•(BH₃)₂ observed at 31.49 ppm, ⁱPrPN^{Ph}P observed at -0.52 ppm, and free PPh₃ observed at -5.43 ppm.

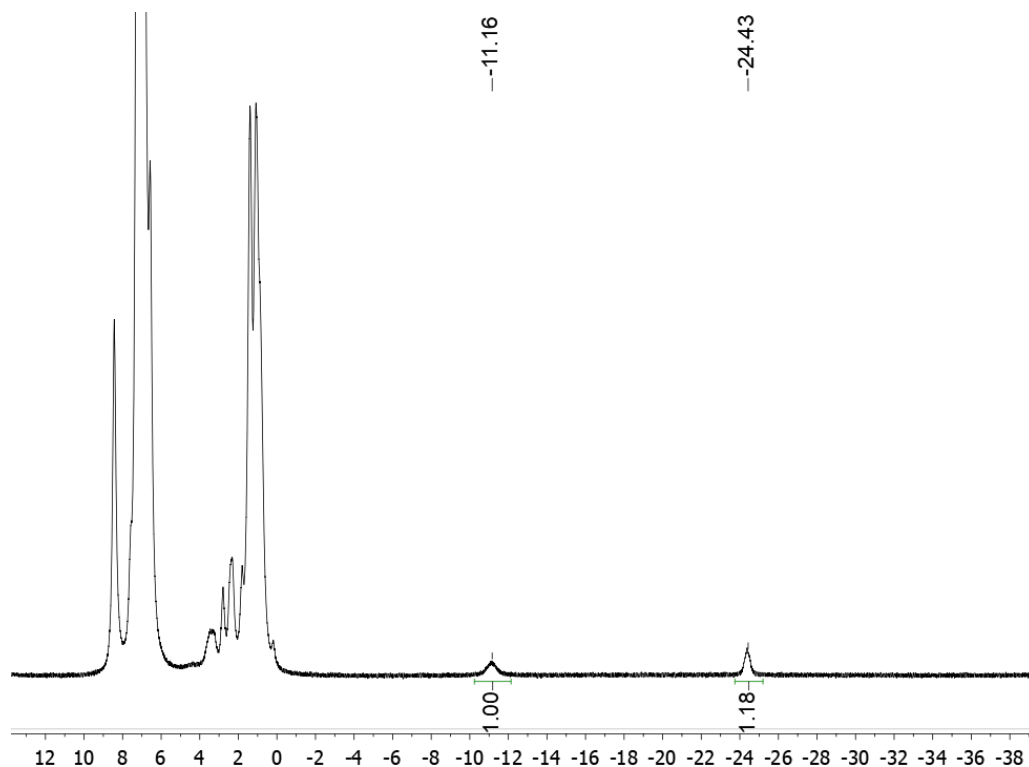
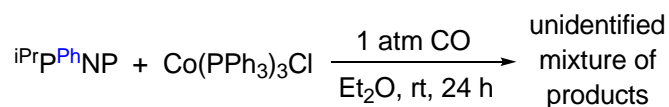


Figure D.33. ^1H NMR spectrum from the reaction of **2** with PPh_3 in C_6D_6 after 15 minutes. All ^1H spectra of this reaction were similarly broad, even after filtering the solution.

XIV. Attempted Synthesis of a $\text{iPrPN}^{\text{Ph}}\text{P}$ Supported Co(I) Species under CO



A solution of $\text{iPrPN}^{\text{Ph}}\text{P}$ and $\text{Co}(\text{PPh}_3)_3\text{Cl}$ in diethyl ether was placed under 1 atm of CO and stirred for 24 hours at room temperature. A green solid was visible at the bottom of the flask. The yellow solution was filtered off and the green solid extracted with THF. The THF was removed *in vacuo*, producing a green oil. A ^1H NMR spectrum of this oil contained both diamagnetic and paramagnetic products and a several signals were observed in the $^{31}\text{P}\{^1\text{H}\}$ NMR spectrum. No clean products could be isolated and attempts at crystallization led to observation of multiple signals in the $^{31}\text{P}\{^1\text{H}\}$ NMR and a significant decrease in signal intensity. The procedure used is the same as that in the literature for

$(i\text{PrPN}^{\text{H}}\text{P})\text{Co}(\text{CO})_2\text{Cl}^4$ and $(i\text{PrPN}^{\text{Me}}\text{P})\text{Co}(\text{CO})_2\text{Cl}^5$ NMR data is shown in Figures D.34-D.37.

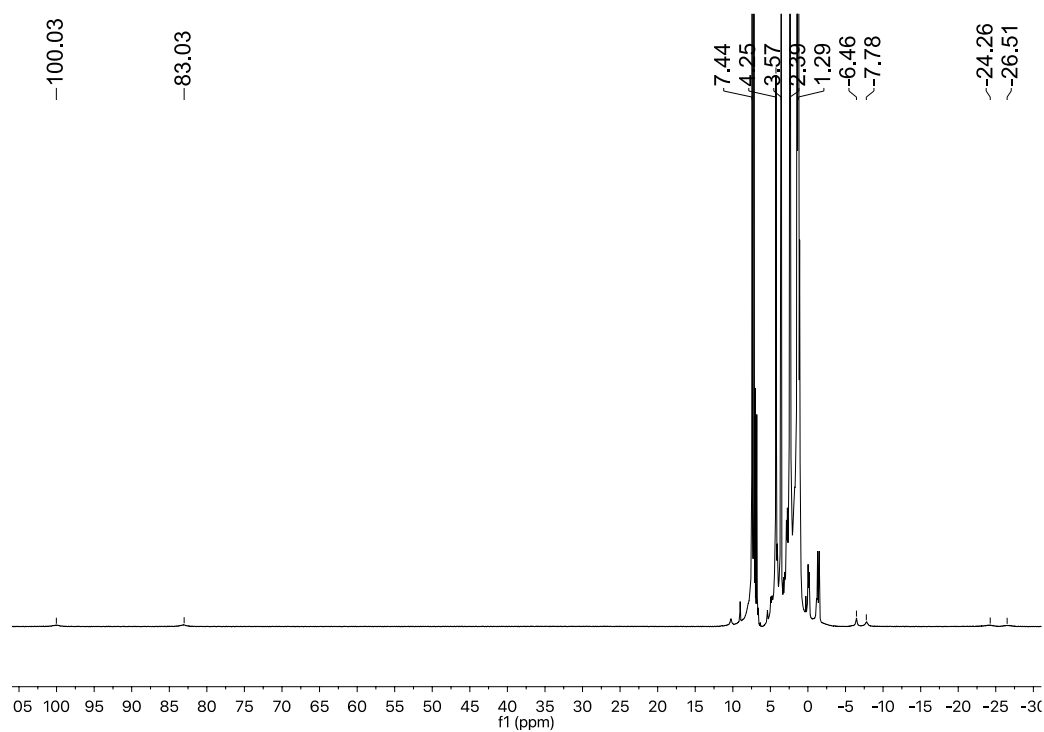


Figure D.34. ^1H NMR spectrum in C_6D_6 from the reaction of $i\text{PrPN}^{\text{Ph}}\text{P}$ and $\text{Co}(\text{PPh}_3)_3\text{Cl}$ under CO after THF extraction.

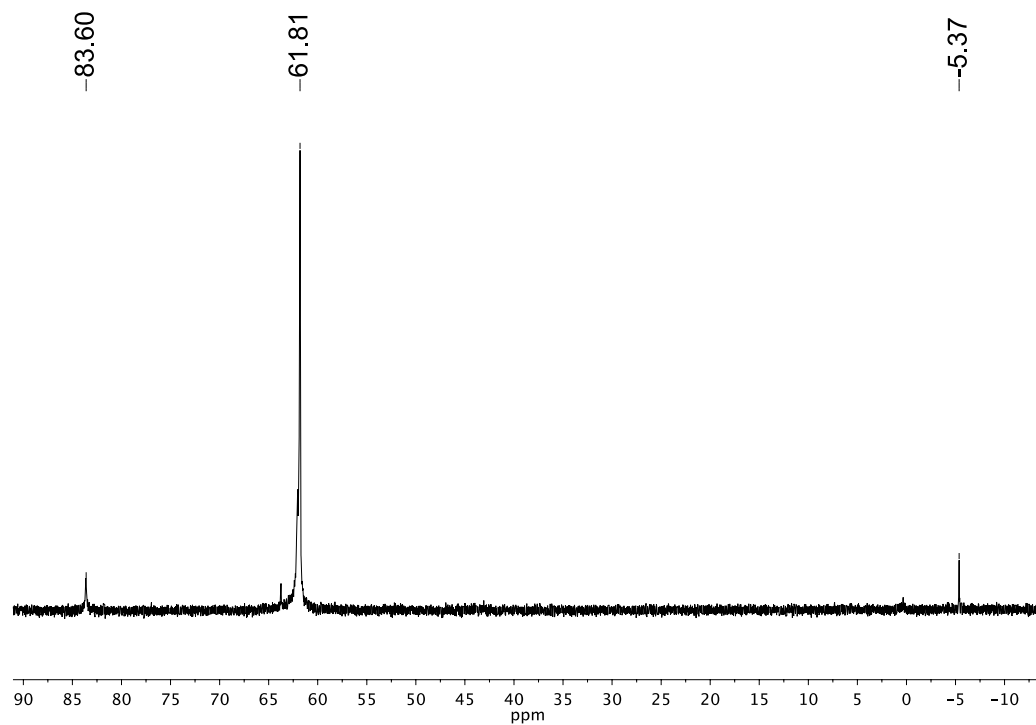


Figure D.35. $^{31}\text{P}\{^1\text{H}\}$ NMR spectrum in C_6D_6 from the reaction of $i\text{PrPN}^{\text{Ph}}\text{P}$ and $\text{Co}(\text{PPh}_3)_3\text{Cl}$ under CO after THF extraction.

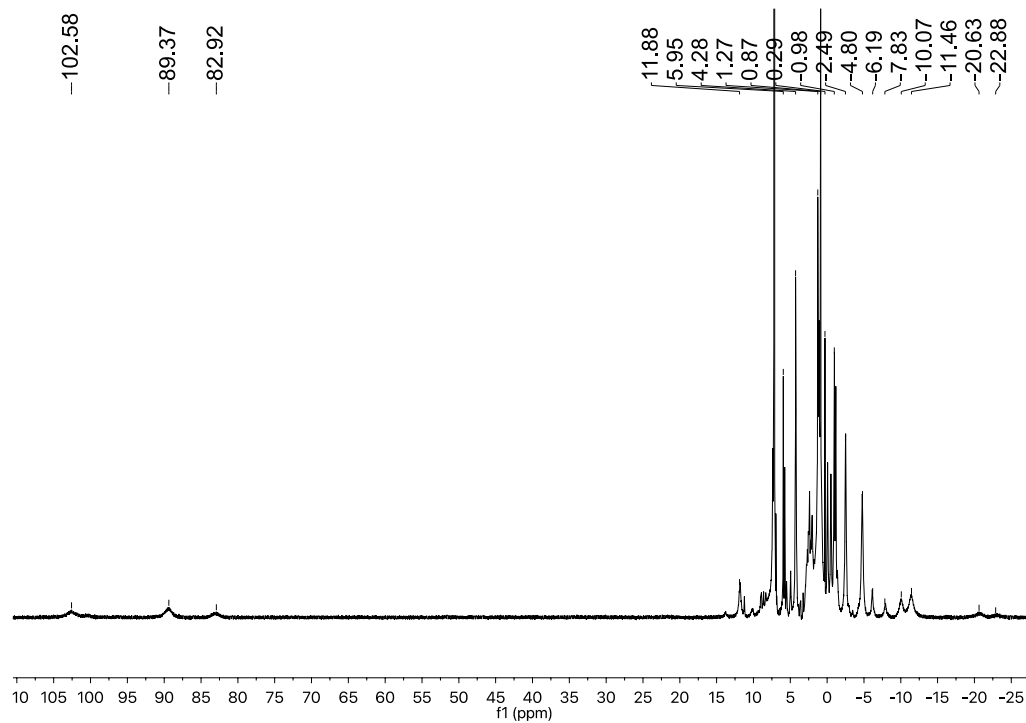


Figure D.36. ^1H NMR spectrum in C_6D_6 from the reaction of $i\text{PrPN}^{\text{Ph}}\text{P}$ and $\text{Co}(\text{PPh}_3)_3\text{Cl}$ under CO after THF extraction and recrystallization.

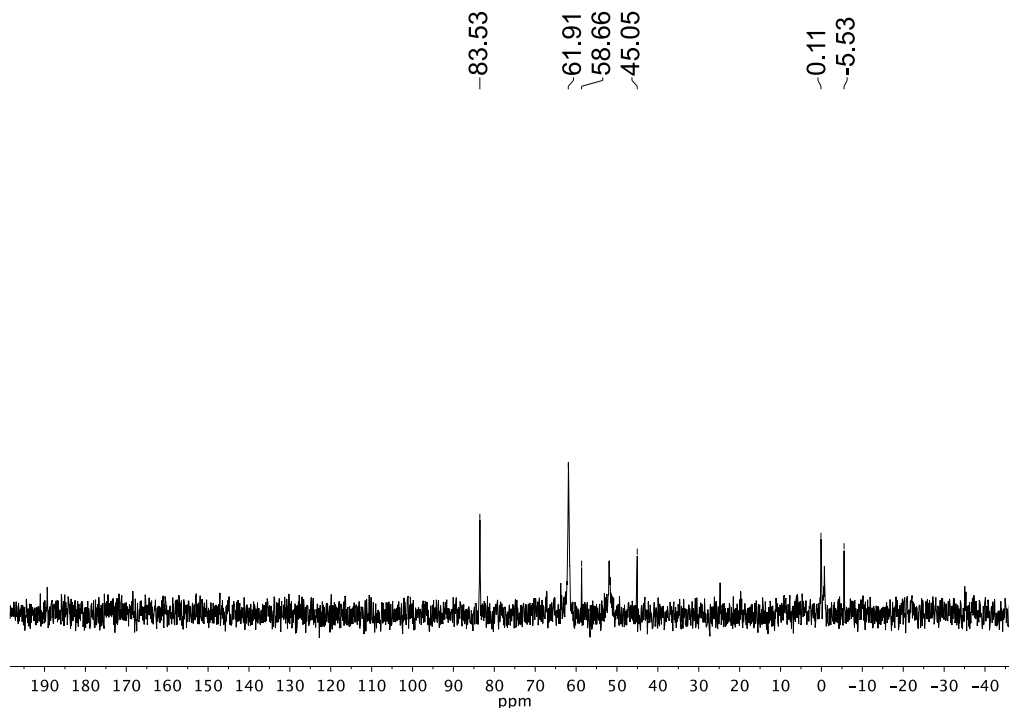
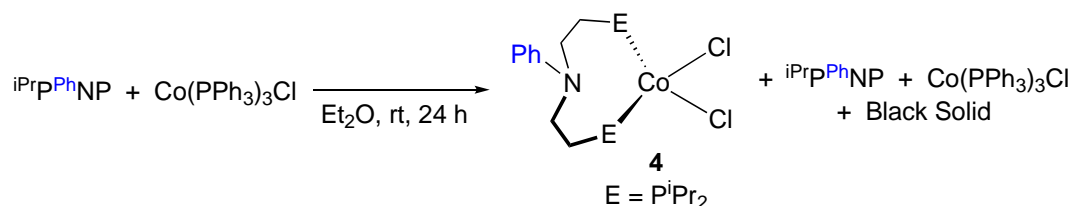


Figure D.37. $^{31}\text{P}\{^1\text{H}\}$ NMR spectrum in C_6D_6 from the reaction of $i\text{PrPN}^{\text{Ph}}\text{P}$ and $\text{Co}(\text{PPh}_3)_3\text{Cl}$ under CO after THF extraction and recrystallization.

XV. Attempted Synthesis of a $i\text{PrPN}^{\text{Ph}}\text{P}$ Supported Co(I) Species under N_2



A solution of $i\text{PrPN}^{\text{Ph}}\text{P}$ and $\text{Co}(\text{PPh}_3)_3\text{Cl}$ in diethyl ether was stirred for 24 hours at room temperature under 1 atm N_2 , producing a pale green solid and a dark green solution. The solvent was removed *in vacuo*, and the residual solid was washed with pentane. An extraction with diethyl ether produced a blue filtrate and left a light green solid. The blue filtrate was dried and a mixture of products was identified by ^1H NMR, including **4**. The remaining green solid was extracted in benzene, leaving an insoluble black solid. The benzene extraction was dried and $\text{Co}(\text{PPh}_3)_3\text{Cl}$ was identified by ^1H NMR spectrum as the

only product. The only signals observed in any of the $^{31}\text{P}\{^1\text{H}\}$ spectra were those for free $i\text{PrPN}^{\text{Ph}}\text{P}$ and PPh_3 . NMR data shown in Figure D.38.

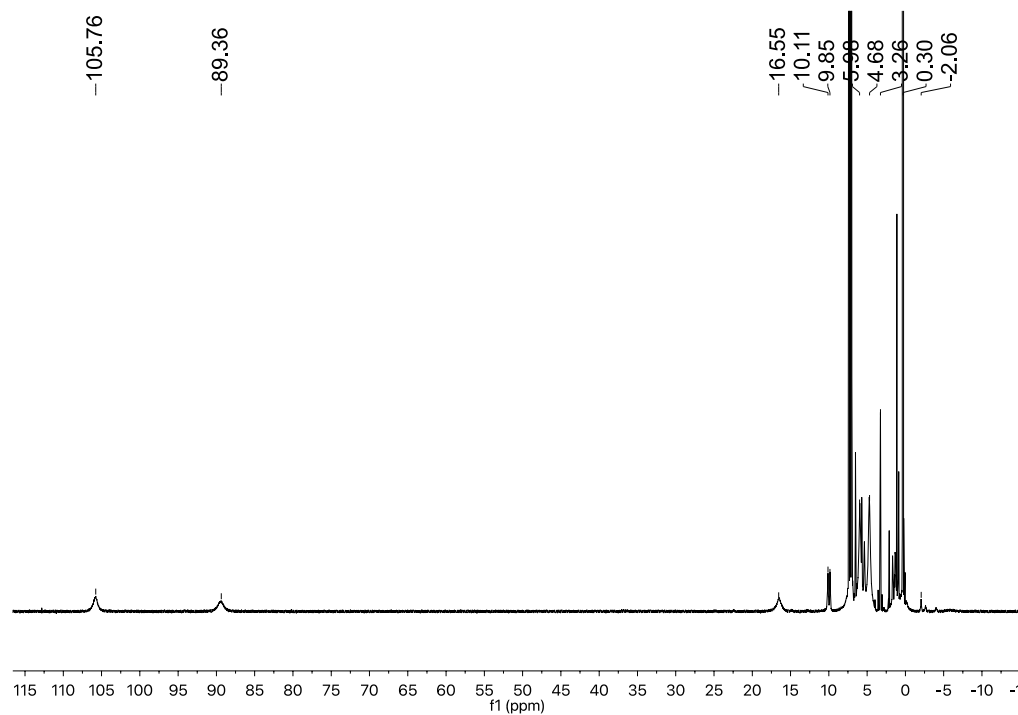
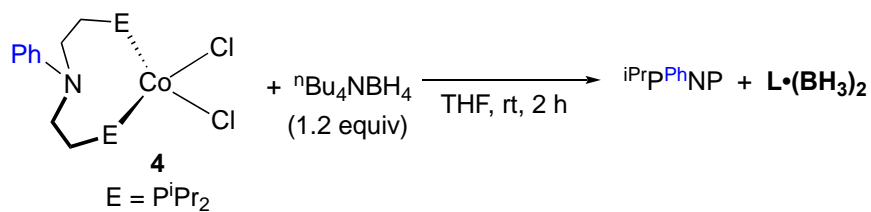


Figure D.38. ^1H NMR spectrum in C_6D_6 from the reaction of $i\text{PrPN}^{\text{Ph}}\text{P}$ and $\text{Co}(\text{PPh}_3)_3\text{Cl}$ under N_2 after diethyl ether extraction.

XVI. Reaction of **4** with $^n\text{Bu}_4\text{NBH}_4$



A solution of **4** and 1.2 equiv. $^n\text{Bu}_4\text{NBH}_4$ was stirred for 2 hours in THF at room temperature, producing a yellow solution and dark blue solid. An *in situ* $^{31}\text{P}\{^1\text{H}\}$ NMR

spectrum contained signals observed for free $i\text{PrPN}^{\text{Ph}}\text{P}$ and $\text{L}\cdot(\text{BH}_3)_2$, as shown in Figure D.39.

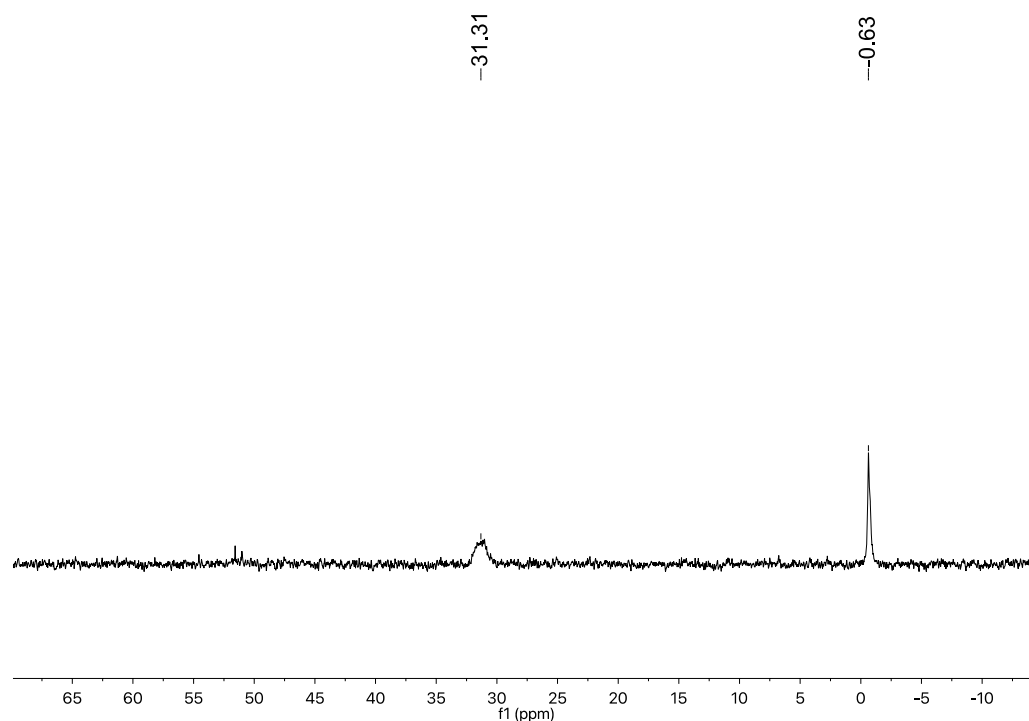
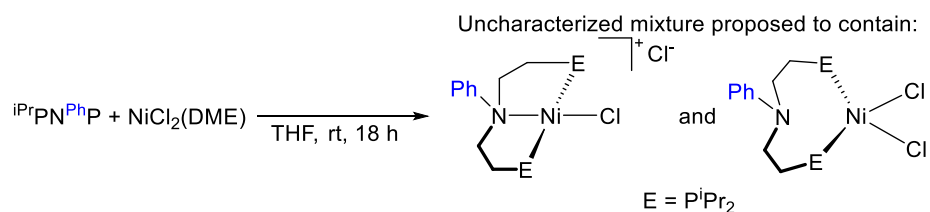


Figure D.39. *In situ* $^{31}\text{P}\{^1\text{H}\}$ NMR spectrum in THF from reaction of **4** and $^n\text{Bu}_4\text{NBH}_4$. $\text{L}\cdot(\text{BH}_3)_2$ is observed at 31.31 ppm, and free $i\text{PrPN}^{\text{Ph}}\text{P}$ is observed at -0.63 ppm.

XVII. Equilibrium in the Reaction of $\text{NiCl}_2(\text{DME})$ and $i\text{PrPN}^{\text{Ph}}\text{P}$



NMR spectra of this proposed mixture are shown in C_6D_6 (Figures D.40-D.41) and CD_2Cl_2 (Figures D.42-D.43). The product was extracted in CH_2Cl_2 before dissolving in the

NMR solvent. Changes in the chemical shift of the ^{31}P peak as well as the paramagnetic peaks in the ^1H NMR spectrum indicate a possible change in speciation between solvents.

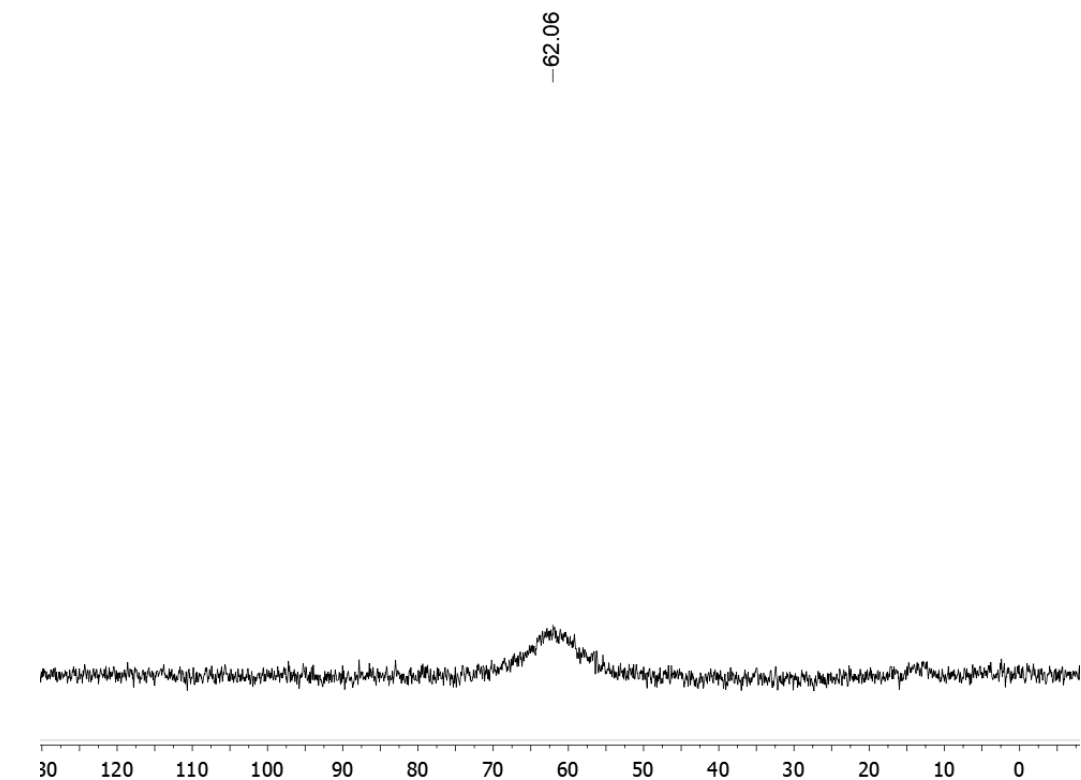


Figure D.40. $^{31}\text{P}\{^1\text{H}\}$ NMR spectrum of the product(s) from the reaction of $\text{NiCl}_2(\text{DME})$ and $i\text{PrPN}^{\text{Ph}}\text{P}$ in C_6D_6 .

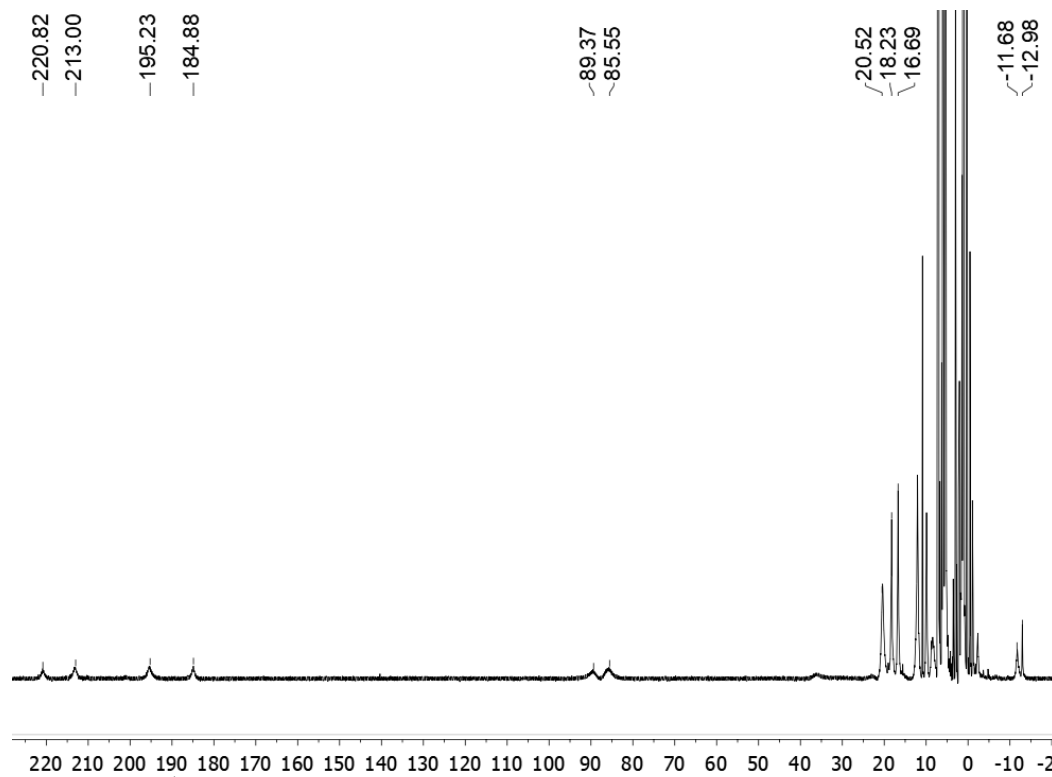


Figure D.41. ^1H NMR spectrum of the product(s) from the reaction of $\text{NiCl}_2(\text{DME})$ and $i\text{PrPN}^{\text{Ph}}\text{P}$ in C_6D_6 .

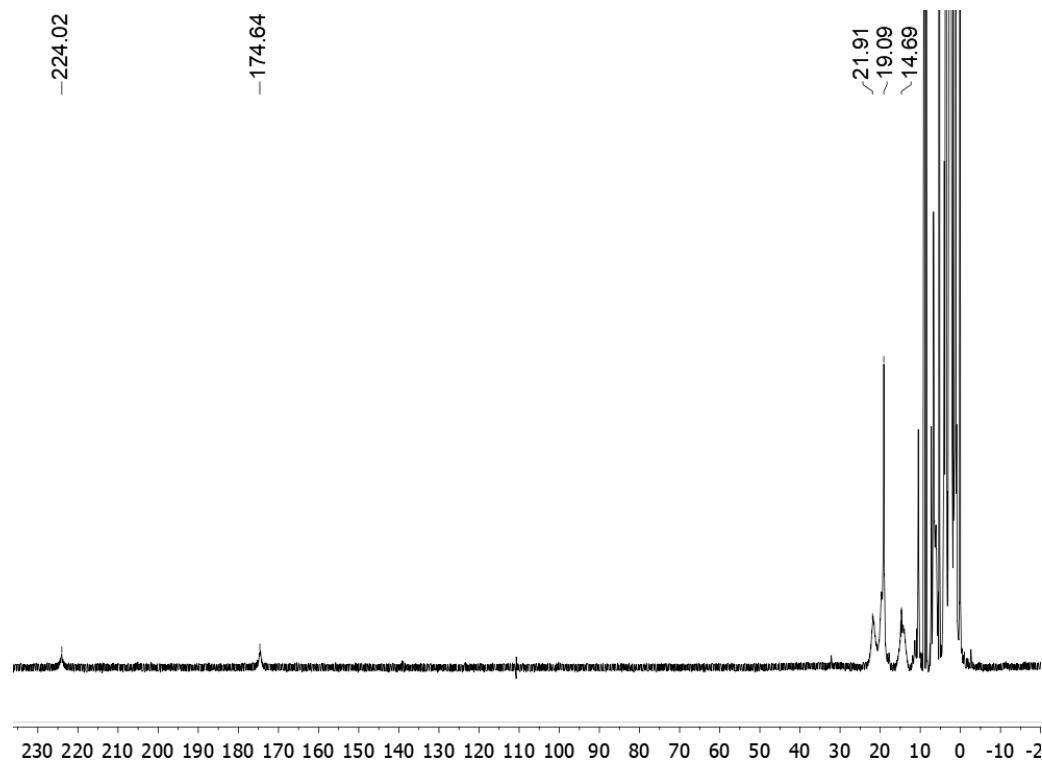


Figure D.42. ^1H NMR spectrum of the product(s) from the reaction of $\text{NiCl}_2(\text{DME})$ and $\text{iPrPN}^{\text{Ph}}\text{P}$ in CD_2Cl_2 .

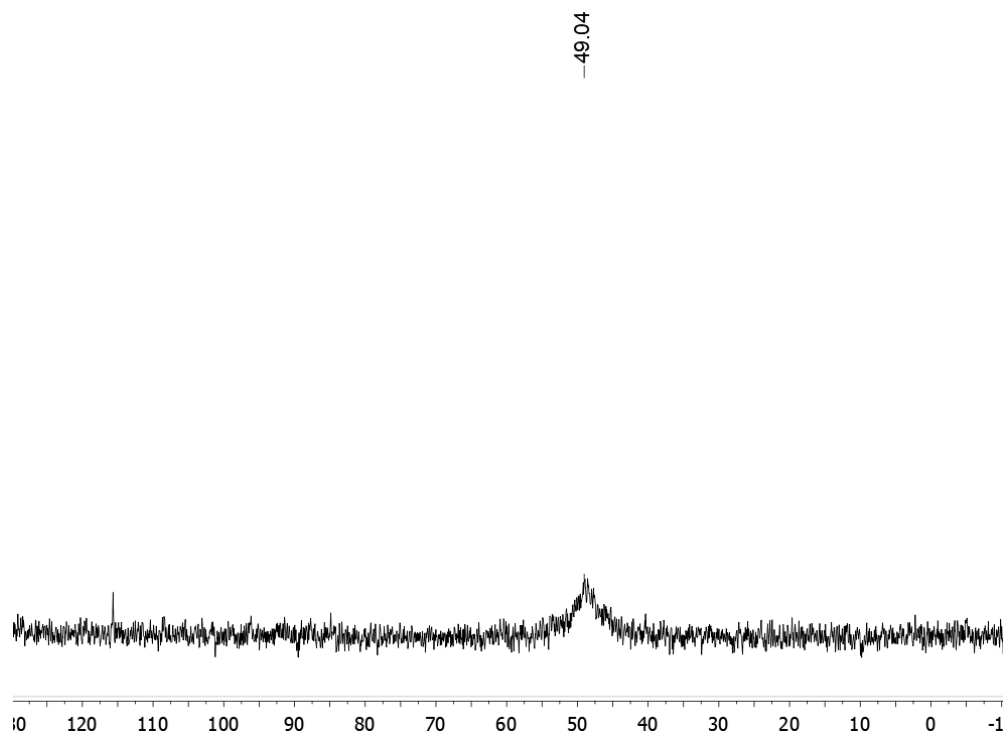
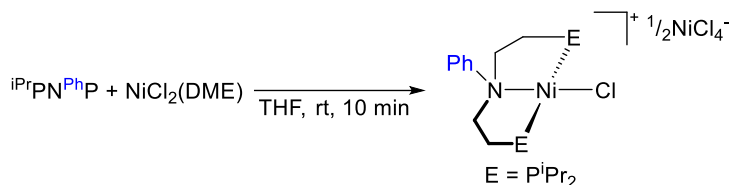
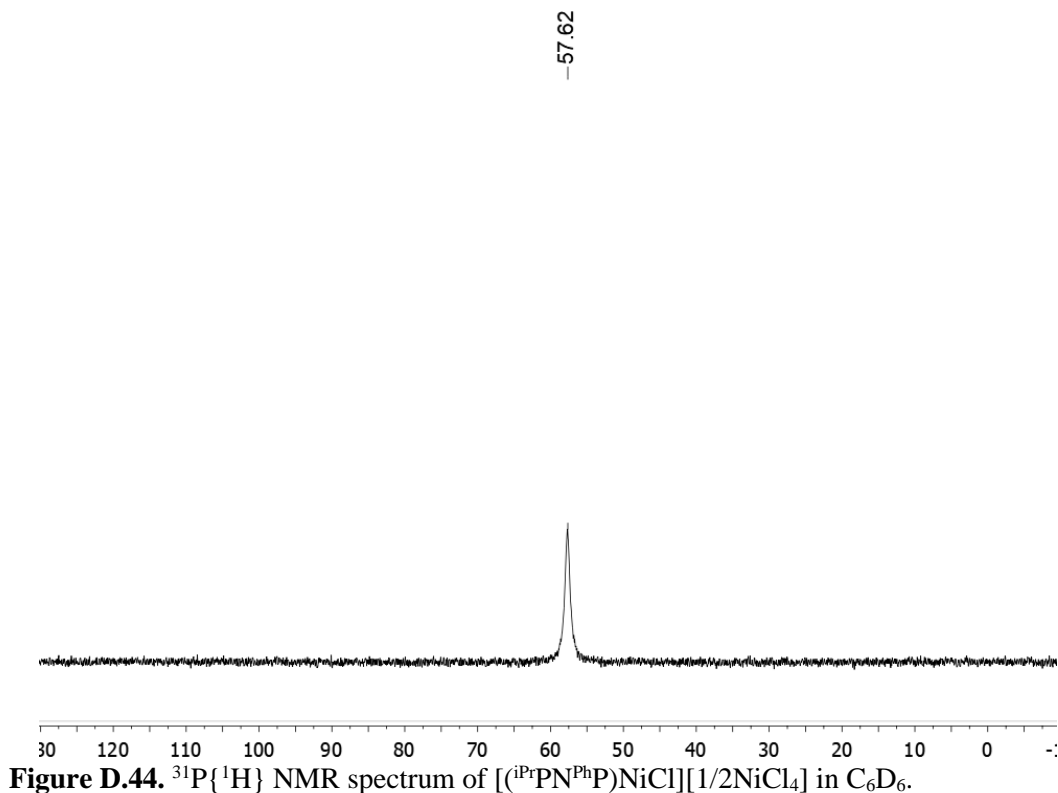


Figure D.43. $^{31}\text{P}\{^1\text{H}\}$ NMR spectrum of the product(s) from the reaction of $\text{NiCl}_2(\text{DME})$ and $\text{iPrPN}^{\text{Ph}}\text{P}$ in CD_2Cl_2 .

XVIII. Isolation of [(ⁱPrPN^{Ph}P)NiCl][1/2NiCl₄]



In a dinitrogen glovebox, to a 15 mL scintillation vial were added ⁱPrPN^{Ph}P (50 mg, 0.13 mmol), NiCl₂(DME) (29 mg, 0.13 mmol), and THF (6 mL). The solution immediately turned crimson orange, and an orange precipitate formed. The vial was capped and shaken vigorously, then the THF was removed *in vacuo* and the residue was extracted in CH₂Cl₂ and the volatiles were removed *in vacuo* to yield an orange solid. Single crystals of the product suitable for X-ray diffraction were grown from a concentrated toluene solution at -35 °C, yield 14 mg (37%). NMR spectra of the product are shown in Figures D.44-D.45; solid state structure shown in Figure D.46.



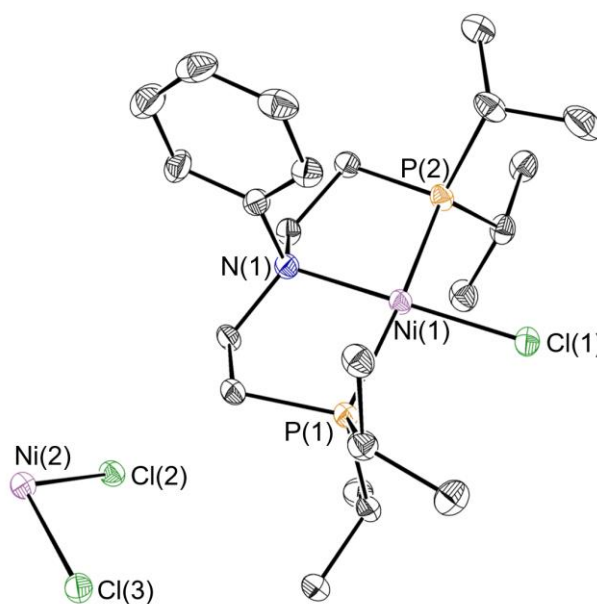
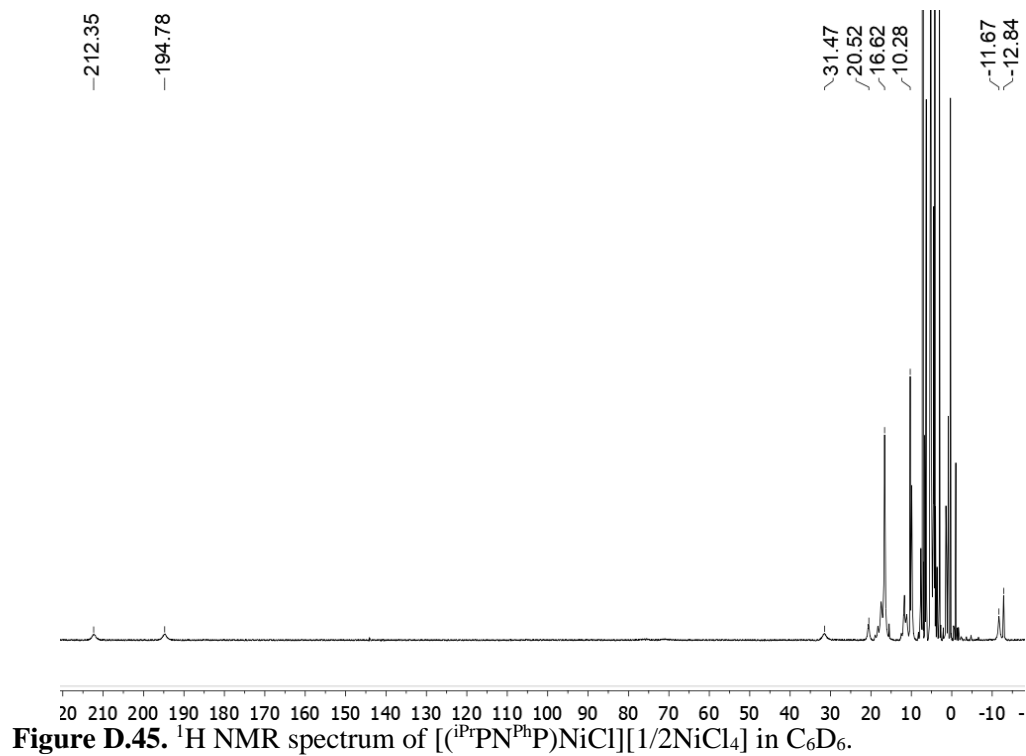


Figure D.46. ORTEP of $[(^i\text{PrPN}^{\text{Ph}}\text{P})\text{NiCl}][1/2\text{NiCl}_4]$ with ellipsoids at 30% probability. Hydrogen atoms omitted for clarity.

Crystals of $[(^i\text{PrPN}^{\text{Ph}}\text{P})\text{NiCl}][1/2\text{NiCl}_4]$ were dissolved in toluene- d_8 in order to assess the nature of the equilibrium between the paramagnetic and diamagnetic species in solution at variable temperatures. A PPh_3 capillary standard was used. NMR data is shown in Figures D.47-D.48.

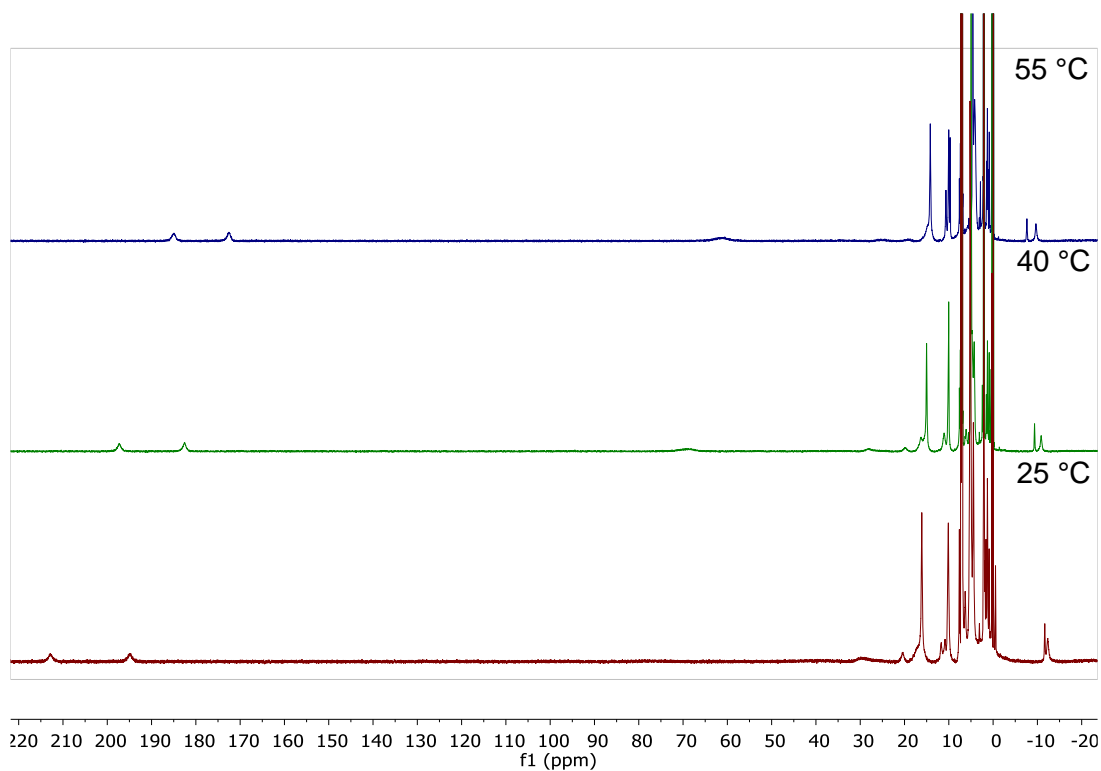


Figure D.47. ^1H NMR spectra of crystals of $[(^i\text{PrPN}^{\text{Ph}}\text{P})\text{NiCl}][1/2\text{NiCl}_4]$ in toluene- d_8 at 25, 40, and 55 °C.

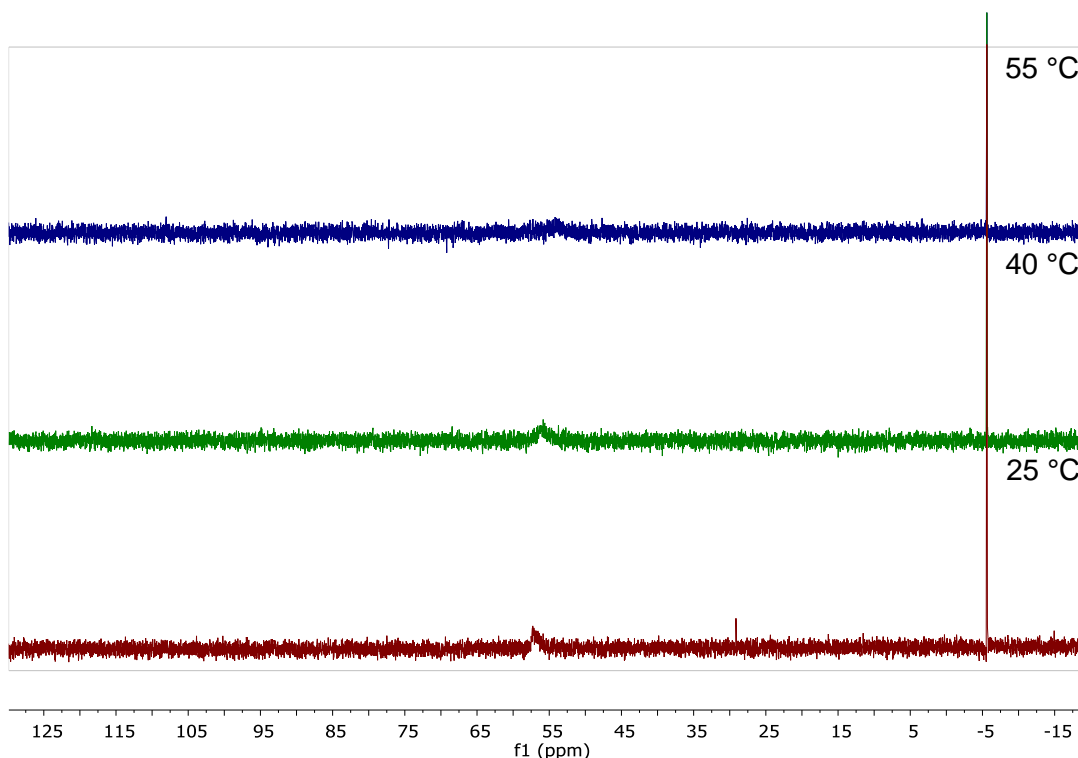
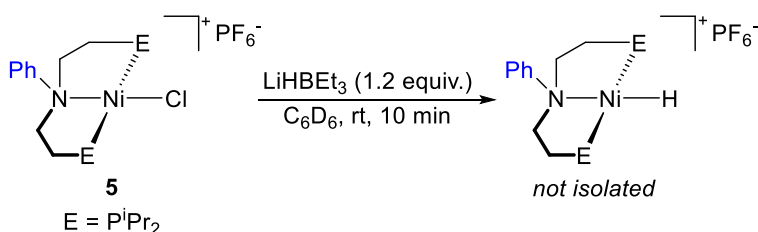


Figure D.48. $^{31}\text{P}\{^1\text{H}\}$ NMR spectra of crystals of $[(i\text{PrPN}^{\text{Ph}}\text{P})\text{NiCl}][1/2\text{NiCl}_4]$ in toluene- d_8 at 25, 40, and 55 °C. PPh_3 capillary standard at -5.6 ppm.

XIX. Attempted Isolation of $[(i\text{PrPN}^{\text{Ph}}\text{P})\text{NiH}][\text{PF}_6]$



In a dinitrogen glovebox, to a J. Young NMR tube were added **5** (5.2 mg, 0.0084 mmol), C_6D_6 (0.5 mL), and LiHBEt_3 (1.7 M solution in THF, 6 μL , 0.010 mmol). The solution immediately darkened from orange to a dark red-brown. *In situ* NMR data for this reaction are shown in Figures D.49-D.50. Based on the similarity of the hydride chemical shift in this reaction (-20.97 ppm) and the previously isolated complex $[(^{\text{Cy}}\text{PN}^{\text{H}}\text{P})\text{NiH}][\text{BPh}_4]$ (-19.59 ppm),⁶ we propose that $[(i\text{PrPN}^{\text{Ph}}\text{P})\text{NiH}][\text{PF}_6]$ is formed.

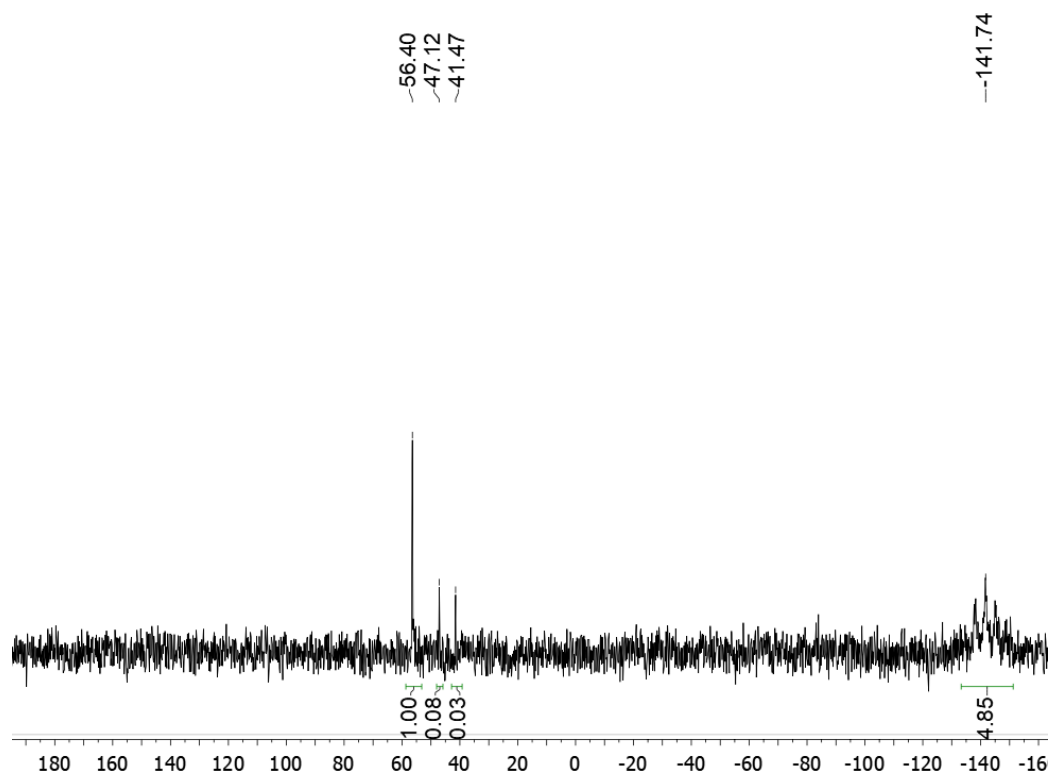


Figure D.49. *In situ* $^{31}\text{P}\{^1\text{H}\}$ NMR spectrum from the reaction of **5** with LiHBEt_3 in C_6D_6 . Small amount of **5** observed at 41.47 ppm.

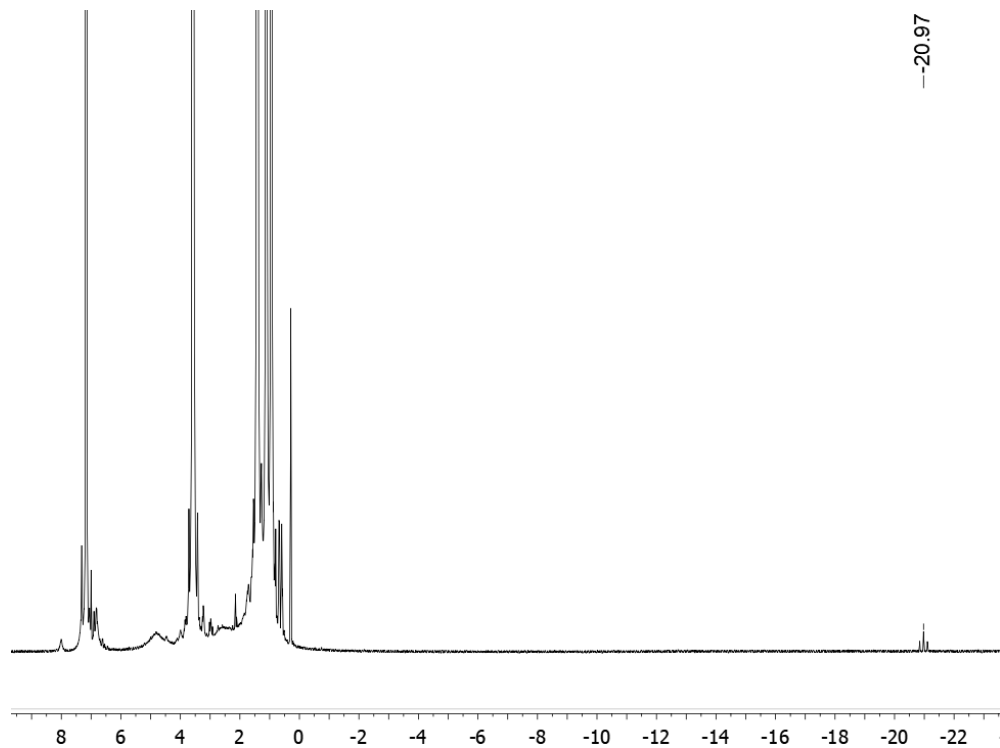


Figure D.50. *In situ* ^1H NMR spectrum from the reaction of **5** with LiHBEt_3 in C_6D_6 .

This solution was filtered, pumped down, and extracted again into C₆D₆. NMR data is shown in Figures D.51-D.52. Significant back conversion to **5** is observed.

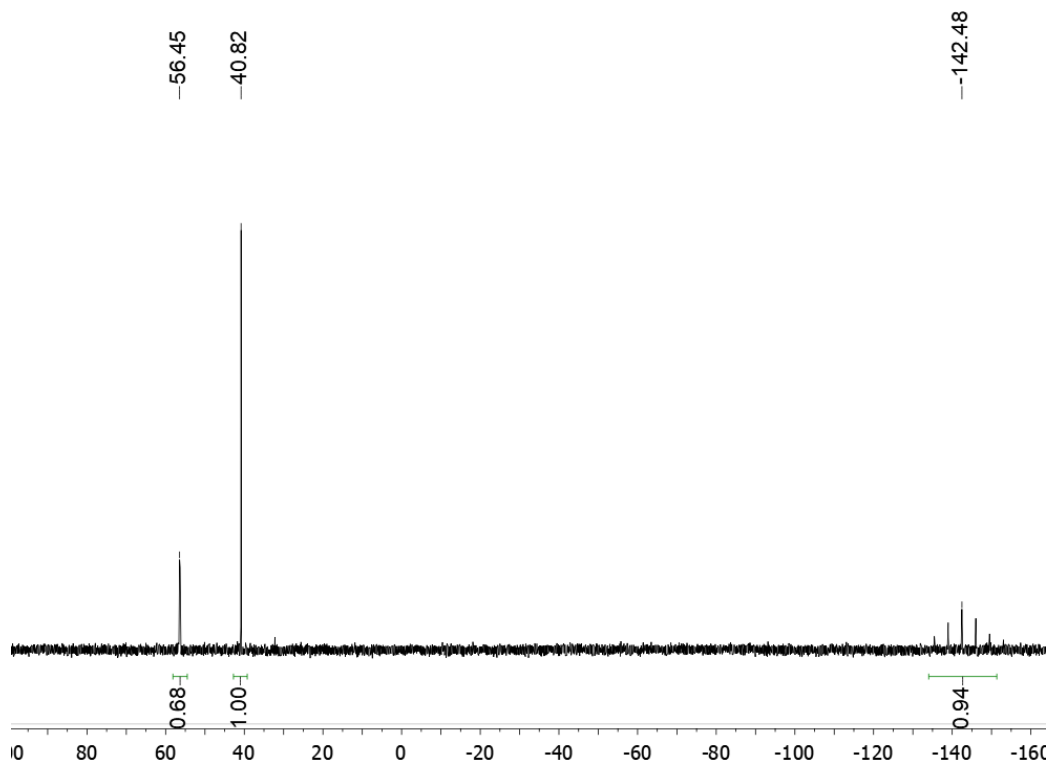


Figure D.51. $^{31}\text{P}\{^1\text{H}\}$ NMR spectrum from the reaction of **5** with LiHBEt₃ in C₆D₆ after filtering and pumping down. **5** observed at 40.82 ppm and is now the major product.

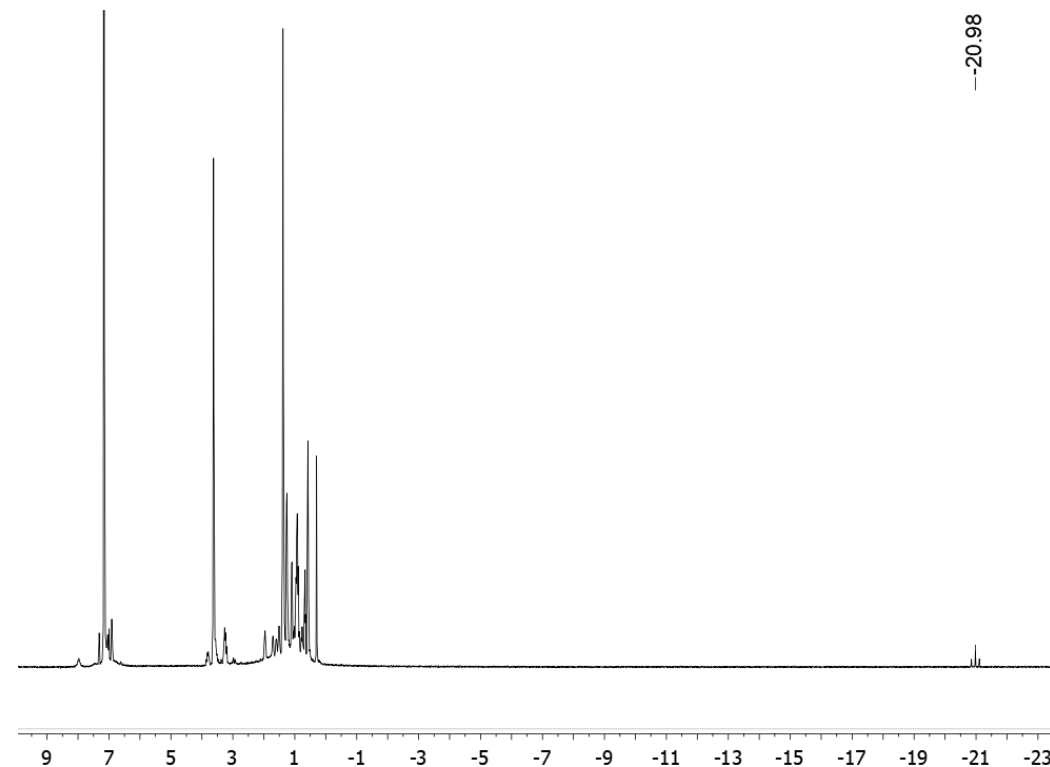


Figure D.52. ^1H NMR spectrum from the reaction of **5** with LiHBet_3 in C_6D_6 after filtering and pumping down.

XX. Formic Acid Dehydrogenation Details

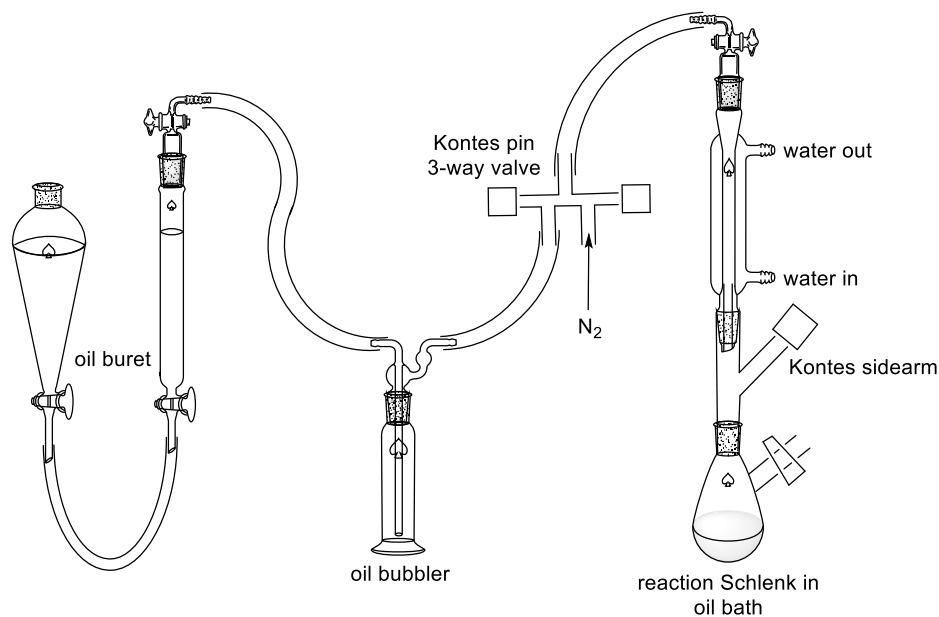


Figure D.53. Diagram of experimental setup for formic acid dehydrogenation.

TON Quantification:

Before running a catalytic reaction, a blank reaction was performed in which no catalyst was added to the reaction solution. The volume of gas obtained from this reaction (trace solvent and FA) was recorded as V_{blank} . The corrected volume of gas produced from a catalytic reaction was then calculated using the following expression:

$$V_{corr} = V_{obs} - V_{blank}$$

Where V_{obs} is the observed change in oil level in the gas buret during catalysis. It was assumed that a 1:1 mixture of H_2 and CO_2 was produced in the catalytic reaction. The number of moles of gas produced (n_{prod}) in the reaction was determined using the following expression that utilizes the ideal gas law:

$$n_{prod} = \frac{V_{corr}}{2(22.4 \frac{L}{mol})}$$

The TON was then determined using the following expression:

$$TON = \frac{n_{prod}}{n_{cat}}$$

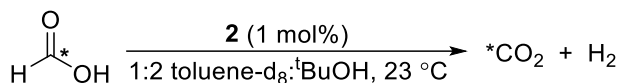
Where n_{cat} is the molar quantity of the catalyst.

The TOF was determined to be the TON that occurred in the first hour.

Gas Volume Determination

The volume/height ratio of each gas buret was determined before using them in catalysis. To do this, water was placed in the buret, and the meniscus was marked. Some water was drained from the column into a tared flask, and the new water level was marked again. The weight of the water drained from the flask was used to determine its volume, and this was divided by the change in height in the buret to determine the mL/cm calibration of the buret.

XXI. Verifying the Products of Catalytic Formic Acid Dehydrogenation Using NMR Spectroscopy



In a glovebox, to a J. Young tube were added **2** (1.6 mg, 3.6 μmol), toluene- d_8 (200 μL), $^t\text{BuOH}$ (400 μL), and ^{13}C -formic acid (14 μL , 0.36 mmol). Upon addition of the acid, effervescence was observed, and the solution color bleached from light brown to colorless along with the formation of a colorless precipitate over the course of a few minutes. ^{13}C NMR spectroscopy was used to detect the formation of $^{13}\text{CO}_2$ from the dehydrogenation reaction, as shown in Figure D.54. The signal to noise in the ^1H spectrum was poor due to the proteo solvent and precipitate formation, but a small H_2 peak could be seen.

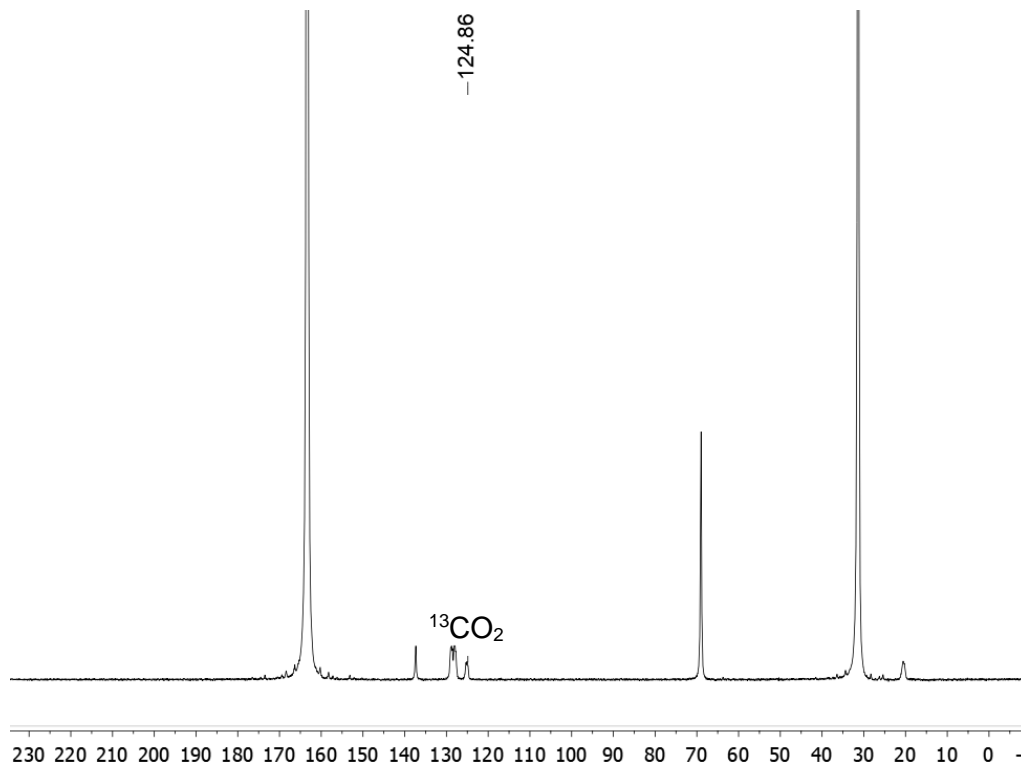


Figure D.54. *In situ* $^{13}\text{C}\{^1\text{H}\}$ NMR spectrum of formic acid dehydrogenation using **2** and ^{13}C -formic acid. $^{13}\text{CO}_2$ is observed at 124.86 ppm, and no ^{13}CO is observed.

XXII. Analysis of Catalysis Decomposition Products

The reaction described in the previous section (D.XXI) was analyzed by $^{31}\text{P}\{^1\text{H}\}$ NMR after 24 hours to investigate the catalytic decomposition product(s). The data is shown in Figure D.55. Only $\text{L}(\text{BH}_3)_2$ and $^{\text{iPr}}\text{PN}^{\text{Ph}}\text{P}$ is observed, indicating that all the ligand has likely demetallated from Fe.

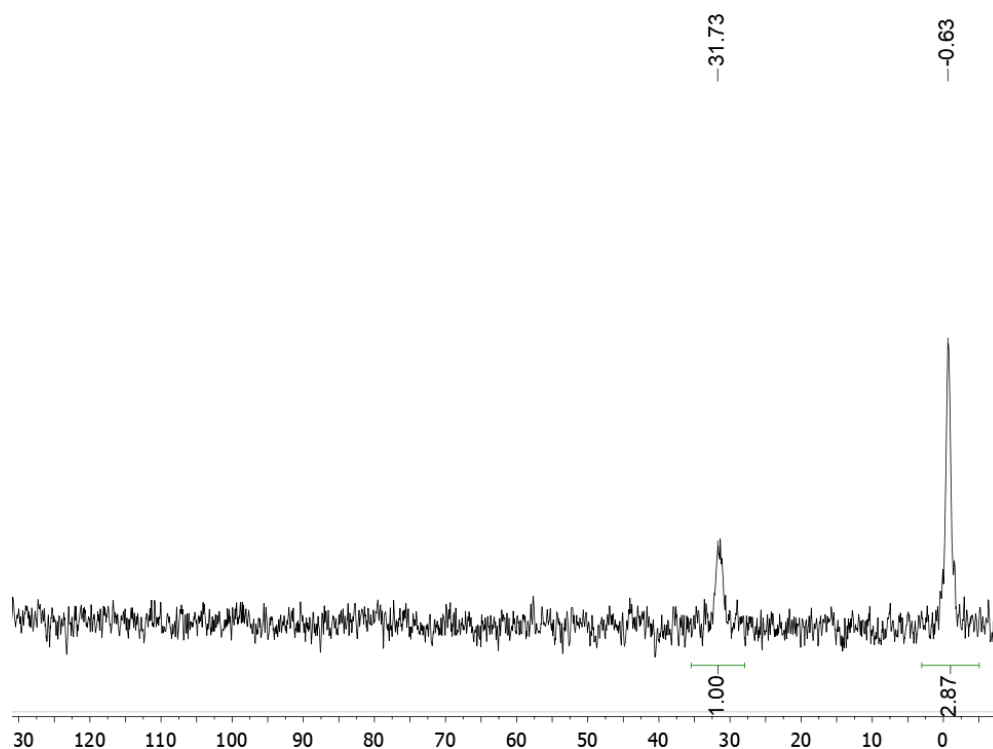


Figure D.55. *In situ* $^{31}\text{P}\{^1\text{H}\}$ NMR spectrum from formic acid dehydrogenation using **2** and ^{13}C -formic acid after 24 hours. $\text{L}(\text{BH}_3)_2$ is observed at 31.73 ppm, and free $^{\text{iPr}}\text{PN}^{\text{Ph}}\text{P}$ is observed at -0.63 ppm.

XXIII. X-ray Crystallographic Information

$(\kappa^2\text{-}^{\text{iPr}}\text{PN}^{\text{Ph}}\text{P})\text{FeCl}_2(\mathbf{1})$ (CCDC: XX)

Low-temperature diffraction data (ω -scans) were collected on a Rigaku SCX Mini diffractometer coupled to a Rigaku Mercury275R CCD with Mo K α radiation ($\lambda = 0.71073$ Å) for the structure of **1**. The diffraction images were processed and scaled using Rigaku

Oxford Diffraction software.⁷ This data was refined as a 2-component twin. The fractional volume contribution of the minor twin component was freely refined to a converged value of 0.30(3). The structure was solved with SHELXT and was refined against F^2 on all data by full-matrix least squares with SHELXL.⁸ All non-hydrogen atoms were refined anisotropically. Hydrogen atoms were included in the model at geometrically calculated positions and refined using a riding model. The isotropic displacement parameters of all hydrogen atoms were fixed to 1.2 times the U value of the atoms to which they are linked (1.5 times for methyl groups). The full numbering scheme of compound **1** can be found in the full details of the X-ray structure determination (CIF), which is included as Supporting Information. CCDC number XXXXXX (**1**) contains the supplementary crystallographic data for this paper. These data can be obtained free of charge from The Cambridge Crystallographic Data Center via www.ccdc.cam.ac.uk/data_request/cif.

Table D.01. Crystal data and structure refinement for **1**.

Empirical formula	C ₂₂ H ₄₁ Cl ₂ Fe N P ₂	
Formula weight	508.25	
Temperature	93(2) K	
Wavelength	0.71073 Å	
Crystal system	Orthorhombic	
Space group	P2 ₁ 2 ₁ 2 ₁	
Unit cell dimensions	a = 8.5123(4) Å	$\alpha = 90^\circ$.
	b = 16.9497(9) Å	$\beta = 90^\circ$.
	c = 18.1195(10) Å	$\gamma = 90^\circ$.
Volume	2614.3(2) Å ³	
Z	4	
Density (calculated)	1.291 Mg/m ³	
Absorption coefficient	0.913 mm ⁻¹	
F(000)	1080	
Crystal size	0.200 x 0.200 x 0.200 mm ³	
Diffractometer	Rigaku Mercury275R CCD	
Theta range for data collection	2.248 to 25.023°.	
Index ranges	-10 ≤ h ≤ 10, -20 ≤ k ≤ 20, -21 ≤ l ≤ 21	
Reflections collected	37476	
Independent reflections	4611 [R(int) = 0.1056]	
Observed reflections (I > 2sigma(I))	3945	

Completeness to theta = 25.023°	99.7 %
Absorption correction	Semi-empirical from equivalents
Max. and min. transmission	1.00000 and 0.91238
Solution method	SHELXT-2018/2 (Sheldrick, 2014)
Refinement method	SHELXL-2014/7 (Sheldrick, 2014)
Data / restraints / parameters	4611 / 0 / 262
Goodness-of-fit on F ²	1.031
Final R indices [I>2sigma(I)]	R1 = 0.0382, wR2 = 0.0753
R indices (all data)	R1 = 0.0540, wR2 = 0.0806
Absolute structure parameter	0.30(3)
Largest diff. peak and hole	0.371 and -0.259 e.Å ⁻³

(ⁱPrPN^{Ph}P)FeH(κ²-BH₄) (**2**) (CCDC: XX)

Low-temperature diffraction data (ω-scans) were collected on a Rigaku SCX Mini diffractometer coupled to a Rigaku Mercury275R CCD with Mo Kα radiation (λ = 0.71073 Å) for the structure of **2**. The diffraction images were processed and scaled using Rigaku Oxford Diffraction software.⁷ The structure was solved with SHELXT and was refined against F² on all data by full-matrix least squares with SHELXL.⁸ This data was refined as a 2-component twin. The fractional volume contribution of the minor twin component was freely refined to a converged value of 0.2668(8). All non-hydrogen atoms were refined anisotropically. Hydrogen atoms were included in the model at geometrically calculated positions and refined using a riding model. The isotropic displacement parameters of all hydrogen atoms were fixed to 1.2 times the U value of the atoms to which they are linked (1.5 times for methyl groups). The borohydrides were found in the difference map and freely refined. The full numbering scheme of compound mini-17056 can be found in the full details of the X-ray structure determination (CIF), which is included as Supporting Information. CCDC number XXXXXX (**2**) contains the supplementary crystallographic

data for this paper. These data can be obtained free of charge from The Cambridge Crystallographic Data Center via www.ccdc.cam.ac.uk/data_request/cif.

Table D.02. Crystal data and structure refinement for **2**.

Empirical formula	C ₂₂ H ₄₅ B Fe N P ₂	
Formula weight	452.19	
Temperature	93(2) K	
Wavelength	0.71073 Å	
Crystal system	Monoclinic	
Space group	P2 ₁ /n	
Unit cell dimensions	a = 9.1005(2) Å	$\alpha = 90^\circ$.
	b = 16.4887(4) Å	$\beta = 90.117(2)^\circ$.
	c = 16.7644(4) Å	$\gamma = 90^\circ$.
Volume	2515.58(10) Å ³	
Z	4	
Density (calculated)	1.194 Mg/m ³	
Absorption coefficient	0.734 mm ⁻¹	
F(000)	980	
Crystal size	0.200 x 0.200 x 0.200 mm ³	
Crystal color and habit	Orange Block	
Diffractometer	Rigaku Mercury275R CCD	
Theta range for data collection	1.732 to 27.521°	
Index ranges	-11 ≤ h ≤ 11, -21 ≤ k ≤ 21, 0 ≤ l ≤ 21	
Reflections collected	5773	
Independent reflections	5773 [R(int) = 0.0337]	
Observed reflections (I > 2σ(I))	5462	
Completeness to theta = 25.242°	99.9 %	
Absorption correction	Semi-empirical from equivalents	
Max. and min. transmission	1.00000 and 0.91576	
Solution method	SHELXT-2018/2 (Sheldrick, 2014)	
Refinement method	SHELXL-2014/7 (Sheldrick, 2014)	
Data / restraints / parameters	5773 / 0 / 269	
Goodness-of-fit on F ²	1.064	
Final R indices [I > 2σ(I)]	R1 = 0.0248, wR2 = 0.0645	
R indices (all data)	R1 = 0.0273, wR2 = 0.0660	
Largest diff. peak and hole	0.612 and -0.295 e.Å ⁻³	

(ⁱPrPN^{Ph}P)Fe(CO)₂ (**3**) (CCDC: XX)

Low-temperature diffraction data (ω -scans) were collected on a Rigaku MicroMax-007HF diffractometer coupled to a Saturn994+ CCD detector with Cu K α ($\lambda = 1.54178$ Å)

for the structure of **3**. The diffraction images were processed and scaled using Rigaku Oxford Diffraction software.⁷ The structure was solved with SHELXT and was refined against F^2 on all data by full-matrix least squares with SHELXL.⁸ All non-hydrogen atoms were refined anisotropically. Hydrogen atoms were included in the model at geometrically calculated positions and refined using a riding model. The isotropic displacement parameters of all hydrogen atoms were fixed to 1.2 times the U value of the atoms to which they are linked (1.5 times for methyl groups). Several low angle reflections were improperly recorded due to instrument artifacts. These reflections were omitted from the refinement. The full numbering scheme of compound **3** can be found in the full details of the X-ray structure determination (CIF), which is included as Supporting Information. CCDC number XXXXXX (**3**) contains the supplementary crystallographic data for this paper. These data can be obtained free of charge from The Cambridge Crystallographic Data Center via www.ccdc.cam.ac.uk/data_request/cif.

Table D.03. Crystal data and structure refinement for **3**.

Empirical formula	C ₂₄ H ₄₁ Fe N O ₂ P ₂	
Formula weight	493.37	
Temperature	93(2) K	
Wavelength	1.54184 Å	
Crystal system	Triclinic	
Space group	P-1	
Unit cell dimensions	a = 11.2048(3) Å	$\alpha = 95.568(2)^\circ$.
	b = 14.3728(4) Å	$\beta = 94.618(2)^\circ$.
	c = 16.4165(4) Å	$\gamma = 101.946(3)^\circ$.
Volume	2560.55(12) Å ³	
Z	4	
Density (calculated)	1.280 Mg/m ³	
Absorption coefficient	6.050 mm ⁻¹	
F(000)	1056	
Crystal size	0.200 x 0.080 x 0.030 mm ³	
Crystal color and habit	orange plate	
Diffractometer	Rigaku Saturn 944+ CCD	
Theta range for data collection	2.719 to 66.601°.	
Index ranges	-13 ≤ h ≤ 13, -17 ≤ k ≤ 17, -19 ≤ l ≤ 19	

Reflections collected	90831
Independent reflections	8923 [R(int) = 0.0479]
Observed reflections ($I > 2\sigma(I)$)	8360
Completeness to $\theta = 66.601^\circ$	98.5 %
Absorption correction	Semi-empirical from equivalents
Max. and min. transmission	1.00000 and 0.85922
Solution method	SHELXT-2014/5 (Sheldrick, 2014)
Refinement method	SHELXL-2014/7 (Sheldrick, 2014)
Data / restraints / parameters	8923 / 0 / 557
Goodness-of-fit on F^2	1.035
Final R indices [$I > 2\sigma(I)$]	R1 = 0.0274, wR2 = 0.0702
R indices (all data)	R1 = 0.0298, wR2 = 0.0717
Largest diff. peak and hole	0.474 and -0.393 e. \AA^{-3}

PhN{CH₂CH₂PⁱPr₂(BH₃)₂}₂ (**L**•(**BH**₃)₂) (CCDC: XX)

Low-temperature diffraction data (ω -scans) were collected on a Rigaku MicroMax-007HF diffractometer coupled to a Saturn994+ CCD detector with Cu K α ($\lambda = 1.54178 \text{ \AA}$) for the structure of **L**•(**BH**₃)₂. The diffraction images were processed and scaled using Rigaku Oxford Diffraction software.⁷ The structure was solved with SHELXT and was refined against F^2 on all data by full-matrix least squares with SHELXL.⁸ All non-hydrogen atoms were refined anisotropically. Hydrogen atoms were included in the model at geometrically calculated positions and refined using a riding model. The isotropic displacement parameters of all hydrogen atoms were fixed to 1.2 times the U value of the atoms to which they are linked (1.5 times for methyl groups). The only exceptions are H1A, H1B, and H1C which were found in the difference map and freely refined. The full numbering scheme of compound **L**•(**BH**₃)₂ can be found in the full details of the X-ray structure determination (CIF), which is included as Supporting Information. CCDC number XXXXXX (**L**•(**BH**₃)₂) contains the supplementary crystallographic data for this

paper. These data can be obtained free of charge from The Cambridge Crystallographic Data Center via www.ccdc.cam.ac.uk/data_request/cif.

Table D.04. Crystal data and structure refinement for **L•(BH₃)₂**.

Empirical formula	C ₂₂ H ₄₇ B ₂ N P ₂	
Formula weight	409.16	
Temperature	93(2) K	
Wavelength	1.54184 Å	
Crystal system	Monoclinic	
Space group	I2/a	
Unit cell dimensions	a = 18.2111(5) Å b = 11.1830(2) Å c = 12.6758(4) Å	$\alpha = 90^\circ$. $\beta = 92.693(3)^\circ$. $\gamma = 90^\circ$.
Volume	2578.64(12) Å ³	
Z	4	
Density (calculated)	1.054 Mg/m ³	
Absorption coefficient	1.555 mm ⁻¹	
F(000)	904	
Crystal size	0.100 x 0.040 x 0.040 mm ³	
Crystal color and habit	Brown Needle	
Diffractometer	Rigaku Saturn 944+ CCD	
Theta range for data collection	4.642 to 66.601°	
Index ranges	-21 ≤ h ≤ 21, -13 ≤ k ≤ 13, -15 ≤ l ≤ 15	
Reflections collected	46239	
Independent reflections	2280 [R(int) = 0.0689]	
Observed reflections (I > 2σ(I))	1946	
Completeness to theta = 66.601°	100.0 %	
Absorption correction	Semi-empirical from equivalents	
Max. and min. transmission	1.00000 and 0.73928	
Solution method	SHELXT-2014/5 (Sheldrick, 2014)	
Refinement method	SHELXL-2014/7 (Sheldrick, 2014)	
Data / restraints / parameters	2280 / 0 / 140	
Goodness-of-fit on F ²	1.065	
Final R indices [I > 2σ(I)]	R1 = 0.0434, wR2 = 0.0981	
R indices (all data)	R1 = 0.0547, wR2 = 0.1040	
Largest diff. peak and hole	0.333 and -0.272 e.Å ⁻³	

(κ²-iPrPN^{Ph}P)CoCl₂ (**4**) (CCDC: XX)

Low-temperature diffraction data (ω-scans) were collected on a Rigaku MicroMax-007HF diffractometer coupled to a Saturn994+ CCD detector with Cu Kα (λ = 1.54178 Å)

for the structure of **4**. The diffraction images were processed and scaled using Rigaku Oxford Diffraction software.⁷ The structure was solved with SHELXT and was refined against F^2 on all data by full-matrix least squares with SHELXL.⁸ All non-hydrogen atoms were refined anisotropically. Hydrogen atoms were included in the model at geometrically calculated positions and refined using a riding model. The isotropic displacement parameters of all hydrogen atoms were fixed to 1.2 times the U value of the atoms to which they are linked (1.5 times for methyl groups). The full numbering scheme of compound **4** can be found in the full details of the X-ray structure determination (CIF), which is included as Supporting Information. CCDC number XXXXXX (**4**) contains the supplementary crystallographic data for this paper. These data can be obtained free of charge from The Cambridge Crystallographic Data Center via www.ccdc.cam.ac.uk/data_request/cif.

Table D.05. Crystal data and structure refinement for **4**.

Identification code	mini-18051	
Empirical formula	C ₄₄ H ₈₂ Cl ₄ Co ₂ N ₂ P ₄	
Formula weight	1022.65	
Temperature	93(2) K	
Wavelength	0.71073 Å	
Crystal system	Orthorhombic	
Space group	P2 ₁ 2 ₁ 2 ₁	
Unit cell dimensions	a = 8.5187(2) Å	$\alpha = 90^\circ$.
	b = 16.9298(4) Å	$\beta = 90^\circ$.
	c = 17.9887(4) Å	$\gamma = 90^\circ$.
Volume	2594.33(10) Å ³	
Z	2	
Density (calculated)	1.309 Mg/m ³	
Absorption coefficient	1.000 mm ⁻¹	
F(000)	1084	
Crystal size	0.5 x 0.5 x 0.2 mm ³	
Crystal color and habit	blue plate	
Theta range for data collection	2.264 to 33.459°.	
Index ranges	-12 ≤ h ≤ 12, -25 ≤ k ≤ 25, -27 ≤ l ≤ 27	
Reflections collected	61592	
Independent reflections	9990 [R(int) = 0.0512]	
Observed reflections (I > 2σ(I))	8498	
Completeness to theta = 25.242°	99.7 %	

Absorption correction	Semi-empirical from equivalents
Max. and min. transmission	1.00000 and 0.88612
Solution method	ShelXT (Sheldrick, 2015)
Refinement method	ShelXL (Sheldrick, 2015)
Data / restraints / parameters	9990 / 0 / 262
Goodness-of-fit on F^2	1.040
Final R indices [$I > 2\sigma(I)$]	$R1 = 0.0389$, $wR2 = 0.0662$
R indices (all data)	$R1 = 0.0543$, $wR2 = 0.0705$
Absolute structure parameter	0.425(11)
Largest diff. peak and hole	0.488 and -0.285 e. \AA^{-3}

$[(^i\text{PrPN}^{\text{Ph}}\text{P})\text{NiCl}][1/2\text{NiCl}_4]$ (CCDC: XX)

Low-temperature diffraction data (ω -scans) were collected on a Rigaku MicroMax-007HF diffractometer coupled to a Saturn994+ CCD detector with Cu $K\alpha$ ($\lambda = 1.54178 \text{ \AA}$) for the structure of $[(^i\text{PrPN}^{\text{Ph}}\text{P})\text{NiCl}][1/2\text{NiCl}_4]$. The diffraction images were processed and scaled using Rigaku Oxford Diffraction software.⁷ The structure was solved with SHELXT and was refined against F^2 on all data by full-matrix least squares with SHELXL.⁸ All non-hydrogen atoms were refined anisotropically. Hydrogen atoms were included in the model at geometrically calculated positions and refined using a riding model. The isotropic displacement parameters of all hydrogen atoms were fixed to 1.2 times the U value of the atoms to which they are linked (1.5 times for methyl groups). One of the toluene solvents is disordered over two equally occupied positions. The models include methyl groups C36 and C43; these models were fixed at half occupancy and were constrained to have ideal geometries. The toluene with methyl C29 is disordered across the crystallographic 2(1) screw axis. It was also constrained to have ideal geometries.⁹ The full numbering scheme of $[(^i\text{PrPN}^{\text{Ph}}\text{P})\text{NiCl}][1/2\text{NiCl}_4]$ can be found in the full details of the X-ray structure determination (CIF), which is included as Supporting Information. CCDC number XXXXXX ($[(^i\text{PrPN}^{\text{Ph}}\text{P})\text{NiCl}][1/2\text{NiCl}_4]$) contains the supplementary crystallographic data

for this paper. These data can be obtained free of charge from The Cambridge Crystallographic Data Center via www.ccdc.cam.ac.uk/data_request/cif.

Table D.06. Crystal data and structure refinement for [(ⁱPrPN^{Ph}P)NiCl][1/2NiCl₄].

Empirical formula	C _{32.50} H ₅₃ Cl ₃ N Ni _{1.50} P ₂	
Formula weight	714.10	
Temperature	93(2) K	
Wavelength	1.54184 Å	
Crystal system	Monoclinic	
Space group	C2/c	
Unit cell dimensions	a = 28.0256(3) Å b = 14.7337(2) Å c = 18.1208(2) Å	α = 90°. β = 105.1600(10)°. γ = 90°.
Volume	7222.06(15) Å ³	
Z	8	
Density (calculated)	1.308 Mg/m ³	
Absorption coefficient	6.645 mm ⁻¹	
F(000)	3008	
Crystal size	0.200 x 0.200 x 0.200 mm ³	
Crystal color and habit	Colorless Block	
Diffractometer	Rigaku Saturn 944+ CCD	
Theta range for data collection	3.268 to 66.593°	
Index ranges	-33 ≤ h ≤ 33, -17 ≤ k ≤ 17, -21 ≤ l ≤ 21	
Reflections collected	129185	
Independent reflections	6386 [R(int) = 0.0696]	
Observed reflections (I > 2σ(I))	5539	
Completeness to theta = 66.593°	100.0 %	
Absorption correction	Semi-empirical from equivalents	
Max. and min. transmission	1.00000 and 0.78500	
Solution method	SHELXT-2014/5 (Sheldrick, 2014)	
Refinement method	SHELXL-2014/7 (Sheldrick, 2014)	
Data / restraints / parameters	6386 / 90 / 437	
Goodness-of-fit on F ²	1.136	
Final R indices [I > 2σ(I)]	R1 = 0.0336, wR2 = 0.0776	
R indices (all data)	R1 = 0.0435, wR2 = 0.0837	
Largest diff. peak and hole	0.267 and -0.341 e.Å ⁻³	

[(ⁱPrPN^{Ph}P)NiCl][PF₆] (**5**) (CCDC: XX)

Low-temperature diffraction data (ω-scans) were collected on a Rigaku MicroMax-007HF diffractometer coupled to a Saturn994+ CCD detector with Cu Kα (λ = 1.54178 Å)

for the structure of **5**. The diffraction images were processed and scaled using Rigaku Oxford Diffraction software.⁷ The structure was solved with SHELXT and was refined against F^2 on all data by full-matrix least squares with SHELXL.⁸ All non-hydrogen atoms were refined anisotropically. Hydrogen atoms were included in the model at geometrically calculated positions and refined using a riding model. The isotropic displacement parameters of all hydrogen atoms were fixed to 1.2 times the U value of the atoms to which they are linked (1.5 times for methyl groups). The full numbering scheme of compound **5** can be found in the full details of the X-ray structure determination (CIF), which is included as Supporting Information. CCDC number XXXXXX (**5**) contains the supplementary crystallographic data for this paper. These data can be obtained free of charge from The Cambridge Crystallographic Data Center via www.ccdc.cam.ac.uk/data_request/cif.

Table D.07. Crystal data and structure refinement for **5**.

Empirical formula	C ₂₂ H ₄₁ Cl F ₆ N Ni P ₃	
Formula weight	620.63	
Temperature	93(2) K	
Wavelength	1.54184 Å	
Crystal system	Orthorhombic	
Space group	Pnma	
Unit cell dimensions	$a = 24.6772(2)$ Å	$\alpha = 90^\circ$.
	$b = 13.12990(10)$ Å	$\beta = 90^\circ$.
	$c = 8.50230(10)$ Å	$\gamma = 90^\circ$.
Volume	$2754.82(4)$ Å ³	
Z	4	
Density (calculated)	1.496 Mg/m ³	
Absorption coefficient	4.037 mm ⁻¹	
F(000)	1296	
Crystal size	0.200 x 0.200 x 0.200 mm ³	
Crystal color and habit	Colorless Block	
Theta range for data collection	3.582 to 66.599°.	
Index ranges	-29 ≤ h ≤ 29, -15 ≤ k ≤ 15, -9 ≤ l ≤ 9	
Reflections collected	96124	
Independent reflections	2527 [R(int) = 0.0278]	
Observed reflections ($I > 2\sigma(I)$)	2514	
Completeness to $\theta = 66.599^\circ$	99.2 %	
Absorption correction	Semi-empirical from equivalents	

Max. and min. transmission	1.00000 and 0.71180
Solution method	SHELXT-2014/5 (Sheldrick, 2014)
Refinement method	SHELXL-2014/7 (Sheldrick, 2014)
Data / restraints / parameters	2527 / 0 / 176
Goodness-of-fit on F^2	1.076
Final R indices [$I > 2\sigma(I)$]	$R1 = 0.0208$, $wR2 = 0.0573$
R indices (all data)	$R1 = 0.0209$, $wR2 = 0.0574$
Largest diff. peak and hole	0.300 and -0.220 e. \AA^{-3}

XXIV. References

1. Harris, R. K.; Becker, E. D.; Cabral de Menezes, S. M.; Granger, P.; Hoffman, R. E.; Zilm, K. W., Further Conventions for NMR Shielding and Chemical Shifts (IUPAC Recommendations 2008). *Pure Appl. Chem.* **2008**, *80*, 59-84.
2. Zhang, Y.; MacIntosh, A. D.; Wong, J. L.; Bielinski, E. A.; Williard, P. G.; Mercado, B. Q.; Hazari, N.; Bernskoetter, W. H., Iron Catalyzed CO₂ Hydrogenation to Formate Enhanced by Lewis Acid Co-Catalysts. *Chem. Sci.* **2015**, *6*, 4291-4299.
3. Koehne, I.; Schmeier, T. J.; Bielinski, E. A.; Pan, C. J.; Lagaditis, P. O.; Bernskoetter, W. H.; Takase, M. K.; Würtele, C.; Hazari, N.; Schneider, S., Synthesis and Structure of Six-Coordinate Iron Borohydride Complexes Supported by PNP Ligands. *Inorg. Chem.* **2014**, *53*, 2133-2143.
4. Mills, M. R.; Barnes, C. L.; Bernskoetter, W. H., Influences of Bifunctional PNP-Pincer Ligands on Low Valent Cobalt Complexes Relevant to CO₂ Hydrogenation. *Inorg. Chem.* **2018**, *57*, 1590-1597.
5. Spentzos, A. Z.; Barnes, C. L.; Bernskoetter, W. H., Effective Pincer Cobalt Precatalysts for Lewis Acid Assisted CO₂ Hydrogenation. *Inorg. Chem.* **2016**, *55*, 8225-8233.

6. Vasudevan, K. V.; Scott, B. L.; Hanson, S. K., Alkene Hydrogenation Catalyzed by Nickel Hydride Complexes of an Aliphatic PNP Pincer Ligand. *Euro. J. Inorg. Chem.* **2012**, *2012*, 4898-4906.
7. *CrysAlis Pro*, Rigaku OD. The Woodlands, TX, **2015**.
8. Sheldrick, G., A Short History of SHELX. *Acta Cryst. A* **2008**, *64*, 112-122.
9. Guzei, I., An idealized molecular geometry library for refinement of poorly behaved molecular fragments with constraints. *Journal of Applied Crystallography* **2014**, *47*, 806-809.